

The Oxidation Capacity of the Summertime Asian Monsoon Anticyclone

-

Airborne measurements of OH and HO₂ radicals in the Upper Troposphere using Laser Induced Fluorescence Spectroscopy

Dissertation

Zur Erlangung des Grades

„Doktor der Naturwissenschaften“
im Promotionsfach Chemie

am Fachbereich Chemie, Pharmazie,
Geographie und Geowissenschaften
der Johannes Gutenberg-Universität
Mainz,

ausgeführt am
Max-Planck-Institut für Chemie,
Mainz

vorgelegt von

Daniel Richard Marno

Mainz, 2021

Tag der mündlichen Prüfung: 4th June 2021

Abstract

The intense summertime heating over Southern Asia forms a strong convective transport system, which is capable of quickly uplifting South Asian polluted air masses into a quasi-stationary anticyclone that is situated within in the upper troposphere and lower stratosphere. This efficient transportation of Asian emissions during the summertime Asian monsoon has the potential to turn a regional-scale pollution problem into a global one.

In July to August 2015, the High Altitude and Long Range aircraft (HALO) performed a series of 24 measurement flights that probed the western reaches of the summertime Asian monsoon anticyclone (AMA) up to altitudes of 15 km, as part of the Oxidation Mechanism Observations over Asia (OMO-Asia) airborne campaign. Measurements and budget calculations of OH and HO₂ (HO_x) are described in depth within this thesis in order to parameterize the self-cleaning capacity of AMA and characterize its impact on the atmospheric lifetimes of South Asian pollutants that it transports. For this study, a *Laser-Induced Fluorescence – Fluorescence Assay by Gas Expansion (LIF-FAGE)* instrument (HORUS) from the Max-Planck Institute for Chemistry, Mainz was developed and installed for use on board HALO. This was the first time that successful HO_x measurements were performed by an airborne LIF-FAGE instrument capable of measuring atmospheric OH and its chemical background interferences (OH-CHEM) in-situ and in-real-time. This was achieved through effective characterization and operation of an *Inlet Pre-Injector (IPI)* system, which enabled the quantification of OH-CHEM and the correction of the OH measurements. Additionally as part of this PhD work, the *All Pressure Altitude based Calibrator for HO_x Experimentation (APACHE)* was developed and utilized to resolve all known pressure dependent and independent terms affecting the HO_x sensitivity of HORUS, and achieved an accuracy of 22.6 % (1σ).

The measured OH and HO₂ concentrations are, on average, 31 % and 68 % higher respectively inside AMA when compared to the observed background upper troposphere. From the OH and HO₂ budget analyses, the oxidative throughput of OH, i.e. the rate at which OH is produced and reacts with pollutants, was calculated to be, on average, ~ 52 % faster within AMA when compared to background upper Troposphere air masses. The average oxidative throughput rate of OH increased from ~ 4.3 (± 0.7) × 10⁵ molec. cm⁻³ s⁻¹ outside to ~ 6.6 (± 0.9) × 10⁵ molec. cm⁻³ s⁻¹ inside AMA, with over 80 % involving HO_x recycling reactions. The main source of OH is the HO₂ + NO channel, which increased from 3.2 (± 0.9) × 10⁵ molec. cm⁻³ s⁻¹ outside AMA to 5.1 (± 1.4) × 10⁵ molec. cm⁻³ s⁻¹ inside AMA. This 59.4 % increase in the production of OH via HO₂ + NO is due the strong convective transport processes that inject anthropogenic and lightning NO_x into AMA, as supported by the observed 16 % higher NO mixing ratio inside AMA when compared to outside. Furthermore, the concentrations of CH₄, CO and RO₂ are also elevated inside AMA, due to the aforementioned convective transport of polluted boundary layer air masses into AMA. This causes the cycling of OH to HO₂ to accelerate by ~ 3.3 (± 0.93) × 10⁵ molec. cm⁻³ s⁻¹ to a rate of ~ 5.5 (± 1.4) × 10⁵ molec. cm⁻³ s⁻¹ inside AMA.

The OH recycling probability (r_{OH}) analysis showed that buffering processes are strengthened within AMA, whereby the local atmospheric oxidative capacity is maintained despite the increased pollutant loading. The injection of NO_x enriched air masses into AMA increases the *NOPR* (Net Ozone Production Rate) by 91.7 %, and elevates O_3 levels by 6 %. This enables the reaction rate of the $\text{HO}_2 + \text{O}_3$ channel to increase, and partially buffer r_{OH} against the photochemical loss of NO that occurs in-between convection events.

Ultimately, AMA promotes cycling within HO_x and buffers the r_{OH} against pollutant loading, which in turn elevates overall HO_x levels. This intensification of HO_x chemistry inside AMA shortens the atmospheric lifetime of the transported South Asian pollutants by a factor of 1.52. This increased self-cleaning capacity of AMA limits the potential accumulation of pollutants before ejecting them out, thus moderates the global-scale impact of the transported South Asian emissions.

Zusammenfassung

Die intensive Sommerhitze über Südasien verursacht ein starkes, konvektives Transportsystem, welches verschmutzte Luftmassen aus dem südasiatischen Raum schnell in einen quasistationären Antizyklon transportiert. Dieser befindet sich innerhalb der oberen Troposphäre und unteren Stratosphäre. Die dort vorherrschenden hohen Windgeschwindigkeiten ermöglichen die globale Verteilung der zunächst regional emittierten Schadstoffe.

Um die Auswirkung zu untersuchen wurde im Juli bis August 2015 die Messkampagne OMO-Asia (Oxidation Mechanism Observation-Asia), mit dem Forschungsflugzeug HALO durchgeführt. In 24 Messflügen wurden die westlichen Ausläufer des Asiatischen Monsun-Antizyklons (AMA) beprobt. Mithilfe von Messungen und Budgetanalysen durch ein numerisches Modell der Radikale OH und HO₂ (HO_x) wurde in dieser Arbeit die Selbstreinigungskapazität des AMA und dessen Einfluss auf die atmosphärische Lebensdauer von Schadstoffen aus dem südasiatischen Raum untersucht. Hierzu wurde das LIF-FAGE (*Laser-Induced Fluorescence – Fluorescence Assay by Gas Expansion*) Instrument (HORUS) des Max-Planck-Instituts für Chemie, für den Einsatz auf HALO angepasst und installiert. Da LIF-FAGE Messungen in belasteter Luft eine Interferenz aufwiesen, wurde hierzu ein IPI-Detektionssystem (*Inlet Pre-Injector*) für HALO entwickelt, das die Quantifizierung des Interferenzanteils erlaubt. So konnte während OMO das erste Mal bei Flugzeugmessungen die OH Konzentrationen in belasteter Luft interferenzbereinigt bestimmt werden. Um die druckabhängige Empfindlichkeit von HORUS zu bestimmen, wurde das Kalibrationssystem APACHE (*All Pressure Altitude-based Calibrator for HO_x Experimentation*) entwickelt. APACHE erlaubt die Empfindlichkeit von HORUS mit einer Genauigkeit von 22,6 % (1σ) zu bestimmen.

Messungen von HORUS haben gezeigt, dass die OH- und HO₂-Konzentrationen innerhalb des AMA im Durchschnitt 31 % bzw. 68 % höher sind, als außerhalb des AMA. Die OH- und HO₂-Budgetanalysen ergaben zudem, dass die Rate, mit der OH produziert und mit Schadstoffen reagiert, innerhalb des AMA mit $\sim 6,6 (\pm 0,9) \times 10^5 \text{ molec. cm}^{-3} \text{ s}^{-1}$ im Durchschnitt 52 % höher liegt als außerhalb mit $\sim 4,3 (\pm 0,7) \times 10^5 \text{ molec. cm}^{-3} \text{ s}^{-1}$. Dies konnte zu 80% auf HO_x-Rezyklierungsreaktionen zurückgeführt werden. Die größte Quelle von OH ist die Reaktion HO₂ + NO, welche von $(3.2 (\pm 0.9) \times 10^5 \text{ molec. cm}^{-3} \text{ s}^{-1})$ außerhalb zu $(5.1 (\pm 1.4) \times 10^5 \text{ molec. cm}^{-3} \text{ s}^{-1})$ innerhalb von AMA ansteigt. Diese Zunahme von 59.4 % ist bedingt durch die starken konvektiven Prozesse, die NO_x, aus anthropogenen Quellen wie auch produziert durch Blitze, in den Antizyklon einbringt und die entlang der Messstrecke zu einer im Mittel 16.6 % größere NO Konzentration innerhalb des Antizyklons führt. Ebenso sind die Konzentrationen von CH₄, CO und RO₂ aufgrund des konvektiven Transports von verschmutzten Luftmassen aus der planetaren Grenzschicht in den AMA erhöht. Dies führt zu einer Beschleunigung des OH zu HO₂ Zyklus um ca. 60 % von $\sim 3.3 (\pm 0.93) \times 10^5 \text{ molec. cm}^{-3} \text{ s}^{-1}$ auf $\sim 5.5 (\pm 1.4) \times 10^5 \text{ molec. cm}^{-3} \text{ s}^{-1}$. Eine Analyse der OH-Rezyklierungswahrscheinlichkeit (r_{OH}) ergab, dass Prozesse, die die OH Konzentration puffern innerhalb des AMA verstärkt werden, wodurch die atmosphärische Oxidationskapazität des AMA, trotz der erhöhten Schadstoffbelastung, stabilisiert wird. Weiterhin erhöht die Injektion von NO_x in den

AMA die Netto Ozon Produktionsrate (NOPR) um 91,7 % und führt zu einer mittleren Zunahme entlang der Messstrecke des O₃-Mischverhältnis um 6 %. Dadurch steigt die OH Rezyklierung durch die OH Bildungsreaktion HO₂ + O₃ und puffert somit r_{OH} gegen die, photochemische Abnahme von NO zwischen Konvektionsevents, die wieder NO aus Blitzen und anthropogenen Quellen einbringen.

Letztendlich fördert der AMA das Zyklieren von HO_x, puffert die r_{OH} gegen Schadstoffbelastung und erhöht insgesamt die OH und HO₂ Konzentrationen. Diese Intensivierung der HO_x-Chemie in AMA verkürzt die atmosphärische Lebensdauer der Schadstoffe aus Südasien um den Faktor 1,52. Die gesteigerte Selbstreinigungskraft im AMA begrenzt die potenzielle Anreicherung von Schadstoffen vor dem Ausstoß und mindert somit die globalen Auswirkungen von Schadstoffemissionen.

Contents

1. The Atmosphere.....	- 1 -
1.1. Composition and structure of the atmosphere	- 1 -
1.2. Oxidation of trace gases	- 3 -
1.3. Atmospheric Oxidative Capacity and the hydroxyl radical.....	- 3 -
1.4. Pollution loading impacts on atmospheric oxidative capacity	- 4 -
2. HO _x Chemistry in the troposphere	- 5 -
2.1. HO _x sources	- 6 -
2.2. HO _x recycling / cycling within HO _x	- 7 -
2.3. HO _x sinks	- 9 -
3. HORUS instrument and HO _x measurements.....	- 10 -
3.1. Techniques, challenges and developments for measuring HO _x	- 10 -
3.1.1. Measurement techniques for atmospheric OH detection	- 10 -
3.1.2. Measurement techniques for atmospheric HO ₂ detection	- 14 -
3.2. The HORUS instrument	- 16 -
4. Calibration	- 27 -
4.1. Parameters affecting instrument sensitivity.....	- 27 -
4.2. Methods for Calibrating HO _x instrumentation.....	- 30 -
4.3. APACHE design and characterization	- 32 -
4.3.1. Pressure control.....	- 32 -
4.3.2. Flow conditions.....	- 34 -
4.3.3. Influence of HO _x wall losses in APACHE	- 39 -
4.4. Characterization of UV conditions in APACHE.....	- 43 -
4.5. Airborne HORUS sensitivity calibrations	- 49 -
5. Interference Characterization.....	- 56 -
5.1. IPI In-flight performance and OH-CHEM	- 56 -
5.2. HORUS HO ₂ measurement, conversion efficiency, HONO and RO ₂ interference.....	- 60 -
6. OMO-Asia 2015	- 69 -
6.1. Measurement Campaign.....	- 70 -
6.2. HO _x measurements during OMO Asia 2015.....	- 72 -
6.3. AMA, HO _x , and oxidation	- 75 -
6.3.1. CAABA-MECCA model	- 75 -
6.3.2. Observations	- 75 -
6.3.3. OH and HO ₂ budget calculated using observations	- 77 -
6.3.4. OH and HO ₂ budget implications	- 89 -
6.4. OH recycling probability and oxidative capacity	- 93 -

7. Summary and Conclusions	- 99 -
8. Published Works	- 101 -
A. Datasheets and Primary Standard Calibrations.....	- 122 -
B. Residual Undescribed values of HORUS calibrations with APACHE.....	- 132 -
C. Trace gas species and meteorological measurements during OMO-ASIA 2015.....	- 133 -
D. Chemical Mechanism (MOM) of CAABA-MECCA box model version 4.0	- 144 -
E. Support figures for the CO _{calc} discussion.....	- 196 -
F. Abbreviations.....	- 200 -
Bibliography	- 202 -
Danksagung	- 213 -
Curriculum Vitae	- 214 -

List of Tables

2.1.: HO _x sources.....	- 7 -
2.2.: Cycling OH into HO ₂	- 7 -
2.3.: Cycling HO ₂ into OH.....	- 7 -
2.4.: HO _x sinks via radical-radical reactions	- 9 -
2.5.: HO _x sinks via acid formation	- 9 -
3.1.: IPI parameters from airborne setup and ground setup	- 19 -
4.1.: The temperature dependency parameterizations of the collisional rate coefficients	- 28 -
4.2.: Various calibration techniques for HO _x instrumentation	- 31 -
4.3.: Evolution of OH in the streamlines created by HORUS sampling inside APACHE	- 42 -
4.4.: Parameters and their uncertainties used in actinometrical method A	- 47 -
4.5.: Parameters and their uncertainties involved in actinometrical method B.....	- 48 -
4.6.: Parameters for OH and HO ₂ production by UV lamp in APACHE	- 49 -
4.7.: Pressure independent sensitivity coefficients of HORUS for OH and HO ₂	- 50 -
4.8.: Pressure dependent HO _x transmission values.....	- 53 -
4.9.: Pressure dependent sensitivities for HORUS, from calibrations with APACHE	- 53 -
6.1.: Instrumentation installed on the HALO aircraft during OMO-Asia 2015.....	- 71 -
6.2.: Comparison of measured HO _x from AirLIF and HORUS during OMO-Asia 2015	- 74 -

List of Figures

Figure 1.1.: Composition of the atmosphere, taken from Seinfeld and Pandis (1998).....	- 1 -
Figure 1.2.: The structure of the atmosphere, taken from Brasseur et al. (1999).....	- 2 -
Figure 1.3.: Lifespan and transport scale of trace gases, from Seinfeld and Pandis (1998)	- 4 -
Figure 2.1.: A simplified chemistry scheme of HO _x	- 5 -
Figure 3.1.: A schematic showing the combined LIF-FAGE sensitivity curve. (A modified version of the schematic in Faloon et al. (2004), taken from Marno et al. (2020)).	- 13 -
Figure 3.2.: A schematic showing the time between laser pulses when photon detection occurs in a LIF-FAGE technique.....	- 14 -
Figure 3.3.: Overview of the airborne HORUS system as installed in the HALO aircraft. (A modified figure, taken from Marno et al. (2020))......	- 18 -
Figure 3.4.: A close up of the inlet shroud.....	- 18 -
Figure 3.5.: A schematic of the dye laser system, taken from Hens (2013).	- 20 -
Figure 3.6.: An image taken from White (1942), showing the optical path of a White Cell	- 21 -
Figure 3.7.: A schematic of the different branches in the rotational structure of OH and the A ² Σ ⁺ - X ² Π, v' = 1 ← v' = 0 transitions used during laser excitation. Modified version from Kubistin (2009).	- 22 -
Figure 3.8.: Figure taken from Chan et al. (1990) showing the absorption spectrum of OH radicals at wavelength ~ 308 nm at pressures of ~ 5 mbar.	- 23 -
Figure 3.9.: Example of on-resonance OH signal and off-resonance background signal, and the alternating laser tuning	- 24 -
Figure 3.10.:An example of in-flight measurement of OH during OMO-Asia 2015.....	- 24 -
Figure 3.11.:Improved efficiency of a two tier pre-compaction vacuum system setup. Modified figure from Hens et al. (2014).....	- 25 -
Figure 4.1.: A schematic of the APACHE system. (Figure taken from Marno et al. (2020)).....	- 33 -
Figure 4.2.: A schematic showing the full experimental setup within the lab for calibrations. Figure was taken from Marno et al. (2020))......	- 35 -
Figure 4.3.: The percentage of the total volume flow that enters APACHE that is sampled by HORUS. Figure taken from Marno et al. (2020)).....	- 36 -
Figure 4.4.: The measured and COMSOL simulated flow speed profiles within APACHE, at 920 mbar. (Modified version taken from Marno et al. (2020)).	- 36 -
Figure 4.5.: COMSOL Multiphysics output data, simulating the flow speed conditions at six discrete pressures within APACHE ranging from 275 to 894 mbar. Figure taken from Marno et al. (2020))	- 38 -
Figure 4.6.: COMSOL Multiphysics output data, simulating OH conditions at six discrete pressures within APACHE ranging from 275 to 894 mbar. The figure was taken from Marno et al. (2020))	- 41 -
Figure 4.7.: The product of Equation 4.12 plotted as a function of oxygen concentration, as part of the actinometrical method (A). (Figure taken from Marno et al. (2020))	- 46 -
Figure 4.8.: The calibrated HORUS sensitivity parameters for OH and HO ₂ . Figure taken from Marno et al. (2020).....	- 51 -

Figure 4.9.: Quantified in-flight sensitivity curves, limit of detection, and HO _x transmission for OH and HO ₂ plotted as a function of altitude. Figure taken from Marno et al. (2020).....	55 -
Figure 5.1.: Series of propane titrations	57 -
Figure 5.2.: The propane chemical residence, η_{scav} , OH data corrected for instrument sensitivity, and atmospheric OH concentrations plotted as a function of altitude.....	58 -
Figure 5.3.: Vertical profiles of the OH _{atm} / OH* ratio from the OMO-Asia 2015 campaign.....	59 -
Figure 5.4.: Series of NO titrations at 4 different altitudes	61 -
Figure 5.5.: The calculated $SI_{[HONO]}$ interference	63 -
Figure 5.6.: The NO chemical residence time, η_{conv} , HO ₂ ' , and HO ₂ * as a function of altitude ...	64 -
Figure 5.7.: RO ₂ interference contribution to the HO ₂ * signal (α_{RO_2}) using output data from the CAABA-MECCA box model.....	66 -
Figure 5.8.: Correlation plot between the two NO injection HO ₂ ' signals, HO ₂ * signals , and atmospheric HO ₂ signals	68 -
Figure 6.1.: Diagram showing the flight tracks for all the flights performed during OMO-Asia 2015 campaign relative to AMA	70 -
Figure 6.2.: Correlation plot for all available atmospheric OH and HO ₂ data between AirLIF and HORUS instruments.....	73 -
Figure 6.3.: Measurement data from flight 21	76 -
Figure 6.4.: Measured CH ₄ vs measured CO mixing ratios for OMO-Asia 2015	77 -
Figure 6.5.: Measured CH ₄ vs measured CO mixing ratios at O ₃ levels above 40ppbv from flights 19, 21 and 23, colored by altitude (km).....	78 -
Figure 6.6.: Measured CO and CO _{calc} mixing ratios for flights 20, 21, 22, and 23.....	79 -
Figure 6.7.: As a function of altitude, the OH primary and secondary production rates outside and inside AMA.....	82 -
Figure 6.8.: As a function of altitude, the OH loss rates outside and inside AMA.....	83 -
Figure 6.9.: As a function of altitude, the kOHcharacterized and kOHuncharacterized outside and inside AMA	85 -
Figure 6.10.:As a function of altitude, the OH loss rates outside and inside AMA.....	85 -
Figure 6.11.:As a function of altitude, the HO ₂ production rates outside and inside AMA	87 -
Figure 6.12.:As a function of altitude, the HO ₂ loss rates outside and inside AMA	88 -
Figure 6.13.:Net ozone production rate (NOPR) outside and inside AMA	90 -
Figure 6.14.:OH and HO ₂ budgets in two contrasting air masses inside AMA calculated directly from available measurements.....	91 -
Figure 6.15.:OH recycling probability (r_{OH}) as a function of the NO mixing ratio from numerous measurement campaigns in various environments. Figure and caption information taken and from Hens (2013) and modified.	94 -
Figure 6.16.:OH recycling probability (r_{OH}) as a function of ambient NO mixing ratio above 11 km altitude inside and outside AMA	96 -
Figure 6.17.:The reaction rate of $k_{G2107}[HO_2][O_3]$ as a function of ambient NO mixing ratio above 11 km altitude inside and outside AMA.....	97 -
Figure 6.18.:The calculated OMO-Asia 2015 r_{OH} values (on a log scale x-axis) superimposed on Figure 6.15 (a desaturated modified figure from Hens (2013)).....	98 -

Appendix Figures

Figure A.1.: The specifications of the UV ring lamp used in APACHE, developed by uv-technik Speziallampen GmbH, Gewerbegebiet Ost 6, 98704, Wolfsberg, Germany	- 122 -
Figure A.2.: National Physical Laboratory – NO standard used for actinic flux density calibration of mercury lamp used for calibration of HORUS instrument in Experiment A	- 123 -
Figure A.3.: Specifications of coated silica fiber used for transmittance of 308 nm light through the HORUS instrument. (Information taken from specification listings, Thorlabs GmbH, Europe, Germany, www.thorlabs.de)	- 124 -
Figure A.4.: Laser Dye, Pyrromethane-597 used in tunable dye laser powered by a diode-pumped Nd:YAG laser emitting 532 nm light. Dye sourced from Radiant Dyes Laser & Accessoires GmbH, Friedrichstr. 58, 42929, Wermelskirchen, Germany. (Information taken from www.radiant-dyes.com)	- 125 -
Figure A.5.: Certificate of the Fluke Ozone generator uncertainty compared to the Deutsche Akkreditierungsstelle primary standard at Hessisches Landsamt für Naturschutz, Umwelt und Geologie, Rheingaustraße 186, 65203, Wiesbaden.....	- 126 -
Figure A.6.: The calibration of the ANYSCO Ozone monitor against the MLU ozone generator which was calibrated to primary standard.....	- 127 -
Figure A.7.: Datasheet for the NTC-EC95302V thermistor used for temperature monitoring in APACHE.....	- 128 -
Figure A.8.: Datasheet for the Edwards ASG2-1000 pressure sensor used for pressure monitoring in APACHE.....	- 129 -
Figure A.9.: Datasheet for the Bronkhorst F-106AI-PAD-03-V mass flow controller to regulate the high flows through APACHE.....	- 130 -
Figure A.10.: Datasheet for the Bronze alloy AMPOR sinter filter from atmag. Company address found on the data sheet	- 131 -
Figure B.1.: $R_{\text{undescribed}}$ fraction plotted against HORUS internal pressure. Taken from calibration of the HORUS instrument setup (OMO-ASIA 2015 campaign) with APACHE.....	- 132 -
Figure B.2.: $R_{\text{undescribed}}$ fraction plotted against HORUS internal pressure. Taken from calibration of the HORUS instrument setup (CAFÉ-AFRICA 2018 campaign) with APACHE.....	- 132 -
Figure C.1.: Measurement Data flight 15.....	- 134 -
Figure C.2.: Measurement Data flight 16.....	- 135 -
Figure C.3.: Measurement Data flight 17.....	- 136 -
Figure C.4.: Measurement Data flight 18.....	- 137 -
Figure C.5.: Measurement Data flight 19.....	- 138 -
Figure C.6.: Measurement Data flight 20.....	- 139 -
Figure C.7.: Measurement Data flight 21.....	- 140 -
Figure C.8.: Measurement Data flight 22.....	- 141 -
Figure C.9.: Measurement Data flight 23.....	- 142 -
Figure C.10.: Measurement Data flight 24.....	- 143 -
Figure E.1.: Flight 20 (15.08.2015), acetone measurements and altitude (top left panel), flight track colored by time as fractional Julian day, UTC (top right panel), and 12 day backward trajectory analysis taken from the supplementary material of Tomsche et al. (2019) (bottom panel)	- 196 -

Figure E.2.: Flight 21 (18.08.2015), acetone measurements and altitude (top left panel), flight track colored by time as fractional Julian day, UTC (top right panel), and 12 day backward trajectory analysis taken from the supplementary material of Tomsche et al. (2019) (bottom panel) - 197 -

Figure E.3.: Flight 22 (23.08.2015), acetone measurements and altitude (top left panel), flight track colored by time as fractional Julian day, UTC (top right panel), and 12 day backward trajectory analysis taken from the supplementary material of Tomsche et al. (2019) (bottom panel) - 198 -

Figure E.4.: Flight 23 (25.08.2015), acetone measurements and altitude (top left panel), flight track colored by time as fractional Julian day, UTC (top right panel), and 12 day backward trajectory analysis taken from the supplementary material of Tomsche et al. (2019) (bottom panel) - 199 -

1. The Atmosphere

1.1. Composition and structure of the atmosphere

The thin fluid layer that encapsulates the Earth, the atmosphere, is the one of the dominant driving forces of nature. It effects countless facets of biological, geological, chemical, and physical processes that occur on this planet. The Earth's atmosphere, consists mainly of N₂ (~ 78 %), oxygen (~ 21 %), and varying levels of H₂O (~ 0-2 %). Additionally, there are aerosols, and trace gases such as volatile organic compounds (VOCs), ozone (O₃), and nitrogen oxides (NO_x) all of which contribute significantly to the chemical and physical characteristics of the atmosphere. The measurement and quantification of such species are critical in understanding their impacts on air quality and climate, particularly as they are being unremittingly emitted into the atmosphere via anthropogenic, biogenic, and geological processes (van Aardenne et al., 2001; Bobrowski et al., 2006; Miller et al., 2012; Artaxo et al., 2013). Figure 1.1 shows an overview of the makeup of the atmosphere including certain trace gases and their involvement in anthropogenic, biogenic, and chemical processes.

Gas	Molecular Weight	Average Mixing Ratio (ppm)	Cycle
Ar	39.948	9340	} No cycle
Ne	20.179	18	
Kr	83.80	1.1	
Xe	131.30	0.09	
N ₂	28.013	780,840	} Biological and } microbiological
O ₂	32	209,460	
CH ₄	16.043	1.72	Biogenic and chemical
CO ₂	44.010	355	Anthropogenic and biogenic
CO	28.010	0.12 (NH) 0.06 (SH)	Anthropogenic and chemical
H ₂	2.016	0.58	Biogenic and chemical
N ₂ O	44.012	0.311	Biogenic and chemical
SO ₂	64.06	10 ⁻⁵ -10 ⁻⁴	Anthropogenic, biogenic, chemical
NH ₃	17	10 ⁻⁴ -10 ⁻³	Biogenic and chemical
NO	30.006	} 10 ⁻⁶ -10 ⁻²	Anthropogenic, biogenic, chemical
NO ₂	46.006		
O ₃	48	10 ⁻² -10 ⁻¹	Chemical
H ₂ O	18.015	Variable	} Physicochemical
He	4.003	5.2	

Figure 1.1.: An overview of the composition of the atmosphere, taken from Seinfeld and Pandis (1998).

The division of the atmosphere into several different layers are characterized by shifts in mass exchange and in the temperature gradient (see Figure 1.2). The lowest layer of the atmosphere, in which the weather takes place and is the air that we breathe, is called the troposphere. The troposphere is characteristic in its adiabatic temperature curve, attributable to the heating of the Earth's surface by the Sun. In the tropics where solar Earth surface heating is most intense, the troposphere can reach altitudes of 15 to 18 km, whereas at the poles altitudes rarely exceed 8 to 9 km. The troposphere is sub divided into two regions: the planetary

boundary layer (PBL) and the free troposphere (FT). The PBL is characterized by the direct heating of air and frictional forces as air moves over the Earth's surface. Depending on location, time of day or year, the PBL can extend from a few meters up to a thickness of 4 km. As the PBL is perpetually extending and collapsing to its full extent, daily, it induces high turbulent air flows which are capable of thoroughly mixing trace gases across its entire thickness within as little as an hour. The upper limit of the PBL is categorized as a region of relatively high atmospheric stability, which acts a barrier that limits the vertical air mass exchange between the PBL and the FT. However, due to the overall decreasing temperature profile of the troposphere, combined with strong and uneven convective currents, winds, air deflection at the Earth's surface etc. the troposphere is known for its turbulent behavior. (The word troposphere is derived from the greek word Tropos meaning "turn", "change").

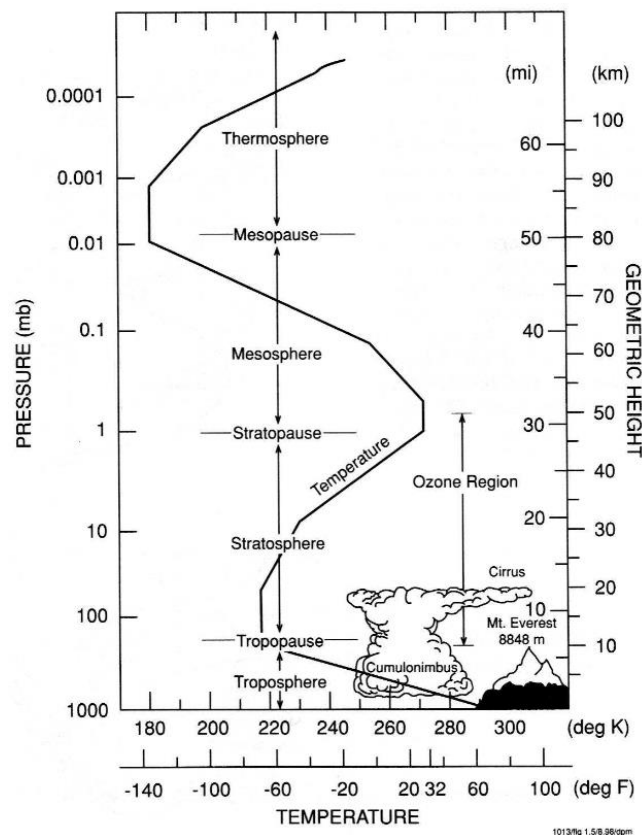


Figure 1.2.: The structure of the atmosphere and the different layers therein, taken from Brasseur et al. (1999).

The stratosphere, which sits above the tropopause, can reach altitudes of 55 km and is home to the ozone layer, where ~ 90 % of all ozone in the Earth's atmosphere is located. Due to the high presence of ozone, the strong absorption of short-wave radiation ($\lambda < 290$ nm) heats the stratosphere resulting in increasing temperatures as altitude increases. Therefore, horizontal mixing of trace gasses occurs much more rapidly within the stratosphere than vertical exchanges. Sitting above the stratosphere is the mesosphere. In this layer the radiative heating is not sufficient to overcome the rate of cooling as altitude increases, thus the mesosphere is characterized by a decreasing temperature curve. In the thermosphere, the temperature gradient switches again to an increasing curve with altitude.

1.2. Oxidation of trace gases

Many trace gasses are pollutants, which can have implications for ecological and human health. Therefore, the intensity of pollution in our atmosphere and the atmosphere's ability to oxidize and/or otherwise remove these pollutants is of paramount importance for the world's general environmental health, society and therefore economy. Within the last half century, the acknowledgment of this phenomenon within science, and largely within global politics, have led to intensified studies and has accelerated our understanding of pollution and atmospheric processes and impacts (Motley et al., 1959; Lelieveld et al., 2020). Usually the first step in the removal of pollutants is oxidation into chemical species that can be more efficiently removed from the atmosphere via wet/dry deposition. However, some species exist that are not readily oxidized in the troposphere, e.g. chlorofluorocarbons (CFCs) and nitrous oxide (N_2O), which often reach the stratosphere via transport processes such as convection, where they are then depleted under the more intense UV conditions.

1.3. Atmospheric Oxidative Capacity and the hydroxyl radical

Despite its relatively low atmospheric concentrations, the major tropospheric oxidizing species during daylight hours is the hydroxyl radical (OH). OH is ubiquitous in our atmosphere and strongly reacts with trace gases to form secondary gas species such as O_3 , highly oxidized VOCs (HVOCs), and non-gaseous species such as aerosol particles. O_3 and peroxides (H_2O_2 and ROOH) also play a part in the oxidative capacity of the atmosphere, particularly with regards to oxidation within cloud droplets (Paulson et al., 2019). There are also chemicals that play a role in nighttime oxidation e.g. the nitrate radical (NO_3), which is formed by reactions of ozone with nitrogen oxides that are sourced from industry and fossil fuel burning (Brown et al., 2011). Nevertheless, due to its exceedingly high reactivity and the ubiquitous availability of its major sources e.g. water vapor, UV radiation, and O_3 ; the OH radical remains the dominant oxidizing chemical that dictates the self-cleansing capacity of the atmosphere and therefore lifetime and abundance of trace gases. Figure 1.3 shows a short overview of the typical lifetimes and spatial scales of trace gas species under atmospheric conditions. From Figure 1.3, one would be forgiven for thinking that OH would play a smaller impact on atmospheric chemistry given its short temporal and small spatial scale. However, due to its high reactivity towards many chemical species, the moment an OH molecule is produced it rapidly reacts with a chemical and is replenished several chemical steps later or is removed from the system entirely. As a result, OH is not transported and is rapidly produced and lost in-situ, therefore intrinsically describing the prevailing oxidative conditions and oxidative capacity of a localized region of the atmosphere. Nevertheless, the combined measurement of OH and of longer-lived chemical species involved in its production and loss can provide a much broader picture of the chemistry occurring within our atmosphere.

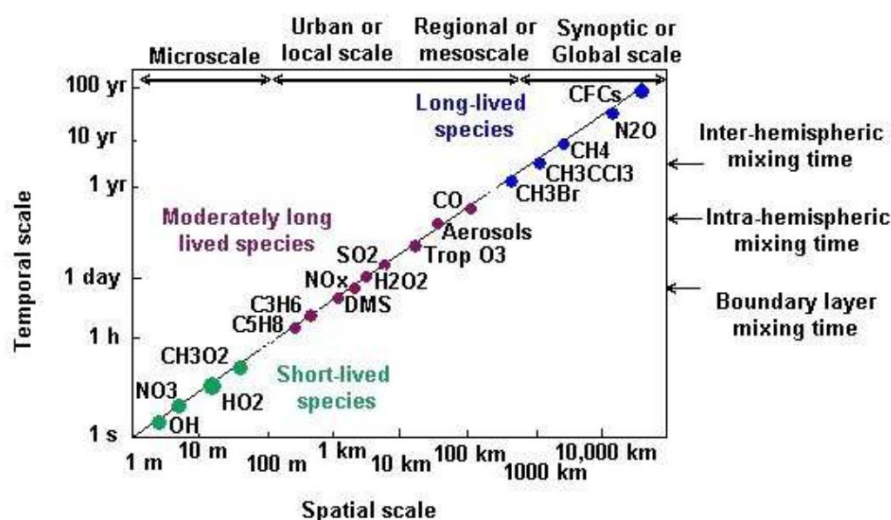


Figure 1.3.: Lifespan and transport scale of trace gas species, taken from Seinfeld and Pandis (1998).

1.4. Pollution loading impacts on atmospheric oxidative capacity

At present, more and more countries are developing and are increasing in their energy consumption. This growth is supported by increasing energy production, which is usually based on fossil fuel burning. Additionally, large-scale land use changes such as urbanization and deforestation also contribute to the increasing anthropogenic pollutant emissions and reduces forestland areas that sequester atmospheric carbon dioxide (CO_2). Through climate warming, the biosphere is also changing and perpetuating this climatic status quo. As a single example of many, warmer temperatures are causing arctic peat soils to thaw and dry out (Voigt et al., 2017). This exposes the previously permafrost locked carbon and nitrogen stocks to the atmosphere (Selvam et al., 2017; Voigt et al., 2017). Additionally, the rate of permafrost thawing is accelerating, which facilitates smoldering combustion within the peat soils, thus causing biogenic emission rates of trace gases such as methane (CH_4), carbon monoxide (CO) and N_2O and brown carbon aerosols to increase (Chakrabarty et al., 2016). Despite this shift in atmospheric chemical makeup and the increases in pollutant loading, the global OH radical concentration has remained stable (Lelieveld et al., 2016). This suggests that there is an atmospheric buffering system present that is capable of oxidizing these trace gases without causing significant losses of OH. For example, the hydroperoxyl radical (HO_2) can produce OH via catalytic cyclic reactions with nitrogen monoxide (NO). The atmospheric background concentrations of HO_2 are approximately two orders of magnitude higher than OH. In addition, HO_2 has a much longer atmospheric lifetime that can extend up to several minutes. The strong chemical coupling between OH and HO_2 , combined with their short lifespan results in the establishment of an equilibrium-state within seconds. The coupling between these two radicals is so dominant; they effectively act as buffers for one another. Such buffering mechanisms are vital in inhibiting huge changes in HO_x (OH and HO_2) and therefore atmospheric oxidation capacity, thus preventing concentrations of toxic and greenhouse gases to accumulate to dangerous levels.

2. HO_x Chemistry in the troposphere

Within the atmosphere, there are many oxidants that are capable of reacting with pollutants. However, oxidation is a two-sided story. On one hand, oxidants can convert emitted toxic pollutants into less toxic chemicals, e.g. CO to CO₂, or oxidize chemical species into forms that are more easily removed from the atmosphere e.g. NO_x to nitric acid (HNO₃) and SO₂ to sulfuric acid (H₂SO₄) both products of which are soluble and more readily removed via wet deposition. Whereas on the other hand, if these acids are at high enough concentrations they can cause acid rain. Additionally, some products formed by oxidation can be more toxic than the originally emitted pollutants themselves. During daytime, the most predominant initiator for most atmospheric oxidation processes is the OH radical (Levy, 1971), making it the principal cleansing agent in our atmosphere (Lelieveld et al., 2004). Figure 2.1 shows the principle chemistry of OH and HO₂.

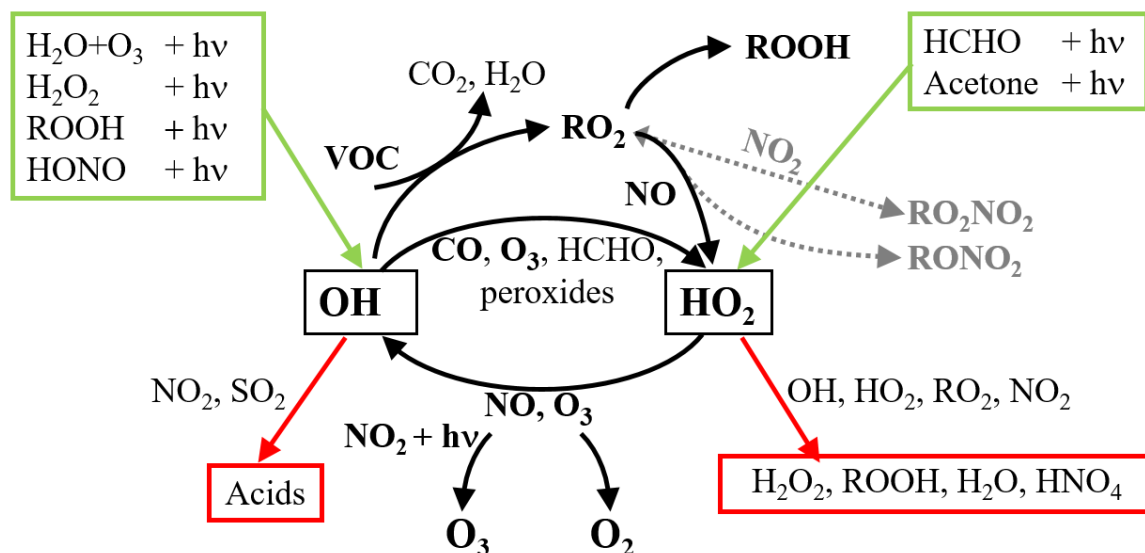
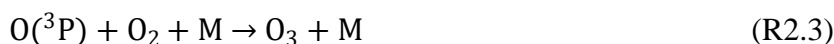
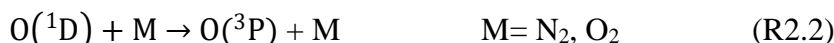


Figure 2.1.: Diagram showing a simplified chemistry scheme of HO_x. The green represents the initial radical production, black the cycling reactions, and red the loss channels for HO_x.

2.1. HO_x sources

The main primary source for OH ($P_{(\text{OH})}^{1^\circ}$) is described as the formation of OH when a water vapor molecule reacts with an excited oxygen atom, O(¹D). O(¹D) atoms are formed when ozone dissociates into molecular oxygen and O(¹D) when absorbing photons of wavelengths (λ) < 320 nm. However, the reaction of O(¹D) atoms with H₂O is a minor reaction channel, as O(¹D) atoms predominately lose their excitation by collision with O₂ and N₂ returning it to ground state, O(³P). The formed O(³P) atoms predominately react with molecular oxygen and recycles back ozone.



Only about 14 % of O(¹D) atoms react with water forming OH at 298 K with 1 % water vapour content (Atkinson et al., 2006). This primary production of OH can be described as:

$$\frac{d[\text{OH}]}{dt} = 2 \cdot \varphi_{\text{OH}} j_{\text{O}(\text{}^1\text{D})} [\text{O}_3] \quad (2.1)$$

where $j_{\text{O}(\text{}^1\text{D})}$ is the photolysis frequency and φ_{OH} is the branching ratio whereby the collision of O(¹D) atoms yield OH:

$$\varphi_{\text{OH}} = \frac{k_{\text{O}(\text{}^1\text{D})+\text{H}_2\text{O}} [\text{H}_2\text{O}]}{k_{\text{O}(\text{}^1\text{D})+\text{O}_2} [\text{O}_2] + k_{\text{O}(\text{}^1\text{D})+\text{N}_2} [\text{N}_2] + k_{\text{O}(\text{}^1\text{D})+\text{H}_2\text{O}} [\text{H}_2\text{O}]} \quad (2.2)$$

In the lower troposphere (LT, is below 4 km), where water vapor mixing ratios are in the order of 10⁻³ mol mol⁻¹, this is the dominant production channel for OH. However, in highly polluted air (rich with NO_x) and in the upper troposphere (> 8 km altitude) where water vapor mixing ratios are in the order of 10⁻⁵ mol mol⁻¹, this OH primary production channel is likely not the dominant source for OH. Other sources of OH and HO₂, such as photolysis of peroxides and aldehydes (e.g. formaldehyde, HCHO) can often play a more dominant role within the initial production HO_x in the much drier upper troposphere (UT) (Ren et al., 2008). An additional source for OH, albeit minor one (particularly within the UT) is the ozonolysis of VOCs.

These aforementioned HO_x radical production channels are shown in Table 2.1:

Table 2.1.: HO_x sources				
^a H ₂ O ₂ + <i>hν</i>	→	2OH	λ < 557 nm	(R2.5)
^b ROOH + <i>hν</i>	→	OH + RO	λ < 360 nm	(R2.6)
^c HCHO + <i>hν</i> + 2O ₂	→	2HO ₂ + products		(R2.7)
^d Alkene + O ₃	→	αOH + products		(R2.8)
^e HONO + <i>hν</i>	→	OH + NO	λ < 380 nm	(R2.9)

^{a+b} The photolysis of peroxides represents, typically, a secondary source of OH since they are formed during the oxidation process of VOCs and radical recombination.

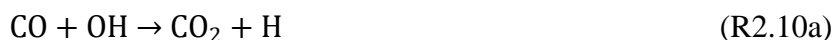
^c HO₂ primary production from formaldehyde (HCHO) photolysis,

^d The ozonolysis of alkenes is a non-photolytic primary OH source. The initial ozonide produces a Criegee Intermediate, which can then decompose releasing OH, (Novelli et al., 2014, and references therein). However, the strong negative temperature dependency of alkene ozonolysis would suggest that this is would be small source for OH in UT, when compared to the other sources listed in Table 1.

^e Nitrous acid (HONO) can photolyze to produce OH and NO. This channel can pose a significant channel of OH production during night. However, HONO quickly decomposes during the morning when solar radiation is present reforming OH and NO (Aumont et al., 2003; Kleffmann et al., 2005).

2.2. HO_x recycling / cycling within HO_x

OH has a very short lifetime (less than a few seconds) and can react quickly with CO and O₃ to produce HO₂. In terms of cycling within HO_x, the OH-initialized oxidation of CO is one of the most important reactions. The first step is a loss process of the OH radical forming CO₂ and a hydrogen atom (H), The H atom then rapidly reacts with O₂ to produce HO₂.



Ozone, HCHO, H₂O₂, and SO₂ are also prominent channels of HO₂ production from OH:

Table 2.2.: Cycling OH into HO₂			
OH + CO (+ O ₂ , M)	→	HO ₂ + CO ₂	(R2.11)
OH + O ₃	→	HO ₂ + O ₂	(R2.12)
OH + HCHO (+ O ₂)	→	HO ₂ + H ₂ O + CO	(R2.13)
OH + H ₂ O ₂	→	HO ₂ + H ₂ O	(R2.14)
OH + SO ₂ (+ O ₂ , H ₂ O)	→	HO ₂ + H ₂ SO ₄	(R2.15)

There are also prevalent channels for HO₂ to cycle into OH. HO₂ can react with ozone and NO, generating another oxidation channel:

Table 2.3.: Cycling HO₂ into OH			
HO ₂ + O ₃	→	OH + 2O ₂	(R2.16)
HO ₂ + NO	→	OH + NO ₂	(R2.17)

Oxidation of VOCs by OH initialization presents another pathway for HO₂ recycling. The most prevalent VOC in the atmosphere is methane (CH₄), which has a lifetime of ~ 9 years and has a mixing ratio in the range of parts per million (ppm). CH₄ therefore, is ubiquitous throughout the troposphere. CH₄ is mainly oxidized by OH resulting in the formation of the methylperoxy radical (CH₃O₂). CH₃O₂ reacts with NO to produce a methoxy radical (CH₃O), which in turn rapidly reacts with O₂ producing HO₂ and HCHO:



With one of the products of OH initiated CH₄ oxidation being HCHO, this HO_x cycling channel can actually increase the total production of HO_x by a median factor of 1.7 (Logan et al., 1981). This factor is calculated from the branching ratio of the radical forming photolysis channel (R.2.8) and none-radical forming photolysis channel of HCHO. The completion of the HO_x-cycle occurs when OH is formed back through reactions (R2.16 & 2.17) (Martinez et al., 2003). Other VOCs oxidize via a similar reaction chain when the initial oxidation occurs by OH, irrespective of the complexity of the initial VOC structure (Jenkin et al., 2015); (the R denotes an organic group):



However, there is a route that can potentially disrupt this HO_x recycling channel and lead to a potential sink for HO_x. RO₂ radicals can be removed via reaction with HO₂ (see reaction R2.32), other RO₂ radicals and NO_x forming peroxides and peroxy nitrates:



The thermal decomposition rates are much slower within the UT, due to subzero temperatures, thus increasing peroxy nitrates atmospheric lifetimes (Fischer et al., 2014). Therefore, branching towards peroxy nitrates formation in the UT can become more prominent, elevating a sink for OH and RO₂ species, and reduces the efficiency of HO_x cycling. On the contrary, due to the warmer temperatures in the LT, peroxy nitrates can quickly thermally decompose, reforming peroxy radicals and NO₂.



Essentially, peroxy nitrates act as transportable reservoirs for peroxy radicals and NO_x, particularly within the UT.

2.3. HO_x sinks

The main sink of HO_x radicals is through radical-radical reactions producing peroxides and other products:

Table 2.4.: HO _x sinks via radical-radical reactions					
HO ₂ + HO ₂		→	H ₂ O ₂ + O ₂		(R2.30)
OH + HO ₂		→	H ₂ O + O ₂		(R2.31)
HO ₂ + RO ₂		→	ROOH + O ₂		(R2.32)

Typically, peroxides are lost through wet and dry deposition, thus removing HO_x from the system and reducing the cycling within HO_x. Conversely, in the UT and above, very little deposition can occur due less available surfaces that peroxides can deposit on (with the exception of aerosol particle surfaces) and lack of precipitation (limiting chemical washout). This means that the photolysis of peroxides (see reactions R2.5 & 2.6) becomes the more dominant loss process for peroxides in the UT, which in turn forms OH. This leads to a reduction in the potential sink of HO_x and organic radicals via peroxide formation.

Another potential sink of HO_x in polluted air masses is the direct formation of nitrogen acids / nitrates in the presence of NO_x.

Table 2.5.: HO _x sinks via acid formation					
OH + NO	(+ M)	→	HONO	(+ M)	(R2.33)
OH + NO ₂	(+ M)	→	HNO ₃	(+ M)	(R2.34)
HO ₂ + NO ₂	(+ M)	→	HNO ₄	(+ M)	(R2.35)

3. HORUS instrument and HO_x measurements

3.1. Techniques, challenges and developments for measuring HO_x

Hydroxyl radicals are notoriously difficult to measure. Due to their high reactivity towards many trace gas species, OH atmospheric lifetimes can be shorter than one second. Therefore, short sample lines with minimal wall losses and fast detection are required to measure OH. Furthermore, OH radicals cannot be directly stored within samples for measurement in a lab. Additionally, daytime OH concentrations can be low, with average concentrations being in the order of 10^5 to 10^7 molec. cm^{-3} . The HO₂ radical has typical average concentrations that are about 100 times larger than OH, and has an atmospheric lifetime ranging from seconds to minutes. Due to the atmospheric characteristics of HO_x, highly sensitive instrumentation is needed to measure the variability of these species in the atmosphere. The following paragraphs discuss the different direct and indirect methods for measuring OH and HO₂.

3.1.1. Measurement techniques for atmospheric OH detection

Spin trapping – electron paramagnetic resonance

Electron paramagnetic resonance (EPR) or otherwise known as electron spin resonance (ESR) spectroscopy is a measurement technique used to detect chemical species with unpaired electrons. EPR involves the resonant absorption of microwaves (electromagnetic radiation) of a sample within a magnetic field. However, this method alone is too slow to detect species such as OH that can have sub second chemical lifetimes. The combining of EPR with spin trapping makes OH detection feasible, but this negatively affects the time resolution. Atmospheric OH has been measured using EPR in conjunction with α -4-pyridyl-N-tert-butyl nitron α -1-oxide (4-POBN) as the spin trapping substrate for OH, whereby the hydroxy-adduct of 4-POBN is detected (Watanabe et al., 1982). This technique has a lower detection limit of 5×10^5 molec. cm^{-3} , requiring an integration time of 20 minutes.

¹⁴CO Tracer Technique

The basis of this technique is the assumption that CO is mainly oxidized by OH radicals. The concentrations of atmospheric OH can be calculated by adding isotopically labeled ¹⁴CO and freeze desalination the subsequently produced ¹⁴CO₂ (Felton et al., 1988). The combined measurement of ¹⁴CO and ¹⁴CO₂ concentrations and application of the known rate constant of OH with CO to these measurements allows OH concentrations to be calculated. However, despite the ¹⁴CO method having a detection limit of 2×10^5 molec. cm^{-3} and requiring integration times of only a few minutes, the intricate sampling method can make this measurement technique less suitable for in-the-field atmospheric OH detection.

Differential optical absorption spectroscopy – DOAS

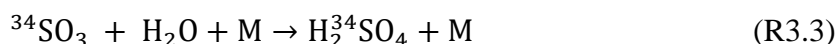
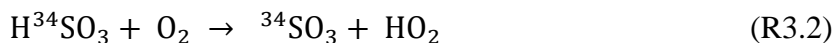
Differential optical absorption spectroscopy (DOAS) uses the principle that different molecular species absorb different wavelengths of light, and measuring molecules in the atmosphere using the Beer-Lambert's law:

$$I(\lambda) = I_o(\lambda) \cdot \exp \left[\int_0^L -\sigma_{\text{OH}}(\lambda) \cdot [\text{OH}] \cdot dL \right] \quad (3.1)$$

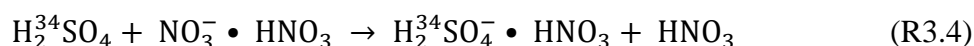
I_o and I are the measured light intensities before and after transmission through a medium of length (L). $\sigma_{\text{OH}}(\lambda)$ denotes the absorption cross section of OH at wavelength (λ). Light from either a laser or the sun passes through the atmosphere and the absorption spectrum is measured with high spectral resolution spectrographs. Many different chemical species can be monitored by extracting their respective absorption spectra. With regards to OH measurement, the uncertainty mainly comes from the uncertainty in the OH absorption cross section, 7 % (Dorn et al., 1995). In order to achieve a limit of detection of 7.3×10^5 molec. cm^{-3} , integration times of 100 seconds and light path lengths of 2240 m are required (Fuchs et al., 2012). However, DOAS is no longer used for in-the-field atmospheric OH detection due to light scattering by aerosols within the light path causing high detection limits.

Chemical Ionization Mass Spectroscopy – CIMS

Chemical Ionization Mass Spectroscopy (CIMS) is an indirect method of acquiring atmospheric mixing ratios of OH. The sampled atmospheric OH is titrated using isotopically labelled $^{34}\text{SO}_2$ and the subsequently produced $\text{H}_2^{34}\text{SO}_4$ is measured.



An excess of $^{34}\text{SO}_2$ is injected into the sample flow to ensure the efficient conversion of sampled atmospheric OH radicals into H_2SO_4 within milliseconds (Eisele and Tanner, 1991; Eisele et al., 1997; Kukui et al., 2008; Petaja et al., 2009). H_2SO_4 is then ionized via a charge transfer reaction with nitrate ions (NO_3^-). Predominately, the NO_3^- ions are present as a chemical complex with HNO_3 or H_2O .



The formed $\text{H}_2^{34}\text{SO}_4^- \cdot \text{HNO}_3$ chemical complex is fragmented inside a collision chamber and mass spectrometry is used to detect the resulting fragments. The measured concentration of $\text{H}_2^{34}\text{SO}_4^-$ ions is directly proportional to the concentration of atmospheric OH involved in the titration reactions. Due to the small natural abundance of ^{34}S isotopes ($\sim 4\%$), it is easily distinguishable from the atmospheric H_2SO_4 and the $\text{H}_2^{34}\text{SO}_4$ produced from the OH titrations. Additionally, propane is injected in front of the sampling in order to remove atmospheric OH. This allows CIMS instruments resolve for interferences caused by chemical species that can also react with SO_2 to form H_2SO_4 within the atmospheric OH signal. As reactions R3.1 to R3.4 occur under ambient conditions within the sampling tube of CIMS instruments, if the residence

times within the sampling tube are too long, HO_x cycling artifacts can occur. In polluted air i.e. urban air, where there are high NO levels, the sampled atmospheric HO₂ and NO can react within the sample tube forming OH (Muller et al., 2018). Therefore, to minimize this OH regeneration interference, the residence times have been shortened from seconds to tens of milliseconds (Kukui et al., 2008). However, like other multi-tier chemical reaction based methods for trace gas detection, the largest uncertainties within this technique come from the reaction rate constants. Typical detection limits are in the order of 1 to 2 x 10⁵ molec. cm⁻³, with an atmospheric OH measurement time resolution of 5 minutes.

Laser-Induced Fluorescence – Fluorescence Assay by Gas Expansion – LIF-FAGE

The first account of using a tunable laser source in the ultraviolet to excite OH in the air and successfully detecting the resulting resonance fluorescence was reported by Wang and Davis (1974). OH radicals can be selectively excited by UV light at a wavelength of 282.58 nm which is on resonance with the P₁(2) line within the A²Σ⁺ - X²Π, v' = 1 ← v'' = 0 transitions of OH. Once excited, OH can transition back, via a series of rotationally and vibrationally excited states, to ground state resulting in fluorescence within the wavelength range of 307 – 315 nm. However, the vast majority of electronically excited state OH molecules would lose their energy through collisional quenching with other molecules in the air at atmospheric pressure. This resulted in sub 1ns collisional lifetimes of electronically excited OH (Hard et al., 1984). Additionally, very few of the initially excited OH molecules fluoresced, as the lifetime of excited state OH is around 700 ns. Combine this poor yield of OH fluorescence with the large background signals from laser light scattering by aerosols and other molecules within the sampled air and from the internal wall surfaces within the instrument, detection limits of only 5 x 10⁶ molec. cm⁻³ were achieved (Wang and Davis. 1974). Further limitations to measuring OH by LIF have also been described in Wang and Davis (1974). The laser wavelength used to excite atmospheric OH radicals, λ ≈ 282 nm, also causes photodissociation of atmospheric O₃, which produces O(¹D) atoms. These laser-generated O(¹D) atoms can react with atmospheric water vapor (see reaction R2.4), yielding artificially elevated OH concentrations, and therefore the laser itself generates OH interference in LIF, which is directly proportional to the power of the laser (Ortgies et al., 1980).

The introduction of fluorescence assay by gas expansion (FAGE) was a significant improvement to LIF measurements of OH. By reducing the internal pressure within the instrument from ambient down to ~ 1 to 5 mbar, the main disadvantages of LIF described above were negated. The reduction in pressure reduces the number density of H₂O and O₃, thus significantly limiting the yield of artificial OH radicals generated from photodissociation of atmospheric O₃ by the 282 nm laser radiation (Hard et al., 1979). Unfortunately, the lower pressures also reduced the number density of atmospheric OH molecules available for excitation, and reduced the transmission of OH molecules to the detection cell by increasing the mean free path for molecules within the instrument, thus increasing wall losses. However, the OH fluorescence quantum yield increased due to the sub 5 mbar internal pressures suppressing the rate of collisional quenching of excited OH thus extending the overall lifetime of the excited state by several hundred nanoseconds. Figure 3.1 shows these different effects, and their impact on a LIF-FAGE instrument detecting OH.

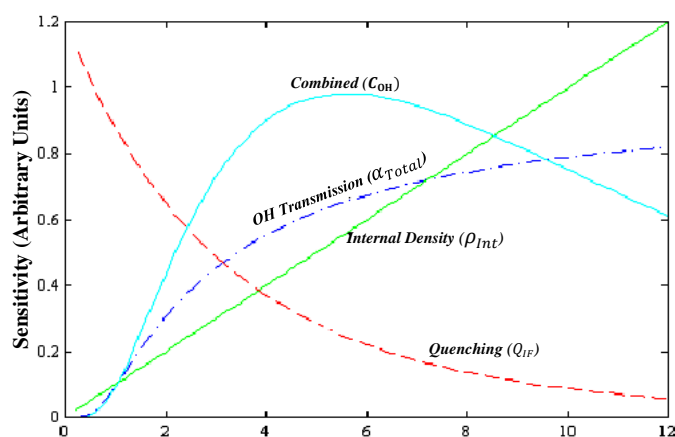


Figure 3.1.: A schematic showing the combined LIF-FAGE sensitivity curve as a function of instrument internal pressure (light blue line), OH transmission (dotted-dashed dark blue line), internal density (green line), and quenching (dashed red line). (A modified version of the schematic in Faloona et al. (2004), taken from Marno et al. (2020)).

Further modifications to LIF-FAGE instruments such as installing baffles and black anodizing the internal walls of the instrument suppresses the potential background signal caused by scattered photons from internal reflections. To differentiate and minimize the impact of fluorescence that show similar temporal characteristics to the laser pulse, electronic detector gating times were introduced (Mather et al., 1997). During and immediately after a laser pulse, where aerosol fluorescence (Mie and Rayleigh scattering) and photon reflections from the internal walls are highest, the detectors are switched off. Then ~ 100 ns after the initial laser pulse (named as the first gating time), the detectors are switched on. Post the first gating time, the significant contribution to the signal is sourced from OH fluorescence. The detectors are left on and the detected signal is integrated over several hundred nanoseconds to capture the best possible measured representation of the initially excited OH radicals before switching off (the second gating time) ahead of the next laser pulse. Figure 3.2 shows a schematic describing the principle of a gated photon detection method.

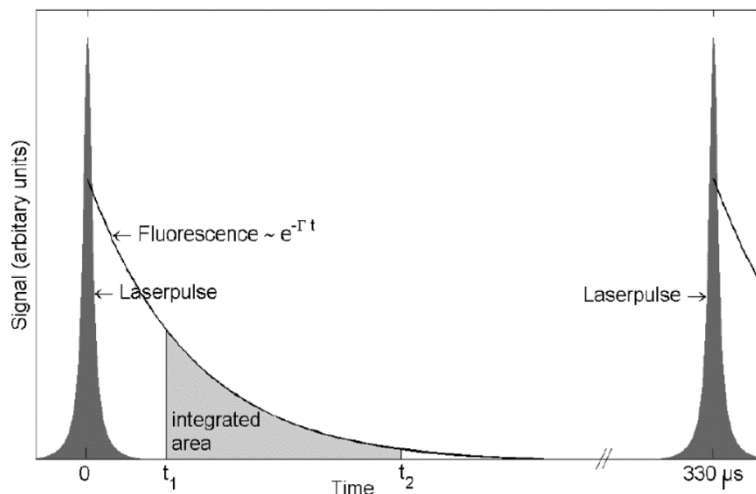


Figure 3.2.: A schematic showing the time between laser pulses (dark grey areas) when photon detection occurs in a LIF-FAGE technique. The first and second gating times are described as t_1 and t_2 respectively. The large background signal caused by events such as Mie and Raleigh scattering and wall reflections are removed by the turning on the detectors sufficiently after the initial laser pulse. The light grey area is the integrated fluorescence signal that is directly proportional to the concentration of the initially excited OH molecules in the sampled air. (A modified version of the schematic in Faloon et al. (2004)).

In modern day LIF-FAGE instruments, the $A^2\Sigma^+ - X^2\Pi, v' = 1 \leftarrow v'' = 0$ excitation of OH is achieved using laser radiation at wavelengths of 308 nm. The OH radicals still reach the ground state in the similar way as described earlier, and fluoresce and are detected at similar wavelengths. The advantage of using 308 nm photons as opposed to 282 nm photons is twofold. The potential for laser-generated OH is roughly a factor 25 times smaller due to lower absorption cross section of O_3 at 308 nm, thus reducing the quantum yield of $O(^1D)$ atoms. Additionally, the efficiency of OH radical excitation is improved due to OH having a factor 4 larger absorption cross section at 308 nm, thus amplifying the OH fluorescence signal (Chan et al., 1990). More recently there have been further developments of LIF-FAGE instrumentation, to characterize other sources of interference which are discussed in detail in sections 4 and 5.

3.1.2. Measurement techniques for atmospheric HO_2 detection

Matrix Isolation ESR

Mihelcic et al. (1978) developed the only selective method for direct HO_2 detection known as Matrix Isolation and Electron Spin Resonance spectroscopy (MIESR). Air is sampled into a chamber with a reduced pressure of ~ 10 mbar, where peroxy radicals are removed from the air by freezing into a D_2O molecular matrix on a sampling finger that is cooled by liquid nitrogen. This is to minimize reactions between the frozen out reactive chemical species. These cryogenically stored samples are then taken to a lab where measurements are performed by electron spin resonance (ESR) spectroscopy. MIESR is capable of simultaneously measuring

concentrations of HO₂, RO₂, NO₂, and NO₃ in one sample. However, in order to collect a sufficient number HO₂ radical molecules, sampling times can be in excess of 30 minutes, resulting in a low time resolution and detection limits of about 1 x10⁷ molec. cm⁻³. Also, the requirement for cryogenically storing the samples and performing the ESR concentration measurements in a lab is time consuming, which has practical implications for in-the-field use therefore resulting in the discontinuation of MIESR in-the-field measurements of HO₂.

Chemical Ionization Mass Spectroscopy – CIMS

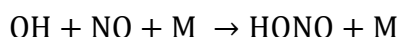
Chemical Ionization Mass Spectroscopy (CIMS) has been used to measure, indirectly, both HO₂ and RO₂ radicals, via chemical conversion to OH (Reiner et al., 1997; Cantrell et al., 2003):



The produced OH from Reactions R3.5 – R3.7 is measured using the same CIMS technique described in section 3.1.1, by further addition of SO₂. The only dissimilarity between the atmospheric OH detection described in section 3.1.1 and HO₂/RO₂ CIMS detection is that isotopically labelled SO₂ is not required when measuring HO₂ and RO₂. As the atmospheric concentrations of HO₂ and RO₂ are in the order of 100 times greater than OH, the background interference of atmospheric H₂SO₄ is small. When specifically measuring atmospheric HO₂, injection of N₂ is used instead of O₂, which suppresses conversion of RO₂ to OH by reducing the rate of the intermediate Reaction R3.6. Only atmospheric O₂ is still available to take place in Reaction R3.6. When under HO₂ only detection conditions, ~ 70 % of the produced H₂SO₄ is sourced from atmospheric HO₂, resulting in detection limits of about 7 x10⁵ molec. cm⁻³ and integration times of about 1 minute (Heard and Pilling, 2003).

Laser-Induced Fluorescence – Fluorescence Assay by Gas Expansion – LIF-FAGE

LIF-FAGE is an other indirect technique for HO₂ radical detection, which is based on the chemical conversion of HO₂ to OH by injecting excess NO into the sample flow, see Reaction R2.17. The subsequently produced OH radicals are measured in a similar fashion as described in section 3.1.1. However, due to the short time period (a few milliseconds) between the point of NO injections and the detection of the subsequently produced OH radicals, fairly high NO mixing ratios of 1000 ± 500 ppmv are required to ensure high conversion efficiency. Other factors such as wall losses and quality of NO mixing during injection also impact conversion efficiency. However, interferences can occur at high NO mixing ratios. Internal formation of HONO, via Reaction R2.33:



can result in a detectable loss of produced OH radicals. However, due to the termolecular nature of the reaction coupled with the low internal pressures inside LIF-FAGE detection systems, this reaction is slow compared to ambient conditions. If the time for reaction between NO injection and detection cell is sufficiently long enough or injected NO levels are high

enough, sampled atmospheric RO₂ can react with NO producing a detectable artificially elevated OH signal (see Reactions R3.5 – R3.7). It is also known that alkene-based RO₂ species can decomposed under low pressure regimes inside LIF-FAGE instruments, thus rapidly forming an excess level of HO₂ (Fuchs et al., 2011). The interferences from RO₂ species can be reduced by shortening the reaction time and/or reducing NO concentrations in the detection cell. However, this will cause HO₂ to OH conversion efficiencies to decrease thus reducing HO₂ detection sensitivity. Typical detection limits of less than 1×10^6 molec. cm⁻³ with integration times of around 30 seconds can be achieved by LIF-FAGE instruments measuring HO₂. The influence of HONO formation and RO₂ within the airborne *HydrOxylRadical Measurement Unit* based on fluorescence Spectroscopy (HORUS) LIF-FAGE instrument will be discussed in section 5.

3.2. The HORUS instrument

The OH and HO₂ observations presented within this work were conducted during the OMO-Asia 2015 airborne campaign by the Max Planck Institute for Chemistry (Mainz, Germany) airborne HO_x instrument based on LIF-FAGE, HORUS (*HydrOxylRadical Measurement Unit* based on fluorescence Spectroscopy). HORUS is based on the original design of GTHOS (Ground Tropospheric Hydrogen Oxide Sensor) described by Faloon et al. (2004) and is described in further detail in Martinez et al. (2010). Different iterations of HORUS have been used during various ground-based, shipborne, and airborne campaigns (Schlosser et al., 2009; Kubistin et al., 2010; Martinez et al., 2010; Regelin et al., 2013; Mallik et al., 2018). The airborne HORUS instrument involved in the OMO-ASIA 2015 airborne campaign, was a revised and altered design to perform under in-flight pressure and temperature conditions and conform to aeronautical regulations. It was primarily developed for installation on the High Altitude and Long Range Research Aircraft (HALO). The system comprises of an external inlet shroud, an inlet pre injector (IPI), laser system, detection axes, and a vacuum system (Figure 3.3).

Inlet Shroud

The inlet shroud was designed to enable in-flight calibrations, monitor instrument sensitivity performance, and improve sampling conditions of HO_x radicals. The in-flight calibrations were used to monitor relative changes of the instrument during flight such as HO₂ conversion efficiency and interference levels, potential degradation of the detectors, and changes in reflectivity of the White Cell mirrors due to intake of VOC rich air from aircraft engines and fuelling trucks when the aircraft was out on the apron. Within the shroud there is a shutter-able UV Pen-Ray lamp. Throughout the flight the UV lamp is kept on, to ensure that it is in thermal steady state and therefore emitting near-constant flux intensity. When HORUS is normally measuring, there is a closed shutter blocking the UV radiation. However, when in-flight calibrations are performed the shutter is opened, allowing the UV radiation to pass through the inner-most shroud. UV radiation is used to photolyze atmospheric water vapor, to produce elevated and stable concentrations of OH and HO₂. The use of this method for HORUS calibrations will be discussed in more detail in section 4. In order to improve sampling conditions of HO_x radicals in flight, as shown, from left to right, in Figure 3.3, the inlet shroud

system is made up of three increasingly smaller shrouds. This not only ensures that the HORUS instrument is sampling air from within the central air flow but also parallelizes the air flow passing through the shroud system to the IPI nozzle. To prevent excessive collisions of OH and HO₂ with the IPI nozzle and its internal walls, thus limiting losses of HO_x during flight, the momentum inertia of the air passing through the inlet shroud had to be overcome in order to promote the airflow direction into IPI. To achieve this, a choke behind IPI was installed, see Figure 3.4. Without the shroud choke, flow speeds in the inlet shroud would readily exceed 200 m s⁻¹. However, with the choke point installed, flow speeds in the shroud did not exceed 21 m s⁻¹ during OMO-Asia 2015, which is sufficiently below the sample velocities of IPI during flight (44 – 53 m s⁻¹). The combination of the parallelized air flow in the inlet shroud, the central sampling location of the IPI nozzle, and the installation of a choke limited the increase in OH variability as the aircraft changes pitch, roll and yaw, to $\pm 4.51 \times 10^4 \text{ cm}^{-3}$ (1 σ). This increase in variability is negligible as it never exceeded 30 % of the detection limit of the HORUS and was only 10 to 15 % higher than the natural variability of OH that was measured during OMO-Asia 2015.

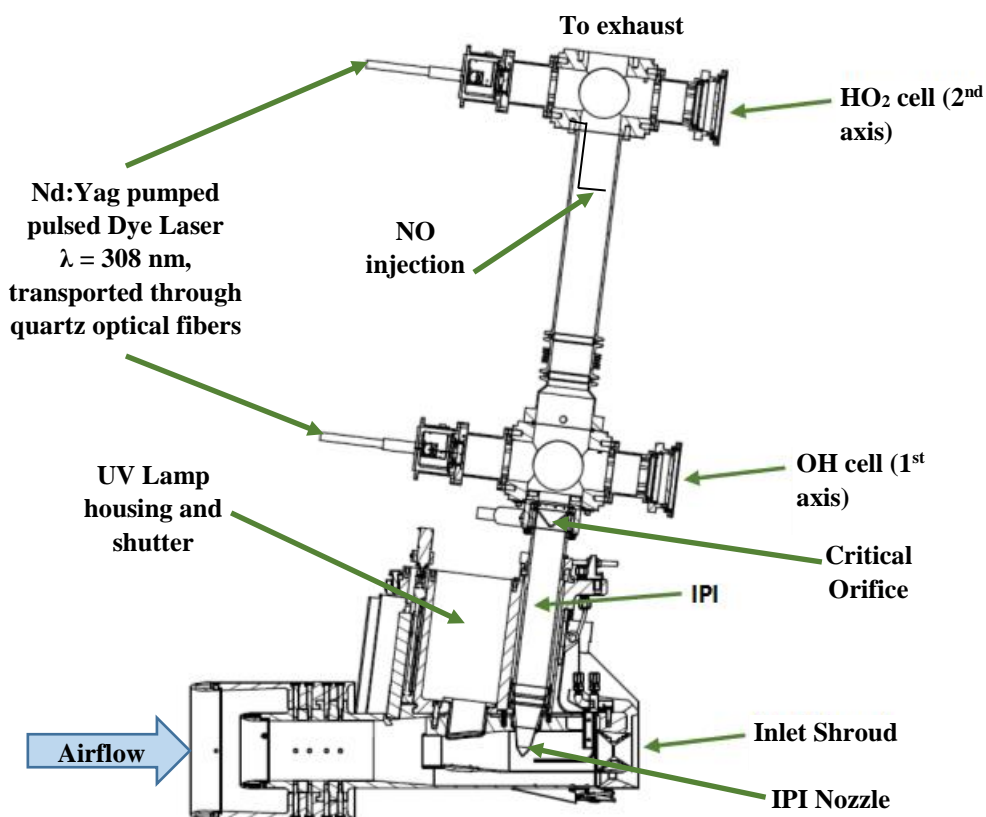


Figure 3.3.: Overview of the airborne HORUS system as installed in the HALO aircraft. An Inlet Pre-Injector (IPI) is mounted inside the inlet shroud and is designed to allow for chemical background detection within HORUS. Post critical orifice, the OH radicals are excited by laser light at around 308 nm within the detection cells. The fluorescence of these molecules is detected using a multi-channel plate detector (MCP) that forms part of one of the detection cell arms. The MCPs look towards the center of the detection cells through a series of focal optics, perpendicular to the incoming laser beam from the fibers. In a second detection axis, HO₂ is detected indirectly through the addition of NO that quantitatively converts HO₂ into OH. The NO injection occurs via a stainless steel 1/8 inch line, shaped into a ring perpendicular to the airflow with several unidirectional apertures of 0.25 mm diameter creating essentially a NO shower. For details refer to text. (A modified figure, taken from Marno et al. (2020)).

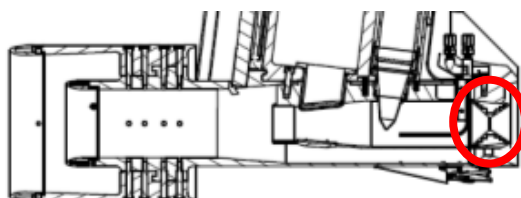


Figure 3.4.: A close up of the inlet shroud. The red circle depicts the location of the installed choke used to reduce in-flight airflow speeds within the inlet shroud.

The Inlet Pre-Injector (IPI)

The HORUS setup as flown during OMO-Asia 2015 was the first airborne LIF-FAGE instrument measuring HO_x that had a dedicated inlet pre injector (IPI) system installed for removing atmospheric OH, to enable real time measurement and quantification of potential chemical background OH interferences, OH-CHEM (Mao et al., 2012). In the HORUS IPI system, propane is injected as a scavenger to remove the atmospheric OH in front of the critical orifice (i.e. before the low pressure section where OH detection occurs). Once removed, the residual chemical background OH signal ($S_{OH-CHEM}$) is measured. The airborne IPI system differs internally compared to the previously used ground-based IPI system, as it does not have a hyperbolic internal shape (Novelli et al., 2014). Additionally, the operation of the airborne IPI system had to conform to aeronautical regulations, and in-flight conditions. This resulted in differing operational IPI flow speeds, propane usage, and subsequent scavenging efficiencies and wall losses. Additionally, due to the low ambient temperatures, the walls of IPI were heated to a constant 30 °C. The IPI system (with a nozzle orifice diameter of 6.5 mm) samples (50 to 230 SL min⁻¹) from the central airflow moving through the internal shroud.

Note: Standard flows e.g. standard liters per minute (SL min⁻¹) or standard cubic centimeters per minute (sccm) used within this thesis are defined using the standard temperature and pressure of 298.15 K and 1013.25 mbar respectively.

A critical orifice is located at the end of IPI in the center of the IPI cross section, which enables the HORUS instrument to sample (3 to 17 SL min⁻¹) from the central flow moving through IPI. This further reduces influences of wall loss within IPI on the overall measured signal in the cells. The removal of excess flow moving through IPI occurs via a perforated ring that surrounds the base of the critical orifice cone, and evacuated by a blower. Table 3.1 shows the primary operational differences between the ground and airborne IPI systems.

Table 3.1.: IPI parameters from airborne setup and ground setup

Campaign	IPI flow Residence time	Scavenger/flow	Carrier flow Synthetic Air	Scavenging Efficiency
OMO-Asia 2015 (Airborne campaign)	50-230 SL min ⁻¹ 22-120 ms	1% Propane/ 0-100 sccm	2000 sccm	82-98%
AQABA 2017 (ship campaign)	150 SL min ⁻¹ ~ 4 ms	Pure Propane/ 0.5-12 sccm	10000 sccm	> 95%

Laser system

A triply ionized neodymium (Nd^{III}) doped yttrium aluminium garnet (YAG) pumped, pulsed tunable dye laser system operating at a pulse repetition rate of 3 kHz is used to provide the 308 nm UV light needed to excite OH radicals (Wennberg et al., 1994; Martinez et al., 2010). To optically pump the custom made dyelaser system with 532 nm light, a diode-pumped, quality-switchable, Type Navigator I, Nd:YAG laser from Spectra Physics is used. To precisely focus the beam of the pump laser onto the dye cell, the initial pump laser beam, with a beam width

of 0.65 mm, is expanded using a tenfold beam expander from Linos - Qioptic. The light beam is then focused through a converging lens with a focal length of 100 mm (Thorlabs), generating a beam focal point within the dye cell. The additional use of two piezo-actuated mirrors allows for active control of the incoupling of the green laser beam, thus compensating for potential thermal and mechanical influences on the laser plate that could cause misalignment. Figure 3.5 shows the schematic of the dye laser, taken from the thesis of Hens (2013). The 532 nm wavelength pump laser beam hits the dye cell at the Brewster angle, where the custom made laser dye absorbs the green laser light and fluoresces at the red wavelength range (including $\lambda = 616$ nm). The custom made laser dye is Pyrromethane-597 (Radiant Dyes Laser, Germany) which is dissolved in 99.9 % purity isopropanol. To prevent over saturation of excited laser dye within the dye cell, the dye is circulated, via a reservoir, at a rate of 1.6 – 1.7 litres per minute, resulting in a full exchange of dye within the dye cell after every two laser pulses. The light emitted from the dye cell is then amplified within the dye laser cavity, as shown in Figure 3.5, which comprises of all optics between the back reflection (end) mirror to the outcoupling mirror. As described before the laser dye fluoresces across a wide range of wavelengths within the red visible light spectrum. However, primary selective amplification of light at the wavelength of 616 nm is acquired through the combined use of three SF10 dispersion prisms (each placed at a 60° Brewster angle from one another) with a rotatable intracavity etalon optic that is controlled by a stepper motor. Within the cavity, frequency doubling in the β -barium borate (BBO) crystal occurs, which feeds 308 nm UV light to the outcoupling mirror. The UV light is then transported to the detection cells via optical fibers, that are angle polished to prevent signal interference from backreflections (Hens. 2013).

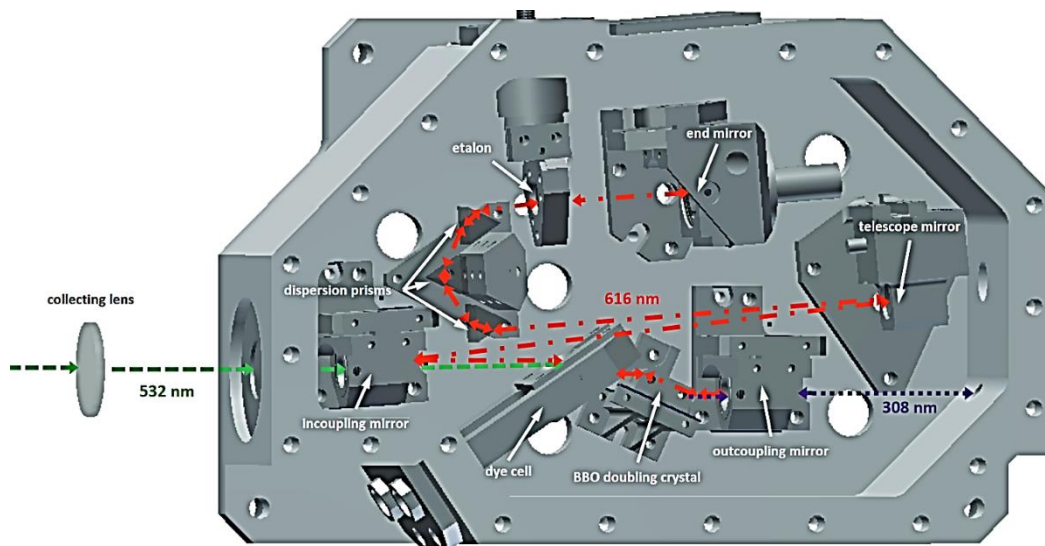


Figure 3.5.: A schematic of the dye laser system. The incoming 532 nm wavelength Nd:YAG laser beam is focused onto the dye cell. The pyrromethane-597 laser dye fluoresces at $\lambda = 616$ nm which is amplified within an optical resonator (the telescope, dispersion prisms, etalon mirror and back reflection (end) mirror). 308 nm wavelength UV light is generated by amplifying selectively 616 nm sufficiently to allow frequency doubling to occur within a nonlinear doubling crystal (β -barium borate, BBO). Taken from Hens (2013).

Low pressure Detection Cell

After passing through IPI, the sampled air is drawn through a critical orifice with a diameter of ~ 1.4 mm, at a volume flow of ~ 17 SL min^{-1} (under standard conditions) into the low-pressure fluorescence chamber. All internal surfaces, including that of IPI is black anodized aluminum. The critical orifice produces an internal cell pressure of about 18 mbar at ground level and causes rapid adiabatic expansion of the measuring gas. This exchange rate of sample air is required to ensure that excitation of the same sample air does not occur from two consecutive laser pulses, which would elevate the production and interference of laser-generated OH. 77.5 mm after the critical orifice, in the direction of airflow, is the center of the first detection block, where atmospheric OH excitation, fluorescence and detection occurs. Beyond increasing the output power of the dye laser, to ensure maximal atmospheric OH excitation and maximizing HORUS sensitivity towards OH, a White Cell setup (Figure 3.6) within the detection cells is used (White. 1942). The reflection mirrors in the White Cells in HORUS are aligned in order to create 32 light paths, which cross the detection volume.

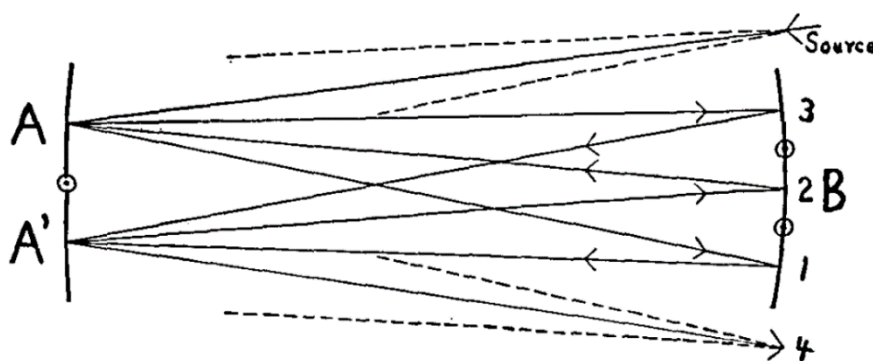


Figure 3.6.: An image taken from White (1942), that represents the optical path of a White Cell. Three aligned mirrors reflect the single incoming laser beam multiple times, creating several beams of light that cross the space between, before leaving the cell.

HORUS, like many other LIF-FAGE instruments, is based on the resonant absorption of laser light by OH molecules, specifically the $Q_1(2)$ transition from the ground state $X^2\Pi_{3/2}$ to the excited $A^2\Sigma^+$ state (Figure 3.7). The resulting return to ground state results in a detectable fluorescence of OH (Dorn et al., 1995; Holland et al., 1995; Mather et al., 1997) in the low-pressure regime (< 18 mbar) within the detection cells. The ground state electron configuration of OH is $(1\sigma)^2 (2\sigma)^2 (3\sigma)^2 (\pi^+)^2 (\pi^-)^1$ with an unpaired electron in the π orbital (Freeman. 1958). In the $A^2\Sigma^+$ electronically excited state, the electron configuration is $(1\sigma)^2 (2\sigma)^2 (3\sigma)^2 (\pi^+)^2 (\pi^-)^2$. There is a separation in the rotational ground states for OH due to spin-orbit coupling forming two electronic substrates $X^2\Pi_{3/2}$ and $X^2\Pi_{1/2}$. The excited $A^2\Sigma^+$ state has no angular momentum, and therefore no spin-orbit coupling. In Figure 3.7, K stands for the quantum number of angular momentum (rotation+orbit), and J stands for the quantum number of the total angular momentum (rotation+orbit+spin).

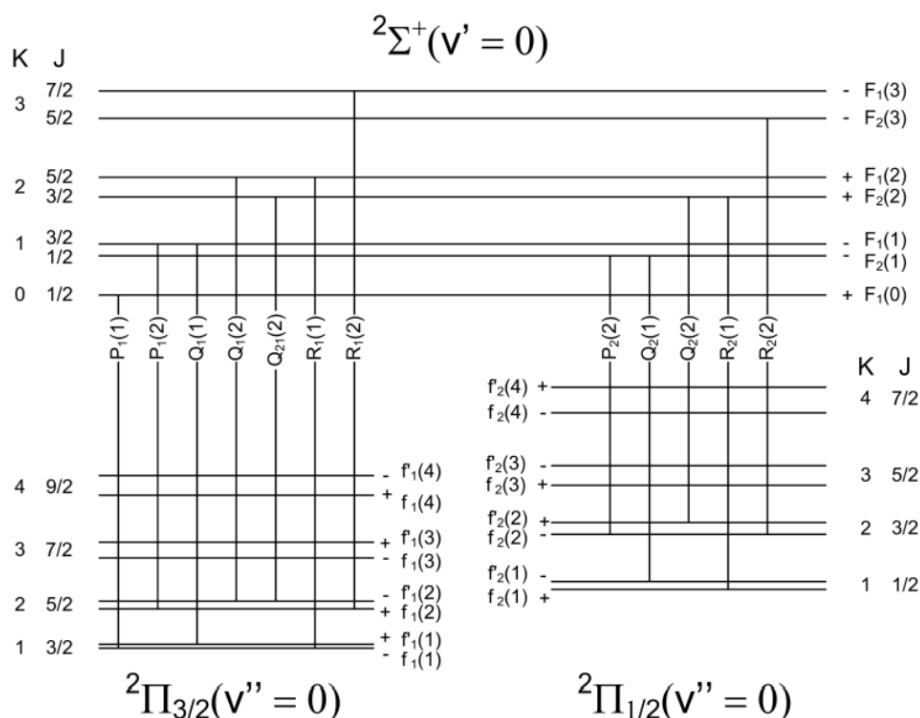


Figure 3.7.: A schematic of the different branches in the rotational structure of OH and the $A^2\Sigma^+ - X^2\Pi$, $v' = 1 \leftarrow v'' = 0$ transitions used during laser excitation. K stands for the quantum number of angular momentum (rotation+orbit), and J stands for the quantum number of the total angular momentum (rotation+orbit+spin). Modified version from Kubistin (2009).

The energy levels of the two ground sub-states are labeled with $f_i(K)$ and $f'_i(K)$, where $i = 1$ represents $K+\Sigma$, and $i = 2$ denotes $K-\Sigma$. The symbol Σ represents the projection of molecular spin in the z -axis. Due to lambda doubling interactions, energetically higher levels exist which are denoted as $f'_i(K)$. Consequently, the energetically differing substrates within the excited $2\Sigma^+$ state are labelled as an analogy to the ground state with capitalized $F_i(K)$ and $F'_i(K)$ labels. The absorption lines are labeled by the rotational branches $P(\Delta K=-1)$, $Q(\Delta K=0)$, or $R(\Delta K=1)$ and where K is the quantum number of the angular momentum in the ground state.

Transitions of spin projections, $K \pm \frac{1}{2}$, known as satellite branches also occur at similar energies, however they show low intensities when compared to the main branches. An overview of the energy states of diatomic molecules and their permitted transitions and intensities is summarized in-depth in Kubistin (2009). More detailed descriptions of the OH absorption spectrum are found in Freeman (1958); Dieke and Crosswhite (1962); Langhoff et al. (1982) and the references therein. Figure 3.8 shows the reasoning behind the use of the relatively high signal intensity of the $Q_1(2)$ transition within the OH absorption spectrum at wavelengths around 308 nm (Chan et al., 1990), when compared to the other transitions shown in Figure 3.7.

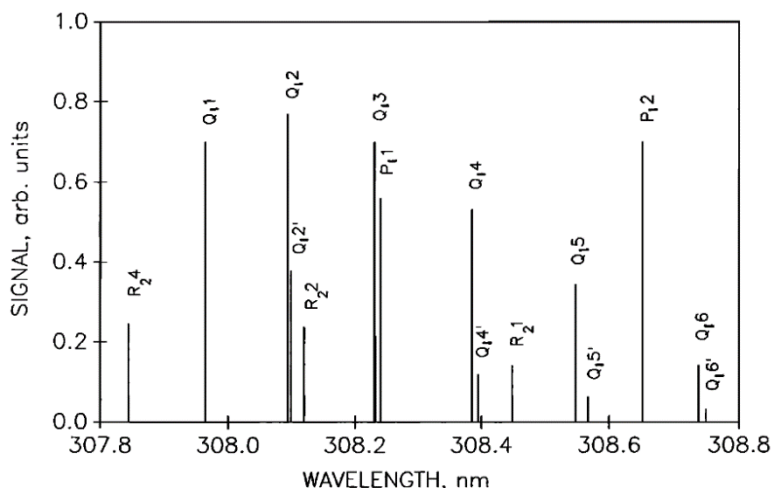


Figure 3.8.: Figure taken from Chan et al. (1990) showing the absorption spectrum of OH radicals at wavelength ~ 308 nm at pressures of ~ 5 mbar.

To measure the signal created from OH fluorescence (S_{OH}), LIF-FAGE HO_x instruments successively cycle the laser tuning from on-resonance (measuring the total signal of OH fluorescence and the signal originating from other fluorescence and electronic sources, OHF_{on}), to off-resonance (measuring all the above except the OH fluorescence, OHF_{off}) (Kubistin. 2009; Regelin et al., 2013). The net OH signal (S_{OH}) is the difference between the on-resonance and off-resonance signals, OH-WAVE (Mao et al., 2012):

$$S_{OH} = OHF_{on} - OHF_{off} \quad (3.2)$$

For the OMO-Asia airborne campaign, the HORUS dye laser was cycled 7 seconds on-resonance followed by 7 seconds off-resonance, with each consecutive off-resonance being alternated by rotating the etalon mirror ± 500 steps (~ 37 GHz) left and right of the $Q_1(2)$ transition line, see Kubistin (2009) for more information. Figure 3.9 shows the on/off signal in the first (OH) detection cell during a calibration. To determine the interference signal $S_{OH-CHEM}$, 100 sccm of propane (C_3H_8) was injected into IPI, to remove the sampled atmospheric OH. Propane is added for 42 seconds for the duration of one on-resonance measurement period, and then the propane injection system is purged by shutting of the propane injection valve and mass flow controller and injecting 1 SL min^{-1} of pure synthetic air (for ~ 1 second) to remove any residual propane from IPI. The propane injection system and then closed off from IPI for 245 seconds (equivalent of 17 on-resonance off-resonance cycles) during which both atmospheric OH and OH_{CHEM} (described in this work as, $OH_{(tot)}$) are measured. Figure 3.10, shows a typical OH and OH_{CHEM} measurement during a flight.

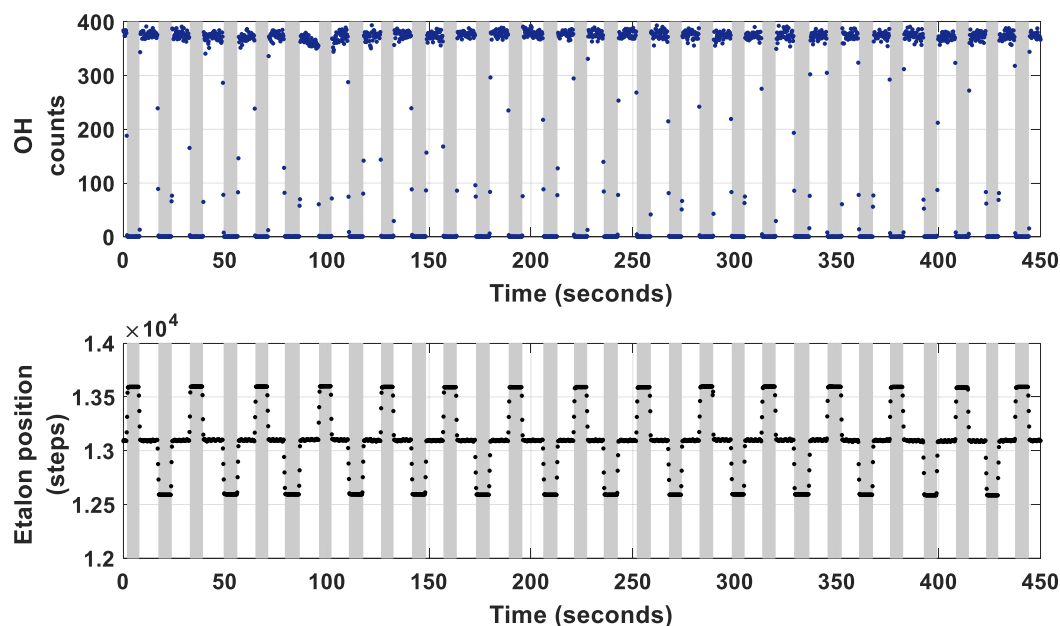


Figure 3.9.: The top panel is an example of on-resonance OH signal (unshaded) and off-resonance background signal (shaded). The bottom panel is shows the alternating laser tuning by rotating the etalon mirror ± 500 steps thus adjusting the laser system left and right of the OH radical $Q_1(2)$ transition line. Data shown here was produced during a calibration of HORUS and is of the time resolution, 5 Hz.

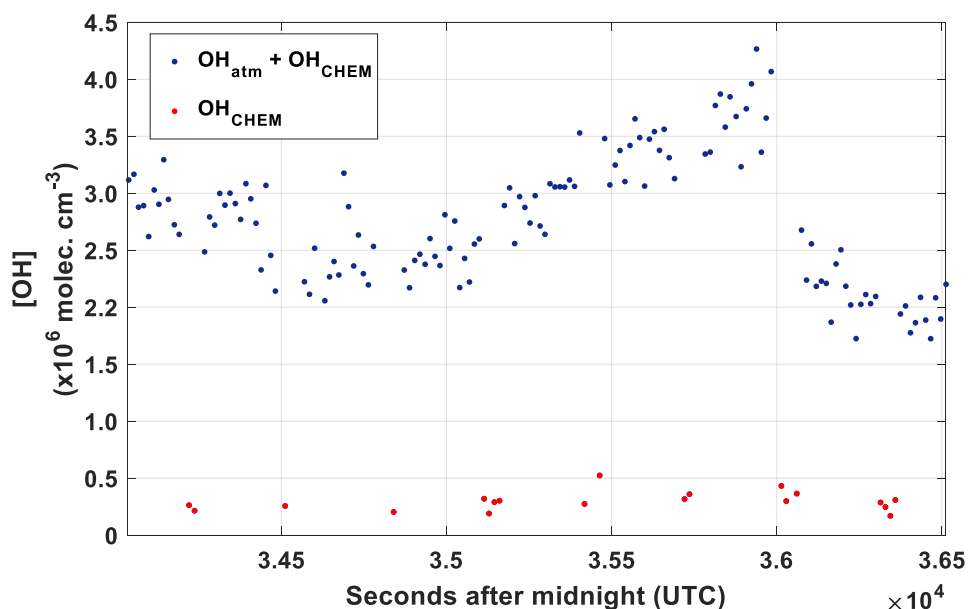


Figure 3.10.: An example of in-flight measurement of OH in the first detection cell during OMO-Asia 2015. The data presented here is averaged over 14 seconds and filtered for noise. The blue data points are the sum of atmospheric OH and OH_{CHEM} (OH_{TOTAL}) concentrations with no propane injection. The red data points is the background interference measurement of OH_{CHEM} when 100 sccm propane is injected into IPI.

HO₂ is measured indirectly in the second detection axis, through the quantitative conversion of atmospheric HO₂ to OH by injecting NO into the low-pressure conditions within HORUS, see Reaction R2.17. The detection of the subsequently produced OH (from atmospheric HO₂) and atmospheric OH occurs in the second detection axis, essentially measuring atmospheric HO_X. The net HO₂ signal (S_{HO_2}) is derived by subtracting the net OH signal from the first detection axis normalized by the ratio of the OH sensitivities in the two detection axes ($C_{OH(2)} / C_{OH}$) from the net HO_X signal (S_{HO_X}). Then S_{HO_2} is corrected by the second detection cell sensitivity towards HO₂ (C_{HO_2}) and laser power ($W_{Z_2\ pwr}$) to reach absolute HO₂ mixing ratio (see Equation 3.4).

$$[OH] = \frac{S_{OH}}{(C_{OH} \cdot W_{Z_1\ pwr})} \quad (3.3)$$

$$[HO_2] = \frac{1}{(C_{HO_2} \cdot W_{Z_2\ pwr})} \cdot \left\{ S_{HO_X} - \frac{(C_{OH(2)} \cdot W_{Z_2\ pwr})}{(C_{OH} \cdot W_{Z_1\ pwr})} S_{OH} \right\} \quad (3.4)$$

where, $W_{Z_1\ pwr}$ is the laser power in the first detection axis, $W_{Z_2\ pwr}$ is the laser power in the second detection axis and C_{OH} and C_{HO_2} are the calibrated sensitivity factors for OH and HO₂ (cts s⁻¹ pptv⁻¹ mW⁻¹) respectively. The bracketed 2 subscript distinguishes the variable in the second detection axis, from the variable of similar name that is referenced towards the first detection axis.

Vacuum system

To achieve stable pressures at 18 mbar and below within the HORUS detection cells, air is sampled through a critical orifice using a two tier vacuum system. The HORUS vacuum system involves a compressor (Type M90 roots blower, Eton) and a vacuum pump (ESDP-30 scroll pump, Edwards). The M90 roots blower compresses and increases the pressure of the sampled air in front of the scroll pump, thus enhancing the ESDP-30 pumping efficiency. Figure 3.11 shows the improved pumping efficiency of a two tier roots blower and scroll pump vacuum system, which has been proven to cope with extended running times of several weeks.

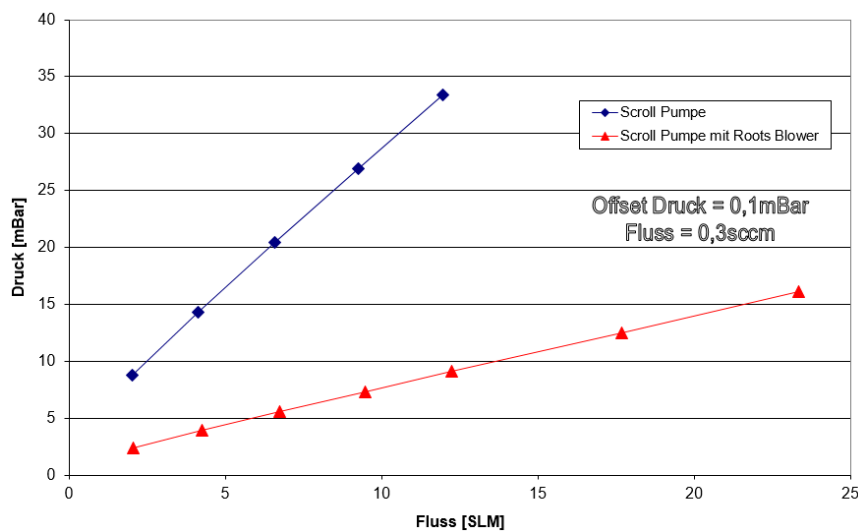


Figure 3.11.: Improved efficiency of a two tier pre-compaction vacuum system setup. Modified figure from Hens et al. (2014).

Instrument control and data acquisition unit

The HORUS instrument is controlled by an integrated PC that runs on a Debian LINUX operating system. A modular system of electronic cards, developed at the Max-Planck-Institute, Mainz is used to connect all sensors, actuators, MFCs (Mass Flow Controller), and other monitoring hardware of the HORUS instrument to the data acquisition unit. An ISA bus is then used to establish a connection to the PC. The software of HORUS is programmed in “C” and is based on a client-server archetype. The communication between the embedded PC and the HORUS hardware is controlled by the server, which collects all the instrument data and then stores it on a harddrive. In order to query data from clients and/or send actuator commands (e.g. close the propane valve) UDP sockets are used. The graphical user interface (GUI, which is programmed in MatLab, Mathworks, Inc.) is actualized as a client, meaning that the data acquisition runs independently of user input and is unaffected by potential GUI malfunctions. Additionally, the GUI can be utilized on multiple computers within the same network, without affecting the data acquisition process, via virtual network computing programmes.

4. Calibration

Note: Parts of this chapter have been taken word for word from my publication Marno et al. (2020), which forms only a fraction of the total scientific accomplishment of this thesis. The aforementioned paper can be found, as published, in chapter 8 as part of the main text of this thesis. The precise contributions, I, Daniel Marno have made to the published paper are the following: the prototyping, development and characterization of the calibration system (APACHE), the development and implementation of the COMSOL CFD simulations, and the writing of the published manuscript itself. The DOI link to the manuscript is: <https://doi.org/10.5194/amt-13-2711-2020>, and is listed in the bibliography.

4.1. Parameters affecting instrument sensitivity

As can be seen in Equations 3.3 and 3.4, the sensitivity factors are the points of proportionality between the amplitude of fluorescence signal and the native concentrations of OH and HO₂, and are found through calibrations. For ground-based HO_x instruments, calibrations are done at one pressure (typically ambient pressure) at the instrument inlet. However, airborne LIF-FAGE HO_x instruments can experience varying cell pressures, internal residence times, temperatures, and humidity during flight. This can provide an additional challenge given that sensitivities of LIF-FAGE instruments like HORUS are dependent on parameters such as the density inside the detection axis, quenching effects (e.g. sampled air water vapour concentration), the overlap of laser and fluorescence transition lines, the quality of the White Cell alignment, as well as the quantum yield of the detectors themselves. Some of those parameters are difficult to be determined separately and are often summed into one variable. Therefore, replication of such variances when calibrating in the lab are essential in acquiring the appropriate sensitivities, which resulted in the development and implementation of a new calibration device, known as the All Pressure Altitude based Calibrator for HO_x Experimentations (APACHE). Equations 4.1a to 4.1c show the terms that affect the sensitivity of OH detection at the first and second detection axes (including HO₂). As highlighted in section 3, the detection of HO₂ within HORUS is an indirect method. Therefore, terms that are labelled with HO₂ within this section are directly related to the detected OH within the second detection axis that was produced by the HO₂ + NO reaction occurring within HORUS between the two detection axes. Take note that the (2) subscript within this chapter refers to the measurement of OH at the second axis.

$$C_{OH}(P, T) = c_0 \cdot \rho_{Int}(P, T) \cdot Q_{IF}(P, T, [M]) \cdot b_c(T) \cdot [\alpha_{IPI\ OH}(P, T) \cdot \alpha_{HORUS\ OH}(P, T)] \quad (4.1a)$$

$$C_{OH(2)}(P, T) = c_1 \cdot \rho_{Int}(P, T) \cdot Q_{IF(2)}(P, T, [M]) \cdot b_c(T) \cdot [\alpha_{IPI\ OH}(P, T) \cdot \alpha_{HORUS\ OH(2)}(P, T)] \quad (4.1b)$$

$$C_{HO_2}(P, T) = c_2 \cdot \rho_{Int}(P, T) \cdot Q_{IF(2)}(P, T, [M]) \cdot b_c(T) \cdot [\alpha_{IPI\ HO_2}(P, T) \cdot \alpha_{HORUS\ HO_2}(P, T)] \cdot \eta_{conv}(P, T) \cdot [SI_{[HONO]}(P, T, [M])] \quad (4.1c)$$

where c_0 , c_1 , and c_2 are the lump sum coefficients of all the pressure independent factors affecting the HORUS sensitivity, e.g. OH absorption cross section at 308nm, the transmissivity efficiency of the White cells, the photon collection efficiency of the optical setup and quantum yield of the detectors, as well as pressure independent wall loss effects. The c_0 , c_1 , and c_2 scale to laser power and therefore are normalized by the respective measured laser power within the two White cells when calibrating, and they have the units (cts pptv⁻¹ s⁻² cm³ molec.⁻¹ mW⁻¹). ρ_{Int} is the internal molecular density within the detection axes. Q_{IF} is the quenching effect (s), which consists of the natural decay frequency of OH, excited OH decay due to collisional quenching that is dependent on pressure, temperature, and concentration of N₂, O₂, and water vapor, and the detector opening and closing gating times after the initial excitation laser pulse. Q_{IF} is calculated using the same approach as described in Faloon et al. (2004) and Martinez et al. (2010):

$$Q_{IF}(P) = \frac{1}{\Gamma} (e^{-\Gamma t_1} - e^{-\Gamma t_2}) \quad (4.2)$$

where t_1 and t_2 are the detector gate opening and closing times after the initial excitation laser pulse, which are set to 104 ns and 600 ns respectively. Γ is the excited state decay frequency (Hz), consisting of the natural decay frequency (γ_{nat}), and excited state deactivation due to collisional quenching of other molecules, mainly N₂, O₂, and water vapor, denoted as [X] in the following:

$$\Gamma = \gamma_{nat} + \sum(k_X(T) \cdot [X]) \quad (4.3)$$

The collisional rate constants (k_X) can be approximated with the temperature range of -70 °C to 50 °C (Faloon et al., 2004):

$$k_X(T) = aT^{\frac{1}{2}} - bT^{\frac{3}{2}} + c \quad (4.4)$$

The a, b, c coefficients shown in Equation 4.4 are experimentally determined (Bailey et al., 1997; Bailey et al., 1999), and are listed in Table 4.1.

Table 4.1.: The temperature dependency parameterizations of the collisional rate coefficients

Collision Gas	a (cm ³ molec. ⁻¹ s ⁻¹ K ^{-$\frac{1}{2}$})	b (cm ³ molec. ⁻¹ s ⁻¹ K ^{-$\frac{3}{2}$})	c (cm ³ molec. ⁻¹ s ⁻¹)
N ₂	-1.668 x10 ⁻¹¹	-1.731 x10 ⁻¹⁴	2.313 x10 ⁻¹⁰
O ₂	1.008 x10 ⁻¹¹	1.655 x10 ⁻¹⁴	5.129 x10 ⁻¹¹
H ₂ O	-4.017 x10 ⁻¹¹	-4.4686 x10 ⁻¹⁴	5.3137 x10 ⁻⁹

In Equations 4.1a, 4.1b, and 4.1c, the temperature dependent Boltzmann correction (b_c) term corrects for OH molecules that are in a thermally excited state within HORUS and therefore are not measurable by fluorescence excitation at 308 nm. The conversion efficiency (η_{conv}) is the percentage of HO₂ that is able to convert to OH for detection. The term $SI_{[HONO]}$ is the percentage loss of the formed OH which reacts further with NO to form HONO within HORUS. Both η_{conv} and $SI_{[HONO]}$ are pressure and temperature dependent, with $SI_{[HONO]}$ being

additionally density dependent. During flights, these terms are quantified using the internal pressures and temperatures measured within HORUS in-flight, in conjunction with NO titrations, which will be discussed within section 5. However, when calibrating HORUS in the lab, η_{conv} is kept close to 1 by injecting in excess of 30 sccm of NO, equating to an internal NO concentration of 6.3×10^{13} molec. cm^{-3} at an internal pressure of ~ 14 mbar. Furthermore, under the same conditions, $SI_{[\text{HONO}]}$ would be less than 10 %, as discussed in detail in section 5. HORUS has two different pressure and flow regimes. During flight, IPI operates across the pressure range of 180 to 1010 mbar with flows ranging 50 to 230 SL min^{-1} . After the critical orifice, the low-pressure detection regime operates across the pressure range of 3.1 to 18.4 mbar with flows of 3 to 17 SL min^{-1} during flight. Therefore, the pressure dependent transmission terms (α), which represent the fraction of OH that reaches the respective detection axes in Equations 4.1a, 4.1b, and 4.1c are calculated separately. The α_{IPI} terms represent the correction for pressure and temperature dependent OH and HO₂ wall losses within IPI. The α_{HORUS} terms represent the correction for pressure and temperature dependent OH and HO₂ wall losses within the HORUS detection axes post critical orifice. The terms that need to be determined through calibration, which are directly applied to the in-flight measurement are the pressure independent sensitivity coefficients. In the case for atmospheric OH measurements, once the c_0 coefficient is calculated, the final in-flight measured OH mixing ratio (ppt_v) is found:

$$\text{OH} = \frac{S_{\text{OH}}}{(c_0 \cdot \rho_{\text{Int}} \cdot Q_{\text{IF}} \cdot b_c \cdot [\alpha_{\text{IPI OH}} \cdot \alpha_{\text{HORUS OH}}] \cdot W_{Z_1 \text{ pwr}})} \quad (4.5)$$

As S_{OH} scales with laser power, the instrument sensitivity terms shown in the denominator in Equation 4.5, which combined have the units $\text{cts s}^{-1} \text{ppt}_v^{-1} \text{mW}^{-1}$, must also be scaled to the measured laser power ($W_{Z_1 \text{ pwr}}$) in order to acquire the absolute measurement of the OH mixing ratio. As will be shown in the following sections, the complete system is calibrated with IPI attached and operating as when it was installed in the aircraft. Therefore, the losses of OH within IPI and within the low-pressure regime of HORUS contribute to the overall calibrated C_{OH} sensitivity factor in the same way during measurement flights and calibrations. This means that once calculated separately, both of the OH transmission terms $\alpha_{\text{IPI OH}}$ and $\alpha_{\text{HORUS OH}}$ can be summarized into one term (α_{Total}).

$$\text{OH} = \frac{S_{\text{OH}}}{(c_0 \cdot \rho_{\text{Int}} \cdot Q_{\text{IF}} \cdot b_c \cdot [\alpha_{\text{Total}}] \cdot W_{Z_1 \text{ pwr}})} \quad (4.6)$$

4.2. Methods for Calibrating HO_x instrumentation

Table 4.2 shows an overview of the common techniques used to calibrate HO_x instruments. The APACHE system is based on the production of known quantified and equal concentrations of OH and HO₂ via the photolysis of water vapor in synthetic air by means of a Hg ring lamp emitting UV radiation at 184.9 nm.



Within the APACHE setup, stable water vapor mixing ratios with a variability of < 2 % were achieved by heating 300 SL min⁻¹ flow of synthetic air to 353 K before introducing deionized water via a peristaltic pump. This resulted in immediate evaporation of the deionized water into the gas phase before entering a 15 L mixing chamber. Heating of the air prevents re-condensation and humidity spikes when the pump is introducing water to the system. The water vapor content in gas flow is then diluted to around 3 mmol mol⁻¹ and mixed further through multiple additions of dry pure synthetic air via a series of mixing blocks to achieve water vapor mixing ratios at the required and desired levels. The photolysis of H₂O occurs in only one spin-allowed and energetically viable dissociation channel at 184.9 nm (Engel et al., 1992), meaning that the quantum yield of OH and H* are unified (Sander et al., 2003). Despite Reaction R4.2 being possible due to H* atoms ability to carry transitional energies of 0.7 eV at 189.4nm (Zhang et al., 2000), the fast removal of energy via Reaction R4.3 allows for the assumption that all produced H* atoms ultimately form to HO₂ (Faloona et al., 2004). The use of water photolysis as a quantifiable source for OH and HO₂ radicals in calibrations of HO_x instruments has been widely adopted in a number of studies (Heard and Pilling, 2003; Ren et al., 2003; Faloona et al., 2004; Dusanter et al., 2008; Novelli et al., 2014; Mallik et al., 2018). To quantify the known concentrations of OH and HO₂ produced by this calibration technique, the following calculation is used:

$$[\text{OH}] = [\text{HO}_2] = [\text{H}_2\text{O}] \cdot \sigma_{\text{H}_2\text{O}} \cdot F_{184.9 \text{ nm}} \cdot \phi_{\text{H}_2\text{O}} \cdot t \quad (4.7)$$

where in the OH and HO₂ concentrations are a product of photolysis of a known concentration of water vapor [H₂O]. $\sigma_{\text{H}_2\text{O}}$ is the absorption cross section of water vapor at $\lambda = 184.9 \text{ nm}$, $7.22 (\pm 0.22) \times 10^{-20} \text{ cm}^2 \text{ molecule}^{-1}$ (Hofzumahaus et al., 1997; Creasey et al., 2000). $F_{184.9 \text{ nm}}$ is the actinic flux (photons cm⁻² s⁻¹) produced by UV mercury lamp, $\phi_{\text{H}_2\text{O}}$ is the quantum yield (which is 1 at 184.9 nm (Creasey et al., 2000)) and t is exposure time (i.e. the time spent in the irradiation zone).

Table 4.2.: Various calibration techniques for HO_x instrumentation, (modified version from Marno et al. (2020)).

Technique	Method	Quoted (1σ) Uncertainty	Limitations	References
(I) Water UV-Photolysis	Described in this work	10-30%	Dependent on lamp, photon flux measurement, and absorption	(Creasey et al., 2003; Heard and Pilling. 2003; Holland et al., 2003; Ren et al., 2003; Faloon et al., 2004; Smith et al., 2006; Martinez et al., 2010; Mallik et al., 2018)
(II) Pulsed N ₂ -H ₂ O RF discharge	At low pressure (0.1 Torr); OH and NO produced using a low power RF discharge.	20%	Requires NO measurement using stable ambient air calibrations	(Dilecce et al., 2004; Verreycken and Bruggeman. 2014)
(III) Low-pressure flow-tube RF discharge	OH radical production by titration of H atoms with NO ₂ . Known amount of H atoms produced using microwave discharge using low pressure flow tube	30%	Stable ambient air calibrations	(Stevens et al., 1994)
(IV) Continuously Stirred Tank Reactor and decay of select hydrocarbons	OH produced through UV-irradiation of humidified air flow with injection of a specific Hydrocarbon (1,3,5-trimethylbenzene, C ₉ H ₁₂) and NO. Recent studies have used Cyclohexane, n-pentane and iso-butene Concentrations of OH relates to decay rate of the Hydrocarbon	24-36%	Time intensive, systematic wall loss of OH in reactor	(Hard et al., 1995, 2002; Winiberg et al., 2015)
(V) Steady-State O ₃ -alkene	A steady state OH concentration produced from ozonolysis of a known concentration of an alkene	42%	Time consuming, large uncertainties compared to other methods	(Heard and Pilling. 2003; Dusanter et al., 2008)
(VI) Laser photolysis of Ozone	Photolysis of O ₃ with 284 nm light producing O(¹ D). Which then reacts with H ₂ O producing OH	40-50%	Requires large apparatus	(Tanner and Eisele. 1995)

4.3. APACHE design and characterization

Figure 4.1 shows the overview of the new APACHE calibration system. In front of the APACHE inlet, there are a series of mixing blocks installed, where multiple stages of dry synthetic air additions are injected into a controlled humidified air supply to ensure that there is thorough mixing of water vapor before being measured by a LI-COR 6262 CO₂/H₂O (Figure 4.1a). This humidified air is fed into a large MFC. The construction of APACHE chamber itself is shown in Figure 4.1b. The first APACHE section contains the diffuser inlet with a sintered filter (bronze alloy, Amtag, filter class 10) that is 2 mm thick with a pore size of 35 μm . The purpose of the sintered filter is to initialize a homogeneous turbulent flow regime and further improve the mixing of water vapor in front of the UV ring lamp, which is critical for the calibrations, as will be shown in later sections. The water photolysis section comprises of a low-pressure, 0.8 A, mercury ring lamp from uv-technik (data sheet in see Appendix A), which produces a constant radial photon flux at $\lambda = 184.9 \text{ nm}$, and is situated 133 mm after the sintered filter. The UV lamp is separated from the main APACHE chamber by an airtight quartz window. Between the lamp and the quartz window there is a black anodized aluminum band with thirty 8 mm apertures that reduce the amount of UV flux entering APACHE and limit the illumination area size. The IPI system is clamped down 169.5 mm behind the photolysis section, causing the sample flow through the IPI nozzle to be perpendicular to the airflow passing through APACHE. The nozzle protrudes 51.5 mm into the APACHE cross section and the union between APACHE and IPI is made air tight with the use of O-rings. Opposite the IPI nozzle, there is an airtight block attachment comprising of a series of monitoring hardware. A pitot tube attached to an Airflow PTSX-K 0-10Pa differential pressure sensor (accuracy rating of 1 % at full scale, 1σ) is installed to monitor internal flow speeds within APACHE. A 3-kOhm NTC-EC95302V thermistor to monitor the air temperature, and an Edwards ASG2-1000 pressure sensor (with an accuracy rating of $\pm 4 \text{ mbar}$, 2σ) monitors the static air pressure are also installed to the attachment block. There are two additional adjacent one-quarter inch airtight apertures in the block, which can be opened to allow other instrumentation to be installed.

4.3.1. Pressure control

The operational pressure range of APACHE used to calibrated HORUS was 227 – 900 mbar, with precision of $\pm 0.1\%$ (1σ) and accuracy of $\pm 2\%$ (1σ), which required mass flows ranging from 200 to 990 SL min^{-1} . This was achieved through the combined use of an Edwards GSX160 scroll pump to control the volume flow and a Bronkhorst F-601A1-PAD-03-V MFC to control the mass flow of air entering APACHE. Air speeds within APACHE ranged from 0.9 to 1.5 m s^{-1} with air temperatures ranging from 282 to 302 K. The temperature inside APACHE is not directly controlled. However, the air temperatures were constantly measured throughout the APACHE calibration device and HORUS. Therefore, any term that is temperature dependent is characterized by using the corresponding measured temperature values.

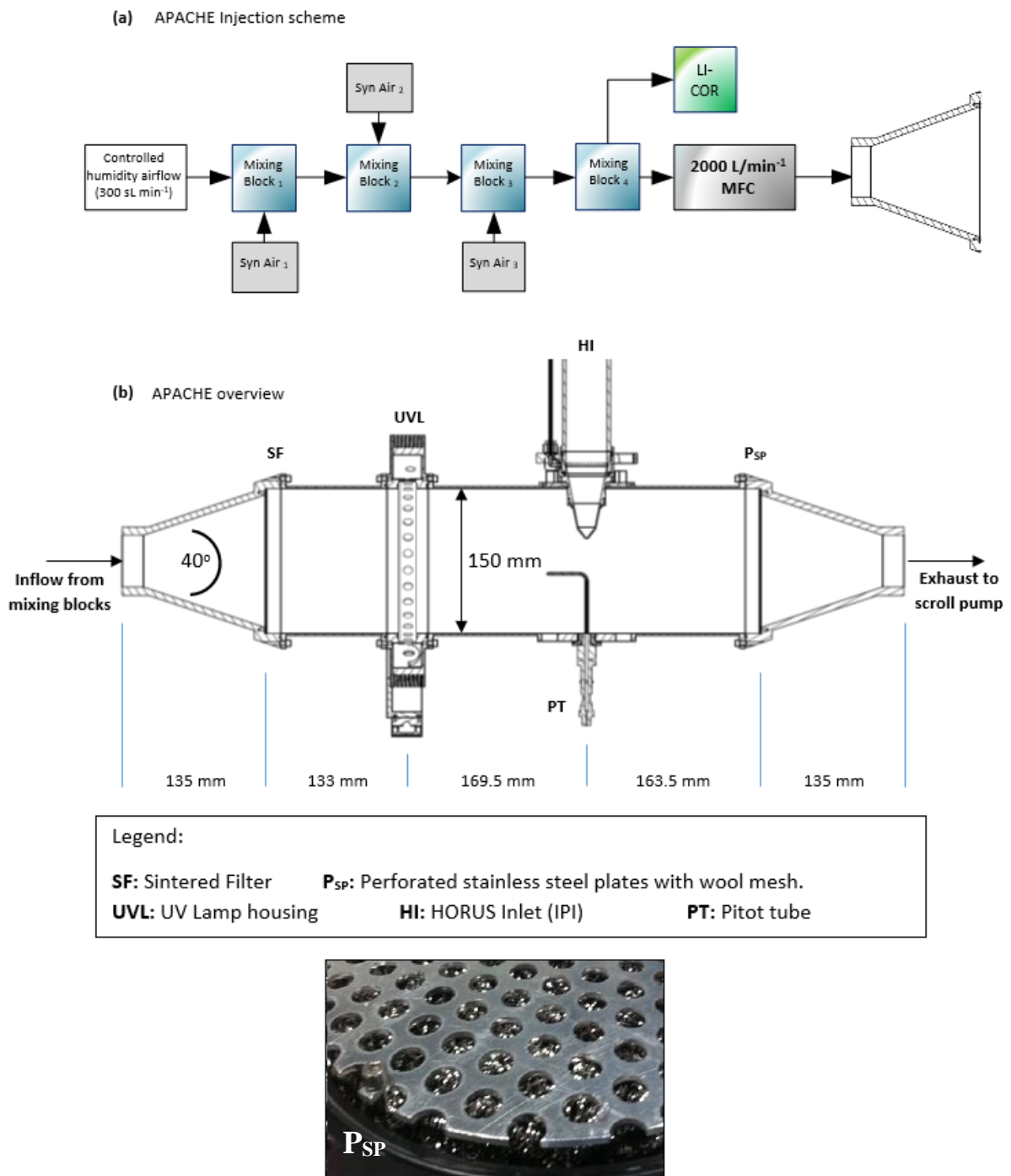


Figure 4.1.: A schematic of the APACHE system and the pre-mixing setup used in the lab to calibrate the HORUS airborne instrument. The bottom panel shows the perforated stainless steel plates with wool mesh that forms part of the APACHE exhaust. (Figure taken from Marno et al. (2020)).

4.3.2. Flow conditions

As with any calibration device, flow conditions must be characterized to inform subsequent methodology and calibrations. For APACHE, experimental and model tests were performed to determine whether the combination of the sintered filter, and the stainless steel perforated plates and wool arrangement could provide a homogeneous flow. Therefore, under operation the air masses passing across the irradiation zone have the same flow speed and thus exposure times irrespective of where they are in the APACHE cross section. The tests focused on resolving two key factors:

- (i) How uniform are the flow speed profiles and exposure times in respect to the APACHE cross section.
- (ii) The impact of wall losses.

Model simulations can provide an indication of the development and scale of boundary air conditions where air parcels experience extended contact time with the interior walls of APACHE, and so have pronounced OH wall losses. Thus highlighting potential pressure and flow conditions where there is sufficient time between the photolysis zone and the IPI nozzle to allow APACHE boundary air to expand into and influence the OH content of the air sampled by HORUS.

Computational Fluid Dynamics (CFD) Modelling

A computational fluid dynamics (CFD) model developed by COMSOL multiphysics was used to simulate the flows inside APACHE and the IPI nozzle. The module within the COMSOL CFD model that was used within this study is based on the Reynolds Averaged Navier-Stokes (RANS) model (COMSOL. 2019). The simulated flows were defined as incompressible within the standard k-epsilon turbulence sub-model as it is applicable when simulating flow speeds below 115 m s^{-1} (COMSOL. 2019). An extra fine gridded mesh of a perforated plate with a high solidity ($\sigma_s = 0.96$) was implemented within the turbulence model to generate the turbulence and replicate the flows created by the bronze sintered filter (Roach. 1987). The model simulations were constrained with the measured pressures and temperature within APACHE and IPI.

Flow speed profiles

When performing calibrations, the pressures within HORUS had to be controlled and monitored in order to replicate in-flight conditions. The pressure inside APACHE is equivalent to the in-flight static pressures measured within the external shroud. The pressure within the detection axes depends on the pressure at the IPI nozzle and the efficiency of the pumps. The airflow passing through IPI is dependent on the pressure gradient between the shroud and the ambient pressure at the IPI exhaust. When calibrating, this translates to the APACHE pressure and pressure in front of the XDS 35 scroll pump (post IPI blower). During OMO-Asia 2015, the exhausts of all blowers and pumps that make up the HORUS exhaust system were attached to the passive exhaust system of the aircraft and were exposed to ambient pressure. Therefore, throughout the calibrations the same blowers and pumps that were installed on HALO were used in the lab. Additionally, the pressure at the exhausts for every blower and pump involved

in the HORUS instrument were matched to the respective ambient pressures measured in-flight by means of attaching a separate pressure sensor, needle valve and XDS 35 scroll pump system. To ensure that within the lab, the pumps are powered by the same power as was on the aircraft, a three-phase mission power supply unit was used during testing and throughout the calibrations. Figure 4.2 shows the described lab setup.

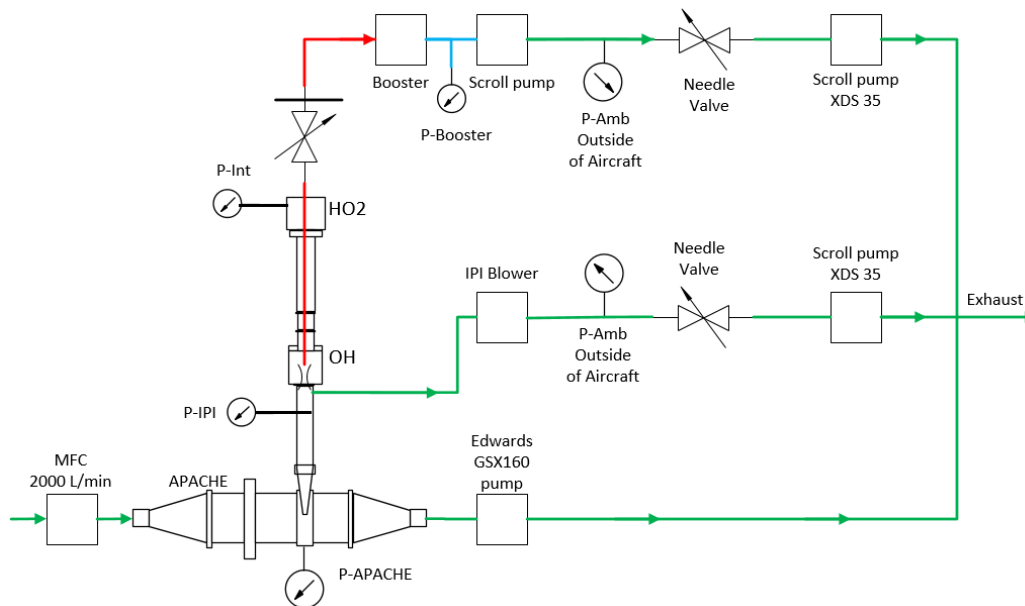


Figure 4.2.: A schematic showing the full experimental setup within the lab for calibrations. The additional needle valves, pressure sensors and XDS 35 scroll pumps are labelled thusly, and were attached to the exhausts of all pumps and blowers of this HORUS instrument to match in-flight pumping efficiencies when calibrating with APACHE. The low-pressure region within HORUS (red lines), the pressure monitoring line between the booster and scroll pump that drive the HORUS sample flow (blue lines), and the external gas lines (green lines) show the respective air flow direction and pathways of the setup. Figure was taken from Marno et al. (2020)).

The HORUS instrument samples air from the core of the APACHE flow and draws a fraction of the total air flow that passes through APACHE, as shown in Figure 4.3. At 900 mbar, the HORUS instrument takes ~ 20 % and at 275 mbar HORUS takes ~ 30 % of the total volume flow that enters APACHE. To confirm that this variable volume flow into HORUS does not disturb the flow speed profile within APACHE, measurements of the flow speed profile were performed using the Prandtl pitot tube that was installed directly opposite the IPI nozzle. The Prandtl pitot tube can be re-positioned from flush against the internal wall up to 60.5 mm into the APACHE cavity (15 mm from the center of APACHE). Figure 4.4 shows the measured flow speed profile (blue data points) when the APACHE pressure was 920 mbar.

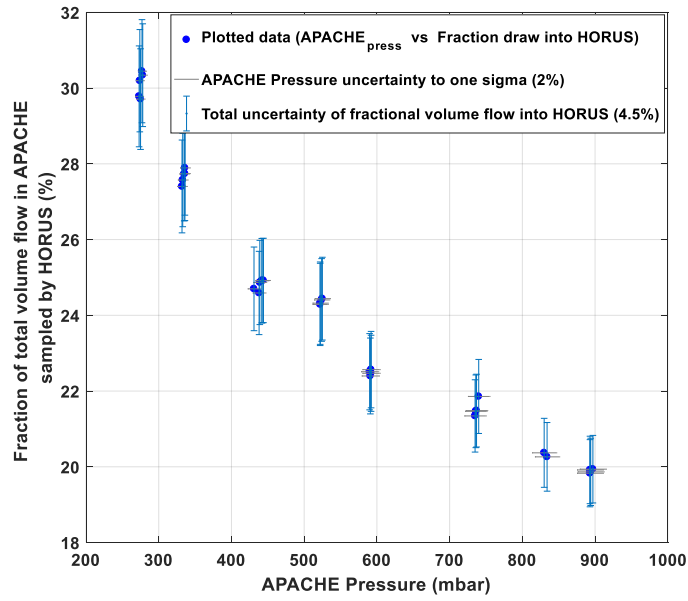


Figure 4.3.: The percentage of the total volume flow that enters APACHE that is sampled by HORUS, plotted as a function of pressure within APACHE. All error bars are quoted to 1σ of the measurement uncertainty of the temperature and pressure sensors involved. Figure taken from Marno et al. (2020)).

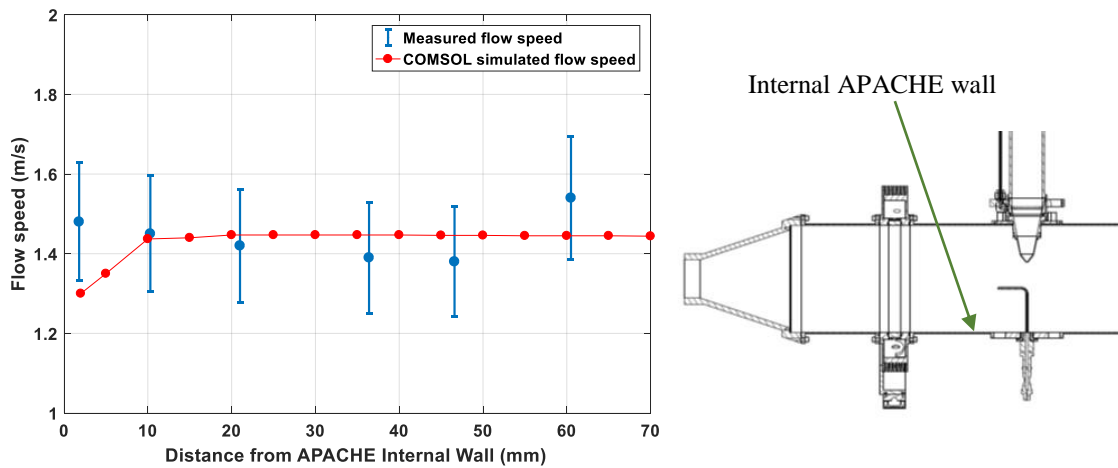


Figure 4.4.: The measured (blue) and COMSOL simulated (red) flow speed profiles within APACHE, at 920 mbar. The x-axis is the distance from the internal wall of APACHE. The error bars are quoted to 2σ . (Modified version taken from Marno et al. (2020)).

As the distance between the APACHE wall and the pitot tube inlet increased, there was no observed significant change in the flow speed. The largest observed change occurred between 46.6 mm and 60.5 mm where the flow speed increased by 0.16 m s^{-1} . This change is not significant, as it equates to only 77.2 % of the combined uncertainty of the 46.6 and 60.5 mm measurements, $\pm 0.21 \text{ m s}^{-1}$ (2σ). However, when performing the speed profile measurements at lower pressures, the measured pressure difference was close to or in some cases below the resolution of the differential pressure sensor. Therefore, COMSOL CFD model simulations constrained by pressure and temperature measurements were performed to gain a better understanding of the flow speed profiles at all pressures of interest.

Figure 4.4 shows the comparison of the CFD flow speed profile with the measured flow speed profile at 920 mbar (the pressure at which the highest confidence in the measurements was achieved). Overall, the CFD flow speed profile did not differ significantly from measured profile; only at the boundary ($< 4 \text{ mm}$ away from the APACHE wall), did the model disagree significantly from measurements. The model predicted a flow speed of 1.3 m s^{-1} , which is 6 % lower than the minimum extent of the 2σ measurement uncertainty (1.38 m s^{-1}). This disagreement could be due to the uncertainty in the boundary conditions that were parameterized within the COMSOL CFD simulations. However, as this disagreement is occurring within a region that ultimately does not influence the OH content of air entering HORUS, as will be described in more depth in the following sections, such disagreements between modelled and measured flow speeds at distances less than 4 mm from the APACHE wall were ignored. Figure 4.5 shows the simulated flow speeds within APACHE and the IPI nozzle across six discrete pressures. From Figure 4.5, it is clear that the pressure dependent variable fractional sample flow of HORUS does not significantly impact the homogenous air flow speed profile within APACHE, particularly (and crucially) within the UV irradiation zone.

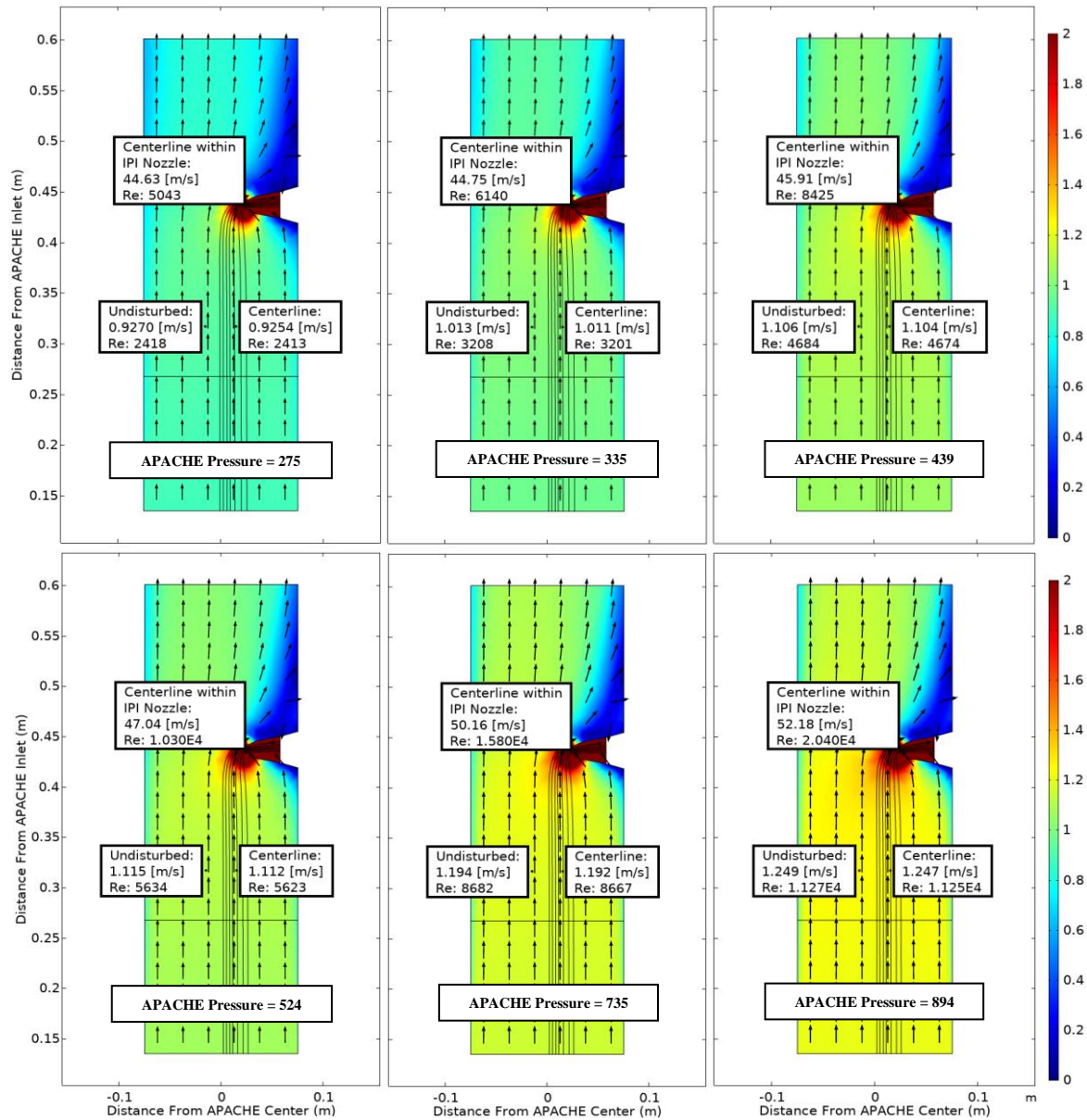
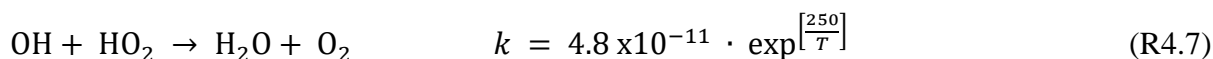
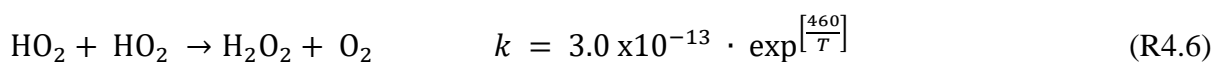
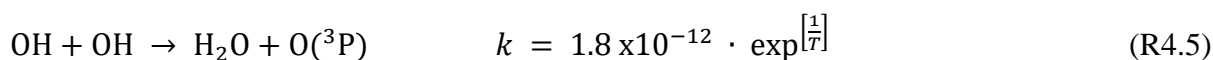


Figure 4.5.: COMSOL Multiphysics output data, simulating the flow speed conditions at six discrete pressures within APACHE ranging from 275 to 894 mbar. The data shown here are calculated flow conditions between the sintered filter and the first perforated stainless steel plate, i.e. the main APACHE chamber. The color is the flow speed in m s^{-1} . The black lines represent the streamlines created by the HORUS sample flow, and the black arrows depict the flow direction of the air passing through APACHE and the IPI nozzle. The x-axis is the distance from the center of APACHE in meters. The y-axis is the distance from the APACHE inlet. The “centerline within the IPI nozzle” tags show the flow conditions in the center of the fully formed flows after the IPI pinhole. The “undisturbed” tags show the flow conditions that are not influenced by HORUS sampling, and the “centerline” tags show the flow conditions in the center of the streamlines (i.e. the area of airflow influenced by HORUS sampling). The horizontal black line at 0.27 m marks the center of the UV irradiation zone. Figure taken from Marno et al. (2020)).

The centerline flow speeds (i.e. the airflow influenced by HORUS sampling) differs by less than 0.1 % when compared to the undisturbed flow (i.e. the airflow not influenced by HORUS sampling). Even at 275 mbar when HORUS is drawing the highest percentage of the total volume flow entering APACHE, the difference between centerline and undisturbed airflows is insignificant. The high calculated Reynolds numbers ($Re > 2300$) support the statement that a turbulent flow regime is created and that the small pores of the sintered filter release a uniform distribution of small turbulent elements across the complete diameter of APACHE, which remain all the way up to the IPI nozzle.

4.3.3. Influence of HO_x wall losses in APACHE

Chemistry was also implemented within COMSOL, to simulate OH and HO₂ levels within APACHE and investigate the potential impact of wall losses on HO_x content within air being sampled by HORUS under calibration conditions. For each simulation, the OH and HO₂ concentrations were initialized to zero, and HO_x losses at the APACHE wall surfaces were fixed to 100 %. The radial photolytic production of OH and HO₂ at the lamp was calculated using Equation 4.11; details of the different variables making up the equation are described in section 4.4. Proxy values of 5.1×10^{14} photons $\text{cm}^{-2} \text{s}^{-1}$ for the flux intensity entering APACHE and 8×10^{-20} $\text{cm}^3 \text{molec.}^{-1}$ for γ_{O_2} were used to calculate the radial OH and HO₂ production at the lamp. For all simulations, the HO_x radical-radical recombination loss reactions (Reactions R4.5 – R4.7) were taken from Burkholder et al. (2015), with temperature (T) in Kelvin:



The recommended molecular diffusion coefficient of OH_{Dm} in air (Tang et al., 2014) was implemented within the simulations:

$$\text{OH}_{Dm} = 179 (\pm 20) \text{ Torr cm}^2 \text{ s}^{-1} \quad (239 \pm 27 \text{ hPa cm}^2 \text{ s}^{-1})$$

In literature, there have been no reports of successful accurate measurements of HO₂ diffusivity coefficients in air. However, calculations of HO₂ diffusion coefficients in air have been performed using models such as the Lennard-Jones potential model (Ivanov et al., 2007). Ivanov et al. (2007) had performed a series of measurements and Lennard-Jones potential model calculations to quantify the polar analogue diffusion coefficients for OH, HO₂ and O₃ in both air and pure helium. The Lennard-Jones potential model calculated OH and O₃ diffusion coefficients in air agreed well, within the given uncertainties, with the recommended measurement values in Tang et al., (2014). Therefore, in order to best replicate HO₂ diffusivity within this study, the diffusion coefficient of HO₂ in air taken from Ivanov et al. (2007) was used:

$$\text{HO}_2_{Dm} = 107.1 \text{ Torr cm}^2 \text{ s}^{-1} \quad (142.8 \text{ hPa cm}^2 \text{ s}^{-1})$$

The COMSOL CFD model calculated OH mixing ratios (ppt_v) are shown in Figure 4.6. Mixing ratios are shown in order to most clearly show how HO_x content, as the air flows along the length of APACHE, changes with changing APACHE pressure. In Figure 4.6, irrespective of APACHE pressure, the boundary air masses where wall losses are 100 % do not have sufficient time to expand into the streamlines of the HORUS sample flow, and therefore do not influence the HO_x content entering HORUS. The lateral exchanges between boundary air at the APACHE walls and the air sampled by HORUS are suppressed due to the preservation of the small turbulence regime inside APACHE. Table 4.3 shows the evolution of OH along the length of APACHE, within the streamlines created by the HORUS sample flow across the six discrete pressures depicted in Figure 4.6.

L and R respectively in Table 4.3 represent the CFD model calculated OH mixing ratios on the left-most and right-most HORUS sample flow streamline shown in Figure 4.6. C represents the OH mixing ratio in the center of the HORUS sample flow streamlines. The mean mixing ratio for each APACHE pressure does not change significantly as the distance from the lamp increases. However, the standard deviation of the OH mixing ratios across the HORUS sampling streamlines decreases as the distance from the lamp increases, thus signifying that the air is homogenizing.

Figure 4.6 and Table 4.3 show that the main loss process influencing HO_x entering IPI is the wall loss occurring at the IPI nozzle itself. The CFD simulations calculate around 22.2 (\pm 0.8) % (1σ) of OH and HO₂ is lost at the IPI nozzle. However, this value does not significantly change with pressure, indicating that HO_x loss at the IPI nozzle is pressure independent. As described in section 4.1, the pressure independent sensitivity coefficients are lump sum values that contain the pressure independent wall losses for OH and HO₂. Therefore, the characterized pressure independent sensitivity coefficients, shown in section 4.5, will contain the experimentally resolved OH and HO₂ losses at the IPI nozzle.

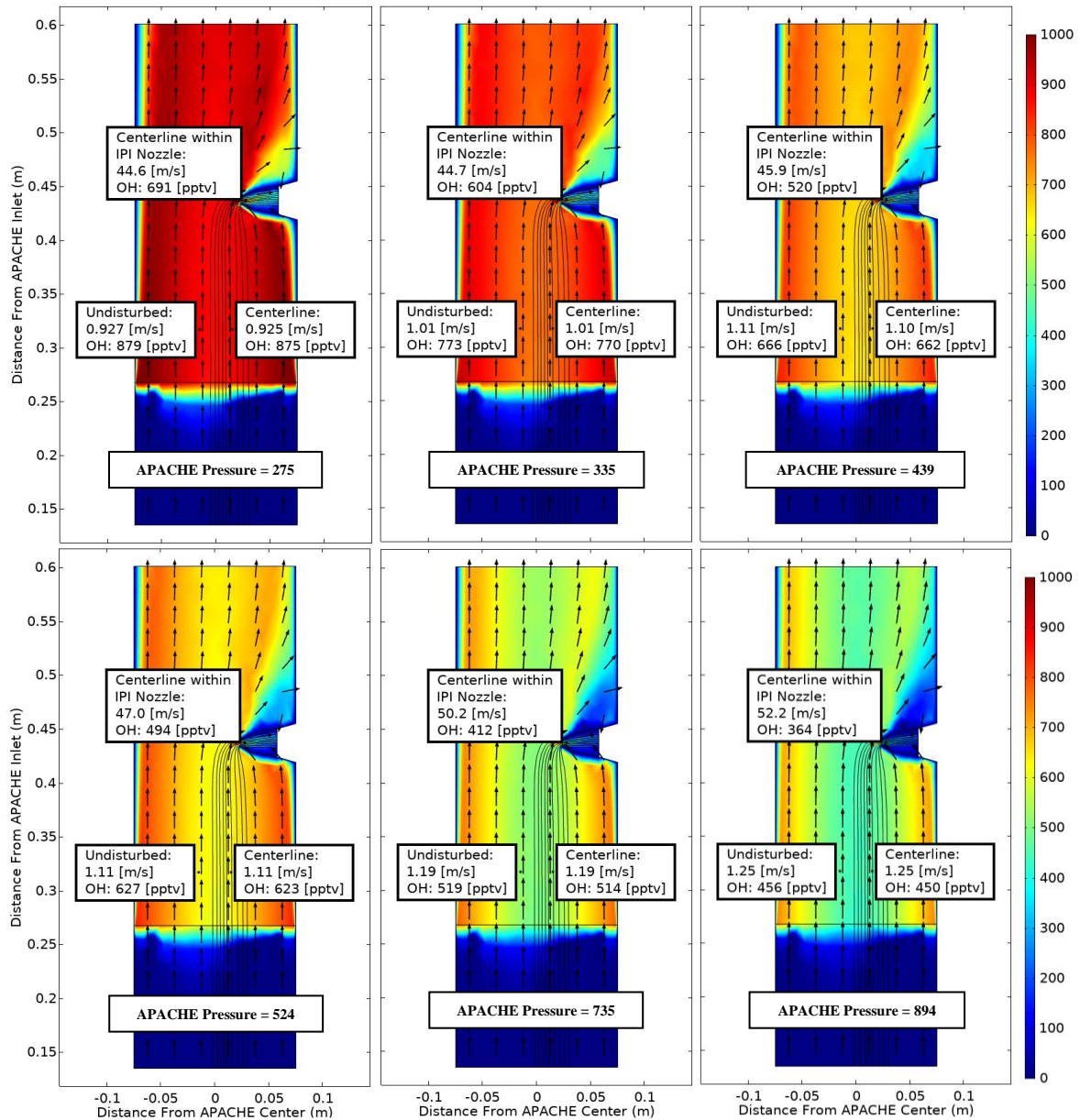


Figure 4.6.: COMSOL Multiphysics output data, simulating OH conditions at six discrete pressures within APACHE ranging from 275 to 894 mbar, between the sintered filter and the first perforated stainless steel plate. The color is OH mixing ratio (pptv), with initial OH production occurring at the lamp (0.27 m from APACHE inlet), using Equation 4.11, with water vapour mixing ratios kept constant at $3.2 \text{ mmol mol}^{-1}$ and Proxy values of $5.1 \times 10^{14} \text{ photons cm}^{-2} \text{ s}^{-1}$ for the flux intensity entering APACHE and $8 \times 10^{-20} \text{ cm}^3 \text{ molec.}^{-1}$ for γ_{O_2} . The black lines are the streamlines created by the HORUS sample flow. The black arrows depict the flow direction. The x-axis is the distance from the center of APACHE in meters. The y-axis is the distance from the APACHE inlet. The “centerline within IPI nozzle” tags represent the flow speed and OH mixing ratio in the center of the fully formed flows within the IPI nozzle. The “undisturbed” tags show the OH and flow conditions in air not sampled by HORUS. The “centerline” tags show the OH and flow conditions in the center of the streamlines created by HORUS sampling. The figure was taken from Marno et al. (2020)).

Table 4.3.: The evolution of OH within the streamlines created by HORUS sampling as depicted in Figure 4.5 at six pressures along the length of APACHE. The L term is the OH mixing ratio on the left most streamline, C is the OH mixing ratio in the center of the streamlines, and R is the OH mixing ratio on the right most streamline. The centerline within IPI nozzle column shows the calculated OH mixing ratios in the center of the fully formed flow within the IPI nozzle. All standard deviations are quoted to 1σ . Table taken from Marmo et al. (2020)).

APACHE Pressure (mbar)	OH (pptv) At the lamp				OH (pptv) 4.2 cm from lamp				OH (pptv) 8.4 cm from lamp				OH (pptv) 12.8 cm from lamp				OH (pptv) 2 cm before HORUS Inlet				In Centerline within IPI Nozzle (pptv)	
	L	C	R	Mean	L	C	R	Mean	L	C	R	Mean	L	C	R	Mean	L	C	R	Mean		Std (1 σ)
894	438	445	513	465	442	446	507	465	438	455	500	464	442	456	501	466	445	457	490	464	30.8	23.3
735	502	508	572	527	506	509	567	527	502	519	560	527	507	519	562	529	509	521	550	527	28.9	21.1
524	611	617	672	633	615	619	668	634	613	627	660	633	617	628	664	636	619	629	651	633	24.1	16.4
439	652	657	706	672	656	659	702	672	654	666	698	673	657	667	699	674	660	669	686	672	22.7	13.2
335	760	765	805	777	764	766	801	777	762	773	799	778	766	774	803	781	768	776	788	777	19.0	10.1
275	866	871	907	881	870	872	907	883	869	879	904	884	873	880	905	886	875	882	889	882	18.0	7.0

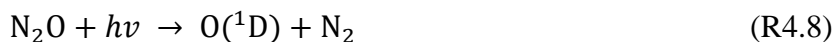
4.4. Characterization of UV conditions in APACHE

As described previously, the UV ring lamp in APACHE is housed within a mount with one side facing into the APACHE chamber. Between the lamp and the quartz wall (which forms part of the internal surface of APACHE chamber within the irradiation zone), there is an anodized aluminum band with thirty 8 mm apertures. The housing was flushed with pure nitrogen to purge it of any present O₂ before the lamp was turned on. The nitrogen flushing was kept on continuously thereafter to ensure the housing remains purged of O₂. Calibrations began once the lamp reached stable operation conditions, i.e the relative flux emission of the lamp reading of the photometer located in the UVL on the underside of the APACHE chamber (see Figure 4.1b) was constant. The flux (F_{β}) entering APACHE is not the same as the flux experienced by the molecules sampled by HORUS (F). Factors influencing the ratio between F_{β} and F are:

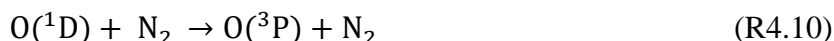
- (i) Absorption of light by O₂, which has a strong absorption cross section at 184.9 nm, and the density of O₂ changes drastically inside APACHE when calibrating at different pressures.
- (ii) The variable radial flux, which varies on the geometric setup of the ring lamp and the location within the irradiation cross section where the molecule is passes through.

To resolve these factors, two actinometrical methods were performed and compared. The main advantage of using actinometrical methods to calculate flux (F) is that F is derived directly from the actual flux experienced by the molecules themselves when passing through the APACHE chamber.

The first actinometrical method (A) involved using the HORUS instrument as a transfer standard in order to relate the flux of a pre-calibrated Hg Pen-Ray lamp to the flux entering APACHE (F_{β}). This required first calibrating the HORUS instrument using a pre-characterized ground-based calibration device (Martinez et al., 2010). The pre-calibrated Pen-Ray lamp flux (ϕ_0) is calculated from the measured NO concentrations produced by irradiating a known mixture of N₂O in nitrogen and helium carrier gases (Edwards et al., 2003; Martinez et al., 2010). N₂O photodissociates under 184.9 nm radiation that produces O(¹D) atoms:



which are then quenched by collisions, or react with N₂ or N₂O (Sander et al., 2006).



Given that the influence of R4.14 is so small compared to the other reactions (Vranckx et al., 2008) and the branching ratio between R4.12 and R4.13 is well known (Burkholder et al., 2015), the pre-calibrated Hg Pen-Ray lamp flux (ϕ_0) (with helium as a carrier gas) is calculated:

$$\phi_0 = \frac{(k_a [\text{N}_2][\text{M}] + k_b [\text{N}_2] + k_c [\text{N}_2\text{O}] + k_d [\text{N}_2\text{O}][\text{NO}])}{2k_d [\text{N}_2\text{O}]^2 \sigma_{\text{N}_2\text{O}} f_{\text{N}_2\text{O}}} \quad (4.8)$$

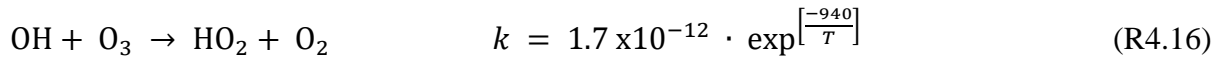
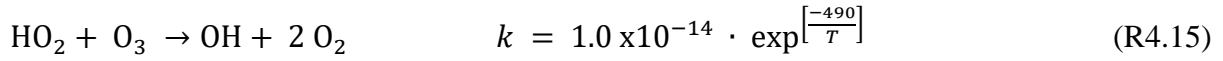
where $\sigma_{\text{N}_2\text{O}}$ is the N_2O absorption cross section at 184.9 nm and $f_{\text{N}_2\text{O}}$ is the correction factor that accounts for the flux reduction via absorption by N_2O . A TEI NO monitor measures the NO concentration. For more details on how the ground calibration device is characterized using the N_2O photolysis, see Martinez et al. (2010). Ultimately, ϕ_0 was calibrated to be 1.27×10^{13} photons $\text{cm}^{-2} \text{s}^{-1}$.

In order to use the pre-characterized ground based calibration system (with the pre-calibrated Hg Pen-Ray lamp installed) to calibrate the airborne HORUS instrument, one key adaption was performed. The pre-characterized ground based calibration device is designed to supply only 50 SL min^{-1} , however the airborne HORUS instrument is optimized for high altitude flying and IPI draws up to 200 SL min^{-1} and the detection axes are at ~ 18 mbar when running with ground-level ambient pressures of ~ 1000 mbar. Therefore, the critical orifice diameter of HORUS was changed from the airborne configuration of 1.4 mm to a 0.8 mm on-ground* configuration, refer back Figure 3.3 to see where the critical orifice is located inside HORUS. This reduced the internal pressure within HORUS from 18 to 3.5 mbar, thus optimizing the peak sensitivity of the HORUS on-ground* configuration towards OH when ambient ground level pressures are at ~ 1000 mbar. Additionally, the reduction of the internal pressure to 3.5 mbar, prevents a detectable interference of HONO formation on the HO_2 signal by inhibiting the termolecular reaction R2.33, thus improving the calibration of the HORUS on-ground* HO_2 sensitivity. More information regarding HONO formation in HORUS will be discussed later in section 5. The IPI system was also switched to passive (i.e. the exhaust line from IPI to the IPI blower was capped) in order to reduce the sample flow through the IPI nozzle to a level that the ground based calibration device is capable of providing.

Note: the same initial 1.4 mm diameter critical orifice that was used during the airborne campaign was reinstalled for the direct calibrations of the airborne HORUS system with the characterized APACHE chamber in section 4.5.

Through calibration using the pre-characterized ground based calibration system with the pre-calibrated Hg Pen-Ray lamp installed, the HORUS on-ground* sensitivities at 1010 mbar for OH and HO_2 were $13.7 (\pm 1.9)$ cts s^{-1} pptv $^{-1}$ mW $^{-1}$ and $17.9 (\pm 2.5)$ cts s^{-1} pptv $^{-1}$ mW $^{-1}$ respectively, the uncertainties are quoted to 1σ . This sensitivity was then used to calculate the OH and HO_2 concentrations at the IPI nozzle with the APACHE system installed and operating at 1010 mbar. To ensure that the flows in APACHE were stable during calibration at this high pressure, the Edwards GSX160 scroll pump was disengaged. The water vapor mixing ratios were kept constant (~ 3.1 mmol mol $^{-1}$), and oxygen levels were varied by adding different pure N_2 and synthetic air mixtures into the mixing blocks through the use of MFCs. The OH and

HO₂ concentrations at the IPI nozzle were 1.41 (± 0.01) and 1.32 (± 0.01) x 10¹⁰ molec. cm⁻³ respectively when water vapor mixing ratio of 3.1 mmol mol⁻¹ in synthetic air was introduced into APACHE. The quoted uncertainties are the measurement variability at the 1σ level. Once OH and HO₂ concentrations at the IPI nozzle were resolved, the OH and HO₂ concentrations at the lamp were then back calculated correcting for radical-radical loss reactions (R4.5 to R4.7) and HO_x reactions with O₃ (R4.15-R4.16) (Burkholder et al., 2015) with temperature (*T*) in Kelvin.



With the Edwards GSX160 scroll pump disengaged, the internal volume flow inside APACHE was 984.1 L min⁻¹, causing the transit time between the UV irradiation zone and the IPI nozzle to be 0.18 seconds, which results in chemical losses of 30 to 37 % for OH and HO₂, depending on oxygen concentration. When accounting for these chemical losses, the calculated OH and HO₂ concentrations at the lamp, at 1010 mbar, are 2.0 (± 0.02) x 10¹⁰ molec. cm⁻³ and 1.9 (± 0.02) x 10¹⁰ molec. cm⁻³ respectively. The photon flux experienced by the air sampled by HORUS (*F*_{184.9 nm}), is quantified using the OH and HO₂ concentrations stated above, and ranged from 3.8 x 10¹⁴ photons cm⁻² s⁻¹ to 6.7 x 10¹⁴ photons cm⁻² s⁻¹ depending on oxygen concentrations and the chemical losses. As described before, Equation 4.7 shows how OH production at the lamp is calculated:

$$[\text{OH}] = [\text{H}_2\text{O}] \cdot \sigma_{\text{H}_2\text{O}} \cdot F_{184.9 \text{ nm}} \cdot \phi_{\text{H}_2\text{O}} \cdot t \quad (4.7)$$

where *F*_{184.9 nm} is the actinic flux experienced by the water molecules as they pass through the irradiation zone, which is dependent on the attenuation of the flux entering APACHE (*F*_β) by water vapor and O₂ molecules. The absorption cross section of water vapor is constant across the 184.9 nm Hg emission linewidth and does not change with varying water vapor and O₂ column density. However, the effective absorption cross section of O₂ (*σ*_{O₂}) changes significantly at 184.9 nm within the Hg lamp emission linewidth and with varying O₂ column density (Creasey et al., 2000). Therefore, *σ*_{O₂} is dependent on O₂ concentration, and the ring lamp linewidth (temperature and applied amperage dependent). Since the actinometrical experiments and the APACHE calibrations were performed once the lamp reached thermal steady state, and the current applied to the lamp (0.8 A) was always kept constant, any effect on *σ*_{O₂} regarding the ring lamp linewidth does not need to be discussed further. The relationship of *F*_{184.9 nm} to *F*_β can be calculated using Beer-Lambert principles:

$$F_{184.9 \text{ nm}} = F_{\beta} \cdot e^{-(\gamma_{\text{H}_2\text{O}}[\text{H}_2\text{O}] + \gamma_{\text{O}_2}[\text{O}_2])} \quad (4.9)$$

where *F*_β is the flux intensity entering APACHE from ring lamp, with:

$$\gamma_{\text{O}_2} = R_{\beta} \cdot \omega \cdot \sigma_{\text{O}_2} \quad (4.10)$$

where *γ*_{O₂} is an effective term that is a product of the terms shown in Equation 4.10. *R*_β is the radial distance between the sampled air parcel and the ring lamp of APACHE. *ω* is

correction factor which is the integrated product of the absorption cross section and the ring lamp's emission line as modified by extent of absorption of the O₂ present between the lamp and the position of the sampled air (Marno et al., 2020). The product of R_β and ω is then scaled by σ_{O_2} . When combining Equation (4.7) and Equation (4.9) the OH concentration formed at the lamp is quantified as:

$$[\text{OH}] = [\text{H}_2\text{O}] \cdot \sigma_{\text{H}_2\text{O}} \cdot \phi_{\text{H}_2\text{O}} \cdot t \cdot F_\beta \cdot e^{-(\gamma_{\text{H}_2\text{O}}[\text{H}_2\text{O}] + \gamma_{\text{O}_2}[\text{O}_2])} \quad (4.11)$$

In order to calculate and characterize the flux intensity entering APACHE and γ_{O_2} , Equation 4.11 can be rearranged to:

$$\ln \left[\frac{[\text{OH}]}{[\text{H}_2\text{O}]} \right] = \ln(F_\beta \cdot t \cdot \phi_{\text{H}_2\text{O}} \cdot \sigma_{\text{H}_2\text{O}}) + (-\gamma_{\text{H}_2\text{O}} \cdot [\text{H}_2\text{O}] - \gamma_{\text{O}_2} \cdot [\text{O}_2]) \quad (4.12)$$

where t is the exposure time spent within the UV irradiation zone and is calculated:

$$t = L_{\text{UV}} / (V_{\text{APACHE}} / A_{\text{APACHE}}) \quad (4.13)$$

where L_{UV} is the length of the UV irradiation zone (the diameter of the 0.008 m apertures that restrict the amount of UV light entering APACHE), V_{APACHE} is the volume flow moving through APACHE with the units $\text{m}^3 \text{s}^{-1}$, and A_{APACHE} is the cross sectional area of APACHE, which is 0.018 m^2 . Figure 4.7, shows the natural log product of the measured OH normalized by water vapor concentration, (the left side of Equation 4.12) plotted against the oxygen concentration within APACHE.

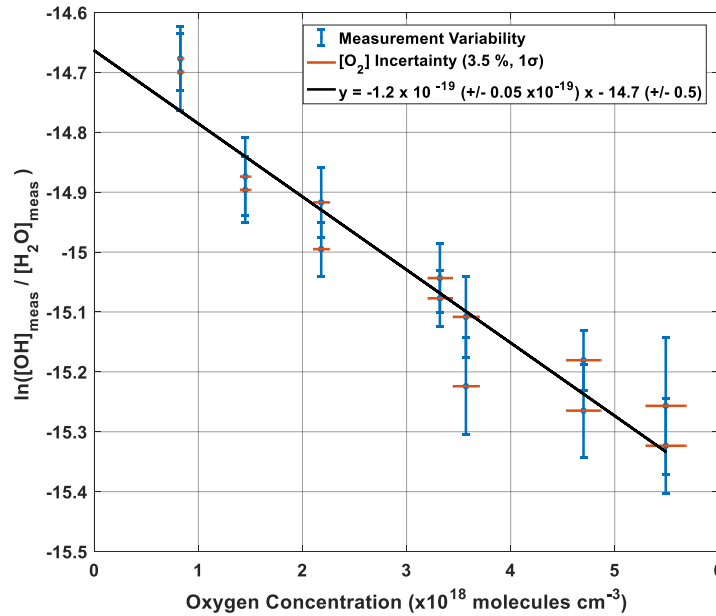


Figure 4.7.: The product of Equation 4.12 plotted as a function of oxygen concentration, as part of the actinometrical method (A) to derive γ_{O_2} and calibrate F_β . The error bars show the total uncertainty at the 1σ level. (Figure taken from Marno et al. (2020)).

As the other terms within Equation 4.12 are independent of changing oxygen concentration, the plotted gradient of the linear regression in Figure 4.7 yields a γ_{O_2} value, as a function of oxygen concentration, of $1.2 \times 10^{-19} (\pm 0.05 \times 10^{-19}) \text{ cm}^3 \text{ molecule}^{-1}$. The y intercept of the linear regression in Figure 4.7, -14.66, is equal to the natural logarithm of $(F_\beta t \phi_{H_2O})$ minus $(\gamma_{H_2O} [H_2O])$, the flux entering APACHE (F_β) can be characterized as:

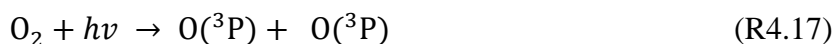
$$F_\beta = \left(\frac{e^{-14.66}}{t \cdot \phi_{H_2O}} \right) - (\gamma_{H_2O} \cdot [H_2O]) = 6.9 \times 10^{14} (\pm 1.1 \times 10^{14}) \text{ photons cm}^{-2} \text{ s}^{-1} \quad (4.14)$$

The accuracy of F_β characterized in the actinometrical method A is 15.9 % (1σ). Table 4.4 shows the parameters and their uncertainties contributing to the characterized F_β found in the actinometrical method A.

Table 4.4.: Parameters and uncertainties used in actinometrical method A, in with the HORUS instrument was used as a transfer standard. The quoted overall uncertainty is the sum of the quadrature of all the individual uncertainties listed within the table, at the 1σ level. $O(^1D)$ yield is taken from Martinez et al., (2010). This table is a modified version from Marno et al. (2020).

Parameter	Comments	Total Uncertainty (1σ)
NO Monitor (TEI)	Calibration uncertainty	5.2 %
NO standard (NPL)	Purity and concentration of the gas	1 %
N ₂ O cross section	JPL recommendation	2 %
H ₂ O cross section	JPL recommendation	2 %
γ_{O_2}	From actinometrical method A	3.5 %
$O(^1D)$ yield	Martinez et al. (2010)	1 %
Kinetic rate coefficients	JPL recommendation	12 %
F_β Variability	From actinometrical method A	3.5 %
APACHE dimensions	Specifications of in-house workshop	3 %
[H ₂ O]	Calibration with NIST standard Dew point generator	2 %
[O ₂]	From actinometrical method A	3.4 %
Mass flow controllers	Calibration with NIST DryCal	2 %
Pressure and Temperature sensors	Validated against NIST standard	2 %
Experimental Stability	Variability of measured terms	4 %
Overall uncertainty		15.9 %

The second actinometrical method (B) involved using an ANSYCO O3 41 M ozone monitor (calibrated to a primary standard, see Appendix A) to measure the ozone mixing ratio profile between the wall surface of APACHE and the IPI nozzle, at a pressure of 1021 mbar. This method utilizes the same approach as method A regarding changing the oxygen concentration using various mixtures of pure N₂ and synthetic air. O₂ photolysis at 184.9 nm produces two O(³P) atoms that react further with two O₂ molecules to produce two O₃ molecules.



The value of $1.2 \times 10^{-19} \text{ cm}^3 \text{ molecule}^{-1}$ for γ_{O_2} found from actinometrical method A was used to calculate the actinic flux entering APACHE:

$$F_{\beta} = \frac{[\text{O}_3]}{[\text{O}_2] \cdot \gamma_{\text{O}_2} \cdot \phi_{\text{O}_2} \cdot t \cdot e^{-(\gamma_{\text{O}_2}[\text{O}_2]t)}} \quad (4.15)$$

Φ_{O_2} is the quantum yield of O_2 at 184.9 nm, which has the value of 1 at wavelengths between 242 and 175 nm (Atkinson et al., 2004). Much like in method A, the ozone produced at the lamp is quantified by back calculating from the position of ozone measurement at the ANSYCO O3 41 M inlet. Inside APACHE, the calculated ozone concentrations at the UV irradiation zone ranged from 1.26×10^{12} to $2.05 \times 10^{12} \text{ molec. cm}^{-3}$, depending on the oxygen concentration. From this approach, F_{β} was found to be $6.11 \times 10^{14} (\pm 0.8 \times 10^{14}) \text{ photons cm}^{-2} \text{ s}^{-1}$ with a total uncertainty of 12.9 % (1σ). Table 4.5 shows the uncertainties of the parameters involved in the F_{β} characterization in the actinometrical method B.

Table 4.5.: Parameters and uncertainties involved in actinometrical method B, using the ANSYCO O3 41 M monitor. The overall uncertainty is the sum of the quadrature of the individual uncertainties listed below. Table taken from Marno et al. (2020).

Parameter	Comments	Total Uncertainty (1σ)
O_3 calibrator	Calibrated against a primary standard	2 %
$[\text{O}_3]$	Calibration of ANSYCO O3 41 M monitor	4 %
$[\text{O}_2]$	From actinometrical method A	3.4 %
γ_{O_2}	From actinometrical method A	3.5 %
F_{β} Variability	From actinometrical method B	3.5 %
Mass flow controllers	Calibration with NIST DryCal	2 %
Pressure and Temperature sensors	Validated against NIST standard	2 %
Experimental Stability	Variability of values	10.1 %
Overall uncertainty		12.9 %

The final value used for the F_{β} in the APACHE calibrations is the average of the two experiments, weighted by their uncertainties:

- Calibrated Actinic flux (F_{β}) = $6.37 \times 10^{14} (\pm 1.3 \times 10^{14}) \text{ photons cm}^{-2} \text{ s}^{-1}$
- Accuracy in F_{β} = 20.5 % (1σ)
- Agreement for F_{β} between actinometrical methods A and B, Zeta score = 0.59.

4.5. Airborne HORUS sensitivity calibrations

Once the APACHE system was fully characterized, the HORUS instrument pressure sensitivity was calibrated. Figure 4.8 shows the finalized HORUS calibration with APACHE. The sensitivity curve of HORUS, the quenching effect, the linear fits to quantify the pressure independent sensitivity coefficients, and relative HO_x transmission values for OH in the first axis, OH in the second axis, and HO₂, all plotted as a function of the HORUS internal density. After all the terms in Equation 4.1 for each of the three measurements were characterized, the sensitivity curves for OH in the first axis, OH in the second axis, and HO₂ were calculated (the red smoothed line in Figure 4.8, Row A) using Equation 4.1 and the characterized variables therein. Given that the calculated sensitivity curves agree within 2σ of the uncertainties in the measured calibration curves, indicates high confidence that each of the terms described in Equation 4.1 have been sufficiently resolved. Table 4.6 shows the values, ranges, precision and total uncertainties of the measured and calculated variables that determine the production of HO_x inside APACHE during the calibrations of HORUS.

Table 4.6.: Parameters for OH and HO₂ production by UV lamp in APACHE. Their overall precision and uncertainty is the sum of the quadrature of the individual parameter precision and uncertainty listed below. Taken from Marno et al. (2020).

Parameter (unit)	Range or typical value	Precision (1σ)	Total Uncertainty (1σ)
F_{β} at 184.9 nm (photons cm ⁻² s ⁻¹)	6.37 x 10 ¹⁴	3.5 %	20.5 %
$\sigma_{\text{H}_2\text{O}}$ (cm ² molecule ⁻¹)	7.22 x 10 ⁻²⁰	-	2 %
γ_{O_2} (cm ³ molecule ⁻¹)	1.22 x 10 ⁻¹⁹	1.8 %	3.5 %
[O ₂] (x10 ¹⁸ molec. cm ⁻³)	1.1 - 4.8	1.4 %	3.4 %
[H ₂ O] (x10 ¹⁶ molec. cm ⁻³)	2.00 - 7.41	1.2 %	2 %
Mass flow controller (SL min ⁻¹)	203 - 988	< 2 %	2 %
Pressure sensors (mbar)	275 - 900	< 1 %	2 %
Temperature sensors (K)	282 - 302	< 1 %	2 %
Overall		5 %	21.5 %

The pressure independent sensitivity coefficients (described as cN in Figure 4.8, Row C) for OH in the 1st axis (c0), OH in the 2nd axis (c1), and HO₂ in the 2nd axis (c2), are calculated by rearranging Equations 4.1a, 4.1b, and 4.1c to form:

$$c0 \cdot \rho_{Int}(P, T) = \frac{c_{\text{OH}}(P, T)}{Q_{IF}(P, T) \cdot b_c(T) \cdot [\alpha_{IPI\text{OH}}(P, T) \cdot \alpha_{HORUS\text{OH}}(P, T)]} \quad (4.16)$$

$$c1 \cdot \rho_{Int}(P, T) = \frac{c_{\text{OH}(2)}(P, T)}{Q_{IF(2)}(P, T) \cdot b_c(T) \cdot [\alpha_{IPI\text{OH}}(P, T) \cdot \alpha_{HORUS\text{OH}(2)}(P, T)]} \quad (4.17)$$

$$c2 \cdot \rho_{Int}(P, T) = \frac{c_{\text{HO}_2}(P, T)}{Q_{IF(2)}(P, T) \cdot b_c(T) \cdot [\alpha_{IPI\text{HO}_2}(P, T) \cdot \alpha_{HORUS\text{HO}_2}(P, T)]} \quad (4.18)$$

The products of Equations 4.16 to 4.18 are plotted as a function HORUS internal density in Figure 4.8, Row C. The slopes of the linear regressions are the pressure independent sensitivity coefficients. Table 4.7 shows the values, precision and total uncertainty of the resolved pressure independent sensitivity coefficients.

Table 4.7.: The pressure independent sensitivity coefficients and their overall uncertainty, characterized from calibrations with APACHE. Taken from Marno et al. (2020).

Parameter (cts pptv ⁻¹ s ⁻² cm ³ molecule ⁻¹ mW ⁻¹)	Value (x10 ⁻⁹)	Precision (± 1σ)	Total Uncertainty (1σ)
<i>c</i> 0 for OH in 1 st axis	3.8	4 %	6.9 %
<i>c</i> 1 for OH in 2 nd axis	2.3	4 %	6.9 %
<i>c</i> 2 for HO ₂ in 2 nd axis	4.5	2 %	5.6 %

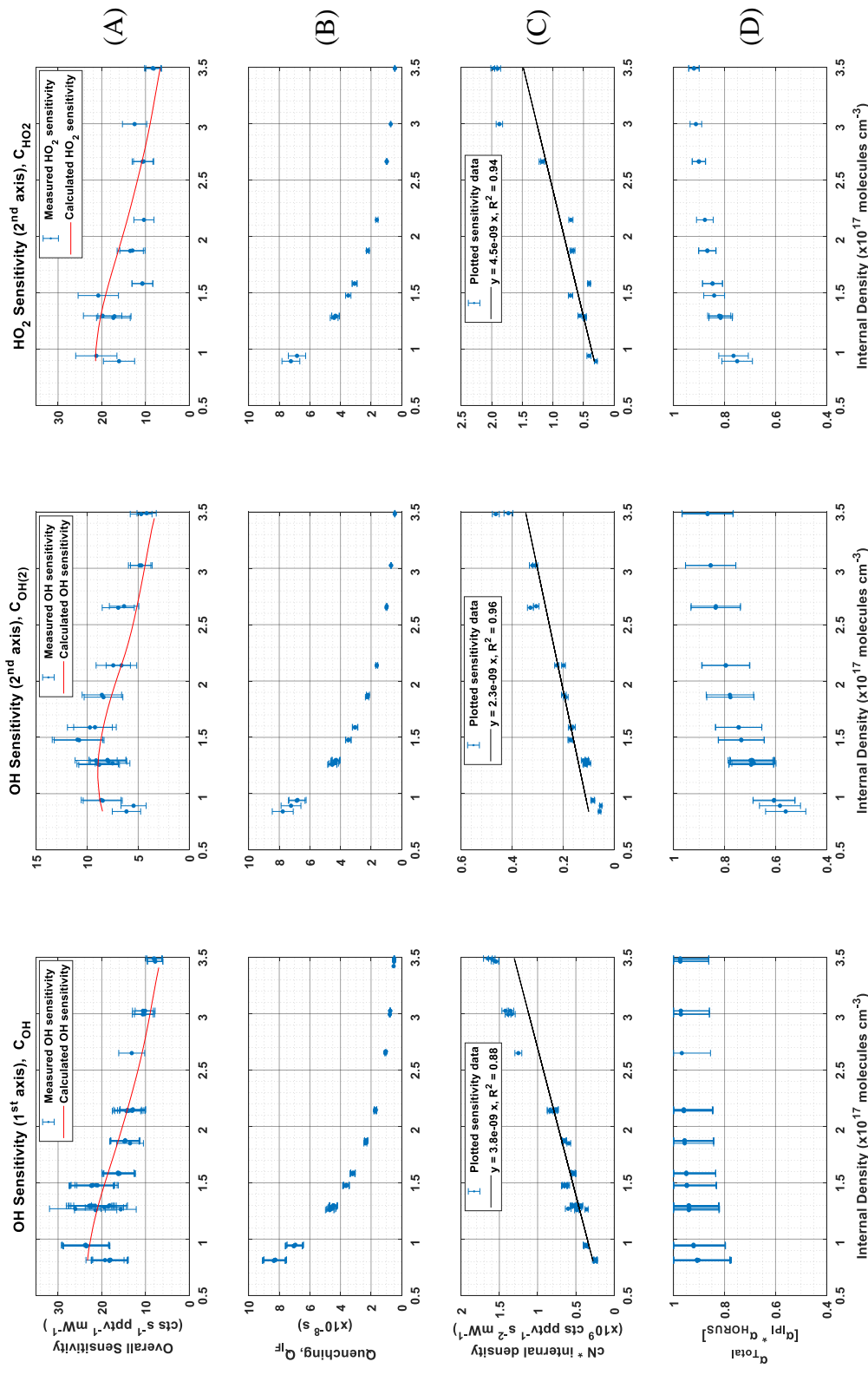


Figure 4.8.: The calibrated HORUS sensitivity parameters for OH in 1st axis (left four panels), for OH in the 2nd axis (middle four panels), and HO₂ in 2nd axis (right four panels) as one-hour averages as a function of ρ_{int} . Row A is the measured (blue) and calculated (red line) HORUS sensitivity curve. Row B is Q_{if} . Row C shows the products of Equations 4.16 to 4.18. Row D is the pressure dependent OH and HO₂ transmissions to the two detection axes. The error bars represent measurement variability (1σ), for rows B and C. In rows A and D, the error bars represent the total uncertainty (1σ). Figure taken from Marno et al. (2020).

As described in section 4.1, the pressure independent sensitivity coefficients are lump sum variables containing pressure independent HO_x wall losses. The pressure dependent HO_x transmission through the HORUS instrument is quantified and described below. Since IPI operates across the pressure range of 180 to 1010 mbar and the pressure within the detection axes of HORUS ranged from 3.1 to 18.4 mbar during flight, the pressure dependent transmission through IPI (α_{IPI}) and through HORUS (α_{HORUS}) must be quantified separately. α_{IPI} and α_{HORUS} are independently calculated using the corresponding measured pressures and calculated transit times, before being combined as the total transmission ($\alpha_{IPI} \cdot \alpha_{HORUS} = \alpha_{Total}$). The following was used to calculate the transmission of HO_x through IPI:

$$\alpha_{IPI\ OH} = 1 - \left[\frac{OH_{DM}(P) \cdot t_{rIPI}(P,T) \cdot \pi}{IPI_A \cdot P_{IPI}} \right] \quad (4.19)$$

$$\alpha_{IPI\ HO_2} = 1 - \left[\frac{HO_{2\ DM}(P) \cdot t_{rIPI}(P,T) \cdot \pi}{IPI_A \cdot P_{IPI}} \right] \quad (4.20)$$

where the OH_{DM} and $HO_{2\ DM}$ terms are the OH and HO₂ diffusion coefficients as described in section previously. t_{rIPI} is the transit time within IPI, i.e. the time taken for air to flow from the IPI nozzle to the critical orifice of HORUS. IPI_A is the internal cross sectional area of IPI. P_{IPI} is the measured pressure inside IPI. $\alpha_{IPI\ OH}$ is the transmission of OH through IPI, and $\alpha_{IPI\ HO_2}$ is the transmission of HO₂ through IPI. During calibrations with APACHE, the P_{IPI} ranged from 198 to 808 mbar and t_{rIPI} times ranged from 90 to 120 milliseconds, resulting in $\alpha_{IPI\ OH}$ and $\alpha_{IPI\ HO_2}$ values of 0.97 to 0.99 and 0.99 to 0.997 respectively. However, in order to calculate the total transmission of HO_x, the OH and HO₂ transmission values post critical orifice, $\alpha_{HORUS\ OH}$, $\alpha_{HORUS\ OH(2)}$, and $\alpha_{HORUS\ HO_2}$, must be resolved. α_{HORUS} transmission terms are calculated by adapting Equations 4.19 and 4.20 to the internal HORUS conditions:

$$\alpha_{HORUS\ OH} = 1 - \left[\frac{OH_{DM}(P) \cdot t_{r1}(P,T) \cdot \pi}{HORUS_A \cdot P_{int}} \right] \quad (4.21)$$

$$\alpha_{HORUS\ OH(2)} = 1 - \left[\frac{OH_{DM}(P) \cdot t_{r2}(P,T) \cdot \pi}{HORUS_A \cdot P_{int}} \right] \quad (4.22)$$

$$\alpha_{HORUS\ HO_2} = 1 - \left[\frac{HO_{2\ DM}(P) \cdot t_{r2}(P,T) \cdot \pi}{HORUS_A \cdot P_{int}} \right] \quad (4.23)$$

where t_{r1} and t_{r2} are the transit times calculated from the critical orifice to the 1st and 2nd detection axis respectively. $HORUS_A$ is the internal cross sectional area of HORUS. P_{int} is the measured internal pressure within HORUS. During calibrations with APACHE, P_{int} ranged from 3.7 to 13.7 mbar and internal transit times to the 1st and 2nd detection axis ranged from 3.8 to 4.3 milliseconds and 23.5 to 27.8 milliseconds respectively. Under these conditions, the calculated OH transmission from the critical orifice to the 1st detection cell ($\alpha_{HORUS\ OH}$), OH transmission from the critical orifice to the 2nd detection cell ($\alpha_{HORUS\ OH(2)}$), and HO₂ transmission from the critical orifice to the 2nd detection cell ($\alpha_{HORUS\ HO_2}$) ranged from 0.93 to 0.98, 0.58 to 0.87, and 0.76 to 0.92 respectively. The combined α_{Total} values for the three measurements are plotted as a function of the internal density of HORUS in Figure 4.8, Row D. Table 4.8 shows the calculated α_{Total} values, their precision and total uncertainty for OH to the first axis, OH to the second axis, and HO₂ to the second axis.

Table 4.8.: Pressure dependent OH and HO₂ transmission values, their precision and overall uncertainty during HORUS calibrations with APACHE. Taken from Marno et al. (2020).

Parameter (%)	Value	Precision ($\pm 1\sigma$)	Total Uncertainty (1σ)
α_{Total} (for OH to 1 st axis)	90 - 97	2.8 %	14.3 - 11.5 %
α_{Total} (for OH to 2 nd axis)	56 - 86	4.3 %	14.1 - 11.5 %
α_{Total} (for HO ₂ to 2 nd axis)	75 - 92	2.9 %	7.9 - 2.2 %

Table 4.9 shows the measured HORUS sensitivity values using APACHE for OH at the first axis (C_{OH}), OH at the second axis ($C_{OH(2)}$), and HO₂ at the second axis (C_{HO_2}). The precision signifies the 1σ variability in the measured HO_X signals from HORUS, with the total uncertainty denoting the root sum square of the total uncertainty values from the variables listed in Tables 4.6 and Table 4.7. The total uncertainties listed in Table 4.9 represent the 1σ OH and HO₂ measurement uncertainty of HORUS for the OMO-Asia 2015 campaign.

Table 4.9.: Pressure dependent sensitivities for the three HO_X measurements within HORUS, their overall uncertainty from calibrations with APACHE. The range in the precision relates to the numbers quoted in the value column. Taken from Marno et al. (2020).

Parameter (unit)	Value	Precision ($\pm 1\sigma$)	Total Uncertainty (1σ)
C_{OH} (cts s ⁻¹ pptv ⁻¹ mW ⁻¹)	7.8 - 26.1	1.1 - 0.5 %	22.6 %
$C_{OH(2)}$ (cts s ⁻¹ pptv ⁻¹ mW ⁻¹)	4.2 - 11.0	2.0 - 0.3 %	22.6 %
C_{HO_2} (cts s ⁻¹ pptv ⁻¹ mW ⁻¹)	8.1 - 21.2	0.4 - 0.7 %	22.2 %

The undescribed remaining fraction influencing the HORUS instrument sensitivity ($R_{undescribed}$), is calculated by dividing the measured overall sensitivity values by characterized terms in Equation 4.1:

$$R_{OH} = \frac{C_{OH}}{c0 \cdot \rho_{Int}(P,T) \cdot Q_{IF}(P,T) \cdot b_c(T) \cdot [\alpha_{IPI_{OH}}(P,T) \cdot \alpha_{HORUS_{OH}}(P,T)]} \quad (4.24)$$

$$R_{OH(2)} = \frac{C_{OH(2)}}{c1 \cdot \rho_{Int}(P,T) \cdot Q_{IF(2)}(P,T) \cdot b_c(T) \cdot [\alpha_{IPI_{OH}}(P,T) \cdot \alpha_{HORUS_{OH(2)}}(P,T)]} \quad (4.25)$$

$$R_{HO_2} = \frac{C_{HO_2}}{c2 \cdot \rho_{Int}(P,T) \cdot Q_{IF(2)}(P,T) \cdot b_c(T) \cdot [\alpha_{IPI_{HO_2}}(P,T) \cdot \alpha_{HORUS_{HO_2}}(P,T)]} \quad (4.26)$$

$$R_{undescribed} = |R_{OH} ; R_{OH(2)} ; R_{HO_2}|$$

where $R_{undescribed}$ is a matrix containing the undescribed remaining factors from the three measurements. When plotting $R_{undescribed}$ as a function of the P_{int} , (see Appendix B), the data scatters ± 0.15 (1σ) around an average value of 1.02 (± 0.23 , 1σ calibration uncertainty). This indicates that, as an upper limit, less than 2 % of the overall instrument sensitivity is still unresolved by the characterized terms in Equation 4.1. Furthermore, the 1σ variability of the

$R_{undescrbed}$ is 34 % smaller than the uncertainty in the APACHE calibration. Therefore, there is no conclusive indication that $R_{undescrbed}$ is pressure dependent or pressure independent, and has a negligible impact on the overall quantified HORUS OH and HO₂ sensitivities.

To apply these in-lab calibrations to the airborne measurements, the pressure and temperature dependent terms listed in Equation 4.1 are calculated using the temperatures and pressures values that were measured in-flight within the instrument. Only the pressure independent sensitivity coefficients are directly transferable from the calibrations with APACHE to the measurements in-flight as they are not subject to change with the large temperature and pressures ranges that HORUS experiences when airborne. Figure 4.9 shows, as a function of altitude, the HORUS sensitivity, limit of detection, and transmission values for OH (blue data points) and HO₂ (red data points) for a typical flight during OMO-Asia 2015, when the corresponding measured in-flight pressures and temperatures are applied the pressure and temperature dependent terms in Equation 4.1.

During this flight (flight 23), the OH sensitivity ranged from 5.4 (\pm 1.2) cts s⁻¹ pptv⁻¹ mW⁻¹ on ground to 24.1 (\pm 5.4) cts s⁻¹ pptv⁻¹ mW⁻¹ at 14 km. The average HORUS sensitivity value for HO₂ was 5.5 (\pm 1.2) cts s⁻¹ pptv⁻¹ mW⁻¹ on ground and reached an average maxima of 20.5 (\pm 4.5) cts s⁻¹ pptv⁻¹ mW⁻¹ at 11.4 km. Above 11.4 km the HO₂ sensitivity decreased, reaching 19.7 (\pm 4.4) cts s⁻¹ pptv⁻¹ mW⁻¹ at 14 km. This shift in HO₂ sensitivity is attributable to the increasing rate of decline in $\alpha_{TOTAL\ HO_2}$ transmission inside HORUS as the aircraft flies higher, which is exceeding the rate of sensitivity improvement via collisional quenching reduction as the air is becoming drier. The average water vapor mixing ratios at 14 km are three orders of magnitude lower than the average 1.5 % water vapor mixing ratios at ground level (see bottom panel in Figure 4.9). This strongly suppresses the collision quenching of OH at the higher altitudes, and is the main causation for the general increasing trend in instrument sensitivity towards HO_x as altitude increases. The tangible effect of improving instrument sensitivity trend as altitude increases is the decreasing limit of detection for both OH and HO₂. The HORUS limit of detection for OH and HO₂ is \sim 0.11 pptv and \sim 1.2 pptv respectively at ground level and drops to \sim 0.02 pptv and \sim 0.23 ppv respectively at 14 km.

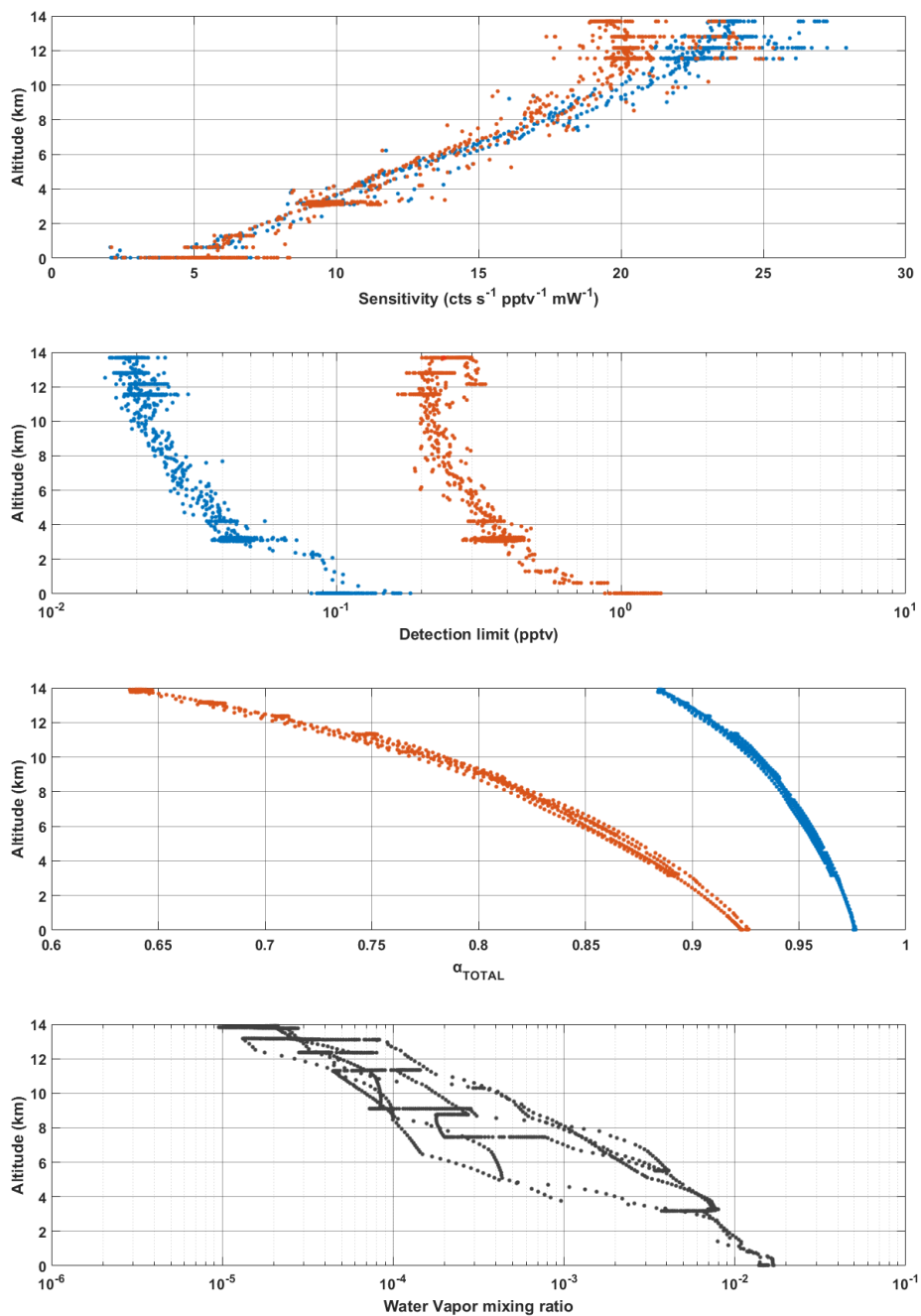


Figure 4.9.: Quantified in-flight sensitivity curves, limit of detection, and HO_x transmission for OH (blue data points) and HO₂ (red data points), plotted as a function of altitude. The water vapour mixing ratios (black data points) are also plotted, in the bottom panel, as a function of altitude. The data shown is from flight 23. Figure taken from Marno et al. (2020).

5. Interference Characterization

5.1. IPI In-flight performance and OH-CHEM

As described previously, the background OH signal ($S_{OH(CHEM)}$) is measured by injecting an OH-scavenger (propane) into IPI in order to remove atmospheric OH. The total OH fluorescence signal ($S_{OH(tot)}$) is measured when no OH scavenger is injected, which includes atmospheric OH, and $S_{OH(CHEM)}$ interference. Once the C_{OH} is applied to the signals, the OH_{CHEM} signal is corrected for the IPI scavenging efficiency (η_{scav}) allowing for the correct acquisition of atmospheric OH concentrations (OH_{atm}). Both $S_{OH(tot)}$ and OH_{CHEM} are normalized by $W_{Z1\ pwr}$.

$$OH_{atm} = \frac{S_{OH(tot)}}{C_{OH} \cdot W_{Z1\ pwr}} - \left[\left\{ \frac{S_{OH(CHEM)}}{C_{OH} \cdot W_{Z1\ pwr}} \right\} \cdot \eta_{scav}(P, T) \right] \quad (5.1)$$

which can be simplified to:

$$OH_{atm} = (OH_{tot} - (OH_{CHEM} \cdot \eta_{scav}(P, T))) \quad (5.2)$$

where η_{scav} is calculated:

$$\eta_{scav}(P, T) = 1 - e^{(-k_{C_3H_8}(T) [C_3H_8] t_{C_3H_8})} \quad (5.3)$$

$k_{C_3H_8}$ is the temperature dependent rate constant for OH reacting with propane (Burkholder et al., 2015), $[C_3H_8]$ is the propane concentration in IPI, and $t_{C_3H_8}$ is the chemical residence time. The chemical residence time is the effective time in which the propane is injected into the sampled air thus removing atmospheric OH and accounts for incomplete mixing of C_3H_8 in IPI. This is different to the t_{IPI} described earlier. To adequately quantify the chemical residence times in IPI and therefore calculate the η_{scav} correction for the OH_{CHEM} signal, multiple propane titrations were performed during flight for every flight level flown during the OMO-Asia 2015. These titrations involve injecting various amounts of propane into IPI and measuring the subsequent OH signals. They provide the required information for the given pressure, temperature, and propane concentrations that occur in IPI during flight in order to quantify the correct $t_{C_3H_8}$ and is quantified by:

$$\ln \left[\frac{OH_{C_3H_8}}{OH_0} \right] = -k_{C_3H_8}(T) [C_3H_8] t_{C_3H_8}(P, T) \quad (5.4)$$

where $OH_{C_3H_8}$ is the OH signal when various C_3H_8 amounts are injected, OH_0 is the OH signal when no C_3H_8 is injected. The natural log of the ratio of these signals are plotted against the corresponding C_3H_8 concentrations that are injected into IPI. The slope of the plotted the linear regression titration curve is a product of the temperature dependent $k_{C_3H_8}$ and $t_{C_3H_8}$. As the temperature in IPI is measured, the $k_{C_3H_8}$ can be calculated and divided from the derived titration curve, revealing $t_{C_3H_8}$ under that specific IPI in-flight condition. Figure 5.1 shows a range of propane titration curves and derived $t_{C_3H_8}$ times for four contrasting altitudes during a flight.

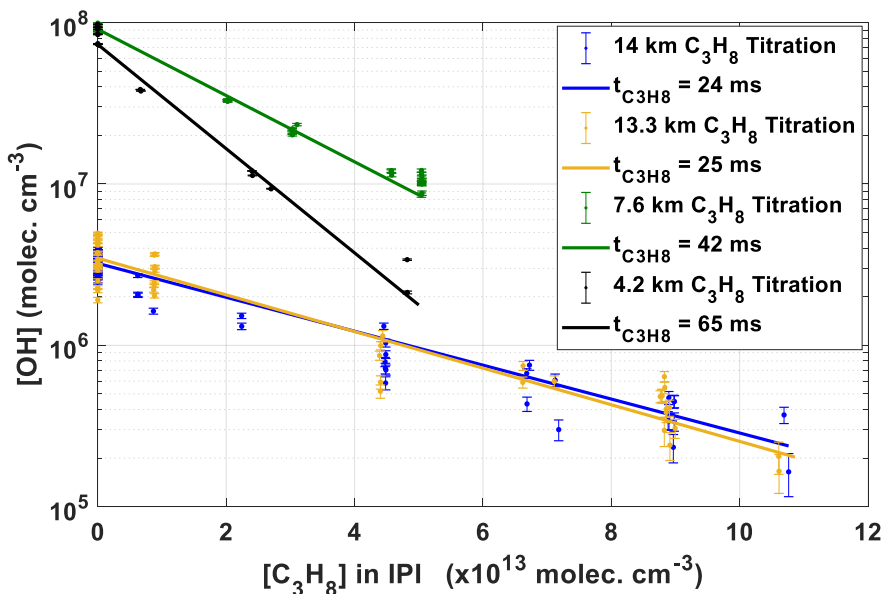


Figure 5.1.: Series of propane titrations showing the measured effect of changing pressures and air temperatures about IPI as a function of altitude. The error bars show the HORUS measurement variability (2σ).

Once the in-flight IPI chemical residence times were characterized for the various in-flight temperatures, pressures, and flow conditions, the corresponding η_{scav} can be calculated and applied to the OH_{CHEM} signal; resolving the measurement for the true atmospheric OH concentrations. With the η_{scav} applied, the uncertainty in the background signal is $\pm 5\%$ (1σ). Figure 5.2 shows the resolved chemical residence times (ranging 20 to 120 ms), η_{scav} , and OH concentrations before (green) and after (blue) the subtraction of the η_{scav} corrected OH_{CHEM} interference. The overall influence the η_{scav} correction on the final atmospheric OH data can be described by taking the ratio of OH_{atm} (when the OH_{CHEM} subtraction is corrected for η_{scav}) and OH^* (when the OH_{CHEM} subtraction is not corrected for η_{scav}), see Figure 5.3 (left). η_{scav} values begin to sharply decrease when increasing in altitude above 11 km (Figure 5.2). This affects the ratio of $\text{OH}_{\text{atm}} / \text{OH}^*$ in Figure 5.3 (left), where an increasing trend with altitude can be seen. In many cases beyond 11 km, more than 5 % of the OH_{CHEM} signal comprises of atmospheric OH if the η_{scav} correction is not applied. This means that without performing propane titrations to quantify η_{scav} , an increasing proportion of atmospheric OH would reside within the background signal, which would cause the measured OH concentrations, particularly in the UT, to be artificially lower than the atmospheric OH concentrations.

The median percentage contribution of the η_{scav} corrected OH_{CHEM} in the $S_{\text{OH}(\text{tot})}$ signal above 11 km is 12 %, with instances exceeding 20 %, (Figure 5.3 right). As the altitude decreases, the interference levels steadily increases with a median value of 29 % at around 3.2 km. During OMO-Asia 2015, the outflow of the Mount Etna eruption was sampled when HALO flew at altitudes 3 – 4 km. The large increase in concentrations of sulphur and halogen compounds associated with volcanic eruption outflows (Bobrowski et al., 2006; Oppenheimer et al., 2006) could be the likely candidates causing interference levels exceed 30 %. However, in-depth

investigations into sulphur and halogen OH_{CHEM} interferences within LIF-FAGE OH instruments are required to conclusively deduce the cause of this high OH_{CHEM} interference of volcanic origin. Overall, the IPI system has proven to be a critical part of the HORUS instrument. Without IPI, it would not be possible to distinguish and resolve for these aforementioned OH_{CHEM} interferences within the atmospheric OH measurements.

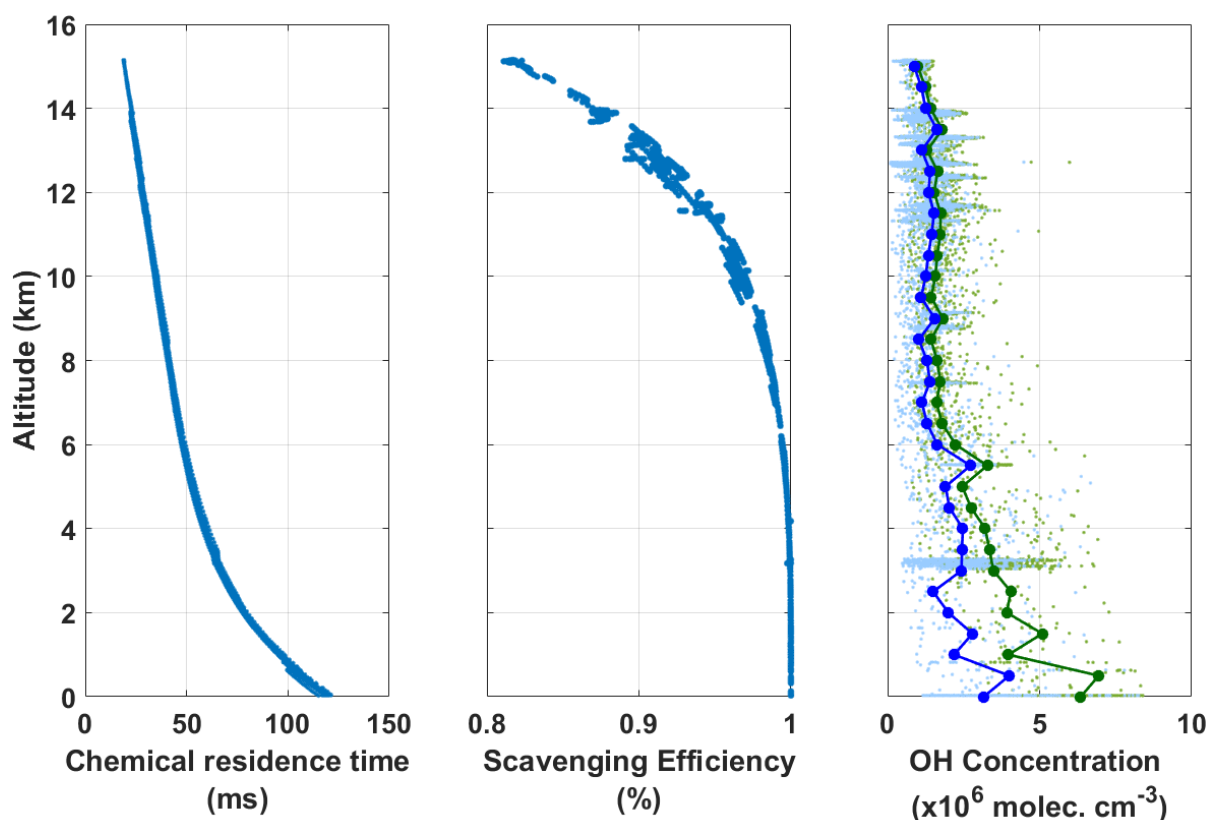


Figure 5.2.: Showing data from OMO-Asia 2015 campaign. The propane chemical residence time as a function of altitude, found from propane titrations (left). The subsequent η_{scav} as a function of altitude, when propane is being injected (center). The right shows the OH data corrected for instrument sensitivity. The light blue data points are atmospheric OH concentrations (OH_{atm}) calculated using the background signal accounting for η_{scav} . The light green data points are calculated total OH concentrations ($S_{\text{OH}(tot)} / (W_{Z1pwr} \cdot C_{\text{OH}})$) i.e. without applying the background signal corrected for η_{scav} . The dark blue and green lines are the corresponding 500 m median values.

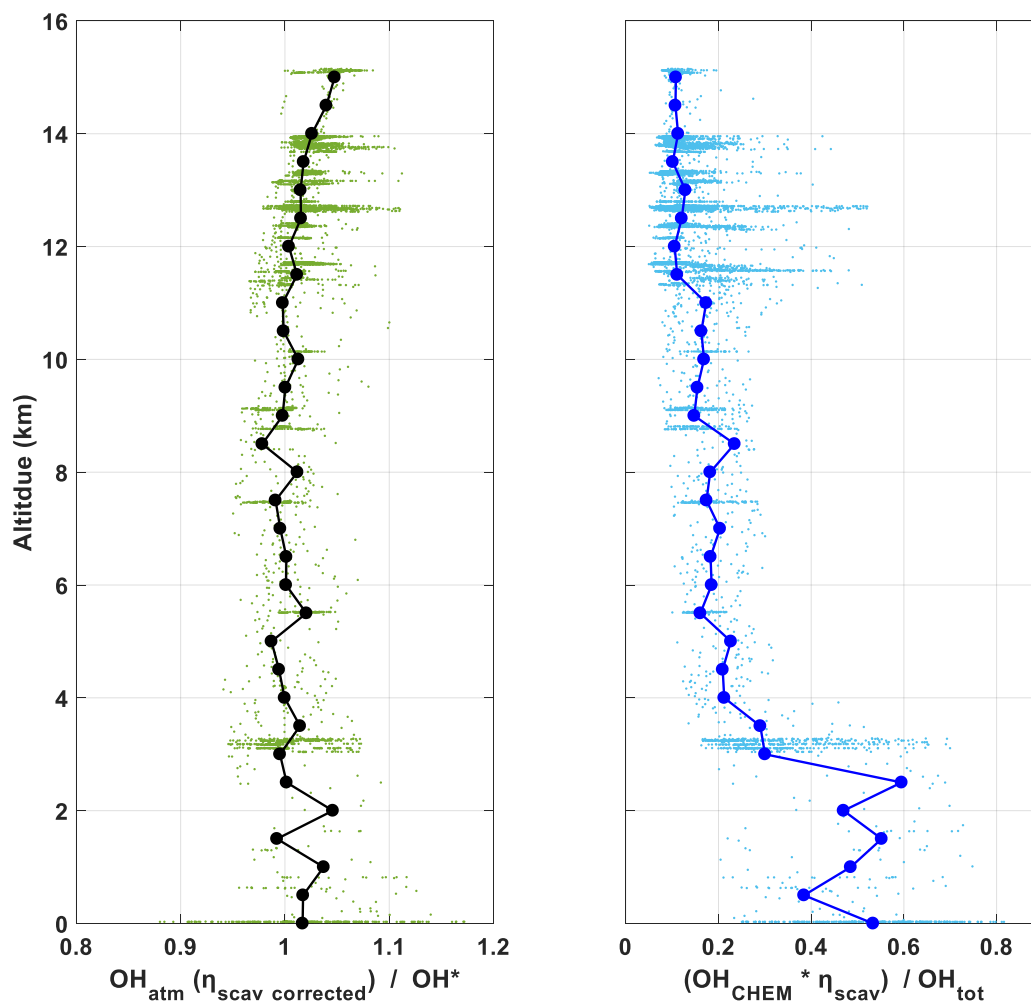


Figure 5.3.: Vertical profiles of the ratio of the $\text{OH}_{\text{atm}} / \text{OH}^*$ with the black linked circles representing the 500 m median (left), and the percentage interference level (OH_{CHEM} corrected for η_{scav}) in the OH_{tot} signal (right) for the whole OMO-Asia 2015 campaign.

5.2. HORUS HO₂ measurement, conversion efficiency, HONO and RO₂ interference

As described in section 3, HO₂ is measured indirectly by first converting atmospheric HO₂ into OH internally using a toggled NO injection system, and detecting the subsequent OH fluorescence. When NO is injected, both atmospheric OH and OH converted from HO₂, i.e. HO_X are detected at the second axis. To quantify and therefore remove the signal produced by atmospheric OH reaching the second detection axis, the OH signal from the first axis (S_{OH}) is multiplied by the ratio of the two axes' OH sensitivities, which are normalized by their respective measured laser power. Equation 5.5 shows how:

$$HO_{2 \text{ atm}} = \frac{1}{(C_{HO_2} \cdot W_{z_2 \text{ pwr}})} \cdot \left\{ S_{HO_X} - \frac{(C_{OH(2)} \cdot W_{z_2 \text{ pwr}})}{(C_{OH} \cdot W_{z_1 \text{ pwr}})} S_{OH} \right\} \cdot [1 - \alpha_{RO_2}(P, T)] \quad (5.5)$$

Equation 5.5 can then be simplified to:

$$HO_{2 \text{ atm}} = \left[\frac{HO_2'}{\eta_{\text{conv}}(P, T) \cdot S_{I[HONO]}(P, T)} \right] \cdot [1 - \alpha_{RO_2}(P, T)] \quad (5.6)$$

where α_{RO_2} is the fractional contribution of RO₂ interference in the HO₂ signal. S_{HO_X} is the net fluorescence signal of OH, (atmospheric and converted from HO₂) when NO is injected. HO_2' is the S_{HO_X} signal corrected for C_{HO_2} , $C_{OH(2)}$, laser power, and atmospheric OH.

NO titrations were also performed during flight to find the chemical residence time and thusly η_{conv} in order to correct the HO₂ data.

$$\eta_{\text{conv}}(P, T) = [1 - e^{(-k_{NO}(T)[NO] t_{NO}(P, T))}] \quad (5.7)$$

where k_{NO} is the rate constant for HO₂ reacting with NO (Burkholder et al., 2015), [NO] is the NO concentration in the sample flow between injection point and the second detection axis, and t_{NO} is the chemical residence time. Figure 5.4 shows a typical range of chemical residence times found from NO titrations during flight. From the NO titrations, t_{NO} ranged from ~ 11 ms at ground level to less than 5 ms at altitudes 13 km and above.

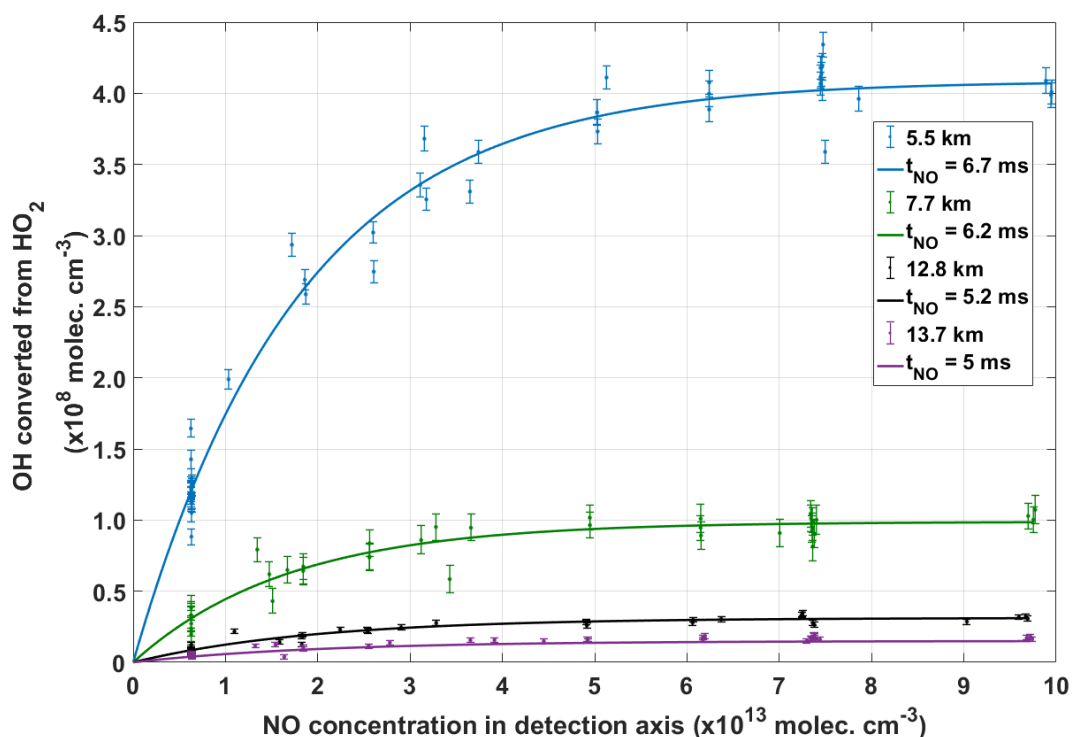


Figure 5.4.: Series of NO titrations to show chemical residence times at 4 different altitudes. The error bars show the HORUS measurement variability for each respective averaged data point (1σ). The NO injection is occurring within HORUS behind the critical orifice, with pressure ranging from 3 to 18.4 mbar. During flight, the total volume flow changed by 10 % (1.08 to 1.2 m^3 min^{-1}) resulting in NO chemical residence times (t_{NO}) to range from 4.8 to 11 milliseconds.

When HORUS is in its standard in-flight measurement status, NO injection is toggled between 2 sccm (yielding NO concentrations of $\sim 6.6 \pm 0.4 \times 10^{12}$ molec. cm^{-3}) and 30 sccm (yielding NO concentrations of $\sim 7.9 \pm 0.3 \times 10^{13}$ molec. cm^{-3}) at pressures ranging from 3 to 18.4 mbar, with internal volume flows ranging from 1.08 to 1.2 m^3 min^{-1} . The NO is stored within a gas cylinder, which is rated to 10 % NO at a NIST standard (see Appendix A). This permits the treatment of potential RO_2 and HONO interferences once the correct η_{conv} is applied to the HO_2 data. The 2 sccm mode has a lower conversion efficiency of HO_2 , which results in a more variable signal. Therefore, requiring longer integration times, which reduces the temporal resolution, in order to achieve the same precision as the 30 sccm mode which efficiently converts HO_2 to OH and has a less variable signal. However, the 2 sccm mode has a nominal HONO and RO_2 interference, whereas the 30 sccm mode can contain a detectable HONO and RO_2 interference. As HONO formation interference causes the HO_2 signal to decrease, it is in direct competition with RO_2 interferences, which increase the HO_2 signal. Therefore, HONO and RO_2 interferences must be calculated separately in order to correct the HO_2 signal.

As described in section 3, when high NO levels are injected into a LIF-FAGE instrument, a detectable loss in the OH radicals produced from the conversion of HO₂ with NO can occur. This chemical loss process occurs via HONO formation:



In order to calculate the relative interference contribution from HONO formation, the CAABA-MECCA (Chemistry As A Box Model Application – Module Efficiently Calculating the Chemistry of the Atmosphere) model was initialized with a HO₂ mixing ratio of 50 pptv and OH was initialized at zero. Details of the CAABA-MECCA model will be discussed later in section 6. The model was constrained to the measured in-flight internal pressures and temperatures. The simulation time was constrained to the characterized t_{NO} found from the NO titrations described earlier in order to reflect the varying quality of the internal mixing of NO and flow conditions that occurred inside HORUS during flight across different altitudes. A large sweep of NO concentrations were used to constrain the model simulations in order to get a broad picture of the potential HONO levels that could be formed inside HORUS. The NO concentrations ranged from 9 x10¹¹ molec. cm⁻³ up to 1.5 x10¹⁵ molec. cm⁻³. The ratio of the calculated CAABA-MECCA formed HONO concentrations ([HONO]_{NO+OH+M}) over the initial HO₂ concentrations within HORUS ([HO₂]_{int}) is used to calculate the correction factor for the signal interference caused by HONO formation (S_{I[HONO]}):

$$S_{I[\text{HONO}]} = 1 - \left(\frac{[\text{HONO}]_{\text{NO+OH+M}}}{[\text{HO}_2]_{\text{int}}} \right) \quad (5.8)$$

Figure 5.5 shows calculated ratio in Equation 5.8 at flight altitudes of 14 km, 9 km, 8 km and 3.5 km, plotted as a function of simulated NO injection concentrations. The black dotted-dashed line is the maximum NO concentration (1.04 x10¹⁴ molec. cm⁻³) injected into HORUS when performing in-flight NO titrations. The blue dotted-dashed line shows the maximum NO concentration (0.79 x10¹⁴ molec. cm⁻³) and the green dotted-dashed line shows the minimum NO concentration (6.61 x10¹² molec. cm⁻³) injected into HORUS when performing normal HO₂ measurements. When 0.79 x10¹⁴ molec. cm⁻³ NO is injected, 0.5 %, 0.8 %, 1.6 %, 3.0 %, and 8.2 % of the HO₂ entering HORUS cannot be detected as OH due to formation of HONO at 13.2 km, 11.6 km, 9km, 7.5 km, and 4.2 km respectively.

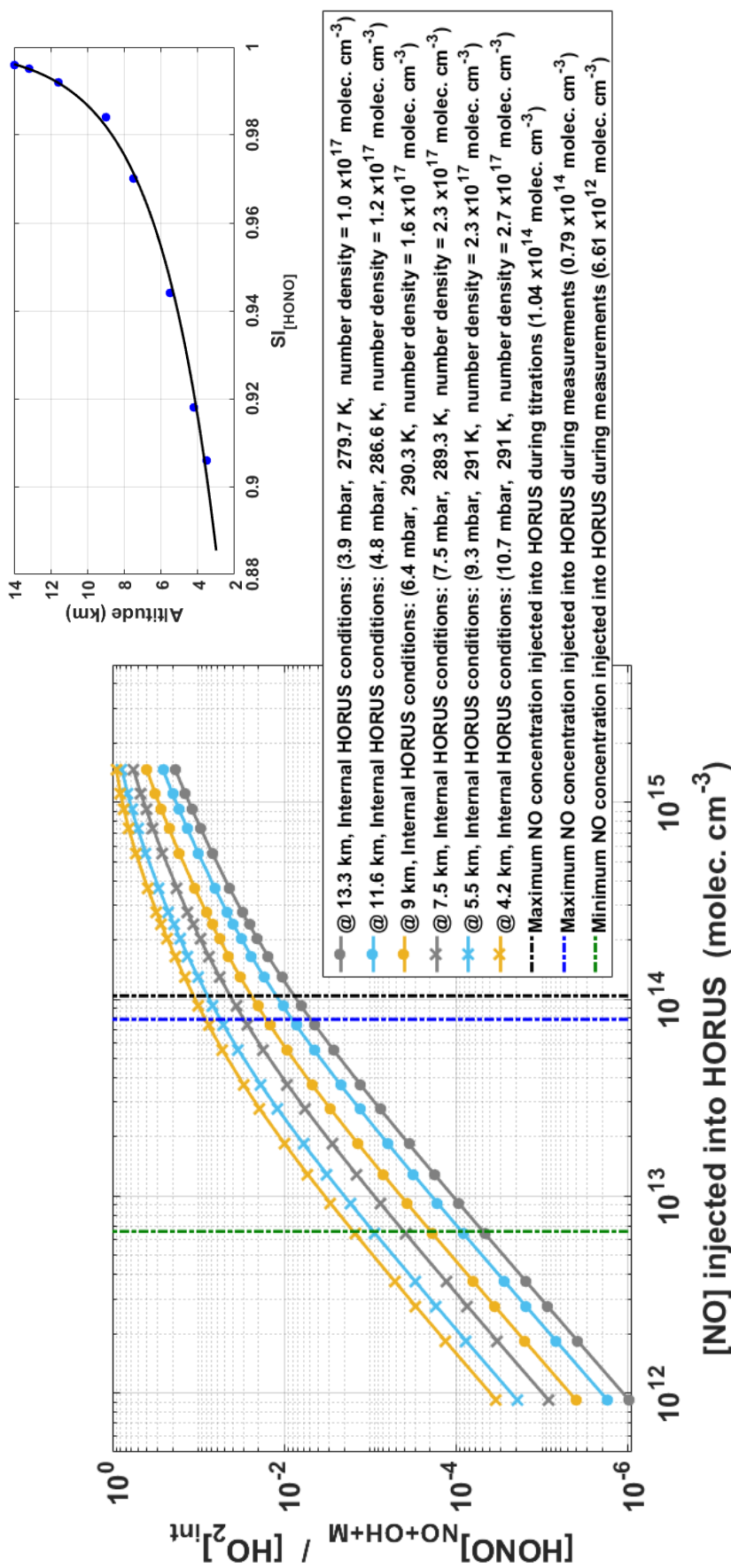


Figure 5.5: The ratio of the calculated CAABA-MECCA formed HONO concentrations (via OH + NO + M) and initial HO₂ concentrations under in-flight HORUS internal conditions plotted as a function of various injectable NO concentrations. The CAABA-MECCA box model was constrained to the measured internal HORUS conditions during flight at altitudes ranging from 13.2 km to 4.2 km. The black dotted-dashed line is the maximum NO concentration (1.04 x 10¹⁴ molec. cm⁻³) injected into HORUS when performing in-flight NO titrations. The blue dotted-dashed line shows the maximum NO concentration (0.79 x 10¹⁴ molec. cm⁻³) and the green dotted-dashed line shows the minimum NO concentration (6.61 x 10¹² molec. cm⁻³) injected into HORUS when performing normal measurements. The top right panel shows the calculated $S^I_{[\text{HO}_2]}$ at the 0.79 x 10¹⁴ molec. cm⁻³ NO injection line, plotted as a function of altitude.

In Figure 5.6, the top left panel shows the t_{NO} values as a function of altitude during OMO-Asia, that were characterized by the in-flight NO titrations. The subsequent η_{conv} values ranged from 25 – 42 % for the 2 sccm NO injection mode, and 96 – 99 % for the 30 sccm injection mode. The bottom left panel shows the measured HO_2' concentrations for the two NO injection modes when η_{conv} is not applied to the signal.

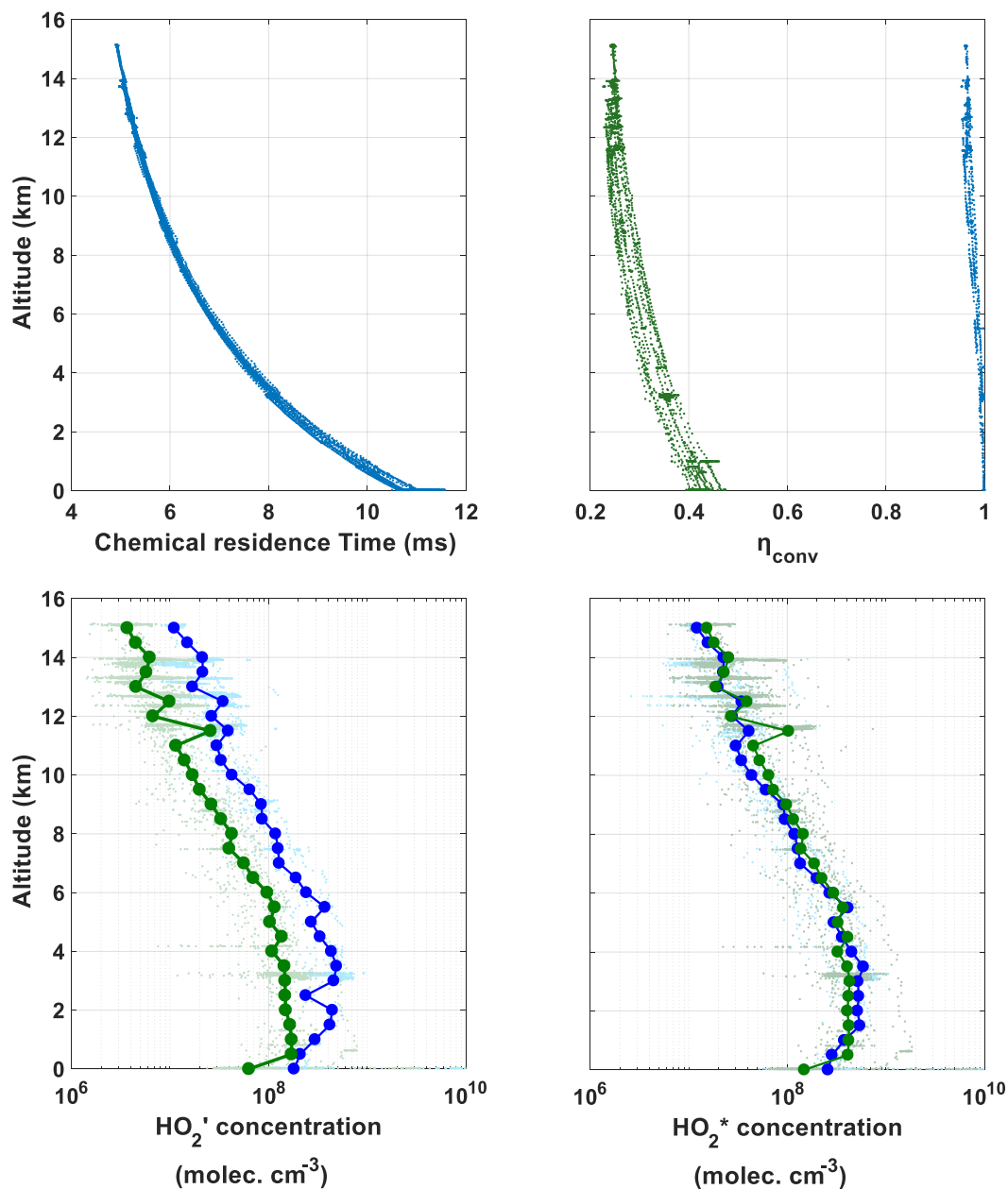


Figure 5.6.: The NO chemical residence time as a function of altitude, found from performed NO titrations (top left). The calculated η_{conv} (top right) as a function of altitude, for the 2 sccm NO injection mode (green) and 30 sccm NO injection mode (blue) are shown. The bottom left panel shows the HO_2' concentrations for 2 (green) and 30 (blue) sccm NO injection modes when η_{conv} is not applied. The HO_2^* concentrations when η_{conv} and $SI_{[\text{HONO}]}$ are applied to the HO_2' data for 2 (green) and 30 (blue) sccm NO injection modes (bottom right).

When η_{conv} and $SI_{[\text{HONO}]}$ are applied to HO_2' (HO_2^*), the two NO injection signals converge (bottom right panel, Figure 5.6). On average, the 30 sccm HO_2^* measurement is 4 % higher than the 2 sccm HO_2^* measurement, indicating a detectable RO_2 interference of ~ 4 % within the 30 sccm mode is present. Reactions R5.1 and R5.2 show how sampled atmospheric RO_2 species can artificially elevate HO_2 levels within a LIF-FAGE instrument when sufficient NO is injected:



See Fuchs et al. (2011) for more information regarding specific RO_2 species and their respective interference contributions in LIF-FAGE measurements of HO_2 . In order to gain a further understanding of the potential scale and altitude dependence of the fractional contribution of RO_2 interference in the 30 sccm HO_2^* signal (α_{RO_2}); the CAABA-MECCA box model was used. The full chemistry scheme in CABBA-MECCA is shown in the Appendix D and an in-depth description of the model is discussed in section 6. An initial CAABA-MECCA simulation was performed with the model constrained to atmospheric pressure, temperature, and available measurement data, with the exception to HO_x . These simulations provided a lower threshold chemical representation of the diversity and levels of different atmospheric RO_2 species that entered HORUS during the campaign. To quantify α_{RO_2} , two further simulations (*A* and *B*) were performed using the aforementioned output data from the previous atmospheric simulation to initialize the chemistry within the model. In both simulations the model was fixed to the in-flight internal pressures, temperatures, and humidity within HORUS. OH was initialized using the measured OH_{atm} values, adjusted for the internal wall losses in order to reproduce the OH levels that occurred the second detection axis. NO was initialized using the calculated NO concentrations internally within HORUS caused by the NO injection system. The only modification between the two simulations is that simulation *A* involved initializing the model with the measured HO_2^* concentrations (adjusted for wall losses) and simulation *B* involved initializing HO_2 levels at zero. Therefore, the increases in OH within simulation *B* is directly attributable to the RO_2 forming HO_2 that then converts into OH. This allowed for the RO_2 contribution in the detected OH signal to be discriminated from the atmospheric HO_2 contribution in the detected OH signal. The output of the two simulations equate to the following:

$$A: \text{OH}_A = (\text{OH}_\tau + \text{OH}_{\text{HO}_2} + \text{OH}_{\text{RO}_2}) \quad (5.9)$$

$$B: \text{OH}_B = (\text{OH}_\tau + \text{OH}_{\text{RO}_2}) \quad (5.10)$$

where OH_τ is the concentration of atmospheric OH that reaches the second detection axis in HORUS. OH_{HO_2} is the OH produced by atmospheric HO_2 reacting with the known NO concentrations from the different injection modes occurring under the internal HORUS conditions. OH_{RO_2} is the OH produced by the computed RO_2 under the same conditions. α_{RO_2} is then calculated by:

$$\alpha_{\text{RO}_2} = 1 - \left[\frac{(\text{OH}_A - \text{OH}_B)}{(\text{OH}_A - \text{OH}_\tau)} \right] \quad (5.11)$$

Figure 5.7 shows the calculated percentage contribution of RO₂ interference on the HO₂* signal (left) from the CAABA-MECCA simulations. The relative contribution of RO₂ species on the HO₂* signal increases from ~ 1 % in the UT to ~ 7 % in the LT. The calculated RO₂ concentrations were subtracted off the HO₂*_(30 sccm NO) data to ultimately reach atmospheric HO₂ (HO_{2 atm}), Figure 5.7 (right).

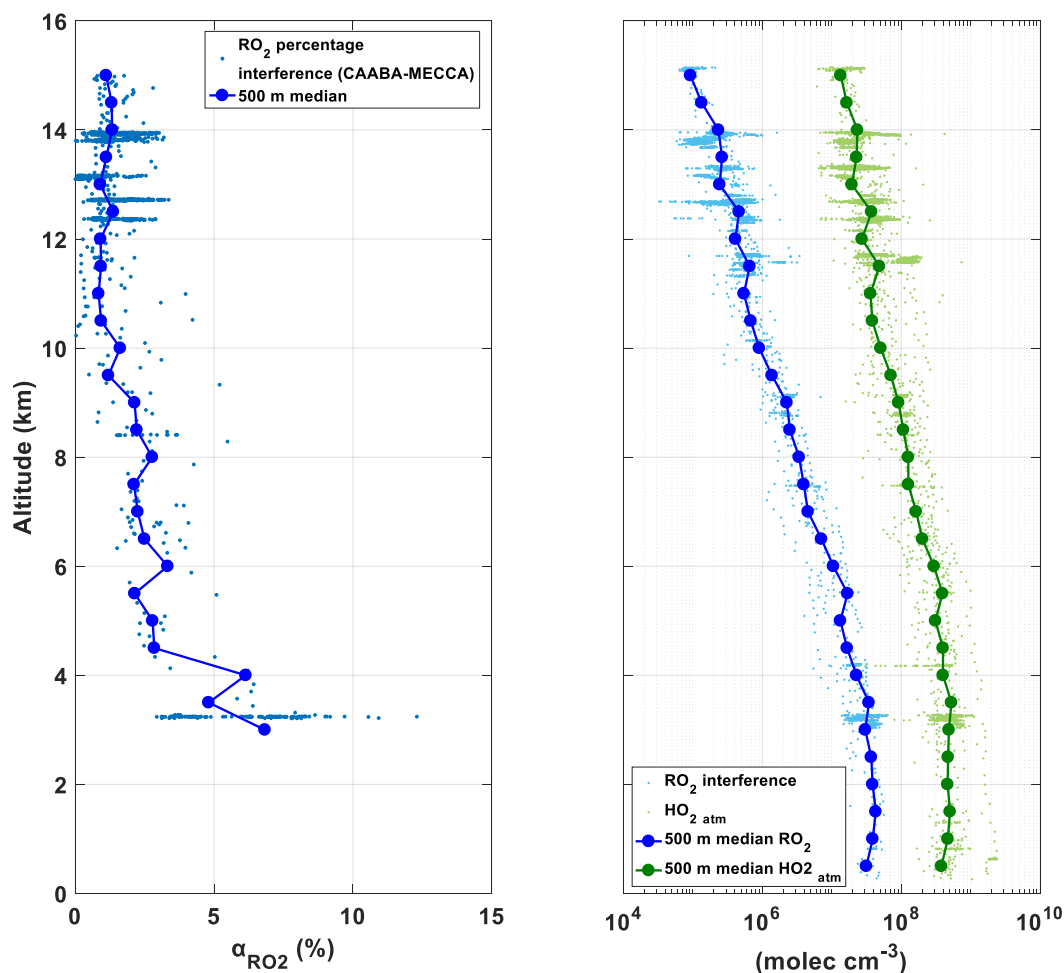


Figure 5.7.: RO₂ interference contribution to the HO₂* signal (α_{RO_2}) using output data from the CAABA-MECCA box model (left panel). The linked blue lines are the 500 m average bins. The model was initialized using data from a previous simulation where it was constrained by available measurements and atmospheric temperature and pressure to get the chemical composition of the air that was sampled by HORUS during the OMO-ASIA 2015 campaign. For the subsequent simulations to acquire α_{RO_2} , the model was fixed to the internal pressure, temperature and humidity occurring within the HORUS instrument, with NO levels being initialized with the concentrations created within by the NO injection system. The absolute concentrations of the RO₂ interference (blue) and the corresponding atmospheric HO₂ (HO₂* - RO₂) (green) (right panel). In this plot the blue and green linked circles represent the 500 m median bins for RO₂ and atmospheric HO₂ (HO_{2 atm}) respectively.

Figure 5.8 shows the incremental improvements in the agreement in the HO₂ data between the two NO injection modes as the η_{conv} , $SI_{[\text{HONO}]}$, and α_{RO_2} corrections are applied. The agreements, shown in Figure 5.8, between the two NO injection signals as η_{conv} , $SI_{[\text{HONO}]}$, and α_{RO_2} corrections are applied are also listed below:

$$\text{HO}_2' (2 \text{ sccm NO}) = 0.28 \text{HO}_2' (30 \text{ sccm NO}) - 1.1 \times 10^5 \text{ molec. cm}^{-3} \quad (\text{R}^2 = 0.84)$$

$$\text{HO}_2^* (2 \text{ sccm NO}) = 0.91 \text{HO}_2^* (30 \text{ sccm NO}) + 3.4 \times 10^6 \text{ molec. cm}^{-3} \quad (\text{R}^2 = 0.96)$$

$$\text{HO}_{2 \text{ atm}} (2 \text{ sccm NO}) = 0.94 \text{HO}_{2 \text{ atm}} (30 \text{ sccm NO}) + 2.8 \times 10^6 \text{ molec. cm}^{-3} \quad (\text{R}^2 = 0.96)$$

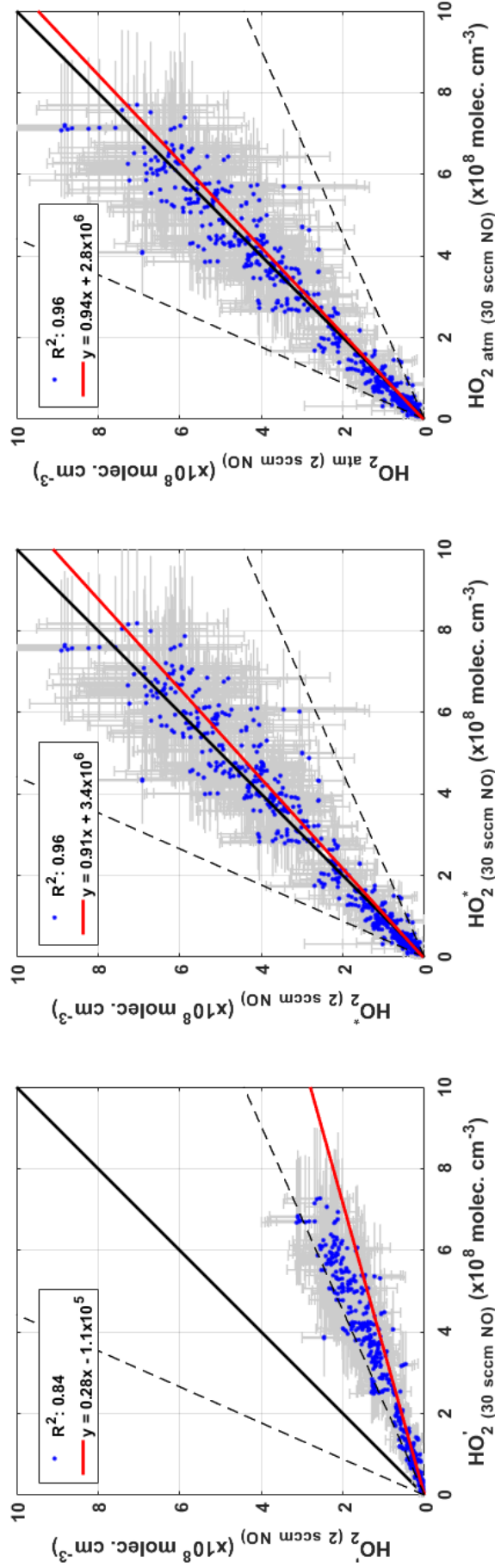


Figure 5.8.: Correlation plot between the two NO injection HO_2' signals (left), where only the HORUS sensitivity to atmospheric HO_2 is applied. Correlation plot between the two NO injection HO_2^* signals (middle), where the HORUS sensitivity to atmospheric HO_2 , η_{conv} , and $S_{[\text{HONO}]}$ corrections are applied. Correlation plot between the two NO injection atmospheric HO_2 signals (right), corrected for HORUS sensitivity to atmospheric HO_2 , η_{conv} , $S_{[\text{HONO}]}$, and RO_2 interferences. The error bars depict the total uncertainty for each measurement at 1σ . The dashed lines signify the average total uncertainty at 2σ (55.7 %).

6. OMO-Asia 2015

Historically, South Asian trace gas emissions were mainly sourced from agriculture and biomass burning, causing releases of large amounts of VOC and relatively low amounts of NO_x (nitric oxide: NO & nitrogen dioxide: NO₂) into the atmosphere. However, within the last three decades, South and East Asia has developed into a booming industrial hub of the world. Even though this transition has brought wealth and development to nations such as China, India, and Indonesia, there is a strong correlation between per capita energy use and development state. In 2014, India and China had the potential growth factor of 10 and 3.5 in energy consumption when compared to the US (International Energy Agency. 2020). The current rate of economic development and growing population sizes increases energy demand that is often met through fossil fuel based energy production, and must be supported by intensified agricultural output resulting in increased biomass burning and expansion of farmable land. A signature of this rapid development is the sharp increase in NO_x and sulfur dioxide (SO₂) emissions, which are worsening air quality and damaging the hydrological cycle in South East Asia (Ghude et al., 2013). Additionally, CO₂ emissions from coal has more than doubled in this region, as countries such as India has implemented policies such as meeting most of its energy requirements by burning Coal, which has the potential to substantially increase NO_x, SO₂, and particulate matter emission rates (Krotkov et al., 2016; Umezawa et al., 2018). This regional situation has the potential to greatly influence the atmosphere and climate on a global scale due to the annual occurrence of the summertime Asian monsoon during the Northern Hemisphere (NH) summertime months of June – August.

The intense NH summertime heating over regions such as the bay of Bengal, forms a strong convective transport system that is capable of quickly uplifting South Asian polluted air masses into the upper troposphere and even the stratosphere (Randel et al., 2010; Ploeger et al., 2017; Lelieveld et al., 2018). Additionally, the strong regional convective transport produces and sustains a giant anticyclone known as the summertime Asian monsoon anticyclone (AMA) (Lawrence and Lelieveld. 2010). AMA is one of the largest air mass formations on the planet as it can extend from the East China sea to the Mediterranean Sea (Scheeren et al., 2003) covering much of South Asia and the Middle East, and is situated in the upper-troposphere-lower-stratosphere (UTLS). The quasi-stationary near-closed anticyclone (Garny and Randel. 2013; Ploeger et al., 2015) can lock up the South Asian sourced anthropogenic air masses inside it for up to several weeks, resulting in extensive chemical and photochemical processing of pollutants. However, due to AMA encompassing the westerly (mid-latitudes) and easterly (tropics) jets, it can also eject these air masses, thus effectively transporting them around the globe. Satellite observations have measured large enhancements of water vapour, trace constituents, and air pollution within AMA (Park et al., 2004; Filipiak et al., 2005), which is a starkly contrasting chemical situation to the drier and cleaner regions within the ‘background’ upper troposphere (Fu et al., 2006; Park et al., 2008; Santee et al., 2017). To better understand the chemistry and the subsequent fate of pollutants in and around AMA, the Oxidation Mechanism Observations over Asia (OMO-Asia) aircraft campaign in summer 2015 took place. This section will address, from a measurement perspective, to what extent AMA acts as

a pollution purifier through the analysis of HO_x budget, oxidative throughput, and local atmospheric oxidative capacity at altitudes above 11 km.

6.1. Measurement Campaign

The OMO-Asia measurement campaign took place in July and August 2015 and involved the installation of an ensemble of instruments on board the High Altitude Long Range Research Aircraft (HALO), a Gulfstream G550 aircraft, operated by Deutsches Zentrum für Luft- und Raumfahrt (DLR). The aircraft flew at altitudes from 9 km to 15 km between eastern Mediterranean (with base of operations on Cyprus) and the Indian Ocean (with base of operations on the Maldivian island of Gan). In total, 24 flights were performed, which probed the western reaches of the anticyclone where air masses were expected to contain emissions of South Asian origin. Additionally, these air masses were expected to have been rapidly uplifted into the UT where, due to the absence of deposition processes, they have accumulated within the anticyclone and have been chemically processed inside AMA for weeks (Lelieveld et al., 2018). Figure 6.1 shows the flight tracks for all 24 flights, with AMA represented as the August average CO mixing ratios (ranging from 50 to 120 ppb) at 200 mbar taken from the atmospheric-chemistry model, EMAC. There was a large array of instrumentation installed on HALO measuring OH and HO₂, peroxides, VOCs, sulfur and nitrogen oxides, actinic radiation, aerosols. Additionally, tracer species (CH₄ and CO) were also measured to track pollution sources and identify the boundaries of the anticyclone. This was the first time such a repertoire of measurements were performed at these altitudes investigating AMA. Table 6.1 shows a list of the instrumentation that took part in OMO-Asia 2015.

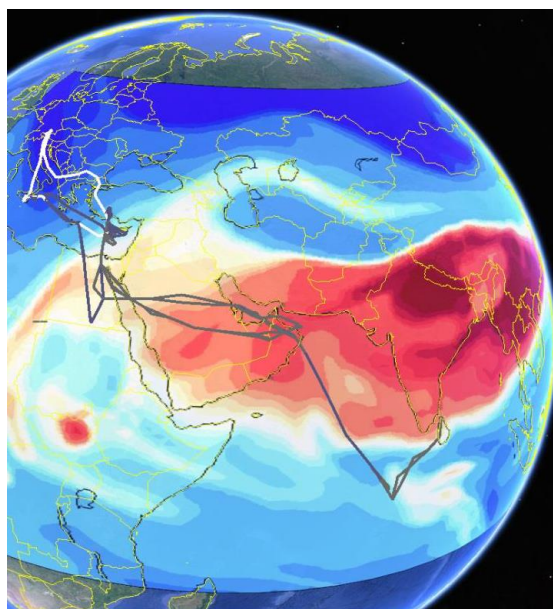


Figure 6.1.: Diagram showing the flight tracks for all the flights performed during OMO-Asia 2015 campaign relative to AMA. The grey flight tracks represent the scientific flights and the white flight tracks show the transfer flights between the base of operations in Cyprus and Oberpfaffenhofen in Germany. The colored overlay shows the output data from the EMAC global model at 200 mbar as monthly average CO mixing ratios for August, ranging from 50 - 120ppb.

Table 6.1.: Instrumentation installed on the HALO aircraft during OMO-Asia 2015.

Species / Quantity	Time resolution	Accuracy (1σ)	Precision (1σ)	Limit of Detection (LOD)	Technique, Instrument
OH	14 s	22.6 %	0.01 – 0.26 pptv [†]	0.02 – 0.11 pptv [†]	IPI-LIF-FAGE, HORUS
HO ₂	14 s	22.2 %	0.11 – 4 pptv [†]	0.23 – 1.2 pptv [†]	IPI-LIF-FAGE, HORUS
OH	40 s	17 % (<10.5 km & >13 km), 34 % (10.5 - 13 km),	0.01 – 0.08 pptv [†]	0.02 – 0.08 pptv [†]	LIF-FAGE, AirLIF
HO ₂	40 s	18 - 26 % (<13.5 km), 35 % (>13.5 km),	0.03 – 3 pptv [†]	0.05 – 1 pptv [†]	LIF-FAGE, AirLIF
CH ₄	1 s	0.25 %	~ 3 ppbv	†††	TDLAS, TRISTAR
CO	1 s	5.1 %	~ 3 ppbv	†††	TDLAS, TRISTAR
O ₃	10 Hz	1.5 %	~ 0.1 ppbv	1.22 % @45 ppbv	CI, FAIRO
H ₂ O	1 s	5 %	1 ppmv	10 ppmv	TDL, SHARC
NO/NO _y	1 s	8 %	< 1 pptv	8 pptv	CI, AENEAS
NO ₂	1 min	4.5 %	3 – 25 pptv [†]	5 – 10 pptv [†]	LIF, GANDALF
H ₂ O ₂ / ROOH	2 min	25 %	0.2% @5.2 ppbv 1.3% @5.9 ppbv for H ₂ O ₂ [†] 0.3% @5.0 ppbv 2.1% @6.0 ppbv for ROOH [†]	8 – 53 pptv for H ₂ O ₂ [†] 9 – 52 pptv for ROOH [†]	DEM-TDLAS, HYPHOP
SO ₂	< 10 s	15 %	8 %	5 pptv	CI-ITMS
Aerosols	1 s	10 %	< 0.00001 # cm ⁻³	10 nm (smallest detectable size)	CPC
Acetone / Acetonitrile	40 s	10 %	2-8 %	57 pptv / 30 pptv	PTRMS, HKMS
VOC's ^{††}	< 3 min	7 %	3.7 – 12.4 % ^{††}	1 – 21 pptv ^{††}	GC-MS, SOFIA
Photolysis Frequencies	2 s	9 – 29 % ^{††††}	< 3 %	-	SR-A, HALO-SR-A

[†] Range of values shown due to temperature / pressure dependencies, additional effects of pitch, roll and yaw of aircraft can lead to precision loss.

^{††} See Bourtsoukidis et al. (2017) for full list of measured VOC species; the precision and LOD have a range due to different VOC sensitivities of SOFIA.

^{†††} See Tadic et al. (2017) for details.

^{††††} Range of uncertainties depending on the photolysis frequency in question.

Acronym meanings: *TDLAS* = Tunable Diode Laser Absorption Spectroscopy, *CI* = Chemical Ionization, *DEM* = Dual Enzyme Monitor, *ITMS* = Ion Trap Mass Spectrometry, *CPC* = Condensation Particle Counter, *PTRMS* = Proton Transfer Reaction Mass Spectrometry, *GC-MS* = Gas Chromatography-Mass Spectrometry, *SR-A* = Spectral Actinic Radiation.

6.2. HO_x measurements during OMO Asia 2015

As described earlier atmospheric OH and HO₂ were measured during OMO-Asia using the Max Planck Institute for Chemistry in Mainz HydrOxyl Radical measurement Unit based on fluorescence Spectroscopy (HORUS) instrument (Martinez et al., 2010). The setup and measurement principle have been described in-depth in section 3. However, onboard HALO during OMO-Asia 2015, an additional LIF-FAGE instrument measuring HO_x was installed from the Forschungszentrum in Jülich (AirLIF). This provided a unique opportunity, as this was the first time two airborne LIF-FAGE instruments measured HO_x at altitudes up to 15 km within AMA.

Overall and regional intercomparison of HORUS and AirLIF

To ensure both datasets show the same temporal variability of HO_x, both HORUS and AirLIF datasets were averaged to the same minute timestamp. Additionally, the Chi-squared linear model (Figure 6.2) was weighted by the combined uncertainty of the measurements (quoted to 1 σ). The average combined measurement uncertainty at 1 σ for OH and HO₂ is 40.8 % and 34.1 % respectively. From Figure 6.2, the overall agreement is $[\text{OH}]_{\text{AirLIF}} = 0.91 [\text{OH}]_{\text{HORUS}} + 1.9 \times 10^5 \text{ molecules cm}^{-3}$ with a correlation coefficient of $r^2 = 0.71$, and $[\text{HO}_2]_{\text{AirLIF}} = 0.87 [\text{HO}_2]_{\text{HORUS}} - 0.12 \text{ pptv}$ with a correlation coefficient of $r^2 = 0.90$. The OH data from the two measurements do not significantly differ as the difference in the means ($0.24 \times 10^6 \text{ cm}^{-3}$) and medians ($0.22 \times 10^6 \text{ cm}^{-3}$) constitute 10.4 % and 9.6 % respectively of the total 2 σ standard deviation of the measurements ($\pm 2.3 \times 10^6 \text{ cm}^{-3}$). The HO₂ data from the two measurements also do not significantly differ as the difference in the means (0.50 pptv) and medians (0.52 pptv) denote 5.2 % and 5.4 % respectively of the total 2 σ standard deviation of the HO₂ measurements ($\pm 9.6 \text{ pptv}$).

To distinguish between background upper troposphere (UT) and AMA, the methane measurements were used (Tomsche et al., 2019). When the measured CH₄ mixing ratios exceed the defined threshold of 1879.8 ppbv these air masses are declared AMA influenced. The overall comparison of AirLIF and HORUS HO_x measurements from the flights where both datasets are available are shown in Table 6.2. The agreement between AIRLIF and HORUS measurements varied from flight to flight and in different regions. MLT_{bg} denotes mid-low troposphere air masses (altitudes 9 km and below). UT denotes the upper troposphere region outside of AMA influence (at altitudes above 9 km where CH₄ levels were below 1879.8 ppbv). AMA denotes the upper troposphere region of AMA influence (at altitudes above 9 km where CH₄ levels were above 1879.8 ppbv). The average and median values for each of the 3 regions and per flight show that the HO_x data from both instruments do not significantly disagree at the 1 σ level, further supporting the conclusions drawn from Figure 6.2.

For OH, the best agreement was reached in the UT regions outside of AMA influence with the mean and median AirLIF/HORUS ratio for OH being 1.10 and 1.09 respectively. The worst agreement in the two OH measurements occurred in flight 21 with the mean and median AirLIF/HORUS ratio for OH being 1.24 and 1.19 respectively, however neither significantly disagree at the 1 σ level. For altitudes below 9 km, the mean OH concentrations for MLT_{bg} are

$3.8 \times 10^6 \text{ cm}^{-3}$ for AirLIF and $3.3 \times 10^6 \text{ cm}^{-3}$ for HORUS, with the mean AirLIF/HORUS OH ratio of 1.13. For HO₂, the largest disagreement exists in flight 24 between the median values, with the median AirLIF/HORUS HO₂ ratio being 0.72. However, this disagreement of 28 % is still 17.9 % smaller than the 1σ combined average measurement uncertainty of 34.1 %, and therefore the two medians do not significantly disagree at the 1σ level. The mean HO₂ mixing ratios for MLT_{bg} was 13.4 pptv for AirLIF and 13.8 pptv for HORUS with the mean AirLIF/HORUS HO₂ ratio of 0.97. This MLT_{bg} comparison does not include the periods when the HALO aircraft flew through the Mt Etna eruption (< 4 km) plume where the background signal in HORUS was large and highly variable ($1.7 \pm 0.5 \times 10^6 \text{ cm}^{-3}$, 2σ). As stated in section 5, volcanic plume chemistry and OH-CHEM interference in HORUS is not fully understood. Additionally, these sub 4 km altitudes are far from the main focus region of the OMO-Asia campaign and of this study (e.g. at altitudes exceeding 11 km). Therefore, no comparisons between the two HO_x instruments involving the Mt Etna eruption outflow were made. With this in mind, the overall high agreement between the two datasets supports a high level of confidence in the atmospheric measurements of OH and HO₂ for the OMO-Asia 2015 campaign.

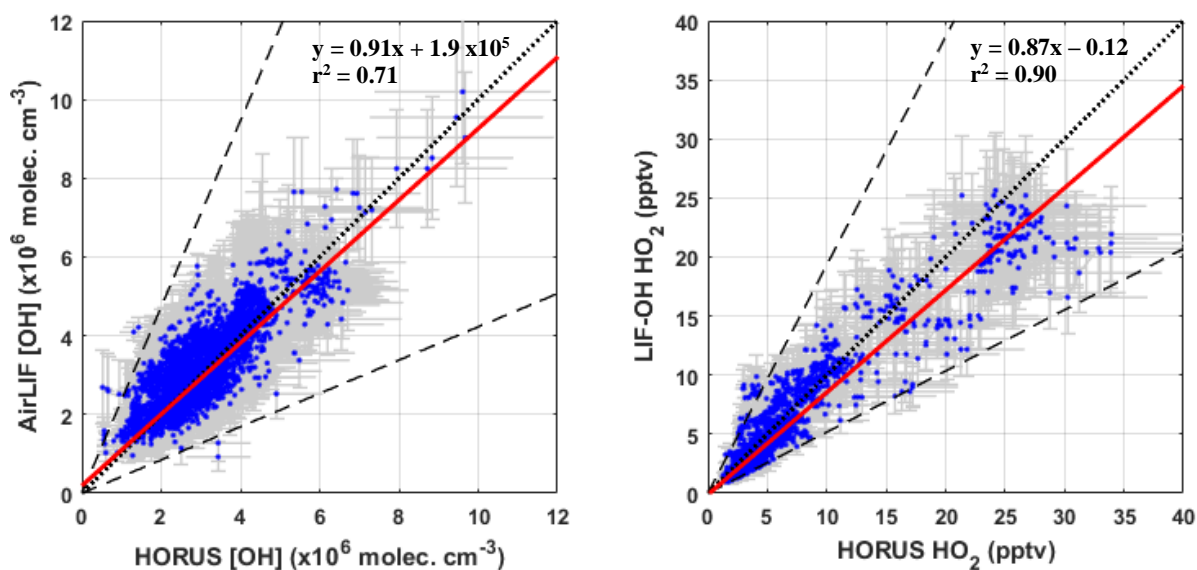


Figure 6.2.: Correlation plot for all available atmospheric OH and HO₂ data between AirLIF and HORUS instruments. The red lines is the linear regression and the black dotted lines are the 1:1 ratio. The grey error bars are the respective measurement total uncertainties (1σ). The dashed lines indicate the combined average measurement accuracy at the 2σ level (57.7 % for OH, and 48.3 % for HO₂).

Table 6.2.: Comparison of measured OH and HO₂ from AirLIF and HORUS during OMO-Asia 2015

Flt #	Flight Description (air masses sampled)	[OH] _{AirLIF} (x10 ⁶ molec. cm ⁻³)		[OH] _{HORUS} (x10 ⁶ molec. cm ⁻³)		[OH] _{AirLIF} / [OH] _{HORUS}		[HO ₂] _{HORUS} (pptv)		[HO ₂] _{AirLIF} / [HO ₂] _{HORUS}	
		mean	median	mean	median	mean	median	mean	median	mean	median
	MLT _{bg}	3.8	3.6	3.3	3.0	1.13	1.19	13.4	10.6	13.8	10.2
	UT	2.7	2.5	2.4	2.3	1.10	1.09	2.6	2.4	3.1	2.9
	AMA	3.5	3.4	3.2	3.1	1.11	1.11	4.9	4.6	5.0	4.8
20	MLT _{bg} , UT, AMA	3.6	3.7	3.3	3.4	1.09	1.09	4.0	3.6	4.7	4.2
21	MLT _{bg} , UT, AMA	3.2	3.1	2.6	2.6	1.24	1.18	4.8	5.1	4.5	4.3
22	MLT _{bg} , UT, AMA	3.2	3.0	2.8	2.7	1.12	1.09	5.4	4.0	6.3	5.1
23	MLT _{bg} , UT, AMA	2.9	2.6	3.0	2.7	0.98	0.96	6.6	3.9	7.4	4.4
24	MLT _{bg} , UT	2.6	2.4	2.8	2.7	0.94	0.90	4.7	2.8	5.9	3.8
All available flight data		3.2	3.1	2.9	2.8	1.1	1.1	5.1	3.7	5.6	4.2
MLT _{bg} = mid-low troposphere air masses (altitudes 9 km and below)											
UT = upper troposphere where air masses were not influenced by AMA (above 9 km and CH ₄ levels were below 1879.8 ppbv)											
AMA = upper troposphere where air masses were influenced by AMA (above 9 km and CH ₄ levels were above 1879.8 ppbv)											

6.3. AMA, HO_x, and oxidation

6.3.1. CAABA-MECCA model

In the pursuit of validating and/or improving our understanding of HO_x chemistry occurring at various spatial and temporal scales within our atmosphere, real-time measurements have frequently been used to parameterize and ratify chemical models. Over the years, this has resulted in numerous developments in chemical mechanisms and their implementations within models. Mechanisms that exist within CAABA-MECCA are the Regional Atmospheric Chemistry Mechanism (RACM) (Stockwell et al., 1997), the Master Chemical Mechanism (MCM) (Jenkin et al., 2015), and the Mainz Isoprene Mechanism (MIM) (Taraborrelli et al., 2009). The MECCA mechanism used in this study is the Mainz Organic mechanism (MOM) (Sander et al., 2019), comprising of 2664 chemical species (including 40 dummy species emulating deposition processes) and 1670 reactions including CH₄, HO_x, O₃, NO_x, non-methane hydrocarbon (NMHC), and sulfur chemistry. The more complex organic reactions in MOM are based on MIM3 but with newly added isoprene oxidation mechanisms (Sander et al., 2019). The original MIM was based on MCM and MIM2 was a further developed to improve the evaluation of a wider range of NO_x regimes with an emphasis in NO_x and nitrogen-containing organic species (Taraborrelli et al., 2009; Mallik et al., 2018). In MIM3, the chemistry involving OH and O₃ oxidation pathways, and HO_x cycling processes were revised and compared well with HO_x measurements under high isoprene mixing ratios (< 1 nmol mol⁻¹) and low NO (< 40 pmol mol⁻¹) (Taraborrelli et al., 2012). However, this study used the CAABA-MECCA model chemical scheme to characterize the budget of HO_x at altitudes exceeding 11 km, in regimes such as AMA, a cocktail containing fresh and highly oxidized Asian emissions where NO mixing ratios regularly exceed 300 pmol mol⁻¹.

6.3.2. Observations

Figure 6.3 shows measurement data from flight 21 (see Appendix C for time series for all flights HORUS measured) where HALO entered AMA (shaded area) at a constant flight altitude. For this flight, OH mixing ratios increased as HALO flew deeper within AMA, with a maximum increase of nearly 50 % (from ~ 0.36 to ~ 0.54 pptv). During this time, $j\text{O}(^1\text{D})$ rates were decreasing from $6.7 (\pm 0.9) \times 10^{-5} \text{ s}^{-1}$ (just outside AMA) to $4.9 (\pm 0.6) \times 10^{-5} \text{ s}^{-1}$ (at the CH₄ maximum), and O₃ mixing ratios were increasing (~ 60 to ~ 90 ppbv). The main source of OH at these high altitudes comes from cycling of HO₂ into OH via the HO₂ + NO channel. In Figure 6.3, the development of OH matches closely with that of NO, and given that AMA is closely linked to anthropogenic and lightning NO_x (Lelieveld et al., 2018), would suggest that the fate of OH in AMA is predominately determined by the cycling within HO_x as opposed to the primary production and loss pathways. On average, the observed OH concentrations inside AMA are $3.1 (\pm 1.4) \times 10^6 \text{ molec. cm}^{-3}$ (2σ), which is 31 % larger than $2.3 (\pm 1.1) \times 10^6 \text{ molec. cm}^{-3}$ (2σ) observed outside AMA at altitudes higher than 11 km and $j\text{O}(^1\text{D})$ values higher than $3 \times 10^{-5} \text{ s}^{-1}$. Additionally under these same conditions, the average observed HO₂ mixing ratios are $4.7 (\pm 2.1) \text{ pptv}$ (2σ) inside AMA, which is 68 % larger than $2.8 (\pm 1.2) \text{ pptv}$ (2σ) outside AMA.

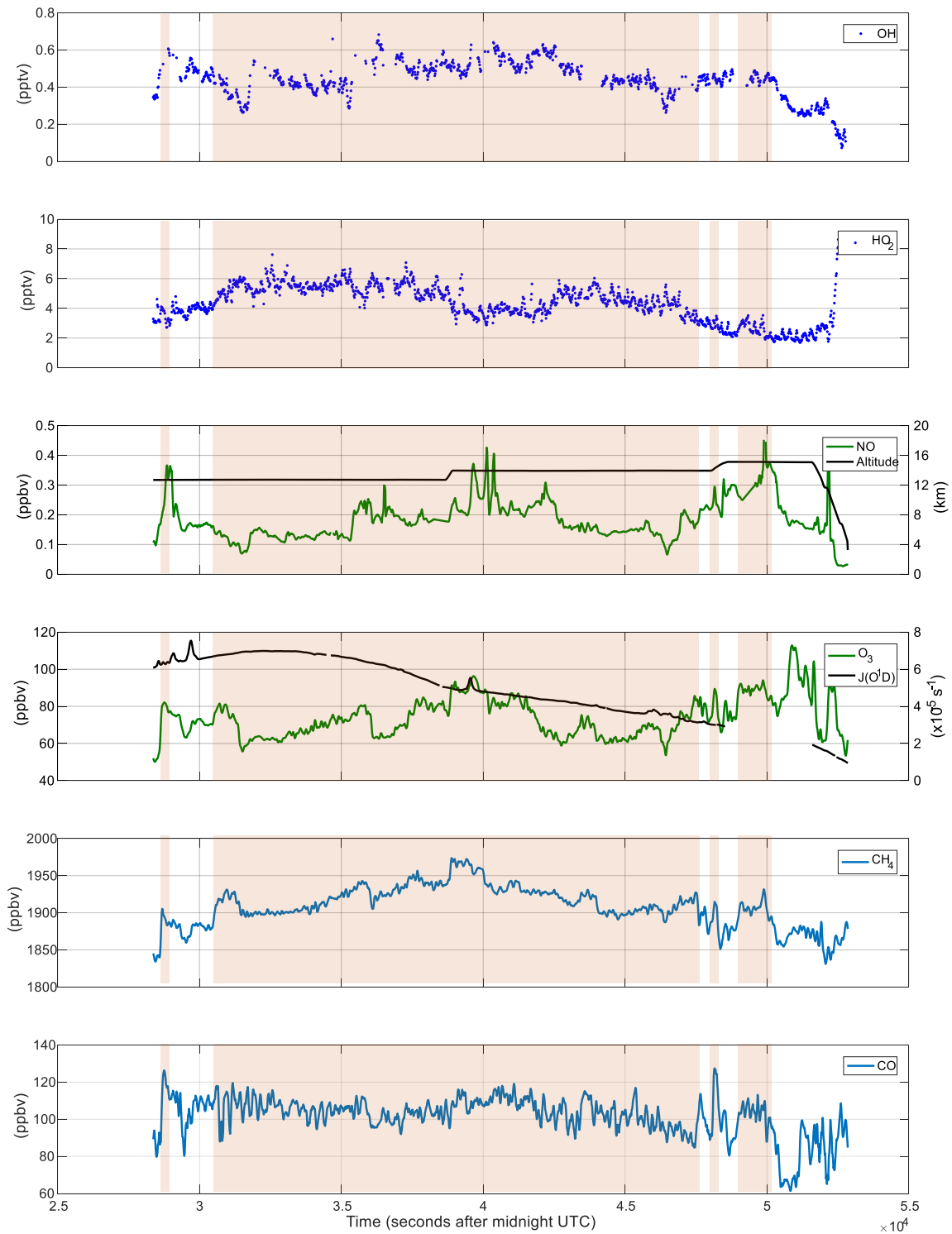


Figure 6.3.: Measurement data from flight 21. The shaded area depicts the period where CH_4 mixing ratio exceeded 1879.8 ppbv, and therefore inside AMA. Data shown for each measurement is averaged within a time window equivalent to 5 times the measurement time resolution, e.g. measurement time resolution = 1 s, the moving average window size = 5 s.

6.3.3. OH and HO₂ budget calculated using observations

In this section, the rate constants labelling is in accordance with that of the MOM chemistry mechanism utilized in the CAABA-MECCA model (Sander et al., 2019), and their temperature dependencies were calculated by applying ambient temperature measurements to the recommended values from JPL (Burkholder et al., 2015) and IUPAC, see Appendix D. Additionally, for any value that represents a single reaction, the quoted uncertainty is the square root of the sum of squares of the reaction rate and measurement uncertainties at the 1 σ level (unless stated otherwise). If a value represents multiple reactions, then the quoted uncertainty is calculated as the square root of the sum of squares of the reaction rates and measurement uncertainty at the 1 σ level (unless stated otherwise) normalized by the degrees of freedom (i.e. the number of reactions involved minus one, N-1). This is to ensure that the quoted uncertainties pertain a useable context. In some cases within this section many reactions are involved, therefore without normalizing the calculated uncertainty by the degrees of freedom, the percentage uncertainty could exceed 100 %.

CO data coverage

As shown in section 2, CO plays a central role within the budget of HO_x. However, CO was not successfully measured during the relevant flights 20, 22, and 24. The following describes how the relationship between the measured CH₄ and CO mixing ratios were used to calculate missing CO data for flights containing air masses of similar origin and have similar flight tracks. As described before, CH₄ is used as a tracer to constrain whether and air mass is AMA influenced or not. Elevated CH₄ concentrations in AMA are typically sourced from regional Asian anthropogenic process such as rice cultivation, urban waste and sewage, biomass and fossil fuel burning (Khalil, 2000; Baker et al., 2012). Elevated CO concentrations are also considered to be a key signature of AMA (Tomsche et al., 2019), as biomass burning, fossil fuel use, and domestic fuels often lead to intense emission rates of CO (Streets et al., 2003; Pandis and Seinfeld, 2006). Figure 6.4, shows the correlation between the measured CO and CH₄ mixing ratio.

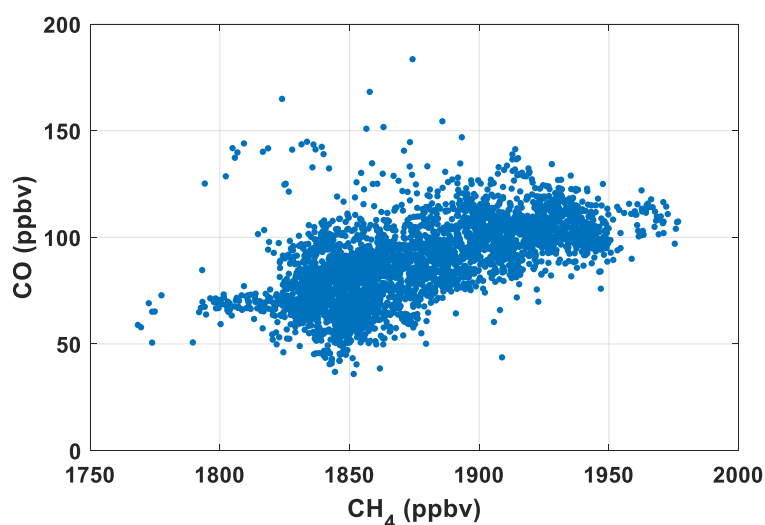


Figure 6.4.: Measured CH₄ vs measured CO mixing ratios for OMO-Asia 2015.

According to the backward trajectory analysis presented within Tomsche et al. (2019), the sampled air masses for flight 20 predominately originated from the same source regions as the those sampled for flight 21, see Appendix E. Additionally, the aircraft flew at altitudes above 11 km across the same region of the Arabian Peninsula at a similar time day for both flights. The same is the case for flights 22 and 23 in terms of the backward trajectories, and the flight tracks are identical, see Appendix E, with the exception of the Mount Etna plume in flight 23 (< 4 km), the data of which as described in section 5 was removed from this study. This provided confidence to use the observed CO-CH₄ relationships from flights 21 and 23 to calculate CO mixing ratios for flights 20 and 22 respectively. If the overall CO-CH₄ relationship plotted in figure 6.4 was to be used to calculate the missing CO data, uncertainties in CO could reach as high as $\pm 35\%$, (quoted as 1σ CO variability in 5 ppbv CH₄ bins). However, the relationship between CO and CH₄ has a dependency on altitude, allowing for further parameterization and minimization of uncertainty, as can be seen in Figure 6.5, the slopes of the observed CO vs CH₄ mixing ratios vary depending on altitude. This could be due to the different sampled air masses at the various altitudes being sourced from specific regions or regional-scale anthropogenic process, and have experienced a varying degree of photochemical ageing, causing distinct CO and CH₄ ratios.

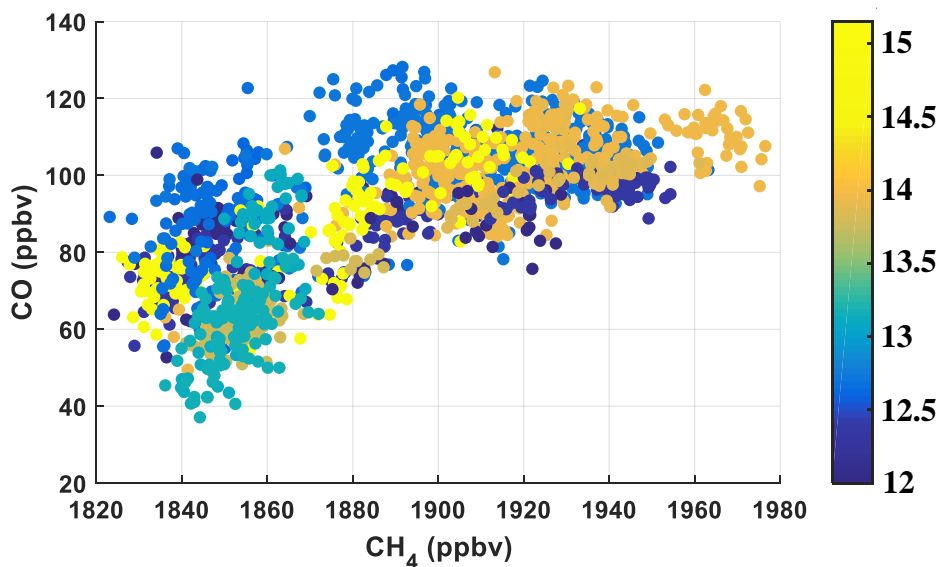


Figure 6.5.: Measured CH₄ vs measured CO mixing ratios at O₃ levels above 40ppbv from flights 19, 21 and 23. Data points are colored by altitude (km).

The missing CO data for flights 20 and 22 (CO_{calc}) was calculated using the available CH_4 measurement data weighted by the resolved altitude-based CO- CH_4 relationship for flights 21 and 23 respectively, which was found by:

$$CO_{calc(i)} = m_{(i)} \cdot CH_{4(i)} - c_{(i)} \quad (6.1)$$

where m and c are the calculated least squares linear correlation coefficients using the measured CO and CH_4 mixing ratios within altitude bins of 250 m (denoted by the (i) subscript) weighted by the measurement uncertainties. Figure 6.6 shows the measured CO and CO_{calc} for flights 20, 21, 22, and 23. By using the approach as described in Equation 6.1, the uncertainty in the CO_{calc} values ranged from 2.9 % to 23.6 %, which represents the 1σ variability the measured CO data about the weighted linear regression within the 250 m bins. The average uncertainty of $9.3 (\pm 3.6) \%$ (1σ) will be quoted for the CO_{calc} data representing CO in flights 20 and 22 within this study. The large shifts in CO_{calc} e.g. 227.52 (flight 20) and at 235.37 (flight 22) occur in instances when HALO entered, at a constant flight altitude, into a chemically contrasting air mass. These calculated CO_{calc} shifts are supported by the observed changes in acetone (CH_3COCH_3) measurements, see Appendix E, which is a strong indication that the method described within Equation 6.1 is capable of capturing and reproducing CO in instances when HALO is entering chemically contrasting air masses.

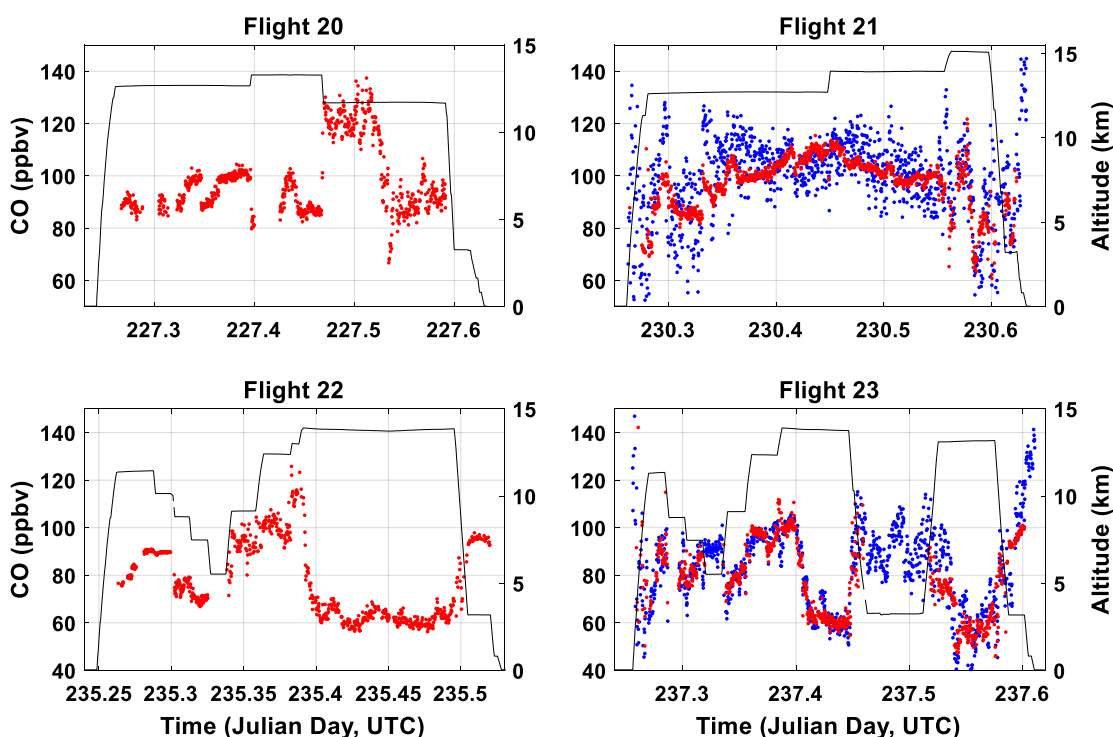


Figure 6.6.: Measured CO (blue points) and CO_{calc} (red points) mixing ratios for flights 20 (top left), 21 (top right), 22 (bottom left), and 23 (bottom right). The black lines represent the flight altitude.

OH budget calculations

One important source of OH is the photolysis of ozone and collision with water, classically described as the primary production of OH ($P_{(\text{OH})}^{1^\circ}$).

$$P_{(\text{OH})}^{1^\circ} = \varphi_{\text{OH}} \cdot j_{\text{O}^1\text{D}} \cdot [\text{O}_3] = 2 \cdot \left(\frac{k_{2111}[\text{H}_2\text{O}]}{k_{2111}[\text{H}_2\text{O}] + k_{1000}[\text{O}_2] + k_{3101}[\text{N}_2]} \right) \cdot j_{\text{O}^1\text{D}} \cdot [\text{O}_3] \quad (6.2)$$

where φ_{OH} is the branching ratio describing the yield of OH when $\text{O}(^1\text{D})$ reacts with H_2O , which is in direct competition with deactivation collisions of $\text{O}(^1\text{D})$ with N_2 and O_2 molecules. As water measurements were not successfully performed above 3 km, the water data was calculated by intersecting the ECMWF reanalysis data (from the operational model, model cycle 4rlr) with the flight track. The uncertainty in water vapor (17.8 %, 1σ) was calculated by moving the intersecting flight track +/- 50 mbar, time +/- 30 minutes, latitude and longitude +/- 0.5 degree.

Another primary source of OH is ozonolysis of alkenes. However, there is limited data coverage of measured alkenes in the upper troposphere. Nevertheless, with the strong negative temperature dependency of alkene ozonolysis reactions suggests that this would be a negligible source for OH in the upper troposphere, especially when compared to other sources discussed within this section. For example, ethene (C_2H_4) which is the most abundant unsaturated hydrocarbon in the atmosphere (Herbin et al., 2009) has been measured to as high as 15 pptv above 9 km over the Eastern Mediterranean and Middle East (Herbin et al., 2009), where the majority of flights during OMO-Asia 2015 took place. From the JPL publication, Burkholder et al. (2015), the rate constant for C_2H_4 with O_3 (E_A/R value of 2630) is $1.7 \times 10^{-19} \text{ cm}^3 \text{ molec.}^{-1} \text{ s}^{-1}$ at the average measured ambient temperature above 9 km of 236.6 K. With the average measured O_3 concentration of $4.9 \times 10^{11} \text{ molec. cm}^{-3}$, the production rate of OH from C_2H_4 ozonolysis would be $10.5 \text{ molec. cm}^{-3} \text{ s}^{-1}$. Even if a more reactive unsaturated hydrocarbon such as 2-methyl-1,3-butadiene (C_5H_8 , known as isoprene) were measured to be 15 pptv above 9 km, the subsequent OH production from isoprene ozonolysis at the same average ambient O_3 concentration of $4.9 \times 10^{11} \text{ molec. cm}^{-3}$ and temperature of 236.6 K would be $144 \text{ molec. cm}^{-3} \text{ s}^{-1}$, which (as an upper limit) is around 3 orders of magnitude smaller than other OH sources discussed within this section. Therefore, alkene ozonolysis as a source for OH will not be further considered within this study.

The secondary production of OH ($P_{(\text{OH})}^{2^\circ}$) considers the photolysis of peroxides and production of OH from reactions involving species such as NO and O_3 reacting with HO_2 as part of cycling within HO_x . Equation 6.3 shows the calculation of $P_{(\text{OH})}^{2^\circ}$ utilizing measurement data of H_2O_2 , NO, O_3 , HO_2 and total ROOH. The photolysis of ROOH (j_{ROOH}) was taken as the measured photolysis frequency of MHP (CH_3OOH).

$$P_{(\text{OH})}^{2^\circ} = j_{\text{H}_2\text{O}_2}[\text{H}_2\text{O}_2] + j_{\text{MHP}}[\text{ROOH}] + k_{\text{G}2107}[\text{O}_3][\text{HO}_2] + k_{\text{G}3201}[\text{NO}][\text{HO}_2] \quad (6.3)$$

Figure 6.7 shows the calculated OH 1° and 2° production rates calculated using Equations 6.2 and 6.3, and averaged into 250 m altitude bins ranging from 11 km to 14.5 km.

Note: Any discussion regarding the OH or HO₂ budget is based on measurement data where $jO(^1D)$ photolysis frequencies are greater than $3 \times 10^{-5} \text{ s}^{-1}$. The lower $jO(^1D)$ threshold of $3 \times 10^{-5} \text{ s}^{-1}$ was implemented in order to minimize the time-of-day bias when comparing photolysis processes inside AMA with photolysis processes outside AMA. With the minimum threshold applied, the average observed $jO(^1D)$ value outside AMA is $5.2 (\pm 0.68) \times 10^{-5} \text{ s}^{-1}$, which is 7.1% lower than the average observed $jO(^1D)$ value inside AMA, $5.6 (\pm 0.73) \times 10^{-5} \text{ s}^{-1}$. As the difference in the means, $0.4 \times 10^{-5} \text{ s}^{-1}$, represents less than 40 % of the combined 1σ uncertainty of the two averages, there is no statistical indication of time-of-day bias, i.e. en masse when the $jO(^1D)$ threshold of $3 \times 10^{-5} \text{ s}^{-1}$ is upheld within this analysis, the photolytic conditions inside AMA are comparable those outside AMA.

In Figure 6.7, the total characterized production rate is significantly driven by secondary production channels of OH, which fundamentally means OH molecules are predominately being recycled back. Based on the observations inside AMA, the average total production rate of OH is $6.5 (\pm 1.1) \times 10^5 \text{ molec. cm}^{-3} \text{ s}^{-1}$, which is 44 % faster than outside AMA ($4.5 (\pm 0.8) \times 10^5 \text{ molec. cm}^{-3} \text{ s}^{-1}$), with more than 80 % of OH being sourced from cycling of HO₂. The dominant source of OH both inside and outside AMA comes from cycling within HO_x via the HO₂ + NO channel. However, inside AMA this channel ($5.1 (\pm 1.4) \times 10^5 \text{ molec. cm}^{-3} \text{ s}^{-1}$) is occurring 59.4 % faster on average than outside AMA ($3.2 (\pm 0.9) \times 10^5 \text{ molec. cm}^{-3} \text{ s}^{-1}$). This is already an indication that observed cycling of HO_x in AMA is being accelerated by the increased NO levels. The primary production contributes ~ 12 % to the total production of OH on average for both inside and outside AMA, equating to $0.76 (\pm 0.3) \times 10^5 \text{ molec. cm}^{-3} \text{ s}^{-1}$ and $0.61 (\pm 0.21) \times 10^5 \text{ molec. cm}^{-3} \text{ s}^{-1}$ respectively. This is attributable to average H₂O mixing ratios being 16 % higher within AMA, thus promoting the primary production of OH. Similar increases in water vapour have been also seen inside AMA in other studies (Santee et al., 2017).

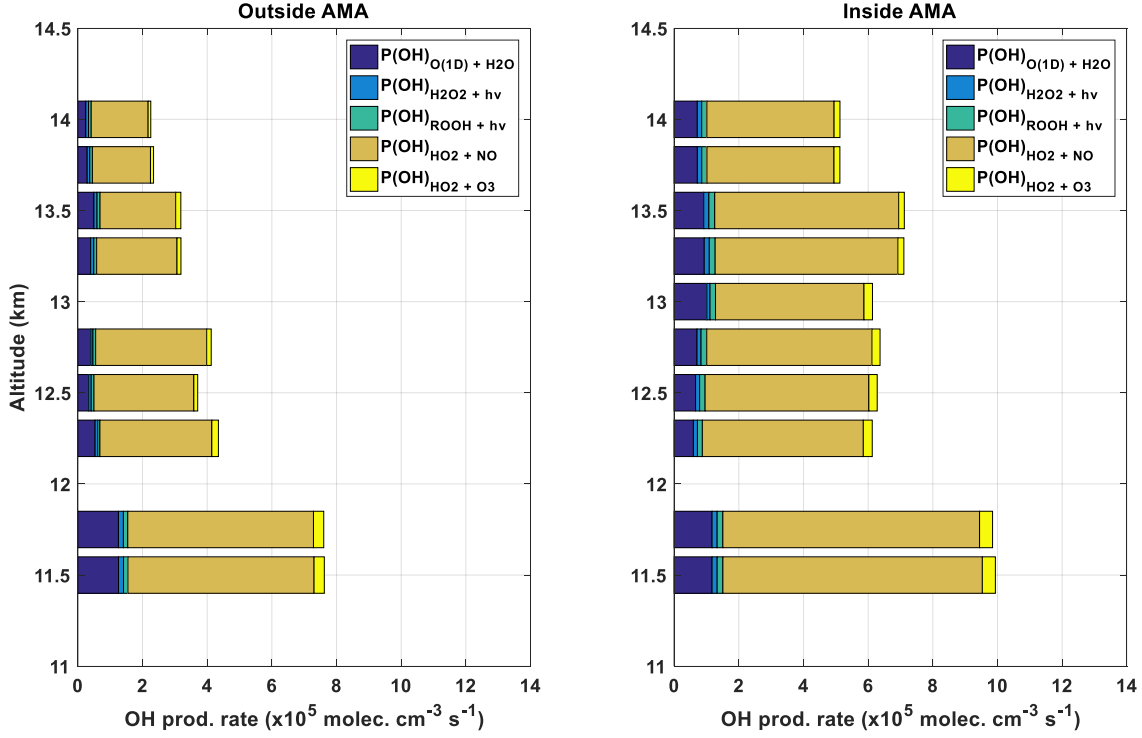


Figure 6.7.: As a function of altitude, the OH primary and secondary production rates outside AMA (left panel) and inside AMA (right panel) calculated directly from available measurements, at altitudes above 11 km and averaged into 250 m bins.

The known loss rate of OH ($L_{(\text{OH})}^{\text{characterized}}$) can be derived from the measured OH concentrations, reaction rates involving the measured species that readily react with OH, and their corresponding concentrations. Equation 6.4 shows how $L_{(\text{OH})}^{\text{characterized}}$ is calculated.

$$\begin{aligned}
 L_{(\text{OH})}^{\text{characterized}} = & k_{G4101}[\text{OH}][\text{CH}_4] + k_{G4110}[\text{OH}][\text{CO}] + k_{G2104}[\text{OH}][\text{O}_3] \\
 & + k_{G2112}[\text{OH}][\text{H}_2\text{O}_2] + k_{G4107}[\text{OH}][\text{ROOH}] + k_{G3202}[\text{OH}][\text{NO}_2] \\
 & + k_{G4108}[\text{OH}][\text{HCHO}] + k_{G2109}[\text{OH}][\text{HO}_2] + k_{G2114a}[\text{OH}]^2 \quad (6.4)
 \end{aligned}$$

As NO_2 is a sink for OH, the NO_2 concentrations used in Equation 6.4 were calculated based on the photostationary state (*PSS*) approximation as reported in other studies (Cantrell et al., 2003; Volz-Thomas et al., 2003). Equation 6.5 shows how the *PSS* NO_2 concentrations are calculated using the available measurements of the involved chemical species and photolysis rate ($j\text{NO}_2$).

$$\text{PSS} [\text{NO}_2] = \frac{k_{G3201}[\text{NO}][\text{HO}_2] + k_{G3103}[\text{O}_3][\text{NO}]}{j\text{NO}_2} \quad (6.5)$$

One consideration to pay mind to is that the production of NO_2 with reaction of NO with RO_2 is not presented within in Equation 6.5. As RO_2 were not measured in OMO-Asia, this

production channel for NO_2 cannot be resolved directly; therefore, the calculated *PSS* NO_2 concentrations represent the lowest quantifiable threshold level. However, the reaction of NO with O_3 contributes over 89 % to the total production term in Equation 6.5. Additionally, the reaction rates of RO_2 species towards NO are typically slower than the reaction rate of HO_2 with NO , therefore suggesting that the missing $\text{RO}_2 + \text{NO}$ production channel for NO_2 would have a minor impact on the calculated *PSS* NO_2 concentrations. Therefore, this *PSS* NO_2 approximation is the best possible quantification of NO_2 concentrations given the lack of RO_2 measurements.

On average, the total characterized loss rate of OH , calculated in Equation 6.4, for inside AMA is $5.4 (\pm 0.8) \times 10^5 \text{ molec. cm}^{-3} \text{ s}^{-1}$, which is 63.6 % larger than outside ($3.3 (\pm 0.5) \times 10^5 \text{ molec. cm}^{-3} \text{ s}^{-1}$). However, as the dominant sinks of OH are involved in the cycling of OH into HO_2 , see Figure 6.8, the amplified OH loss rate inside AMA actually equates to an increase in oxidative throughput of OH . As will be highlighted in the following HO_2 section, the formed HO_2 predominately cycles back OH as opposed to being removed from the chemical system. The main sink of OH for both inside and outside AMA is reaction $\text{OH} + \text{CO}$, which cycles OH into HO_2 . However, the observed cycling of OH to HO_2 with CO is occurring, on average, 74.4 % faster inside AMA ($3.3 (\pm 0.9) \times 10^5 \text{ molec. cm}^{-3} \text{ s}^{-1}$) than outside ($1.9 (\pm 0.6) \times 10^5 \text{ molec. cm}^{-3} \text{ s}^{-1}$).

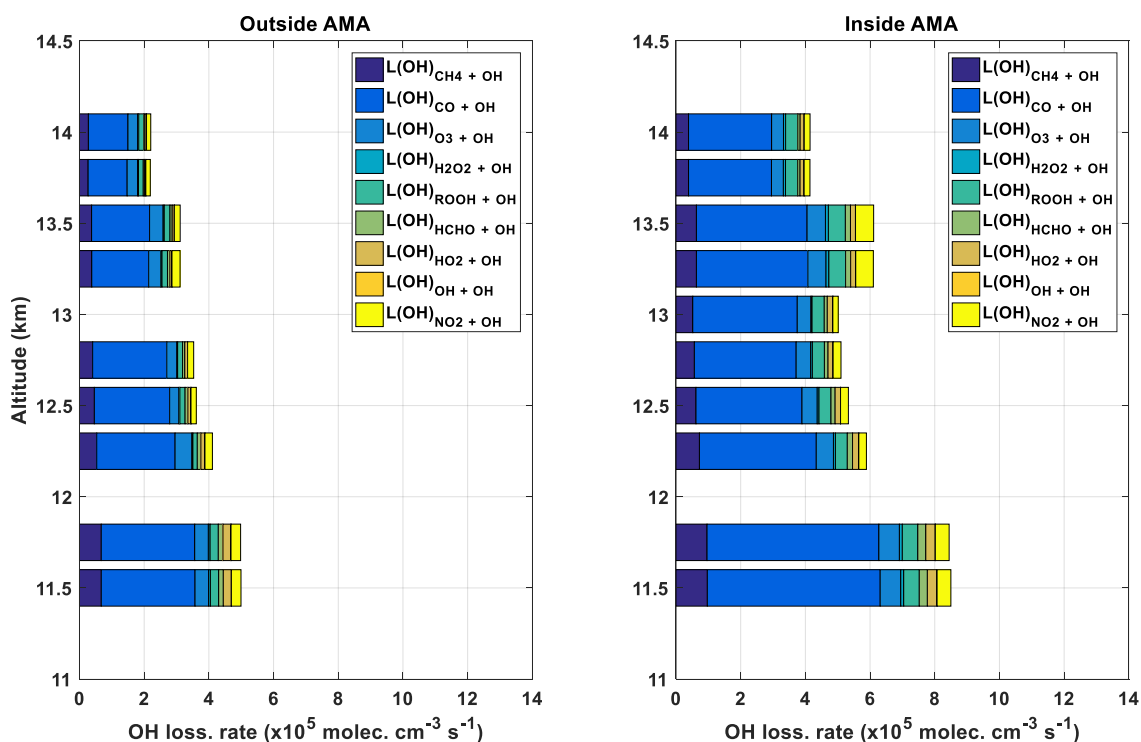


Figure 6.8.: As a function of altitude, the OH loss rates outside AMA (left panel) and inside AMA (right panel) calculated directly from available measurements, at altitudes above 11 km and averaged into 250 m bins.

The second most dominant sink for OH is the reaction with CH₄ yielding an average loss rate of 0.6 (± 0.2) × 10⁵ molec. cm⁻³ s⁻¹ inside AMA, which is 39.5 % faster than outside AMA. However, oxidation of CH₄ with OH leads to the formation of CH₃O₂ radicals, which predominately react further with NO, cycling back a HO₂ radical, which will be described in more detail in the HO₂ budget section.

Due short lifetime of OH in the atmosphere (< 5 seconds) it can be assumed that the measured OH is in steady-state. Therefore, the total loss rate ($L_{(OH)}^{Total}$) should equal the total production rate for OH ($P_{(OH)}^{Total} = P_{(OH)}^{1^\circ} + P_{(OH)}^{2^\circ}$). In order to verify if the known OH reactivity of the species listed in Equation 6.4, ($k_{OH}^{characterized}$):

$$k_{OH}^{characterized} = L_{(OH)}^{characterized} \cdot \frac{1}{[OH]} \quad (6.6)$$

describes the total OH reactivity, Equation 6.6 can be adapted whereby the known loss rate $L_{(OH)}^{characterized}$ is subtracted off the total OH production, $P_{(OH)}^{Total}$, before being normalized by the measured OH concentration to produce the reactivity units of s⁻¹:

$$k_{OH}^{uncharacterized} = (P_{(OH)}^{Total} - L_{(OH)}^{characterized}) \cdot \frac{1}{[OH]} \quad (6.7)$$

From Equation 6.7, it was found that the observations used in Equation 6.4 can only explain, on average, 80 % to 96 % of OH reactivity inside AMA and 66 % to 98 % of the OH reactivity outside AMA, see Figure 6.9. This is attributable to limited representation of k_{OH} posed by NMVOCs, (Non-Methane VOC, which were not measured). Fresh emissions are rapidly transported from the ground and lower troposphere into the UT within hours (Lelieveld et al., 2018) via deep convection, and can be injected into AMA within 2-3 days (Tomsche et al., 2019). The emissions sourced from south Asia are dominated by biomass and bio fuel burning, producing fresh air masses enriched with CO, hydrocarbons, and organic aerosols (Scheeren et al., 2003; Lawrence and Lelieveld. 2010). This means that there are air masses that have experienced extended oxidation periods (1 to 2 weeks) and relatively fresh air masses that pose a higher reactivity towards OH present within AMA. Therefore, to close the OH budget, this uncharacterized reactivity shown in Figure 6.9 is attributed to the missing NMVOC reactivity, which equates to an average loss rate of OH of 1.4 (± 0.4) × 10⁵ molec. cm⁻³ s⁻¹ in AMA and 1.0 (± 0.3) × 10⁵ molec. cm⁻³ s⁻¹ outside AMA.

Figure 6.10 shows the resulting loss rates for OH including the NMVOC contribution, thus closing the OH budget. When NMVOCs are included, the average loss rate for OH increases to 6.7(± 1.0) × 10⁵ molec. cm⁻³ s⁻¹ and 4.2 (± 0.6) × 10⁵ molec. cm⁻³ s⁻¹ for inside and outside AMA respectively.

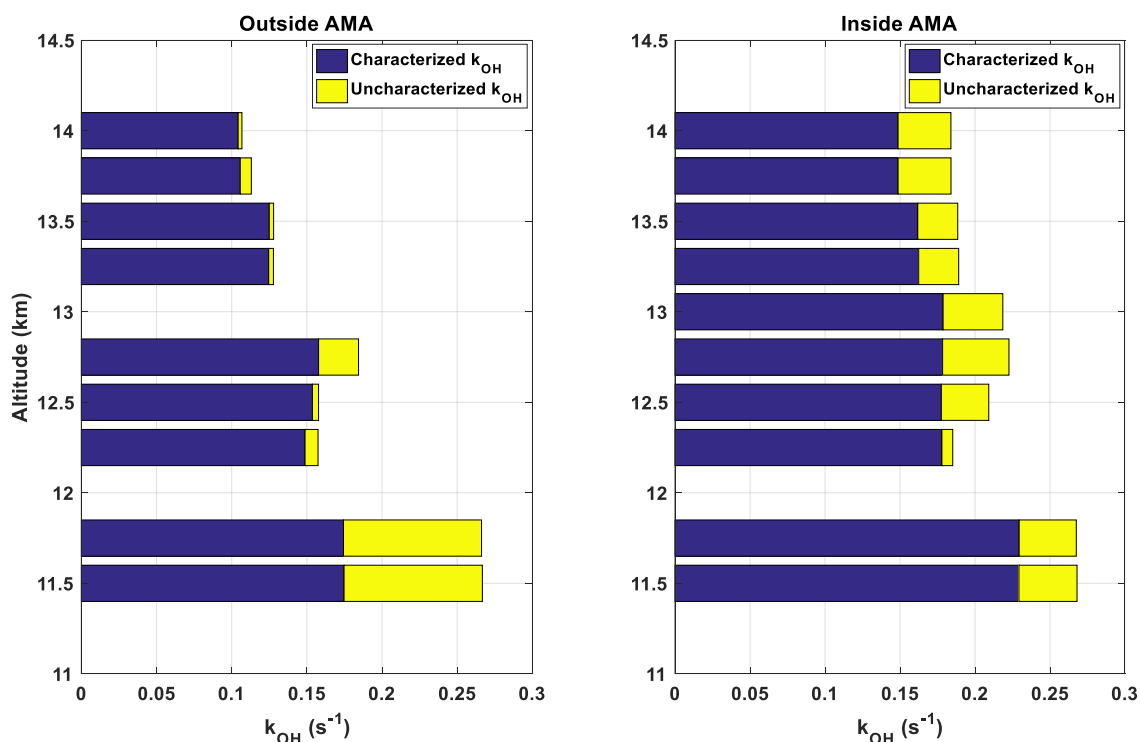


Figure 6.9.: As a function of altitude, the $k_{\text{OH}}^{\text{characterized}}$ (blue bars) and $k_{\text{OH}}^{\text{uncharacterized}}$ (yellow bars) outside AMA (left panel) and inside AMA (right panel) calculated directly from available measurements, at altitudes above 11 km and averaged into 250 m bins.

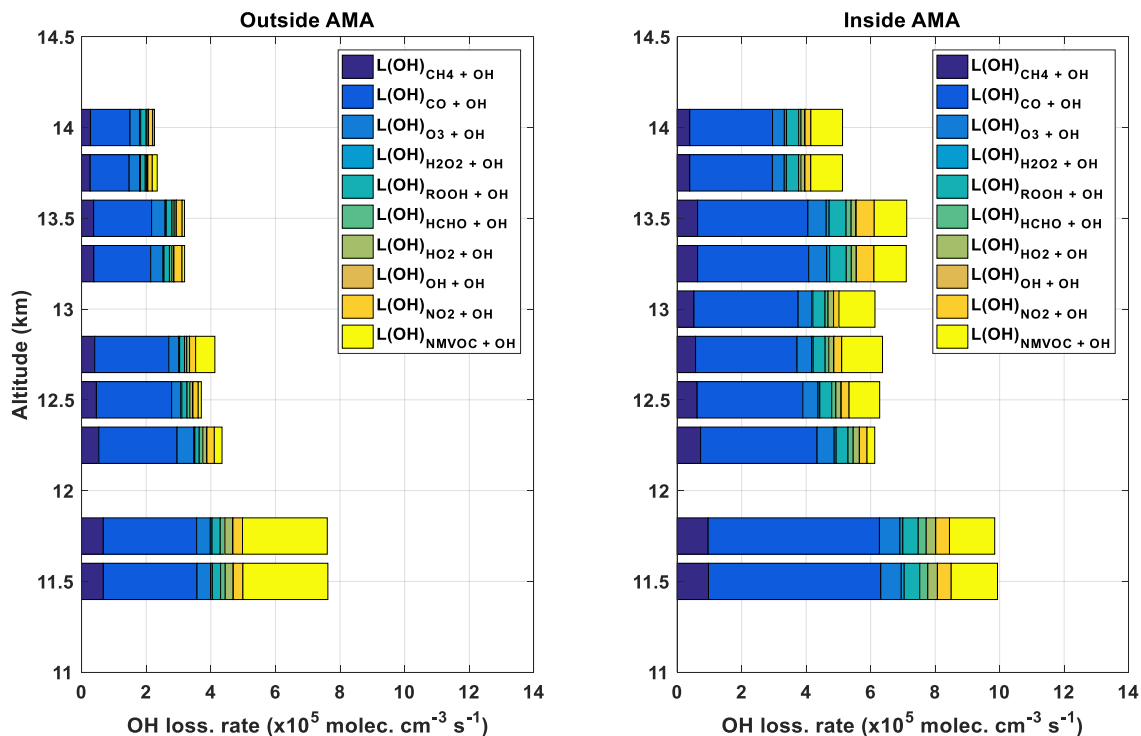


Figure 6.10.: As a function of altitude, the OH loss rates outside AMA (left panel) and inside AMA (right panel) calculated directly from available measurements, including the calculated NMVOC reactivity, at altitudes above 11 km and averaged into 250 m bins.

HO₂ budget calculations

HO₂ plays a critical role in the budget of OH and acts as a reservoir for OH in the atmosphere with HO₂ concentrations being in the order of 100 times greater than OH. Consequently, to understand the oxidative potential of HO_x in the atmosphere, it is important to characterize the HO₂ budget. Equation 6.8 shows how the known production of HO₂ ($P_{(\text{HO}_2)}^{\text{characterized}}$) is calculated:

$$\begin{aligned} P_{(\text{HO}_2)}^{\text{characterized}} = & k_{G4110}[\text{OH}][\text{CO}] + k_{G2104}[\text{OH}][\text{O}_3] + k_{G2112}[\text{OH}][\text{H}_2\text{O}_2] \\ & + k_{G4104}\Phi_{\text{HO}_2}[\text{NO}][\text{RO}_2] + k_{G4108}[\text{OH}][\text{HCHO}] \\ & + 2(j_{41001b}[\text{HCHO}]) + j_{3202}PSS[\text{HNO}_4] \end{aligned} \quad (6.8)$$

where the k are the corresponding rate constants and j are the corresponding measured photolysis rates, which are labelled using the nomenclature from the CAABA-MECCA model. Φ_{HO_2} is the branching ratio whereby the RO₂ + NO reaction yields HO₂. Photolysis of HCHO is multiplied by 2 as the formed H atom from the radical photolysis channel (j_{41001b}) rapidly reacts with atmospheric O₂, producing a second HO₂ molecule.

As RO₂ species were not measured during OMO-Asia, their concentrations are calculated based on the steady-state assumption using the following known and characterizable RO₂ sinks and sources:

$$[\text{RO}_2] = \frac{(k_{G4101}[\text{OH}][\text{CH}_4] + L(\text{OH})_{\text{NMVOC+OH}} + k_{G4107}[\text{OH}][\text{ROOH}])}{(k_{G4104}[\text{NO}] + k_{G4103}[\text{HO}_2] + k_{G4114}[\text{NO}_2])} \quad (6.9)$$

In Equation 6.9 the main source pathway for RO₂ is the OH initiated oxidation of VOCs. Once a VOC is attacked by an OH radical, the subsequent VOC free radical reacts quickly with atmospheric O₂ forming an RO₂, irrespective of the complexity of the initial VOC structure (Jenkin et al., 2015).



Take note that the calculated RO₂ concentrations from Equation 6.9 is the upper limit, as the loss of RO₂ via RO₂ + RO₂ cannot be resolved independently. However, the impact of the missing RO₂ + RO₂ sink can be declared negligible given that the reaction rates are typically two orders of magnitude smaller than the rate constants shown in the denominator in Equation 6.9. Within its 1.5 to 2 day photolytic atmospheric lifetime, upper tropospheric HNO₄ acts as a buffer for HO₂. HNO₄ concentrations were not measured. Therefore, the PSS HNO₄ concentrations were calculated using the measured HO₂ concentrations, measured j_{HNO_4} photolysis frequencies and the PSS NO₂ concentration calculated in Equation 6.5. The rate constant k_{G3207} is the thermo-dissociation rate constant of HNO₄. Equation 6.10 shows the PSS HNO₄ concentration calculation:

$$PSS [\text{HNO}_4] = \frac{k_{G3203}[\text{NO}_2][\text{HO}_2]}{j_{\text{HNO}_4} + k_{G3207}} \quad (6.10)$$

As evident in Figure 6.11, HO₂ production is mainly coming from reactions involving OH. Considering that ~ 82 % of the total production of OH is being sourced from HO₂, as was shown in Figure 6.7, further demonstrates the dominance of cycling within HO_x. Figure 6.11 shows the calculated HO₂ production rates using the reactions and available measurements shown in Equations 6.8 to 6.10, averaged into 250 m altitude bins ranging from 11 km to 14.5 km. Amplification of cycling reactions such as OH + CO, RO₂ + NO and OH + O₃ causes the average HO₂ production rate to increase by 59.5 % from 3.7 (± 0.4) × 10⁵ molec. cm⁻³ s⁻¹ outside AMA to 5.9 (± 0.7) × 10⁵ molec. cm⁻³ s⁻¹ inside AMA. Therefore, additionally supporting the idea that AMA amplifies oxidative throughput, via HO_x cycling reactions, resulting in the 68 % higher measured HO₂ concentrations. The most dominant source for HO₂ is the reaction OH + CO. Inside the observed AMA, this channel equates to 55.9 % (3.3 (± 0.9) × 10⁵ molec. cm⁻³ s⁻¹) of the total production of HO₂, and is occurring 1.7 times faster than outside AMA (1.9 (± 0.6) × 10⁵ molec. cm⁻³ s⁻¹). The second most dominant source for HO₂ is the reaction of RO₂ with NO generating an average production rate of 1.6 (± 0.3) × 10⁵ molec. cm⁻³ s⁻¹ inside AMA, which is 63 % faster than outside AMA (1.0 (± 0.2) × 10⁵ molec. cm⁻³ s⁻¹). As described before, RO₂ compounds, which are largely sourced from OH initiated oxidation of VOCs, predominately react with NO to produce HO₂. Therefore, the amplified RO₂ chemistry is further supporting the faster cycling of HO_x inside AMA.

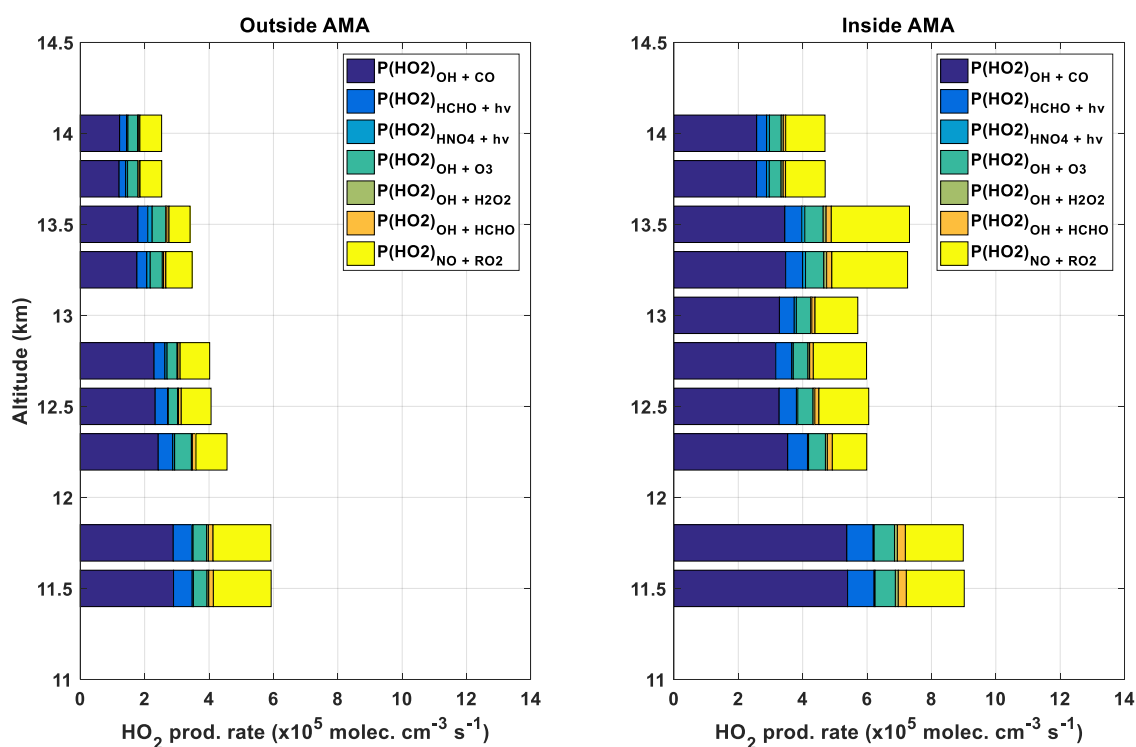


Figure 6.11.: As a function of altitude, the HO₂ production rates outside AMA (left panel) and inside AMA (right panel) calculated directly from available measurements, at altitudes above 11 km and averaged into 250 m bins.

The total characterized loss of HO₂ ($L_{(\text{HO}_2)}^{\text{characterized}}$) is calculated in Equation 6.11 using the measured HO₂ concentrations, reaction rates involving HO₂ and the measured species that readily react with HO₂ and their corresponding concentrations.

$$L_{(\text{HO}_2)}^{\text{characterized}} = k_{\text{G3201}}[\text{NO}][\text{HO}_2] + k_{\text{G2107}}[\text{O}_3][\text{HO}_2] + k_{\text{G3203}}[\text{NO}_2][\text{HO}_2] + k_{\text{G2109}}[\text{OH}][\text{HO}_2] + k_{\text{G2110}}[\text{HO}_2]^2 + k_{\text{G4103}}[\text{RO}_2][\text{HO}_2] \quad (6.11)$$

Overall, the total characterized loss rate for HO₂ is, on average, $6.2 (\pm 0.9) \times 10^5$ molec. cm⁻³ s⁻¹ inside the observed AMA, which is 55 % faster than $4.0 (\pm 0.6) \times 10^5$ molec. cm⁻³ s⁻¹ outside AMA. However, as shown in Figure 6.12, the three most dominant sinks for HO₂ are involved in the cycling and of HO_x. Thus indicating that the 55 % increase in the loss rate of HO₂ inside AMA is only amplifying the rate of cycling within HO_x and therefore oxidative throughput. The dominant sink for HO₂ is the reaction with NO. On average, the reaction of HO₂ with NO inside AMA yields a HO₂ loss rate of $5.1 (\pm 1.4) \times 10^5$ molec. cm⁻³ s⁻¹, which is 59.4 % faster than outside AMA ($3.2 (\pm 0.9) \times 10^5$ molec. cm⁻³ s⁻¹). The second-most significant sink of HO₂ is the reaction of HO₂ with NO₂, resulting in a loss rate of $0.4 (\pm 0.1) \times 10^5$ molec. cm⁻³ s⁻¹ inside and $0.3 (\pm 0.07) \times 10^5$ molec. cm⁻³ s⁻¹ outside AMA respectively. However, the reaction of HO₂ with NO₂ results in the production of HNO₄, which essentially acts as a reservoir for its precursors and readily photolyzes in sunlight and recycles back HO₂ and NO₂. The reaction of HO₂ with O₃ represents the third most dominant channel, with a HO₂ loss rate of $0.25 (\pm 0.07) \times 10^5$ molec. cm⁻³ s⁻¹ inside AMA and $0.18 (\pm 0.05) \times 10^5$ molec. cm⁻³ s⁻¹ outside AMA.

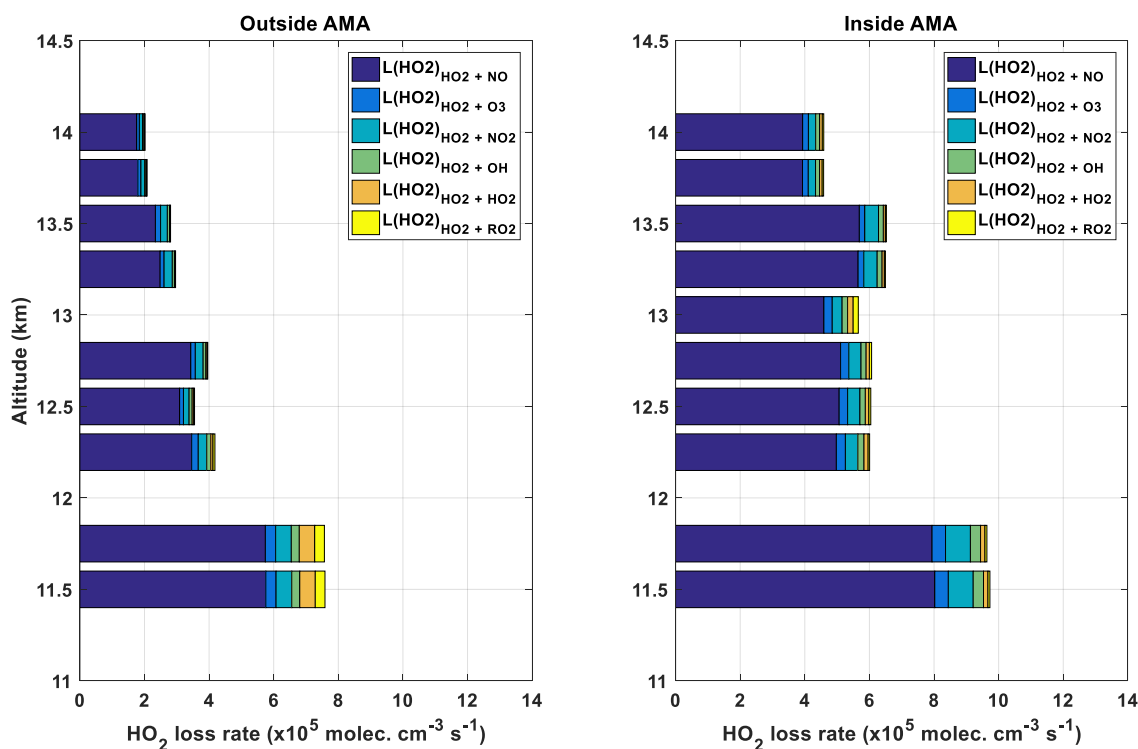
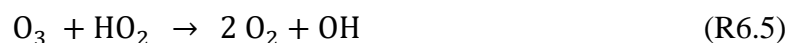
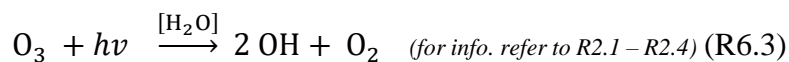


Figure 6.12.: As a function of altitude, the HO₂ loss rates outside AMA (left panel) and inside AMA (right panel) calculated directly from available measurements, at altitudes above 11 km and averaged into 250 m bins.

6.3.4. OH and HO₂ budget implications

From the analysis of the OH and HO₂ budgets, there is a clear acceleration in HO_x chemistry occurring within the sampled air masses of AMA. The oxidation throughput of OH (i.e. the average rate at which OH is produced and lost) increases by 52 %, from ~ 4.3 (± 0.7) x10⁵ molec. cm⁻³ s⁻¹ outside to ~ 6.6 (± 0.9) x10⁵ molec. cm⁻³ s⁻¹ within AMA. This amplification in OH chemistry is predominately supported by the 2.3 (± 0.6) x10⁵ molec. cm⁻³ s⁻¹ increase in the absolute production rate of OH via the HO₂ + NO channel, which is a direct result of increased injection of NO into AMA from lightning and anthropogenic sources (Brune et al., 1998; Schumann and Huntrieser, 2007; Lelieveld et al., 2018). Additionally, HO₂ not only acts as a reservoir for OH, but it is also an oxidizer. The subsequently produced NO₂ from the HO₂ + NO reaction can rapidly photolyze producing O(³P) atoms. These O(³P) atoms readily collide with atmospheric oxygen forming O₃. Therefore, the HO₂ + NO reaction ultimately plays an important role in ozone formation within the UT and lower stratosphere (Faloona et al., 2000). When combining the reaction rates of the main loss channels for O₃ in the UT:



the threshold for O₃ formation / destruction conditions can be resolved. If the sum of the reaction rates HO₂ + NO and RO₂ + NO exceed the sum of the reaction rates of reactions R6.3 to R6.5, then the system is considered to be in an ozone formation condition (Hegglin et al., 2006; Bozem et al., 2017). The net ozone production rate (*NOPR*) essentially describes if the prevailing conditions result in ozone formation (*NOPR* is positive) or ozone destruction (*NOPR* is negative). *NOPR* has the units of ppbv h⁻¹ and is calculated:

$$\text{NOPR} = \frac{(\text{P}_{(\text{O}_3)} - \text{L}_{(\text{O}_3)})}{(1 \times 10^{-9} \cdot N_A)} \cdot \left(V_{mol} \cdot \frac{T}{T_0} \cdot \frac{P_0}{P} \right) \cdot 3600 \quad (6.12)$$

where N_A is Avogadro's constant (6.022x10²³ mol⁻¹), 1x10⁻⁹ is the conversion to ppbv, V_{mol} is the molar volume = 22413 m³ mol⁻¹, T is ambient temperature in Kelvin, T_0 is standard temperature (273.15 K), P is ambient pressure (mbar), P_0 is standard pressure (1013.25 mbar). The value 3600 is to convert from s⁻¹ to h⁻¹. The production rate of O₃ ($\text{P}_{(\text{O}_3)}$) and loss rate of O₃ ($\text{L}_{(\text{O}_3)}$) (units: molec. cm⁻³ s⁻¹) are calculated using the following:

$$\text{P}_{(\text{O}_3)} = k_{\text{G3201}}[\text{NO}][\text{HO}_2] + k_{\text{G4104}}[\text{NO}][\text{RO}_2] \quad (6.13)$$

$$\text{L}_{(\text{O}_3)} = \left(0.5 \cdot \text{P}_{(\text{OH})}^{\circ} + k_{\text{G2104}}[\text{OH}][\text{O}_3] + k_{\text{G2107}}[\text{O}_3][\text{HO}_2] \right) \quad (6.14)$$

It is critical to note here that the primary production rate of OH used in Equation 6.14 is halved, as $\text{P}_{(\text{OH})}^{\circ}$ leads to formation of two OH molecules whilst only consuming one O₃ molecule. The primary production rate of OH already considers the collision of O(¹D) atoms with N₂ or O₂, which is important as such collisions ultimately reform O₃. Figure 6.13 shows the calculated *NOPR* values averaged within 250 m altitude bins.

It is clear that the increased presence of HO₂, RO₂, and particularly NO within AMA greatly enhances the observed production rate of O₃. Despite UT conditions universally supporting O₃ formation, on average, the observationally resolved *NOPR* inside AMA (0.23 (± 0.04) ppbv h⁻¹) is 91.7 % faster than outside AMA (0.12 (± 0.02) ppbv h⁻¹). At altitudes above 13 km, *NOPR* values inside AMA can be up to 7 times faster than calculated *NOPR* values at similar altitudes in background UT air masses. This is in agreement with other studies that have also found strong enhancements in potential O₃ formation (*NOPR*) in convective outflows of electrified thunderstorms, i.e. convected air masses containing lightning NO_x (Bozem et al., 2017) such as those found within AMA. With respects to the enhancement of HO₂, the convection of lightning NO into AMA causes HO₂ oxidation throughput to increase by a 57 %, which supports the 31 % increase in OH concentrations, which in turn enhances OH oxidation throughput, and additionally proliferates the rate of ozone formation. The calculated OH and HO₂ budgets inside AMA and in undisturbed UT air masses have shown that once the pollutants are convected into and locked within AMA, their respective atmospheric lifetimes become shortened by a factor of 1.52. This factor is directly derived from the 52 % increase in OH oxidative throughput inside AMA, i.e. the average of the OH production and loss rate. Consequently, the AMA enhancement of HO_x chemistry oxidizes pollutants out of the system sooner, before potentially being ejected out of AMA and transported globally.

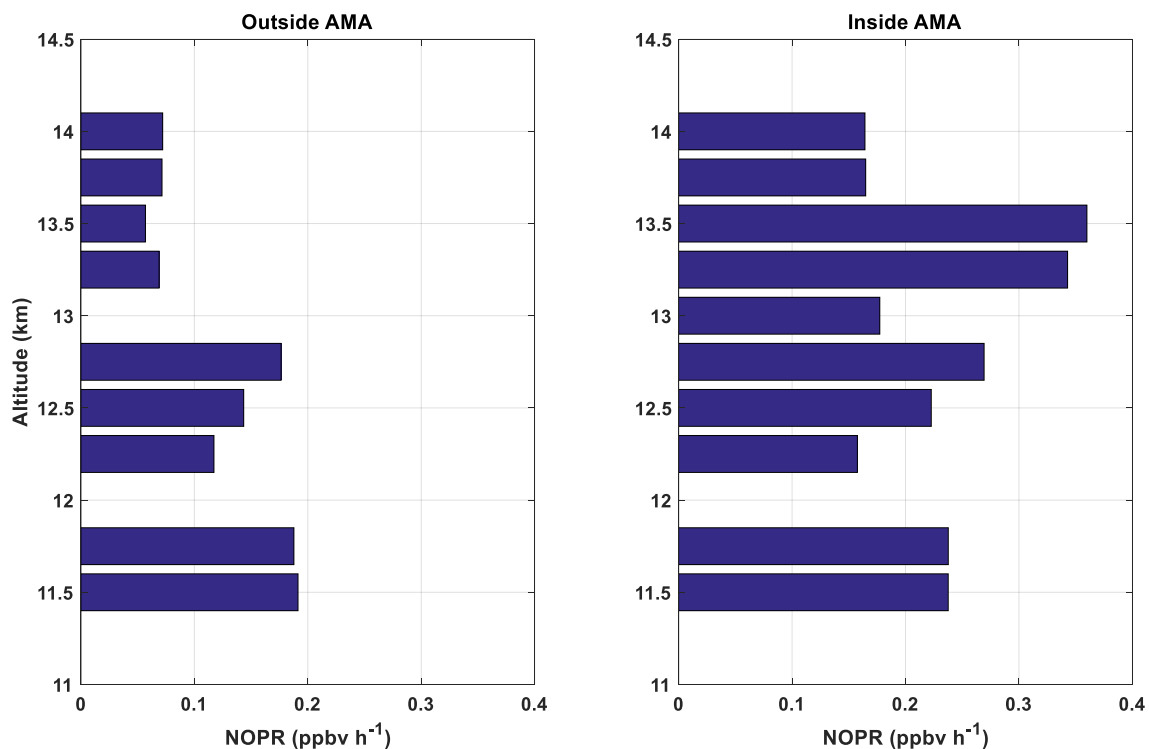


Figure 6.13.: Net ozone production rate (*NOPR*) outside AMA (left panel) and inside AMA (right panel) averaged into 250 m altitude bins, applying the threshold where $jO(^1D)$ photolysis frequencies are greater than $3 \times 10^{-5} \text{ s}^{-1}$, which equates to $\sim 60 \%$ of the daylight hours centered around the photolysis rate peak.

During the OH and HO₂ budget analysis within this study, two distinctly contrasting air masses were observed in AMA, see Figure 6.14. There are instances where OH reactivity posed by NMVOCs increases from ~ 15 % up to 40 - 50 %, see Figures 6.10 and 6.14, whereas the reactivity posed by CO decreases from ~ 54 % down to 22 – 30 % of the total OH loss rate. Within these same air masses, the source of HO₂ via the RO₂ + NO channel can increase up to a rate of 3.1 (± 0.7) x10⁵ molec. cm⁻³ s⁻¹. This equates to 55 % of the total production of HO₂, which exceeds the HO₂ production rate via the CO + OH channel, and is ~ 2.5 times larger than the production rate of HO₂ via RO₂ + NO (1.3 (± 0.3) x10⁵ molec. cm⁻³ s⁻¹) in air masses where CO is dominating OH reactivity. In the air masses where OH reactivity is dominated by NMVOC's, the oxidative throughput of OH is on average 6.1 (± 0.9) x10⁵ molec. cm⁻³ s⁻¹, which is not significantly different than the 5.9 (± 0.8) x10⁵ molec. cm⁻³ s⁻¹ throughput rate of OH in air masses where OH reactivity is dominated by CO. Therefore, this increase in NMVOC reactivity on OH actually buffers cycling within HO_x in the instances where CO levels are dropping, as many NMVOCs that undergo oxidation with OH form RO₂ species. Due to the elevated NO levels in AMA, RO₂ species ultimately cycle back HO₂ by undergoing a further reaction with NO (Butkovskaya et al., 2012; Chai et al., 2014).

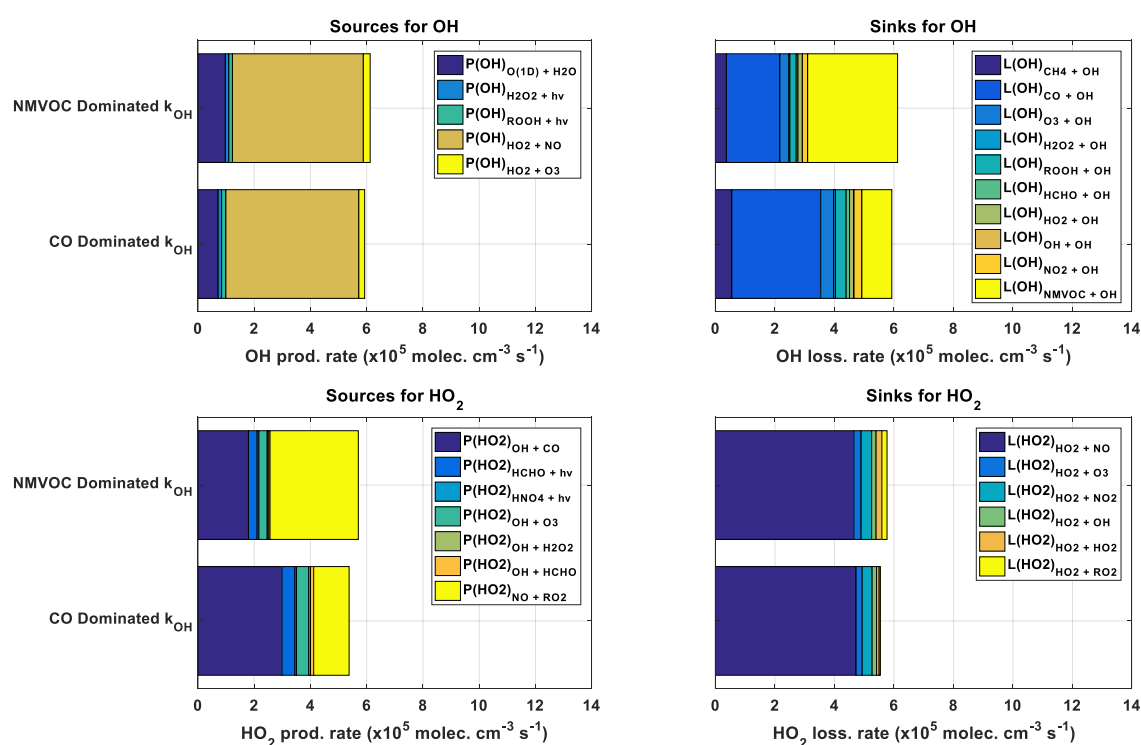


Figure 6.14.: OH and HO₂ budgets in two contrasting air masses inside AMA calculated directly from available measurements, at altitudes above 11 km for all available HO_x data from the OMO-Asia 2015 campaign. The labelling on the y-axis denotes the main contrasts. NMVOC label is for air masses where NMVOCs dominate OH reactivity. The CO label is for air masses where CO dominates OH reactivity.

As mentioned before, there are air masses present within AMA that have experienced 1-2 weeks (Lawrence and Lelieveld. 2010; Lelieveld et al., 2018) of oxidation and have become aged, meaning that much of the reactive NMVOCs have been oxidized by OH forming aldehydes, which in turn are rapidly photolyzed producing CO. Conversely, many air masses originating from ground and lower tropospheric sources can be rapidly uplifted within a matter of days into AMA and its outer reaches (Scheeren et al., 2003; Tomsche et al., 2019). Such air masses have not yet experienced extensive ageing, thus contain higher levels of reactive NMVOCs and NO_x (Lawrence and Lelieveld. 2010), and therefore can pose an increased reactive loading on the HO_x chemical system. However, as demonstrated in Figure 6.14 and in section 6.3.3, the increased NMVOC and NO reactive loading on HO_x actually promotes cycling within HO_x.

In addition, the primary production of OH is 38.9 % faster inside air masses ($1.0 (\pm 0.3) \times 10^5 \text{ molec. cm}^{-3} \text{ s}^{-1}$) where OH reactivity is more dominated by NMVOCs than in the more aged air masses ($0.72 (\pm 0.2) \times 10^5 \text{ molec. cm}^{-3} \text{ s}^{-1}$). This is mostly due to the average water vapor mixing ratio being 32.3 % larger in fresh air masses ($84.8 (\pm 15.1) \mu\text{mol mol}^{-1}$) than in aged air masses ($64.1 (\pm 11.4) \mu\text{mol mol}^{-1}$). The drying of air masses locked within AMA occurs predominately by diffusion, ice particle formation, or by dilution via stratospheric-tropospheric exchange events (Skerlak et al., 2014) and convective overshooting (Sherwood and Dessler. 2001). As described in Tomsche et al. (2019), the average time taken for air masses produced within the PBL to be transported into AMA is around 10 days. Considering that, the atmospheric lifetimes of many NMVOCs range from hours to a few days, photochemical age determinations are required in order to calculate the extent of ageing of the air masses (Rudolph and Johnen. 1990; Kleinman et al., 2003; Saito et al., 2009; Irei et al., 2016) shown in Figure 6.14. Such approaches require high data coverage of multiple NMVOCs that have disparate atmospheric lifetimes but originate from similar sources e.g. Toluene (2 days) and Benzene (12 days) (Lanz et al., 2009), along with emission tracers such as CO and CH₄. Unfortunately, despite the high data coverage of CO and CH₄, they alone cannot be used to determine the photochemical age of air masses as the lifetimes of 2-3 months for CO and ~ 9 years for CH₄ (Tomsche et al., 2019), are orders of magnitude longer than the typical 1-2 weeks residence time of air masses within AMA. Therefore, due lack of the required measurement coverage of various NMVOCs such as Toluene and Benzene, it is not possible to conclusively determine the photochemical age of air masses within this study. However, as shown in Figure 6.14, there is evidence showing that both fresh and photochemically aged air masses were observed within AMA.

To summarize

In section 6.3, the budget analysis of HO_x has revealed that oxidative chemistry is occurring at an elevated rate within AMA. Not only are the measured OH and HO₂ levels within AMA 31 % and 68 % larger respectively, but the increased pollutant loading observed inside AMA causes the oxidative throughput of OH to accelerate by a factor of 1.52 times when compared to sampled air masses outside AMA. This is predominately due

to amplified cycling within HO_x. The increased injection of lightning and anthropogenic NO_x into AMA elevates NO levels by 16.6 %, which promotes cycling of HO₂ into OH. This enhancement in cycling by the elevated NO presence in AMA, supports the acute buffering processes that cycle back HO₂. The accelerated VOC oxidation with OH within AMA contributes a significant fraction towards cycling OH to HO₂, and buffers against instances where cycling via CO + OH is less favored. This buffering is critical for AMA's ability to remove pollutants at an elevated rate whilst still maintaining its oxidative capacity.

6.4. OH recycling probability and oxidative capacity

The OH radical defines the oxidative capacity of the atmosphere. The oxidative capacity of the atmosphere otherwise known as the self-cleansing capacity means the ability of the atmosphere to oxidize and remove pollutant trace gases that are emitted or produced in-situ (Prinn, 2003; Lelieveld et al., 2004). As described before, beyond primary production of the oxidant (OH), recycling within HO_x plays an essential role in maintaining OH concentrations within the atmosphere. So much so, that in autocatalytic conditions, HO_x levels could be amplified to such an extent that the chemical system could become unstable. On the other hand, the complete deficiency of HO_x cycling would lead to catastrophic accumulation of reduced gases and pollutants (Lelieveld et al., 2002). Therefore, the probability of a single OH molecule recycling back through the atmospheric chemical system is an indicator of stability and oxidative strength. Primary sources of OH essentially produce OH without previously involving in-situ oxidation by an OH radical. Secondary sources either produce OH from a compound that was previously formed from in-situ oxidation by OH or involves HO₂ reacting with a chemical species that results in the direct production of at least one OH molecule. The recycling probability of OH (r_{OH}) is calculated by taking the ratio of the secondary sources (S) to the total hydroxyl radical production, e.g. primary (P) plus S (Lelieveld et al., 2002):

$$r_{OH} = \frac{S}{P+S} \quad (6.15)$$

which when adapted to the nomenclature used within this work:

$$r_{OH} = \frac{P_{(OH)}^{2^{\circ}}}{P_{(OH)}^{1^{\circ}} + P_{(OH)}^{2^{\circ}}} \quad (6.16)$$

The budget analysis in section 6.3 shows that NO controls the recycling of OH by reacting with HO₂ and RO₂, see reactions R2.20, R2.21, and R2.17. Therefore, NO concentrations contribute significantly to both the nominator and denominator in Equation 6.16. Consequently, the approximation of r_{OH} can be parameterized as a function of the NO concentration. Figure 6.15 shows, with high data coverage, the NO dependency of r_{OH} , calculated using measurement data from numerous ground-based, ship, and airborne campaigns spanning various environments (Hens, 2013). In Figure 6.15, the calculated r_{OH} shows a strong dependence on NO levels. When NO levels are in the <10 ppt_v range, r_{OH} values are typically low at around 0.2. Conversely, when NO levels reach the ppbv range,

r_{OH} levels increase up to a maximum plateau with values exceeding 0.95. There have been studies that show that there are conditions where high levels of atmospheric NO can adversely affect r_{OH} . If NO levels are high enough to produce ppbv levels of NO_2 , reactions such as $RO_2 + NO$ (forming organic nitrates) and $OH + NO_2$ (a direct sink for OH and forms HNO_3) can become prevalent enough to limit or even reduce recycling probabilities of OH (Crawford et al., 2000; Jaegle et al., 2001; Cariolle et al., 2008). This is critical in preventing r_{OH} values from exceeding 1 and therefore preventing OH autocatalytic oxidation (Lelieveld et al., 2004). However, given the temperature dependence of the $NO + O_3$ reaction (Burkholder et al., 2015), which dominates NO_2 formation, the required NO levels needed to push NO_2 mixing ratios to a ppbv range within the UT have to be much higher than the NO levels stated in other (ground-based) publications, see Ehhalt (1999) and Rohrer et al. (2014). These aforementioned nitrate formations reactions are in direct competition with reactions that directly convert OH to HO_2 . If there is sufficient CO present and NO levels are near the optimum level for OH recycling (i.e. at that given ambient temperature and O_3 level), then the direct OH to HO_2 conversion (and vice versa) reactions are favored and dominate the cycling within HO_x and pushes r_{OH} closer to a value of 1.

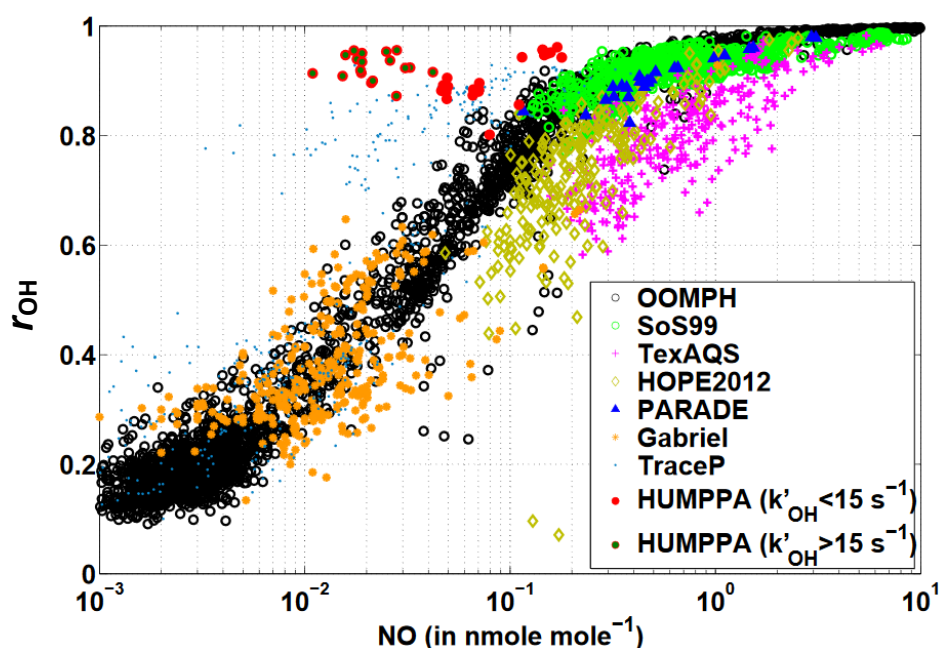


Figure 6.15.: OH recycling probability (r_{OH}) as a function of the NO mixing ratio from numerous measurement campaigns in various environments. OOMPH – marine boundary layer, ship stack plume; SOS99 – metropolitan, biogenic VOCs; HOPE12 and PARADE – biogenic and anthropogenic VOCs; TexAQS – metropolitan, anthropogenic VOCs; Gabriel – tropical rainforest; Trace-P – Airborne East Asia and western pacific; HUMPPA–COPEC–2010 – boreal forest. Figure and caption information taken and from Hens (2013) and modified.

As stated in section 6.3, the measurements of atmospheric species such as H₂O₂ and their photolysis are considered as a secondary source for OH. However, when investigating air masses that are associated with strong transport processes, such as AMA (convection), an additional consideration regarding transported and in-situ produced concentrations is critical in the appropriate determination of r_{OH} . If a chemical's atmospheric lifetime is sufficiently long enough, a fraction of the measurement of this chemical species was produced over three HO_x lifetimes earlier, which is therefore not a product of the measured in-situ HO_x. Consequently, when this fraction decomposes or photolyzes, producing OH at a rate less or equivalent to one HO_x lifetime (~ 4 minutes), it is acting as a primary source for HO_x. This fraction therefore must be distinguished from the fraction that is produced within one lifetime of HO_x, i.e. is a product of the in-situ measured HO_x, of which when decomposing or photolyzing into OH is functioning as a secondary source for OH. To separate H₂O₂ and ROOH with regards to their secondary and primary production contributions, their *PSS* concentrations are calculated to represent the in-situ produced fraction:

$$[H_2O_2]_{PSS} = \frac{k_{G2110}[HO_2]^2}{j_{H_2O_2} + k_{G2112}[OH]} \quad (6.17)$$

$$[ROOH]_{PSS} = \frac{k_{G4103a}[HO_2][RO_2]}{j_{MHP} + k_{G4107}[OH]} \quad (6.18)$$

where the photolysis of $[H_2O_2]_{PSS}$ and $[ROOH]_{PSS}$ is the calculated secondary production of OH from peroxides. Equations 6.19 to 6.21 show how r_{OH} is calculated using the characterized *PSS* peroxides. As the measured $[H_2O_2]$ and $[ROOH]$ contain both $P_{(OH)}^{1^\circ}$ and $P_{(OH)}^{2^\circ}$ sources, the total measured values are used within the denominator in Equation 6.21:

$$P_{(OH)}^{1^\circ} + P_{(OH)}^{2^\circ} = \left(\begin{array}{l} \varphi_{OH}j_{O^1D}[O_3] + j_{H_2O_2}[H_2O_2] + j_{MHP}[ROOH] \\ + k_{G2107}[O_3][HO_2] + k_{G3201}[NO][HO_2] \end{array} \right) \quad (6.19)$$

$$P_{(OH)}^{2^\circ} = \left(\begin{array}{l} j_{H_2O_2}[H_2O_2]_{PSS} + j_{MHP}[ROOH]_{PSS} + k_{G2107}[O_3][HO_2] \\ + k_{G3201}[NO][HO_2] \end{array} \right) \quad (6.20)$$

$$r_{OH} = \frac{[j_{H_2O_2}[H_2O_2]_{PSS} + j_{MHP}[ROOH]_{PSS} + k_{G2107}[O_3][HO_2] + k_{G3201}[NO][HO_2]}{[\varphi_{OH}j_{O^1D}[O_3] + j_{H_2O_2}[H_2O_2] + j_{MHP}[ROOH] + k_{G2107}[O_3][HO_2] + k_{G3201}[NO][HO_2]} \quad (6.21)$$

Figure 6.16 shows the calculated r_{OH} values for both inside and outside AMA using Equation 6.21 plotted as a function of the measured NO mixing ratios.

Note: The x-axis in Figure 6.16 is linear scale (unlike the logarithmic scale shown in Figure 6.15) due to the measured NO values not spanning multiple orders of magnitude.

Figure 6.16 shows that AMA is capable of maintaining r_{OH} at 0.84 on average, and can buffer the cycling of HO_x against potential peroxide and nitrate formation, despite the increase in pollution loading within the observed air masses. There were very few instances when measured NO levels inside AMA dropped into a low NO regime (< 0.1 ppbv), whereas outside AMA this occurred much more frequently, causing r_{OH} to drop to ~ 0.76 on average. This indicates that peroxide formation can have a more pronounced impact (Tan et al., 2001) on r_{OH} stability outside AMA. However, within AMA, the observed increased presence of NO limits the potential impact and frequency of conditions that would promote peroxide formation and cause r_{OH} to significantly drop. At NO levels above 0.4 ppbv the r_{OH} values inside AMA remain unaffected, averaging around 0.86.

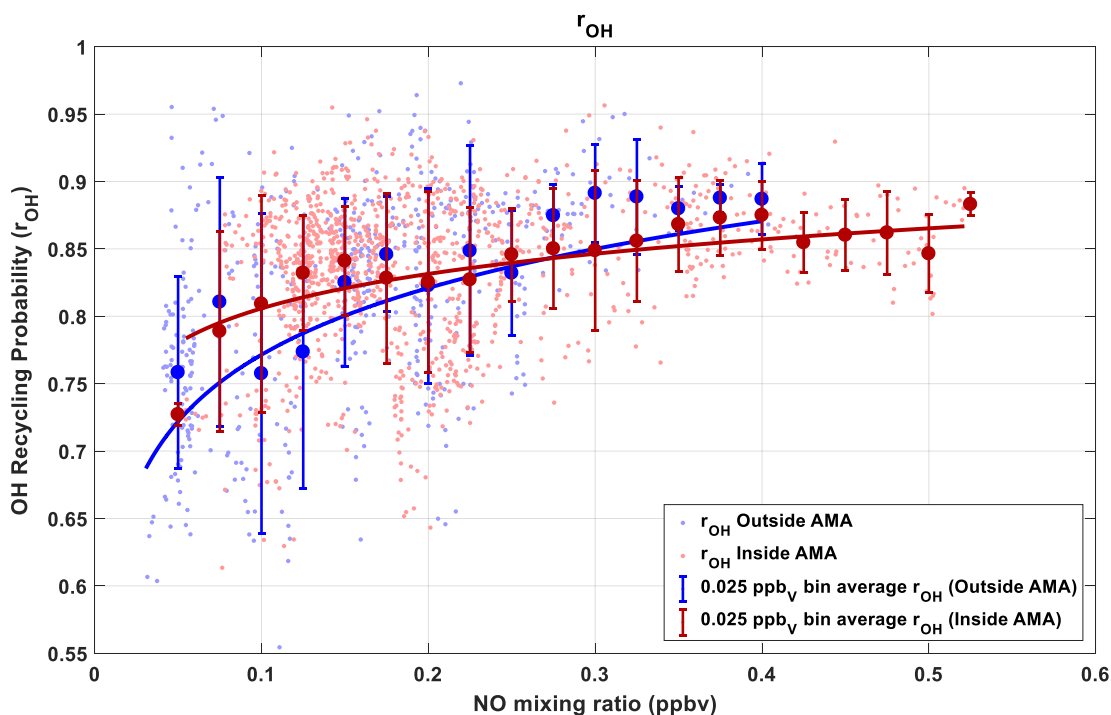


Figure 6.16.: OH recycling probability (r_{OH}) as a function of ambient NO mixing ratio above 11 km altitude inside AMA (red) and outside AMA (blue). The error bars shows the 1σ standard deviation about the r_{OH} values averaged into 0.025 ppbv NO bins.

This flatter response in r_{OH} with respects to changing NO levels inside AMA is a product of the improved OH cycling buffering via the $\text{HO}_2 + \text{O}_3$ channel. This is attributable to the 6 % higher O_3 levels observed within AMA. As can be seen in Figure 6.17, as NO decreases within AMA, the reaction rate of $\text{HO}_2 + \text{O}_3$ increases, which buffers the cycling back of OH. When NO levels do drop to below 0.1 ppbv inside AMA, the $\text{HO}_2 + \text{O}_3$ channel accelerates from $3.2 (\pm 1.7) \times 10^{-4}$ molec. $\text{cm}^{-3} \text{ s}^{-1}$ to $5.1 (\pm 2.5) \times 10^{-4}$ molec.

$\text{cm}^{-3} \text{s}^{-1}$ on average, thereby negating a fraction of the reduction in r_{OH} posed by the slowing $\text{HO}_2 + \text{NO}$ channel when NO levels decrease. On the other hand, outside AMA this buffering effect does not occur to the same extent. At $\sim 0.05 \text{ ppbv}$ NO, outside AMA, there is some evidence that the $\text{HO}_2 + \text{O}_3$ channel is buffering r_{OH} against the low NO levels. However, the overall trend shows that reaction rate of the $\text{HO}_2 + \text{O}_3$ channel in the probed air masses outside AMA remains near constant irrespective of changing NO levels. This means that within the observed AMA, the $\text{HO}_2 + \text{O}_3$ channel is more efficient at buffering HO_x cycling against changing NO levels, thus making r_{OH} less sensitive to NO variability, and stabilizes the local atmospheric oxidative capacity.

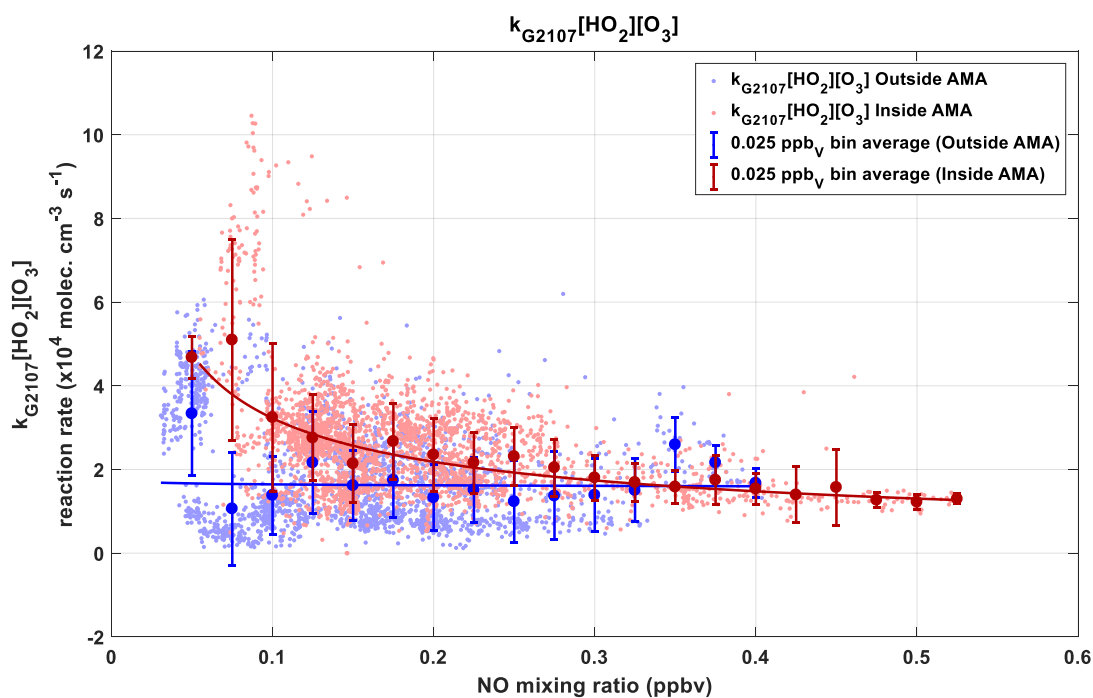


Figure 6.17.: The reaction rate of $k_{\text{G2107}}[\text{HO}_2][\text{O}_3]$ as a function of ambient NO mixing ratio above 11 km altitude inside AMA (red) and outside AMA (blue). The error bars shows the 1σ standard deviation about the $k_{\text{G2107}}[\text{HO}_2][\text{O}_3]$ values averaged into 0.025 ppbv NO bins.

In order to see how r_{OH} values calculated from the OMO-Asia 2015 campaign compare to those calculated from previous campaigns, Figure 6.18 shows the calculated OMO-Asia 2015 r_{OH} values (on a log scale x-axis) superimposed on Figure 6.15. Figure 6.18 highlights that the calculated r_{OH} values from this study falls in accordance with the “S” profile of the calculated r_{OH} values from previous campaigns.

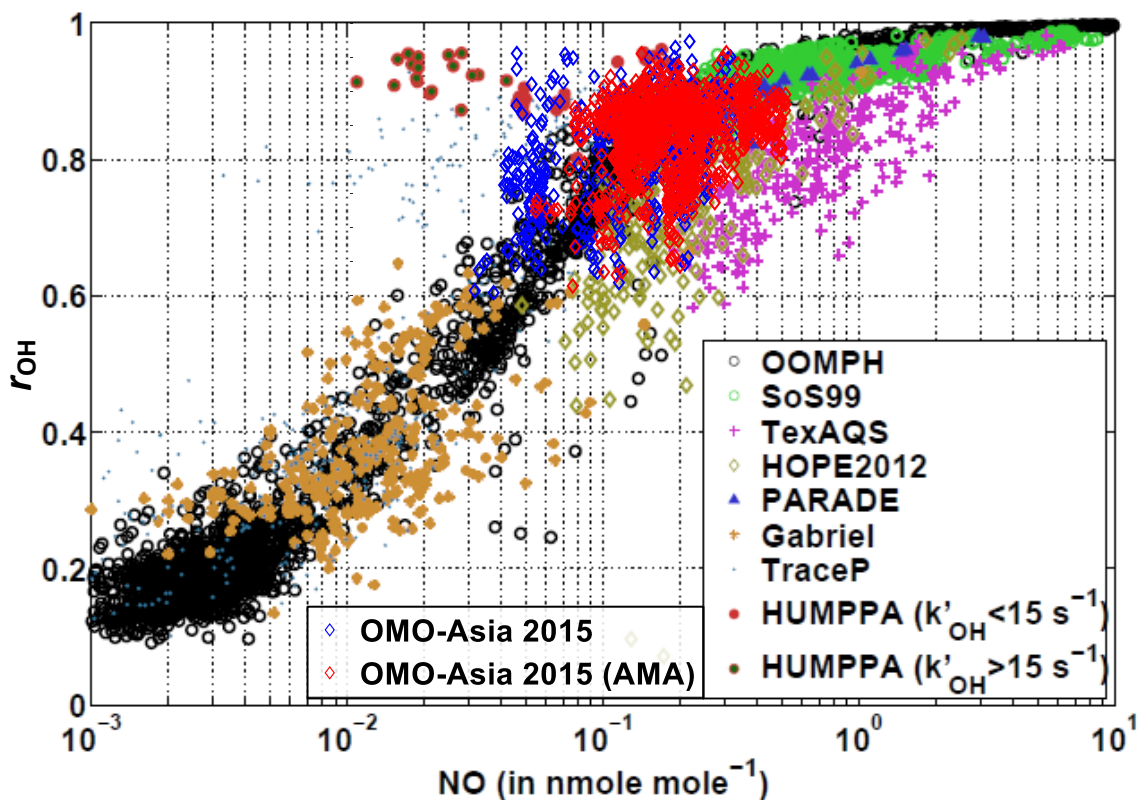


Figure 6.18.: The calculated OMO-Asia 2015 r_{OH} values (on a log scale x-axis) superimposed on Figure 6.15 (a desaturated modified figure from Hens (2013)). The red diamonds are the calculated r_{OH} values inside AMA, and the blue diamonds are the calculated r_{OH} values outside AMA.

7. Summary and Conclusions

Successful airborne measurements of OH and HO₂ were performed to probe one of the largest air mass formations on Earth, the summertime Asian monsoon anticyclone (AMA). In order to understand to what extent oxidation is affected by AMA, the OMO-Asia airborne campaign took place in summer 2015. Onboard the aircraft were an ensemble of instrumentation, including two LIF-FAGE instruments measuring HO_x. From the available OH and HO₂ measurements, over 97 % of the data from both instruments agreed to within 2σ of their combined measurement uncertainty. In the case of HORUS, the development and characterization of the APACHE calibration system was essential in achieving such an agreement. APACHE provided the high flows required by the airborne HORUS system, whilst maintaining stable pressures in front of the IPI nozzle at all pressures measured in-flight during the OMO-Asia 2015 campaign. The sensitivity of HORUS to OH and HO₂ ranged from 7.8 – 26.1 cts s⁻¹ pptv⁻¹ mW⁻¹ and 8.1 – 21.2 cts s⁻¹ pptv⁻¹ mW⁻¹ respectively, with < 2 % of the instrument sensitivity remaining unresolved and declared neither pressure dependent or pressure independent. The achieved overall calibration uncertainty of 22.6 % (1σ) for OH and 22.2 % (1σ) for HO₂ compares well with other calibration methods, as was highlighted in section 4 of this work.

The average observed OH levels within AMA were 3.1 (± 1.4) × 10⁶ molec. cm⁻³ (2σ), which is 31 % higher than the average observed OH levels outside AMA, 2.3 (± 1.1) × 10⁶ molec. cm⁻³ (2σ). For HO₂, the average observed level inside AMA was 4.7 (± 2.1) pptv (2σ), which is 68 % higher than the average observed 2.8 (± 1.2) pptv (2σ) HO₂ in the UT air masses outside of AMA. This elevation in HO_x levels within AMA is present despite the increased pollutant loading, which is indicative of intensified HO_x oxidative throughput. The rate at which OH is being produced and lost is occurring, on average, 1.52 times faster in the probed air masses of AMA than in the observed UT not influenced by AMA. Therefore, the observed HO_x chemistry inside AMA is cutting the lifetimes of pollutants by 52 %, once they are locked with the anticyclone. This is attributable to the amplified cycling of HO_x inside AMA. The dominant driver for this increased cycling of HO_x is the intensified injection of lightning and anthropogenic NO_x into AMA. Overall, the cycling of HO₂ into OH is accelerated by 50 % in the observed AMA, increasing from 3.6 × 10⁵ molec. cm⁻³ s⁻¹ to 5.4 × 10⁵ molec. cm⁻³ s⁻¹, of which 95.3 % is occurring via the HO₂ + NO channel. Additionally, the cycling of OH to HO₂ is accelerated by 62.8 % in AMA, which is attributable to combined effect of the 34.9 % higher CO levels and a 63 % increase in the production rate of HO₂ via reaction of RO₂ with NO.

Despite the observed increased pollutant loading, AMA is capable of maintaining the local atmospheric oxidative capacity. The calculated OH recycling probability (*r*_{OH}) inside the probed air masses of AMA is equivalent in amplitude to the calculated *r*_{OH} values of those outside AMA. However, *r*_{OH} inside AMA shows a lower sensitivity towards changing NO levels due to strengthened chemical buffering. The higher injection frequency of lightning NO_x enriched air masses into AMA, increases the *NOPR* by 91.7 % and O₃ levels by 6 % higher. This enables the HO₂ + O₃ channel inside AMA to increase in reaction rate

and in importance when the NO levels drop. Crucially, the HO₂ + O₃ channel inside the observed AMA partially buffers r_{OH} against the photochemical loss of NO, which occurs in-between convection events.

To conclude, the summertime Asian monsoon anticyclone not only aids in the accumulation and global-scale transport of South Asian emissions, but it also oxidizes and cleanses these pollutants at an elevated rate. This limits the potential global-scale impact of the transported South Asian pollution. In contrast to observed UT air masses outside AMA, the intensified influx of lightning and anthropogenic NO_x into AMA elevates HO_x levels, accelerates the cycling within HO_x, and stabilizes the local atmospheric oxidative capacity; causing atmospheric lifetimes of pollutants to shorten by 52 %.

8. Published Works

Atmos. Meas. Tech., 13, 2711–2731, 2020
https://doi.org/10.5194/amt-13-2711-2020
© Author(s) 2020. This work is distributed under
the Creative Commons Attribution 4.0 License.



Atmospheric
Measurement
Techniques
Open Access
EGU

Calibration of an airborne HO_x instrument using the All Pressure Altitude-based Calibrator for HO_x Experimentation (APACHE)

Daniel Marno¹, Cheryl Ernest^{1,a}, Korbinian Hens^{1,b}, Umar Javed^{1,2}, Thomas Klimach¹, Monica Martinez¹, Markus Rudolf¹, Jos Lelieveld¹, and Hartwig Harder¹

¹Atmospheric Chemistry Department, Max Planck Institute for Chemistry, 55128 Mainz, Germany

²Forschungszentrum Jülich GmbH, IEK-8, 52425 Jülich, Germany

^anow at: Department of Neurology, University Medical Center of the Johannes Gutenberg University Mainz, 55131 Mainz, Germany

^bnow at: Hübner GmbH & Co KG – Division Hübner Photonics, 34123 Kassel, Germany

Correspondence: Daniel Marno (daniel.marno@mpic.de) and Hartwig Harder (hartwig.harder@mpic.de)

Received: 18 November 2019 – Discussion started: 26 November 2019

Revised: 26 February 2020 – Accepted: 3 April 2020 – Published: 27 May 2020

Abstract. Laser-induced fluorescence (LIF) is a widely used technique for both laboratory-based and ambient atmospheric chemistry measurements. However, LIF instruments require calibrations in order to translate instrument response into concentrations of chemical species. Calibration of LIF instruments measuring OH and HO₂ (HO_x) typically involves the photolysis of water vapor by 184.9 nm light, thereby producing quantitative amounts of OH and HO₂. For ground-based HO_x instruments, this method of calibration is done at one pressure (typically ambient pressure) at the instrument inlet. However, airborne HO_x instruments can experience varying cell pressures, internal residence times, temperatures, and humidity during flight. Therefore, replication of such variances when calibrating in the lab is essential to acquire the appropriate sensitivities. This requirement resulted in the development of the APACHE (All Pressure Altitude-based Calibrator for HO_x Experimentation) chamber to characterize the sensitivity of the airborne LIF-FAGE (fluorescence assay by gas expansion) HO_x instrument, HORUS, which took part in an intensive airborne campaign, OMO-Asia 2015. It utilizes photolysis of water vapor but has the additional ability to alter the pressure at the nozzle of the HORUS instrument. With APACHE, the HORUS instrument sensitivity towards OH (26.1–7.8 cts s⁻¹ pptv⁻¹ mW⁻¹, ±22.6% 1σ; cts stands for counts by the detector) and HO₂ (21.2–8.1 cts s⁻¹ pptv⁻¹ mW⁻¹, ±22.1% 1σ) was characterized to the external pressure range at the instrument nozzle of 227–900 mbar. Measure-

ments supported by a computational fluid dynamics model, COMSOL Multiphysics, revealed that, for all pressures explored in this study, APACHE is capable of initializing a homogenous flow and maintaining near-uniform flow speeds across the internal cross section of the chamber. This reduces the uncertainty regarding average exposure times across the mercury (Hg) UV ring lamp. Two different actinometrical approaches characterized the APACHE UV ring lamp flux as $6.37 \times 10^{14} (\pm 1.3 \times 10^{14})$ photons cm⁻² s⁻¹. One approach used the HORUS instrument as a transfer standard in conjunction with a calibrated on-ground calibration system traceable to NIST standards, which characterized the UV ring lamp flux to be $6.9 (\pm 1.1) \times 10^{14}$ photons cm⁻² s⁻¹. The second approach involved measuring ozone production by the UV ring lamp using an ANSYCO O3 41 M ozone monitor, which characterized the UV ring lamp flux to be $6.11 (\pm 0.8) \times 10^{14}$ photons cm⁻² s⁻¹. Data presented in this study are the first direct calibrations of an airborne HO_x instrument, performed in a controlled environment in the lab using APACHE.

1 Introduction

It is well known that the hydroxyl (OH) radical is a potent oxidizing agent in daytime photochemical degradation of pollutants sourced from anthropogenic and biogenic processes, thus accelerating their removal from our atmosphere. The hy-

Published by Copernicus Publications on behalf of the European Geosciences Union.

droperoxyl radical (HO_2) also plays a central role in atmospheric oxidation as it not only acts as a reservoir for OH but is involved in formation of other oxidants such as peroxides and impacts the cycling of pollutants such as NO_x ($=\text{NO} + \text{NO}_2$) (Lelieveld et al., 2002). Therefore, measurements of OH and HO_2 (HO_x) within the troposphere are essential in understanding the potential global-scale impacts of pollutants in both the present day and in climate predictions. One common HO_x measurement method is laser-induced fluorescence (LIF) (Stevens et al., 1994; Brune et al., 1995; Hard et al., 1995; Martinez et al., 2003; Faloon et al., 2004; Stone et al., 2010; Hens et al., 2014; Novelli et al., 2014). Other methods have been successfully implemented to measure HO_x . Chemical ionization mass spectrometry (CIMS) (Cantrell et al., 2003; Mauldin et al., 2004; Sjostedt et al., 2007; Dusanter et al., 2008; Kukui et al., 2008; Albrecht et al., 2019) and differential optical absorption spectroscopy (DOAS) (Brauers et al., 1996, 2001; Schlosser et al., 2007) have also been used in the measurement of HO_x in the field and in intercomparison projects with LIF instrumentation. However, low atmospheric concentrations of HO_x (Schlosser et al., 2009) and potential interferences (Faloon et al., 2004; Fuchs et al., 2011, 2016; Mao et al., 2012; Hens et al., 2014; Novelli et al., 2014) can make HO_x measurements especially challenging. Airborne LIF-FAGE (LIF-fluorescence assay by gas expansion) instruments experience large variability in pressure, humidity, instrument internal air density, and internal quenching during flights, which cause a wide array of instrumental sensitivities (Faloon et al., 2004; Martinez et al., 2010; Regelin et al., 2013; Winiberg et al., 2015). Therefore, it is critical to utilize a calibration system that can suitably reproduce in-flight conditions to determine the instrument response to known levels of OH and HO_2 to acquire robust HO_x measurements.

The first stage of the Hydroxyl Radical measurement Unit based on fluorescence Spectroscopy (HORUS) inlet is an inlet preinjector (IPI), used to determine the concentration of background OH interferences by removing atmospheric OH from the signal via addition of an OH scavenger such as propane. IPI draws $50\text{--}230\text{ sL min}^{-1}$ depending on altitude and is susceptible to temperature- and pressure-driven changes in internal reaction rates and residence times under flight conditions. This has implications for the removal of atmospheric OH in the inlet and for the characterization of background interference signals in HORUS. Therefore, a device capable of providing stable high flows while reproducing a wide range of pressures and temperatures is needed in order to calibrate the airborne HORUS instrument. This led to the production, characterization, and utilization of the calibration device APACHE (All Pressure Altitude-based Calibrator for HO_x Experimentation) which is described in depth in this work.

2 Experimental design and setup

2.1 APACHE design overview

Figure 1 shows the overview of the APACHE system. In front of the APACHE inlet, a series of mixing blocks are installed where multiple dry synthetic air additions are injected into a controlled humidified air supply ensuring thorough mixing of water vapor before being measured by a LI-COR 6262 $\text{CO}_2/\text{H}_2\text{O}$ (Fig. 1a). This air is then fed into a large mass flow controller (MFC). The construction of the APACHE chamber itself is shown in Fig. 1b. The first section contains the diffuser inlet with a sintered filter (bronze alloy, Amtag, filter class 10). This 2 mm thick sintered filter, with a pore size of $35\text{ }\mu\text{m}$, initializes a homogeneous flow and further improves the mixing of water vapor in front of the UV ring lamp (described further in Sect. 4). The water photolysis section contains a low-pressure, 0.8 A, mercury ring lamp (uv-technik; see Fig. S1 in the Supplement) which produces a constant radial photon flux at 184.9 nm , situated 133 mm after the sintered filter and separated from the main APACHE chamber by an airtight quartz window. Between the lamp and the quartz window there is an anodized aluminum band with thirty 8 mm apertures blocking all light apart from that going through the apertures, which reduces the amount of UV flux entering APACHE and limits the size of the illuminated area. The IPI system is clamped down 169.5 mm behind the photolysis section in such a way that the instrument sample flow is perpendicular to the airflow passing over the IPI nozzle. The nozzle protrudes 51.5 mm into the APACHE cavity much like it is when installed in the aircraft shroud system (see Fig. 2), and it is made airtight with the use of O-rings. Opposite the IPI nozzle, there is an airtight block attachment containing a series of monitoring systems. A pitot tube attached to an Airflow PTSX-K 0-10Pa differential pressure sensor (accuracy rating of 1% at full scale, 1σ) is used to monitor the internal flow speeds within APACHE. A $3\text{ k}\Omega$ NTC-EC95302V thermistor is used to monitor the air temperature, and an Edwards ASG2-1000 pressure sensor (with an accuracy rating of $\pm 4\text{ mbar}$, 2σ) monitors the static air pressure. Additionally, there are two $1/4\text{ in.}$ (6.35 mm) airtight apertures in the monitoring block that can be opened to enable other instrumentation to be installed.

2.2 Pressure control

For this study, the operational pressure range of APACHE used was $227\text{--}900\text{ mbar}$, with a precision of $\pm 0.1\%$ (1σ) and accuracy of $\pm 2\%$ (1σ) and with mass flows ranging from 200 to 990 sL min^{-1} (sL stands for standard liter). This was achieved using an Edwards GSX160 scroll pump controlling the volume flow in combination with a MFC (Bronkhorst F-601A1-PAD-03-V) controlling the mass flow of air entering APACHE. This system reached air speeds of 0.9 to 1.5 m s^{-1} through APACHE at pressures ranging from 250 to 900 mbar .

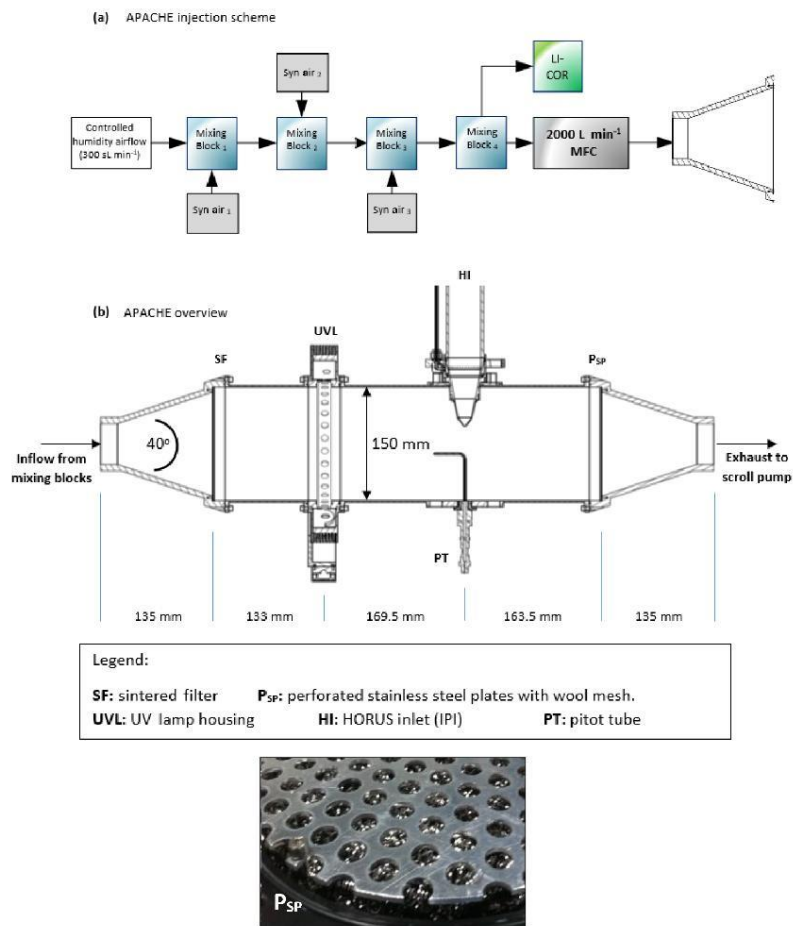


Figure 1. Overview of the APACHE system and the premixing setup used in the lab to calibrate the HORUS airborne instrument. A picture at the bottom shows the perforated stainless-steel plates with wool mesh.

and at temperatures ranging from 282 to 302 K. Temperature changes inside APACHE are not controlled. However, as air temperature is measured throughout the calibration device and HORUS, any term that is affected by temperature is characterized using the corresponding measured temperature values. Although not critical for this study, the operational pressure range of APACHE can be extended by changing the draw speed of the Edwards scroll pump. However, that may cause the flow speeds and potentially the flow speed profiles across the UV ring lamp to vary in between different pressure calibrations.

2.3 The airborne HORUS instrument

The LIF-FAGE instrument developed by our group (HORUS) is based on the original design of GTHOS (Ground-based Tropospheric Hydrogen Oxides Sensor) described by Faloona et al. (2004) and is described in further detail by Martinez et al. (2010). The airborne instrument is a revised and altered design to perform under conditions experienced during flight and conform to aeronautical regulations. It was primarily developed for installation on the High Altitude and Long Range Research Aircraft (HALO) and took place in the

OMO-Asia 2015 airborne campaign. The system comprises of an external inlet shroud, detection axes, a laser system, and a vacuum system (Fig. 2). Additionally, this is the first airborne LIF-FAGE instrument measuring HO_x with a dedicated inlet preinjector (IPI) system installed for the purpose of removing atmospheric OH, enabling real-time measurements and quantification of potential chemical background OH interferences, OH-CHEM (Mao et al., 2012). The airborne IPI system is redesigned to fit within the shroud inlet system, and its walls are heated to 30°C , while maintaining similar operational features to the on-ground IPI installation (Novelli et al., 2014). To prevent excessive collisions of OH and HO_2 with the IPI nozzle and internal walls, thus limiting losses of HO_x during flight, the momentum inertia of the air passing through the external shroud system had to be overcome to promote flow direction into the instrument. This was achieved by installing a choke point behind the IPI nozzle in the inlet shroud, resulting in a reduction in airflow speed. For example without the shroud choke, flow speeds in excess of 200 m s^{-1} could occur in the shroud during flight. However, with the choke point, flow speeds in the shroud during flight did not exceed 21 m s^{-1} during OMO-Asia 2015, which is sufficiently below the sample velocities of IPI during flight ($44\text{--}53\text{ m s}^{-1}$). Additionally, it limits non-parallel flows across the IPI nozzle created by variable pitch, roll, and yaw changes of the aircraft. As the aircraft changes pitch, roll, and yaw, the measured OH variability increases by $\pm 4.51 \times 10^4\text{ cm}^{-3}$ (1σ), which is only 10% to 15% higher than the natural variability of OH. This increase in variability is negligible as it represents, depending on internal pressure, 19% to 30% of the detection limit of the instrument. Both of these effects of the external shroud improve the measurement performance by reducing variable wall losses of HO_x at the IPI nozzle under flight conditions. The IPI system (with a nozzle orifice diameter of 6.5 mm) samples (51 to 230 sL min^{-1}) from the central airflow moving through the internal shroud. A critical orifice is located at the end of IPI in the center of the IPI cross section, which enables the HORUS instrument to sample (3 to 17 sL min^{-1}) from the central flow moving through IPI. This further reduces influences of wall loss within IPI on the overall measured signal in the cells. The removal of excess flow moving through IPI occurs via a perforated ring that surrounds the base of the critical orifice cone, evacuated by a blower.

As with other LIF-FAGE HO_x instruments, HORUS measures an off-resonance signal to discern the net OH fluorescence signal. This is achieved by successive cycling of the laser tuning from on-resonance (measuring the total signal of OH fluorescence and the signal originating from other fluorescence and electronic sources) to off-resonance (measuring all the above except the OH fluorescence). The HORUS instrument utilizes the $Q_1(2)$ transition $X^2\Pi_{3/2}(v''=0) \rightarrow A^2\Sigma^+(v'=0)$ (Freeman, 1958; Dieke and Crosswhite, 1962; Langhoff et al., 1982; Dorn et al., 1995; Holland et al., 1995; Mather et al., 1997). The net OH signal (S_{OH}) is the differ-

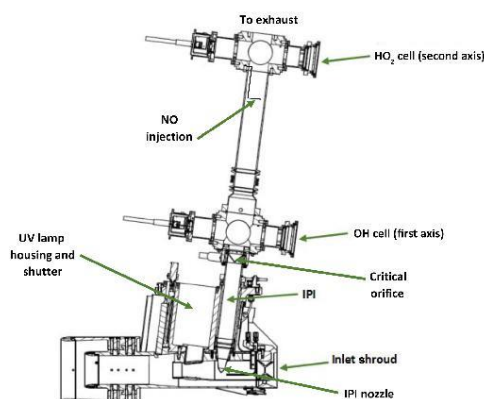


Figure 2. Overview of the airborne HORUS system as installed in the HALO aircraft. HO_2 is measured indirectly through the addition of NO that quantitatively converts HO_2 into OH. The NO injection occurs via a stainless-steel 1/8 in. (3.175 mm) line, shaped into a ring perpendicular to the airflow with several unidirectional apertures of 0.25 mm diameter creating essentially a NO shower.

ence between the on-resonance and off-resonance signals, OH-WAVE (Mao et al., 2012). The OH sensitivity (C_{OH}) and average laser power within the detection axis ($W_{z1\text{ pwr}}$) are then used to calculate the absolute OH mixing ratio (see Eq. 1). HO_2 is measured indirectly through the quantitative conversion of atmospheric HO_2 to OH by injection of nitric oxide (NO) under the low-pressure conditions within HORUS.



When NO is injected into the instrument, both ambient OH and HO_2 are measured in the second detection axis. The net HO_2 signal (S_{HO_2}) in the second axis is therefore derived from subtracting the net OH signal from the first detection axis normalized by the ratio of the OH sensitivities for the two detection axes ($C_{\text{OH}(2)}/C_{\text{OH}}$) from the net HO_x signal (S_{HO_x}). Then S_{HO_2} is corrected by the sensitivity to HO_2 (C_{HO_2}) and laser power ($W_{z2\text{ pwr}}$) to reach the absolute HO_2 mixing ratio (see Eq. 2).

$$[\text{OH}] = \frac{S_{\text{OH}}}{(C_{\text{OH}} \cdot W_{z1\text{ pwr}})}, \quad (1)$$

$$[\text{HO}_2] = \frac{1}{(C_{\text{HO}_2} \cdot W_{z2\text{ pwr}})} \cdot \left\{ S_{\text{HO}_x} - \frac{(C_{\text{OH}(2)} \cdot W_{z2\text{ pwr}})}{(C_{\text{OH}} \cdot W_{z1\text{ pwr}})} S_{\text{OH}} \right\}, \quad (2)$$

where $W_{z1\text{ pwr}}$ is the laser power in the first detection axis, $W_{z2\text{ pwr}}$ is the laser power in the second detection axis, and

C_{OH} and C_{HO_2} are the calibrated sensitivity factors for OH and HO_2 ($\text{cts s}^{-1} \text{pptv}^{-1} \text{mW}^{-1}$) respectively. By calibrating using a known OH mixing ratio, the instrument sensitivity C_{OH} can be determined by rearranging Eq. (1) to

$$C_{\text{OH}(\text{cal})} = S_{\text{OH}(\text{cal})} / ([\text{OH}] \cdot W_{z1\text{pwr}}). \quad (3)$$

The sensitivity of HORUS depends on the internal pressure, water vapor mixing ratios, and temperature, which are subject to change quite significantly during flight. Therefore, further parameterization when calibrating is required to fully constrain the sensitivity response of the instrument at various flight conditions. Equation (4) shows the terms that affect the sensitivity of the first HORUS axis that measures OH.

$$C_{\text{OH}}(P, T) = c_0 \cdot \rho_{\text{int}}(P, T) \cdot Q_{\text{IF}}(P, T, \text{H}_2\text{O}) \cdot b_c(T) \cdot [\alpha_{\text{IPI}}(P, T) \cdot \alpha_{\text{HORUS}}(P, T)], \quad (4)$$

where c_0 is determined by calibrations and is the lump sum coefficient of all the pressure-independent factors affecting the HORUS sensitivity, for example, OH absorption cross section at 308 nm, the photon collection efficiency of the optical setup and quantum yield of the detectors, and pressure-independent wall loss effects. For calibrations, c_0 is normalized by laser power and has the units $\text{cts pptv}^{-1} \text{s}^{-2} \text{cm}^3 \text{molecule}^{-1} \text{mW}^{-1}$. ρ_{int} is the internal molecular density. Q_{IF} is the quenching effect(s), which consists of the natural decay frequency of OH; OH decay due to collisional quenching that is dependent on pressure, temperature, and water vapor mixing ratio; and the detector opening and closing gating times after the initial excitation laser pulse. Both are pressure-dependent terms as denoted in Eq. (4). The Boltzmann correction (b_c) has a temperature dependency as it corrects for any OH molecules that enter the HORUS instrument in a thermally excited state and are therefore not measurable by fluorescence excitation at the wavelength used. α is the pressure-dependent OH transmission, which is the fraction of OH that reaches the point of detection. This term is separated for the two-tier pressure conditions present in the instrument. The term α_{IPI} represents the correction for pressure- and temperature-dependent OH loss on the walls within IPI. The term α_{HORUS} is the correction for pressure-dependent OH loss to the walls within the HORUS detection axes post critical orifice. While the quenching effects, internal densities, and Boltzmann corrections can be quantified by calculation, and the power entering the measurement cell is measured, the two factors that need to be determined through calibration are c_0 and OH transmission, α . Once the c_0 coefficient and α terms are known, the final in-flight-measured OH mixing ratio (pptv) is found:

$$[\text{OH}] = S_{\text{OH}} / (c_0 \cdot \rho_{\text{int}} \cdot Q_{\text{IF}} \cdot b_c \cdot [\alpha_{\text{IPI}} \cdot \alpha_{\text{HORUS}}] \cdot W_{z1\text{pwr}}). \quad (5)$$

As S_{OH} scales with laser power, the terms that describe the instrument sensitivity shown as the denominator in Eq. (5), which ultimately have the units $\text{cts s}^{-1} \text{pptv}^{-1} \text{mW}^{-1}$, must

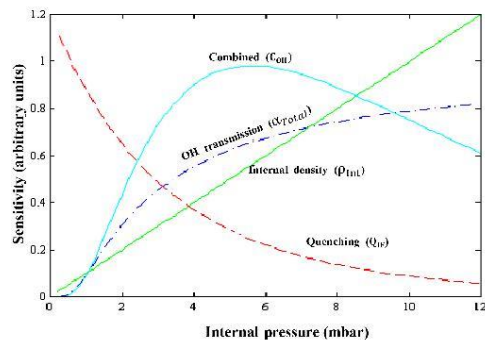


Figure 3. A schematic showing the overall sensitivity curve as a function of internal pressure (light blue line), OH transmission (dotted-dashed dark blue line), internal density (green line), and the quenching (dashed red line).

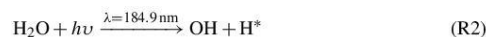
also be scaled to the measured laser power ($W_{z1\text{pwr}}$) during flight to acquire the absolute measurement of OH mixing ratio. As depicted in both Figs. 1b and 2, the complete system is calibrated with IPI attached and operating as it did when installed in the aircraft. Therefore, the combined losses of OH within IPI and in the low-pressure regime post critical orifice (that has a diameter of 1.4 mm) contribute to the overall calibrated C_{OH} sensitivity factor in the same way during measurement and calibrations, meaning that the OH transmission of HORUS can be quantified with both OH transmission terms (α_{IPI} and α_{HORUS}) combined into one term (α_{Total}).

$$[\text{OH}] = S_{\text{OH}} / (c_0 \cdot \rho_{\text{int}} \cdot Q_{\text{IF}} \cdot b_c \cdot [\alpha_{\text{Total}}] \cdot W_{z1\text{pwr}}) \quad (6)$$

Figure 3 shows the schematic of the different factors described above and their impact on the overall sensitivity.

3 Calibration method and theory

As an overview, Table 1 shows common calibration techniques for OH instruments. The APACHE system is based on the production of known quantified and equal concentrations of OH and HO_2 via photolysis of water vapor in only synthetic air using a Hg ring lamp emitting UV radiation at 184.9 nm.



Stable water mixing ratios with a variability of $< 2\%$ were achieved by heating 300 sL min^{-1} flow of synthetic air to

353 K and introducing deionized water using a peristaltic pump into this heated gas flow, causing it to evaporate before entering a 15 L mixing chamber. This prevents recondensation and humidity spikes when the pump is introducing the water. The humidified gas flow is then diluted (to around 3 mmol mol^{-1}) and mixed further with additional dry pure synthetic air via a series of mixing blocks to achieve the required and desired stable water vapor mixing ratios. The photolysis of H_2O has only one spin-allowed and energetically viable dissociation channel at 184.9 nm (Engel et al., 1992), meaning the quantum yields of OH and H^* are unified (Sander et al., 2003). Even though Reaction (R3) is possible particularly since the H^* atoms can carry transitional energies of 0.7 eV at 189.4 nm (Zhang et al., 2000), the fast removal of energy by Reaction (R4) allows for the general assumption that all H^* atoms produced lead to HO_2 production (Fuchs et al., 2011). The use of water photolysis as a OH and HO_2 radical source for calibration of HO_x instruments has been adopted in a number of studies (Heard and Pilling, 2003; Ren et al., 2003; Faloon et al., 2004; Dusanter et al., 2008; Novelli et al., 2014; Mallik et al., 2018). As an example, the factors required to quantify the known concentrations of OH and HO_2 during calibrations are shown below:

$$[\text{OH}] = [\text{HO}_2] = [\text{H}_2\text{O}] \cdot \sigma_{\text{H}_2\text{O}} \cdot F_{184.9 \text{ nm}} \cdot \phi_{\text{H}_2\text{O}} \cdot t, \quad (7)$$

where in Eq. (7) the OH and HO_2 concentrations are a product of photolysis of a known concentration of water vapor $[\text{H}_2\text{O}]$, and $\sigma_{\text{H}_2\text{O}}$ is the absorption cross section of water vapor, $7.22(\pm 0.22) \times 10^{-20} \text{ cm}^2$ per molecule at 184.9 nm (Hofzumahaus et al., 1997; Creasey et al., 2000). $F_{184.9 \text{ nm}}$ is the actinic flux ($\text{photons cm}^{-2} \text{ s}^{-1}$) of the mercury lamp used for photolysis, $\phi_{\text{H}_2\text{O}}$ is the quantum yield, and t is exposure time. The quantum yield of water vapor photolysis at the 184.9 nm band is 1 (Creasey et al., 2000).

4 Results and discussion

4.1 Flow conditions

With any calibration device, the flow conditions must be characterized to inform subsequent methods and calibrations. Regarding APACHE, the two main factors to be resolved are (i) how uniform the flow speed profiles and therefore exposure times in respect to the APACHE cross section are and (ii) the impact of OH wall losses.

To this end, experimental and model tests were performed to determine whether the combination of the sintered filter as well as the stainless-steel perforated plates and wool arrangement could provide a homogeneous flow. This means that under operation the flow speeds should be uniform along the cross section of APACHE to within the uncertainty of the measurements. This is to ensure that the air masses passing across the lamp have the same exposure times irrespective

of where they are in the cross section. Additionally, model simulations can provide an indication of, as a function of APACHE pressure, the development and scale of boundary air conditions where air parcels experience extended contact time with the interior walls of APACHE and so have pronounced OH wall losses. This highlights potential flow conditions where there is sufficient time between the photolysis zone and the IPI nozzle to allow APACHE boundary air to expand into and influence the OH content of the air being sampled by HORUS.

4.1.1 Flow speed profiles

During calibration, the pressures within the HORUS instrument had to be controlled and monitored to replicate the in-flight conditions. The APACHE chamber pressure is equivalent to the in-flight pressure in the shroud where the HORUS system samples. The pressure of the detection axes depends on the pressure at the IPI nozzle and the efficiency of the pumps. Within IPI itself, the airflow through it is dependent on the pressure gradient between the shroud and the ambient pressure at the IPI exhaust or alternatively the APACHE pressure and pressure in front of the XDS35 scroll pump (post IPI blower). During the campaign, the exhausts of all blowers and pumps of the HORUS system were attached to the passive exhaust system of the aircraft and were thus exposed to ambient pressure. Therefore, the same IPI blower and pumps that were installed on HALO were used in the lab, and throughout the calibrations the pressure at the exhaust for every blower and pumps involved in the HORUS instrument was matched to the respective in-flight ambient pressures by attaching a separate pressure sensor, needle valve, and XDS35 scroll pump system. Additionally, to match the power that is provided on the aircraft, a three-phase mission power supply unit was used to power the pumps in the lab during testing and throughout the calibrations. Figure 4 shows the lab setup described above.

To limit the effect of wall loss, HORUS samples air from the core of the APACHE flow system and draws only a fraction of the total airflow as shown in Fig. 5. At 900 hPa the HORUS instrument takes 20 % and at 275 hPa HORUS takes 30 % of the total volume flow entering APACHE. To validate that this proportional volume flow into HORUS does not disturb the flow conditions within APACHE, flow speed profiles were performed using the Prandtl pitot tube installed directly opposite the IPI nozzle, which can be positioned flush against the internal wall up to 60.5 mm into the APACHE cavity, which is 15 mm from the APACHE center. Figure 6 shows the measured flow speed profile (blue data points) when the APACHE pressure was 920 hPa. As the distance between the APACHE wall and the pitot tube inlet increased, no significant change in the flow speed was observed. The largest change observed was between 46.6 and 60.5 mm where the flow speed increased by 0.16 m s^{-1} , which is 22.8 % smaller than the combined uncertainty of these two measurements

Table 1. Various known methods for OH instrument calibrations. CSTR stands for continuously stirred tank reactor.

	Technique	Method	Quoted (1σ) uncertainty	Limitations	References
(I)	Water UV photolysis	See Sects. 3 and 4	10 %–30 %	Dependent on lamp, photon flux measurement, and absorption	Creasey et al. (2003), Heard and Pilling (2003), Holland et al. (2003), Ren et al. (2003), Faloona et al. (2004), Smith et al. (2006), Martinez et al. (2010), Mallik et al. (2018)
(II)	Pulsed N ₂ –H ₂ O RF discharge	At low pressure (0.1 Torr); OH and NO produced using a low-power RF discharge. Concentrations of NO and OH are closely linked.	20 %	Requires NO measurement using stable ambient air calibrations	Dilecce et al. (2004), Verreycken and Bruggeman (2014)
(III)	Low-pressure flow-tube RF discharge	OH radical production by titration of H atoms with NO ₂ . Known amount of H atoms produced using microwave discharge using low-pressure flow tube.	30 %	Stable ambient air calibrations	Stevens et al. (1994)
(IV)	Continuously stirred tank reactor and decay of select hydrocarbons	In a CSTR, OH produced through UV irradiation of humidified airflow with injection of a specific hydrocarbon (1,3,5-trimethylbenzene, C ₉ H ₁₂) and NO. More recent studies have used cyclohexane, <i>n</i> -pentane and iso-butene. Concentrations of OH relate to decay rate of the hydrocarbon.	24 %–36 %	Time intensive, systematic wall loss of OH in reactor	Hard et al. (1995, 2002), Winiberg et al. (2015)
(V)	Steady-state O ₃ alkene	A steady-state OH concentration produced from ozonolysis of a known concentration of an alkene.	42 %	Time-consuming, large uncertainties compared to other methods	Heard and Pilling (2003), Dusanter et al., (2008)
(VI)	Laser photolysis of ozone	Photolysis of O ₃ with 284 nm light producing O(¹ D), which then reacts with H ₂ O producing OH.	40 %–50 %	Requires large apparatus	Tanner and Eisele (1995)

$\pm 0.21 \text{ m s}^{-1}$ (2σ). Compared to the other four measurement points performed at 920 mbar, the 1.54 m s^{-1} measured at 60.5 mm is not significantly different. However, when performing the speed profile tests at lower pressures, the pressure difference measured was close to or below the resolution of the differential pressure sensor. Consequently, the flow inside APACHE and the IPI nozzle was simulated using the computational fluid dynamics (CFD) model from COMSOL Multiphysics to gain a better understanding of the flow speed profiles at all pressures. The CFD module in COMSOL uses Reynolds-averaged Navier–Stokes (RANS) models (COM-

SOL, 2019). The standard *k*-epsilon turbulence model with incompressible flows was used for this study as it is applicable when investigating flow speeds below 115 m s^{-1} (COMSOL, 2019). An extra fine gridded mesh of a perforated plate with a high solidity ($\sigma_s = 0.96$) was implemented in the turbulence model to generate the turbulence and replicate the flows created by the bronze sintered filter (Roach, 1987). The model was constrained with the pressures measured within APACHE and IPI. The volume flow was calculated from the measured mass flow entering APACHE, and temperatures were constrained using the thermistor readings.

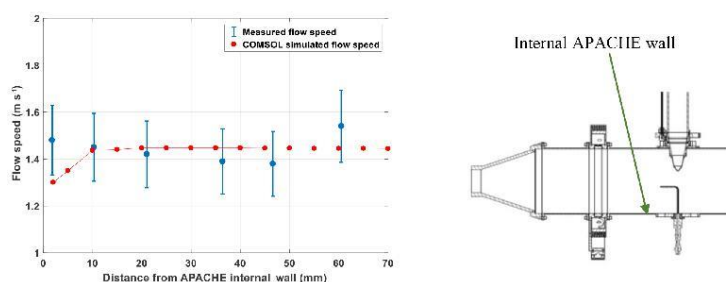


Figure 6. The measured (blue) and COMSOL simulated (red) flow speed profiles within APACHE, at 920 hPa. The x axis is the distance from the internal wall of APACHE. The error bars are quoted to 2σ .

APACHE, which remain prevalent all the way up to the IPI nozzle.

4.1.2 HO_x losses in APACHE

The modeled OH mixing ratios (pptv) in Fig. 8 show the change in OH content as the air flows along the length of APACHE. Mixing ratios were used as they are independent of the changing density within APACHE. In every simulation, the OH and HO₂ concentrations were initialized at zero, and losses at the walls were fixed to 100% for both OH and HO₂. The radial photolytic production of OH and HO₂, as calculated using Eqs. (7) and (9), occurred when the air passed the UV ring lamp. For all simulations, the HO_x radical–radical recombination loss reactions (Reactions R6–R8) and the measured molecular diffusion coefficient of OH_{Dm} in air (Tang et al., 2014) were used:

$$\text{OH}_{\text{Dm}} = 179(\pm 20) \text{ Torr cm}^2 \text{ s}^{-1} \quad (239 \pm 27 \text{ hPa cm}^2 \text{ s}^{-1}).$$

In literature, there have been no reports of successfully performed tests that accurately measure HO₂ diffusivity coefficients in air. However, calculations of HO₂ diffusion coefficients using the Lennard-Jones potential model have been performed (Ivanov et al., 2007). Ivanov et al. (2007) performed a series of measurements and Lennard-Jones potential model calculations to quantify the polar analogue diffusion coefficients for OH, HO₂, and O₃ in both air and pure helium. The calculated OH and O₃ diffusion coefficients in air from the Lennard-Jones potential model were in good agreement with the recommended measurement values in Tang et al. (2014) and were well within the given uncertainties. Therefore, to best replicate the diffusivity of HO₂ within the simulations, the following diffusion coefficient of HO₂ in air from the Ivanov et al. (2007) paper was used:

$$\text{HO}_{2\text{Dm}} = 107.1 \text{ Torr cm}^2 \text{ s}^{-1} \quad (142.8 \text{ hPa cm}^2 \text{ s}^{-1}).$$

<https://doi.org/10.5194/amt-13-2711-2020>

It is clear from Fig. 8 that irrespective of pressure the air masses at the boundary (where wall losses are 100%) do not have sufficient time to expand into the HORUS sample flow streamlines and influence HO_x content entering HORUS. Lateral exchanges between air at the walls of APACHE and the free air in the center are suppressed due to the preservation of the small turbulence regime between the sintered filter and IPI. Table 2 provides, for six pressures, the evolution of OH along the length of APACHE, within the streamlines created by the HORUS sample flow as depicted in Fig. 8.

In Table 2, the L term represents OH mixing ratios on the leftmost HORUS sample flow streamline shown in Figs. 7 and 8. C represents OH mixing ratios in the center of the HORUS sample flow streamlines shown in Figs. 7 and 8. R represents OH mixing ratios on the rightmost HORUS sample flow streamline shown in Figs. 7 and 8. The mean mixing ratio at each APACHE pressure does not change significantly and is thus independent of the distance from the lamp. Conversely, the standard deviations of the OH mixing ratios within the HORUS sampling streamlines decrease as the distance from the lamp increases, indicating that the air is homogenizing. However, Fig. 8 and Table 2, with support from available measurements, indicate that the OH-depleted air masses (i.e., air masses that have experienced loss of OH on the APACHE walls) do not expand into and influence the OH content of air that is being sampled by HORUS. The main loss process that influences HO_x entering HORUS is the wall loss occurring at the IPI nozzle itself. According to the COMSOL simulations, around 22.2(±0.8)% (1σ) of OH and HO₂ is lost at the nozzle. This value does not significantly change with pressure, indicating that the HO_x loss at the nozzle is pressure independent. As described in Sect. 2.3, the pressure-independent sensitivity coefficients are a lump sum value containing the pressure-independent wall losses for OH and HO₂. Therefore, the characterized pressure-independent sensitivity coefficients, shown in Sect. 4.3, have the OH and HO₂ losses at the IPI nozzle constrained within them.

Atmos. Meas. Tech., 13, 2711–2731, 2020

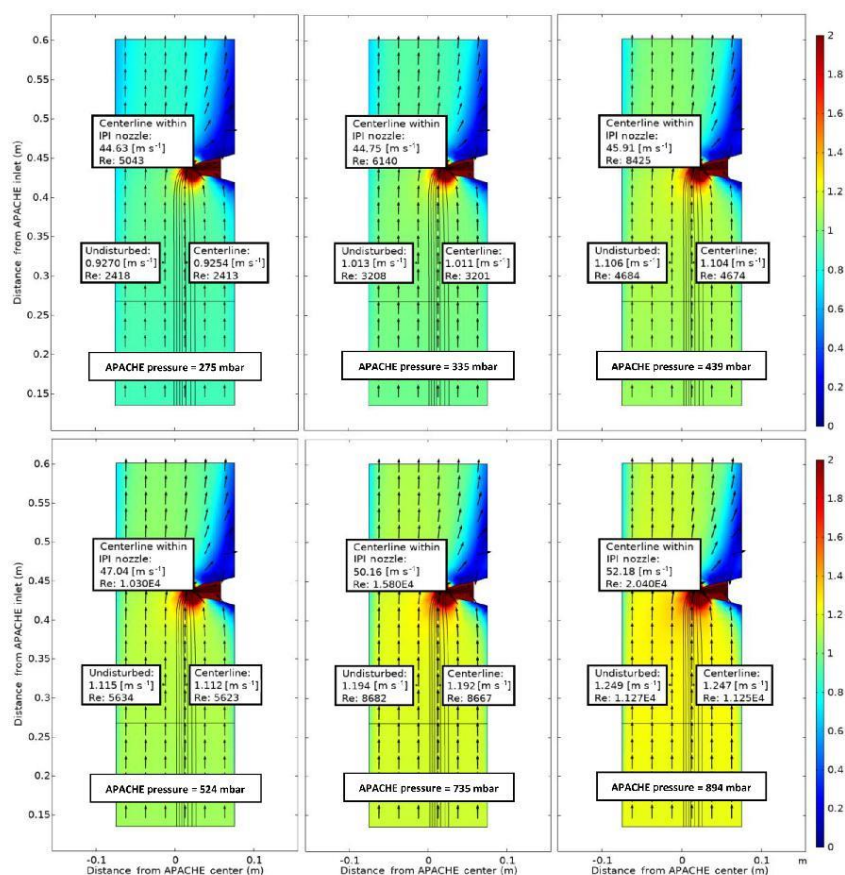


Figure 7. COMSOL Multiphysics output data, simulating the flow speed conditions at six discrete pressures within APACHE ranging from 275 to 894 mbar, between the sintered filter and the first perforated stainless-steel plate. The color represents flow speed in meters per second (m s^{-1}). The black lines are the streamlines created by the HORUS sample flow. The black arrows depict the flow direction. The x axis is the distance from the center of APACHE in meters. The y axis is the distance from the APACHE inlet. The “centerline within the IPI nozzle” labels show the flow conditions in the center of the fully formed flows after the HORUS pinhole, the “undisturbed” labels show the flow conditions outside of the HORUS streamlines, and the “centerline” labels show the flow conditions in the center of the streamlines (i.e., the area of flow influenced by HORUS sampling).

4.2 UV conditions

The photolysis lamp is housed in a mount with the side facing into the chamber having an anodized aluminum band with thirty 8 mm apertures installed between the lamp and a quartz wall. The housing was flushed with pure nitrogen to purge any O_2 present before the lamp was turned on. The nitrogen flushing was kept on continuously thereafter. After approximately 1 h, the lamp reached stable operation conditions; i.e.,

the relative flux emitted by the lamp as measured by a photometer (seen in Fig. 1b at the UVL (ultraviolet lamp) on the underside of the APACHE chamber) was constant. The flux (F_β) entering APACHE is not the same as the flux experienced by the molecules sampled by HORUS (F). Factors influencing the ratio between F_β and F are as follows: (i) absorption of light by O_2 , which is particularly important as O_2 has a strong absorption band at 184.9 nm and the O_2

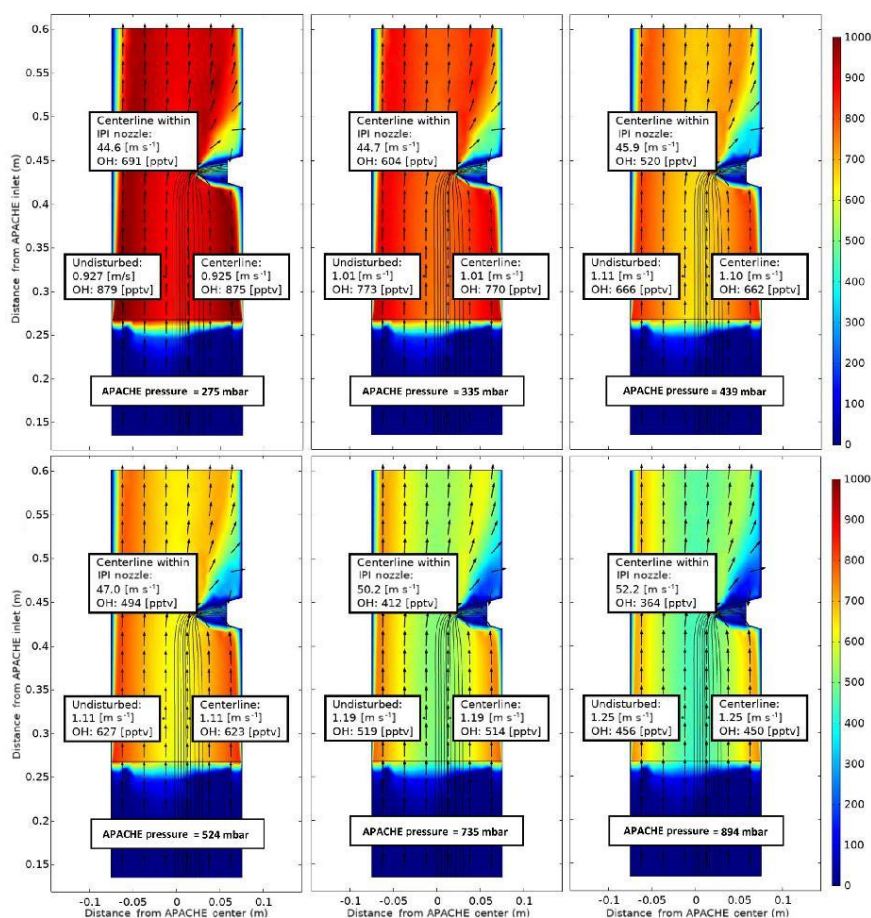


Figure 8. COMSOL Multiphysics output data, simulating OH conditions at six discrete pressures within APACHE ranging from 275 to 894 mbar, between the sintered filter and the first perforated stainless-steel plate. The color gradient is the OH mixing ratio (pptv), with initial OH production occurring at the lamp (0.26 m from APACHE inlet), using Eqs. (7) and (9), with water vapor mixing ratios kept constant at $3.2 \text{ mmol mol}^{-1}$. The black lines are the streamlines created by the HORUS sample flow. The black arrows depict the flow direction. The x axis is the distance from the center of APACHE in meters. The y axis is the distance from the APACHE inlet. The “centerline within IPI nozzle” labels represent the flow and OH concentrations in the center of the fully formed flows after the HORUS pinhole. The “undisturbed” labels show the flow conditions outside of the HORUS streamlines, and the “centerline” labels show the flow conditions in the center of the streamlines (i.e., influenced by HORUS sampling).

density changes in APACHE when calibrating at the different pressures; (ii) the variable radial flux, which is dependent on the geometric setup of the ring lamp and on the location within the irradiation cross section where the molecule is passing. These factors were resolved through the combination of two actinometrical cross-check methods. The advan-

tage of actinometrical methods is that the flux calculated is derived directly from the actual flux that is experienced by the molecules themselves as they pass through the APACHE chamber.

The first actinometrical method (A) used the HORUS instrument as a transfer standard to relate the flux of a precal-

APACHE pressure (mbar)	OH (ppv) at the lamp				OH (ppv) 4.2 cm from lamp				OH (ppv) 8.4 cm from lamp				OH (ppv) 12.8 cm from lamp				OH (ppv) 2 cm before HORUS inlet				In centreline within IPI nozzle (ppv)					
	L	C	R	Mean	L	C	R	Mean	L	C	R	Mean	L	C	R	Mean	L	C	R	Mean						
894	438	445	513	465	41.4	442	446	507	465	36.4	438	455	500	464	32.0	442	456	501	466	30.8	445	457	490	464	23.3	364
735	502	508	572	527	38.8	502	506	509	507	34.4	502	519	560	527	29.8	507	519	562	529	28.9	509	521	550	527	21.1	412
524	611	617	672	633	33.6	615	619	668	634	29.5	613	627	660	633	24.1	617	628	664	636	24.6	619	629	651	633	16.4	403
439	652	657	706	672	29.5	656	659	702	672	25.7	654	666	698	673	22.7	657	667	699	674	21.9	660	669	686	672	15.2	520
335	760	765	805	777	24.7	764	766	801	777	20.8	762	773	799	778	19.0	766	774	803	781	19.5	768	776	788	777	10.1	603
275	866	871	907	881	22.4	870	872	907	883	20.8	869	879	904	884	18.0	873	880	905	886	16.8	875	882	889	882	7.0	689

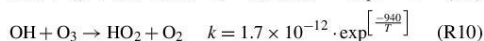
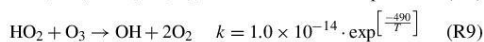
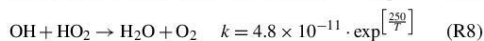
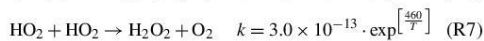
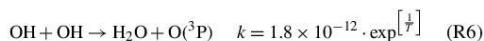
Table 2. The evolution of OH within the HORUS sample flow streamlines, along the length of APACHE at all six pressures, within the streamlines created by HORUS sampling as depicted in Fig. 8. The *L* term represents OH mixing ratios on the left most streamline, *C* represents OH mixing ratios in the center of the streamlines, and *R* represents OH mixing ratios on the right most streamline. The centreline within IPI nozzle column shows the OH mixing ratios in the center of the flow in the HORUS inlet. All standard deviations are quoted to 1σ .

ibrated Pen-Ray lamp used on the ground-based calibration device to F_{β} entering APACHE. This entailed first calibrating the HORUS instrument using a precharacterized ground-based calibration device (Martinez et al., 2010). The precalibrated Pen-Ray lamp flux (ϕ_0) is calculated from the measured NO concentrations that are produced by irradiating a known mixture of N_2O in a carrier gas:

$$\phi_0 = \frac{(k_a [N_2] [LM] + k_b [N_2] + k_c [N_2O] + k_d [N_2O] [NO])}{2k_d [N_2O]^2 \sigma_{N_2O} f_{N_2O}}, \quad (8)$$

where σ_{N_2O} is the absorption cross section of N_2O at 184.9 nm and f_{N_2O} is the correction factor that accounts for the flux reduction via absorption by N_2O . A TEI NO monitor measures the NO concentration. For more details on how the ground calibration device is characterized using the photolysis of N_2O in conjunction with a TEI NO monitor, see Martinez et al. (2010). Since the precharacterized ground-based calibration device is designed to supply only 50 sL min^{-1} , and the sensitivity of the airborne HORUS instrument is optimized for high-altitude flying, the critical orifice diameter in HORUS was changed from the airborne configuration of 1.4 to a 0.8 mm on-ground* configuration. Additionally, the IPI system was switched to passive (i.e., the exhaust line from IPI to the IPI blower was capped). This was to adapt HORUS to a mass flow that the ground-based calibration device is able to provide and reduces the internal pressure within HORUS (from 18 to 3.5 mbar) to optimize the sensitivity towards OH at ambient ground level pressures (~ 1000 mbar). The asterisk discerns terms that were quantified when the smaller 0.8 mm critical orifice was used. The calculated instrument on-ground* sensitivity was then used to translate OH and HO_2 concentrations produced by the uv-technik Hg ring lamp into a value for F_{β} . Take note that for the direct calibrations of the airborne HORUS system using the characterized APACHE system, discussed in Sect. 4.3, the same initial 1.4 mm diameter critical orifice as used during the airborne campaign was installed. The HORUS on-ground* sensitivities at 1010 mbar for OH and HO_2 are $13.7(\pm 1.9)$ and $17.9(\pm 2.5) \text{ cts s}^{-1} \text{ pptv}^{-1} \text{ mW}^{-1}$ respectively, with the uncertainties quoted to 1σ . This sensitivity was then used to calculate the OH and HO_2 concentrations at the instrument nozzle with the APACHE system installed and operating at 1010 mbar. To ensure sufficient flow stability during calibration at this high pressure, the Edwards GSX160 scroll pump was disengaged. Additionally, the water mixing ratios were kept constant ($\sim 3.1 \text{ mmol mol}^{-1}$) and oxygen levels were varied by adding different pure N_2 and synthetic air mixtures, via MFCs. The OH and HO_2 concentrations at the IPI nozzle were $1.41(\pm 0.01)$ and $1.31(\pm 0.01) \times 10^{10} \text{ molecules cm}^{-3}$ respectively when using a water vapor mixing ratio of $3.1 \text{ mmol mol}^{-1}$ in synthetic air injected into APACHE. The uncertainties are quoted as measurement variability at 1σ . Using these values, the OH and HO_2 concentrations at the lamp were back calculated accounting for radical–radical loss Reactions (R6–R8) and HO_x reactions

with O₃ (Reactions R9–R10) using rate constants taken from Burkholder et al. (2015) with temperature (T) in Kelvin.



In APACHE when the Edwards GSX160 scroll pump was disengaged, the transit time between the UV radiation zone and the IPI nozzle was 0.18 s, resulting in chemical losses of 30 % to 33 % for OH and 27 % to 30 % HO₂, depending on oxygen concentration. Accounting for these chemical losses yields OH concentrations of $2.0(\pm 0.02) \times 10^{10}$ molecules cm⁻³ and HO₂ concentrations of $1.9(\pm 0.02) \times 10^{10}$ molecules cm⁻³ at the lamp, at 1010 mbar. The photon flux (F) experienced by the air sampled by HORUS, quantified using the OH and HO₂ concentrations stated above, ranged from 3.8×10^{14} to 6.7×10^{14} photons cm⁻² s⁻¹ depending on oxygen concentrations and considering the chemical losses. As described before, Eq. (7) shows how the production of OH at the lamp is calculated:

$$[\text{OH}] = [\text{H}_2\text{O}] \cdot \sigma_{\text{H}_2\text{O}} \cdot F_{184.9\text{nm}} \cdot \phi_{\text{H}_2\text{O}} \cdot t. \quad (9)$$

$F_{184.9\text{nm}}$ is the actinic flux encountered by the water molecules as they pass across the photolysis region, which is dependent on the attenuation of the flux (F_β) entering APACHE due to water vapor and O₂ molecules. Whereas the absorption coefficient of water vapor is constant across the linewidth of the 184.9 nm Hg emission line, the effective absorption cross section of molecular oxygen (σ_{O_2}) changes significantly at 184.9 nm within the linewidth of the Hg lamp (Creasey et al., 2000). Therefore, σ_{O_2} affecting the APACHE calibrations is dependent on O₂ concentration and the ring lamp temperature and current. Since the operating temperature of the uv-technic Hg lamp and the current applied (0.8 A) was kept constant during the actinometrical experiments and during the APACHE calibrations, any effect on σ_{O_2} regarding the ring lamp linewidth does not need to be investigated further in this study. The relationship of $F_{184.9\text{nm}}$ to F_β can be derived using Beer–Lambert principles:

$$F_{184.9\text{nm}} = F_\beta \cdot e^{-\left(\gamma_{\text{H}_2\text{O}}[\text{H}_2\text{O}] + \gamma_{\text{O}_2}[\text{O}_2]\right)}, \quad (10)$$

where F_β is the flux intensity entering APACHE from the ring lamp, with

$$\gamma_{\text{O}_2} = R_\beta \cdot \omega \cdot \sigma_{\text{O}_2}, \quad (11)$$

where R_β is the radial distance of the sampled air parcel to the ring lamp of APACHE; ω is a correction factor replicating

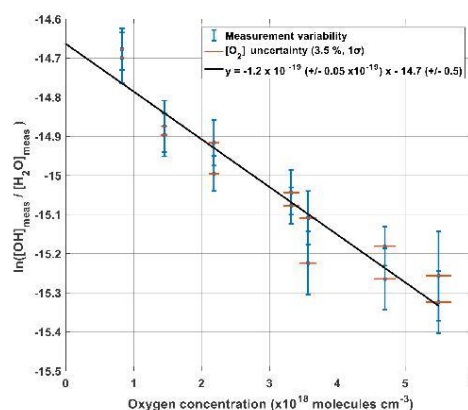


Figure 9. Plot showing the result of Eq. (11) as a function of oxygen concentration.

the integrated product of the absorption cross section and the ring lamp's emission line as modified by the effect of the absorption of O₂ present in between the lamp; and the flight path of the sampled air, normalized by σ_{O_2} , is the effective cross section of O₂. When combining Eqs. (7) and (9) the OH concentration produced at the lamp is quantified as

$$[\text{OH}] = [\text{H}_2\text{O}] \cdot \sigma_{\text{H}_2\text{O}} \cdot \phi_{\text{H}_2\text{O}} \cdot t \cdot F_\beta \cdot e^{-\left(\gamma_{\text{H}_2\text{O}}[\text{H}_2\text{O}] + \gamma_{\text{O}_2}[\text{O}_2]\right)}. \quad (12)$$

Equation (11) can be rearranged to

$$\ln\left[\frac{[\text{OH}]}{[\text{H}_2\text{O}]}\right] = \ln\left(F_\beta \cdot t \cdot \phi_{\text{H}_2\text{O}} \cdot \sigma_{\text{H}_2\text{O}}\right) + \left(-\gamma_{\text{H}_2\text{O}} \cdot [\text{H}_2\text{O}] - \gamma_{\text{O}_2} \cdot [\text{O}_2]\right). \quad (13)$$

Figure 9 shows the measured production of OH (left side of Eq. 12) plotted against oxygen concentration. Given that the other terms within Eq. (12) are constant with changing oxygen levels, the plotted gradient of the linear regression in Fig. 9 yields γ_{O_2} as a function of oxygen concentration being $1.2 \times 10^{-19}(\pm 0.05 \times 10^{-19})$ cm³ per molecule.

Given that the y intercept of the linear regression, -14.66 , is equal to the natural logarithm of ($F_\beta t \phi_{\text{H}_2\text{O}}$) minus ($\gamma_{\text{H}_2\text{O}}[\text{H}_2\text{O}]$), the flux entering APACHE F_β can be characterized:

$$F_\beta = \left(\frac{e^{-14.66}}{t \cdot \phi_{\text{H}_2\text{O}}}\right) - \left(\gamma_{\text{H}_2\text{O}} \cdot [\text{H}_2\text{O}]\right) = 6.9 \times 10^{14}(\pm 1.1 \times 10^{14}) \text{ photons cm}^{-2} \text{ s}^{-1}. \quad (14)$$

The accuracy in F_β from method A is 15.9 % (1σ). Table 3 shows the parameters and their uncertainties contributing to the F_β characterized in method A.

Table 3. Parameters and uncertainties used in method A, using HORUS as a transfer standard. Overall uncertainty is the sum of the quadrature of the individual uncertainties. O(¹D) yield is taken from Martínez et al. (2010).

Parameter	Comments	Total uncertainty (1σ)
NO monitor (TEI)	Calibration uncertainty	5.2 %
NO standard (NPL)	Purity and concentration of the gas	1 %
N ₂ O cross section	JPL recommendation	2 %
H ₂ O cross section	JPL recommendation	2 %
γ _{O₂}	From method A	3.5 %
O(¹ D) yield	Martínez et al. (2010)	1 %
Kinetic rate coefficients	JPL recommendation	12 %
F _β variability	From method A	3.5 %
Photolysis chamber dimensions	Specifications of in-house workshop	3 %
[H ₂ O]	Calibration with NIST standard dew point generator	2 %
[O ₂]	From method A	3.4 %
Mass flow controllers	Calibration with NIST DryCal	2 %
Pressure and temperature sensors	Validated against NIST standard	2 %
Overall experimental stability	Variability of measured terms	4 %
Overall uncertainty		15.9 %

The second actinometrical method (B) involved using an ANSYCO O3 41 M ozone monitor to measure the ozone mixing ratio profile between the IPI nozzle and the wall surface of APACHE, at ground pressure (1021 mbar). This method utilizes O₂ photolysis at 184.9 nm, which produces two O(³P) atoms capable of reacting with a further two O₂ molecules to produce O₃.



The value of $1.2 \times 10^{-19} \text{ cm}^3$ per molecule for γ_{O₂} found in the previous method was used to calculate the actinic flux entering APACHE:

$$F_\beta = \frac{[\text{O}_3]}{[\text{O}_2] \cdot \gamma_{\text{O}_2} \cdot \phi_{\text{O}_2} \cdot t \cdot e^{-(\gamma_{\text{O}_2}[\text{O}_2])}} \quad (15)$$

Φ_{O₂} is the quantum yield of O₂ at 184.9 nm, which has been determined to be 1 between 242 and 175 nm (Atkinson et al., 2004). As in method A, the ozone produced at the lamp is quantified by back calculating from the ozone measured at the ANSYCO O3 41 M inlet position. Inside APACHE, typical ozone concentrations ranged from 1.26×10^{12} to $2.05 \times 10^{12} \text{ molecules cm}^{-3}$ depending on the oxygen concentration. From this approach, the calculated F_β is $6.11 \times 10^{14} (\pm 0.8 \times 10^{14}) \text{ photons cm}^{-2} \text{ s}^{-1}$ with a total uncertainty of 12.9 % (1σ). The final value taken for F_β is the average of the two experiments, weighted by their uncertainties:

- actinic flux (F_β) = $6.37 \times 10^{14} (\pm 1.3 \times 10^{14}) \text{ photons cm}^{-2} \text{ s}^{-1}$

- accuracy in F_β = 20.5 % (1σ)

- agreement for F_β between method A and B, zeta score = 0.59.

Table 4 shows the parameters and their uncertainties which contribute to the F_β characterized in method B.

4.3 Evaluation of instrumental sensitivity

Figure 10 shows the sensitivity curve of HORUS; the quenching effect; the linear fits used to quantify the pressure-independent sensitivity coefficients; and relative HO_x transmission values for OH, OH in the second axis, and HO₂ plotted as a function of the HORUS internal density. The red smoothed line in Fig. 10a represents the calculated sensitivity curve for each measurement using Eq. (4) and the characterized variables therein. Given that this calculated sensitivity curve for each measurement agrees to within 2σ of the uncertainties in measured calibration curves, we are confident that each of the terms described in Eq. (4) has been sufficiently resolved. Table 5 shows the ranges, precision, and uncertainties of measured or calculated variables affecting OH and HO₂ concentrations formed in APACHE.

The pressure-independent sensitivity coefficients (cN) for OH in the first axis (c0), OH in the second axis (c1), and HO₂ in the second axis (c2) are calculated by rearranging Eq. (4) to

$$c0 \cdot \rho_{\text{int}}(P, T) = \frac{C_{\text{OH}}(P, T)}{Q_{\text{IF}}(P, T) \cdot b_c(T) \cdot [\alpha_{\text{IPI OH}}(P, T) \cdot \alpha_{\text{HORUS OH}}(P, T)]}, \quad (16)$$

$$c1 \cdot \rho_{\text{int}}(P, T) = \frac{C_{\text{OH}(2)}(P, T)}{Q_{\text{IF}(2)}(P, T) \cdot b_c(T) \cdot [\alpha_{\text{IPI OH}}(P, T) \cdot \alpha_{\text{HORUS OH}(2)}(P, T)]}, \quad (17)$$

Table 4. Parameters and uncertainties involved in method B, using the ANSYCO O3 41 M monitor. The total uncertainty is the sum of the quadrature of the individual uncertainties.

Parameter	Comments	Total uncertainty (1σ)
O ₃ calibrator	Calibrated against a primary standard	2 %
[O ₃]	Calibration of ANSYCO O3 41 M monitor	4 %
[O ₂]	From method A	3.4 %
γ_{O_2}	From method A	3.5 %
F_{β} variability	From method A	3.5 %
Mass flow controllers	Calibration with NIST DryCal	2 %
Pressure and temperature sensors	Validated against NIST standard	2 %
Experimental stability	Variability of values	10.1 %
Overall uncertainty		12.9 %

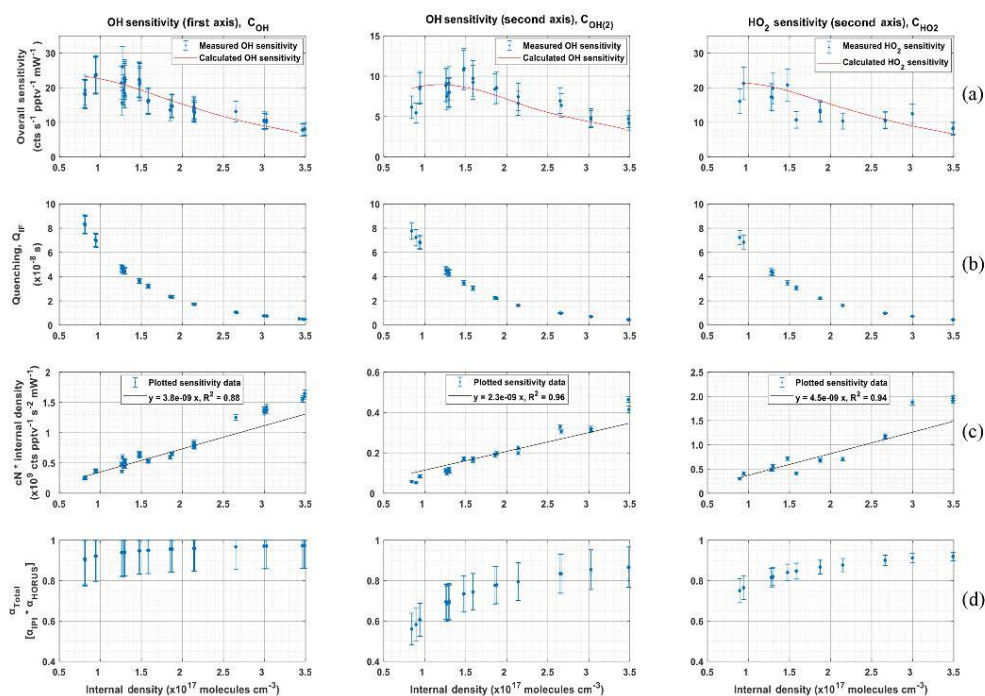
**Figure 10.** The determination of the pressure-based sensitivity of OH in both axes and HO₂ for HORUS. The data shown are 1 h averages for the tested pressures, all plotted with the internal density on the x axis. Row (a) is the measured (blue data points) HORUS sensitivity curve and calculated (red line) sensitivity curve. Row (b) is internal quenching by N₂, O₂, and water vapor. Row (c) is internal density and the pressure-independent sensitivity coefficient (cN: c0 for the OH first axis, c1 for OH second axis, and c2 for HO₂). Row (d) is the total OH and HO₂ transmissions, all plotted against internal density. The error bars represent measurement variability (1σ) for rows (b, c). In rows (a, d), the error bars represent the total uncertainty (1σ).

Table 5. Parameters within APACHE, their ranges, and uncertainties, contributing to the uncertainty in the three measurement sensitivities within HORUS.

Parameter (unit)	Range or typical value	Precision (1σ)	Total uncertainty (1σ)
F_β at 184.9 nm (photons $\text{cm}^{-2} \text{s}^{-1}$)	6.37×10^{14}	3.5 %	20.5 %
$\sigma_{\text{H}_2\text{O}}$ (cm^2 per molecule)	7.22×10^{-20}	–	2 %
γ_{O_2} (cm^3 per molecule)	1.22×10^{-19}	1.8 %	3.5 %
$[\text{O}_2]$ ($\times 10^{18}$ molecules cm^{-3})	1.1–4.8	1.4 %	3.4 %
$[\text{H}_2\text{O}]$ ($\times 10^{16}$ molecules cm^{-3})	2.00–7.41	1.2 %	2 %
Mass flow controller (sL min^{-1})	203–988	< 2 %	2 %
Pressure sensors (mbar)	275–900	< 1 %	2 %
Temperature sensors (K)	282–302	< 1 %	2 %
Overall		5 %	21.5 %

$$c2 \cdot \rho_{\text{Int}}(P, T) = \frac{C_{\text{HO}_2}(P, T)}{Q_{\text{IF}(2)}(P, T) \cdot b_c(T) \cdot [\alpha_{\text{IPIHO}_2}(P, T) \cdot \alpha_{\text{HORUSHO}_2}(P, T)]}. \quad (18)$$

The products of Eq. (15) to (17) are plotted against internal density in Fig. 10c, where the slopes of the linear regressions are the pressure-independent sensitivity coefficients. Note that in Eqs. (16) and (17) the two bracketed terms are in relation to the OH measurement at the second axis. Table 6 shows the values, precision, and uncertainty in the quantified pressure-independent sensitivity coefficients.

In Fig. 10c the quenching (Q_{IF}) is plotted against internal density. Q_{IF} is calculated using the same approach as described in Faloon et al. (2004) and Martinez et al. (2010):

$$Q_{\text{IF}}(P) = \frac{1}{\Gamma} (e^{-\Gamma g_1} - e^{-\Gamma g_2}), \quad (19)$$

where Γ is the excited state decay frequency (Hz), consisting of the natural decay frequency, and decay due to collisional quenching that is dependent on pressure, temperature, and water vapor mixing ratio. g_1 and g_2 are the detector gate opening and closing times after the initial excitation laser pulse, which are set to 104 and 600 ns respectively.

As described in Sect. 2.3, the pressure-independent sensitivity coefficients are lump sum variables containing pressure-independent HO_x wall loss. The pressure-dependent HO_x transmission through the HORUS instrument is quantified and described below. In flight, IPI operates across the pressure range of 180 to 1010 mbar. However, within HORUS, post critical orifice, at detection axes where HO_x is measured the pressure ranges from 3.1 to 18.4 mbar. Therefore, the transmission through IPI (α_{IPI}) and through HORUS (α_{HORUS}) must be quantified separately using the corresponding measured pressures and transit times, before being combined as the total transmission ($\alpha_{\text{IPI}} \cdot \alpha_{\text{HORUS}} = \alpha_{\text{Total}}$). To calculate the transmission of HO_x within IPI, the following was used:

$$\alpha_{\text{IPIOH}} = 1 - \left[\frac{\text{OH}_{\text{DM}}(P) \cdot t_{\text{rIPI}}(P, T) \cdot \pi}{\text{IPI}_A \cdot P_{\text{IPI}}} \right], \quad (20)$$

$$\alpha_{\text{IPIHO}_2} = 1 - \left[\frac{\text{HO}_{2\text{DM}}(P) \cdot t_{\text{rIPI}}(P, T) \cdot \pi}{\text{IPI}_A \cdot P_{\text{IPI}}} \right], \quad (21)$$

where t_{rIPI} is the transit time within IPI, i.e., the time it takes for air to flow from the IPI nozzle to the critical orifice of HORUS. IPI_A is the internal cross-sectional area of IPI and P_{IPI} is the measured pressure within IPI. The OH_{DM} and $\text{HO}_{2\text{DM}}$ terms are the OH and HO_2 diffusion coefficients as described in Sect. 4.1.2. α_{IPIOH} is the transmission of OH through IPI, and α_{IPIHO_2} is the transmission of HO_2 through IPI. By applying Eqs. (19) and (20), α_{IPIOH} and α_{IPIHO_2} ranged from 0.97 to 0.99 and 0.99 to 0.997 respectively across the pressure range within IPI of 198–808 mbar and IPI transit times of 90–120 ms. However, to calculate α_{Total} , the OH and HO_2 transmission post critical orifice, α_{HORUSOH} and $\alpha_{\text{HORUSHO}_2}$, must be resolved. α_{HORUS} regarding OH and HO_2 can be calculated by adapting Eqs. (19) and (20) to the internal HORUS conditions producing:

$$\alpha_{\text{HORUSOH}} = 1 - \left[\frac{\text{OH}_{\text{DM}}(P) \cdot t_{\text{r1}}(P, T) \cdot \pi}{\text{HORUS}_A \cdot P_{\text{int}}} \right], \quad (22)$$

$$\alpha_{\text{HORUSOH}(2)} = 1 - \left[\frac{\text{OH}_{\text{DM}}(P) \cdot t_{\text{r2}}(P, T) \cdot \pi}{\text{HORUS}_A \cdot P_{\text{int}}} \right], \quad (23)$$

$$\alpha_{\text{HORUSHO}_2} = 1 - \left[\frac{\text{HO}_{2\text{DM}}(P) \cdot t_{\text{r2}}(P, T) \cdot \pi}{\text{HORUS}_A \cdot P_{\text{int}}} \right], \quad (24)$$

where t_{r1} and t_{r2} are the transit times within HORUS from the critical orifice to the first and second detection axis respectively. HORUS_A is the internal cross-sectional area of HORUS, and P_{int} is the measured internal pressure within HORUS. The OH transmission from the critical orifice to the first detection cell (α_{HORUSOH}) ranged from 0.93 to 0.98, the OH transmission from the critical orifice to the second detection cell ($\alpha_{\text{HORUSOH}(2)}$) ranged from 0.58 to 0.87, and the HO_2 transmission from the critical orifice to the second detection cell ($\alpha_{\text{HORUSHO}_2}$) ranged from 0.76 to 0.92. These ranges are quoted under the HORUS internal pressure range of 3.7 to 13.7 mbar and internal transit times to the first detection axis (3.8 to 4.3 ms) and second detection axis (23.5

Table 6. Pressure-independent sensitivities and their overall uncertainty from calibrations with APACHE.

Parameter (cts pptv ⁻¹ s ⁻² cm ³ molecule ⁻¹ mW ⁻¹)	Value (×10 ⁻⁹)	Precision (±1σ)	Total uncertainty (1σ)
c0 for OH in OH axis	3.8	4 %	6.9 %
c1 for OH in HO ₂ axis	2.3	4 %	6.9 %
c2 for HO ₂ in HO ₂ axis	4.5	2 %	5.6 %

to 27.8 ms). The combined α_{Total} values for OH, OH at the second detection axis, and HO₂ are plotted in Fig. 10d as a function of the internal density of HORUS. Table 7 shows the calculated α_{Total} transmission terms; their precision; and uncertainty for OH to the first axis, OH to the second axis, and HO₂ to the second axis.

Table 8 shows the measured sensitivity values using APACHE for OH at the first axis (C_{OH}), OH at the second axis ($C_{\text{OH}(2)}$), and HO₂ at the second axis (C_{HO_2}). The precision denotes the 1σ variability in the measured HO_x signals from HORUS; the total uncertainty is the root sum square of the total uncertainty values from the variables listed in Tables 5 and 6.

The undescribed remaining fraction that influences the instrument sensitivity ($R_{\text{undescribed}}$) is calculated by dividing the overall sensitivity values described in Eq. (4):

$$R_{\text{OH}} = \frac{C_{\text{OH}}}{c0 \cdot \rho_{\text{int}}(P, T) \cdot Q_{\text{IF}}(P, T) \cdot b_c(T) \cdot [\sigma_{\text{PI OH}}(P, T) \cdot \sigma_{\text{HORUS OH}}(P, T)]}, \quad (25)$$

$$R_{\text{OH}(2)} = \frac{C_{\text{OH}(2)}}{c1 \cdot \rho_{\text{int}}(P, T) \cdot Q_{\text{IF}(2)}(P, T) \cdot b_c(T) \cdot [\sigma_{\text{PI OH}}(P, T) \cdot \sigma_{\text{HORUS OH}(2)}(P, T)]}, \quad (26)$$

$$R_{\text{HO}_2} = \frac{C_{\text{HO}_2}}{c2 \cdot \rho_{\text{int}}(P, T) \cdot Q_{\text{IF}(2)}(P, T) \cdot b_c(T) \cdot [\sigma_{\text{PI HO}_2}(P, T) \cdot \sigma_{\text{HORUS HO}_2}(P, T)]}, \quad (27)$$

$$R_{\text{undescribed}} = \{R_{\text{OH}}; R_{\text{OH}(2)}; R_{\text{HO}_2}\},$$

where $R_{\text{undescribed}}$ is a matrix containing the undescribed remaining factors from the three measurements. When plotting $R_{\text{undescribed}}$ against the internal pressure of HORUS, (see Fig. S10), the data scatters $\pm 0.15(1\sigma)$ about the average value of 1.02 (± 0.23 , 1σ calibration uncertainty). This means that (as an upper limit) < 2 % of the overall instrument sensitivity is unresolved by the terms described in Eq. (4). Additionally, the 1σ variability of the $R_{\text{undescribed}}$ is 34 % smaller than the uncertainty in the APACHE calibration, meaning that this remaining fraction is declared as neither pressure dependent nor pressure independent.

It is important to note here that all data shown in Fig. 10, with the exception of the pressure-independent sensitivity coefficients, are in relation to temperatures and pressures HORUS experienced during calibrations in the lab. To apply these findings to real airborne measurements, the pressure- and temperature-dependent terms in Eq. (4) are calculated using the temperatures and pressures that are measured

within the instrument during flight. The only terms that affect measurement sensitivity and are directly transferable from the calibrations with APACHE to the measurements in flight shown in Eq. (4) are the pressure-independent sensitivity coefficient as they are not subject to change with the large temperature and pressures ranges HORUS experiences when airborne. Figure 11 shows the pressure- and temperature-dependent terms from Eq. (4) characterized for a typical flight that took place during the OMO-Asia 2015 airborne campaign. In Fig. 11, the sensitivity values, limit of detection, transmission values for OH (blue data points) and HO₂ (red data points), and the ambient water mixing ratios (black data points) that occurred during flight 23 are plotted as a function of altitude. During flight, the OH sensitivity ranged from 5.4(±1.2) cts s⁻¹ pptv⁻¹ mW⁻¹ on the ground to 24.1(±5.4) cts s⁻¹ pptv⁻¹ mW⁻¹ at 14 km. The HORUS sensitivity values for HO₂ ranged from 5.5(±1.2) cts s⁻¹ pptv⁻¹ mW⁻¹ and reached an average maxima of 20.5(±4.5) cts s⁻¹ pptv⁻¹ mW⁻¹ at 11.4 km. Above 11.4 km the HO₂ sensitivity decreased with altitude, reaching 19.7(±4.4) cts s⁻¹ pptv⁻¹ mW⁻¹ at 14 km. This drop in HO₂ sensitivity is attributable to the increasing decline in HO₂ transmission inside HORUS as the aircraft flies higher, despite the sensitivity improvements via quenching as the air is becoming drier. The water vapor mixing ratios at 14 km on average are 3 orders of magnitude lower than the average water vapor mixing ratio of 1.5 % at ground level, which greatly suppresses quenching of OH and thus is the main driver for the general increasing trend in the instrument sensitivity towards HO_x as altitude increases. Additionally, Fig. 11 shows that the limit of detection for both OH and HO₂ decrease with increasing altitude. For OH, the HORUS limit of detection is ~ 0.11 pptv at ground level and drops to ~ 0.02 pptv at 14 km. For HO₂ the limit of detection is ~ 1.2 pptv at ground level and drops to 0.23 pptv at 14 km.

5 Conclusions

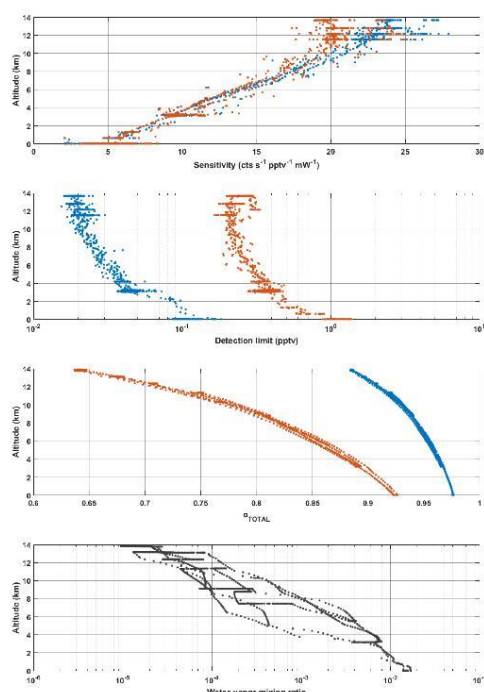
The overall goal of this study was to develop and test a new calibration system capable of providing the high flows required by the airborne HORUS system while maintaining stable pressures across the pressure ranges experienced during flight. Such systems are critical to suitably characterize airborne systems (such as a LIF-FAGE measuring HO_x) that have a strong pressure-dependent sensitivity. In addition, this

Table 7. Pressure-dependent OH and HO₂ transmission and their overall uncertainty from calibrations with APACHE.

Parameter (%)	Value	Precision ($\pm 1\sigma$)	Total uncertainty (1σ)
α_{Total} (for OH to OH axis)	90–97	2.8 %	14.3%–11.5 %
α_{Total} (for OH to HO ₂ axis)	56–86	4.3 %	14.1%–11.5 %
α_{Total} (for HO ₂ to HO ₂ axis)	75–92	2.9 %	7.9%–2.2 %

Table 8. Pressure-dependent sensitivities for the three measurement within HORUS and their overall uncertainty from calibrations with APACHE. The range in the precision relates to the numbers quoted in the value column.

Parameter (unit)	Value	Precision ($\pm 1\sigma$)	Total uncertainty (1σ)
C_{OH} (cts s ⁻¹ pptv ⁻¹ mW ⁻¹)	7.8–26.1	1.1%–0.5 %	22.6 %
$C_{\text{OH}(2)}$ (cts s ⁻¹ pptv ⁻¹ mW ⁻¹)	4.2–11.0	2.0%–0.3 %	22.6 %
C_{HO_2} (cts s ⁻¹ pptv ⁻¹ mW ⁻¹)	8.1–21.2	0.4%–0.7 %	22.2 %

**Figure 11.** In-flight sensitivity curves, limit of detection, and HO_x transmission plotted against altitude for OH (blue data points) and HO₂ (red data points), and the water vapor mixing ratio (black data points) plotted against altitude in kilometers (bottom plot). Data taken from flight 23.

system is purely based on the use of water vapor photolysis, which is a frequently adopted technique for HO_x instrument calibration (Martinez et al., 2003; Faloon et al., 2004; Dusanter et al., 2008). The COMSOL Multiphysics simulations constrained by temperature, pressure, and mass flow measurements demonstrated that air masses at the boundary of the APACHE system do not have sufficient time to expand into the streamlines created by the HORUS sample flow and influence the HO_x content entering HORUS. The largest uncertainties result from constraining the flux (F_{β}) entering APACHE ($6.37 \pm 1.3 \times 10^{14}$ photons cm⁻² s⁻¹, 1σ) and the total uncertainty in the pressure-independent sensitivity coefficients (ranging from 5.6 % to 6.9 %, 1σ). The two actinometrical methods used to derive F_{β} proved to be in good agreement with a zeta score of 0.59, considering 1σ of their uncertainties. The HORUS transfer standard method yielded an F_{β} value of $6.9 \pm 1.1 \times 10^{14}$ photons cm⁻² s⁻¹ (1σ), and the ozone monitor method yielded an F_{β} value of $6.11 \pm 0.8 \times 10^{14}$ photons cm⁻² s⁻¹ (1σ). Furthermore, the APACHE system enabled the total OH and HO₂ pressure-dependent transmission factors to be characterized as a function of internal pressure. Calculations of HO_x diffusivity to the walls within IPI and the low-pressure regime within HORUS yielded 90%–97% for OH transmission to the first detection axis, 56%–86% for OH transmission to the second detection axis, and 75%–92% for HO₂ transmission to the second detection axis. Future studies with APACHE are planned to expand upon the findings within this paper, with a particular focus on temperature control and on improving operational pressure and flow speed ranges. However, in this study, the APACHE calibration system has demonstrated that, within the lab, it is sufficiently capable of calibrating the airborne HORUS instrument across the pressure ranges the instrument had experienced in flight during the OMO-Asia 2015 airborne campaign. The overall uncertainty of 22.1%–22.6% (1σ) demonstrates that this calibration approach with APACHE compares well with other

calibration methods described earlier in Table 1. Nevertheless, there is potential for improvement. Accurate calibrations of instruments, particularly airborne instruments that have strong pressure-dependent sensitivities, are critical to acquiring concentrations of atmospheric species with minimal uncertainties. Only through calibrations can the accuracy of measurements be characterized and allow for robust comparisons with other measurements and with models to expand our current understanding of chemistry that occurs within our atmosphere.

Data availability. The research dataset is fully and openly accessible via <https://doi.org/10.5281/zenodo.3821976> (Marno and Harder, 2020).

Supplement. The supplement related to this article is available online at: <https://doi.org/10.5194/amt-13-2711-2020-supplement>.

Author contributions. KH, CE, MM, HH, UJ, and MR formulated the original concept and designed the APACHE system. DM, HH, and UJ prototyped, developed, and characterized the APACHE system. TK, DM, and HH developed and performed the CFD simulations. DM prepared the manuscript with contributions from all coauthors.

Competing interests. The authors declare that they have no conflict of interest.

Acknowledgements. We would like to take this opportunity to give a thank you to the in-house workshop at the Max Planck Institute for Chemistry for construction and guidance in the development of APACHE. Additionally, we would like to extend a special thank you to Dieter Scharffe for his assistance and advice during the development stage of this project.

Financial support. The article processing charges for this open-access publication were covered by the Max Planck Society.

Review statement. This paper was edited by Lisa Whalley and reviewed by two anonymous referees.

References

- Albrecht, S. R., Novelli, A., Hofzumahaus, A., Kang, S., Baker, Y., Mentel, T., Wahner, A., and Fuchs, H.: Measurements of hydroperoxy radicals (HO_2) at atmospheric concentrations using bromide chemical ionisation mass spectrometry, *Atmos. Meas. Tech.*, 12, 891–902, <https://doi.org/10.5194/amt-12-891-2019>, 2019.
- Atkinson, R., Baulch, D. L., Cox, R. A., Crowley, J. N., Hampson, R. F., Hynes, R. G., Jenkin, M. E., Rossi, M. J., and Troe, J.: Evaluated kinetic and photochemical data for atmospheric chemistry: Volume I – gas phase reactions of O_x , HO_x , NO_x and SO_x species, *Atmos. Chem. Phys.*, 4, 1461–1738, <https://doi.org/10.5194/acp-4-1461-2004>, 2004.
- Brauers, T., Aschmutat, U., Brandenburger, U., Dorn, H. P., Hausmann, M., Hessling, M., Hofzumahaus, A., Holland, F., Plass-Dulmer, C., and Ehhalt, D. H.: Intercomparison of tropospheric OH radical measurements by multiple folded long-path laser absorption and laser induced fluorescence, *Geophys. Res. Lett.*, 23, 2545–2548, <https://doi.org/10.1029/96gl02204>, 1996.
- Brauers, T., Hausmann, M., Bister, A., Kraus, A., and Dorn, H. P.: OH radicals in the boundary layer of the Atlantic Ocean I. Measurements by long-path laser absorption spectroscopy, *J. Geophys. Res.*, 106, 7399–7414, <https://doi.org/10.1029/2000jd900679>, 2001.
- Brune, W. H., Stevens, P. S., and Mather, J. H.: Measuring OH and HO_2 in the Troposphere by Laser-Induced Fluorescence at Low-Pressure, *J. Atmos. Sci.*, 52, 3328–3336, [https://doi.org/10.1175/1520-0469\(1995\)052<3328:Moahit>2.0.Co;2](https://doi.org/10.1175/1520-0469(1995)052<3328:Moahit>2.0.Co;2), 1995.
- Burkholder, J. B., Sander, S. P., Abbatt, J., Barker, J. R., Huie, R. E., Kolb, C. E., Kurylo, M. J., Orkin, V. L., Wilmouth, D. M., and Wine, P. H.: Chemical Kinetics and Photochemical Data for Use in Atmospheric Studies, Evaluation No. 18, JPL Publication 15-10, 2015.
- Cantrell, C. A., Edwards, G. D., Stephens, S., Mauldin, L., Kosciuch, E., Zondlo, M., and Eisele, F.: Peroxy radical observations using chemical ionization mass spectrometry during TOPSE, *J. Geophys. Res.*, 108, 8371, <https://doi.org/10.1029/2002JD002715>, 2003.
- COMSOL: Multiphysics Documentation, version 5.4, software, available at: <https://www.comsol.com/>, last access: 30 October 2019.
- Creasey, D. J., Heard, D. E., and Lee, J. D.: Absorption cross-section measurements of water vapour and oxygen at 185 nm. Implications for the calibration of field instruments to measure OH, HO_2 and RO_2 radicals *Geophys. Res. Lett.*, 27, 1651–1654, <https://doi.org/10.1029/1999gl011014>, 2000.
- Creasey, D. J., Evans, G. E., Heard, D. E., and Lee, J. D.: Measurements of OH and HO_2 concentrations in the Southern Ocean marine boundary layer, *J. Geophys. Res.-Atmos.*, 108, 4475, <https://doi.org/10.1029/2002jd003206>, 2003.
- Dieke, G. H. and Crosswhite, H. M.: The Ultraviolet Bands of OH Fundamental Data, *J. Quant. Spectrosc. Ra.*, 2, 97–199, [https://doi.org/10.1016/0022-4073\(62\)90061-4](https://doi.org/10.1016/0022-4073(62)90061-4), 1962.
- Dilecce, G., Ambrico, P. F., and De Benedictis, S.: An ambient air RF low-pressure pulsed discharge as an OH source for LIF calibration, *Plasma Sources Sci. T.*, 13, 237–244, <https://doi.org/10.1088/0963-0252/13/2/007>, 2004.
- Dorn, H. P., Neuroth, R., and Hofzumahaus, A.: Investigation of OH Absorption Cross-Sections of Rotational Transitions in the Band under Atmospheric Conditions: Implications for Tropospheric Long-Path Absorption-Measurements, *J. Geophys. Res.*, 100, 7397–7409, <https://doi.org/10.1029/94JD03323>, 1995.
- Dusanter, S., Vimal, D., and Stevens, P. S.: Technical note: Measuring tropospheric OH and HO_2 by laser-induced fluorescence at low pressure. A comparison of calibration techniques. *At-*

- mos. Chem. Phys., 8, 321–340, <https://doi.org/10.5194/acp-8-321-2008>, 2008.
- Engel, V., Staemmler, V., Vanderwal, R. L., Crim, F. F., Sensation, R. J., Hudson, B., Andresen, P., Hennig, S., Weide, K., and Schinke, R.: Photodissociation of Water in the 1st Absorption-Band – a Prototype for Dissociation on a Repulsive Potential-Energy Surface, *J. Phys. Chem.*, 96, 3201–3213, <https://doi.org/10.1021/j100187a007>, 1992.
- Faloona, I. C., Tan, D., Leshner, R. L., Hazen, N. L., Frame, C. L., Simpasa, J. B., Harder, H., Martinez, M., Di Carlo, P., Ren, X. R., and Brune, W. H.: A laser-induced fluorescence instrument for detecting tropospheric OH and HO₂: Characteristics and calibration, *J. Atmos. Chem.*, 47, 139–167, <https://doi.org/10.1023/B:JOCH.0000021036.53185.0e>, 2004.
- Freeman, A. J.: Configuration Interaction Study of the Electronic Structure of the Oh Radical by the Atomic and Molecular Orbital Methods, *J. Chem. Phys.*, 28, 230–243, <https://doi.org/10.1063/1.1744098>, 1958.
- Fuchs, H., Bohn, B., Hofzumahaus, A., Holland, F., Lu, K. D., Nehr, S., Rohrer, F., and Wahner, A.: Detection of HO₂ by laser-induced fluorescence: calibration and interferences from RO₂ radicals, *Atmos. Meas. Tech.*, 4, 1209–1225, <https://doi.org/10.5194/amt-4-1209-2011>, 2011.
- Fuchs, H., Tan, Z., Hofzumahaus, A., Broch, S., Dorn, H.-P., Holland, F., Künstler, C., Gomm, S., Rohrer, F., Schrade, S., Tillmann, R., and Wahner, A.: Investigation of potential interferences in the detection of atmospheric RO_x radicals by laser-induced fluorescence under dark conditions, *Atmos. Meas. Tech.*, 9, 1431–1447, <https://doi.org/10.5194/amt-9-1431-2016>, 2016.
- Hard, T. M., George, L. A., and O'Brien, R. J.: Fage Determination of Tropospheric OH and HO₂, *J. Atmos. Sci.*, 52, 3354–3372, [https://doi.org/10.1175/1520-0469\(1995\)052<3354:F0thas>2.0.Co;2](https://doi.org/10.1175/1520-0469(1995)052<3354:F0thas>2.0.Co;2), 1995.
- Hard, T. M., George, L. A., and O'Brien, R. J.: An absolute calibration for gas-phase hydroxyl measurements, *Environ. Sci. Technol.*, 36, 1783–1790, <https://doi.org/10.1021/es0156461>, 2002.
- Heard, D. E. and Pilling, M. J.: Measurement of OH and HO₂ in the troposphere, *Chem. Rev.*, 103, 5163–5198, <https://doi.org/10.1021/cr020522s>, 2003.
- Hens, K., Novelli, A., Martinez, M., Auld, J., Axinte, R., Bohn, B., Fischer, H., Keronen, P., Kubistin, D., Nölscher, A. C., Oswald, R., Paasonen, P., Petäjä, T., Regelin, E., Sander, R., Sinha, V., Sipilä, M., Taraborrelli, D., Tatum Ernest, C., Williams, J., Lelieveld, J., and Harder, H.: Observation and modelling of HO_x radicals in a boreal forest, *Atmos. Chem. Phys.*, 14, 8723–8747, <https://doi.org/10.5194/acp-14-8723-2014>, 2014.
- Hofzumahaus, A., Brauers, T., Aschmutat, U., Brandenburger, U., Dorn, H. P., Hausmann, M., Hessling, M., Holland, F., Plass-Dulmer, C., Sedlacek, M., Weber, M., and Ehhalt, D. H.: Reply to "Comment on 'The measurement of tropospheric OH radicals by laser-induced fluorescence spectroscopy during the POPCORN field campaign' by Hofzumahaus et al. and 'Inter-comparison of tropospheric OH radical measurements by multiple folded long-path laser absorption and laser induced fluorescence' by Brauers et al.", *Geophys. Res. Lett.*, 24, 3039–3040, <https://doi.org/10.1029/97gl02947>, 1997.
- Holland, F., Hessling, M., and Hofzumahaus, A.: In-Situ Measurement of Tropospheric Oh Radicals by Laser-Induced Fluorescence – a Description of the Kfa Instrument, *J. Atmos. Sci.*, 52, 3393–3401, [https://doi.org/10.1175/1520-0469\(1995\)052<3393:ismoto>2.0.Co;2](https://doi.org/10.1175/1520-0469(1995)052<3393:ismoto>2.0.Co;2), 1995.
- Holland, F., Hofzumahaus, A., Schafer, R., Kraus, A., and Patz, H. W.: Measurements of OH and HO₂ radical concentrations and photolysis frequencies during BERLIOZ, *J. Geophys. Res.*, 108, 8246, <https://doi.org/10.1029/2001JD001393>, 2003.
- Ivanov, A. V., Trakhtenberg, S., Bertram, A. K., Gershenzon, Y. M., and Molina, M. J.: OH, HO₂, and ozone gaseous diffusion coefficients, *J. Phys. Chem. A*, 111, 1632–1637, <https://doi.org/10.1021/jp066558w>, 2007.
- Kukui, A., Ancellet, G., and Le Bras, G.: Chemical ionisation mass spectrometer for measurements of OH and Peroxy radical concentrations in moderately polluted atmospheres, *J. Atmos. Chem.*, 61, 133–154, <https://doi.org/10.1007/s10874-009-9130-9>, 2008.
- Langhoff, S. R., Vandishoeck, E. F., Wetmore, R., and Dalgarno, A.: "Radiative Lifetimes and Dipole-Moments of the A²Σ⁺, B²Σ⁺, and C²Σ⁺ States of OH, *J. Chem. Phys.*, 77, 1379–1390, <https://doi.org/10.1063/1.443962>, 1982.
- Lelieveld, J., Peters, W., Dentener, F. J., and Krol, M. C.: Stability of tropospheric hydroxyl chemistry, *J. Geophys. Res.*, 107, 4715, <https://doi.org/10.1029/2002jd002272>, 2002.
- Mallik, C., Tomsche, L., Bourtsoukidis, E., Crowley, J. N., Derstroff, B., Fischer, H., Hafermann, S., Hüser, I., Javed, U., Keßel, S., Lelieveld, J., Martinez, M., Meusel, H., Novelli, A., Phillips, G. J., Pozzer, A., Reiffs, A., Sander, R., Taraborrelli, D., Sauvage, C., Schuladen, J., Su, H., Williams, J., and Harder, H.: Oxidation processes in the eastern Mediterranean atmosphere: evidence from the modelling of HO_x measurements over Cyprus, *Atmos. Chem. Phys.*, 18, 10825–10847, <https://doi.org/10.5194/acp-18-10825-2018>, 2018.
- Mao, J., Ren, X., Zhang, L., Van Duin, D. M., Cohen, R. C., Park, J.-H., Goldstein, A. H., Paulot, F., Beaver, M. R., Crouse, J. D., Wennberg, P. O., DiGangi, J. P., Henry, S. B., Keutsch, F. N., Park, C., Schade, G. W., Wolfe, G. M., Thornton, J. A., and Brune, W. H.: Insights into hydroxyl measurements and atmospheric oxidation in a California forest, *Atmos. Chem. Phys.*, 12, 8009–8020, <https://doi.org/10.5194/acp-12-8009-2012>, 2012.
- Mamo, D. and Harder, H.: HORUS pressure dependent calibrations using the APACHE calibrator, Data set, Zenodo, <https://doi.org/10.5281/zenodo.3821976>, 2020.
- Martinez, M., Harder, H., Kovacs, T. A., Simpasa, J. B., Bassis, J., Leshner, R., Brune, W. H., Frost, G. J., Williams, E. J., Stroud, C. A., Jobson, B. T., Roberts, J. M., Hall, S. R., Shetter, R. E., Wert, B., Fried, A., Alicke, B., Stutz, J., Young, V. L., White, A. B., and Zamora, R. J.: OH and HO₂ concentrations, sources, and loss rates during the Southern Oxidants Study in Nashville, Tennessee, summer 1999, *J. Geophys. Res.*, 108, 4617, <https://doi.org/10.1029/2003jd003551>, 2003.
- Martinez, M., Harder, H., Kubistin, D., Rudolf, M., Bozem, H., Eerdeken, G., Fischer, H., Klüpfel, T., Gurk, C., Königstedt, R., Parchatka, U., Schiller, C. L., Stickler, A., Williams, J., and Lelieveld, J.: Hydroxyl radicals in the tropical troposphere over the Suriname rainforest: airborne measurements, *Atmos. Chem. Phys.*, 10, 3759–3773, <https://doi.org/10.5194/acp-10-3759-2010>, 2010.
- Mather, J. H., Stevens, P. S., and Brune, W. H.: OH and HO₂ measurements using laser-induced fluorescence, *J. Geophys. Res.*, 102, 6427–6436, <https://doi.org/10.1029/96JD01702>, 1997.

- Mauldin, R. L., Kosciuch, E., Henry, B., Eisele, F. L., Shetter, R., Lefer, B., Chen, G., Davis, D., Huey, G., and Tanner, D.: Measurements of OH, HO₂ + RO₂, H₂SO₄, and MSA at the south pole during ISCAT 2000. *Atmos. Environ.*, 38, 5423–5437, <https://doi.org/10.1016/j.atmosenv.2004.06.031>, 2004.
- Novelli, A., Hens, K., Tatum Ernest, C., Kubistin, D., Regelin, E., Elste, T., Plass-Dülmer, C., Martinez, M., Lelieveld, J., and Harder, H.: Characterisation of an inlet pre-injector laser-induced fluorescence instrument for the measurement of atmospheric hydroxyl radicals. *Atmos. Meas. Tech.*, 7, 3413–3430, <https://doi.org/10.5194/amt-7-3413-2014>, 2014.
- Regelin, E., Harder, H., Martinez, M., Kubistin, D., Tatum Ernest, C., Bozem, H., Klippel, T., Hosaynali-Beygi, Z., Fischer, H., Sander, R., Jücker, P., Königstedt, R., and Lelieveld, J.: HO_x measurements in the summertime upper troposphere over Europe: a comparison of observations to a box model and a 3-D model. *Atmos. Chem. Phys.*, 13, 10703–10720, <https://doi.org/10.5194/acp-13-10703-2013>, 2013.
- Ren, X. R., Harder, H., Martinez, M., Leshner, R. L., Olinger, A., Simpas, J. B., Brune, W. H., Schwab, J. J., Demerjian, K. L., He, Y., Zhou, X. L., and Gao, H. G.: OH and HO₂ chemistry in the urban atmosphere of New York City. *Atmos. Environ.*, 37, 3639–3651, [https://doi.org/10.1016/S1352-2310\(03\)00459-X](https://doi.org/10.1016/S1352-2310(03)00459-X), 2003.
- Roach, P. E.: The Generation of Nearly Isotropic Turbulence by Means of Grids. *Int. J. Heat Fluid Fl.*, 8, 82–92, [https://doi.org/10.1016/0142-727x\(87\)90001-4](https://doi.org/10.1016/0142-727x(87)90001-4), 1987.
- Sander, S. P., Finlayson-Pitts, B. J., Friedl, R. R., Golden, D. M., Huie, R. E., Kolb, C. E., Kurylo, M. J., Molina, M. J., Moortgat, G. K., Orkin, V. L., and Ravishankara, A. R.: Chemical Kinetics and Photochemical Data for Use in Atmospheric Studies, JPL Publication 02-25, 2003.
- Schlosser, E., Bohn, B., Brauers, T., Dorn, H. P., Fuchs, H., Haseler, R., Hofzumahaus, A., Holland, F., Rohrer, F., Rupp, L. O., Siese, M., Tillmann, R., and Wahner, A.: Intercomparison of two hydroxyl radical measurement techniques at the atmosphere simulation chamber SAPHIR. *J. Atmos. Chem.*, 56, 187–205, <https://doi.org/10.1007/s10874-006-9049-3>, 2007.
- Schlosser, E., Brauers, T., Dorn, H.-P., Fuchs, H., Haseler, R., Hofzumahaus, A., Holland, F., Wahner, A., Kanaya, Y., Kajii, Y., Miyamoto, K., Nishida, S., Watanabe, K., Yoshino, A., Kubistin, D., Martinez, M., Rudolf, M., Harder, H., Berresheim, H., Elste, T., Plass-Dülmer, C., Stange, G., and Schurath, U.: Technical Note: Formal blind intercomparison of OH measurements: results from the international campaign HO_xComp. *Atmos. Chem. Phys.*, 9, 7923–7948, <https://doi.org/10.5194/acp-9-7923-2009>, 2009.
- Sjostedt, S. J., Huey, L. G., Tanner, D. J., Peischl, J., Chen, G., Dibb, J. E., Lefer, B., Hutterli, M. A., Beyersdorf, A. J., Blake, N. J., Blake, D. R., Sueper, D., Ryerson, T., Burkhart, J., and Stohl, A.: Observations of hydroxyl and the sum of peroxy radicals at Summit, Greenland during summer 2003. *Atmos. Environ.*, 41, 5122–5137, <https://doi.org/10.1016/j.atmosenv.2006.06.065>, 2007.
- Smith, S. C., Lee, J. D., Bloss, W. J., Johnson, G. P., Ingham, T., and Heard, D. E.: Concentrations of OH and HO₂ radicals during NAMBLEX: measurements and steady state analysis. *Atmos. Chem. Phys.*, 6, 1435–1453, <https://doi.org/10.5194/acp-6-1435-2006>, 2006.
- Stevens, P. S., Mather, J. H., and Brune, W. H.: Measurement of Tropospheric OH and HO₂ by Laser-Induced Fluorescence at Low-Pressure. *J. Geophys. Res.*, 99, 3543–3557, <https://doi.org/10.1029/93JD03342>, 1994.
- Stone, D., Evans, M. J., Commane, R., Ingham, T., Floquet, C. F. A., McQuaid, J. B., Brookes, D. M., Monks, P. S., Purvis, R., Hamilton, J. F., Hopkins, J., Lee, J., Lewis, A. C., Stewart, D., Murphy, J. G., Mills, G., Oram, D., Reeves, C. E., and Heard, D. E.: HO_x observations over West Africa during AMMA: impact of isoprene and NO_x. *Atmos. Chem. Phys.*, 10, 9415–9429, <https://doi.org/10.5194/acp-10-9415-2010>, 2010.
- Tang, M. J., Cox, R. A., and Kalberer, M.: Compilation and evaluation of gas phase diffusion coefficients of reactive trace gases in the atmosphere: volume 1. Inorganic compounds. *Atmos. Chem. Phys.*, 14, 9233–9247, <https://doi.org/10.5194/acp-14-9233-2014>, 2014.
- Tanner, D. J. and Eisele, F. L.: Present OH Measurement Limits and Associated Uncertainties. *J. Geophys. Res.*, 100, 2883–2892, <https://doi.org/10.1029/94JD02609>, 1995.
- Verreycken, T. and Bruggeman, P. J.: OH density measurements in nanosecond pulsed discharges at atmospheric pressure N₂–H₂O mixtures. *Plasma Sources Sci. T.*, 23, 015009, <https://doi.org/10.1088/0963-0252/23/1/015009>, 2014.
- Winiberg, F. A. F., Smith, S. C., Bejan, I., Brumby, C. A., Ingham, T., Malkin, T. L., Orr, S. C., Heard, D. E., and Seakins, P. W.: Pressure-dependent calibration of the OH and HO₂ channels of a FAGE HO_x instrument using the Highly Instrumented Reactor for Atmospheric Chemistry (HIRAC). *Atmos. Meas. Tech.*, 8, 523–540, <https://doi.org/10.5194/amt-8-523-2015>, 2015.
- Zhang, D. H., Collins, M. A., and Lee, S. Y.: First-principles theory for the H + H₂O, D₂O reactions. *Science*, 290, 961–963, <https://doi.org/10.1126/science.290.5493.961>, 2000.

A. Datasheets and Primary Standard Calibrations

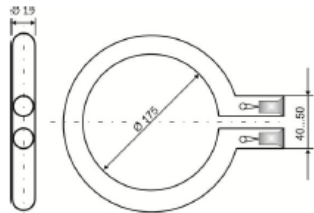
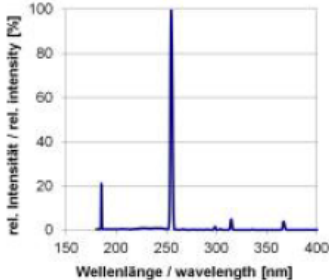
Stand: 26.02.14	Technisches Datenblatt	
UVN 50 N Ringstrahler di=175mm mit 200 mm Litze maximaler Lampenstrom IL=800 mA, PN Quarz		
Artikel-Nummer:		151 02501 0000
1. Geometrische Daten Gesamtlänge GL: ohne Kontaktstifte Leuchtlänge BL: Material Lampenrohr: QGR PS 19,0±0,4 x 1,4±0,2 x ... Sockelmaße: 2x x kundenspez. Markierung: nein		
		
2. Elektrische Daten - Lampenstrom: 0,8 A - Lampenspannung: 62 ± 3 V - Lampenleistung: 50 W Vorschaltgerät des Kunden - Typ: EVG UVT 40WHO ACHTUNG: Rücksprache notwendig, falls ein anderes VG verwendet wird!		
3. Betriebsweise - Brennlage: beliebig - Lampenrohrtemperatur: min. 40°C, optimal 40-50°C, max. 60°C		
4. Strahlenphysikalische Daten Messabstand: Bestrahlungsstärke: mW/cm ² bei 254 nm UVC Leistung: 15 W UVC 100 Stunden-Wert, gemessen frei brennend unter Laborbedingungen. Unter realen Bedingungen können die Werte teilweise extrem abweichen. garantierte Lebensdauer: 6000 h Nutzlebensdauer: 6000 h Leistungsabfall nach Nutzlebensd.: 35 % Betriebsweise: Dauerbetrieb max. 1 Schaltung pro Tag		
		
<p>Die Nutzlebensdauer ist abhängig von Anlagenauslegung und Betriebsweise (EIN-AUS-Schaltzyklen, Kühlung, Verschmutzung). Die tatsächliche Strahlerleistung ist vom gewählten Vorschaltgerät abhängig. Durch Änderung des Strahlerstromes kann nach Rücksprache mit uns eine andere als die oben angegebene Leistung eingestellt werden.</p> <p>Eine funktionsgerechte Anwendung dieses Strahlers ist nur in speziellen, dafür geeigneten Anlagen gewährleistet.</p> <p>Der sachgemäße Einsatz kann deshalb nur durch den jeweiligen Gerätehersteller erfolgen. Kundenspezifische Sonderausführungen auf Anfrage.</p>		
<div style="display: flex; align-items: center;">  <p>ACHTUNG: Die von diesem Strahler ausgehende Strahlung ist schädlich für Haut und Augen. Deshalb dürfen sie nur in dafür vorgesehen Anlagen betrieben werden, die für einen ausreichenden Strahlenschutz sorgen. Arbeitsschutzvorschriften sind zu beachten!</p> </div>		

Figure A.1.: The specifications of the UV ring lamp used in APACHE, developed by uv-technik Speziallampen GmbH, Gewerbegbiet Ost 6, 98704, Wolfsberg, Germany.



NATIONAL PHYSICAL LABORATORY

Teddington Middlesex UK TW11 0LW Telephone +44 20 8977 3222

Certificate of Calibration



4002

NPL PRIMARY REFERENCE MATERIAL

Cylinder Number: 2336

This certificate is issued in accordance with the laboratory accreditation requirements of the United Kingdom Accreditation Service. It provides traceability of measurement to the SI system of units and/or to units of measurement realised at the National Physical Laboratory or other recognised national metrology institutes. This certificate may not be reproduced other than in full, except with the prior written approval of the issuing laboratory.

CUSTOMER: Max-Planck-Institut für Chemie
ADDRESS: Atmospheric Chemistry, Hahn-Meitner-Weg 1,
55128 Mainz, Germany
CALIBRATION DATE: 27 September 2017

AMOUNT FRACTION:

Component	Amount fraction / ($\mu\text{mol/mol}$)
Nitrogen monoxide	5.004 ± 0.025
Nitrogen	Balance

The reported expanded uncertainty is based on a standard uncertainty multiplied by a coverage factor $k = 2$, providing a coverage probability of approximately 95 %. The uncertainty evaluation has been carried out in accordance with UKAS requirements.

METHODS: Preparation: gravimetry; Analysis: non-dispersive ultraviolet
TRACEABILITY: The values on this certificate are traceable to NPL Primary Standards
EXPIRY: Certificate valid for 1 year from the date of issue
PRESSURE: Fill pressure: 100 bar; Minimum utilisation pressure: 5 bar
STORAGE: No special precautions are required
HANDLING: Refer to ISO 16664
OUTLET: BS341 No. 14 valve
INTENDED USE: Calibration standard

Reference: 2017060311 **Date of issue:** 28 September 2017

Signed:  (Authorised Signatory)

Name: Dr P J Brewer (on behalf of NPLML)

Checked by: 

Page 1 of 1



This certificate is consistent with the capabilities that are included in Appendix C of the MRA drawn up by the CIPM. Under the MRA, all participating institutes recognise the validity of each other's calibration and measurement certificates for the quantities, ranges and measurement uncertainties specified in Appendix C (for details see <http://www.bipm.org>).

NPLC05-08/13

Figure A.2.: National Physical Laboratory – NO standard used for actinic flux density calibration of mercury lamp that was used for calibration of HORUS instrument in Experiment A.

Ø273 µm Core TECS-Coated Multimode Optical Fiber

Item #	Wavelength Range	Hydroxyl Content	Core Diameter	Cladding Diameter	Coating Diameter	Buffer Diameter	Core/Cladding	Coating ^a	Buffer	Proof Test
FG273UEC	250 - 1200 nm ^b	High OH	273 ± 10 µm	300 ± 6 µm	330 ± 10 µm	400 ± 30 µm	Pure Silica / Fluorine-Doped Silica	TECS Hard Fluoropolymer	Tefzel	≥100 kpsi
FG273LEC	400 - 2200 nm	Low OH								

Item #	NA	Max Power Capability		Max Attenuation @ 808 nm	Max Core-Cladding Offset	Max Core-TECS Offset	Bend Radius		Operating Temperature	Strip Tool	Core Index	Cladding Index
		Pulsed ^c	CW ^d				Short Term	Long Term				
FG273UEC	0.22 ± 0.02	1.87 MW	0.37 kW	10 dB/km	4 µm	7 µm	16 mm	32 mm	-60 to 125 °C	T14S18 ^e	See Table in Overview Tab	Proprietary ^f
FG273LEC												

- a. This coating acts as a second cladding with an NA of 0.39, which is calculated from the index difference between the TECS coating to the core, rather than between the silica cladding and the TECS coating/second cladding.
- b. Solarization may occur at wavelengths below 300 nm. We also offer [solarization-resistant multimode fiber](#).
- c. Based on 5 GW/cm² for 1064 nm Nd:YAG laser with 10 ns pulse length and input spot size equal to 80% of the core diameter.
- d. Based on 1 MW/cm² for 1064 nm Nd:YAG laser and input spot size equal to 80% of the core diameter.
- e. This tool will strip off the buffer for termination to the coating.
- f. We regret that we cannot provide this proprietary information.

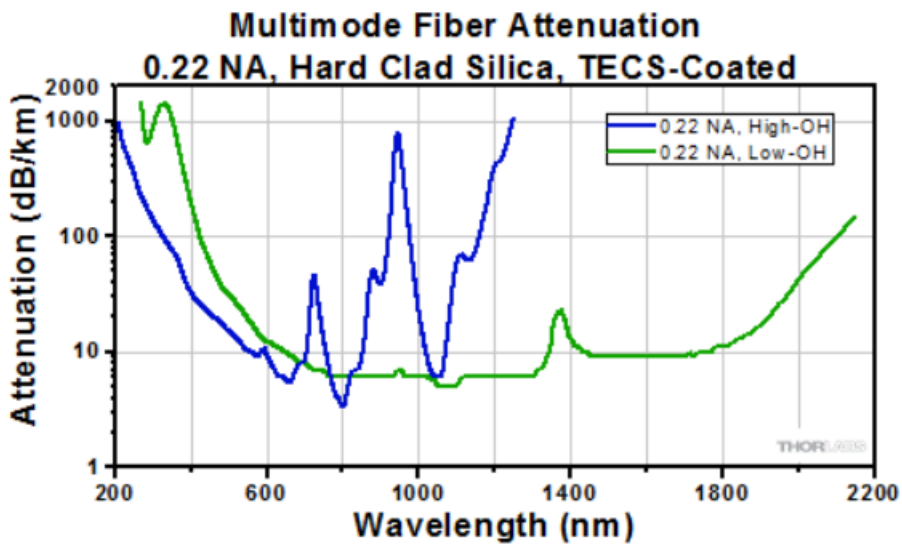


Figure A.3.: Specifications of coated silica fiber used for transmittance of 308 nm light through the HORUS instrument. (Information taken from specification listings, Thorlabs GmbH, Europe, Germany, www.thorlabs.de)

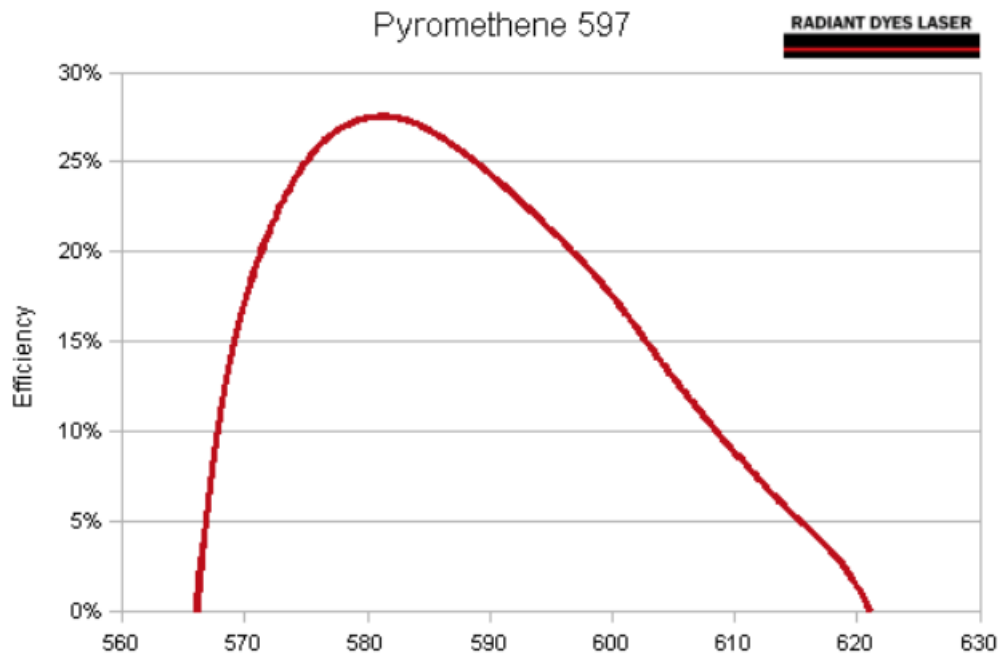


Figure A.4.: Laser Dye, Pyromethane-597 used in tunable dye laser powered by a diode-pumped Nd:YAG laser emitting 532 nm light. Dye sourced from Radiant Dyes Laser & Accessoires GmbH, Friedrichstr. 58, 42929, Wermelskirchen, Germany. (Information taken from www.radiant-dyes.com)

Hessisches Landesamt für Naturschutz, Umwelt und Geologie

HESSEN



Prüfbericht der Kalibrierung

PB-Nr: **24B04_S/N0711521534_20190219**

Auftraggeber: **Max Planck-Institut für Chemie
Hahn-Meitner-Weg 1
55128 Mainz**

Auftragsnummer **n.n.**
Prüfgegenstand **O₃-Generator**
Zustand **gebraucht**
Hersteller **Thermo Fisher Scientific Inc.**
Modell **49i.PS**
Serien-Nr. **711521534**
Messbereich **0-1 ppm O₃**
Ausgangssignal **seriell**
Eingangsdatum **11.02.2019**
Prüfdatum **14.02.2019**
Ausgangsdatum **19.02.2019**

Die Überprüfung erfolgte mit selbsthergestellten Prüfgasen nach den Vorgaben des ISO-Guide 34.

Rückführung **UBA
zuletzt am 24.05.2018**
Messunsicherheit **2%**

Die Prüfergebnisse beziehen sich nur auf den zur Prüfung vorgelegten Gegenstand.
Die Ergebnisse des Berichts gelten für den Gegenstand wie vom Kunden erhalten.

Für die Einhaltung einer angemessenen Frist zur Wiederholung der Überprüfung ist der Benutzer verantwortlich.

Dieser Prüfbericht darf ohne die schriftliche Zustimmung des Unterzeichners nicht auszugsweise vervielfältigt werden.

Datum

27. FEB. 2019

Prof. Dr. Stefan Jacobi
Technische Leitung

Jens Kettenbach
Bearbeiter



Rheingaustraße 186, 65203 Wiesbaden
Tel. 0611-6939-0, Fax 0611-6939-236

Seite 1 von 4

Figure A.5.: Certificate of the Fluke Ozone generator uncertainty compared to the Deutsche Akkreditierungsstelle primary standard at Hessisches Landesamt für Naturschutz, Umwelt und Geologie, Rheingaustraße 186, 65203, Wiesbaden.

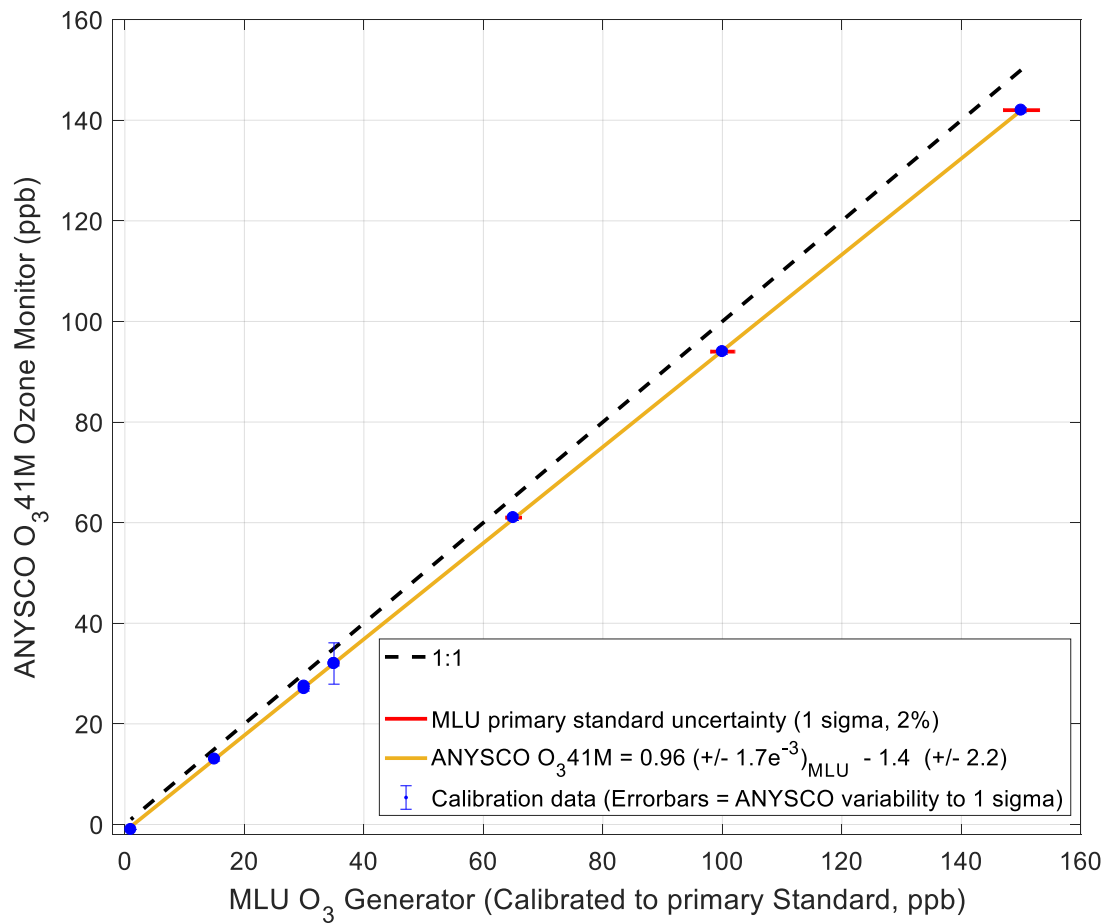


Figure A.6.: The calibration of the ANYSCO Ozone monitor against the MLU ozone generator which was calibrated to primary standard.



NTC THERMISTORS: TYPE EC95

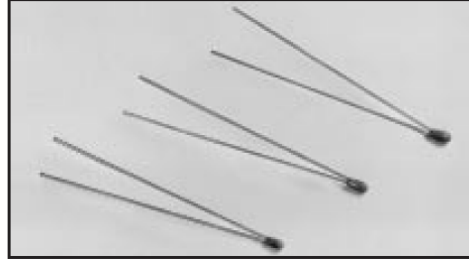
INTERCHANGEABLE CHIP THERMISTOR

DESCRIPTION:

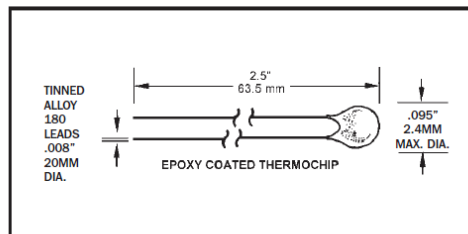
Epoxy Coated interchangeable chip thermistors with bare tinned 180 alloy lead-wires.

FEATURES:

- Precision, solid state temperature sensor
- Interchangeability down to $\pm 0.1^\circ\text{C}$
- Suitable for use over range of -80°C to $+150^\circ\text{C}$
- High sensitivity greater than $-4\%/^\circ\text{C}$ at 25°C
- Suitable for temperature measurement, control and compensation
- High reliability and stability over interchangeable range
- Most popular R-vs-T curves are available
- Resin coated for good mechanical strength and resistance to solvents
- .008" (.2 mm) dia. bare tinned 180 alloy lead-wires



DIMENSIONS:



Select appropriate part number below for resistance and temperature tolerance desired

R _{25°C}	MATERIAL SYSTEM	$\pm .2^\circ\text{C}$ -20°C to +50°C	$\pm .1^\circ\text{C}$ 0°C to 70°C	$\pm .2^\circ\text{C}$ 0°C to 70°C
100	Q	EC95Q101U		
300	Q	EC95Q301U		
1000	R	EC95R102U		EC95R102W
1000	S	EC95S102U		EC95S102W
2252	F	EC95F232U	EC95F232V	EC95F232W
3000	F	EC95F302U	EC95F302V	EC95F302W
5000	F	EC95F502U	EC95F502V	EC95F502W
10000	F	EC95F103U	EC95F103V	EC95F103W
10000	Y	EC95Y103U	EC95Y103V	EC95Y103W
30000	H	EC95H303U	EC95H303V	EC95H303W
50000	G	EC95G503U	EC95G503V	EC95G503W
100000	G		EC95G104V	EC95G104W

RS 151-215 = EC95F302W
RS 151-221 = EC95F502W
RS 151-237 = EC95F103W
RS 151-243 = EC95G104W

OPTIONS:

Consult factory for availability of options:

- Other resistance values in the range of 100Ω - 100kΩ
- Other tolerances or ranges
- Alternative lead-wires or lengths
- Non standard R-vs-T curves
- Controlled dimensions

DATA:

THERMAL AND ELECTRICAL PROPERTIES:

Dissipation constant:.....(still air) 1 mW/°C
(stirred oil) 8 mW/°C

Thermal time constant:.....(still air) 10 sec.
(stirred oil) 1 sec.

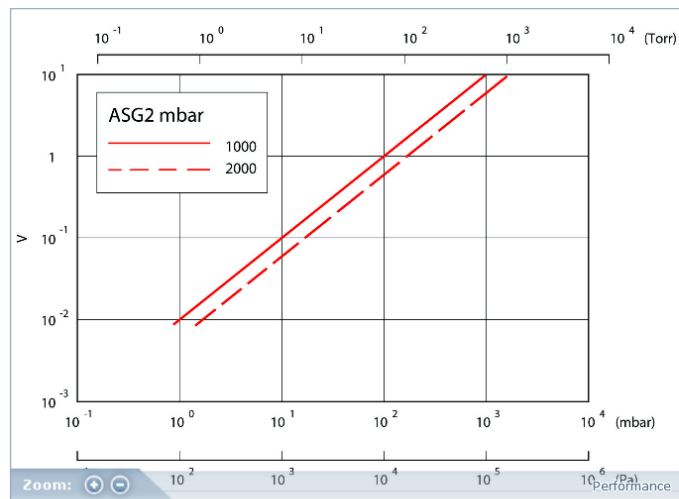
Maximum power at 25°C75mW
(derated from 100% at 25°C to 0% at 100°C)

Figure A.7.: Datasheet for the NTC-EC95302V thermistor used for temperature monitoring in APACHE.

Technical Data

Full scale pressure range	ASG2-1000, 1000 to 1 mbar ASG2-2000, 2000 to 1 mbar
Accuracy	±0.2% full scale
Stability	±0.1% full scale
Temperature coefficient	±0.03% full scale per oC
Power supply	12 to 32 V d.c.
Maximum power	0.1 W
Output signal	0 to 10 V d.c. linear
Output impedance	51 (Ohms)
Minimum load	>10 (Ohms)
Adjustments	Set full scale and set zero
Temperature range	
Compensated	-10 to +50 oC
Operating / Storage	-40 to +80 oC
Materials exposed to vacuum	Stainless steel 316L, Hastelloy C276
Internal volume	NW16 2.78 cm ³ 1/8" NTP 2.74 cm ³
Weight	NW16 150 g 1/8" NTP 130 g
Electrical connector	4 pin Din 43650 Form A
Vacuum fitting	NW16 or 1/8" NTP
Enclosure rating	IP65

Performance



Dimensions

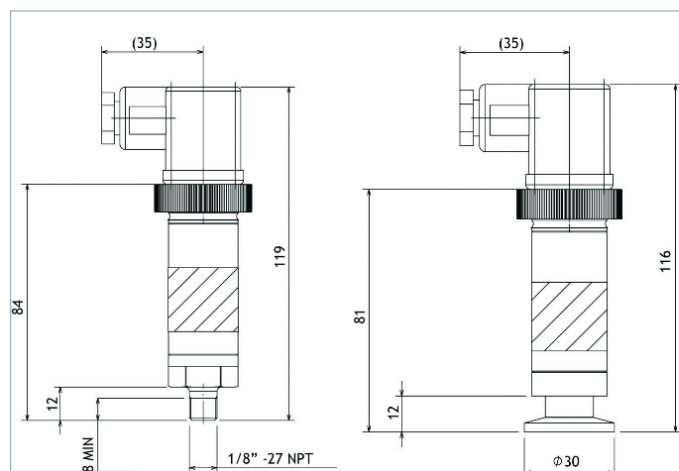


Figure A.8.: Datasheet for the Edwards ASG2-1000 pressure sensor used for pressure monitoring in APACHE.

Technical specifications

IN-FLOW 'HIGH-FLOW' F-106AI

Industrial Style Mass Flow Meter for High Gas Flow

- High accuracy, excellent repeatability
- Virtually pressure and temperature independent
- Compact design
- Rugged, weatherproof housing (IP65, dust and waterproof)
- "Wafer type" for mounting between flanges (DN40 / 1½")



Measurement / control system	
Flow range, based on N ₂ (intermediate ranges available)	min. 1...50 m ³ _n /h max. 10...500 m ³ _n /h
Accuracy (incl. linearity) (based on actual calibration)	±1% FS
Turndown	1:50
Multi fluid capability	storage of max. 8 calibration curves
Repeatability	< 0,2% Rd
Response time	typical: 0,5 seconds
Operating temperature	-10...+70°C; for ATEX cat. 3 and FM Class 1 Div 2: 0...50°C
Temperature sensitivity	zero: < 0,05% FS/°C; span: < 0,05% Rd/°C
Pressure sensitivity	0,1% Rd/bar typical N ₂ ; 0,01% Rd/bar typical H ₂
Leak integrity, outboard	tested < 2 x 10 ⁻⁹ mbar l/s He
Attitude sensitivity	max. error at 90° off horizontal 0,2% FS at 1 bar, typical N ₂
Warm-up time	30 min. for optimum accuracy 2 min for accuracy ± 2% FS

Mechanical parts	
Material (wetted parts)	stainless steel 316L or comparable
Pressure rating	up to 40 bar abs (PN10, 16, 40); for hazardous gases such as O ₂ , H ₂ , etc. do not exceed operating pressure of 10 bar; for higher pressure select a flanged type MFM, series F-107/F-117.
Process connections	Wafer type, for mounting between flanges according to DIN DN50 or ANSI 2"
Seals	standard: Viton [®] ; options: EPDM, Kalrez [®] (FFKM)
Weight	4,6 kg
Ingress protection (housing)	IP65

Electrical properties			
Power supply	+15...24 Vdc		
Max. power consumption	Supply	at voltage I/O	at current I/O
	15 V	95 mA	125 mA
	24 V	65 mA	85 mA
PROFIBUS DP	add 53 mA (15 V supply) or 30 mA (24 V supply)		
DeviceNet™	add 48 mA (24 V supply)		
Analog output/command	0...5 (10) Vdc or 0 (4)...20 mA (sourcing output)		
Digital communication	standard: RS232; options: PROFIBUS DP, PROFINET, DeviceNet™, Modbus RTU or ASCII, FLOW-BUS		

Electrical connection	
Analog/RS232	8 DIN (male);
PROFIBUS DP	bus: 5-pin M12 (female); power: 8 DIN (male);
PROFINET	bus: 2 x 5-pin M12 (female) (in/out); power: 8 DIN (male);
Devicenet™	5-pin M12 (male);
FLOW-BUS/Modbus-RTU/ASCII	5-pin M12 (male)

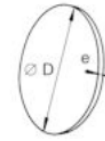
Figure A.9.: Datasheet for the Bronkhorst F-106AI-PAD-03-V mass flow controller to regulate the high flows through APACHE.

AMPOR® - BRONZE - P BC (Scheiben)

Aufbau der Materialbezeichnung

Die Materialbezeichnung ist wie folgt aufgebaut:
Typ . Dicke e (x 10) . Filterklasse.

Beispiel: die Materialbezeichnung einer Scheibe mit einem Durchmesser D von 114 mm und einer Dicke e von 2 mm der Filterklasse 10 lautet:
AMPOR-P BC 114.20.10.



Standardabmessungen (Überblick)

Typ BC	Durchmesser D (mm)	Filterfläche (cm ²)	Dicke e (mm)	Filterklasse
006	6	0,3	2-3	03-60
013	13	1,3		
021	21	3,5		
030	30	7,0		
042	42	14,0		
060	60	28,0		
090	90	63,5		
114	20	102,0		
250	250	450,0		
Filterklasse 03-30: Toleranz js 15, Filterklasse 40 und 60: k 15				

Temperatur	max. zulässige Temperatur (°C)	Anmerkungen
bei Zinnlötung	100	Mit Zinn verbundene Teile dürfen auf keinen Fall über 100°C zum Einsatz kommen.
bei Hartlötung	150	-
an der Luft	150	-
im Reduktionsmedium	abhängig vom Medium	In CO ₂ z.B. bis zu 400°C. Es ist aber die Abschwächung der mechanischen Eigenschaften des Werkstoffs unter dem Temperatureinfluss zu berücksichtigen.
Koeffizient der linearen Ausdehnung (1/°C): 18,4 x 10 ⁻⁶		

© by **amtag**



amtag
Alfred Merkelbach Technologies AG

33

Lise-Meitner-Str. 2 • 40670 Meerbusch
Telefon: (02159) 69 599-0
Telefax: (02159) 69 599-33
www.amtag.de • info@amtag.de

Figure A.10.: Datasheet for the Bronze alloy AMPOR sinter filter from atmag. Company address found on the data sheet.

B. Residual Undescribed values of HORUS calibrations with APACHE

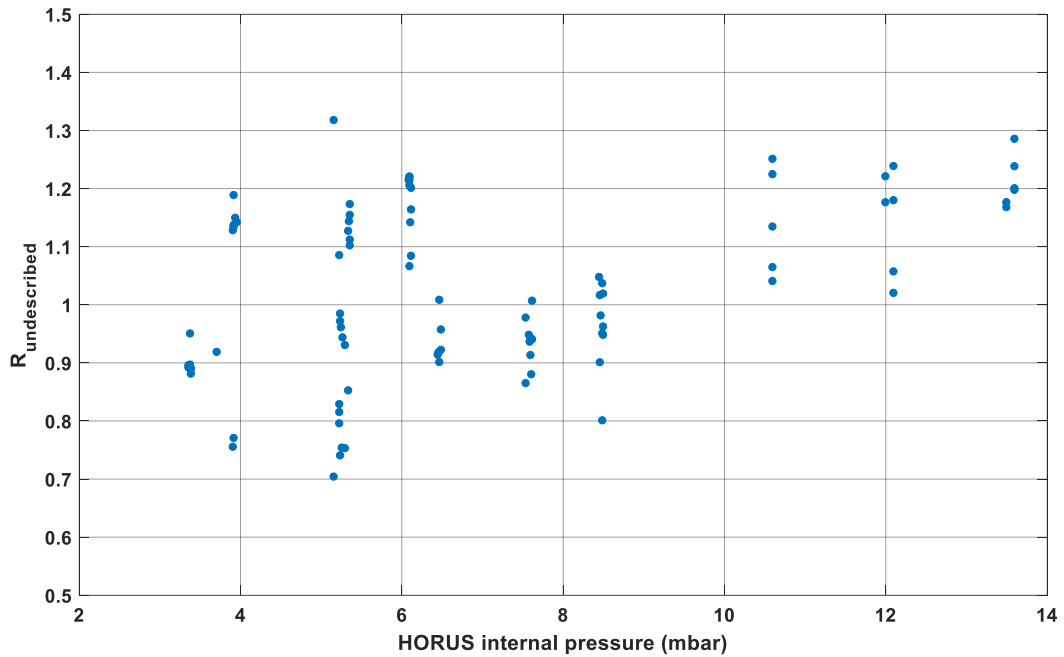


Figure B.1.: $R_{\text{undescribed}}$ fraction plotted against HORUS internal pressure. Taken from calibration of the HORUS instrument setup (OMO-ASIA 2015 campaign) with APACHE.

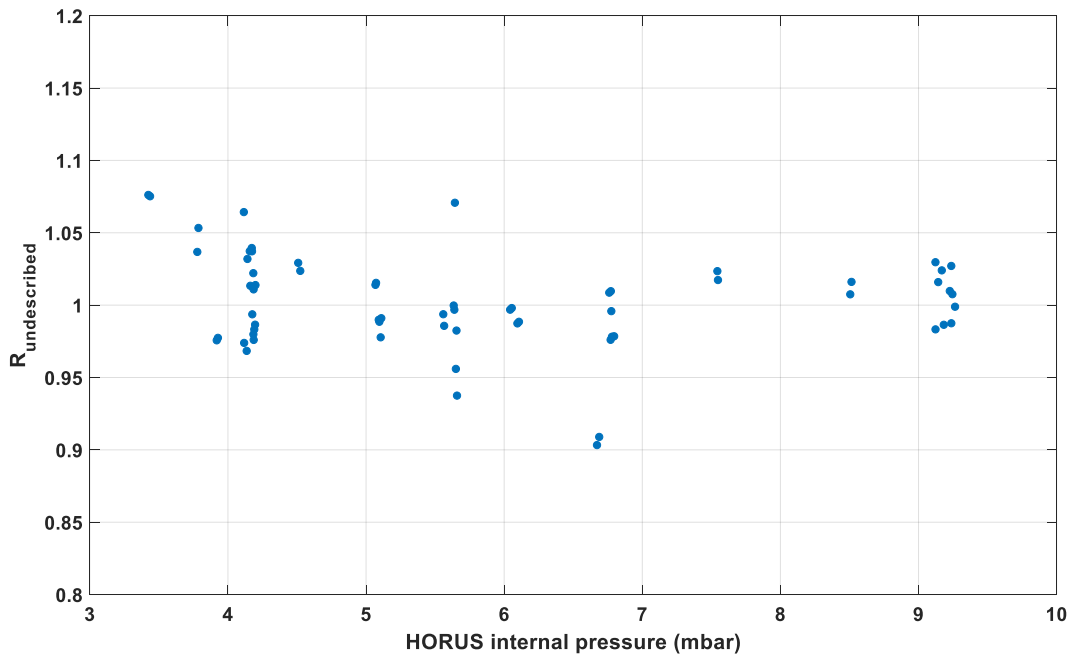


Figure B.2.: $R_{\text{undescribed}}$ fraction plotted against HORUS internal pressure. Taken from calibration of the HORUS instrument setup (CAFÉ-AFRICA 2018 campaign) with APACHE.

C. Trace gas species and meteorological measurements during OMO-ASIA 2015

Note for Appendix C: Grey shaded areas signify AMA influenced air masses.

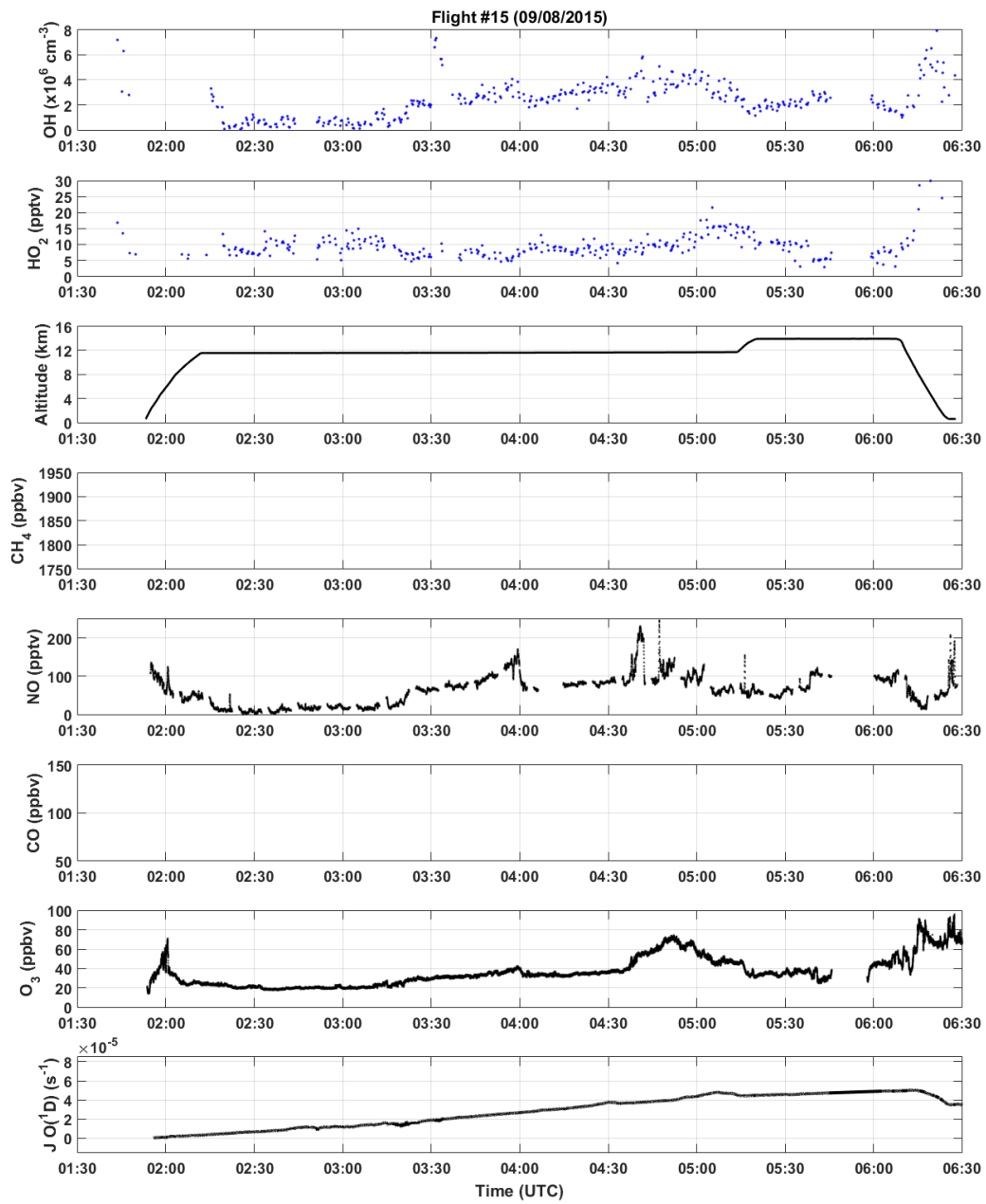


Figure C.1.: Measurement Data flight 15.

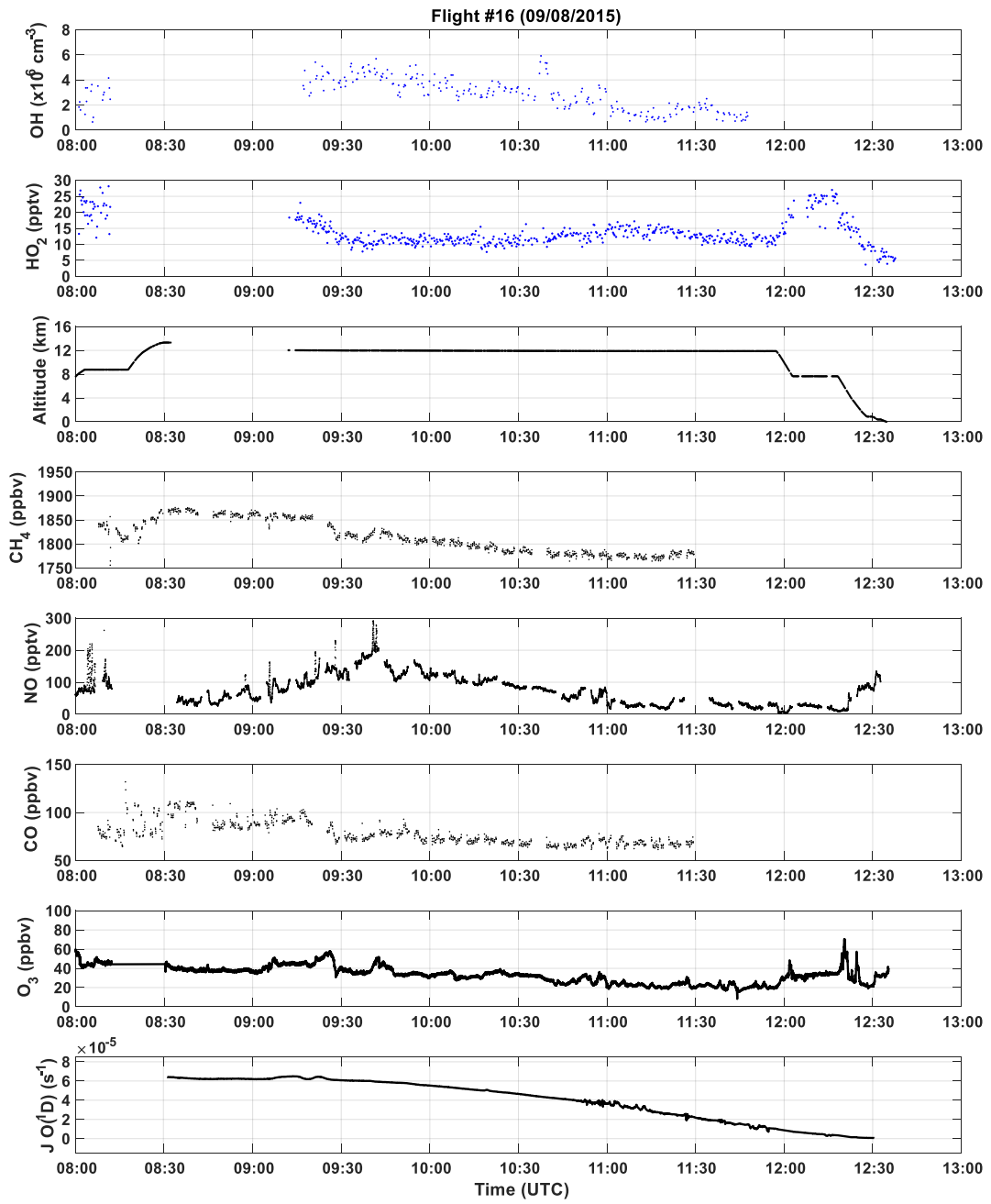


Figure C.2.: Measurement Data flight 16.

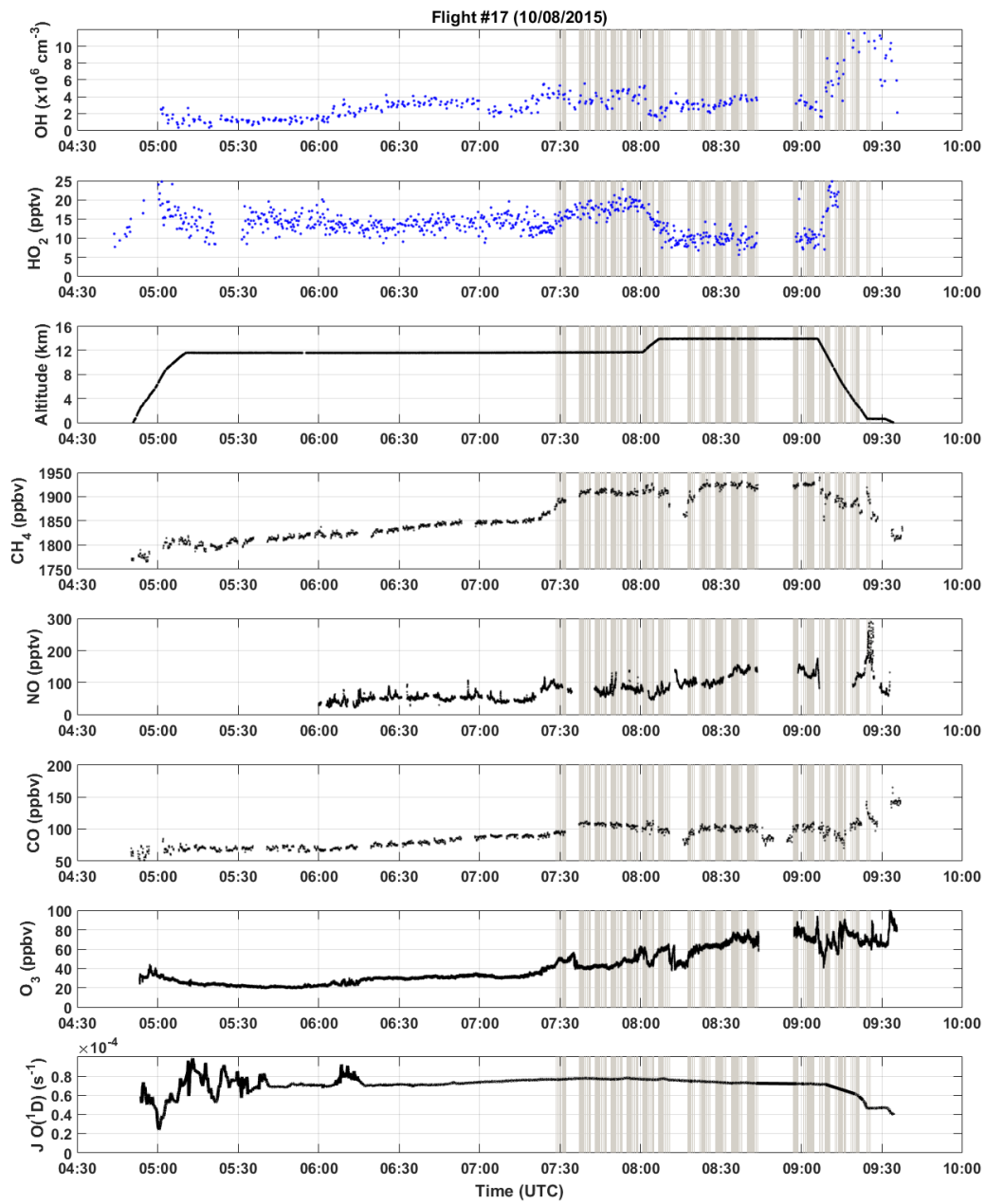


Figure C.3.: Measurement Data flight 17.

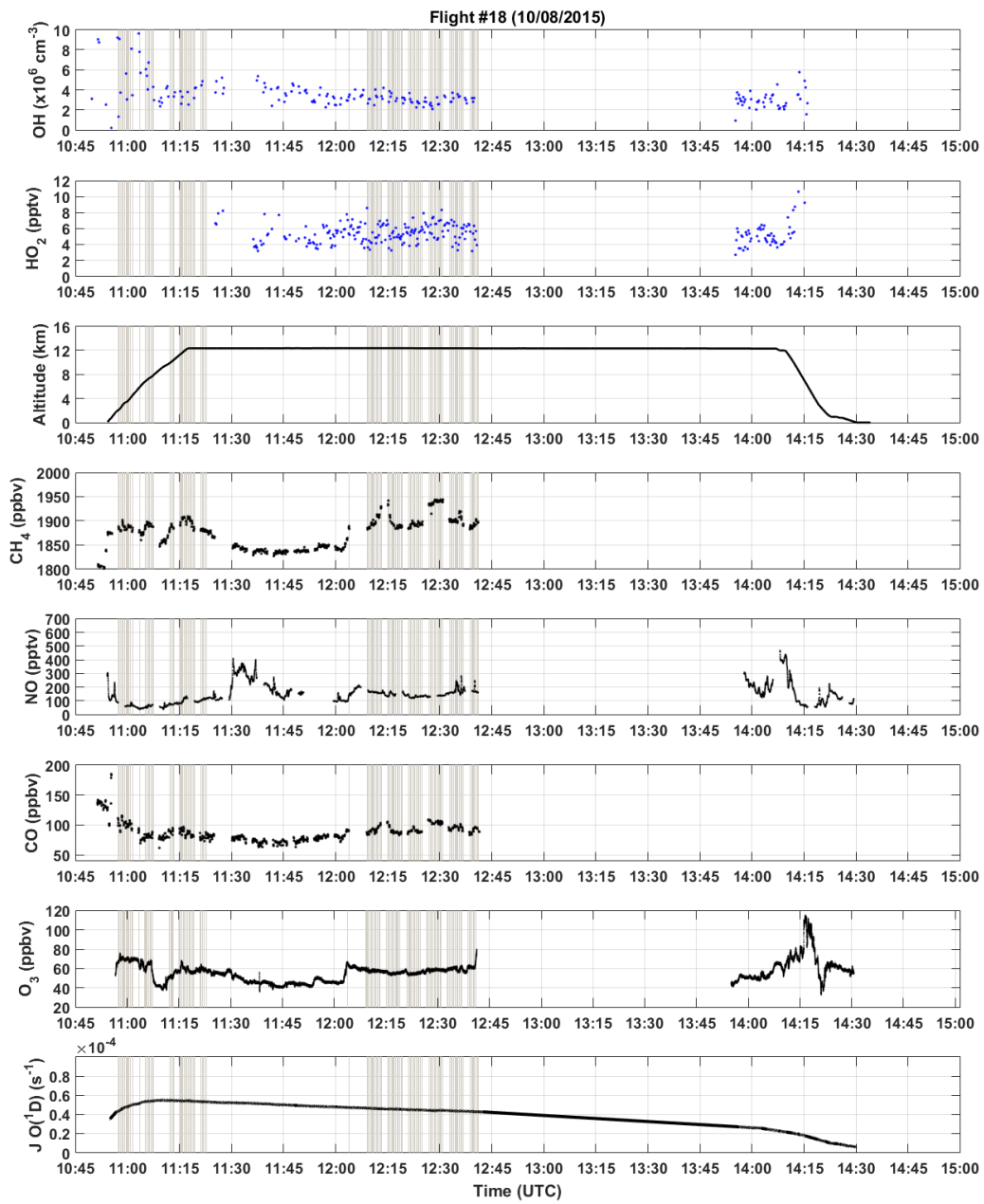


Figure C.4.: Measurement Data flight 18.

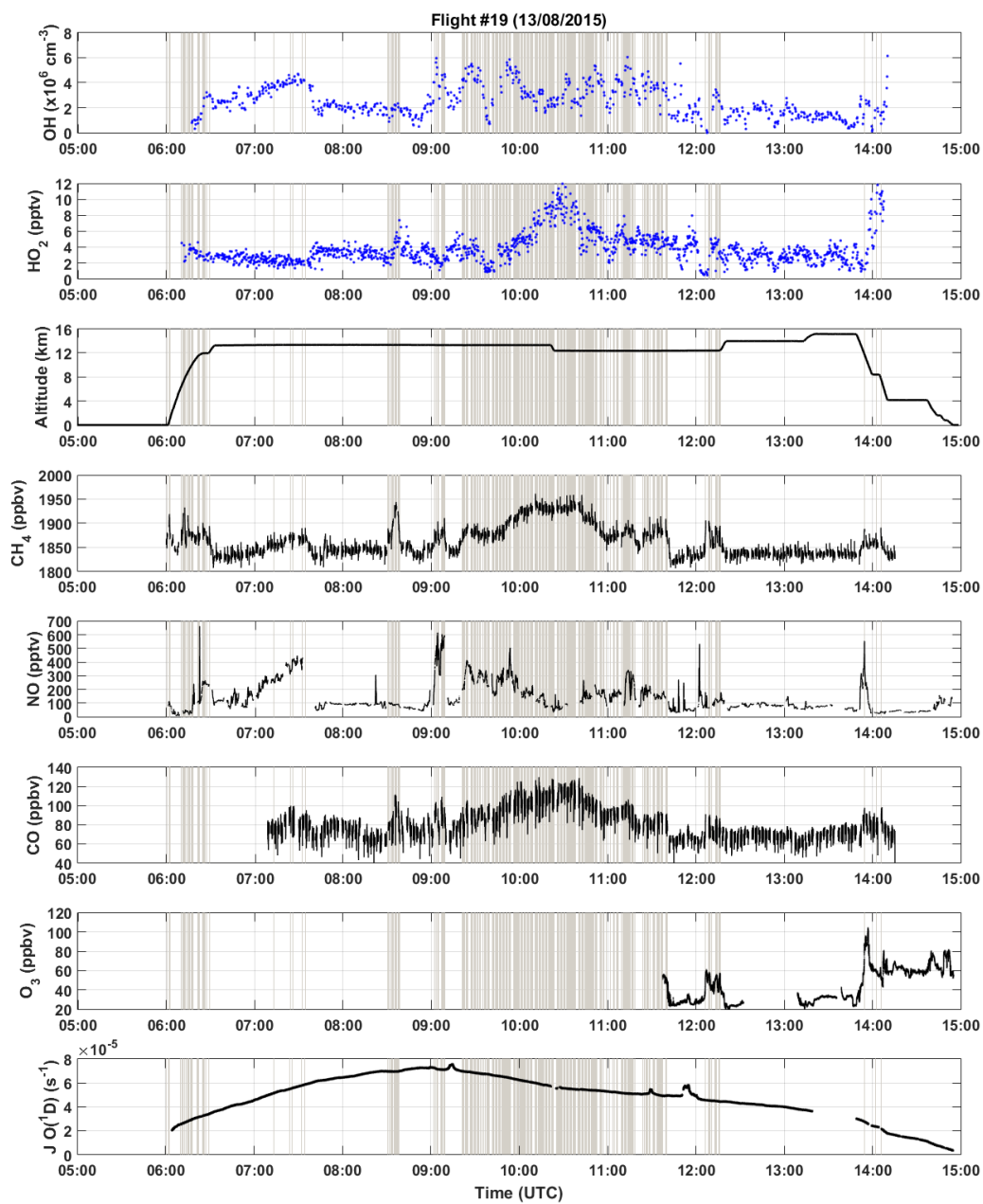


Figure C.5: Measurement Data flight 19.

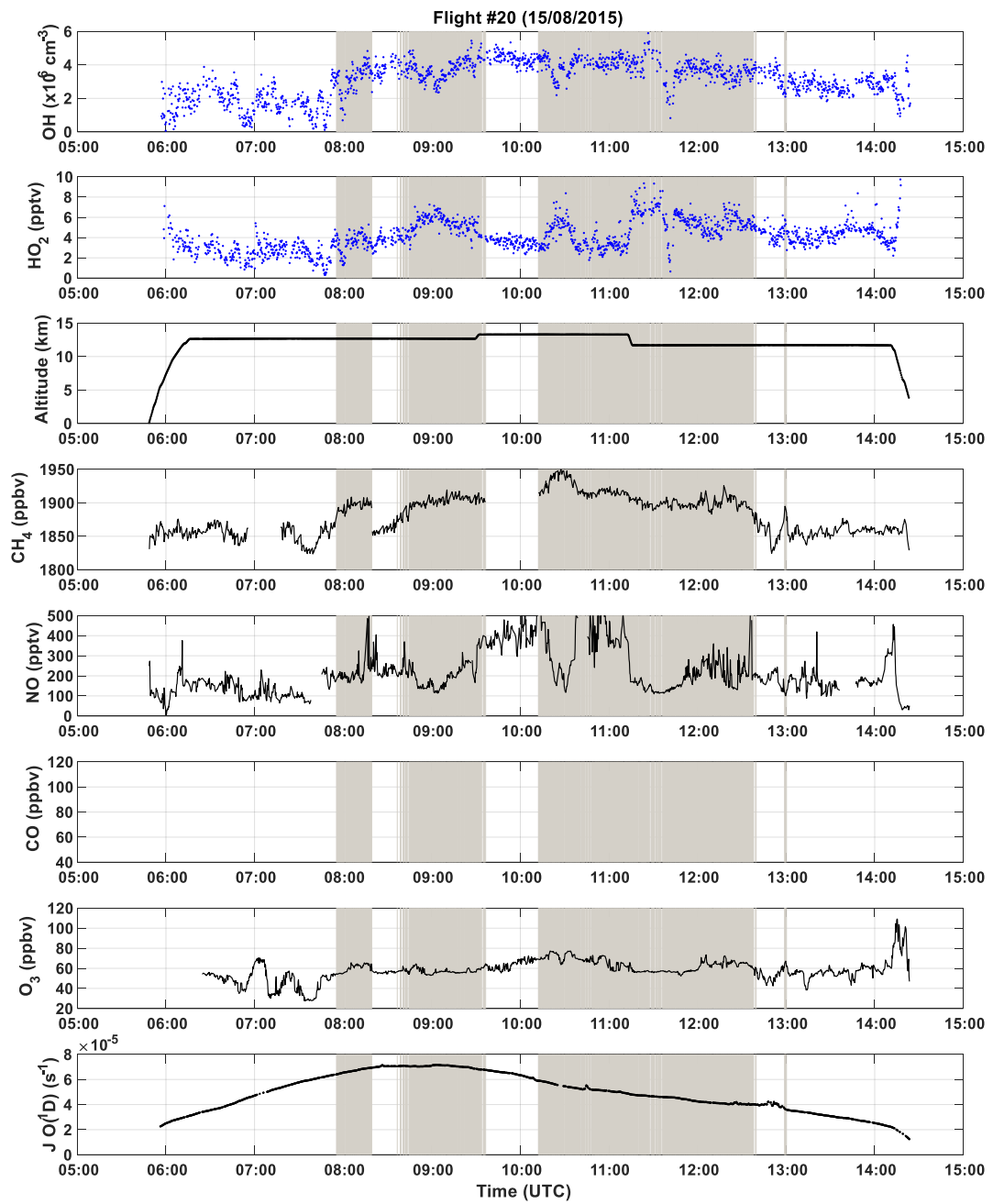


Figure C.6.: Measurement Data flight 20.

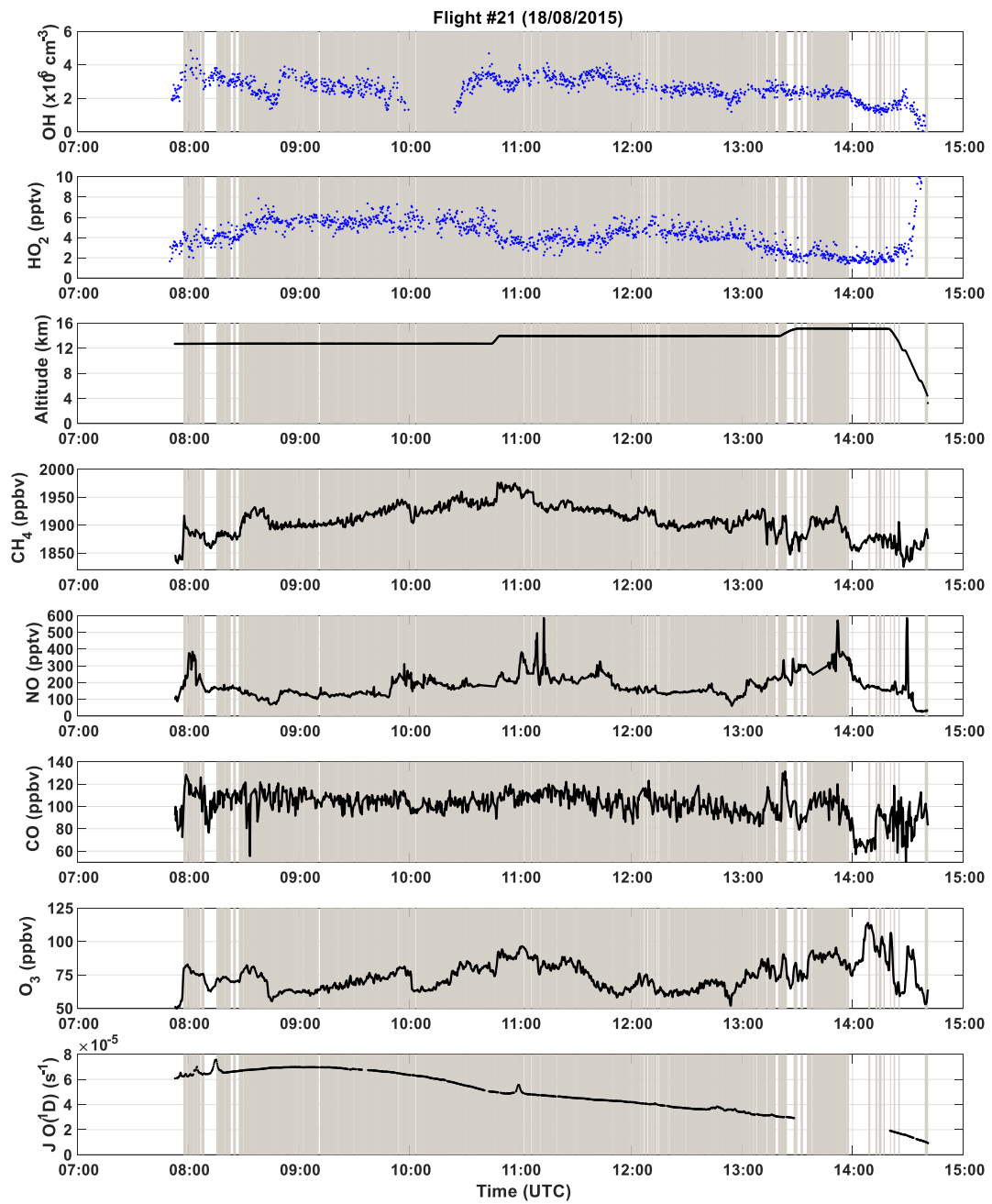


Figure C.7.: Measurement Data flight 21.

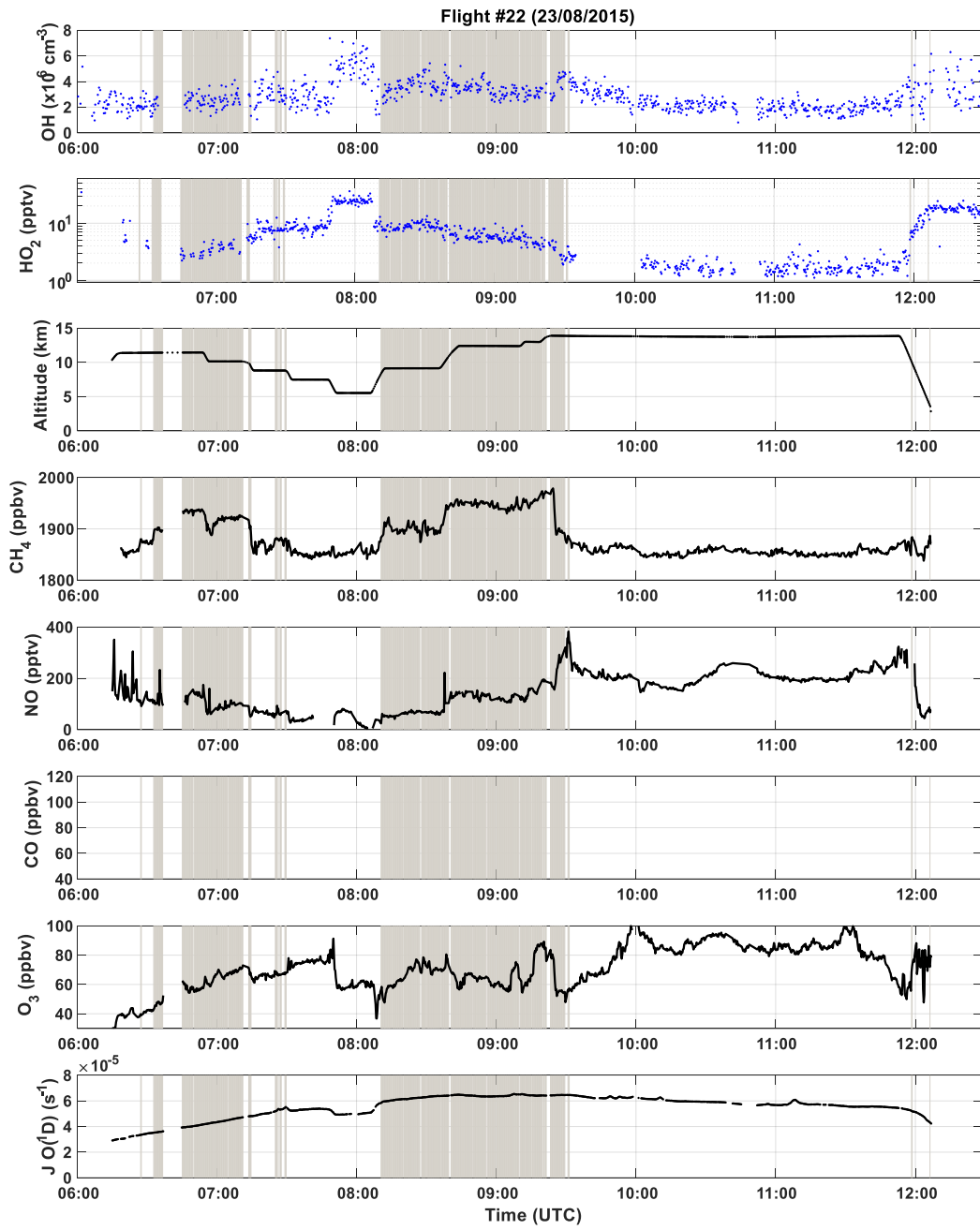


Figure C.8.: Measurement Data flight 22.

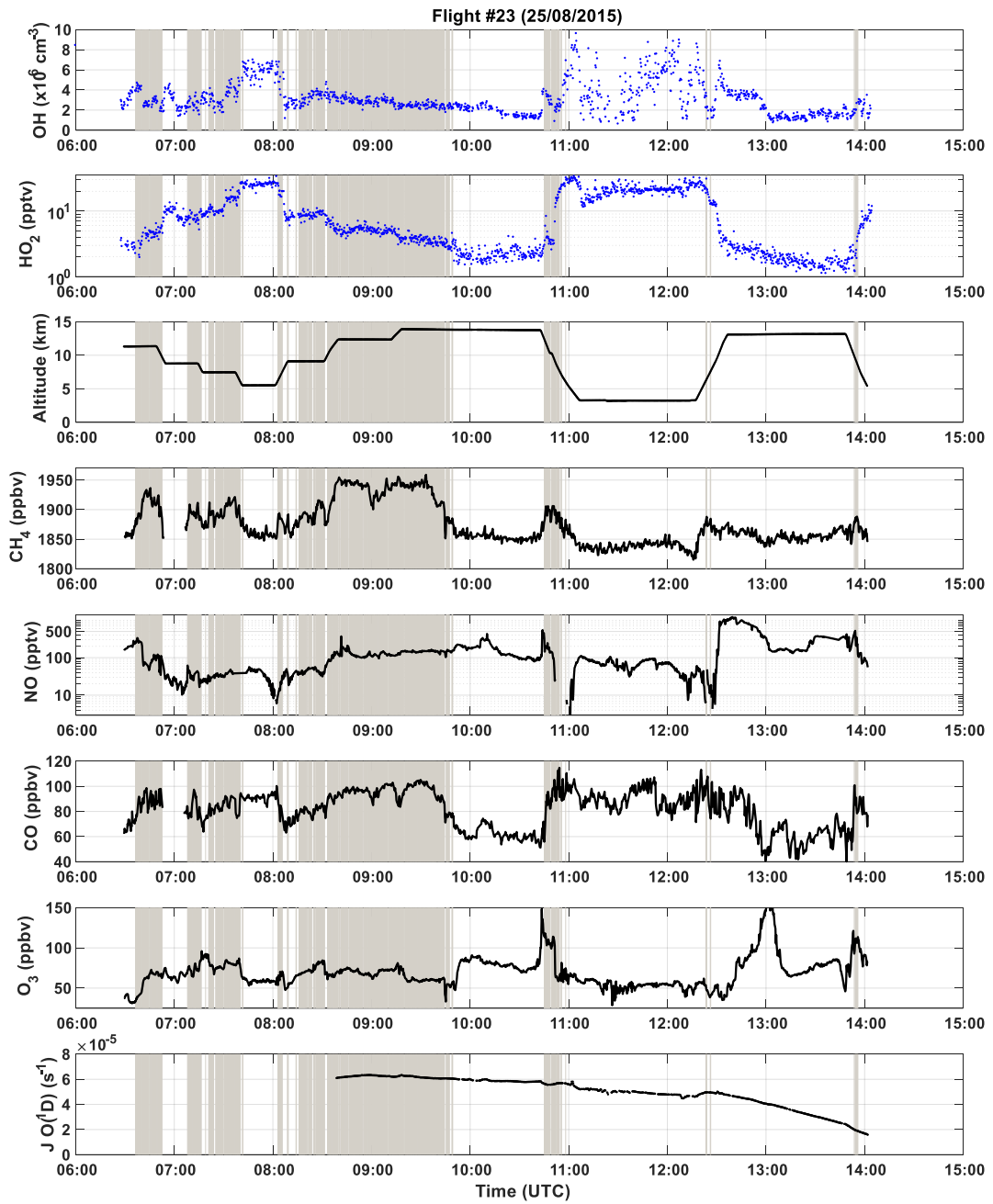


Figure C.9.: Measurement Data flight 23.

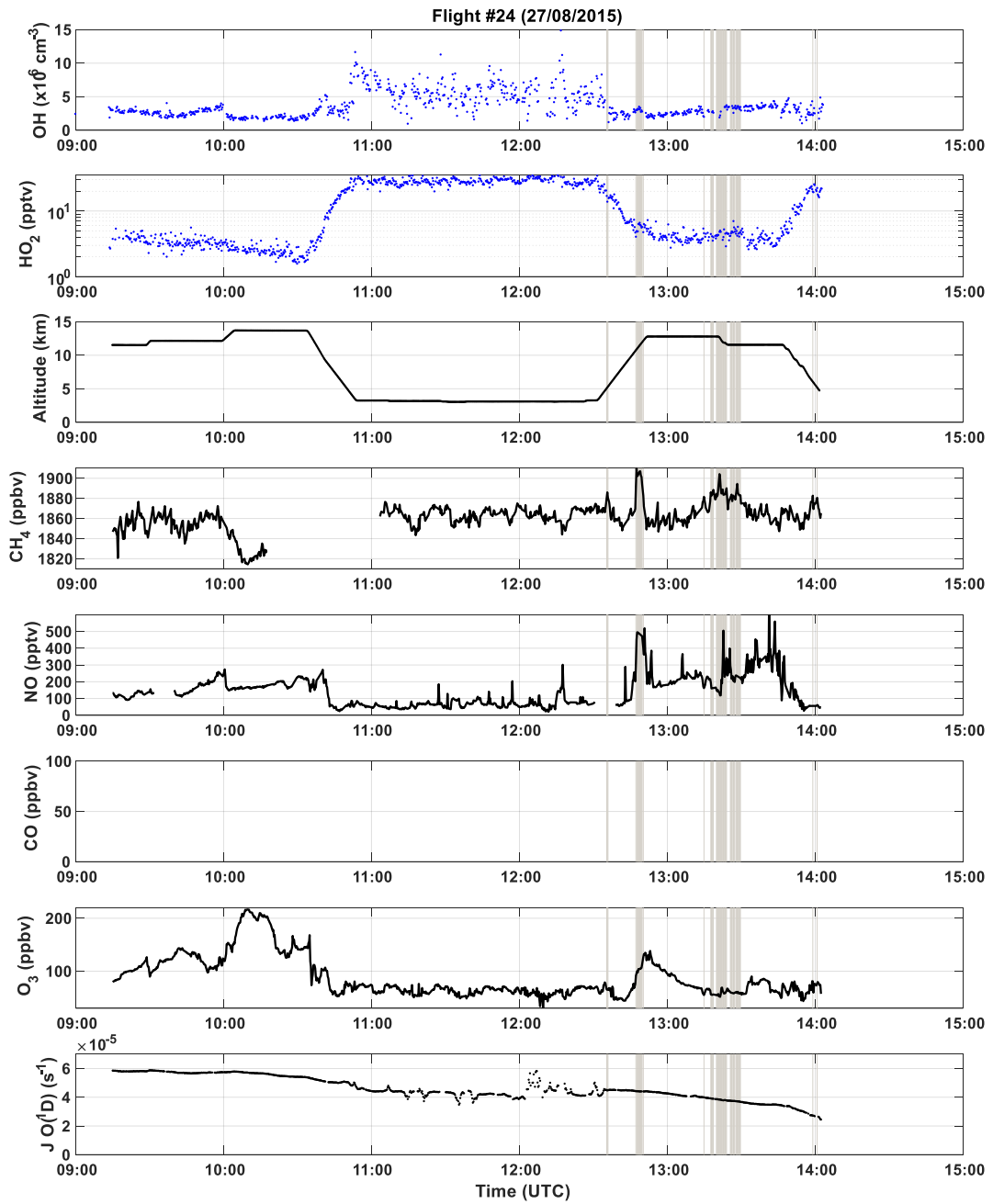


Figure C.10.: Measurement Data flight 24.

D. Chemical Mechanism (MOM) of CAABA-MECCA box model version 4.0

The Chemical Mechanism of MECCA

KPP version: 2.2.3_rs3
MECCA version: 4.0gmdd4
Date: April 8, 2020
Batch file: OM0.bat
Integrator: rosenbrock_posdef
Gas equation file: gas.eqn
Replacement file:
Selected reactions:
"Tr && G && !S && !Cl && !Br && !I && !Hg"
Number of aerosol phases: 0
Number of species in selected mechanism:
Gas phase: 2566
Aqueous phase: 0
All species: 2566
Number of reactions in selected mechanism:
Gas phase (Gmn): 1618
Aqueous phase (Annn): 0
Henry (Hnnn): 0
Photolysis (Jnnn): 324
Aqueous phase photolysis (PHnnn): 0
Heterogeneous (HETnnn): 0
Equilibria (EQnn): 0
Isotope exchange (IEXnnn): 0
Tagging equations (TAGnnn): 0
Dummy (Dnn): 0
All equations: 1942

Table 1: Gas phase reactions

#	labels	reaction	rate coefficient	reference
G1000	UpStTrG	$O_2 + O(^1D) \rightarrow O(^3P) + O_2$	$3.3E-11*EXP(55./temp)$	Burkholder et al. (2015)
G1001	UpStTrG	$O_2 + O(^3P) \rightarrow O_3$	$6.0E-34*((temp/300.)**(-2.4))$ *cair	Burkholder et al. (2015)
G2100	UpStTrG	$H + O_2 \rightarrow HO_2$	$k_3rd(temp, cair, 4.4E-32, 1.3,$ $7.5E-11, -0.2, 0.6)$	Burkholder et al. (2015)
G2104	UpStTrG	$OH + O_3 \rightarrow HO_2 + O_2$	$1.7E-12*EXP(-940./temp)$	Burkholder et al. (2015)
G2105	UpStTrG	$OH + H_2 \rightarrow H_2O + H$	$2.8E-12*EXP(-1800./temp)$	Burkholder et al. (2015)
G2107	UpStTrG	$HO_2 + O_3 \rightarrow OH + 2 O_2$	$1.E-14*EXP(-490./temp)$	Burkholder et al. (2015)
G2109	UpStTrG	$HO_2 + OH \rightarrow H_2O + O_2$	$4.8E-11*EXP(250./temp)$	Burkholder et al. (2015)
G2110	UpStTrG	$HO_2 + HO_2 \rightarrow H_2O_2 + O_2$	k_H02_H02	Burkholder et al. (2015)*
G2111	UpStTrG	$H_2O + O(^1D) \rightarrow 2 OH$	$1.63E-10*EXP(60./temp)$	Burkholder et al. (2015)
G2112	UpStTrG	$H_2O_2 + OH \rightarrow H_2O + HO_2$	$1.8E-12$	Burkholder et al. (2015)
G2117	UpStTrG	$H_2O + H_2O \rightarrow (H_2O)_2$	$6.521E-26*temp*EXP(1851.09/temp)$ *EXP(-5.10485E-3*temp)	Scribano et al. (2006)*
G2118	UpStTrG	$(H_2O)_2 \rightarrow H_2O + H_2O$	$1.E0$	see note*
G3101	UpStTrGN	$N_2 + O(^1D) \rightarrow O(^3P) + N_2$	$2.15E-11*EXP(110./temp)$	Burkholder et al. (2015)
G3103	UpStTrGN	$NO + O_3 \rightarrow NO_2 + O_2$	$3.0E-12*EXP(-1500./temp)$	Burkholder et al. (2015)
G3106	StTrGN	$NO_2 + O_3 \rightarrow NO_3 + O_2$	$1.2E-13*EXP(-2450./temp)$	Burkholder et al. (2015)
G3108	StTrGN	$NO_3 + NO \rightarrow 2 NO_2$	$1.5E-11*EXP(170./temp)$	Burkholder et al. (2015)
G3109	UpStTrGN	$NO_3 + NO_2 \rightarrow N_2O_5$	k_N03_N02	Burkholder et al. (2015)*
G3110	StTrGN	$N_2O_5 \rightarrow NO_2 + NO_3$	$k_N03_N02/(5.8E-27*EXP(10840./$ $temp))$	Burkholder et al. (2015)*
G3200	TrGN	$NO + OH \rightarrow HONO$	$k_3rd(temp, cair, 7.0E-31, 2.6,$ $3.6E-11, 0.1, 0.6)$	Burkholder et al. (2015)
G3201	UpStTrGN	$NO + HO_2 \rightarrow NO_2 + OH$	$3.3E-12*EXP(270./temp)$	Burkholder et al. (2015)
G3202	UpStTrGN	$NO_2 + OH \rightarrow HNO_3$	$k_3rd(temp, cair, 1.8E-30, 3.0,$ $2.8E-11, 0., 0.6)$	Burkholder et al. (2015)
G3203	StTrGN	$NO_2 + HO_2 \rightarrow HNO_4$	k_N02_H02	Burkholder et al. (2015)*
G3204	TrGN	$NO_3 + HO_2 \rightarrow NO_2 + OH + O_2$	$3.5E-12$	Burkholder et al. (2015)
G3205	TrGN	$HONO + OH \rightarrow NO_2 + H_2O$	$1.8E-11*EXP(-390./temp)$	Burkholder et al. (2015)
G3206	StTrGN	$HNO_3 + OH \rightarrow H_2O + NO_3$	k_HNO3_OH	Dulitz et al. (2018)*
G3207	StTrGN	$HNO_4 \rightarrow NO_2 + HO_2$	$k_N02_H02/(2.1E-27*EXP(10900./$ $temp))$	Burkholder et al. (2015)*
G3208	StTrGN	$HNO_4 + OH \rightarrow NO_2 + H_2O$	$1.3E-12*EXP(380./temp)$	Burkholder et al. (2015)

2

Table 1: Gas phase reactions (... continued)

#	labels	reaction	rate coefficient	reference
G3209	TrGN	$NH_3 + OH \rightarrow NH_2 + H_2O$	$1.7E-12*EXP(-710./temp)$	Kohlmann and Poppe (1999)
G3210	TrGN	$NH_3 + O_3 \rightarrow NH_2O + O_2$	$4.3E-12*EXP(-930./temp)$	Kohlmann and Poppe (1999)
G3211	TrGN	$NH_2 + HO_2 \rightarrow NH_2O + OH$	$4.8E-07*EXP(-628./temp)$ *temp**(-1.32)	Kohlmann and Poppe (1999)
G3212	TrGN	$NH_2 + HO_2 \rightarrow HNO + H_2O$	$9.4E-09*EXP(-356./temp)$ *temp**(-1.12)	Kohlmann and Poppe (1999)
G3213	TrGN	$NH_2 + NO \rightarrow HO_2 + OH + N_2$	$1.92E-12*((temp/298.)**(-1.5))$	Kohlmann and Poppe (1999)
G3214	TrGN	$NH_2 + NO \rightarrow N_2 + H_2O$	$1.41E-11*((temp/298.)**(-1.5))$	Kohlmann and Poppe (1999)
G3215	TrGN	$NH_2 + NO_2 \rightarrow N_2O + H_2O$	$1.2E-11*((temp/298.)**(-2.0))$	Kohlmann and Poppe (1999)
G3216	TrGN	$NH_2 + NO_2 \rightarrow NH_2O + NO$	$0.8E-11*((temp/298.)**(-2.0))$	Kohlmann and Poppe (1999)
G3217	TrGN	$NH_2O + O_3 \rightarrow NH_2 + O_2$	$1.2E-14$	Kohlmann and Poppe (1999)
G3218	TrGN	$NH_2O \rightarrow NHOH$	$1.3E3$	Kohlmann and Poppe (1999)
G3219	TrGN	$HNO + OH \rightarrow NO + H_2O$	$8.0E-11*EXP(-500./temp)$	Kohlmann and Poppe (1999)
G3220	TrGN	$HNO + NHOH \rightarrow NH_2OH + NO$	$1.66E-12*EXP(-1500./temp)$	Kohlmann and Poppe (1999)
G3221	TrGN	$HNO + NO_2 \rightarrow HONO + NO$	$1.0E-12*EXP(-1000./temp)$	Kohlmann and Poppe (1999)
G3222	TrGN	$NHOH + OH \rightarrow HNO + H_2O$	$1.66E-12$	Kohlmann and Poppe (1999)
G3223	TrGN	$NH_2OH + OH \rightarrow NHOH + H_2O$	$4.13E-11*EXP(-2138./temp)$	Kohlmann and Poppe (1999)
G3224	TrGN	$HNO + O_2 \rightarrow HO_2 + NO$	$3.65E-14*EXP(-4600./temp)$	Kohlmann and Poppe (1999)
G4101	StTrG	$CH_4 + OH \rightarrow CH_3 + H_2O$	$1.85E-20*EXP(2.82*LOG(temp)$ $-987./temp)$	Atkinson (2003)
G4102	TrG	$CH_3OH + OH \rightarrow .85 HCHO + .85 HO_2 + .15 CH_3O + H_2O$	$6.38E-18*(temp**2)*EXP(144./temp)$	Atkinson et al. (2006)
G4103a	StTrG	$CH_3O_2 + HO_2 \rightarrow CH_3OOH + O_2$	$3.8E-13*EXP(780./temp)/(1.+1./$ $498.*EXP(1160./temp))$	Atkinson et al. (2006)
G4103b	StTrG	$CH_3O_2 + HO_2 \rightarrow HCHO + H_2O + O_2$	$3.8E-13*EXP(780./temp)/(1.+$ $498.*EXP(-1160./temp))$	Atkinson et al. (2006)
G4104a	StTrGN	$CH_3O_2 + NO \rightarrow CH_3O + NO_2$	$2.3E-12*EXP(360./temp)*(1.-beta_$ $CH3NO3)$	Atkinson et al. (2006), Butkovskaya et al. (2012), Flocke et al. (1998)
G4104b	StTrGN	$CH_3O_2 + NO \rightarrow CH_3ONO_2$	$2.3E-12*EXP(360./temp)*beta_$ $CH3NO3$	Atkinson et al. (2006), Butkovskaya et al. (2012), Flocke et al. (1998)*
G4105	TrGN	$CH_3O_2 + NO_3 \rightarrow CH_3O + NO_2 + O_2$	$1.2E-12$	Atkinson et al. (2006)
G4106a	StTrG	$CH_3O_2 \rightarrow CH_3O + .5 O_2$	$7.4E-13*EXP(-520./temp)*R02*2.$	Atkinson et al. (2006)

3

Table 1: Gas phase reactions (... continued)

#	labels	reaction	rate coefficient	reference
G4106b	SeTrG	$\text{CH}_3\text{O}_2 \rightarrow .5 \text{HCHO} + .5 \text{CH}_3\text{OH} + .5 \text{O}_2$	$(k_{\text{CH3O2}} - 7.4\text{E}-13 * \text{EXP}(-520./\text{temp})) * \text{R02} * 2.$	Atkinson et al. (2006)
G4107	SeTrG	$\text{CH}_3\text{OOH} + \text{OH} \rightarrow .6 \text{CH}_3\text{O}_2 + .4 \text{HCHO} + .4 \text{OH} + \text{H}_2\text{O}$	$k_{\text{CH3OOH_OH}}$	Wallington et al. (2018)
G4108	SeTrG	$\text{HCHO} + \text{OH} \rightarrow \text{CO} + \text{H}_2\text{O} + \text{HO}_2$	$9.52\text{E}-18 * \text{EXP}(2.03 * \text{LOG}(\text{temp}) + 636./\text{temp})$	Sivakumaran et al. (2003)
G4109	TrGN	$\text{HCHO} + \text{NO}_3 \rightarrow \text{HNO}_3 + \text{CO} + \text{HO}_2$	$3.4\text{E}-13 * \text{EXP}(-1900./\text{temp})$	Burkholder et al. (2015)*
G4110	UpSeTrG	$\text{CO} + \text{OH} \rightarrow \text{H} + \text{CO}_2$	$(1.57\text{E}-13 + \text{cair} * 3.54\text{E}-33)$	McCabe et al. (2001)
G4111	TrG	$\text{HCOOH} + \text{OH} \rightarrow \text{CO}_2 + \text{HO}_2 + \text{H}_2\text{O}$	$2.94\text{E}-14 * \text{exp}(786./\text{temp}) + 9.85\text{E}-13 * \text{EXP}(-1036./\text{temp})$	Paulot et al. (2011)
G4114	SeTrGN	$\text{CH}_3\text{O}_2 + \text{NO}_2 \rightarrow \text{CH}_3\text{O}_2\text{NO}_2$	$k_{\text{NO2_CH3O2}}$	Burkholder et al. (2015)
G4115	SeTrGN	$\text{CH}_3\text{O}_2\text{NO}_2 \rightarrow \text{CH}_3\text{O}_2 + \text{NO}_2$	$k_{\text{NO2_CH3O2}} / (9.5\text{E}-29 * \text{EXP}(11234./\text{temp}))$	Burkholder et al. (2015)*
G4116	SeTrGN	$\text{CH}_3\text{O}_2\text{NO}_2 + \text{OH} \rightarrow \text{HCHO} + \text{NO}_3 + \text{H}_2\text{O}$	$3.00\text{E}-14$	see note*
G4117	SeTrGN	$\text{CH}_3\text{ONO}_2 + \text{OH} \rightarrow \text{H}_2\text{O} + \text{HCHO} + \text{NO}_2$	$4.0\text{E}-13 * \text{EXP}(-845./\text{temp})$	Atkinson et al. (2006)
G4118	SeTrG	$\text{CH}_3\text{O} \rightarrow \text{HO}_2 + \text{HCHO}$	$1.3\text{E}-14 * \text{exp}(-663./\text{temp}) * c(\text{ind_O2})$	Chai et al. (2014)
G4119a	SeTrGN	$\text{CH}_3\text{O} + \text{NO}_2 \rightarrow \text{CH}_3\text{ONO}_2$	$k_{\text{3rd_iupac}}(\text{temp}, \text{cair}, 8.1\text{E}-29, 4.5, 2.1\text{E}-11, 0., 0.44)$	Atkinson et al. (2006)
G4119b	SeTrGN	$\text{CH}_3\text{O} + \text{NO}_2 \rightarrow \text{HCHO} + \text{HONO}$	$9.6\text{E}-12 * \text{EXP}(-1150./\text{temp})$	Atkinson et al. (2006)
G4120a	SeTrGN	$\text{CH}_3\text{O} + \text{NO} \rightarrow \text{CH}_3\text{ONO}$	$k_{\text{3rd_iupac}}(\text{temp}, \text{cair}, 2.6\text{E}-29, 2.8, 3.3\text{E}-11, 0.6, \text{REAL}(\text{EXP}(-\text{temp}/900.), \text{SP}))$	Atkinson et al. (2006)
G4120b	SeTrGN	$\text{CH}_3\text{O} + \text{NO} \rightarrow \text{HCHO} + \text{HNO}$	$2.3\text{E}-12 * (\text{temp}/300.) ** 0.7$	Atkinson et al. (2006)
G4121	SeTrG	$\text{CH}_3\text{O}_2 + \text{O}_3 \rightarrow \text{CH}_3\text{O} + 2 \text{O}_2$	$2.9\text{E}-16 * \text{exp}(-1000./\text{temp})$	Burkholder et al. (2015)
G4122	SeTrGN	$\text{CH}_3\text{ONO} + \text{OH} \rightarrow \text{H}_2\text{O} + \text{HCHO} + \text{NO}$	$1\text{E}-10 * \text{exp}(-1764./\text{temp})$	Nielsen et al. (1991)
G4123	SeTrG	$\text{HCHO} + \text{HO}_2 \rightarrow \text{HOCH}_2\text{O}_2$	$9.7\text{E}-15 * \text{EXP}(625./\text{temp})$	Atkinson et al. (2006)
G4124	SeTrG	$\text{HOCH}_2\text{O}_2 \rightarrow \text{HCHO} + \text{HO}_2$	$2.4\text{E}12 * \text{EXP}(-7000./\text{temp})$	Atkinson et al. (2006)
G4125	SeTrG	$\text{HOCH}_2\text{O}_2 + \text{HO}_2 \rightarrow .5 \text{HOCH}_2\text{OOH} + .5 \text{HCOOH} + .2 \text{OH} + 2 \text{H}_2\text{O} + 3 \text{H}_2\text{O} + .8 \text{O}_2$	$5.6\text{E}-15 * \text{EXP}(2300./\text{temp})$	Atkinson et al. (2006)
G4126	SeTrGN	$\text{HOCH}_2\text{O}_2 + \text{NO} \rightarrow \text{NO}_2 + \text{HO}_2 + \text{HCOOH}$	$0.7275 * 2.3\text{E}-12 * \text{EXP}(360./\text{temp})$	Atkinson et al. (2006)*
G4127	SeTrGN	$\text{HOCH}_2\text{O}_2 + \text{NO}_3 \rightarrow \text{NO}_2 + \text{HO}_2 + \text{HCOOH}$	$1.2\text{E}-12$	see note*
G4129a	SeTrG	$\text{HOCH}_2\text{O}_2 \rightarrow \text{HCOOH} + \text{HO}_2$	$(k_{\text{CH3O2}} * 5.5\text{E}-12) ** 0.5 * \text{R02} * 2.$	Atkinson et al. (2006)
G4129b	SeTrG	$\text{HOCH}_2\text{O}_2 \rightarrow .5 \text{HCOOH} + .5 \text{HOCH}_2\text{OH} + .5 \text{O}_2$	$(k_{\text{CH3O2}} * 5.7\text{E}-14 * \text{EXP}(750./\text{temp})) ** 0.5 * \text{R02} * 2.$	Atkinson et al. (2006)
G4130a	SeTrG	$\text{HOCH}_2\text{OOH} + \text{OH} \rightarrow \text{HOCH}_2\text{O}_2 + \text{H}_2\text{O}$	k_{roohro}	Taraborrelli (2010)*
G4130b	SeTrG	$\text{HOCH}_2\text{OOH} + \text{OH} \rightarrow \text{HCOOH} + \text{H}_2\text{O} + \text{OH}$	$k_{\text{rohro}} + k_{\text{s*f_soh}} * f_{\text{soh}}$	Taraborrelli (2010)*

4

Table 1: Gas phase reactions (... continued)

#	labels	reaction	rate coefficient	reference
G4132	SeTrG	$\text{HOCH}_2\text{OH} + \text{OH} \rightarrow \text{HO}_2 + \text{HCOOH} + \text{H}_2\text{O}$	$2 * k_{\text{rohro}} + k_{\text{s*f_soh}} * f_{\text{soh}}$	Taraborrelli (2010)*
G4133	SeTrG	$\text{CH}_3\text{O}_2 + \text{OH} \rightarrow \text{CH}_3\text{O} + \text{HO}_2$	$1.4\text{E}-10$	Bossolasco et al. (2014)*
G4134	SeTrG	$\text{CH}_2\text{OO} \rightarrow \text{CO} + \text{HO}_2 + \text{OH}$	$1.124\text{E}14 * \text{EXP}(-10000./\text{temp})$	see note*
G4135	SeTrG	$\text{CH}_2\text{OO} + \text{H}_2\text{O} \rightarrow \text{HOCH}_2\text{OOH}$	$k_{\text{CH2OO_N02}} * 3.6\text{E}-6$	Ouyang et al. (2013)*
G4136	SeTrG	$\text{CH}_2\text{OO} + (\text{H}_2\text{O})_2 \rightarrow \text{HOCH}_2\text{OOH} + \text{H}_2\text{O}$	$5.2\text{E}-12$	Chao et al. (2015), Lewis et al. (2015)*
G4137	SeTrGN	$\text{CH}_2\text{OO} + \text{NO} \rightarrow \text{HCHO} + \text{NO}_2$	$6\text{E}-14$	Welz et al. (2012)*
G4138	SeTrGN	$\text{CH}_2\text{OO} + \text{NO}_2 \rightarrow \text{HCHO} + \text{NO}_3$	$k_{\text{CH2OO_N02}}$	Welz et al. (2012), Stone et al. (2014)*
G4140	SeTrG	$\text{CH}_2\text{OO} + \text{CO} \rightarrow \text{HCHO} + \text{CO}_2$	$3.6\text{E}-14$	Vereecken et al. (2012)
G4141	SeTrG	$\text{CH}_2\text{OO} + \text{HCOOH} \rightarrow 2 \text{HCOOH}$	$1\text{E}-10$	Welz et al. (2014)*
G4142	SeTrG	$\text{CH}_2\text{OO} + \text{HCHO} \rightarrow 2 \text{LCARBON}$	$1.7\text{E}-12$	Stone et al. (2014)*
G4143	SeTrG	$\text{CH}_2\text{OO} + \text{CH}_3\text{OH} \rightarrow 2 \text{LCARBON}$	$5\text{E}-12$	Vereecken et al. (2012)*
G4144	SeTrG	$\text{CH}_2\text{OO} + \text{CH}_3\text{O}_2 \rightarrow 2 \text{LCARBON}$	$5\text{E}-12$	Vereecken et al. (2012)*
G4145	SeTrG	$\text{CH}_2\text{OO} + \text{HO}_2 \rightarrow \text{LCARBON}$	$5\text{E}-12$	Vereecken et al. (2012)
G4146	SeTrG	$\text{CH}_2\text{OO} + \text{O}_3 \rightarrow \text{HCHO} + 2 \text{O}_2$	$1\text{E}-12$	Vereecken et al. (2014)
G4147	SeTrG	$\text{CH}_2\text{OO} + \text{CH}_2\text{OO} \rightarrow 2 \text{HCHO} + \text{O}_2$	$6\text{E}-11$	Buras et al. (2014)
G4148	SeTrGN	$\text{HOCH}_2\text{O}_2 + \text{NO}_2 \rightarrow \text{HOCH}_2\text{O}_2\text{NO}_2$	$k_{\text{NO2_CH3O2}}$	see note*
G4149	SeTrGN	$\text{HOCH}_2\text{O}_2\text{NO}_2 \rightarrow \text{HOCH}_2\text{O}_2 + \text{NO}_2$	$k_{\text{NO2_CH3O2}} / (9.5\text{E}-29 * \text{EXP}(11234./\text{temp}))$	Barnes et al. (1985)*
G4150	SeTrGN	$\text{HOCH}_2\text{O}_2\text{NO}_2 + \text{OH} \rightarrow \text{HCOOH} + \text{NO}_3 + \text{H}_2\text{O}$	$9.50\text{E}-13 * \text{EXP}(-650./\text{temp}) * f_{\text{soh}}$	see note*
G4151	SeTrG	$\text{CH}_3 + \text{O}_2 \rightarrow \text{CH}_3\text{O}_2$	$k_{\text{3rd_iupac}}(\text{temp}, \text{cair}, 7.0\text{E}-31, 3., 1.8\text{E}-12, -1.1, 0.33)$	Atkinson et al. (2006)
G4152	SeTrG	$\text{CH}_3 + \text{O}_3 \rightarrow .956 \text{HCHO} + .956 \text{H} + .044 \text{CH}_3\text{O} + \text{O}_2$	$5.1\text{E}-12 * \text{exp}(-210./\text{temp})$	Albaladejo et al. (2002), Ogryzlo et al. (1981)
G4153	SeTrG	$\text{CH}_3 + \text{O}(^3\text{P}) \rightarrow .83 \text{HCHO} + .83 \text{H} + .17 \text{CO} + .17 \text{H}_2 + .17 \text{H}$	$1.3\text{E}-10$	Atkinson et al. (2006)
G4154	SeTrG	$\text{CH}_3\text{O} + \text{O}_3 \rightarrow \text{CH}_3\text{O}_2 + \text{O}_2$	$2.53\text{E}-14$	Albaladejo et al. (2002)*
G4155	SeTrG	$\text{CH}_3\text{O} + \text{O}(^3\text{P}) \rightarrow .75 \text{CH}_3 + .75 \text{O}_2 + .25 \text{HCHO} + .25 \text{OH}$	$2.5\text{E}-11$	Baulch et al. (2005)
G4156	SeTrG	$\text{CH}_3\text{O}_2 + \text{O}(^3\text{P}) \rightarrow \text{CH}_3\text{O} + \text{O}_2$	$4.3\text{E}-11$	Zellner et al. (1988)
G4157	SeTrG	$\text{HCHO} + \text{O}(^3\text{P}) \rightarrow .7 \text{OH} + .7 \text{CO} + .3 \text{H} + .3 \text{CO}_2 + \text{HO}_2$	$3.4\text{E}-11 * \text{EXP}(-1600./\text{temp})$	Burkholder et al. (2015)
G4158	TrG	$\text{CH}_2\text{OO}^* \rightarrow .37 \text{CH}_2\text{OO} + .47 \text{CO} + .47 \text{H}_2\text{O} + .16 \text{HO}_2 + .16 \text{CO} + .16 \text{OH}$	KDEC	Atkinson et al. (2006)

5

Table 1: Gas phase reactions (... continued)

#	labels	reaction	rate coefficient	reference
G4159	TrGN	HCN + OH → H ₂ O + CN	k_3rd(temp, cair, 4.28E-33, 1.0, REAL(4.25E-13*EXP(-1150./temp), SP), 1.0, 0.8)	Kleinböhl et al. (2006)
G4160a	TrGN	HCN + O(¹ D) → O(³ P) + HCN	1.08E-10*EXP(105./temp) *0.15*EXP(200./temp)	Strekowski et al. (2010)
G4160b	TrGN	HCN + O(¹ D) → H + NCO	1.08E-10*EXP(105./temp)*0.68/2.	Strekowski et al. (2010)*
G4160c	TrGN	HCN + O(¹ D) → OH + CN	1.08E-10*EXP(105./temp)*(1.-(0.68/2.+0.15*EXP(200./temp)))	Strekowski et al. (2010)*
G4161	TrGN	HCN + O(³ P) → H + NCO	1.0E-11*EXP(-4000./temp)	Burkholder et al. (2015)*
G4162	TrGN	CN + O ₂ → NCO + O(³ P)	1.2E-11*EXP(210./temp)*0.75	Baulch et al. (2005)
G4163	TrGN	CN + O ₂ → CO + NO	1.2E-11*EXP(210./temp)*0.25	Baulch et al. (2005)
G4164	TrGN	NCO + O ₂ → CO ₂ + NO	7.E-15	Becker et al. (2000)*
G42000	TrGC	C ₂ H ₆ + OH → C ₂ H ₅ O ₂ + H ₂ O	1.49E-17*temp*temp*EXP(-499./temp)	Atkinson et al. (2006)
G42001	TrGC	C ₂ H ₄ + O ₃ → HCHO + CH ₂ OO*	9.1E-15*EXP(-2580./temp)	Atkinson et al. (2006)*
G42002	TrGC	C ₂ H ₄ + OH → HOCH ₂ CH ₂ O ₂	k_3rd_iupac(temp, cair, 8.6E-29, 3.1, 9.E-12, 0.85, 0.48)	Atkinson et al. (2006), Rickard and Pascoe (2009)
G42003	TrGC	C ₂ H ₅ O ₂ + HO ₂ → C ₂ H ₅ OOH	7.5E-13*EXP(700./temp)	Burkholder et al. (2015)
G42004a	TrGCN	C ₂ H ₅ O ₂ + NO → CH ₃ CHO + HO ₂ + NO ₂	2.55E-12*EXP(380./temp)*(1.-beta_C2H5NO3)	Atkinson et al. (2006), Butkovskaya et al. (2010)
G42004b	TrGCN	C ₂ H ₅ O ₂ + NO → C ₂ H ₅ ONO ₂	2.55E-12*EXP(380./temp)*beta_C2H5NO3	Atkinson et al. (2006), Butkovskaya et al. (2010)
G42005	TrGCN	C ₂ H ₅ O ₂ + NO ₃ → CH ₃ CHO + HO ₂ + NO ₂	2.3E-12	Wallington et al. (2018)
G42006	TrGC	C ₂ H ₅ O ₂ → .8 CH ₃ CHO + .6 HO ₂ + .2 C ₂ H ₅ OH	2.*(7.6E-14*k_CH3O2)**(5)*R02	Sander et al. (2018), Atkinson et al. (2006)
G42007a	TrGC	C ₂ H ₅ OOH + OH → C ₂ H ₅ O ₂ + H ₂ O	k_roohro	Sander et al. (2018)
G42007b	TrGC	C ₂ H ₅ OOH + OH → CH ₃ CHO + OH	k_s*f_sooH	Sander et al. (2018)
G42008a	TrGC	CH ₃ CHO + OH → CH ₃ C(O) + H ₂ O	4.4E-12*EXP(365./temp)*0.95	Atkinson et al. (2006)
G42008b	TrGC	CH ₃ CHO + OH → HCOCH ₂ O ₂ + H ₂ O	4.4E-12*EXP(365./temp)*0.05	Atkinson et al. (2006)
G42009	TrGCN	CH ₃ CHO + NO ₃ → CH ₃ C(O) + HNO ₃	KN03AL	Rickard and Pascoe (2009)
G42010	TrGC	CH ₃ COOH + OH → CH ₃ + CO ₂ + H ₂ O	k_CH3CO2H_OH	Atkinson et al. (2006)*
G42011a	TrGC	CH ₃ C(O)OO + HO ₂ → OH + CH ₃ + CO ₂	5.20E-13*EXP(980./temp)*1.507*0.61	Groß et al. (2014)
G42011b	TrGC	CH ₃ C(O)OO + HO ₂ → CH ₃ C(O)OOH	5.20E-13*EXP(980./temp)*1.507*0.23	Groß et al. (2014)
G42011c	TrGC	CH ₃ C(O)OO + HO ₂ → CH ₃ COOH + O ₃	5.20E-13*EXP(980./temp)*1.507*0.16	Groß et al. (2014)
G42012	TrGCN	CH ₃ C(O)OO + NO → CH ₃ + CO ₂ + NO ₂	8.1E-12*EXP(270./temp)	Tyndall et al. (2001a)

6

Table 1: Gas phase reactions (... continued)

#	labels	reaction	rate coefficient	reference
G42013	TrGCN	CH ₃ C(O)OO + NO ₂ → PAN	k_CH3CO3_NO2	Burkholder et al. (2015)*
G42014	TrGCN	CH ₃ C(O)OO + NO ₃ → CH ₃ + NO ₂ + CO ₂	4.E-12	Canosa-Mas et al. (1996)
G42017a	TrGC	CH ₃ C(O)OO → CH ₃ + CO ₂	k1_R02RC03*0.9	Sander et al. (2018)
G42017b	TrGC	CH ₃ C(O)OO → CH ₃ COOH	k1_R02RC03*0.1	Sander et al. (2018)
G42018	TrGC	CH ₃ C(O)OOH + OH → CH ₃ C(O)OO + H ₂ O	k_roohro	Rickard and Pascoe (2009)*
G42020	TrGCN	PAN + OH → HCHO + CO + NO ₂ + H ₂ O	3.00E-14	Rickard and Pascoe (2009)
G42021	TrGCN	PAN → CH ₃ C(O)OO + NO ₂	k_PAN_M	Burkholder et al. (2015)*
G42022a	TrGC	C ₂ H ₂ + OH → GLYOX + OH	k_3rd(temp, cair, 5.5e-30, 0.0, 8.3e-13, -2., 0.6)*0.71	Burkholder et al. (2015)*
G42022b	TrGC	C ₂ H ₂ + OH → HCOOH + CO + HO ₂	k_3rd(temp, cair, 5.5e-30, 0.0, 8.3e-13, -2., 0.6)*0.29	Burkholder et al. (2015)*
G42023a	TrGC	HOCH ₂ CHO + OH → HOCH ₂ CO + H ₂ O	8.00E-12*0.80	Atkinson et al. (2006)
G42023b	TrGC	HOCH ₂ CHO + OH → HOCHCHO + H ₂ O	8.00E-12*0.20	Atkinson et al. (2006)
G42024a	TrGC	HOCH ₂ CO + O ₂ → HOCH ₂ CO ₃	5.1E-12*(1.-1./(1+1.85E-18*cair))	Atkinson et al. (2006), Beyersdorf et al. (2010)*
G42024b	TrGC	HOCH ₂ CO + O ₂ → OH + HCHO + CO ₂	5.1E-12*1./(1+1.85E-18*cair)	Atkinson et al. (2006), Beyersdorf et al. (2010)*
G42025	TrGC	HOCHCHO → GLYOX + HO ₂	KDEC	Sander et al. (2018)
G42026	TrGCN	HOCH ₂ CHO + NO ₃ → HOCH ₂ CO + HNO ₃	KN03AL	Rickard and Pascoe (2009)
G42027a	TrGC	HOCH ₂ CO ₃ → HCHO + CO ₂ + HO ₂	k1_R02RC03*0.9	Sander et al. (2018)
G42027b	TrGC	HOCH ₂ CO ₃ → HOCH ₂ CO ₂ H	k1_R02RC03*0.1	Sander et al. (2018)
G42028a	TrGC	HOCH ₂ CO ₃ + HO ₂ → HCHO + HO ₂ + OH + CO ₂	KAPH02*rc03_oh	Sander et al. (2018), Groß et al. (2014)
G42028b	TrGC	HOCH ₂ CO ₃ + HO ₂ → HOCH ₂ CO ₃ H	KAPH02*rc03_ooH	Sander et al. (2018), Groß et al. (2014)
G42028c	TrGC	HOCH ₂ CO ₃ + HO ₂ → HOCH ₂ CO ₂ H + O ₃	KAPH02*rc03_o3	Sander et al. (2018), Groß et al. (2014)
G42029	TrGCN	HOCH ₂ CO ₃ + NO → NO ₂ + HO ₂ + HCHO + CO ₂	KAPNO	Rickard and Pascoe (2009)
G42030	TrGCN	HOCH ₂ CO ₃ + NO ₂ → PHAN	k_CH3CO3_NO2	Rickard and Pascoe (2009)
G42031	TrGCN	HOCH ₂ CO ₃ + NO ₃ → NO ₂ + HO ₂ + HCHO + CO ₂	KR02N03*1.74	Rickard and Pascoe (2009)
G42032	TrGC	HOCH ₂ CO ₂ H + OH → .09 HCHO + .09 CO ₂ + .91 HCOCO ₂ H + HO ₂ + H ₂ O	k_co2h*k_s*f_soh*f_co2h	Sander et al. (2018)
G42033a	TrGC	HOCH ₂ CO ₃ H + OH → HOCH ₂ CO ₃ + H ₂ O	k_roohro	Sander et al. (2018)
G42033b	TrGC	HOCH ₂ CO ₃ H + OH → HCOCO ₃ H + HO ₂	k_s*f_soh*f_co2h	Sander et al. (2018)
G42034	TrGCN	PHAN → HOCH ₂ CO ₃ + NO ₂	k_PAN_M	Rickard and Pascoe (2009)

7

Table 1: Gas phase reactions (... continued)

#	labels	reaction	rate coefficient	reference
G42035	TrGCN	PHAN + OH → HCHO + CO + NO ₂ + H ₂ O	k_s*f_soh*f_cpan+k_rohro	Sander et al. (2018)
G42036	TrGC	GLYOX + OH → HCOCO + H ₂ O	3.1E-12*EXP(340./temp)	Atkinson et al. (2006), Orlando and Tyndall (2001), Lockhart et al. (2013)
G42037	TrGCN	GLYOX + NO ₃ → HCOCO + HNO ₃	KN03AL	Rickard and Pascoe (2009)
G42038a	TrGC	HCOCO → CO + CO + HO ₂	7.E11*EXP(-3160./temp) +5.E-12*c(ind_02)	Orlando and Tyndall (2001), Lockhart et al. (2013), Rickard and Pascoe (2009)
G42037b	TrGC	HCOCO → HCOCO ₃	5.E-12*(ind_02)*3.2*exp(-550./temp)	Lockhart et al. (2013), Rickard and Pascoe (2009)
G42037c	TrGC	HCOCO → OH + CO + CO ₂	5.E-12*c(ind_02) *(1.-3.2*exp(-550./temp))	Lockhart et al. (2013), Rickard and Pascoe (2009)
G42039a	TrGC	HCOCO ₃ → CO + HO ₂ + CO ₂	k1_R02RC03*0.9	Sander et al. (2018)
G42039b	TrGC	HCOCO ₃ → HCOCO ₂ H	k1_R02RC03*0.1	Sander et al. (2018)
G42040	TrGC	HCOCO ₃ + HO ₂ → HO ₂ + CO + CO ₂ + OH	KAPH02	Feierabend et al. (2008), Sander et al. (2018)
G42041	TrGCN	HCOCO ₃ + NO → HO ₂ + CO + NO ₂ + CO ₂	KAPND	Rickard and Pascoe (2009)
G42042	TrGCN	HCOCO ₃ + NO ₃ → HO ₂ + CO + NO ₂ + CO ₂	KR02N03*1.74	Rickard and Pascoe (2009)
G42043	TrGCN	HCOCO ₃ + NO ₂ → HO ₂ + CO + NO ₃ + CO ₂	k_CH3CO3_NO2	Orlando and Tyndall (2001), Sander et al. (2018)
G42044	TrGC	HCOCO ₂ H + OH → CO + HO ₂ + CO ₂ + H ₂ O	k_co2h+k_t*f_o*f_co2h	Sander et al. (2018)
G42045a	TrGC	HCOCO ₂ H + OH → HCOCO ₃ + H ₂ O	k_roohro	Sander et al. (2018)
G42045b	TrGC	HCOCO ₂ H + OH → CO + CO ₂ + H ₂ O + OH	k_t*f_o*f_co2h	Sander et al. (2018)
G42046	TrGC	HOCH ₂ CH ₂ O ₂ → .6 HOCH ₂ CH ₂ O + .2 HOCH ₂ CHO + .2 ETHGLY	2.*(7.8E-14*EXP(1000./temp) *k_CH3O2)**(.5)*R02	Atkinson et al. (2006), Rickard and Pascoe (2009)
G42047	TrGCN	HOCH ₂ CH ₂ O ₂ + NO → .25 HO ₂ + .5 HCHO + .75 HOCH ₂ CH ₂ O + NO ₂	KR02N0*(1.-alpha_AN(3,1,0,0,0, temp, cair))	Rickard and Pascoe (2009)*
G42048	TrGCN	HOCH ₂ CH ₂ O ₂ + NO → ETHOHNO3	KR02N0*alpha_AN(3,1,0,0,0, temp, cair)	Sander et al. (2018)
G42049a	TrGC	HOCH ₂ CH ₂ O ₂ + HO ₂ → HYETHO2H	1.53E-13*EXP(1300./temp) *(1.-rchohch2o2_oh)	Rickard and Pascoe (2009)
G42049b	TrGC	HOCH ₂ CH ₂ O ₂ + HO ₂ → HOCH ₂ CH ₂ O + OH	1.53E-13*EXP(1300./temp) *rchohch2o2_oh	Rickard and Pascoe (2009)
G42050	TrGCN	ETHOHNO3 + OH → .93 NO ₃ CH ₂ CHO + .93 HO ₂ + .07 HOCH ₂ CHO + .07 NO ₂ + H ₂ O	k_s*(f_soh*f_ch2ono2+f_ono2*f_pch2oh)+k_rohro	Sander et al. (2018)

8

Table 1: Gas phase reactions (... continued)

#	labels	reaction	rate coefficient	reference
G42051a	TrGC	HYETHO2H + OH → HOCH ₂ CH ₂ O ₂ + H ₂ O	k_roohro	Rickard and Pascoe (2009)*
G42051b	TrGC	HYETHO2H + OH → HOCH ₂ CHO + OH + H ₂ O	k_s*f_sooh*f_pch2oh	Sander et al. (2018)
G42051c	TrGC	HYETHO2H + OH → HOOCH ₂ CHO + HO ₂ + H ₂ O	k_s*f_soh*f_pch2oh+k_rohro	Sander et al. (2018)
G42052a	TrGC	HOCH ₂ CH ₂ O → HO ₂ + HOCH ₂ CHO	6.00E-14*EXP(-550./temp) *C(ind_02)	Rickard and Pascoe (2009)
G42052b	TrGC	HOCH ₂ CH ₂ O → HO ₂ + HCHO + HCHO	9.50E13*EXP(-5988./temp)	Rickard and Pascoe (2009)
G42053	TrGC	ETHGLY + OH → HOCH ₂ CHO + HO ₂ + H ₂ O	2*k_s*f_soh*f_pch2oh+2*k_rohro	Sander et al. (2018)
G42054	TrGC	HCOCH ₂ O ₂ → .6 HCHO + .6 CO + .6 HO ₂ + .2 GLYOX + .2 HOCH ₂ CHO	k1_R02p0R02	Sander et al. (2018)
G42055a	TrGC	HCOCH ₂ O ₂ + HO ₂ → HOOCH ₂ CHO	KR02H02(2)*rcoch2o2_oh	Sander et al. (2018)
G42055b	TrGC	HCOCH ₂ O ₂ + HO ₂ → HCHO + CO + HO ₂ + OH	KR02H02(2)*rcoch2o2_oh	Sander et al. (2018)
G42056a	TrGCN	HCOCH ₂ O ₂ + NO → NO ₂ + HCHO + CO + HO ₂	KR02N0*(1.-alpha_AN(3,1,1,0,0, temp, cair))	Sander et al. (2018)
G42056b	TrGCN	HCOCH ₂ O ₂ + NO → NO ₃ CH ₂ CHO	KR02N0*alpha_AN(3,1,1,0,0, temp, cair)	Sander et al. (2018)
G42057	TrGCN	HCOCH ₂ O ₂ + NO ₃ → HCHO + CO + HO ₂ + NO ₂	KR02N03	Sander et al. (2018)
G42058a	TrGC	HOOCH ₂ CHO + OH → HCOCH ₂ O ₂	k_roohro	Sander et al. (2018)
G42058b	TrGC	HOOCH ₂ CHO + OH → HCHO + CO + OH	0.8*8.E-12	Sander et al. (2018)*
G42058c	TrGC	HOOCH ₂ CHO + OH → GLYOX + OH	k_s*f_sooh*f_cho	Sander et al. (2018)
G42059	TrGCN	HOOCH ₂ CHO + NO ₃ → OH + HCHO + CO + HNO ₃	KN03AL	Rickard and Pascoe (2009)
G42060	TrGCN	HOOCH ₂ CO ₃ + NO → NO ₂ + OH + HCHO + CO ₂	KAPND	Sander et al. (2018)
G42061	TrGCN	HOOCH ₂ CO ₃ + NO ₃ → NO ₂ + OH + HCHO + CO ₂	KR02N03*1.74	Sander et al. (2018)
G42062a	TrGC	HOOCH ₂ CO ₃ + HO ₂ → 2 OH + HCHO + CO ₂	KAPH02*rco3_oh	Sander et al. (2018)
G42062b	TrGC	HOOCH ₂ CO ₃ + HO ₂ → HOOCH ₂ CO ₃ H	KAPH02*rco3_oh	Sander et al. (2018)
G42062c	TrGC	HOOCH ₂ CO ₃ + HO ₂ → HOOCH ₂ CO ₂ H + O ₃	KAPH02*rco3_o3	Sander et al. (2018)
G42063a	TrGC	HOOCH ₂ CO ₃ → OH + HCHO + CO ₂	k1_R02RC03*0.9	Sander et al. (2018)
G42063b	TrGC	HOOCH ₂ CO ₃ → HOOCH ₂ CO ₂ H	k1_R02RC03*0.1	Sander et al. (2018)
G42064a	TrGC	HOOCH ₂ CO ₃ H + OH → HOOCH ₂ CO ₃ + H ₂ O	2.*k_roohro	Sander et al. (2018)
G42064b	TrGC	HOOCH ₂ CO ₃ H + OH → HCOCO ₃ H + OH + H ₂ O	k_s*f_sooh*f_co2h	Sander et al. (2018)
G42065	TrGC	HOOCH ₂ CO ₂ H + OH → HCOCO ₂ H + OH + H ₂ O	k_s*f_sooh*f_co2h+k_co2h	Sander et al. (2018)
G42066	TrGC	CH ₂ CO + OH → .6 HCHO + .6 HO ₂ + .6 CO + .4 HOOCH ₂ CO ₂ H	2.8E-12*exp(510./temp)	Baulch et al. (2005), Sander et al. (2018)
G42067a	TrGC	CH ₃ CHOHOH + OH → CH ₃ COOH + OH	(k_t*f_tooh*f_toh + k_rohro)	Sander et al. (2018)
G42067b	TrGC	CH ₃ CHOHOH + OH → CH ₃ CHOH ₂ O	k_roohro	Sander et al. (2018)

9

Table 1: Gas phase reactions (... continued)

#	labels	reaction	rate coefficient	reference
G42068	TrGC	$\text{CH}_3\text{CHOHO}_2 \rightarrow \text{CH}_3\text{CHO} + \text{HO}_2$	$3.46\text{E}12 \cdot \text{EXP}(-12500./ (1.98 \cdot \text{temp}))$	Hermans et al. (2005), Sander et al. (2018)
G42069	TrGC	$\text{CH}_3\text{CHO} + \text{HO}_2 \rightarrow \text{CH}_3\text{CHOHO}_2$	$3.46\text{E}12 \cdot \text{EXP}(-12500./ (1.98 \cdot \text{temp})) / (6.34\text{E}26 \cdot \text{EXP}(-14700./ (1.98 \cdot \text{temp})))$	Hermans et al. (2005), Sander et al. (2018)
G42070	TrGC	$\text{CH}_3\text{CHOHO}_2 + \text{HO}_2 \rightarrow .5 \text{CH}_3\text{CHOHOOH} + .3 \text{CH}_3\text{COOH} + .2 \text{CH}_3 + .2 \text{HCOOH} + .2 \text{OH}$	$5.6\text{E}-15 \cdot \text{EXP}(2300./ \text{temp})$	Sander et al. (2018)
G42071	TrGC	$\text{CH}_3\text{CHOHO}_2 \rightarrow \text{CH}_3 + \text{HCOOH} + \text{OH}$	k1_R02s0R02	Sander et al. (2018)
G42072	TrGCN	$\text{CH}_3\text{CHOHO}_2 + \text{NO} \rightarrow \text{CH}_3 + \text{HCOOH} + \text{OH} + \text{NO}_2$	KR02N0	Sander et al. (2018)
G42073	TrGCN	$\text{C}_2\text{H}_5\text{ONO}_2 + \text{OH} \rightarrow \text{CH}_3\text{CHO} + \text{H}_2\text{O} + \text{NO}_2$	$6.7\text{E}-13 \cdot \text{EXP}(-395./ \text{temp})$	Atkinson et al. (2006)
G42074a	TrGCN	$\text{NO}_3\text{CH}_2\text{CHO} + \text{OH} \rightarrow \text{GLYOX} + \text{NO}_2 + \text{H}_2\text{O}$	k_s*f_ch2ono2*f_cho	Paulot et al. (2009a), Sander et al. (2018)*
G42074b	TrGCN	$\text{NO}_3\text{CH}_2\text{CHO} + \text{OH} \rightarrow \text{NO}_3\text{CH}_2\text{CO}_3 + \text{H}_2\text{O}$	k_t*f_o*f_ch2ono2*3.	Paulot et al. (2009a), Sander et al. (2018)*
G42075	TrGCN	$\text{NO}_3\text{CH}_2\text{CO}_3 + \text{HO}_2 \rightarrow \text{HCHO} + \text{NO}_2 + \text{CO}_2 + \text{OH}$	KAPH02	Rickard and Pascoe (2009)*
G42076	TrGCN	$\text{NO}_3\text{CH}_2\text{CO}_3 + \text{NO} \rightarrow \text{HCHO} + \text{NO}_2 + \text{CO}_2 + \text{NO}_2$	KAPN0	Rickard and Pascoe (2009)
G42077	TrGCN	$\text{NO}_3\text{CH}_2\text{CO}_3 + \text{NO}_2 \rightarrow \text{NO}_3\text{CH}_2\text{CHO}$	k_CH3CO3_N02	Rickard and Pascoe (2009)
G42078	TrGCN	$\text{NO}_3\text{CH}_2\text{CO}_3 \rightarrow \text{HCHO} + \text{NO}_2 + \text{CO}_2$	k1_R02RC03	Rickard and Pascoe (2009)*
G42079	TrGCN	$\text{NO}_3\text{CH}_2\text{CHO} \rightarrow \text{NO}_3\text{CH}_2\text{CO}_3 + \text{NO}_2$	k_PAN_M	Rickard and Pascoe (2009)
G42080	StTrGCN	$\text{C}_2\text{H}_5\text{O}_2 + \text{NO}_2 \rightarrow \text{C}_2\text{H}_5\text{O}_2\text{NO}_2$	k_3rd_iupac(temp, cair, 1.3E-29, 6.2, 8.8E-12, 0.0, 0.31)	Atkinson et al. (2006)
G42081	StTrGCN	$\text{C}_2\text{H}_5\text{O}_2\text{NO}_2 \rightarrow \text{C}_2\text{H}_5\text{O}_2 + \text{NO}_2$	k_3rd_iupac(temp, cair, REAL(4.8E-4*EXP(-9285./temp), SP), 0.0, REAL(8.8E15*EXP(-10440./temp), SP), 0.0, 0.31)	Atkinson et al. (2006)
G42082	StTrGCN	$\text{C}_2\text{H}_5\text{O}_2\text{NO}_2 + \text{OH} \rightarrow \text{CH}_3\text{CHO} + \text{NO}_3 + \text{H}_2\text{O}$	$9.5\text{E}-13 \cdot \text{EXP}(-650./ \text{temp})$	Sander et al. (2018)*
G42083a	TrGC	$\text{CH}_3\text{C}(\text{O}) + \text{O}_2 \rightarrow \text{CH}_3\text{C}(\text{O})\text{OO}$	$5.1\text{E}-12 \cdot (1. - 1./ (1. + 9.4\text{E}-18 \cdot \text{cair}))$	Atkinson et al. (2006), Beyersdorf et al. (2010)*
G42083b	TrGC	$\text{CH}_3\text{C}(\text{O}) + \text{O}_2 \rightarrow \text{OH} + \text{HCHO} + \text{CO}$	$5.1\text{E}-12 \cdot 1./ (1. + 9.4\text{E}-18 \cdot \text{cair})$	Atkinson et al. (2006), Beyersdorf et al. (2010)*
G42084	TrGC	$\text{C}_2\text{H}_5\text{OH} + \text{OH} \rightarrow .95 \text{C}_2\text{H}_5\text{O}_2 + .95 \text{HO}_2 + .05 \text{HOCH}_2\text{CH}_2\text{O}_2 + \text{H}_2\text{O}$	$3.0\text{E}-12 \cdot \text{EXP}(20./ \text{temp})$	Sander et al. (2018), Atkinson et al. (2006)
G42085a	TrGCN	$\text{CH}_3\text{CN} + \text{OH} \rightarrow \text{NCCH}_2\text{O}_2 + \text{H}_2\text{O}$	$8.1\text{E}-13 \cdot \text{EXP}(-1080./ \text{temp}) \cdot 0.40$	Atkinson et al. (2006), Tyndall et al. (2001b)*

10

Table 1: Gas phase reactions (... continued)

#	labels	reaction	rate coefficient	reference
G42085b	TrGCN	$\text{CH}_3\text{CN} + \text{OH} \rightarrow \text{OH} + \text{CH}_3\text{C}(\text{O}) + \text{NO}$	$8.1\text{E}-13 \cdot \text{EXP}(-1080./ \text{temp}) \cdot (1. - 0.40)$	Atkinson et al. (2006), Tyndall et al. (2001b)*
G42086a	TrGCN	$\text{CH}_3\text{CN} + \text{O}(^1\text{D}) \rightarrow \text{O}(^3\text{P}) + \text{CH}_3\text{CN}$	$2.54\text{E}-10 \cdot \text{EXP}(-24./ \text{temp}) \cdot 0.0269 \cdot \text{EXP}(137./ \text{temp})$	Strekowski et al. (2010)
G42086b	TrGCN	$\text{CH}_3\text{CN} + \text{O}(^1\text{D}) \rightarrow 2 \text{H} + \text{CO} + \text{HCN}$	$2.54\text{E}-10 \cdot \text{EXP}(-24./ \text{temp}) \cdot 0.16$	Strekowski et al. (2010)*
G42086c	TrGCN	$\text{CH}_3\text{CN} + \text{O}(^1\text{D}) \rightarrow .5 \text{CH}_3 + .5 \text{NCO} + .5 \text{NCCH}_2\text{O}_2 + .5 \text{OH}$	$2.54\text{E}-10 \cdot \text{EXP}(-24./ \text{temp}) \cdot (1. - (0.16 + 0.0269 \cdot \text{EXP}(137./ \text{temp})))$	Strekowski et al. (2010)*
G42087	TrGCN	$\text{NCCH}_2\text{O}_2 + \text{NO} \rightarrow \text{HCN} + \text{CO}_2 + \text{HO}_2 + \text{NO}_2$	KR02N0	see note*
G42088	TrGCN	$\text{NCCH}_2\text{O}_2 + \text{HO}_2 \rightarrow \text{HCN} + \text{CO}_2 + \text{HO}_2$	KR02HO2(2)	see note*
G42089a	TrGC	$\text{CH}_2\text{CHOH} + \text{OH} \rightarrow \text{HCOOH} + \text{OH} + \text{HCHO}$	k_CH2CHOH_OH_HCOOH	Sander et al. (2018), So et al. (2014)*
G42089b	TrGC	$\text{CH}_2\text{CHOH} + \text{OH} \rightarrow \text{HOCH}_2\text{CHO} + \text{HO}_2$	k_CH2CHOH_OH_ALD	Sander et al. (2018), So et al. (2014)
G42090	TrGC	$\text{CH}_2\text{CHOH} + \text{HCOOH} \rightarrow \text{CH}_3\text{CHO} + \text{HCOOH}$	k_CH2CHOH_HCOOH	Sander et al. (2018), da Silva (2010)*
G42091	TrGC	$\text{CH}_3\text{CHO} + \text{HCOOH} \rightarrow \text{CH}_2\text{CHOH} + \text{HCOOH}$	k_ALD_HCOOH	Sander et al. (2018), da Silva (2010)*
G43000a	TrGC	$\text{C}_3\text{H}_8 + \text{OH} \rightarrow \text{iC}_3\text{H}_7\text{O}_2 + \text{H}_2\text{O}$	k_s	Sander et al. (2018)
G43000b	TrGC	$\text{C}_3\text{H}_8 + \text{OH} \rightarrow \text{C}_3\text{H}_7\text{O}_2 + \text{H}_2\text{O}$	2.*k_p	Sander et al. (2018)
G43001a	TrGC	$\text{C}_3\text{H}_6 + \text{O}_3 \rightarrow \text{HCHO} + .16 \text{CH}_3\text{CHOHOOH} + .50 \text{OH} + .50 \text{HCOCH}_2\text{O}_2 + .05 \text{CH}_2\text{CO} + .09 \text{CH}_3\text{OH} + .09 \text{CO} + .2 \text{CH}_4 + .2 \text{CO}_2$	$5.5\text{E}-15 \cdot \text{EXP}(-1880./ \text{temp}) \cdot 57$	Atkinson et al. (2006)*
G43001b	TrGC	$\text{C}_3\text{H}_6 + \text{O}_3 \rightarrow \text{CH}_3\text{CHO} + \text{CH}_2\text{OO}^*$	$5.5\text{E}-15 \cdot \text{EXP}(-1880./ \text{temp}) \cdot 43$	Atkinson et al. (2006)*
G43002	TrGC	$\text{C}_3\text{H}_6 + \text{OH} \rightarrow \text{HYPROPO}_2$	k_3rd_iupac(temp, cair, 8.6E-27, 3.5, 3.E-11, 1., 0.5)	Atkinson et al. (2006), Rickard and Pascoe (2009)
G43003	TrGCN	$\text{C}_3\text{H}_6 + \text{NO}_3 \rightarrow \text{PRONO}_3\text{BO}_2$	$4.6\text{E}-13 \cdot \text{EXP}(-1155./ \text{temp})$	Wallington et al. (2018)
G43004	TrGC	$\text{iC}_3\text{H}_7\text{O}_2 + \text{HO}_2 \rightarrow \text{iC}_3\text{H}_7\text{OOH}$	$1.9\text{E}-13 \cdot \text{EXP}(1300./ \text{temp})$	Atkinson (1997)*
G43005a	TrGCN	$\text{iC}_3\text{H}_7\text{O}_2 + \text{NO} \rightarrow \text{CH}_3\text{COCH}_3 + \text{HO}_2 + \text{NO}_2$	$2.7\text{E}-12 \cdot \text{EXP}(360./ \text{temp}) \cdot (1. - \alpha_{\text{AN}}(3, 2, 0, 0, \text{temp}, \text{cair}))$	Wallington et al. (2018)
G43005b	TrGCN	$\text{iC}_3\text{H}_7\text{O}_2 + \text{NO} \rightarrow \text{iC}_3\text{H}_7\text{ONO}_2$	$2.7\text{E}-12 \cdot \text{EXP}(360./ \text{temp}) \cdot \alpha_{\text{AN}}(3, 2, 0, 0, \text{temp}, \text{cair})$	Wallington et al. (2018)
G43006	TrGC	$\text{iC}_3\text{H}_7\text{O}_2 \rightarrow .8 \text{CH}_3\text{COCH}_3 + .2 \text{IPROPOL} + .6 \text{HO}_2$	$2. \cdot (1.6\text{E}-12 \cdot \text{EXP}(-2200./ \text{temp}) \cdot \text{k}_{\text{CH3O2}}) \cdot (5) \cdot \text{RD2}$	Rickard and Pascoe (2009), Atkinson et al. (2006)
G43007a	TrGC	$\text{iC}_3\text{H}_7\text{OOH} + \text{OH} \rightarrow \text{iC}_3\text{H}_7\text{O}_2 + \text{H}_2\text{O}$	k_roohro	Sander et al. (2018)
G43007b	TrGC	$\text{iC}_3\text{H}_7\text{OOH} + \text{OH} \rightarrow \text{CH}_3\text{COCH}_3 + \text{H}_2\text{O} + \text{OH}$	k_t*f_tooh	Sander et al. (2018)

11

Table 1: Gas phase reactions (... continued)

#	labels	reaction	rate coefficient	reference
G43008	TrGC	$C_3H_7O_2 + HO_2 \rightarrow C_3H_7OOH$	$1.9E-13*EXP(1300./temp)$	Atkinson (1997)*
G43009a	TrGCN	$C_3H_7O_2 + NO \rightarrow C_2H_5CHO + HO_2 + NO_2$	$2.7E-12*EXP(360./temp)*(1-alpha_{AN}(3,1,0,0,0,temp,cair))$	Wallington et al. (2018)
G43009b	TrGCN	$C_3H_7O_2 + NO \rightarrow C_3H_7ONO_2$	$2.7E-12*EXP(360./temp)*alpha_{AN}(3,1,0,0,0,temp,cair)$	Wallington et al. (2018)
G43010	TrGC	$C_3H_7O_2 \rightarrow .8 CH_3COCH_3 + .2 NPROPOL + .6 HO_2$	$2.*(k_{CH3O2*3.E-13})**(5)*R02$	Rickard and Pascoe (2009), Atkinson et al. (2006)
G43011	TrGC	$CH_3COCH_3 + OH \rightarrow CH_3COCH_2O_2 + H_2O$	$(8.8E-12*EXP(-1320./temp) + 1.7E-14*EXP(423./temp))$	Atkinson et al. (2006)*
G43012a	TrGC	$CH_3COCH_2O_2 + HO_2 \rightarrow CH_3COCH_2O_2H$	$8.6E-13*EXP(700./temp)*rcoch2o2_{ooh}$	Tyndall et al. (2001a), Sander et al. (2018)
G43012b	TrGC	$CH_3COCH_2O_2 + HO_2 \rightarrow OH + CH_3C(O) + HCHO$	$8.6E-13*EXP(700./temp)*rcoch2o2_{oh}$	Tyndall et al. (2001a), Sander et al. (2018)
G43013a	TrGCN	$CH_3COCH_2O_2 + NO \rightarrow CH_3C(O) + HCHO + NO_2$	$2.9E-12*EXP(300./temp)*(1-alpha_{AN}(4,1,1,0,0,temp,cair))$	Burkholder et al. (2015)
G43013b	TrGCN	$CH_3COCH_2O_2 + NO \rightarrow NOA$	$2.9E-12*EXP(300./temp)*alpha_{AN}(4,1,1,0,0,temp,cair)$	Burkholder et al. (2015)
G43014	TrGC	$CH_3COCH_2O_2 \rightarrow .3 CH_3C(O) + .3 HCHO + .5 MGLYOX + .2 CH_3COCH_2OH$	$k1_{R02pR02}$	Orlando and Tyndall (2012)
G43015a	TrGC	$CH_3COCH_2O_2H + OH \rightarrow CH_3COCH_2O_2 + H_2O$	k_{roohro}	see note*
G43015b	TrGC	$CH_3COCH_2O_2H + OH \rightarrow MGLYOX + OH + H_2O$	$k_{s*f_{sooh*f_{co}}}$	Sander et al. (2018)
G43016	TrGC	$CH_3COCH_2OH + OH \rightarrow MGLYOX + HO_2 + H_2O$	$1.6E-12*EXP(305./temp)$	Rickard and Pascoe (2006)
G43017	TrGC	$MGLYOX + OH \rightarrow .4 CH_3 + .6 CH_3C(O) + 1.4 CO + H_2O$	$1.9E-12*EXP(575./temp)$	Baeza-Romero et al. (2007), Atkinson et al. (2006)
G43020	TrGCN	$iC_3H_7ONO_2 + OH \rightarrow CH_3COCH_3 + NO_2$	$6.2E-13*EXP(-230./temp)$	Wallington et al. (2018)
G43021	TrGCN	$CH_3COCH_2O_2 + NO_3 \rightarrow CH_3C(O) + HCHO + NO_2$	$KR02N03$	Rickard and Pascoe (2009)
G43022	TrGC	$HYPPOPO_2 \rightarrow CH_3CHO + HCHO + HO_2$	$k1_{R02sR02}$	Rickard and Pascoe (2009)
G43023a	TrGC	$HYPPOPO_2 + HO_2 \rightarrow HYPPOPO_2H$	$KR02H02(3)*(1-rchohch2o2_{oh})$	Rickard and Pascoe (2009)
G43023b	TrGC	$HYPPOPO_2 + HO_2 \rightarrow CH_3CHO + HCHO + HO_2 + OH$	$KR02H02(3)*rchohch2o2_{oh}$	Rickard and Pascoe (2009)
G43024a	TrGCN	$HYPPOPO_2 + NO \rightarrow CH_3CHO + HCHO + HO_2 + NO_2$	$KR02N0*(1-alpha_{AN}(4,1,0,0,0,temp,cair))$	Rickard and Pascoe (2009)
G43024b	TrGCN	$HYPPOPO_2 + NO \rightarrow PROPOLNO_3$	$KR02N0*alpha_{AN}(4,1,0,0,0,temp,cair)$	Rickard and Pascoe (2009)
G43025	TrGCN	$HYPPOPO_2 + NO_3 \rightarrow CH_3CHO + HCHO + HO_2 + NO_2$	$KR02N03$	Rickard and Pascoe (2009)
G43026a	TrGC	$HYPPOPO_2H + OH \rightarrow HYPPOPO_2$	k_{roohro}	Rickard and Pascoe (2009)

12

Table 1: Gas phase reactions (... continued)

#	labels	reaction	rate coefficient	reference
G43026b	TrGC	$HYPPOPO_2H + OH \rightarrow CH_3COCH_2OH + OH$	$(k_{s*f_{soh*f_{pch2oh}+k_{t*f_{tooh*f_{pch2oh}}}})$	Sander et al. (2018)
G43027	TrGCN	$PRONO_3BO_2 + HO_2 \rightarrow PR_2O_2HNO_3$	$KR02H02(3)$	Rickard and Pascoe (2009)
G43028	TrGCN	$PRONO_3BO_2 + NO \rightarrow NOA + HO_2 + NO_2$	$KR02N0$	Rickard and Pascoe (2009)*
G43029	TrGCN	$PRONO_3BO_2 + NO_3 \rightarrow NOA + HO_2 + NO_2$	$KR02N03$	Rickard and Pascoe (2009)
G43030a	TrGCN	$PR_2O_2HNO_3 + OH \rightarrow PRONO_3BO_2$	k_{roohro}	Rickard and Pascoe (2009)
G43030b	TrGCN	$PR_2O_2HNO_3 + OH \rightarrow NOA + OH$	$k_{t*f_{tooh*f_{ch2ono2}}}$	Sander et al. (2018)
G43031	TrGCN	$MGLYOX + NO_3 \rightarrow CH_3C(O) + CO + HNO_3$	$KN03AL*2.4$	Rickard and Pascoe (2009)
G43032	TrGCN	$NOA + OH \rightarrow MGLYOX + NO_2$	$(k_{s*f_{co*f_{ono2}+k_{p*f_{co}}})$	Sander et al. (2018)
G43033	TrGC	$HOCH_2COCHO + OH \rightarrow .8609 HOCH_2CO + .8609 CO + .1391 HCOCOCHO + .1391 HO_2$	$(1.9E-12*EXP(575./temp))+k_{s*f_{soh*f_{co}}}$	Sander et al. (2018)
G43034	TrGCN	$HOCH_2COCHO + NO_3 \rightarrow HOCH_2CO + CO + HNO_3$	$KN03AL*2.4$	Sander et al. (2018)
G43035	TrGC	$CH_3COCO_2H + OH \rightarrow CH_3C(O) + H_2O + CO_2$	$4.9E-14*EXP(276./temp)$	Mellouki and Mu (2003), Sander et al. (2018)
G43036	TrGC	$HCOCOCH_2O_2 \rightarrow .6 HCOCO + .6 HCHO + .2 HCOCOCHO + .2 HOCH_2COCHO$	$k1_{R02pR02}$	Sander et al. (2018)
G43037	TrGCN	$HCOCOCH_2O_2 + NO \rightarrow HCOCO + HCHO + NO_2$	$KR02N0$	Sander et al. (2018)*
G43038a	TrGC	$HCOCOCH_2O_2 + HO_2 \rightarrow HCOCOCH_2OOH$	$KR02H02(3)*rcoch2o2_{ooh}$	Sander et al. (2018)
G43038b	TrGC	$HCOCOCH_2O_2 + HO_2 \rightarrow HCOCO + HCHO + OH$	$KR02H02(3)*rcoch2o2_{oh}$	Sander et al. (2018)
G43039	TrGCN	$HCOCOCH_2O_2 + NO_3 \rightarrow HCOCO + HCHO + NO_2$	$KR02N03$	Sander et al. (2018)
G43040a	TrGC	$HCOCOCH_2OOH + OH \rightarrow HOCH_2CO_3 + CO + H_2O$	$k_{t*f_{co*f_{o}}}$	Sander et al. (2018)*
G43040b	TrGC	$HCOCOCH_2OOH + OH \rightarrow HCOCOCHO + H_2O + OH$	$k_{s*f_{sooh*f_{co}}}$	Sander et al. (2018)*
G43040c	TrGC	$HCOCOCH_2OOH + OH \rightarrow HCOCOCH_2O_2 + H_2O$	k_{roohro}	Sander et al. (2018)
G43041	TrGCN	$HCOCOCH_2OOH + NO_3 \rightarrow HOCH_2CO_3 + CO + HNO_3$	$KN03AL*2.4$	Sander et al. (2018)
G43042	TrGC	$HOCH_2COCH_2O_2 \rightarrow HCHO + HOCH_2CO$	$k1_{R02pR02}$	Sander et al. (2018)
G43043a	TrGC	$HOCH_2COCH_2O_2 + HO_2 \rightarrow HOCH_2COCH_2OOH$	$KR02H02(3)*rcoch2o2_{ooh}$	Sander et al. (2018)
G43043b	TrGC	$HOCH_2COCH_2O_2 + HO_2 \rightarrow HCHO + HOCH_2CO + OH$	$KR02H02(3)*rcoch2o2_{oh}$	Sander et al. (2018)
G43044	TrGCN	$HOCH_2COCH_2O_2 + NO \rightarrow HCHO + HOCH_2CO + NO_2$	$KR02N0$	Sander et al. (2018)*
G43045a	TrGC	$HOCH_2COCH_2OOH + OH \rightarrow HOCH_2COCHO + OH$	$k_{s*f_{sooh*f_{co}}}$	Sander et al. (2018)
G43045b	TrGC	$HOCH_2COCH_2OOH + OH \rightarrow HOCH_2COCH_2O_2$	k_{roohro}	Sander et al. (2018)
G43045c	TrGC	$HOCH_2COCH_2OOH + OH \rightarrow HCOCOCH_2OOH + HO_2$	$1.60E-12*EXP(305./temp)$	Sander et al. (2018)*
G43046	TrGC	$CH_3COCO + OH \rightarrow .72 CO + .72 CH_3CHO + .72 HO_2 + .21 CH_3COCO_2H + .07 CH_3CHO + .07 HO_2 + .07 CO_2$	$7.6E-11$	Hatakeyama et al. (1985), Sander et al. (2018)
G43047	TrGCN	$PROPOLNO_3 + OH \rightarrow CH_3COCH_2OH + NO_2$	$k_{t*f_{ono2*f_{pch2oh}+k_{s*f_{soh*f_{ch2ono2}}}}}$	Sander et al. (2018)

13

Table 1: Gas phase reactions (... continued)

#	labels	reaction	rate coefficient	reference
G43048	TrGCN	$\text{CH}_3\text{COCH}_2\text{O}_2 + \text{NO}_2 \rightarrow \text{CH}_3\text{COCH}_2\text{OONO}_2$	$2.3\text{E}-12 \cdot \text{EXP}(300./\text{temp})$	Tyndall et al. (2001a)*
G43049	TrGCN	$\text{CH}_3\text{COCH}_2\text{OONO}_2 \rightarrow \text{CH}_3\text{COCH}_2\text{O}_2 + \text{NO}_2$	$1.9\text{E}16 \cdot \text{EXP}(-10830./\text{temp})$	Sehested et al. (1998)*
G43050	TrGCN	$\text{CH}_3\text{COCH}_2\text{OONO}_2 + \text{OH} \rightarrow \text{MGLYOX} + \text{NO}_3 + \text{H}_2\text{O}$	$9.50\text{E}-13 \cdot \text{EXP}(-650./\text{temp}) \cdot \text{f_co}$	Sander et al. (2018)*
G43051a	TrGC	$\text{C}_3\text{H}_7\text{OOH} + \text{OH} \rightarrow \text{C}_3\text{H}_7\text{O}_2 + \text{H}_2\text{O}$	k_{roohro}	Sander et al. (2018)
G43051b	TrGC	$\text{C}_3\text{H}_7\text{OOH} + \text{OH} \rightarrow \text{C}_2\text{H}_5\text{CHO} + \text{H}_2\text{O} + \text{OH}$	$k_{\text{s*f_sooh}}$	Sander et al. (2018)
G43051c	TrGC	$\text{C}_3\text{H}_7\text{OOH} + \text{OH} \rightarrow \text{C}_2\text{H}_5\text{CHO} + \text{HO}_2 + \text{H}_2\text{O}$	$k_{\text{s*f_pch2oh}}$	Sander et al. (2018)*
G43052	TrGC	$\text{C}_2\text{H}_5\text{CHO} + \text{OH} \rightarrow \text{C}_2\text{H}_5\text{CO}_3 + \text{H}_2\text{O}$	$4.9\text{E}-12 \cdot \text{EXP}(405./\text{temp})$	Atkinson et al. (2006)*
G43053	TrGCN	$\text{C}_2\text{H}_5\text{CHO} + \text{NO}_3 \rightarrow \text{C}_2\text{H}_5\text{CO}_3 + \text{HNO}_3$	$6.3\text{E}-15$	Atkinson et al. (2006)
G43054a	TrGC	$\text{C}_2\text{H}_5\text{CO}_3 \rightarrow \text{C}_2\text{H}_5\text{O}_2 + \text{CO}_2$	$k1_{\text{R02RC03}} \cdot 0.9$	Sander et al. (2018)
G43054b	TrGC	$\text{C}_2\text{H}_5\text{CO}_3 \rightarrow \text{C}_2\text{H}_5\text{CO}_2\text{H}$	$k1_{\text{R02RC03}} \cdot 0.1$	Sander et al. (2018)
G43055a	TrGC	$\text{C}_2\text{H}_5\text{CO}_3 + \text{HO}_2 \rightarrow \text{C}_2\text{H}_5\text{O}_2 + \text{CO}_2 + \text{OH}$	KAPH02*rc03_oh	Sander et al. (2018), Groß et al. (2014)
G43055b	TrGC	$\text{C}_2\text{H}_5\text{CO}_3 + \text{HO}_2 \rightarrow \text{C}_2\text{H}_5\text{CO}_3\text{H}$	KAPH02*rc03_ooh	Sander et al. (2018), Groß et al. (2014)
G43055c	TrGC	$\text{C}_2\text{H}_5\text{CO}_3 + \text{HO}_2 \rightarrow \text{C}_2\text{H}_5\text{CO}_2\text{H} + \text{O}_3$	KAPH02*rc03_o3	Sander et al. (2018), Groß et al. (2014)
G43056	TrGCN	$\text{C}_2\text{H}_5\text{CO}_3 + \text{NO} \rightarrow \text{NO}_2 + \text{C}_2\text{H}_5\text{O}_2 + \text{CO}_2$	KAPNO	Rickard and Pascoe (2009)
G43057	TrGCN	$\text{C}_2\text{H}_5\text{CO}_3 + \text{NO}_2 \rightarrow \text{PPN}$	$k_{\text{CH3CO3_NO2}}$	Rickard and Pascoe (2009)
G43058	TrGCN	$\text{PPN} \rightarrow \text{C}_2\text{H}_5\text{CO}_3 + \text{NO}_2$	$k_{\text{PAN_M}}$	Rickard and Pascoe (2009)
G43059	TrGC	$\text{C}_2\text{H}_5\text{CO}_3\text{H} + \text{OH} \rightarrow \text{CH}_3\text{CHO} + \text{CO}_2 + \text{H}_2\text{O}$	$k_{\text{co2h+k_p+k_s*f_co2h}}$	Sander et al. (2018)*
G43060a	TrGC	$\text{C}_2\text{H}_5\text{CO}_3\text{H} + \text{OH} \rightarrow \text{C}_2\text{H}_5\text{CO}_3 + \text{H}_2\text{O}$	k_{roohro}	Sander et al. (2018)
G43060b	TrGC	$\text{C}_2\text{H}_5\text{CO}_3\text{H} + \text{OH} \rightarrow \text{CH}_3\text{CHO} + \text{CO}_2 + \text{H}_2\text{O}$	$k_{\text{s*f_co2h+k_p}}$	Sander et al. (2018)*
G43061	TrGCN	$\text{PPN} + \text{OH} \rightarrow \text{CH}_3\text{CHO} + \text{CO}_2 + \text{NO}_2 + \text{H}_2\text{O}$	$k_{\text{s*f_cpan+k_p}}$	Sander et al. (2018)*
G43062	TrGC	$\text{CH}_3\text{COCOC}_3\text{H} + \text{OH} \rightarrow \text{CH}_3\text{COCOC}_3 + \text{H}_2\text{O}$	k_{roohro}	Sander et al. (2018)
G43063a	TrGC	$\text{CH}_3\text{COCOC}_3 + \text{HO}_2 \rightarrow \text{CH}_3\text{C}(\text{O}) + \text{CO}_2 + \text{OH}$	KAPH02*rc03_oh	Sander et al. (2018)
G43063b	TrGC	$\text{CH}_3\text{COCOC}_3 + \text{HO}_2 \rightarrow \text{CH}_3\text{COCOC}_3\text{H}$	$\text{KAPH02*(rc03_ooh+rc03_o3)}$	Sander et al. (2018)
G43064	TrGCN	$\text{CH}_3\text{COCOC}_3 + \text{NO} \rightarrow \text{CH}_3\text{C}(\text{O}) + \text{CO}_2 + \text{NO}_2$	KAPNO	Sander et al. (2018)
G43065	TrGCN	$\text{CH}_3\text{COCOC}_3 + \text{NO}_2 \rightarrow \text{CH}_3\text{C}(\text{O}) + \text{CO}_2 + \text{NO}_3$	$k_{\text{CH3CO3_NO2}}$	Sander et al. (2018)*
G43066	TrGCN	$\text{CH}_3\text{COCOC}_3 + \text{NO}_3 \rightarrow \text{CH}_3\text{C}(\text{O})\text{OO} + \text{CO}_2 + \text{NO}_2$	$\text{KR02N03} \cdot 1.74$	Sander et al. (2018)
G43067	TrGC	$\text{CH}_3\text{COCOC}_3 \rightarrow \text{CH}_3\text{C}(\text{O})\text{OO} + \text{CO}_2$	$k1_{\text{R02RC03}}$	Sander et al. (2018)
G43068	TrGC	$\text{HCOCOCHO} + \text{OH} \rightarrow 3 \text{CO} + \text{HO}_2$	$2 \cdot k_{\text{t*f_co*f_o}}$	Sander et al. (2018)
G43069	TrGC	$\text{IPROPOL} + \text{OH} \rightarrow \text{CH}_3\text{COCH}_3 + \text{HO}_2 + \text{H}_2\text{O}$	$4.6\text{E}-12 \cdot \text{EXP}(200./\text{temp})$	Atkinson et al. (2006)
G43070a	TrGC	$\text{NPROPOL} + \text{OH} \rightarrow \text{C}_2\text{H}_5\text{CHO} + \text{HO}_2 + \text{H}_2\text{O}$	$4.6\text{E}-12 \cdot \text{EXP}(70./\text{temp}) \cdot (k_{\text{s*f_soh}} / (k_{\text{p+k_s*f_pch2oh+k_s*f_soh}}))$	Atkinson et al. (2006), Sander et al. (2018)*

14

Table 1: Gas phase reactions (... continued)

#	labels	reaction	rate coefficient	reference
G43070b	TrGC	$\text{NPROPOL} + \text{OH} \rightarrow \text{HYPROPO2} + \text{H}_2\text{O}$	$4.6\text{E}-12 \cdot \text{EXP}(70./\text{temp}) \cdot ((k_{\text{p+k_s*f_pch2oh}}) / (k_{\text{p+k_s*f_pch2oh+k_s*f_soh}}))$	Atkinson et al. (2006), Sander et al. (2018)*
G43071a	TrGC	$\text{CH}_2\text{CHCH}_2\text{OH} + \text{OH} \rightarrow \text{HCOOH} + \text{OH} + \text{CH}_3\text{CHO}$	$k_{\text{CH2CHOH_OH_HCOOH}}$	Sander et al. (2018), So et al. (2014)*
G43072	TrGC	$\text{CH}_2\text{CHCH}_2\text{OH} + \text{HCOOH} \rightarrow \text{C}_2\text{H}_5\text{CHO} + \text{HCOOH}$	$k_{\text{CH2CHOH_HCOOH}}$	Sander et al. (2018), da Silva (2010)*
G43073	TrGC	$\text{C}_2\text{H}_5\text{CHO} + \text{HCOOH} \rightarrow \text{CH}_2\text{CHCH}_2\text{OH} + \text{HCOOH}$	$k_{\text{ALD_HCOOH}}$	Sander et al. (2018), da Silva (2010)*
G43074	TrGC	$\text{HCOCOCH}_2\text{OOH} + \text{OH} \rightarrow \text{HCOCO} + \text{CO} + \text{HO}_2 + \text{OH}$	$k_{\text{s*f_sooh*f_co+k_roohro}}$	Sander et al. (2018)*
G43202	TrGTerC	$\text{HCOCH}_2\text{CHO} + \text{OH} \rightarrow \text{HCOCH}_2\text{CO}_3$	$4.29\text{E}-11$	Rickard and Pascoe (2009)
G43203	TrGTerCN	$\text{HCOCH}_2\text{CHO} + \text{NO}_3 \rightarrow \text{HCOCH}_2\text{CO}_3 + \text{HNO}_3$	$2 \cdot \text{KN03AL} \cdot 2.4$	Rickard and Pascoe (2009)
G43204a	TrGTerC	$\text{HCOCH}_2\text{CO}_3 \rightarrow \text{HCOCH}_2\text{O}_2 + \text{CO}_2$	$k1_{\text{R02RC03}} \cdot 0.9$	Sander et al. (2018)
G43204b	TrGTerC	$\text{HCOCH}_2\text{CO}_3 \rightarrow \text{HCOCH}_2\text{CO}_2\text{H}$	$k1_{\text{R02RC03}} \cdot 0.1$	Sander et al. (2018)
G43205	TrGTerCN	$\text{HCOCH}_2\text{CO}_3 + \text{NO} \rightarrow \text{HCOCH}_2\text{O}_2 + \text{CO}_2 + \text{NO}_2$	KAPNO	Rickard and Pascoe (2009)
G43206	TrGTerCN	$\text{HCOCH}_2\text{CO}_3 + \text{NO}_2 \rightarrow \text{C}_3\text{PAN2}$	$k_{\text{CH3CO3_NO2}}$	Rickard and Pascoe (2009)
G43207a	TrGTerC	$\text{HCOCH}_2\text{CO}_3 + \text{HO}_2 \rightarrow \text{HCOCH}_2\text{CO}_3\text{H}$	KAPH02*rc03_ooh	Rickard and Pascoe (2009)
G43207b	TrGTerC	$\text{HCOCH}_2\text{CO}_3 + \text{HO}_2 \rightarrow \text{HCOCH}_2\text{CO}_2\text{H} + \text{O}_3$	KAPH02*rc03_o3	Rickard and Pascoe (2009)
G43207c	TrGTerC	$\text{HCOCH}_2\text{CO}_3 + \text{HO}_2 \rightarrow \text{HCOCH}_2\text{O}_2 + \text{CO}_2 + \text{OH}$	KAPH02*rc03_oh	Rickard and Pascoe (2009)
G43210	TrGTerCN	$\text{C}_3\text{PAN2} \rightarrow \text{HCOCH}_2\text{CO}_3 + \text{NO}_2$	$k_{\text{PAN_M}}$	Rickard and Pascoe (2009)
G43211	TrGTerCN	$\text{C}_3\text{PAN2} + \text{OH} \rightarrow \text{GLYOX} + \text{CO} + \text{NO}_2$	$2.10\text{E}-11$	Rickard and Pascoe (2009)
G43212	TrGTerC	$\text{HCOCH}_2\text{CO}_2\text{H} + \text{OH} \rightarrow \text{HCOCH}_2\text{O}_2 + \text{CO}_2$	$2.14\text{E}-11$	Rickard and Pascoe (2009)
G43213a	TrGTerC	$\text{HOC}_2\text{H}_4\text{CO}_3 \rightarrow \text{HOC}_2\text{H}_2\text{O}_2 + \text{CO}_2$	$k1_{\text{R02RC03}} \cdot 0.9$	Sander et al. (2018)
G43213b	TrGTerC	$\text{HOC}_2\text{H}_4\text{CO}_3 \rightarrow \text{HOC}_2\text{H}_4\text{CO}_2\text{H}$	$k1_{\text{R02RC03}} \cdot 0.1$	Sander et al. (2018)
G43214	TrGTerCN	$\text{HOC}_2\text{H}_4\text{CO}_3 + \text{NO} \rightarrow \text{HOC}_2\text{H}_2\text{O}_2 + \text{CO}_2 + \text{NO}_2$	KAPNO	Rickard and Pascoe (2009)
G43215a	TrGTerC	$\text{HOC}_2\text{H}_4\text{CO}_3 + \text{HO}_2 \rightarrow \text{HOC}_2\text{H}_4\text{CO}_3\text{H}$	KAPH02*rc03_ooh	Rickard and Pascoe (2009)
G43215b	TrGTerC	$\text{HOC}_2\text{H}_4\text{CO}_3 + \text{HO}_2 \rightarrow \text{HOC}_2\text{H}_2\text{O}_2 + \text{CO}_2 + \text{OH}$	KAPH02*rc03_oh	Rickard and Pascoe (2009)
G43215c	TrGTerC	$\text{HOC}_2\text{H}_4\text{CO}_3 + \text{HO}_2 \rightarrow \text{HOC}_2\text{H}_4\text{CO}_2\text{H} + \text{O}_3$	KAPH02*rc03_o3	Rickard and Pascoe (2009)
G43218	TrGTerCN	$\text{HOC}_2\text{H}_4\text{CO}_3 + \text{NO}_2 \rightarrow \text{C}_3\text{PAN1}$	$k_{\text{CH3CO3_NO2}}$	Rickard and Pascoe (2009)
G43219	TrGTerC	$\text{HOC}_2\text{H}_4\text{CO}_2\text{H} + \text{OH} \rightarrow \text{HOC}_2\text{H}_2\text{O}_2 + \text{CO}_2$	$1.39\text{E}-11$	Rickard and Pascoe (2009)
G43220	TrGTerC	$\text{HOC}_2\text{H}_4\text{CO}_3\text{H} + \text{OH} \rightarrow \text{HOC}_2\text{H}_4\text{CO}_3$	$1.73\text{E}-11$	Rickard and Pascoe (2009)
G43221	TrGTerCN	$\text{C}_3\text{PAN1} \rightarrow \text{HOC}_2\text{H}_4\text{CO}_3 + \text{NO}_2$	$k_{\text{PAN_M}}$	Rickard and Pascoe (2009)
G43222	TrGTerCN	$\text{C}_3\text{PAN1} + \text{OH} \rightarrow \text{HOC}_2\text{H}_2\text{O}_2 + \text{CO} + \text{NO}_2$	$4.51\text{E}-12$	Rickard and Pascoe (2009)
G43223	TrGTerC	$\text{HCOCH}_2\text{CO}_3\text{H} + \text{OH} \rightarrow \text{HCOCH}_2\text{O}_2 + \text{CO}_2 + \text{H}_2\text{O}$	$2.49\text{E}-11$	Rickard and Pascoe (2009)*
G43415	TrGAroC	$\text{C3DIALOOH} + \text{OH} \rightarrow \text{HCOCOCHO} + \text{OH}$	$1.44\text{E}-10$	Rickard and Pascoe (2009)

15

Table 1: Gas phase reactions (... continued)

#	labels	reaction	rate coefficient	reference
G43418a	TrGAroC	C3DIALO2 + HO2 → C3DIALOOH	KR02H02(3)*(rco3_ooH+rco3_o3)	Rickard and Pascoe (2009)
G43418b	TrGAroC	C3DIALO2 + HO2 → GLYOX + CO + HO2 + OH	KR02H02(3)*rco3_oh	Rickard and Pascoe (2009)
G43419	TrGAroCN	C3DIALO2 + NO → GLYOX + CO + HO2 + NO2	KR02N0	Rickard and Pascoe (2009)*
G43420	TrGAroCN	C3DIALO2 + NO3 → GLYOX + CO + HO2 + NO2	KR02N03	Rickard and Pascoe (2009)*
G43421	TrGAroC	C3DIALO2 → GLYOX + CO + HO2	k1_R02sR02	Rickard and Pascoe (2009)*
G43422a	TrGAroC	HCOCOHC03 + HO2 → GLYOX + CO2 + HO2 + OH	KAPH02*rco3_oh	Rickard and Pascoe (2009)
G43422b	TrGAroC	HCOCOHC03 + HO2 → HCOCOHC03H	KAPH02*(rco3_ooH+rco3_o3)	Rickard and Pascoe (2009)
G43424	TrGAroCN	HCOCOHC03 + NO → GLYOX + CO2 + HO2 + NO2	KAPN0	Rickard and Pascoe (2009)
G43425	TrGAroCN	HCOCOHC03 + NO2 → HCOCOHPAN	k_CH3C03_N02	Rickard and Pascoe (2009)
G43426	TrGAroCN	HCOCOHC03 + NO3 → GLYOX + CO2 + HO2 + NO2	KR02N03*1.74	Rickard and Pascoe (2009)
G43427	TrGAroC	HCOCOHC03 → GLYOX + CO2 + HO2	k1_R02RC03	Rickard and Pascoe (2009)
G43428	TrGAroC	METACETHO + OH → CH3C(O) + CO2	9.82E-11	Rickard and Pascoe (2009)
G43442	TrGAroCN	HCOCOHPAN + OH → GLYOX + CO + NO2	6.97E-11	Rickard and Pascoe (2009)
G43443	TrGAroCN	HCOCOHPAN → HCOCOHC03 + NO2	k_PAN_M	Rickard and Pascoe (2009)
G43444	TrGAroC	C32OH13CO + OH → HCOCOHC03	1.36E-10	Rickard and Pascoe (2009)
G43446	TrGAroC	HCOCOHC03H + OH → HCOCOHC03	7.33E-11	Rickard and Pascoe (2009)
G44000	TrGC	C4H10 + OH → LC4H9O2 + H2O	2.03E-17*temp*temp*EXP(78./temp)	Atkinson et al. (2006)*
G44001a	TrGC	LC4H9O2 → C3H7CHO + HO2	(k1_R02pR02*0.1273+k1_R02sR02*0.8727)*0.1273	Rickard and Pascoe (2009), Sander et al. (2018)
G44001b	TrGC	LC4H9O2 → .636 MEK + .636 HO2 + .364 CH3CHO + .364 C2H5O2	(k1_R02pR02*0.1273+k1_R02sR02*0.8727)*0.8727	Rickard and Pascoe (2009), Sander et al. (2018)*
G44002	TrGC	LC4H9O2 + HO2 → LC4H9OOH	KR02H02(4)	Rickard and Pascoe (2009)
G44003a	TrGCN	LC4H9O2 + NO → NO2 + C3H7CHO + HO2	KR02N0*(1-(0.1273*alpha_AN(4,1,0,0,0,temp,cair))+0.8727*alpha_AN(4,2,0,0,0,temp,cair)))*0.1273	Rickard and Pascoe (2009), Sander et al. (2018)
G44003b	TrGCN	LC4H9O2 + NO → NO2 + .636 MEK + .636 HO2 + .364 CH3CHO + .364 C2H5O2	KR02N0*(1-(0.1273*alpha_AN(4,1,0,0,0,temp,cair))+0.8727*alpha_AN(4,2,0,0,0,temp,cair)))*0.8727	Rickard and Pascoe (2009), Sander et al. (2018)
G44003c	TrGCN	LC4H9O2 + NO → LC4H9NO3	KR02N0*(0.1273*alpha_AN(4,1,0,0,0,temp,cair))+0.8727*alpha_AN(4,2,0,0,0,temp,cair))	Rickard and Pascoe (2009)*
G44004a	TrGCN	LC4H9O2 + NO3 → NO2 + C3H7CHO + HO2	KR02N03*0.1273	Rickard and Pascoe (2009), Sander et al. (2018)
G44004b	TrGCN	LC4H9O2 + NO3 → NO2 + .636 MEK + .636 HO2 + .364 CH3CHO + .364 C2H5O2	KR02N03*0.8727	Rickard and Pascoe (2009), Sander et al. (2018)

16

Table 1: Gas phase reactions (... continued)

#	labels	reaction	rate coefficient	reference
G44005a	TrGC	LC4H9OOH + OH → LC4H9O2 + H2O	k_roohro	Sander et al. (2018)
G44005b	TrGC	LC4H9OOH + OH → C3H7CHO + H2O + OH	k_s*f_tooh*f_alk*(k_p/(k_p+k_s))	Sander et al. (2018)
G44005c	TrGC	LC4H9OOH + OH → MEK + H2O + OH	k_t*f_tooh*f_alk*(k_s/(k_p+k_s))	Sander et al. (2018)
G44006a	TrGC	iC4H10 + OH → TC4H9O2 + H2O	1.17E-17*temp*temp*EXP(213./temp)	Atkinson (2003)
G44006b	TrGC	iC4H10 + OH → IC4H9O2 + H2O	*k_t/(3.*k_p+k_t)	Atkinson (2003)
G44007	TrGC	TC4H9O2 → CH3COCH3 + CH3	1.17E-17*temp*temp*EXP(213./temp)	Atkinson (2003)
G44008	TrGC	TC4H9O2 → CH3COCH3 + CH3	k1_R02tR02	Rickard and Pascoe (2009), Sander et al. (2018)
G44009a	TrGCN	TC4H9O2 + NO → NO2 + CH3COCH3 + CH3	KR02H02(4)	Rickard and Pascoe (2009)
G44009b	TrGCN	TC4H9O2 + NO → TC4H9NO3	KR02N0*(1-alpha_AN(4,3,0,0,0,temp,cair))	Rickard and Pascoe (2009), Sander et al. (2018)
G44009c	TrGCN	TC4H9O2 + NO → TC4H9NO3	KR02N0*alpha_AN(4,3,0,0,0,temp,cair)	Rickard and Pascoe (2009)
G44010a	TrGC	TC4H9OOH + OH → TC4H9O2 + H2O	k_roohro	Sander et al. (2018)
G44010b	TrGC	TC4H9OOH + OH → CH3COCH3 + HCHO + OH + H2O	3.*k_p*f_tch2oh	Sander et al. (2018)*
G44011	TrGCN	TC4H9NO3 + OH → CH3COCH3 + HCHO + NO2 + H2O	3.*k_p*f_ch2ono2	Sander et al. (2018)*
G44012	TrGC	IC4H9O2 → IPRCHO	k1_R02sR02	Rickard and Pascoe (2009), Sander et al. (2018)
G44013	TrGC	IC4H9O2 + HO2 → IC4H9OOH	KR02H02(4)	Rickard and Pascoe (2009)
G44014a	TrGCN	IC4H9O2 + NO → NO2 + IPRCHO	KR02N0*(1-alpha_AN(4,2,0,0,0,temp,cair))	Rickard and Pascoe (2009), Sander et al. (2018)
G44014b	TrGCN	IC4H9O2 + NO → IC4H9NO3	KR02N0*alpha_AN(4,2,0,0,0,temp,cair)	Rickard and Pascoe (2009)
G44015a	TrGC	IC4H9OOH + OH → IC4H9O2 + H2O	k_roohro	Sander et al. (2018)
G44015b	TrGC	IC4H9OOH + OH → IPRCHO + OH + H2O	k_s*f_sooH+2.*k_s+k_t*f_pch2oh	Sander et al. (2018)*
G44016	TrGCN	IC4H9NO3 + OH → IPRCHO + NO2 + H2O	k_s*f_ono2+2.*k_p+k_t*f_ch2ono2	Sander et al. (2018)*
G44017	TrGC	MVK + O3 → .87 MGLYOX + .5481 CO + .1392 HO2 + .1392 OH + .3219 CH2OO + .13 HCHO + .04680 OH + .04680 CO + .07280 CH3C(O) + .026 CH3CHO + .026 CO2 + .026 HCHO + .026 HO2 + .02402 MGLYOX + .02402 H2O2 + .00718 CH3COCO2H	8.5E-16*EXP(-1520./temp)	Sander et al. (2018)
G44018	TrGC	MVK + OH → LHMVKABO2	2.6E-12*EXP(610./temp)	Sander et al. (2018), Atkinson et al. (2006)*

17

Table 1: Gas phase reactions (... continued)

#	labels	reaction	rate coefficient	reference
G44019	TrGC	MEK + OH → LMEKO2 + H ₂ O	1.5E-12*EXP(-90./temp)	Atkinson et al. (2006), Sander et al. (2018)*
G44020	TrGC	LMEKO2 + HO ₂ → LMEKOOH	KR02H02(4)	Sander et al. (2018)
G44021a	TrGCN	LMEKO2 + NO → .62 CH ₃ CHO + .62 CH ₃ C(O) + .38 HCHO + .38 CO ₂ + .38 HOCH ₂ CH ₂ O ₂ + NO ₂	KR02N0*(1-(.62*alpha_AN(4,2,1,0,0,temp,cair)+.38*alpha_AN(4,1,0,1,0,temp,cair)))	Sander et al. (2018)*
G44021b	TrGCN	LMEKO2 + NO → LMEKNO3	KR02N0*(.62*alpha_AN(4,2,1,0,0,temp,cair)+.38*alpha_AN(4,1,0,1,0,temp,cair))	Sander et al. (2018)
G44022a	TrGC	LMEKOOH + OH → LMEKO2 + H ₂ O	k_roohro	Sander et al. (2018)
G44022b	TrGC	LMEKOOH + OH → .62 BIACET + .38 HCHO + .38 CO ₂ + .38 HOCH ₂ CH ₂ O ₂ + H ₂ O + OH	(.62*k_t*f_tooh*f_co+.38*k_s*f_sooH)	Sander et al. (2018)
G44023a	TrGCN	LC4H9NO3 + OH → MEK + NO ₂ + H ₂ O	(k_t*f_ono2*f_alk+k_p*f_alk+k_s*f_ch2ono2+k_p)*(k_s/(k_p+k_s))	Sander et al. (2018)*
G44023b	TrGCN	LC4H9NO3 + OH → C ₃ H ₇ CHO + NO ₂ + H ₂ O	(k_p+k_s*(1+f_ch2ono2+f_ono2)*f_alk)*(k_p/(k_p+k_s))	Sander et al. (2018)*
G44024	TrGCN	MPAN + OH → CH ₃ COCH ₂ OH + CO + NO ₂	3.2E-11	Orlando et al. (2002)
G44025	TrGCN	MPAN → MACO3 + NO ₂	k_PAN_M	see note*
G44026	TrGC	LMEKO2 → .538 HCHO + .538 CO ₂ + .459 HOCH ₂ CH ₂ O ₂ + .079 C ₂ H ₅ O ₂ + .462 CH ₃ C(O) + .462 CH ₃ CHO	(.62*k1_R02s0R02+.38*k1_R02p0R02)	Rickard and Pascoe (2009)*
G44027	TrGC	MACR + OH → .45 MACO3 + .55 MACRO2	8.E-12*EXP(380./temp)	Orlando et al. (1999b), Sander et al. (2018)
G44028	TrGC	MACR + O ₃ → .5481 CO + .1392 HO ₂ + .1392 OH + .3219 CH ₂ OO + .87 MGLYOX + .13 HCHO + .13 OH + .065 HCOCOCH ₂ O ₂ + .065 CO + .065 CH ₃ C(O)	1.36E-15*EXP(-2112./temp)	Sander et al. (2018)
G44029	TrGCN	MACR + NO ₃ → MACO3 + HNO ₃	KN03AL*2.0	Rickard and Pascoe (2009)
G44030a	TrGC	MACO3 → CH ₃ C(O) + HCHO + CO ₂	k1_R02RC03*0.9	Sander et al. (2018)
G44030b	TrGC	MACO3 → MACO2H	k1_R02RC03*0.1	Sander et al. (2018)
G44031a	TrGC	MACO3 + HO ₂ → MACO2 + OH	KAPH02*rc03_oh	Sander et al. (2018)
G44031b	TrGC	MACO3 + HO ₂ → MACO3H	KAPH02*rc03_ooH	Sander et al. (2018)
G44031c	TrGC	MACO3 + HO ₂ → MACO2H + O ₃	KAPH02*rc03_c03	Sander et al. (2018)
G44032	TrGCN	MACO3 + NO → MACO2 + NO ₂	8.70E-12*EXP(290./temp)	Sander et al. (2018)
G44033	TrGCN	MACO3 + NO ₂ → MPAN	k_CH3C03_N02	Rickard and Pascoe (2009)
G44034	TrGCN	MACO3 + NO ₃ → MACO2 + NO ₂	KR02N03*1.74	Sander et al. (2018)

18

Table 1: Gas phase reactions (... continued)

#	labels	reaction	rate coefficient	reference
G44035	TrGC	MACRO2 → .7 CH ₃ COCH ₂ OH + .7 HCHO + .7 HO ₂ + .3 MACROH	k1_R02t0R02	Rickard and Pascoe (2009)*
G44036a	TrGC	MACRO2 + HO ₂ → MACRO + OH	KR02H02(4)*rc0ch2o2_oh	Sander et al. (2018)
G44036b	TrGC	MACRO2 + HO ₂ → MACROOH	KR02H02(4)*rc0ch2o2_ooH	Sander et al. (2018)
G44037a	TrGCN	MACRO2 + NO → MACRO + NO ₂	KR02N0*(1-alpha_AN(6,3,1,0,0,temp,cair))	Sander et al. (2018)
G44037b	TrGCN	MACRO2 + NO → MACRNO3	KR02N0*alpha_AN(6,3,1,0,0,temp,cair)	Sander et al. (2018)
G44038	TrGCN	MACRO2 + NO ₃ → MACRO + NO ₂	KR02N03	Sander et al. (2018)
G44039a	TrGC	MACROOH + OH → MACRO2	k_roohro	Sander et al. (2018)
G44039b	TrGC	MACROOH + OH → CO + CH ₃ COCH ₂ OH + OH	k_t*f_o*f_tch2oh*f_alk	Sander et al. (2018)
G44039c	TrGC	MACROOH + OH → CO + MGLYOX + HO ₂	(k_s*f_soh*f_pch2oh + k_rohro)	Sander et al. (2018)
G44040	TrGC	MACROH + OH → CH ₃ COCH ₂ OH + CO + HO ₂	k_t*f_o*f_tch2oh*f_alk	Sander et al. (2018)
G44041	TrGC	MACRO → .885 CH ₃ COCH ₂ OH + .885 CO + .115 MGLYOX + .115 HCHO + HO ₂	KDEC	Sander et al. (2018)
G44042	TrGC	MACO2H + OH → CH ₃ COCH ₂ OH + HO ₂ + CO ₂	((k_adt+k_adp)*a_co2h+k_co2h)	Sander et al. (2018)
G44043a	TrGC	MACO3H + OH → CH ₃ COCH ₂ OH + CO ₂ + OH	(k_adt+k_adp)*a_co2h	Sander et al. (2018)
G44043b	TrGC	MACO3H + OH → MACO3	k_roohro	Sander et al. (2018)
G44044	TrGC	LHMKABO2 → .024 CO ₂ H ₃ CHO + .072 MGLYOX + .072 HO ₂ + .072 HCHO + .5280 CH ₃ C(O) + .5280 HOCH ₂ CHO + .176 BIACETOH + .2 HO12CO3C4	(.12*k1_R02p0R02+.88*k1_R02s0R02)	Sander et al. (2018)
G44045a	TrGC	LHMKABO2 + HO ₂ → OH + HOCH ₂ CHO + CH ₃ C(O)	KR02H02(4)*.88*rc0ch2o2_oh	Sander et al. (2018)
G44045b	TrGC	LHMKABO2 + HO ₂ → LHMKABOOH	KR02H02(4)*(.12+.88*rc0ch2o2_ooH)	Sander et al. (2018)
G44046a	TrGCN	LHMKABO2 + NO → .12 MGLYOX + .12 HO ₂ + .88 HOCH ₂ CHO + .88 CH ₃ C(O) + .12 HCHO + NO ₂	KR02N0*(1-(.12*alpha_AN(6,1,0,1,0,temp,cair)+.88*alpha_AN(6,2,1,0,0,temp,cair)))	Sander et al. (2018)
G44046b	TrGCN	LHMKABO2 + NO → MVKNO3	KR02N0*(.12*alpha_AN(6,1,0,1,0,temp,cair)+.88*alpha_AN(6,2,1,0,0,temp,cair))	Sander et al. (2018)*
G44047	TrGCN	LHMKABO2 + NO ₃ → .12 MGLYOX + .12 HO ₂ + .88 HOCH ₂ CHO + .88 CH ₃ C(O) + .12 HCHO + .12 HO ₂ + NO ₂	KR02N03	Sander et al. (2018)
G44048a	TrGC	LHMKABOOH + OH → LHMKABO2	k_roohro	Sander et al. (2018)
G44048b	TrGC	LHMKABOOH + OH → .12 CO ₂ H ₃ CHO + .88 BIACETOH + OH	(.12*k_s*f_soh*f_pch2oh+.88*k_t*f_tooh*f_pch2oh*f_co)	Sander et al. (2018)

19

Table 1: Gas phase reactions (... continued)

#	labels	reaction	rate coefficient	reference
G44049a	TrGC	CO2H3CHO + OH → CO2H3CO3	k_t*f_o*f_alk	Sander et al. (2018)
G44049b	TrGC	CO2H3CHO + OH → CH3COCOCOCHO + HO2 + H2O	k_t*f_co*f_toh*f_cho	Sander et al. (2018)
G44050	TrGCN	CO2H3CHO + NO3 → CO2H3CO3 + HNO3	KN03AL*4.0	Rickard and Pascoe (2009)
G44051	TrGC	CO2H3CO3 → MGLYOX + HO2 + CO2	k1_R02R03	Sander et al. (2018)
G44052a	TrGC	CO2H3CO3 + HO2 → OH + MGLYOX + HO2 + CO2	KAPH02*rc03_oh	Sander et al. (2018)
G44052b	TrGC	CO2H3CO3 + HO2 → CO2H3CO2H + O3	KAPH02*rc03_o3	Sander et al. (2018)
G44052c	TrGC	CO2H3CO3 + HO2 → CO2H3CO3H	KAPH02*rc03_ooH	Sander et al. (2018)
G44053	TrGCN	CO2H3CO3 + NO → MGLYOX + HO2 + NO2 + CO2	KAPNO	Sander et al. (2018)
G44054	TrGCN	CO2H3CO3 + NO3 → MGLYOX + HO2 + NO2 + CO2	KR02N03*1.74	Sander et al. (2018)
G44055a	TrGC	CO2H3CO3H + OH → CO2H3CO3	k_roohro	Sander et al. (2018)
G44055b	TrGC	CO2H3CO3H + OH → CH3C(O) + CO + CO2 + OH	(k_t*f_co2h*f_co*f_toh)	Sander et al. (2018)
G44056	TrGC	CO2H3CO2H + OH → CH3COCOCO2H + HO2	k_t*f_co2h*f_co*f_toh+k_co2h	Sander et al. (2018)
G44057a	TrGC	HO12CO3C4 + OH → BIACETOH + HO2	k_t*f_toh*f_alk*f_co	Sander et al. (2018)
G44057b	TrGC	HO12CO3C4 + OH → CO2H3CHO + HO2	k_s*f_soh*f_alk	Sander et al. (2018)
G44058	TrGC	MACO2 → .65 CH3 + .65 CO + .65 HCHO + .35 OH + .35 CH3COCH2O2 + CO2	KDEC	Sander et al. (2018)
G44059	TrGC	LHMVKABO2 → .88 MGLYOX + .88 HCHO + .12 HOCH2CHO + .12 CH3C(O) + OH	KHSD	Sander et al. (2018)
G44060	TrGC	MACRO2 → MGLYOX + HCHO + OH	KHSB	Sander et al. (2018)
G44061a	TrGCN	MVKNO3 + OH → MGLYOX + CO2 + HO2 + NO2 + H2O	k_s*f_soh*f_ch2ono2+k_rohro	Sander et al. (2018)*
G44061b	TrGCN	MVKNO3 + OH → BIACETOH + NO2 + H2O	k_t*f_ono2*f_co*f_pch2oh	Sander et al. (2018)*
G44062a	TrGCN	MACRNO3 + OH → CH3COCH2OH + CO2 + NO2 + H2O	k_t*f_o*f_ch2ono2	Sander et al. (2018)*
G44062b	TrGCN	MACRNO3 + OH → MGLYOX + CO + NO2 + H2O	k_rohro+k_s*f_soh*f_ch2ono2	Sander et al. (2018)*
G44063	TrGC	MACRO2 → CH3COCH2OH + OH + CO	K14HSAL	Sander et al. (2018)
G44064	TrGC	EZCH3CO2CHCHO → .9 CH3COCHCO + .1 CH3C(O) + .01 GLYOX + .18 CO + .09 HO2 + OH	K15HS24VYNAL	Sander et al. (2018)
G44065	TrGC	EZCH3CO2CHCHO + HO2 → CH3COOHCHCHO	KR02H02(4)	Sander et al. (2018)
G44066	TrGCN	EZCH3CO2CHCHO + NO → CH3COCHO2CHO + NO2	KR02N0	Sander et al. (2018)*
G44067	TrGCN	EZCH3CO2CHCHO + NO3 → CH3COCHO2CHO + NO2	kR02N03	Sander et al. (2018)
G44068	TrGC	EZCH3CO2CHCHO → CH3COCHO2CHO	k1_R02s0R02	Sander et al. (2018)
G44069	TrGC	EZCHOCCH3CHO2 → HCOCCH3CO + OH	K15HS24VYNAL	Sander et al. (2018)
G44070	TrGCN	EZCHOCCH3CHO2 + NO → HCOCO2CH3CHO + NO2	KR02N0	Sander et al. (2018)*
G44071	TrGC	EZCHOCCH3CHO2 + HO2 → HCOCCH3CHOOH	KR02H02(4)	Sander et al. (2018)

20

Table 1: Gas phase reactions (... continued)

#	labels	reaction	rate coefficient	reference
G44072	TrGCN	EZCHOCCH3CHO2 + NO3 → HCOCO2CH3CHO + NO2	KR02N03	Sander et al. (2018)
G44073	TrGC	EZCHOCCH3CHO2 → HCOCO2CH3CHO	k1_R02p0R02	Sander et al. (2018)
G44074	TrGC	CH3COOHCHCHO → CH3COCHO2CHO + OH	KHYDEC	Sander et al. (2018)
G44075	TrGC	HCOCCH3CHOOH → HCOCO2CH3CHO + OH	KHYDEC	Sander et al. (2018)
G44076	TrGCN	CH3COCHO2CHO + NO → CH3C(O) + GLYOX + NO2	KR02N0	Sander et al. (2018)*
G44077	TrGCN	CH3COCHO2CHO + NO3 → CH3C(O) + GLYOX + NO2	KR02N03	Sander et al. (2018)
G44078	TrGC	CH3COCHO2CHO + HO2 → CH3C(O) + GLYOX + OH	KR02H02(4)	Sander et al. (2018)*
G44079	TrGC	CH3COCHO2CHO → CH3C(O) + GLYOX	k1_R02s0R02	Sander et al. (2018)
G44080	TrGC	HCOCO2CH3CHO → MGLYOX + CO + HO2	k1_R02t0R02	Sander et al. (2018)
G44081	TrGCN	HCOCO2CH3CHO + NO → MGLYOX + CO + HO2 + NO2	KR02N0	Sander et al. (2018)*
G44082	TrGC	HCOCO2CH3CHO + HO2 → MGLYOX + CO + HO2 + OH	KR02H02(4)	Sander et al. (2018)*
G44083	TrGCN	HCOCO2CH3CHO + NO3 → MGLYOX + CO + HO2 + NO2	KR02N03	Sander et al. (2018)
G44084	TrGC	HCOCCH3CO + OH → CO + MGLYOX + HO2	1E-10*a_cho	Hatakeyama et al. (1985), Sander et al. (2018)
G44085	TrGC	CH3COCHCO + OH → CO + MGLYOX + HO2	7.6E-11*a_coch3	Hatakeyama et al. (1985), Sander et al. (2018)*
G44086	TrGCN	LMEKNO3 + OH → .62 MGLYOX + .62 HCHO + .62 HO2 + .62 NO2 + .38 CH3C(O) + .38 NO3CH2CHO	.62*(k_p*(f_co+f_ch2ono2)) + .38*(k_s*f_ch2ono2*f_co)	Sander et al. (2018)*
G44087	TrGC	MEPROPENE + OH → IBUTOLBO2	9.4E-12*EXP(505./temp)	Atkinson et al. (2006)
G44088a	TrGC	MEPROPENE + O3 → CH3COCH3 + CH2OO*	2.7E-15*EXP(-1630./temp)*0.33	Atkinson et al. (2006), Sander et al. (2018)
G44088b	TrGC	MEPROPENE + O3 → CH3COCH2O2 + OH + HCHO	2.7E-15*EXP(-1630./temp)*0.67	Atkinson et al. (2006), Sander et al. (2018)
G44089	TrGCN	MEPROPENE + NO3 → CH3COCH3 + HCHO + NO2	3.4E-13	Atkinson et al. (2006), Sander et al. (2018)*
G44090	TrGC	IBUTOLBO2 → CH3COCH3 + HCHO + HO2	k1_R02t0R02	Sander et al. (2018)
G44091a	TrGC	IBUTOLBO2 + HO2 → IBUTOLBOOH	KR02H02(4)*rcoch2o2_ooH	Sander et al. (2018)
G44091b	TrGC	IBUTOLBO2 + HO2 → CH3COCH3 + HCHO + HO2 + OH	KR02H02(4)*rcoch2o2_oh	Sander et al. (2018)
G44092a	TrGCN	IBUTOLBO2 + NO → CH3COCH3 + HCHO + HO2 + NO2	KR02N0*(1.-alpha_AN(5,3,0,0,0,temp,cair))	Sander et al. (2018)

21

Table 1: Gas phase reactions (... continued)

#	labels	reaction	rate coefficient	reference
G44092b	TrGCN	IBUTOLBO2 + NO → IBUTOLBNO3	KR02N0*alpha_AN(5,3,0,0,0,temp,cair)	Sander et al. (2018)
G44093	TrGCN	IBUTOLBO2 + NO ₃ → CH ₃ COCH ₃ + HCHO + HO ₂ + NO ₂	KR02N03	Sander et al. (2018)
G44094a	TrGC	IBUTOLBOOH + OH → IBUTOLBO2	k_roohro	Sander et al. (2018)
G44094b	TrGC	IBUTOLBOOH + OH → CH ₃ COCH ₃ + HCHO + HO ₂	k_s*f_sooh*f_pch2oh	Sander et al. (2018)
G44095	TrGCN	IBUTOLBNO3 + OH → CH ₃ COCH ₃ + HCHO + HO ₂ + NO ₂	3.*k_p	Sander et al. (2018)
G44096	TrGC	BUT1ENE + OH → LBUT1ENO2	6.6E-12*EXP(465./temp)	Atkinson et al. (2006)*
G44097a	TrGC	BUT1ENE + O ₃ → HCHO + .5 C ₂ H ₅ CHO + .5 H ₂ O ₂ + .5 CH ₃ CHO + .5 CO + 5 HO ₂	3.35E-15*EXP(-1745./temp)*.57	Atkinson et al. (2006), Sander et al. (2018)*
G44097b	TrGC	BUT1ENE + O ₃ → C ₂ H ₅ CHO + CH ₂ OO*	3.35E-15*EXP(-1745./temp)*.43	Atkinson et al. (2006), Sander et al. (2018)*
G44098	TrGCN	BUT1ENE + NO ₃ → C ₂ H ₅ CHO + HCHO + NO ₂	3.2E-13*EXP(-950./temp)	Atkinson et al. (2006), Sander et al. (2018)*
G44099	TrGC	LBUT1ENO2 → C ₂ H ₅ CHO + HCHO + HO ₂	k1_R02s0R02	Sander et al. (2018)
G44100a	TrGC	LBUT1ENO2 + HO ₂ → LBUT1ENOOH	KR02H02(4)*rcoch2o2_ooH	Sander et al. (2018)
G44100b	TrGC	LBUT1ENO2 + HO ₂ → C ₂ H ₅ CHO + HCHO + HO ₂ + OH	KR02H02(4)*rcoch2o2_oh	Sander et al. (2018)
G44101a	TrGCN	LBUT1ENO2 + NO → C ₂ H ₅ CHO + HCHO + HO ₂ + NO ₂	KR02N0*(1.-alpha_AN(5,2,0,0,0,temp,cair))	Sander et al. (2018)
G44101b	TrGCN	LBUT1ENO2 + NO → LBUT1ENNO3	KR02N0*alpha_AN(5,2,0,0,0,temp,cair)	Sander et al. (2018)
G44102	TrGCN	LBUT1ENO2 + NO ₃ → C ₂ H ₅ CHO + HCHO + HO ₂ + NO ₂	KR02N03	Sander et al. (2018)
G44103a	TrGC	LBUT1ENOOH + OH → LBUT1ENO2	k_roohro	Sander et al. (2018)
G44103b	TrGC	LBUT1ENOOH + OH → C ₂ H ₅ CO ₃ + HCHO + HO ₂	k_t*f_tooh*f_pch2oh	Sander et al. (2018)*
G44104	TrGCN	LBUT1ENNO3 + OH → C ₂ H ₅ CHO + CO + HO ₂ + NO ₂	k_s*f_soh*f_ch2ono2	Sander et al. (2018)*
G44105	TrGC	CBUT2ENE + OH → BUT2OLO2	1.1E-11*EXP(485./temp)	Atkinson et al. (2006)
G44106	TrGC	CBUT2ENE + O ₃ → CH ₃ CHO + .16 CH ₃ CHOHOH + .50 OH + .50 HCOCH ₂ O ₂ + .05 CH ₂ CO + .09 CH ₃ OH + .09 CO + .2 CH ₄ + 2 CO ₂	3.2E-15*EXP(-965./temp)	Atkinson et al. (2006), Sander et al. (2018)*
G44107	TrGCN	CBUT2ENE + NO ₃ → 2 CH ₃ CHO + NO ₂	3.5E-13	Atkinson et al. (2006), Sander et al. (2018)*
G44108	TrGC	TBUT2ENE + OH → BUT2OLO2	1.0E-11*EXP(553./temp)	Atkinson et al. (2006)

22

Table 1: Gas phase reactions (... continued)

#	labels	reaction	rate coefficient	reference
G44109	TrGC	TBUT2ENE + O ₃ → CH ₃ CHO + .16 CH ₃ CHOHOH + .50 OH + .50 HCOCH ₂ O ₂ + .05 CH ₂ CO + .09 CH ₃ OH + .09 CO + .2 CH ₄ + 2 CO ₂	6.6E-15*EXP(-1060./temp)	Atkinson et al. (2006), Sander et al. (2018)
G44110	TrGCN	TBUT2ENE + NO ₃ → 2 CH ₃ CHO + NO ₂	1.78E-12*EXP(-530./temp) +1.28E-14*EXP(570./temp)	Atkinson et al. (2006), Sander et al. (2018)*
G44111	TrGC	BUT2OLO2 → C ₂ H ₅ CHO + HCHO + HO ₂	k1_R02s0R02	Sander et al. (2018)
G44112a	TrGC	BUT2OLO2 + HO ₂ → BUT2OLOOH	KR02H02(4)*rcoch2o2_ooH	Sander et al. (2018)
G44112b	TrGC	BUT2OLO2 + HO ₂ → 2 CH ₃ CHO + HO ₂ + OH	KR02H02(4)*rcoch2o2_oh	Sander et al. (2018)
G44113a	TrGCN	BUT2OLO2 + NO → 2 CH ₃ CHO + HO ₂ + NO ₂	KR02N0*(1.-alpha_AN(5,2,0,0,0,temp,cair))	Sander et al. (2018)
G44113b	TrGCN	BUT2OLO2 + NO → BUT2OLNO3	KR02N0*alpha_AN(5,2,0,0,0,temp,cair)	Sander et al. (2018)
G44114	TrGCN	BUT2OLO2 + NO ₃ → 2 CH ₃ CHO + HO ₂ + NO ₂	KR02N03	Sander et al. (2018)
G44115a	TrGC	BUT2OLOOH + OH → BUT2OLO2	k_roohro	Sander et al. (2018)
G44115b	TrGC	BUT2OLOOH + OH → LMEKOOH + HO ₂	k_t*f_toh*f_pch2oh	Sander et al. (2018)
G44115c	TrGC	BUT2OLOOH + OH → BUT2OLO + OH	k_t*f_tooh*f_pch2oh	Sander et al. (2018)
G44116	TrGCN	BUT2OLNO3 + OH → LMEKNO3 + HO ₂	k_t*f_toh*f_ch2ono2	Sander et al. (2018)
G44117	TrGC	BUT2OLO + OH → BIACET + HO ₂	k_t*f_toh*f_co	Sander et al. (2018)
G44118	TrGC	IPRCHO + OH → IPRCO3 + H ₂ O	6.8E-12*EXP(410./temp)	Atkinson et al. (2006)
G44119	TrGCN	IPRCHO + NO ₃ → IPRCO3 + HNO ₃	1.67E-12*EXP(-1460./temp)	Atkinson et al. (2006)
G44120	TrGC	IPRCO3 → iC ₃ H ₇ O ₂ + CO ₂	k1_R02RC03	Rickard and Pascoe (2009)
G44121a	TrGC	IPRCO3 + HO ₂ → PERIBUACID	KAPH02*rco3_ooH	Rickard and Pascoe (2009), Sander et al. (2018)
G44121b	TrGC	IPRCO3 + HO ₂ → iC ₃ H ₇ O ₂ + CO ₂ + OH	KAPH02*(1-rco3_ooH)	Rickard and Pascoe (2009), Sander et al. (2018)
G44122	TrGCN	IPRCO3 + NO ₂ → PIPN	k_CH3CO3_N02	Rickard and Pascoe (2009)
G44123	TrGCN	IPRCO3 + NO → iC ₃ H ₇ O ₂ + CO ₂ + NO ₂	KAPN0	Rickard and Pascoe (2009)
G44124a	TrGC	PERIBUACID + OH → IPRCO3 + H ₂ O	k_roohro	Rickard and Pascoe (2009)
G44124b	TrGC	PERIBUACID + OH → CH ₃ COCH ₃ + H ₂ O + CO ₂	k_s*f_co2h	Sander et al. (2018)*
G44125	TrGCN	PIPN → IPRCO3 + NO ₂	k_PAN_M	Rickard and Pascoe (2009)
G44126	TrGCN	PIPN + OH → CH ₃ COCH ₃ + CO ₂ + NO ₂	k_s*f_cpan	Sander et al. (2018)*
G44127	TrGC	MPROPENOL + OH → HCOOH + OH + CH ₃ COCH ₃	k_CH2CHOH_OH_HCOOH	Sander et al. (2018), So et al. (2014)*
G44128	TrGC	MPROPENOL + HCOOH → IPRCHO + HCOOH	k_CH2CHOH_HCOOH	Sander et al. (2018), da Silva (2010)*

23

Table 1: Gas phase reactions (... continued)

#	labels	reaction	rate coefficient	reference
G44129	TrGC	IPRCHO + HCOOH → MPROPENOL + HCOOH	k_ALD_HCOOH	Sander et al. (2018), da Silva (2010)*
G44130	TrGC	BUTENOL + OH → HCOOH + OH + C ₂ H ₅ CHO	k_CH2CHOH_OH_HCOOH	Sander et al. (2018), So et al. (2014)*
G44131	TrGC	BUTENOL + HCOOH → C ₃ H ₇ CHO + HCOOH	k_CH2CHOH_HCOOH	Sander et al. (2018), da Silva (2010)*
G44132	TrGC	C ₃ H ₇ CHO + HCOOH → BUTENOL + HCOOH	k_ALD_HCOOH	Sander et al. (2018), da Silva (2010)*
G44133	TrGC	HVMK + OH → HCOOH + OH + MGLYOX	8.8E-11	Sander et al. (2018), So et al. (2014), Messaadia et al. (2015)*
G44134	TrGC	HVMK + HCOOH → CO ₂ C ₃ CHO + HCOOH	k_CH2CHOH_HCOOH	Sander et al. (2018), da Silva (2010)*
G44135	TrGC	CO ₂ C ₃ CHO + HCOOH → HVMK + HCOOH	k_ALD_HCOOH	Sander et al. (2018), da Silva (2010)*
G44136	TrGC	HMAC + OH → HCOOH + OH + MGLYOX	8.8E-11	Sander et al. (2018), So et al. (2014), Messaadia et al. (2015)*
G44137	TrGC	HMAC + HCOOH → IBUTDIAL + HCOOH	k_CH2CHOH_HCOOH	Sander et al. (2018), da Silva (2010)*
G44138	TrGC	IBUTDIAL + HCOOH → HMAC + HCOOH	k_ALD_HCOOH	Sander et al. (2018), da Silva (2010)*
G44139	TrGC	CO ₂ C ₃ CHO + OH → CH ₃ COCCH ₂ O ₂ + CO ₂ + H ₂ O	k_t*f_o*f_alk+k_s*f_cho*f_co	Sander et al. (2018)*
G44140	TrGCN	CO ₂ C ₃ CHO + NO ₃ → CH ₃ COCCH ₂ O ₂ + CO ₂ + HNO ₃	KN03AL*4.0	Sander et al. (2018)*
G44141	TrGC	IBUTDIAL + OH → CH ₃ CHO + CO + HO ₂ + CO ₂ + H ₂ O	2.*k_t*f_o*f_alk+k_t*f_cho*f_cho	Sander et al. (2018)*
G44142	TrGCN	IBUTDIAL + NO ₃ → CH ₃ CHO + CO + HO ₂ + CO ₂ + HNO ₃	2.*KN03AL*4.0	Sander et al. (2018)*
G44200	TrGTerC	CH ₃ COCOCCH ₂ O ₂ → CH ₃ C(O) + HCHO + CO	k1_R02p0R02	Rickard and Pascoe (2009)
G44201	TrGTerC	CH ₃ COCOCCH ₂ O ₂ + HO ₂ → CH ₃ COCOCCH ₂ OOH	KR02H02(4)	Rickard and Pascoe (2009)
G44202	TrGTerCN	CH ₃ COCOCCH ₂ O ₂ + NO → CH ₃ C(O) + HCHO + CO + NO ₂	KR02N0	Rickard and Pascoe (2009)*
G44203a	TrGTerC	CH ₃ COCOCCH ₂ OOH + OH → CH ₃ COCOCCHO + OH	k_s*f_co*f_sooH	Rickard and Pascoe (2009)*
G44203b	TrGTerC	CH ₃ COCOCCH ₂ OOH + OH → CH ₃ COCOCCH ₂ O ₂	k_roohro	Rickard and Pascoe (2009)
G44204	TrGTerC	C44O ₂ + HO ₂ → C44OOH	KR02H02(4)	Rickard and Pascoe (2009)
G44205	TrGTerCN	C44O ₂ + NO → HCOCH ₂ CHO + CO ₂ + HO ₂ + NO ₂	KR02N0	Rickard and Pascoe (2009)*
G44206	TrGTerC	C44O ₂ → HCOCH ₂ CHO + CO ₂ + HO ₂	k1_R02s0R02	Rickard and Pascoe (2009)

24

Table 1: Gas phase reactions (... continued)

#	labels	reaction	rate coefficient	reference
G44207	TrGTerC	C44OOH + OH → C44O ₂	7.46E-11	Rickard and Pascoe (2009)
G44208	TrGTerC	CHOC ₃ COO ₂ → HCOCCH ₂ CO ₃ + HCHO	k1_R02p0R02	Rickard and Pascoe (2009)
G44209	TrGTerC	CHOC ₃ COO ₂ + HO ₂ → C413COOOH	KR02H02(4)	Rickard and Pascoe (2009)
G44210	TrGTerCN	CHOC ₃ COO ₂ + NO → HCOCCH ₂ CO ₃ + HCHO + NO ₂	KR02N0	Rickard and Pascoe (2009)*
G44211	TrGTerC	C413COOOH + OH → CHOC ₃ COO ₂	8.33E-11	Rickard and Pascoe (2009)
G44212	TrGTerC	C4CODIAL + OH → C312COCO ₃	3.39E-11	Rickard and Pascoe (2009)
G44213	TrGTerCN	C4CODIAL + NO ₃ → C312COCO ₃ + HNO ₃	2.*KN03AL*4.0	Rickard and Pascoe (2009)
G44214	TrGTerC	C312COCO ₃ → HCOCOCCH ₂ O ₂ + CO ₂	k1_R02RCO3	Rickard and Pascoe (2009)
G44215a	TrGTerC	C312COCO ₃ + HO ₂ → C312COCO ₃ H	KAPH02*rco3_ooH	Rickard and Pascoe (2009)
G44215b	TrGTerC	C312COCO ₃ + HO ₂ → HCOCOCCH ₂ O ₂ + CO ₂ + OH	KAPH02*(1-rco3_ooH)	Rickard and Pascoe (2009)
G44216	TrGTerCN	C312COCO ₃ + NO ₂ → C312COPAN	k_CH3CO3_N02	Rickard and Pascoe (2009)
G44217	TrGTerCN	C312COCO ₃ + NO → HCOCOCCH ₂ O ₂ + CO ₂ + NO ₂	KAPN0	Rickard and Pascoe (2009)
G44218	TrGTerC	C312COCO ₃ H + OH → C312COCO ₃	1.63E-11	Rickard and Pascoe (2009)
G44219	TrGTerCN	C312COPAN → C312COCO ₃ + NO ₂	k_PAN_M	Rickard and Pascoe (2009)
G44220	TrGTerCN	C312COPAN + OH → HCOCOCCHO + CO + NO ₂	1.27E-11	Rickard and Pascoe (2009)
G44221	TrGTerC	CH ₃ COCOCCHO + OH → CH ₃ C(O) + 2 CO	8.4E-13*EXP(830./temp)	Sander et al. (2018)*
G44222	TrGTerCN	CH ₃ COCOCCHO + NO ₃ → CH ₃ C(O) + 2 CO + HNO ₃	KN03AL*4.0	Rickard and Pascoe (2009)
G44223	TrGTerC	IBUTALOH + OH → IPRHOCO ₃	1.4E-11	Rickard and Pascoe (2009)
G44224a	TrGTerC	IPRHOCO ₃ + HO ₂ → CH ₃ COCH ₃ + CO ₂ + HO ₂ + OH	KAPH02*rco3_oh	Rickard and Pascoe (2009), Sander et al. (2018)
G44224b	TrGTerC	IPRHOCO ₃ + HO ₂ → IPRHOCO ₂ H + O ₃	KAPH02*rco3_o3	Rickard and Pascoe (2009), Sander et al. (2018)
G44224c	TrGTerC	IPRHOCO ₃ + HO ₂ → IPRHOCO ₃ H	KAPH02*rco3_ooH	Rickard and Pascoe (2009), Sander et al. (2018)
G44225	TrGTerCN	IPRHOCO ₃ + NO → CH ₃ COCH ₃ + CO ₂ + HO ₂ + NO ₂	KAPN0	Rickard and Pascoe (2009)
G44226	TrGTerCN	IPRHOCO ₃ + NO ₂ → CIPAN5	k_CH3CO3_N02	Rickard and Pascoe (2009)
G44227	TrGTerCN	IPRHOCO ₃ + NO ₃ → CH ₃ COCH ₃ + CO ₂ + HO ₂ + NO ₂	KR02N03*1.74	Rickard and Pascoe (2009)
G44228a	TrGTerC	IPRHOCO ₃ → CH ₃ COCH ₃ + CO ₂ + HO ₂	k1_R02RCO3*0.7	Rickard and Pascoe (2009)
G44228b	TrGTerC	IPRHOCO ₃ → IPRHOCO ₂ H	k1_R02RCO3*0.3	Rickard and Pascoe (2009)
G44229	TrGTerC	IPRHOCO ₂ H + OH → CH ₃ COCH ₃ + CO ₂ + HO ₂ + H ₂ O	1.72E-12	Rickard and Pascoe (2009)
G44230	TrGTerC	OH + IPRHOCO ₃ H → IPRHOCO ₃	4.80E-12	Rickard and Pascoe (2009)
G44231	TrGTerCN	C4PAN5 → IPRHOCO ₃ + NO ₂	K_PAN_M	Rickard and Pascoe (2009)
G44232	TrGTerCN	C4PAN5 + OH → CH ₃ COCH ₃ + CO + NO ₂	4.75E-13	Rickard and Pascoe (2009)
G44233a	TrGTerC	MBOOO → IPRHOCO ₂ H	1.60E-17*(ind_H20)*(0.08+0.15)	Rickard and Pascoe (2009), Sander et al. (2018)

25

Table 1: Gas phase reactions (... continued)

#	labels	reaction	rate coefficient	reference
G44233b	TrGTerC	MBOOO → IBUTALOH + H ₂ O ₂	1.60E-17*C(ind_H2O)*0.77	Rickard and Pascoe (2009), Sander et al. (2018)
G44234	TrGTerC	MBOOO + CO → IBUTALOH + CO ₂	1.20E-15	Rickard and Pascoe (2009)
G44235	TrGTerCN	MBOOO + NO → IBUTALOH + NO ₂	1.00E-14	Rickard and Pascoe (2009)
G44236	TrGTerCN	MBOOO + NO ₂ → IBUTALOH + NO ₃	1.00E-15	Rickard and Pascoe (2009)
G44400	TrGAroC	MALANHY + OH → MALANHYO ₂	1.4E-12	Rickard and Pascoe (2009)
G44401a	TrGAroC	MALDIALOOH + OH → HOCOC4DIAL + OH	1.22E-10	Rickard and Pascoe (2009)
G44401b	TrGAroC	MALDIALOOH + OH → MALDIALO ₂	k_roohro	Rickard and Pascoe (2009)
G44402	TrGAroCN	NC4DCO ₂ H + OH → MALANHY + NO ₂	k_roohro	Rickard and Pascoe (2009)*
G44403	TrGAroC	CO14O ₃ CO ₂ H + OH → HCOCH ₂ O ₂ + 2 CO ₂	2.19E-11	Rickard and Pascoe (2009)
G44404	TrGAroC	BZFUOOH + OH → BZFUO ₂	3.68E-11	Rickard and Pascoe (2009)
G44405	TrGAroC	HOCOC4DIAL + OH → CO2C4DIAL + HO ₂	3.67E-11	Rickard and Pascoe (2009)
G44406a	TrGAroC	MALDIALCO ₃ + HO ₂ → MALDALCO ₂ H + O ₃	KAPH02*rco3_o3	Rickard and Pascoe (2009)
G44406b	TrGAroC	MALDIALCO ₃ + HO ₂ → MALDALCO ₃ H	KAPH02*rco3_ooh	Rickard and Pascoe (2009)
G44406c	TrGAroC	MALDIALCO ₃ + HO ₂ → .6 MALANHY + HO ₂ + .4 GLYOX + .4 CO + .4 CO ₂ + OH	KAPH02*rco3_oh	Rickard and Pascoe (2009)*
G44407	TrGAroCN	MALDIALCO ₃ + NO → .6 MALANHY + HO ₂ + .4 GLYOX + .4 CO + .4 CO ₂ + NO ₂	KAPNO	Rickard and Pascoe (2009)*
G44408	TrGAroCN	MALDIALCO ₃ + NO ₂ → MALDIALPAN	k_CH3CO3_NO2	Rickard and Pascoe (2009)
G44409	TrGAroCN	MALDIALCO ₃ + NO ₃ → .6 MALANHY + HO ₂ + .4 GLYOX + .4 CO + .4 CO ₂ + NO ₂	KR02N03*1.74	Rickard and Pascoe (2009)*
G44410	TrGAroC	MALDIALCO ₃ → .6 MALANHY + HO ₂ + .4 GLYOX + .4 CO + .4 CO ₂	k1_R02RC03	Rickard and Pascoe (2009)*
G44411	TrGAroCN	BZFUONE + NO ₃ → NBZFUO ₂	3.00E-13	Rickard and Pascoe (2009)
G44412	TrGAroC	BZFUONE + O ₃ → .3125 CO14O ₃ CO ₂ H + .1875 CO14O ₃ CHO + .1875 H ₂ O ₂ + .5 CO + .5 CO ₂ + .5 HCOCH ₂ O ₂ + .5 OH	2.20E-19	see note*
G44413	TrGAroC	BZFUONE + OH → BZFUO ₂	4.45E-11	Rickard and Pascoe (2009)
G44414	TrGAroCN	NBZFUOOH + OH → NBZFUO ₂	6.18E-12	Rickard and Pascoe (2009)
G44415	TrGAroC	MALDALCO ₃ H + OH → MALDIALCO ₃	4.00E-11	Rickard and Pascoe (2009)
G44416	TrGAroC	EPXDLCO ₂ H + OH → C3DIALO ₂ + CO ₂	2.31E-11	Rickard and Pascoe (2009)
G44417a	TrGAroC	EPXDLCO ₃ + HO ₂ → C3DIALO ₂ + CO ₂ + OH	KAPH02*rco3_oh	Rickard and Pascoe (2009)
G44417b	TrGAroC	EPXDLCO ₃ + HO ₂ → EPXDLCO ₂ H + O ₃	KAPH02*rco3_o3	Rickard and Pascoe (2009)
G44417c	TrGAroC	EPXDLCO ₃ + HO ₂ → EPXDLCO ₃ H	KAPH02*rco3_ooh	Rickard and Pascoe (2009)
G44418	TrGAroCN	EPXDLCO ₃ + NO → C3DIALO ₂ + CO ₂ + NO ₂	KAPNO	Rickard and Pascoe (2009)

26

Table 1: Gas phase reactions (... continued)

#	labels	reaction	rate coefficient	reference
G44419	TrGAroCN	EPXDLCO ₃ + NO ₂ → EPXDLPAN	k_CH3CO3_NO2	Rickard and Pascoe (2009)
G44420	TrGAroCN	EPXDLCO ₃ + NO ₃ → C3DIALO ₂ + CO ₂ + NO ₂	KR02N03*1.74	Rickard and Pascoe (2009)
G44421	TrGAroC	EPXDLCO ₃ → C3DIALO ₂ + CO ₂	k1_R02RC03	Rickard and Pascoe (2009)*
G44422	TrGAroC	MALNHYOHCO + OH → CO + CO + CO + CO ₂ + HO ₂	5.68E-12	Rickard and Pascoe (2009)
G44423	TrGAroCN	MALDIAL + NO ₃ → MALDIALCO ₃ + HNO ₃	2*KNO3AL*2.0	Rickard and Pascoe (2009)
G44424	TrGAroC	MALDIAL + O ₃ → 1.0675 GLYOX + .125 HCHO + .1125 HCOCO ₂ H + .0675 H ₂ O ₂ + .82 HO ₂ + .57 OH + 1.265 CO + .25 CO ₂	2.00E-18	Rickard and Pascoe (2009)*
G44425	TrGAroC	MALDIAL + OH → .83 MALDIALCO ₃ + .17 MALDIALO ₂	5.20E-11	Rickard and Pascoe (2009)*
G44426	TrGAroC	MALANHYOOH + OH → MALNHYOHCO + OH	4.66E-11	Rickard and Pascoe (2009)
G44427	TrGAroCN	MALDIALPAN + OH → GLYOX + CO + CO + NO ₂	3.70E-11	Rickard and Pascoe (2009)
G44428	TrGAroCN	MALDIALPAN → MALDIALCO ₃ + NO ₂	k_PAN_M	Rickard and Pascoe (2009)
G44429a	TrGAroC	MALANHYO ₂ + HO ₂ → MALANHYOOH	KR02H02(4)*(1-rcoch2o2_oh-rchohch2o2_oh)	Rickard and Pascoe (2009), Sander et al. (2018)
G44429b	TrGAroC	MALANHYO ₂ + HO ₂ → HCOCOHCOC ₃ + CO ₂ + OH	KR02H02(4)*(rcoch2o2_oh+rchohch2o2_oh)	Rickard and Pascoe (2009), Sander et al. (2018)
G44430	TrGAroCN	MALANHYO ₂ + NO → HCOCOHCOC ₃ + CO ₂ + NO ₂	KR02NO	Rickard and Pascoe (2009)*
G44431	TrGAroCN	MALANHYO ₂ + NO ₃ → HCOCOHCOC ₃ + CO ₂ + NO ₂	KR02N03	Rickard and Pascoe (2009)*
G44432	TrGAroC	MALANHYO ₂ → HCOCOHCOC ₃ + CO ₂	k1_R02s0R02	Rickard and Pascoe (2009)*
G44433	TrGAroC	EPXDLCO ₃ H + OH → EPXDLCO ₃	2.62E-11	Rickard and Pascoe (2009)
G44434	TrGAroC	CO2C4DIAL + OH → CO + CO + CO + HO ₂	2.45E-11	Rickard and Pascoe (2009)
G44435a	TrGAroCN	NBZFUO ₂ + HO ₂ → NBZFUOOH	KR02H02(4)*(1-rcoch2o2_oh)	Rickard and Pascoe (2009), Sander et al. (2018)
G44435b	TrGAroCN	NBZFUO ₂ + HO ₂ → .5 CO14O ₃ CHO + .5 NO ₂ + .5 NBZFUONE + .5 HO ₂ + OH	KR02H02(4)*rcoch2o2_oh	Rickard and Pascoe (2009), Sander et al. (2018)
G44436	TrGAroCN	NBZFUO ₂ + NO → .5 CO14O ₃ CHO + .5 NO ₂ + .5 NBZFUONE + .5 HO ₂ + NO ₂	KR02NO	Rickard and Pascoe (2009)*
G44437	TrGAroCN	NBZFUO ₂ + NO ₃ → .5 CO14O ₃ CHO + .5 NO ₂ + .5 NBZFUONE + .5 HO ₂ + NO ₂	KR02N03	Rickard and Pascoe (2009)*
G44438	TrGAroCN	NBZFUO ₂ → .5 CO14O ₃ CHO + .5 NO ₂ + .5 NBZFUONE + .5 HO ₂	k1_R02s0R02	Rickard and Pascoe (2009)*
G44439	TrGAroC	MALDALCO ₂ H + OH → .6 MALANHY + HO ₂ + .4 GLYOX + .4 CO + .4 CO ₂	3.70E-11	Rickard and Pascoe (2009)*
G44440	TrGAroCN	EPXC4DIAL + NO ₃ → EPXDLCO ₃ + HNO ₃	2*KNO3AL*4.0	Rickard and Pascoe (2009)

27

Table 1: Gas phase reactions (... continued)

#	labels	reaction	rate coefficient	reference
G44441	TrGAroC	EPXC4DIAL + OH → EPXDLCO3	4.32E-11	Rickard and Pascoe (2009)
G44442a	TrGAroC	MECOACETO2 + HO ₂ → MECOACEOOH	KR02H02(4)*(1-rcoch2o2_oh)	Rickard and Pascoe (2009), Sander et al. (2018)
G44442b	TrGAroC	MECOACETO2 + HO ₂ → CH ₃ C(O)OO + HCHO + CO ₂ + OH	KR02H02(4)*rcoch2o2_oh	Rickard and Pascoe (2009), Sander et al. (2018)
G44443	TrGAroCN	MECOACETO2 + NO → CH ₃ C(O)OO + HCHO + CO ₂ + NO ₂	KR02N0	Rickard and Pascoe (2009)*
G44444	TrGAroCN	MECOACETO2 + NO ₃ → CH ₃ C(O)OO + HCHO + CO ₂ + NO ₂	KR02N03	Rickard and Pascoe (2009)*
G44445	TrGAroC	MECOACETO2 → CH ₃ C(O)OO + HCHO + CO ₂	k1_R02pOR02	Rickard and Pascoe (2009)*
G44446	TrGAroCN	CO14O3CHO + NO ₃ → CO + HCOCH ₂ O ₂ + CO ₂ + HNO ₃	KN03AL*8.0	Rickard and Pascoe (2009)
G44447	TrGAroC	CO14O3CHO + OH → CO + HCOCH ₂ O ₂ + CO ₂	3.44E-11	Rickard and Pascoe (2009)
G44448	TrGAroCN	NBZFUONE + OH → BZFUOCO + NO ₂	1.16E-12	Rickard and Pascoe (2009)
G44449a	TrGAroC	BZFUO2 + HO ₂ → BZFUOOH	KR02H02(4)*(1-rcoch2o2_oh-rchohch2o2_oh)	Rickard and Pascoe (2009), Sander et al. (2018)
G44449b	TrGAroC	BZFUO2 + HO ₂ → CO14O3CHO + HO ₂ + OH	KR02H02(4)*(rcoch2o2_oh+rchohch2o2_oh)	Rickard and Pascoe (2009), Sander et al. (2018)
G44450	TrGAroCN	BZFUO2 + NO → CO14O3CHO + HO ₂ + NO ₂	KR02N0	Rickard and Pascoe (2009)*
G44451	TrGAroCN	BZFUO2 + NO ₃ → CO14O3CHO + HO ₂ + NO ₂	KR02N03	Rickard and Pascoe (2009)*
G44452	TrGAroC	BZFUO2 → CO14O3CHO + HO ₂	k1_R02sOR02	Rickard and Pascoe (2009)*
G44453	TrGAroC	BZFUOCO + OH → CO14O3CHO + HO ₂	1.78E-11	Rickard and Pascoe (2009)
G44456a	TrGAroC	MALDIALO2 + HO ₂ → MALDIALOOH	KR02H02(4)*(1-rcoch2o2_oh-rchohch2o2_oh)	Rickard and Pascoe (2009)
G44456b	TrGAroC	MALDIALO2 + HO ₂ → GLYOX + GLYOX + HO ₂ + OH	KR02H02(4)*(rcoch2o2_oh+rchohch2o2_oh)	Rickard and Pascoe (2009)
G44457	TrGAroCN	MALDIALO2 + NO → GLYOX + GLYOX + HO ₂ + NO ₂	KR02N0	Rickard and Pascoe (2009)*
G44458	TrGAroCN	MALDIALO2 + NO ₃ → GLYOX + GLYOX + HO ₂ + NO ₂	KR02N03	Rickard and Pascoe (2009)*
G44459	TrGAroC	MALDIALO2 → GLYOX + GLYOX + HO ₂	k1_R02sOR02	Rickard and Pascoe (2009)*
G44460	TrGAroCN	EPXDLPAN + OH → HCOCOCHO + CO + NO ₂	2.29E-11	Rickard and Pascoe (2009)
G44461	TrGAroCN	EPXDLPAN → EPXDLCO3 + NO ₂	k_PAN_M	Rickard and Pascoe (2009)*
G44462	TrGAroC	MECOACEOOH + OH → MECOACETO2	3.59E-12	Rickard and Pascoe (2009)

28

Table 1: Gas phase reactions (... continued)

#	labels	reaction	rate coefficient	reference
G45000	TrGC	C ₅ H ₈ + O ₃ → .3508 MACR + .01518 MACO2H + .2440 MVK + .7085 HCHO + .11 CH ₂ OO + .1275 C ₃ H ₆ + .1575 CH ₃ C(O) + .0510 CH ₃ + .2625 HO ₂ + .27 OH + .09482 H ₂ O ₂ + .255 CO ₂ + .522 CO + .07182 HCHO + .03618 HCOCH ₂ O ₂ + .01782 CO + 0.05408 L-CARBON	1.03E-14*EXP(-1995./temp)	Atkinson et al. (2006), Sander et al. (2018)
G45001	TrGC	C ₅ H ₈ + OH → .63 LISOPAB + .30 LISOPCD + .07 LISOPEFO2	2.7E-11*EXP(390./temp)	Atkinson et al. (2006), Sander et al. (2018)
G45002	TrGCN	C ₅ H ₈ + NO ₃ → NISOPO2	3.0E-12*EXP(-450./temp)	Atkinson et al. (2006)
G45003a	TrGC	LISOPAB + O ₂ → LISOPACO2	5.530E-13	Sander et al. (2018)
G45003b	TrGC	LISOPAB + O ₂ → ISOPBO2	3.E-12	Sander et al. (2018)
G45004a	TrGC	LISOPCD + O ₂ → LDISOPACO2	6.780E-13	Sander et al. (2018)
G45004b	TrGC	LISOPCD + O ₂ → ISOPDO2	3.E-12	Sander et al. (2018)
G45005	TrGC	LISOPACO2 → LISOPAB + O ₂	3.1E12*exp(-7900./temp)*.6+7.8E13*exp(-8600./temp)*.4	Sander et al. (2018)
G45006	TrGC	ISOPBO2 → LISOPAB + O ₂	3.7E14*exp(-9570./temp)+4.2E14*exp(-9970./temp)	Sander et al. (2018)
G45007	TrGC	LDISOPACO2 → LISOPCD + O ₂	5.65E12*exp(-8410./temp)*.42+1.4E14*exp(-9110./temp)*.58	Sander et al. (2018)
G45008	TrGC	ISOPDO2 → LISOPCD + O ₂	5.0E14*exp(-10120./temp)+8.25E14*exp(-10220./temp)	Sander et al. (2018)
G45009a	TrGC	LISOPACO2 → C10DC2O2C4OOH	K16HSZ14 * 2./3.*(1-fhpal)	Sander et al. (2018)
G45009b	TrGC	LISOPACO2 → LZCODC23DBC0OH + HO ₂	K16HSZ14 * (2./3.*fhpal + 1./3.)	Sander et al. (2018)
G45010a	TrGC	LDISOPACO2 → C10OHC3O2C4OD	k16HSZ41 * 2./3.*(1-fhpal)	Sander et al. (2018)
G45010b	TrGC	LDISOPACO2 → LZCODC23DBC0OH + HO ₂	k16HSZ41 * (2./3.*fhpal + 1./3.)	Sander et al. (2018)
G45011	TrGC	LISOPACO2 → .9 LISOPACO + .1 ISOPA0H	k1_R02LISOPACO2	Rickard and Pascoe (2009), Sander et al. (2018)
G45012	TrGC	LISOPACO2 + HO ₂ → LISOPACOOH	KR02H02(5)	Rickard and Pascoe (2009)
G45013a	TrGCN	LISOPACO2 + NO → LISOPACO + NO ₂	KR02N0*(1-alpha_AN(6,1,0,0,0,temp,cair))	Lockwood et al. (2010), Paulot et al. (2009a), Sander et al. (2018)
G45013b	TrGCN	LISOPACO2 + NO → LISOPACNO3	KR02N0*alpha_AN(6,1,0,0,0,temp,cair)	Lockwood et al. (2010), Paulot et al. (2009a), Sander et al. (2018)
G45014	TrGCN	LISOPACO2 + NO ₃ → LISOPACO + NO ₂	KR02N03	Rickard and Pascoe (2009)

29

Table 1: Gas phase reactions (... continued)

#	labels	reaction	rate coefficient	reference
G45015	TrGC	LDISOPACO2 → .9 LISOPACO + .1 ISOPA0H	k1_R02LISOPACO2	Rickard and Pascoe (2009), Sander et al. (2018)
G45016	TrGC	LDISOPACO2 + HO2 → LISOPACOOH	KR02H02(5)	Rickard and Pascoe (2009)
G45017a	TrGCN	LDISOPACO2 + NO → LISOPACO + NO2	KR02N0*(1.-alpha_AN(6,1,0,0,0, temp, cair))	Lockwood et al. (2010), Paulot et al. (2009a), Sander et al. (2018)
G45017b	TrGCN	LDISOPACO2 + NO → LISOPACNO3	KR02N0*alpha_AN(6,1,0,0,0, temp, cair)	Lockwood et al. (2010), Paulot et al. (2009a), Sander et al. (2018)
G45018	TrGCN	LDISOPACO2 + NO3 → LISOPACO + NO2	KR02N03	Rickard and Pascoe (2009)
G45019a	TrGC	LISOPACOOH + OH → LISOPACO2	k_roohro	Sander et al. (2018)
G45019b	TrGC	LISOPACOOH + OH → LZCODC23DBCOOH + HO2	k_s*f_allyl*f_soh	Sander et al. (2018)
G45019c	TrGC	LISOPACOOH + OH → LHC4ACCHO + OH	(k_s*f_soh*f_allyl+ k_roohro)	Sander et al. (2018)
G45019d	TrGC	LISOPACOOH + OH → LIEPOX + OH	(k_adt+k_ads)*a_ch2oh*a_ch2ooh	Sander et al. (2018)*
G45020	TrGC	ISOPA0H + OH → LHC4ACCHO + HO2	(k_adt+k_ads)*a_ch2oh*a_ch2oh+k_s*f_soh*f_allyl+k_roohro	Sander et al. (2018)
G45021	TrGCN	LISOPACNO3 + OH → LISOPACNO3O2	(k_adt+k_ads)*a_ch2ono2*a_ch2oh	Sander et al. (2018)*
G45022	TrGC	ISOPBO2 → .8 MVK + .8 HCHO + .8 HO2 + .2 ISOPBOH	k1_R02ISOPBO2	Rickard and Pascoe (2009)
G45023a	TrGC	ISOPBO2 + HO2 → ISOPBOOH	KR02H02(5)*(1.-rchohch2o2_oh)	Sander et al. (2018)
G45023b	TrGC	ISOPBO2 + HO2 → MVK + HCHO + HO2 + OH	KR02H02(5)*rchohch2o2_oh	Sander et al. (2018)
G45024a	TrGCN	ISOPBO2 + NO → MVK + HCHO + HO2 + NO2	KR02N0*(1.-alpha_AN(6,3,0,0,0, temp, cair))	Lockwood et al. (2010), Sander et al. (2018)
G45024b	TrGCN	ISOPBO2 + NO → ISOPBNO3	KR02N0*alpha_AN(6,3,0,0,0, temp, cair)	Lockwood et al. (2010), Sander et al. (2018)
G45025	TrGCN	ISOPBO2 + NO3 → MVK + .75 HCHO + .75 HO2 + .25 CH3 + NO2	KR02N03	Rickard and Pascoe (2009)
G45026a	TrGC	ISOPBOOH + OH → LIEPOX + OH	(k_ads+k_adp)*a_ch2ooh	Paulot et al. (2009b), Sander et al. (2018)
G45026b	TrGC	ISOPBOOH + OH → ISOPBO2	k_roohro	Sander et al. (2018)
G45026c	TrGC	ISOPBOOH + OH → MGLYOX + HOCH2CHO	k_roohro+k_s*f_alk*f_soh	Sander et al. (2018)
G45027	TrGC	ISOPBOOH + O3 → .1368 MACROOH + .1368 H2O2 + .2280 HO2 + .4332 CH3COCH2OH + .2280 CO2 + .6384 OH + .2052 CO + .57 HCHO + .43 MACROOH + .06880 HO2 + .06880 OH + .2709 CO + .1591 CH2OO	1.E-17	Sander et al. (2018)

30

Table 1: Gas phase reactions (... continued)

#	labels	reaction	rate coefficient	reference
G45028	TrGC	ISOPBOH + OH → MVK + .75 HCHO + .75 HO2 + .25 CH3	k_s*f_alk*f_soh+(k_adp+k_ads)*a_ch2oh	Sander et al. (2018)
G45029	TrGCN	ISOPBNO3 + OH → ISOPBDNO3O2	(k_adt+k_adp)*f_ch2ono2	Sander et al. (2018)
G45030	TrGC	ISOPDO2 → .8 MACR + .8 HCHO + .8 HO2 + .1 HCOC5 + .1 ISOPDOH	k1_R02ISOPDO2	Rickard and Pascoe (2009)
G45031a	TrGC	ISOPDO2 + HO2 → ISOPDOOH	KR02H02(5)*(1.-rchohch2o2_oh)	Sander et al. (2018)
G45031b	TrGC	ISOPDO2 + HO2 → MACR + HCHO + HO2 + OH	KR02H02(5)*rchohch2o2_oh	Sander et al. (2018)
G45032a	TrGCN	ISOPDO2 + NO → MACR + HCHO + HO2 + NO2	KR02N0*(1.-alpha_AN(6,2,0,0,0, temp, cair))	Lockwood et al. (2010), Sander et al. (2018)
G45032b	TrGCN	ISOPDO2 + NO → ISOPDN03	KR02N0*alpha_AN(6,2,0,0,0, temp, cair)	Lockwood et al. (2010), Sander et al. (2018)
G45033	TrGCN	ISOPDO2 + NO3 → MACR + HCHO + HO2 + NO2	KR02N03	Rickard and Pascoe (2009)
G45034a	TrGC	ISOPDOOH + OH → LIEPOX + OH	(k_adt+k_adp)*a_ch2ooh	Paulot et al. (2009b), Sander et al. (2018)
G45034b	TrGC	ISOPDOOH + OH → ISOPDO2	k_roohro	Sander et al. (2018)
G45034c	TrGC	ISOPDOOH + OH → HCOC5 + OH	k_t*f_tooh*f_allyl*f_pch2oh	Sander et al. (2018)
G45034d	TrGC	ISOPDOOH + OH → CH3COCH2OH + GLYOX + OH	k_s*f_pch2oh*f_soh	Sander et al. (2018)
G45035	TrGC	ISOPDOOH + O3 → 1.393 OH + BIACETOH + .67 HCHO + .05280 HO2 + .2079 CO + .1221 CH2OO	1.E-17	Sander et al. (2018)
G45036	TrGC	ISOPDOH + OH → HCOC5 + HO2	2.*k_roohro+(k_t*f_toh*f_allyl+k_s*f_soh)*f_pch2oh+(k_adt+k_adp)*a_ch2oh	Sander et al. (2018)
G45037	TrGCN	ISOPDN03 + OH → ISOPBDNO3O2	(k_adp+k_ads)*a_ch2ono2	Sander et al. (2018)*
G45038	TrGCN	NISOP02 → .8 NC4CHO + .6 HO2 + .2 LISOPACNO3	k1_R02LISOPACO2	Rickard and Pascoe (2009)
G45039	TrGCN	NISOP02 + HO2 → NISOP0OH	KR02H02(5)	Rickard and Pascoe (2009)
G45040	TrGCN	NISOP02 + NO → NC4CHO + HO2 + NO2	KR02N0	Rickard and Pascoe (2009)*
G45041	TrGCN	NISOP02 + NO3 → NC4CHO + HO2 + NO2	KR02N03	Rickard and Pascoe (2009)
G45042	TrGCN	NISOP0OH + OH → NC4CHO + OH	1.03E-10	Rickard and Pascoe (2009)
G45043	TrGCN	NC4CHO + OH → LNISO3	(k_adt+k_ads)*a_cho*a_ch2ono2	Sander et al. (2018)*
G45044	TrGCN	NC4CHO + O3 → .27 NOA + .027 HCOCO2H + .0162 GLYOX + .0162 H2O2 + .1458 HCOCO + .0405 HCOOH + .0405 CO + .8758 OH + .365 MGLYOX + .73 NO2 + 0.7705 HCHO + .4055 CO2 + .73 GLYOX	2.40E-17	Sander et al. (2018)
G45045	TrGCN	NC4CHO + NO3 → LNISO3 + HNO3	KN03AL*4.25	Rickard and Pascoe (2009)
G45046	TrGCN	LNISO3 + HO2 → LNISOOH	0.5*KR02H02(5)+0.5*KAPH02	Rickard and Pascoe (2009)

31

Table 1: Gas phase reactions (... continued)

#	labels	reaction	rate coefficient	reference
G45047	TrGCN	LNISO3 + NO → NOA + .5 HOCHCHO + .5 CO + .5 HO ₂ + NO ₂ + .5 CO ₂	0.5*KAPNO+0.5*KR02NO	Rickard and Pascoe (2009)*
G45048	TrGCN	LNISO3 + NO ₃ → NOA + .5 HOCHCHO + .5 CO + .5 HO ₂ + NO ₂ + .5 CO ₂	KR02NO3*1.37	Rickard and Pascoe (2009)
G45049	TrGCN	LNISOOH + OH → LNISO3	2.65E-11	Rickard and Pascoe (2009)
G45050a	TrGC	LHC4ACCHO + OH → LC578O2	(k_adtertprim+k_ads)*a_cho*a_ch2oh	Sander et al. (2018)
G45050b	TrGC	LHC4ACCHO + OH → LHC4ACCO3	k_t*f_o	Sander et al. (2018)
G45050c	TrGC	LHC4ACCHO + OH → C4MDIAL + HO ₂	k_s*f_soh*f_allyl	Sander et al. (2018)
G45051	TrGC	LHC4ACCHO + O ₃ → .2225 CH ₃ C(O) + .89 CO + .0171875 HOCH ₂ CO ₂ H + .075625 H ₂ O ₂ + .0171875 HCOCO ₂ H + .2775 CH ₃ COCH ₂ OH + .6675 HO ₂ + .2603125 GLYOX + .2225 HCHO + .89 OH + .2603125 HOCH ₂ CHO + .5 MGLYOX	2.40E-17	Rickard and Pascoe (2009)
G45052	TrGCN	LHC4ACCHO + NO ₃ → LHC4ACCO3 + HNO ₃	KN03AL*4.25	Rickard and Pascoe (2009)
G45053	TrGC	LC578O2 → .25 CH ₃ COCH ₂ OH + .75 MGLYOX + .25 HOCHCHO + .75 HOCH ₂ CHO + .75 HO ₂	k1_R02t0R02	Rickard and Pascoe (2009)
G45054a	TrGC	LC578O2 + HO ₂ → MGLYOX + HOCH ₂ CHO + OH	KR02H02(5)*rcoch2o2_oh	Rickard and Pascoe (2009)
G45054b	TrGC	LC578O2 + HO ₂ → LC578OOH	KR02H02(5)*rcoch2o2_ooH	Rickard and Pascoe (2009)
G45055	TrGCN	LC578O2 + NO → .25 CH ₃ COCH ₂ OH + .75 MGLYOX + .25 HOCHCHO + .75 HOCH ₂ CHO + .75 HO ₂ + NO ₂	KR02NO	Rickard and Pascoe (2009)*
G45056	TrGCN	LC578O2 + NO ₃ → .25 CH ₃ COCH ₂ OH + .75 MGLYOX + .25 HOCHCHO + .75 HOCH ₂ CHO + .75 HO ₂ + NO ₂	KR02NO3	Rickard and Pascoe (2009)
G45057	TrGC	LC578O2 → .25 CH ₃ COCH ₂ OH + .75 MGLYOX + .25 HOCH ₂ CHO + .75 HOCH ₂ CHO + HO ₂ + OH	KHSB	Sander et al. (2018)
G45058a	TrGC	LC578OOH + OH → LC578O2	k_roohro	Sander et al. (2018)
G45058b	TrGC	LC578OOH + OH → C1ODC2OOHC4OD + HO ₂	k_t*f_o*f_tch2oh*f_alk+k_t*f_toh*f_pch2oh*f_pch2oh+k_s*f_soh*f_pch2oh	Sander et al. (2018)
G45059a	TrGC	LHC4ACCO3 → OH + .5 MACRO2 + .5 LHMVKABO2 + CO ₂	k1_R02RC03*0.9	Sander et al. (2018)
G45059b	TrGC	LHC4ACCO3 → LHC4ACCO2H	k1_R02RC03*0.1	Sander et al. (2018)
G45060a	TrGC	LHC4ACCO3 + HO ₂ → 2 OH + .5 MACRO2 + .5 LHMVKABO2 + CO ₂	KAPH02*rco3_oh	Sander et al. (2018)
G45060b	TrGC	LHC4ACCO3 + HO ₂ → LHC4ACCO3H	KAPH02*rco3_ooH	Sander et al. (2018)

32

Table 1: Gas phase reactions (... continued)

#	labels	reaction	rate coefficient	reference
G45060c	TrGC	LHC4ACCO3 + HO ₂ → LHC4ACCO2H + O ₃	KAPH02*rco3_o3	Sander et al. (2018)
G45061	TrGCN	LHC4ACCO3 + NO → .5 MACRO2 + .5 LHMVKABO2 + NO ₂ + CO ₂	KAPNO	Sander et al. (2018)
G45062	TrGCN	LHC4ACCO3 + NO ₂ → LC5PAN1719	k_CH3C03_N02	Rickard and Pascoe (2009)
G45063	TrGCN	LHC4ACCO3 + NO ₃ → .5 MACRO2 + .5 LHMVKABO2 + NO ₂ + CO ₂	KR02NO3*1.74	Sander et al. (2018)
G45064a	TrGC	LHC4ACCO2H + OH → OH + .5 MACRO2 + .5 LHMVKABO2 + CO ₂	2.52E-11	Sander et al. (2018)
G45064b	TrGC	LHC4ACCO3H + OH → LHC4ACCO3	2.88E-11	Rickard and Pascoe (2009)
G45065	TrGCN	LC5PAN1719 → LHC4ACCO3 + NO ₂	k_PAN_M	Rickard and Pascoe (2009)
G45066	TrGCN	LC5PAN1719 + OH → .5 MACROH + .5 HO12CO3C4 + CO + NO ₂	2.52E-11	Rickard and Pascoe (2009)
G45067	TrGC	HCOC5 + OH → C59O2	3.81E-11	Rickard and Pascoe (2009)
G45068	TrGC	HCOC5 + O ₃ → BIACETOH + .335 H ₂ O ₂ + .67 HCHO + .2079 CO + .1221 CH ₂ OO + .05280 OH	7.51E-16*EXP(-1521./temp)	Sander et al. (2018)
G45069	TrGC	C59O2 → CH ₃ COCH ₂ OH + HOCH2CO	k1_R02t0R02	Sander et al. (2018)
G45070a	TrGC	C59O2 + HO ₂ → OH + CH ₃ COCH ₂ OH + HOCH2CO	KR02H02(5)*rcoch2o2_oh	Sander et al. (2018)
G45070b	TrGC	C59O2 + HO ₂ → C59OOH	KR02H02(5)*rcoch2o2_ooH	Sander et al. (2018)
G45071	TrGCN	C59O2 + NO → CH ₃ COCH ₂ OH + HOCH2CO + NO ₂	KR02NO	Sander et al. (2018)*
G45072	TrGCN	C59O2 + NO ₃ → CH ₃ COCH ₂ OH + HOCH2CO + NO ₂	KR02NO3	Sander et al. (2018)
G45073	TrGC	C59OOH + OH → C59O2	9.7E-12	Rickard and Pascoe (2009)
G45074	TrGC	LIEPOX + OH → DB1O2 + H ₂ O	5.78E-11*EXP(-400./temp) *(1.52/3.+0.98*2./3.)/1.51	Paulot et al. (2009b), Bates et al. (2014), Sander et al. (2018)*
G45075	TrGC	ISOPBO2 → MVK + HCHO + OH	KHSB	Sander et al. (2018)
G45076	TrGC	ISOPDO2 → MACR + HCHO + OH	KHSD	Sander et al. (2018)
G45077a	TrGC	LZCODC23DBC0OH + OH → .6 C1ODC2O2C4OOH + .4 C1OOHC2O2C4OD	k_adt*a_cho*a_ch2ooh	Sander et al. (2018)
G45077b	TrGC	LZCODC23DBC0OH + OH → .6 C1ODC3O2C4OOH + .4 C1OOHC3O2C4OD	k_ads*a_cho*a_ch2ooh	Sander et al. (2018)
G45077c	TrGC	LZCODC23DBC0OH + OH → LZCO3HC23DBCOD	k_t*f_o*f_alk+k_roohro	Sander et al. (2018)
G45077d	TrGC	LZCODC23DBC0OH + OH → C4MDIAL + OH	k_s*f_soh*f_allyl	Sander et al. (2018)

33

Table 1: Gas phase reactions (... continued)

#	labels	reaction	rate coefficient	reference
G45078	TrGC	LZCOC23DBCOOH + O ₃ → .4672 OH + .2336 HCOCOCH ₂ O ₂ + .2336 CO + .2336 CH ₃ C(O) + .4672 HOOCH ₂ CHO + .1728 MGLYOX + .1901 OH + .0864 GLYOX + .02765 HOOCH ₂ CHO + .02765 H ₂ O ₂ + .02592 CH ₃ OOH + .02592 CO ₂ + .01037 HCOCO + .01555 CH ₂ OO + .01555 CO + .006908 HOOCH ₂ CO ₃ + .2628 OH + .1314 MGLYOX + .1314 OH + .1314 HCOCOCH ₂ OOH + .2628 GLYOX + .0972 CH ₃ COCH ₂ O ₂ H + .00972 HCOCO ₂ H + .005832 GLYOX + .005832 H ₂ O ₂ + .05249 OH + .05249 HCOCO + .01458 HCHO + .01458 CO ₂ + .01458 HCOOH + .01458 CO	2.4E-17	Sander et al. (2018)
G45079	TrGC	C1OOHC2O2C4OD → .78 CH ₃ COCH ₂ O ₂ H + .78 HOCHCHO + .22 CO ₂ H ₃ CHO + .22 HCHO + .22 OH	k1_R02tOR02	Sander et al. (2018)
G45080	TrGCN	C1OOHC2O2C4OD + NO → .78 CH ₃ COCH ₂ O ₂ H + .78 HOCHCHO + .22 CO ₂ H ₃ CHO + .22 HCHO + .22 OH + NO ₂	KR02N0	Sander et al. (2018)*
G45081a	TrGC	C1OOHC2O2C4OD + HO ₂ → C1OOHC2OOHC4OD	KR02H02(5)*rcoch2o2_ooH	Sander et al. (2018)
G45081b	TrGC	C1OOHC2O2C4OD + HO ₂ → .78 CH ₃ COCH ₂ O ₂ H + .78 HOCHCHO + .22 CO ₂ H ₃ CHO + .22 HCHO + 1.22 OH	KR02H02(5)*rcoch2o2_oh	Sander et al. (2018)
G45082	TrGC	C1OOHC2O2C4OD → CH ₃ COCH ₂ O ₂ H + GLYOX + OH	KHSB	Sander et al. (2018)
G45083	TrGC	C1ODC2O2C4OOH → OH + C1ODC2OOHC4OD	K15HSDHB	Sander et al. (2018)
G45084a	TrGC	C1OOHC2OOHC4OD + OH → C1ODC2OOHC4OD + OH	2.*k_s*f_sooh*f_tch2oh	Sander et al. (2018)
G45084b	TrGC	C1OOHC2OOHC4OD + OH → CH ₃ COCH ₂ O ₂ H + 2 CO + 2 HO ₂ + OH	k_t*f_toh*f_pch2oh*f_pch2oh	Sander et al. (2018)
G45084c	TrGC	C1OOHC2OOHC4OD + OH → C1OOHC2O2C4OD	k_roohro	Sander et al. (2018)
G45085	TrGC	C1ODC2OOHC4OD + OH → CO ₂ H ₃ CHO + CO + H ₂ O + OH	k_t*f_o*f_tch2oh+k_t*f_toh*f_toh*f_cho	Sander et al. (2018)
G45086	TrGC	C1ODC3O2C4OOH → MGLYOX + HOOCH ₂ CHO + HO ₂	k1_R02sOR02	Sander et al. (2018)
G45087	TrGCN	C1ODC3O2C4OOH + NO → MGLYOX + HOOCH ₂ CHO + HO ₂ + NO ₂	KR02N0	Sander et al. (2018)
G45088	TrGC	C1ODC3O2C4OOH + HO ₂ → .5 CH ₃ C(O) + .5 CO + .5 MGLYOX + .5 HO ₂ + HOOCH ₂ CO ₃	KR02H02(5)	Sander et al. (2018)
G45089	TrGC	C1ODC3O2C4OOH → MGLYOX + OH + HOOCH ₂ CHO	KHSD	Sander et al. (2018)

34

Table 1: Gas phase reactions (... continued)

#	labels	reaction	rate coefficient	reference
G45090	TrGC	C1OOHC3O2C4OD → .625 MGLYOX + 2 CO + 1.625 HO ₂ + .375 CH ₃ C(O) + .375 CO ₂ + OH	K15HSDHB	Sander et al. (2018)
G45091	TrGC	LHC4ACCO3 → LZCO3HC23DBCOD + HO ₂	K16HS	Sander et al. (2018)
G45092a	TrGC	C4MDIAL + OH → C1ODC2O2C4OD	(k_adt+k_ads)*a_cho*a_cho	Sander et al. (2018)*
G45092b	TrGC	C4MDIAL + OH → LZCO3C23DBCOD	2*k_t*f_o*f_alk	Sander et al. (2018)*
G45093	TrGCN	C4MDIAL + NO ₃ → LZCO3C23DBCOD + HNO ₃	KN03AL*4.25*2.	Sander et al. (2018)*
G45094a	TrGC	C1ODC2O2C4OD + HO ₂ → OH + MGLYOX + HOCHCHO	KR02H02(5)*rcoch2o2_oh	Sander et al. (2018)
G45094b	TrGC	C1ODC2O2C4OD + HO ₂ → C1ODC2OOHC4OD	KR02H02(5)*rcoch2o2_ooH	Sander et al. (2018)
G45095	TrGCN	C1ODC2O2C4OD + NO → NO ₂ + MGLYOX + HOCHCHO	KR02N0	Sander et al. (2018)*
G45096	TrGC	C1ODC2O2C4OD → MGLYOX + HOCHCHO	k1_R02tOR02	Sander et al. (2018)
G45097a	TrGC	C1ODC2OOHC4OD + OH → MGLYOX + 2 CO	(2.*k_t*f_o*f_tch2oh*f_alk+k_t*f_toh*f_cho*f_pch2oh)*.5	Sander et al. (2018)
G45097b	TrGC	C1ODC2OOHC4OD + OH → MGLYOX + 2 CO + OH	(2.*k_t*f_o*f_tch2oh*f_alk+k_t*f_toh*f_cho*f_pch2oh)*.5	Sander et al. (2018)
G45098	TrGCN	LISOPACNO3O2 + NO → .21 NOA + .21 HOCH ₂ CHO + .21 HO ₂ + .49 HO12CO3C4 + .49 HCHO + .49 NO ₂ + .045 MVKNO ₃ + .045 HCHO + .255 CH ₃ COCH ₂ OH + .255 NO ₃ CH ₂ CHO + .225 H ₂ O ₂ + NO ₂	KR02N0	Sander et al. (2018)*
G45099	TrGCN	LISOPACNO3O2 → .21 NOA + .21 HOCH ₂ CHO + .21 HO ₂ + .49 HO12CO3C4 + .49 HCHO + .49 NO ₂ + .045 MVKNO ₃ + .045 HCHO + .255 CH ₃ COCH ₂ OH + .255 NO ₃ CH ₂ CHO + .225 H ₂ O ₂	k1_R02tOR02+KR02H02(5)*c(ind_H02)	Sander et al. (2018)
G45100	TrGCN	ISOPBDNO3O2 + NO → .6 CH ₃ COCH ₂ OH + .6 HOCH ₂ CHO + .26 MACRNO ₃ + .14 MVKNO ₃ + .4 HCHO + 4 HO ₂ + 1.6 NO ₂	KR02N0	Sander et al. (2018)*
G45101	TrGCN	ISOPBDNO3O2 → .6 CH ₃ COCH ₂ OH + .6 HOCH ₂ CHO + .26 MACRNO ₃ + .14 MVKNO ₃ + .4 HCHO + .4 HO ₂ + .6 NO ₂	k1_R02sOR02+KR02H02(5)*c(ind_H02)	Sander et al. (2018)
G45102	TrGCN	LISOPACNO ₃ + O ₃ → .8704 OH + .365 HO ₂ + .73 MGLYOX + .4325 NO ₃ CH ₂ CHO + .135 CH ₃ COCH ₂ OH + .0675 GLYOX + .4325 NO ₂ + .0891 H ₂ O ₂ + .135 NOA + .0675 HOCHCHO + .3866 HOCH ₂ CHO + .0405 CH ₃ OH + .0405 CO + .0054 HOCH ₂ CO	2.8E-17	Feierabend et al. (2008), Sander et al. (2018)

35

Table 1: Gas phase reactions (... continued)

#	labels	reaction	rate coefficient	reference
G45103	TrGC	DBIO2 → DBIO2	k1_R02s0R02	Sander et al. (2018)
G45104a	TrGC	DBIO2 + HO2 → DBIOOH	KR02H02(5)*(1.-rchohch2o2_oh)	Sander et al. (2018)*
G45104b	TrGC	DBIO2 + HO2 → DBIO2 + OH	KR02H02(5)*rchohch2o2_oh	Sander et al. (2018)
G45105a	TrGCN	DBIO2 + NO → DBIO2 + NO2	KR02N0*(1.-alpha_AN(7,2,0,0,0, temp, cair))	Sander et al. (2018)
G45105b	TrGCN	DBIO2 + NO → DB1NO3	KR02N0*alpha_AN(7,2,0,0,0, temp, cair)	Sander et al. (2018)
G45106	TrGCN	DBIO2 + NO3 → DBIO2 + NO2	KR02N03	Sander et al. (2018)
G45107	TrGC	DBIO2 → DBIO2 + OH	1.E4	Peeters and Nguyen (2012)*
G45108a	TrGC	DBIO2 → DBIO2	KDEC*0.72	see note*
G45108b	TrGC	DBIO2 → .5 HVMK + .5 HMAc + HCHO + HO2	KDEC*0.28	see note*
G45109	TrGC	DBIO2 → .48 CH3COCH2OH + .52 HOCH2CHO + .52 MGLYOX + .48 GLYOX + HO2	k1_R02s0R02	Sander et al. (2018)
G45110a	TrGC	DBIO2 + HO2 → DB2OOH	KR02H02(5)*(1.-rchohch2o2_oh)	Sander et al. (2018)
G45110b	TrGC	DBIO2 + HO2 → .48 CH3COCH2OH + .52 HOCH2CHO + .52 MGLYOX + .48 GLYOX + HO2 + OH	KR02H02(5)*rchohch2o2_oh	Sander et al. (2018)
G45111	TrGCN	DBIO2 + NO → .48 CH3COCH2OH + .52 HOCH2CHO + .52 MGLYOX + .48 GLYOX + HO2 + NO2	KR02N0	see note*
G45112	TrGCN	DBIO2 + NO3 → .48 CH3COCH2OH + .52 HOCH2CHO + .52 MGLYOX + .48 GLYOX + HO2 + NO2	KR02N03	Sander et al. (2018)
G45113	TrGC	DBIO2 → .48 MACROOH + .52 LHMVKABOOH + CO + OH	K14HSAL	Sander et al. (2018)
G45114a	TrGC	DBIOOH + OH → DBIO2	k_roohro	Sander et al. (2018)
G45114b	TrGC	DBIOOH + OH → HCOOH + HO2 + CH3COCHO2CHO	k_adt	Sander et al. (2018)*
G45115	TrGC	DBIOOH + HCOOH → C10DC2OOHC4OD + HCOOH	4.67E-26*temp**3.286*EXP(4509./ (1.987*temp))	Sander et al. (2018), da Silva (2010)*
G45116	TrGCN	DB1NO3 + OH → HCOOH + NO2 + CH3COCHO2CHO	k_adt	Sander et al. (2018)*
G45117	TrGC	DB2OOH + OH → DBIO2	k_roohro	Sander et al. (2018)*
G45118	TrGC	LISOPACOOH + O3 → 1.3272 OH + .36986 HO2 + .0432 H2O2 + .08422 CO + .2025 CH3OOH + .01215 CH2OO + .3704 HCHO + .00405 CH3OH + .0405 CO2 + .1825 HOCH2COCH2O2 + .365 MGLYOX + .3866 HOOCH2CHO + .135 CH3COCH2OH + .0675 GLYOX + .00324 HCOCO + .3866 HOCH2CHO + .135 CH3COCH2O2H + .0675 HOCHCHO + .0054 HOCH2CO	4.829E-16	Sander et al. (2018)

36

Table 1: Gas phase reactions (... continued)

#	labels	reaction	rate coefficient	reference
G45119a	TrGC	LZCO3HC23DBCOD + OH → .62 CO2H3CHO + .62 OH + .62 CO2 + .38 MGLYOX + .38 HCOCO3H + .38 HO2	k_adt*a_cho*a_co2h	Sander et al. (2018)
G45119b	TrGC	LZCO3HC23DBCOD + OH → .62 CH3COCO3H + 1.24 CO + 1.24 HO2 + .38 MGLYOX + .38 HO2 + .38 CO + .38 HO2 + .38 OH + .38 CO2	k_ads*a_cho*a_co2h	Sander et al. (2018)
G45120	TrGC	LISOPEFO2 → LISOPEFO	k1_R02p0R02	Sander et al. (2018)
G45121a	TrGCN	LISOPEFO2 + NO → LISOPEFO + NO2	KR02N0*(1.-alpha_AN(6,1,0,0,0, temp, cair))	Sander et al. (2018)
G45121b	TrGCN	LISOPEFO2 + NO → ISOPDNO3	KR02N0*alpha_AN(6,1,0,0,0, temp, cair)	Sander et al. (2018)*
G45122a	TrGC	LISOPEFO2 + HO2 → .7143 ISOPDOOH + .2857 ISOPBOOH	KR02H02(5)*(1.-rchohch2o2_oh)	Sander et al. (2018)
G45122b	TrGC	LISOPEFO2 + HO2 → LISOPEFO + OH	KR02H02(5)*rchohch2o2_oh	Sander et al. (2018)
G45123	TrGCN	LISOPEFO2 + NO3 → LISOPEFO + NO2	KR02N03	Sander et al. (2018)
G45124	TrGC	LISOPEFO2 → .7143 MACR + .2857 MVK + HCHO + OH	0.7143*KHSD+.2857*KHSB	Sander et al. (2018)
G45125	TrGC	LISOPEFO → .7143 MACR + .2857 MVK + HCHO + HO2	KDEC	Sander et al. (2018)
G45126a	TrGC	LISOPACO → 3METHYLFURAN + HO2	KDEC*0.37	Sander et al. (2018), Paulot et al. (2009a), Francisco-Marquez et al. (2003)
G45126b	TrGC	LISOPACO → .65 LHC4ACCHO + .65 HO2 + .35 DBIO2	KDEC*(1.-0.37)	Sander et al. (2018), Paulot et al. (2009a), Francisco-Marquez et al. (2003)
G45127a	TrGC	LISOPACO → 3METHYLFURAN + HO2	KDEC*0.37	Sander et al. (2018), Paulot et al. (2009a), Francisco-Marquez et al. (2003)
G45127b	TrGC	LISOPACO → .65 LHC4ACCHO + .65 HO2 + .35 DBIO2	KDEC*(1.-0.37)	Sander et al. (2018), Paulot et al. (2009a), Francisco-Marquez et al. (2003)
G45128	TrGC	3METHYLFURAN + OH → L3METHYLFURANO2	3.2E-11*EXP(310./temp)	Sander et al. (2018)*
G45129	TrGCN	3METHYLFURAN + NO3 → L3METHYLFURANO2 + NO2	1.9E-11	Sander et al. (2018), Atkinson et al. (2006)*
G45130	TrGC	L3METHYLFURANO2 → C4MDIAL + HO2	k1_R02s0R02	Sander et al. (2018)

37

Table 1: Gas phase reactions (... continued)

#	labels	reaction	rate coefficient	reference
G45131	TrGCN	L3METHYLFURANO2 + NO → C4MDIAL + HO ₂ + NO ₂	KR02N0	Sander et al. (2018)*
G45132	TrGC	L3METHYLFURANO2 + HO ₂ → C4MDIAL + HO ₂	KR02H02(5)	Sander et al. (2018)*
G45133	TrGC	LZCO3C23DBCOD → .62 EZCH3CO2CHCHO + .38 EZCHOCCH3CHO2 + CO ₂	k1_R02RC03	Sander et al. (2018)
G45134a	TrGC	LZCO3C23DBCOD + HO ₂ → .62 EZCH3CO2CHCHO + .38 EZCHOCCH3CHO2 + CO ₂ + OH	KAPH02*rc03_oh	Sander et al. (2018)
G45134b	TrGC	LZCO3C23DBCOD + HO ₂ → LZCO3HC23DBCOD	KAPH02*(rc03_oh+rc03_o3)	Sander et al. (2018)*
G45135	TrGCN	LZCO3C23DBCOD + NO → .62 EZCH3CO2CHCHO + .38 EZCHOCCH3CHO2 + CO ₂ + NO ₂	KAPN0	Sander et al. (2018)
G45136	TrGCN	LZCO3C23DBCOD + NO ₂ → LZCPANC23DBCOD	k_CH3CO3_N02	Rickard and Pascoe (2009)
G45137	TrGCN	LZCO3C23DBCOD + NO ₃ → .62 EZCH3CO2CHCHO + .38 EZCHOCCH3CHO2 + CO ₂ + NO ₂	KR02N03*1.74	Sander et al. (2018)
G45138	TrGCN	LZCPANC23DBCOD → LZCO3C23DBCOD + NO ₂	k_PAN_M	Rickard and Pascoe (2009)
G45139	TrGCN	LZCPANC23DBCOD + OH → .62 EZCH3CO2CHCHO + .38 EZCHOCCH3CHO2 + CO ₂ + NO ₂	2.52E-11	Sander et al. (2018)*
G45200	TrGTerC	C511O2 → CH ₃ C(O) + HCOCH2CHO	k1_R02s0R02	Rickard and Pascoe (2009)
G45201	TrGTerCN	C511O2 + NO → CH ₃ C(O) + HCOCH2CHO + NO ₂	KR02N0	Rickard and Pascoe (2009)*
G45202a	TrGTerC	C511O2 + HO ₂ → C511OOH	KR02H02(5)*rcoch2o2_oh	Rickard and Pascoe (2009), Sander et al. (2018)
G45202b	TrGTerC	C511O2 + HO ₂ → CH ₃ C(O) + HCOCH2CHO + OH	KR02H02(5)*rcoch2o2_oh	Rickard and Pascoe (2009), Sander et al. (2018)
G45203	TrGTerC	C511OOH + OH → C511O2	7.49E-11	Rickard and Pascoe (2009)
G45204	TrGTerC	CO23C4CHO + OH → CO23C4CO3	6.65E-11	Rickard and Pascoe (2009)
G45205	TrGTerCN	CO23C4CHO + NO ₃ → CO23C4CO3 + HNO ₃	KN03AL*5.5	Rickard and Pascoe (2009)
G45206	TrGTerC	CO23C4CO3 → CH ₃ COCOCH ₂ O ₂ + CO ₂	k1_R02RC03	Rickard and Pascoe (2009)
G45207	TrGTerCN	CO23C4CO3 + NO → CH ₃ COCOCH ₂ O ₂ + CO ₂ + NO ₂	KAPN0	Rickard and Pascoe (2009)*
G45208	TrGTerCN	CO23C4CO3 + NO ₂ → C5PAN9	k_CH3CO3_N02	Rickard and Pascoe (2009)
G45209a	TrGTerC	CO23C4CO3 + HO ₂ → CO23C4CO3H	KAPH02*(rc03_oh+rc03_o3)	Rickard and Pascoe (2009)
G45209b	TrGTerC	CO23C4CO3 + HO ₂ → CH ₃ COCOCH ₂ O ₂ + CO ₂ + OH	KAPH02*rc03_oh	Rickard and Pascoe (2009)
G45210	TrGTerCN	C5PAN9 → CO23C4CO3 + NO ₂	k_PAN_M	Rickard and Pascoe (2009)
G45211	TrGTerCN	C5PAN9 + OH → CH ₃ COCOCHO + CO + NO ₂	3.12E-13	Rickard and Pascoe (2009)
G45212	TrGTerC	C512O2 → C513O2	k1_R02pR02	Rickard and Pascoe (2009)
G45213	TrGTerC	C512O2 + HO ₂ → C512OOH	KR02H02(5)	Rickard and Pascoe (2009)
G45214	TrGTerCN	C512O2 + NO → C513O2 + NO ₂	KR02N0	Rickard and Pascoe (2009)*

38

Table 1: Gas phase reactions (... continued)

#	labels	reaction	rate coefficient	reference
G45215	TrGTerC	C512OOH + OH → CO13C4CHO + OH	1.01E-10	Rickard and Pascoe (2009)
G45216	TrGTerC	C513O2 → GLYOX + HOC ₂ H ₄ CO ₃	k1_R02s0R02	Rickard and Pascoe (2009)
G45217	TrGTerCN	C513O2 + NO → GLYOX + HOC ₂ H ₄ CO ₃ + NO ₂	KR02N0	Rickard and Pascoe (2009)*
G45218a	TrGTerC	C513O2 + HO ₂ → C513OOH	KR02H02(5)*rcoch2o2_oh	Rickard and Pascoe (2009), Sander et al. (2018)
G45218b	TrGTerC	C513O2 + HO ₂ → GLYOX + HOC ₂ H ₄ CO ₃ + OH	KR02H02(5)*rcoch2o2_oh	Rickard and Pascoe (2009), Sander et al. (2018)
G45219	TrGTerC	CO13C4CHO + OH → CHOC3COCO3	1.33E-10	Rickard and Pascoe (2009)
G45220	TrGTerCN	CO13C4CHO + NO ₃ → CHOC3COCO3 + HNO ₃	2.*KN03AL*5.5	Rickard and Pascoe (2009)
G45221	TrGTerC	C513OOH + OH → C513CO + OH	9.23E-11	Rickard and Pascoe (2009)
G45222	TrGTerC	CHOC3COCO3 → CHOC3COO2 + CO ₂	k1_R02RC03	Rickard and Pascoe (2009)
G45223	TrGTerC	CHOC3COCO3 + HO ₂ → CHOC3COOOH	KAPH02	Rickard and Pascoe (2009)
G45224	TrGTerCN	CHOC3COCO3 + NO ₂ → CHOC3COPAN	k_CH3CO3_N02	Rickard and Pascoe (2009)
G45225	TrGTerCN	CHOC3COCO3 + NO → CHOC3COO2 + CO ₂ + NO ₂	KAPN0	Rickard and Pascoe (2009)*
G45226	TrGTerC	C513CO + OH → HOC ₂ H ₄ CO ₃ + CO + CO	2.64E-11	Rickard and Pascoe (2009)
G45227	TrGTerC	C514O2 + HO ₂ → C514OOH	KR02H02(5)	Rickard and Pascoe (2009)
G45228a	TrGTerCN	C514O2 + NO → CO13C4CHO + HO ₂ + NO ₂	KR02N0*(1.-alpha_AN(7,2,0,1,0,temp,cair))	Rickard and Pascoe (2009), Sander et al. (2018)
G45228b	TrGTerCN	C514O2 + NO → C514NO3	KR02N0*alpha_AN(7,2,0,1,0,temp,cair)	Rickard and Pascoe (2009), Sander et al. (2018)
G45229	TrGTerCN	C514O2 + NO ₃ → CO13C4CHO + HO ₂ + NO ₂	KR02N03	Rickard and Pascoe (2009)
G45230	TrGTerC	C514O2 → CO13C4CHO + HO ₂	k1_R02sR02	Rickard and Pascoe (2009)
G45231	TrGTerC	C514OOH + OH → CO13C4CHO + OH	1.10E-10	Rickard and Pascoe (2009)
G45232	TrGTerCN	C514NO3 + OH → CO13C4CHO + NO ₂	4.33E-11	Rickard and Pascoe (2009)
G45233	TrGTerC	CHOC3COOOH + OH → CHOC3COCO3	7.55E-11	Rickard and Pascoe (2009)
G45234	TrGTerCN	CHOC3COPAN → CHOC3COCO3 + NO ₂	k_PAN_M	Rickard and Pascoe (2009)
G45235	TrGTerCN	CHOC3COPAN + OH → C4CODIAL + CO + NO ₂	7.19E-11	Rickard and Pascoe (2009)
G45236	TrGTerC	MBO + OH → LMBOABO2	8.1E-12*EXP(610./TEMP)	Rickard and Pascoe (2009), Sander et al. (2018)*
G45237a	TrGTerC	MBO + O ₃ → HCHO + .16 CH ₃ COCH ₃ + .16 HO ₂ + .16 CO + .16 OH + .84 MBOOO	1.0E-17*0.57	Rickard and Pascoe (2009), Sander et al. (2018)
G45237b	TrGTerC	MBO + O ₃ → IBUTALOH + .63 CO + .37 HOCH ₂ OOH + .16 OH + .16 HO ₂	1.0E-17*0.43	Rickard and Pascoe (2009), Sander et al. (2018)
G45238	TrGTerCN	MBO + NO ₃ → LNMBOABO2	4.6E-14*EXP(-400./TEMP)	Rickard and Pascoe (2009), Sander et al. (2018)

39

Table 1: Gas phase reactions (... continued)

#	labels	reaction	rate coefficient	reference
G45239	TrGTerC	LMBOABO2 + HO2 → LMBOABOOH	KR02H02(5)	Rickard and Pascoe (2009), Sander et al. (2018)
G45240a	TrGTerCN	LMBOABO2 + NO → LMBOABNO3	KR02N0*(.67*alpha_AN(7,2,0,0,0,0,temp,cair)+.33*alpha_AN(7,1,0,0,0,temp,cair))	Rickard and Pascoe (2009), Sander et al. (2018)
G45240b	TrGTerCN	LMBOABO2 + NO → HOCH2CHO + CH3COCH3 + HO2 + NO2	KR02N0*(1-(.67*alpha_AN(7,2,0,0,0,0,temp,cair)+.33*alpha_AN(7,1,0,0,0,temp,cair)))*.67	Rickard and Pascoe (2009), Sander et al. (2018)
G45240c	TrGTerCN	LMBOABO2 + NO → IBUTALOH + HCHO + HO2 + NO2	KR02N0*(1-(.67*alpha_AN(7,2,0,0,0,0,temp,cair)+.33*alpha_AN(7,1,0,0,0,temp,cair)))*.33	Rickard and Pascoe (2009), Sander et al. (2018)
G45241a	TrGTerC	LMBOABO2 → HOCH2CHO + CH3COCH3 + HO2	k1_R02s0R02*.67	Rickard and Pascoe (2009), Sander et al. (2018)
G45241b	TrGTerC	LMBOABO2 → IBUTALOH + HCHO + HO2	k1_R02p0R02*.33	Rickard and Pascoe (2009), Sander et al. (2018)
G45242a	TrGTerC	LMBOABOOH + OH → MBOACO	0.67*2.93E-11+.33*2.05E-12	Rickard and Pascoe (2009), Sander et al. (2018)
G45242b	TrGTerC	LMBOABOOH + OH → LMBOABO2	k_roohro	Rickard and Pascoe (2009), Sander et al. (2018)
G45243	TrGTerCN	LMBOABNO3 + OH → MBOACO + NO2	0.67*1.75E-12+.33*2.69E-12	Rickard and Pascoe (2009), Sander et al. (2018)
G45244	TrGTerC	MBOACO + OH → MBOCOCO + HO2	3.79E-12	Rickard and Pascoe (2009)
G45245	TrGTerC	MBOCOCO + OH → CO + IPRHOCO3	1.38E-11	Rickard and Pascoe (2009)
G45246	TrGTerCN	LNMBOABO2 + HO2 → LNMBOABOOH	KR02H02(5)	Rickard and Pascoe (2009), Sander et al. (2018)
G45247	TrGTerCN	LNMBOABO2 + NO → .65 NO3CH2CHO + .65 CH3COCH3 + .65 HO2 + .35 IBUTALOH + .35 HCHO + .35 NO2 + NO2	KR02N0	Rickard and Pascoe (2009), Sander et al. (2018)*
G45248	TrGTerCN	LNMBOABO2 + NO3 → .65 NO3CH2CHO + .65 CH3COCH3 + .65 HO2 + .35 IBUTALOH + .35 HCHO + .35 NO2 + NO2	KR02N03	Rickard and Pascoe (2009), Sander et al. (2018)
G45249	TrGTerCN	LNMBOABO2 → .65 NO3CH2CHO + .65 CH3COCH3 + .65 HO2 + .35 IBUTALOH + .35 HCHO + .35 NO2	k1_R02s0R02	Rickard and Pascoe (2009), Sander et al. (2018)
G45250a	TrGTerCN	LNMBOABOOH + OH → .65 C4MCONO3OH + .35 NMBOBOCO	0.65*4.89E-12+.35*2.52E-12	Rickard and Pascoe (2009), Sander et al. (2018)

40

Table 1: Gas phase reactions (... continued)

#	labels	reaction	rate coefficient	reference
G45250b	TrGTerCN	LNMBOABOOH + OH → LNMBOABO2	k_roohro	Rickard and Pascoe (2009), Sander et al. (2018)
G45251	TrGTerCN	NMBOBCO + OH → NC4OHCO3	4.26E-12	Rickard and Pascoe (2009)
G45252a	TrGTerCN	NC4OHCO3 + HO2 → IBUTALOH + CO2 + NO2 + OH	KAPH02*rc03_oh	Rickard and Pascoe (2009), Sander et al. (2018)
G45252b	TrGTerCN	NC4OHCO3 + HO2 → NC4OHCO3H	KAPH02*(rc03_o3+rc03_ooH)	Rickard and Pascoe (2009), Sander et al. (2018)
G45253	TrGTerCN	NC4OHCO3 + NO → IBUTALOH + CO2 + NO2 + NO2	KAPNO	Rickard and Pascoe (2009)
G45254	TrGTerCN	NC4OHCO3 + NO2 → NC4OHCPAN	k_CH3CO3_N02	Rickard and Pascoe (2009)
G45255	TrGTerCN	NC4OHCO3 + NO3 → IBUTALOH + CO2 + NO2 + NO2	KR02N03*1.74	Rickard and Pascoe (2009)
G45256	TrGTerCN	NC4OHCO3 → IBUTALOH + CO2 + NO2	k1_R02RC03	Rickard and Pascoe (2009)
G45257	TrGTerCN	NC4OHCO3H + OH → NC4OHCO3	4.50E-12	Rickard and Pascoe (2009)
G45258	TrGTerCN	NC4OHCPAN + OH → IBUTALOH + CO + NO2 + NO2	1.27E-12	Rickard and Pascoe (2009)
G45259	TrGTerCN	NC4OHCPAN → NC4OHCO3 + NO2	K_PAN_M	Rickard and Pascoe (2009)
G45260	TrGTerCN	C4MCONO3OH + OH → CH3COCH3 + HCHO + CO2 + NO2	1.23E-12	Rickard and Pascoe (2009), Sander et al. (2018)
G45400	TrGAroCN	NC4MDCO2HN + OH → MMALANHY + NO2	k_roohro	Rickard and Pascoe (2009)*
G45401	TrGAroCN	C54CO + NO3 → 3 CO + CH3C(O)OO + HNO3	KN03AL*5.5	Rickard and Pascoe (2009)
G45402	TrGAroC	C54CO + OH → 3 CO + CH3C(O)OO	1.72E-11	Rickard and Pascoe (2009)
G45403a	TrGAroCN	NTLFUO2 + HO2 → NTLFUOOH	KR02H02(5)*(1-rc0ch2o2_oh)	Rickard and Pascoe (2009)
G45403b	TrGAroCN	NTLFUO2 + HO2 → ACCOMECHO + NO2 + OH	KR02H02(5)*rc0ch2o2_oh	Rickard and Pascoe (2009)
G45404	TrGAroCN	NTLFUO2 + NO → ACCOMECHO + NO2 + NO2	KR02N0	Rickard and Pascoe (2009)*
G45405	TrGAroCN	NTLFUO2 + NO3 → ACCOMECHO + NO2 + NO2	KR02N03	Rickard and Pascoe (2009)*
G45406	TrGAroCN	NTLFUO2 → ACCOMECHO + NO2	k1_R02t0R02	Rickard and Pascoe (2009)*
G45407	TrGAroC	C5134CO2OH + OH → C54CO + HO2	7.48E-11	Rickard and Pascoe (2009)
G45408	TrGAroCN	C5COO2NO2 + OH → MGLYOX + CO + CO + NO2	5.43E-11	Rickard and Pascoe (2009)
G45409	TrGAroCN	C5COO2NO2 → C5CO14O2 + NO2	k_PAN_M	Rickard and Pascoe (2009)*
G45410	TrGAroC	C5DIALOOH + OH → C5DIALCO + OH	7.52E-11	Rickard and Pascoe (2009)
G45411a	TrGAroC	C4CO2DBCO3 + HO2 → C4CO2DCO3H	KAPH02*(rc03_ooH+rc03_o3)	Rickard and Pascoe (2009)
G45411b	TrGAroC	C4CO2DBCO3 + HO2 → HO2 + CO + HCOCOCHO + CO2 + OH	KAPH02*rc03_oh	Rickard and Pascoe (2009), Sander et al. (2018)
G45412	TrGAroCN	C4CO2DBCO3 + NO → HO2 + CO + HCOCOCHO + CO2 + NO2	KAPNO	Rickard and Pascoe (2009)
G45413	TrGAroCN	C4CO2DBCO3 + NO2 → C4CO2DBPAN	k_CH3CO3_N02	Rickard and Pascoe (2009)*

41

Table 1: Gas phase reactions (... continued)

#	labels	reaction	rate coefficient	reference
G45414	TrGAroCN	C4CO2DBCO3 + NO ₃ → HO ₂ + CO + HCOCOCHO + CO ₂ + NO ₂	KR02N03*1.74	Rickard and Pascoe (2009)
G45415	TrGAroC	C4CO2DBCO3 → HO ₂ + CO + HCOCOCHO + CO ₂	k1_R02RC03	Rickard and Pascoe (2009)
G45416	TrGAroC	MMALANHY + OH → MMALANHYO2	1.50E-12	Rickard and Pascoe (2009)
G45421a	TrGAroC	MMALANHYO2 + HO ₂ → MMALNHYOOH	KR02H02(5)*(1-rcoch2o2_oh-rchohch2o2_oh)	Rickard and Pascoe (2009), Sander et al. (2018)
G45421b	TrGAroC	MMALANHYO2 + HO ₂ → CO2H3CO3 + CO ₂ + OH	KR02H02(5)*(rcoch2o2_oh+rchohch2o2_oh)	Rickard and Pascoe (2009), Sander et al. (2018)
G45422	TrGAroCN	MMALANHYO2 + NO → CO2H3CO3 + CO ₂ + NO ₂	KR02N0	Rickard and Pascoe (2009)*
G45423	TrGAroCN	MMALANHYO2 + NO ₃ → CO2H3CO3 + CO ₂ + NO ₂	KR02N03	Rickard and Pascoe (2009)*
G45424	TrGAroC	MMALANHYO2 → CO2H3CO3 + CO ₂	k1_R02t0R02	Rickard and Pascoe (2009)*
G45428	TrGAroCN	C4CO2DBPAN + OH → HCOCOCHO + CO ₂ + CO + NO ₂	2.74E-11	Rickard and Pascoe (2009)
G45429	TrGAroCN	C4CO2DBPAN → C4CO2DBCO3 + NO ₂	k_PAN_M	Rickard and Pascoe (2009)*
G45430a	TrGAroC	C5CO14O2 + HO ₂ → .83 MALANHY + .83 CH ₃ + .17 MGLYOX + .17 HO ₂ + .17 CO + .17 CO ₂ + OH	KAPH02*rc03_oh	Rickard and Pascoe (2009)*
G45430b	TrGAroC	C5CO14O2 + HO ₂ → C5CO14OH + O ₃	KAPH02*rc03_03	Rickard and Pascoe (2009)
G45430c	TrGAroC	C5CO14O2 + HO ₂ → C5CO14OOH	KAPH02*rc03_0oh	Rickard and Pascoe (2009)
G45431	TrGAroCN	C5CO14O2 + NO → .83 MALANHY + .83 CH ₃ + .17 MGLYOX + .17 HO ₂ + .17 CO + .17 CO ₂ + NO ₂	KAPN0	Rickard and Pascoe (2009)*
G45432	TrGAroCN	C5CO14O2 + NO ₂ → C5COO2NO2	k_CH3CO3_N02	Rickard and Pascoe (2009)*
G45433	TrGAroCN	C5CO14O2 + NO ₃ → .83 MALANHY + .83 CH ₃ + .17 MGLYOX + .17 HO ₂ + .17 CO + .17 CO ₂ + NO ₂	KR02N03*1.74	Rickard and Pascoe (2009)*
G45434	TrGAroC	C5CO14O2 → .83 MALANHY + .83 CH ₃ + .17 MGLYOX + .17 HO ₂ + .17 CO + .17 CO ₂	k1_R02RC03	Rickard and Pascoe (2009)*
G45436	TrGAroC	C5CO14OH + OH → .83 MALANHY + .83 CH ₃ + .17 MGLYOX + .17 HO ₂ + .17 CO + .17 CO ₂	5.44E-11	Rickard and Pascoe (2009)*
G45441	TrGAroCN	C5DICARB + NO ₃ → C5CO14O2 + HNO ₃	KN03AL*2.75	Rickard and Pascoe (2009)
G45442	TrGAroC	C5DICARB + O ₃ → .5338 GLYOX + .063 CH ₃ CHO + .348 CH ₃ C(O)OO + .918 CO + .57 OH + .473 HO ₂ + .0563 CH ₃ COCO ₂ H + .5338 MGLYOX + .676 H ₂ O ₂ + .063 HCHO + .0563 HCOCO ₂ H + .2465 CO ₂	2.00E-18	Rickard and Pascoe (2009)
G45443	TrGAroC	C5DICARB + OH → .48 C5CO14O2 + .52 C5DICARBO2	6.2E-11	Rickard and Pascoe (2009)
G45444	TrGAroC	MC3ODBCO2H + OH → .35 GLYOX + .35 CH ₃ + .35 CO + .35 CO ₂ + .65 MMALANHY + .65 HO ₂	4.38E-11	Rickard and Pascoe (2009)*

42

Table 1: Gas phase reactions (... continued)

#	labels	reaction	rate coefficient	reference
G45451	TrGAroCN	TLFUONE + NO ₃ → NTLFUO2	1.00E-12	Rickard and Pascoe (2009)
G45452	TrGAroC	TLFUONE + O ₃ → .5 CO + .5 OH + .5 MECOACETO2 + .3125 C24O3CCO2H + .1875 ACCOMECHO + .1875 H ₂ O ₂	8.00E-19	see note*
G45453	TrGAroC	TLFUONE + OH → TLFUO2	6.90E-11	Rickard and Pascoe (2009)
G45454a	TrGAroC	ACCOMECO3 + HO ₂ → ACCOMECHO3H	KAPH02*(rc03_0oh+rc03_03)	Rickard and Pascoe (2009)
G45454b	TrGAroC	ACCOMECO3 + HO ₂ → MECOACETO2 + CO ₂ + OH	KAPH02*rc03_oh	Rickard and Pascoe (2009)
G45455	TrGAroCN	ACCOMECO3 + NO → MECOACETO2 + CO ₂ + NO ₂	KAPN0	Rickard and Pascoe (2009)
G45456	TrGAroCN	ACCOMECO3 + NO ₂ → ACCOMECHAN	k_CH3CO3_N02	Rickard and Pascoe (2009)*
G45457	TrGAroCN	ACCOMECO3 + NO ₃ → MECOACETO2 + CO ₂ + NO ₂	KR02N03*1.74	Rickard and Pascoe (2009)
G45458	TrGAroC	ACCOMECO3 → MECOACETO2 + CO ₂	k1_R02RC03	Rickard and Pascoe (2009)
G45459	TrGAroC	C4CO2DCO3H + OH → C4CO2DBCO3	3.06E-11	Rickard and Pascoe (2009)
G45464	TrGAroCN	ACCOMECO3 + NO ₃ → ACCOMECHO3 + HNO ₃	KN03AL*5.5	Rickard and Pascoe (2009)
G45465	TrGAroC	ACCOMECO3 + OH → ACCOMECHO3	7.09E-11	Rickard and Pascoe (2009)
G45466	TrGAroC	MMALNHYOOH + OH → MMALANHYO2	1.69E-11	Rickard and Pascoe (2009)
G45467a	TrGAroC	C5DICAROOH + OH → C5134CO2OH + OH	1.21E-10	Rickard and Pascoe (2009)
G45467b	TrGAroC	C5DICAROOH + OH → C5DICARBO2	k_roohro	Rickard and Pascoe (2009)
G45468	TrGAroC	C24O3CCO2H + OH → MECOACETO2 + CO ₂	8.76E-13	Rickard and Pascoe (2009)
G45469	TrGAroCN	NTLFUOOH + OH → NTLFUO2	4.44E-12	Rickard and Pascoe (2009)
G45470	TrGAroCN	ACCOMEPAN + OH → METACETHO + CO + CO + NO ₂	1.00E-14	Rickard and Pascoe (2009)
G45471	TrGAroCN	ACCOMEPAN → ACCOMECHO3 + NO ₂	k_PAN_M	Rickard and Pascoe (2009)
G45476a	TrGAroC	TLFUO2 + HO ₂ → TLFUOOH	KR02H02(5)*(1-rcoch2o2_oh-rchohch2o2_oh)	Rickard and Pascoe (2009)
G45476b	TrGAroC	TLFUO2 + HO ₂ → ACCOMECHO + HO ₂ + OH	KR02H02(5)*(rcoch2o2_oh+rchohch2o2_oh)	Rickard and Pascoe (2009)*
G45477	TrGAroCN	TLFUO2 + NO → ACCOMECHO + HO ₂ + NO ₂	KR02N0	Rickard and Pascoe (2009)*
G45478	TrGAroCN	TLFUO2 + NO ₃ → ACCOMECHO + HO ₂ + NO ₂	KR02N03	Rickard and Pascoe (2009)*
G45479	TrGAroC	TLFUO2 → ACCOMECHO + HO ₂	k1_R02t0R02	Rickard and Pascoe (2009)*
G45480	TrGAroC	C5CO14OOH + OH → C5CO14O2	3.59E-12	Rickard and Pascoe (2009)
G45483	TrGAroC	TLFUOOH + OH → TLFUO2	2.53E-11	Rickard and Pascoe (2009)
G45485	TrGAroC	ACCOMECO3H + OH → ACCOMECHO3	3.59E-12	Rickard and Pascoe (2009)
G45486a	TrGAroC	C5DIALO2 + HO ₂ → C5DIALOOH	KR02H02(5)*(1-rcoch2o2_oh)	Rickard and Pascoe (2009)
G45486b	TrGAroC	C5DIALO2 + HO ₂ → MALDIAL + CO + HO ₂ + OH	KR02H02(5)*rcoch2o2_oh	Rickard and Pascoe (2009)*
G45487	TrGAroCN	C5DIALO2 + NO → MALDIAL + CO + HO ₂ + NO ₂	KR02N0	Rickard and Pascoe (2009)*

43

Table 1: Gas phase reactions (... continued)

#	labels	reaction	rate coefficient	reference
G45488	TrGAroCN	C5DIALO2 + NO ₃ → MALDIAL + CO + HO ₂ + NO ₂	KR02N03	Rickard and Pascoe (2009)*
G45489	TrGAroC	C5DIALO2 → MALDIAL + CO + HO ₂	k1_R02s0R02	Rickard and Pascoe (2009)*
G45490a	TrGAroC	C5DICARBO2 + HO ₂ → C5DICAROOH	KR02H02(5)*(rco3_ooH+rco3_o3)	Rickard and Pascoe (2009)
G45491b	TrGAroC	C5DICARBO2 + HO ₂ → MGLYOX + GLYOX + HO ₂ + OH	KR02H02(5)*rco3_oh	Rickard and Pascoe (2009)*
G45492	TrGAroCN	C5DICARBO2 + NO → MGLYOX + GLYOX + HO ₂ + NO ₂	KR02N0	Rickard and Pascoe (2009)*
G45493	TrGAroCN	C5DICARBO2 + NO ₃ → MGLYOX + GLYOX + HO ₂ + NO ₂	KR02N03	Rickard and Pascoe (2009)*
G45494	TrGAroC	C5DICARBO2 → MGLYOX + GLYOX + HO ₂	k1_R02s0R02	Rickard and Pascoe (2009)*
G46200a	TrGTerC	CO235C6O2 + HO ₂ → CO235C6OOH	KR02H02(6)*rcoch2o2_ooH	Rickard and Pascoe (2009), Sander et al. (2018)
G46200b	TrGTerC	CO235C6O2 + HO ₂ → CO23C4CO3 + HCHO + OH	KR02H02(6)*rcoch2o2_oh	Rickard and Pascoe (2009), Sander et al. (2018)
G46201	TrGTerCN	CO235C6O2 + NO → CO23C4CO3 + HCHO + NO ₂	KR02N0	Rickard and Pascoe (2009)*
G46202	TrGTerC	CO235C6O2 → CO23C4CO3 + HCHO	k1_R02p0R02	Rickard and Pascoe (2009)
G46203	TrGTerC	CO235C6OOH + OH → CO235C6O2	1.01E-11	Rickard and Pascoe (2009)
G46204	TrGTerC	C614O2 → CO23C4CHO + HCHO + HO ₂	k1_R02s0R02	Rickard and Pascoe (2009)
G46205a	TrGTerCN	C614O2 + NO → CO23C4CHO + HCHO + HO ₂ + NO ₂	KR02N0*(1-alpha_AN(9,2,0,1,0,temp,cair))	Rickard and Pascoe (2009)
G46205b	TrGTerCN	C614O2 + NO → C614NO3	KR02N0*alpha_AN(9,2,0,1,0,temp,cair)	Rickard and Pascoe (2009)
G46206a	TrGTerC	C614O2 + HO ₂ → C614OOH	KR02H02(6)*(1-rchohch2o2_oh)	Rickard and Pascoe (2009), Sander et al. (2018)
G46206b	TrGTerC	C614O2 + HO ₂ → CO23C4CHO + HCHO + HO ₂ + OH	KR02H02(6)*rchohch2o2_oh	Rickard and Pascoe (2009), Sander et al. (2018)
G46207	TrGTerCN	C614NO3 + OH → C614CO + NO ₂	7.11E-12	Rickard and Pascoe (2009)
G46208	TrGTerC	C614OOH + OH → C614CO + OH	8.69E-11	Rickard and Pascoe (2009)
G46209	TrGTerC	C614CO + OH → CO235C5CHO + HO ₂	3.22E-12	Rickard and Pascoe (2009)
G46210	TrGTerC	CO235C5CHO + OH → CO23C4CO3 + CO	1.33E-11	Rickard and Pascoe (2009)
G46211	TrGTerCN	CO235C5CHO + NO ₃ → CO23C4CO3 + CO + HNO ₃	KN03AL*5.5	Rickard and Pascoe (2009)
G46400	TrGAroC	PHENO0H + OH → PHENO2	1.16E-10	Rickard and Pascoe (2009)
G46401	TrGAroC	C6CO4DB + OH → CO + CO + HO ₂ + CO + HCOCOCHO	7.70E-11	Rickard and Pascoe (2009)
G46402	TrGAroC	C5CO2DCO3H + OH → C5CO2DBC03	3.60E-11	Rickard and Pascoe (2009)

44

Table 1: Gas phase reactions (... continued)

#	labels	reaction	rate coefficient	reference
G46403	TrGAroCN	NDNPHEOOH + OH → NDNPHENO2	k_roohro	Rickard and Pascoe (2009)
G46404a	TrGAroC	C615CO2O2 + HO ₂ → C615CO2OOH	KR02H02(6)*(1-rcoch2o2_oh)	Rickard and Pascoe (2009)
G46404b	TrGAroC	C615CO2O2 + HO ₂ → C5DICARB + CO + HO ₂ + OH	KR02H02(6)*rcoch2o2_oh	Rickard and Pascoe (2009)*
G46405	TrGAroCN	C615CO2O2 + NO → C5DICARB + CO + HO ₂ + NO ₂	KR02N0	Rickard and Pascoe (2009)*
G46406	TrGAroCN	C615CO2O2 + NO ₃ → C5DICARB + CO + HO ₂ + NO ₂	KR02N03	Rickard and Pascoe (2009)*
G46407	TrGAroC	C615CO2O2 → C5DICARB + CO + HO ₂	k1_R02s0R02	Rickard and Pascoe (2009)*
G46408	TrGAroCN	BZEMUCPAN + OH → MALDIAL + CO + CO ₂ + NO ₂	4.05E-11	Rickard and Pascoe (2009)
G46409	TrGAroCN	BZEMUCPAN → BZEMUCCO3 + NO ₂	k_PAN_M	Rickard and Pascoe (2009)
G46410	TrGAroCN	BZBIPERNO3 + OH → BZOBIPEROH + NO ₂	7.30E-11	Rickard and Pascoe (2009)
G46411	TrGAroCN	HOC6H4NO2 + NO ₃ → NPHEN10 + HNO ₃	9.00E-14	Rickard and Pascoe (2009)
G46412	TrGAroCN	HOC6H4NO2 + OH → NPHEN10	9.00E-13	Rickard and Pascoe (2009)
G46413a	TrGAroCN	NDNPHENO2 + HO ₂ → NDNPHENO0H	KR02H02(6)*(1-rchohch2o2_oh)	Rickard and Pascoe (2009)
G46413b	TrGAroCN	NDNPHENO2 + HO ₂ → NC4DCO2H + HNO ₃ + CO + CO + NO ₂ + OH	KR02H02(6)*rchohch2o2_oh	Rickard and Pascoe (2009)*
G46414	TrGAroCN	NDNPHENO2 + NO → NC4DCO2H + HNO ₃ + CO + CO + NO ₂ + NO ₂	KR02N0	Rickard and Pascoe (2009)*
G46415	TrGAroCN	NDNPHENO2 + NO ₃ → NC4DCO2H + HNO ₃ + CO + CO + NO ₂ + NO ₂	KR02N03	Rickard and Pascoe (2009)*
G46416	TrGAroCN	NDNPHENO2 → NC4DCO2H + HNO ₃ + CO + CO + NO ₂	k1_R02IS0P02	Rickard and Pascoe (2009)*
G46417	TrGAroC	PBZQCO + OH → C5CO2OHC03	6.07E-11	Rickard and Pascoe (2009)
G46418	TrGAroCN	CATECHOL + NO ₃ → CATEC10 + HNO ₃	9.9E-11	Rickard and Pascoe (2009)*
G46419	TrGAroC	CATECHOL + O ₃ → MALDALCO2H + HCOCO2H + HO ₂ + OH	9.2E-18	Rickard and Pascoe (2009)
G46420	TrGAroC	CATECHOL + OH → CATEC10	1.0E-10	Rickard and Pascoe (2009)
G46421	TrGAroC	C5COOHCO3H + OH → C5CO2OHC03	8.01E-11	Rickard and Pascoe (2009)
G46422	TrGAroCN	NCATECHOL + NO ₃ → NNCATECO2	2.60E-12	Rickard and Pascoe (2009)
G46423	TrGAroCN	NCATECHOL + OH → NCATECO2	3.47E-12	Rickard and Pascoe (2009)
G46424a	TrGAroC	C5CO2OHC03 + HO ₂ → C5COOHCO3H	KAPH02*(rco3_ooH+rco3_o3)	Rickard and Pascoe (2009)
G46424b	TrGAroC	C5CO2OHC03 + HO ₂ → HOCOC4DIAL + HO ₂ + CO + CO ₂ + OH	KAPH02*rco3_oh	Rickard and Pascoe (2009)
G46425	TrGAroCN	C5CO2OHC03 + NO → HOCOC4DIAL + HO ₂ + CO + CO ₂ + NO ₂	KAPN0	Rickard and Pascoe (2009)
G46426	TrGAroCN	C5CO2OHC03 + NO ₂ → C5CO2OHPAN	k_CH3C03_N02	Rickard and Pascoe (2009)*

45

Table 1: Gas phase reactions (... continued)

#	labels	reaction	rate coefficient	reference
G46427	TrGAroCN	$C_5CO_2OHCOC_3 + NO_3 \rightarrow HOCOC_4DIAL + HO_2 + CO + CO_2 + NO_2$	$KR02N03*1.74$	Rickard and Pascoe (2009)
G46428	TrGAroC	$C_5CO_2OHCOC_3 \rightarrow HOCOC_4DIAL + HO_2 + CO + CO_2$	$k1_R02R0C03$	Rickard and Pascoe (2009)
G46429	TrGAroCN	$BZEPOXMUC + NO_3 \rightarrow BZEMUCCO_3 + HNO_3$	$2*KN03AL*2.75$	Rickard and Pascoe (2009)
G46430	TrGAroC	$BZEPOXMUC + O_3 \rightarrow EPXC_4DIAL + .125 HCHO + .1125 HCOCO_2H + .0675 GLYOX + .0675 H_2O_2 + .82 HO_2 + .57 OH + 1.265 CO + .25 CO_2$	$2.00E-18$	Rickard and Pascoe (2009)*
G46431	TrGAroC	$BZEPOXMUC + OH \rightarrow .31 BZEMUCCO_3 + .69 BZEMUCO_2$	$6.08E-11$	Rickard and Pascoe (2009)
G46432a	TrGAroCN	$NCATECO_2 + HO_2 \rightarrow NCATECOOH$	$KR02H02(6)*(1-rchohch2o2_oh)$	Rickard and Pascoe (2009)
G46432b	TrGAroCN	$NCATECO_2 + HO_2 \rightarrow NC_4DCO_2H + HCOCO_2H + HO_2 + OH$	$KR02H02(6)*rchohch2o2_oh$	Rickard and Pascoe (2009)*
G46433	TrGAroCN	$NCATECO_2 + NO \rightarrow NC_4DCO_2H + HCOCO_2H + HO_2 + NO_2$	$KR02N0$	Rickard and Pascoe (2009)*
G46434	TrGAroCN	$NCATECO_2 + NO_3 \rightarrow NC_4DCO_2H + HCOCO_2H + HO_2 + NO_2$	$KR02N03$	Rickard and Pascoe (2009)*
G46435	TrGAroCN	$NCATECO_2 \rightarrow NC_4DCO_2H + HCOCO_2H + HO_2$	$k1_R02IS0PD02$	Rickard and Pascoe (2009)*
G46436	TrGAroCN	$NPHEN1OOH + OH \rightarrow NPHEN1O_2$	$9.00E-13$	Rickard and Pascoe (2009)
G46437a	TrGAroCN	$NPHENO_2 + HO_2 \rightarrow NPHENOOH$	$KR02H02(6)*(1-rchohch2o2_oh)$	Rickard and Pascoe (2009)
G46437b	TrGAroCN	$NPHENO_2 + HO_2 \rightarrow MALDALCO_2H + GLYOX + NO_2 + OH$	$KR02H02(6)*rchohch2o2_oh$	Rickard and Pascoe (2009)*
G46438	TrGAroCN	$NPHENO_2 + NO \rightarrow MALDALCO_2H + GLYOX + NO_2 + NO_2$	$KR02N0$	Rickard and Pascoe (2009)*
G46439	TrGAroCN	$NPHENO_2 + NO_3 \rightarrow MALDALCO_2H + GLYOX + NO_2 + NO_2$	$KR02N03$	Rickard and Pascoe (2009)*
G46440	TrGAroCN	$NPHENO_2 \rightarrow MALDALCO_2H + GLYOX + NO_2$	$k1_R02IS0PD02$	Rickard and Pascoe (2009)*
G46441	TrGAroC	$BENZENE + OH \rightarrow .352 BZBIPERO_2 + .118 BZEPOXMUC + .118 HO_2 + .53 PHENOL + .53 HO_2$	$2.3E-12*EXP(-190/TEMP)$	Rickard and Pascoe (2009)*
G46442	TrGAroCN	$C_5CO_2OHPAN + OH \rightarrow HOCOC_4DIAL + CO + CO + NO_2$	$7.66E-11$	Rickard and Pascoe (2009)
G46443	TrGAroCN	$C_5CO_2OHPAN \rightarrow C_5CO_2OHCOC_3 + NO_2$	k_PAN_M	Rickard and Pascoe (2009)
G46444	TrGAroCN	$CATEC1O + NO_2 \rightarrow NCATECHOL$	k_C6H5O_N02	Rickard and Pascoe (2009), Platz et al. (1998)
G46445	TrGAroC	$CATEC1O + O_3 \rightarrow CATEC1O_2$	k_C6H5O_03	Rickard and Pascoe (2009), Tao and Li (1999)

46

Table 1: Gas phase reactions (... continued)

#	labels	reaction	rate coefficient	reference
G46446	TrGAroC	$BZEMUCCO + OH \rightarrow EPXDLCO_3 + GLYOX$	$9.20E-11$	Rickard and Pascoe (2009)
G46447a	TrGAroCN	$NNCATECO_2 + HO_2 \rightarrow NNCATECOOH$	$KR02H02(6)*(1-rchohch2o2_oh)$	Rickard and Pascoe (2009)
G46447b	TrGAroCN	$NNCATECO_2 + HO_2 \rightarrow NC_4DCO_2H + HCOCO_2H + NO_2 + OH$	$KR02H02(6)*rchohch2o2_oh$	Rickard and Pascoe (2009)*
G46448	TrGAroCN	$NNCATECO_2 + NO \rightarrow NC_4DCO_2H + HCOCO_2H + NO_2 + NO_2$	$KR02N0$	Rickard and Pascoe (2009)*
G46449	TrGAroCN	$NNCATECO_2 + NO_3 \rightarrow NC_4DCO_2H + HCOCO_2H + NO_2 + NO_2$	$KR02N03$	Rickard and Pascoe (2009)*
G46450	TrGAroCN	$NNCATECO_2 \rightarrow NC_4DCO_2H + HCOCO_2H + NO_2$	$k1_R02IS0PD02$	Rickard and Pascoe (2009)*
G46451	TrGAroC	$BZEMUCCO_2H + OH \rightarrow C_5DIALO_2 + CO_2$	$4.06E-11$	Rickard and Pascoe (2009)
G46452	TrGAroCN	$NNCATECOOH + OH \rightarrow NNCATECO_2$	k_roohro	Rickard and Pascoe (2009)
G46453	TrGAroCN	$NPHEN1O + NO_2 \rightarrow DNPHEN$	k_C6H5O_N02	Rickard and Pascoe (2009), Platz et al. (1998)
G46454	TrGAroCN	$NPHEN1O + O_3 \rightarrow NPHEN1O_2$	k_C6H5O_03	Rickard and Pascoe (2009), Tao and Li (1999)
G46455	TrGAroCN	$DNPHEN + NO_3 \rightarrow NDNPHENO_2$	$2.25E-15$	Rickard and Pascoe (2009)
G46456	TrGAroCN	$DNPHEN + OH \rightarrow DNPHEO_2$	$3.00E-14$	Rickard and Pascoe (2009)
G46457	TrGAroCN	$PHENOL + NO_3 \rightarrow .742 C_6H_5O + .742 HNO_3 + .258 NPHENO_2$	$3.8E-12$	Rickard and Pascoe (2009)*
G46458	TrGAroC	$PHENOL + OH \rightarrow .06 C_6H_5O + .8 CATECHOL + .8 HO_2 + .14 PHENO_2$	$4.7E-13*EXP(1220/TEMP)$	Rickard and Pascoe (2009)*
G46459	TrGAroCN	$PBZQONE + NO_3 \rightarrow NBZQO_2$	$3.00E-13$	Rickard and Pascoe (2009)
G46460	TrGAroC	$PBZQONE + OH \rightarrow PBZQO_2$	$4.6E-12$	Rickard and Pascoe (2009)
G46461a	TrGAroC	$PHENO_2 + HO_2 \rightarrow PHENOOH$	$KR02H02(6)*(1-rchohch2o2_oh)$	Rickard and Pascoe (2009)
G46461b	TrGAroC	$PHENO_2 + HO_2 \rightarrow .71 MALDALCO_2H + .71 GLYOX + .29 PBZQONE + HO_2 + OH$	$KR02H02(6)*rchohch2o2_oh$	Rickard and Pascoe (2009)*
G46462	TrGAroCN	$PHENO_2 + NO \rightarrow .71 MALDALCO_2H + .71 GLYOX + .29 PBZQONE + HO_2 + NO_2$	$KR02N0$	Rickard and Pascoe (2009)*
G46463	TrGAroCN	$PHENO_2 + NO_3 \rightarrow .71 MALDALCO_2H + .71 GLYOX + .29 PBZQONE + HO_2 + NO_2$	$KR02N03$	Rickard and Pascoe (2009)*
G46464	TrGAroC	$PHENO_2 \rightarrow .71 MALDALCO_2H + .71 GLYOX + .29 PBZQONE + HO_2$	$k1_R02IS0PD02$	Rickard and Pascoe (2009)*
G46465	TrGAroC	$C_615CO_2OOH + OH \rightarrow C_6125CO + OH$	$9.42E-11$	Rickard and Pascoe (2009)
G46466a	TrGAroC	$C_5CO_2DICO_3 + HO_2 \rightarrow C_5CO_2DCO_3H$	$KAPH02*(rco3_ooh+rco3_o3)$	Rickard and Pascoe (2009)

47

Table 1: Gas phase reactions (... continued)

#	labels	reaction	rate coefficient	reference
G46466b	TrGAroC	C5CO2DBCO3 + HO ₂ → CH ₃ C(O) + HCOCOCHO + CO ₂ + OH	KAPH02*rc03_oh	Rickard and Pascoe (2009)
G46467	TrGAroCN	C5CO2DBCO3 + NO → CH ₃ C(O) + HCOCOCHO + CO ₂ + NO ₂	KAPNO	Rickard and Pascoe (2009)
G46468	TrGAroCN	C5CO2DBCO3 + NO ₂ → C5CO2DBPAN	k_CH3CO3_NO2	Rickard and Pascoe (2009)*
G46469	TrGAroCN	C5CO2DBCO3 + NO ₃ → CH ₃ C(O) + HCOCOCHO + CO ₂ + NO ₂	KR02N03*1.74	Rickard and Pascoe (2009)
G46470	TrGAroC	C5CO2DBCO3 → CH ₃ C(O) + HCOCOCHO + CO ₂	k1_R02RC03	Rickard and Pascoe (2009)
G46471	TrGAroCN	NPHEN1O2 + HO ₂ → NPHEN1OOH	KR02H02(6)	Rickard and Pascoe (2009)
G46472a	TrGAroCN	NPHEN1O2 + NO → NPHEN1O + NO ₂	KR02N0	Rickard and Pascoe (2009)
G46472b	TrGAroCN	NPHEN1O2 + NO ₂ → NPHEN1O + NO ₃	k_C6H5O2_NO2	Jagiella and Zabel (2007)*
G46473	TrGAroCN	NPHEN1O2 + NO ₃ → NPHEN1O + NO ₂	KR02N03	Rickard and Pascoe (2009)
G46474	TrGAroCN	NPHEN1O2 → NPHEN1O	k1_R02sR02	Rickard and Pascoe (2009)
G46475	TrGAroCN	NPHEOOH + OH → NPHEO2	1.07E-10	Rickard and Pascoe (2009)
G46476	TrGAroCN	C6H5O + NO ₂ → HOC6H4NO2	k_C6H5O_NO2	Rickard and Pascoe (2009), Platz et al. (1998)*
G46477	TrGAroC	C6H5O + O ₃ → C6H5O2	k_C6H5O_O3	Rickard and Pascoe (2009), Tao and Li (1999)
G46478	TrGAroCN	NCATECOOH + OH → NCATECO2	k_roohro	Rickard and Pascoe (2009)
G46479	TrGAroC	PBZQOOH + OH → PBZQCO + OH	1.23E-10	Rickard and Pascoe (2009)
G46480a	TrGAroC	PBZQO2 + HO ₂ → PBZQOOH	KR02H02(6)*(1-rchohch2o2_oh-rcoch2o2_oh)	Rickard and Pascoe (2009)
G46480b	TrGAroC	PBZQO2 + HO ₂ → C5CO2OHCO3 + OH	KR02H02(6)*(rchohch2o2_oh+rcoch2o2_oh)	Rickard and Pascoe (2009)*
G46481	TrGAroCN	PBZQO2 + NO → C5CO2OHCO3 + NO ₂	KR02N0	Rickard and Pascoe (2009)*
G46482	TrGAroCN	PBZQO2 + NO ₃ → C5CO2OHCO3 + NO ₂	KR02N03	Rickard and Pascoe (2009)*
G46483	TrGAroC	PBZQO2 → C5CO2OHCO3	k1_R02s0R02	Rickard and Pascoe (2009)*
G46484	TrGAroC	BZOBIPEROH + OH → MALDIALCO3 + GLYOX	8.16E-11	Rickard and Pascoe (2009)
G46485a	TrGAroCN	DNPHENO2 + HO ₂ → DNPHENO2 + OH	KR02H02(6)*(1-rchohch2o2_oh)	Rickard and Pascoe (2009)
G46485b	TrGAroCN	DNPHENO2 + HO ₂ → NC4DCO2H + HCOCO2H + NO ₂ + OH	KR02H02(6)*rchohch2o2_oh	Rickard and Pascoe (2009)*
G46486	TrGAroCN	DNPHENO2 + NO → NC4DCO2H + HCOCO2H + NO ₂ + NO ₂	KR02N0	Rickard and Pascoe (2009)*
G46487	TrGAroCN	DNPHENO2 + NO ₃ → NC4DCO2H + HCOCO2H + NO ₂ + NO ₂	KR02N03	Rickard and Pascoe (2009)*

48

Table 1: Gas phase reactions (... continued)

#	labels	reaction	rate coefficient	reference
G46488	TrGAroCN	DNPHENO2 → NC4DCO2H + HCOCO2H + NO ₂	k1_R02ISOPD02	Rickard and Pascoe (2009)*
G46489	TrGAroC	BZBIPEROOH + OH → BZOBIPEROH + OH	9.77E-11	Rickard and Pascoe (2009)
G46490a	TrGAroC	BZEMUCO2 + HO ₂ → BZEMUCOOH	KR02H02(6)	Rickard and Pascoe (2009)
G46490b	TrGAroC	BZEMUCO2 + HO ₂ → .5 EPXC4DIAL + .5 GLYOX + .5 HO ₂ + .5 C3DIALO2 + .5 C32OH13CO + OH	KR02H02(6)	Rickard and Pascoe (2009)*
G46491a	TrGAroCN	BZEMUCO2 + NO → BZEMUCNO3	KR02N0*alpha_AN(10,2,0,1,0,temp_cair)	Rickard and Pascoe (2009)
G46491b	TrGAroCN	BZEMUCO2 + NO → .5 EPXC4DIAL + .5 GLYOX + .5 HO ₂ + .5 C3DIALO2 + .5 C32OH13CO + NO ₂	KR02N0*(1.-alpha_AN(10,2,0,1,0,temp_cair))	Rickard and Pascoe (2009)*
G46492	TrGAroCN	BZEMUCO2 + NO ₃ → .5 EPXC4DIAL + .5 GLYOX + .5 HO ₂ + .5 C3DIALO2 + .5 C32OH13CO + NO ₂	KR02N03	Rickard and Pascoe (2009)*
G46493	TrGAroC	BZEMUCO2 → .5 EPXC4DIAL + .5 GLYOX + .5 HO ₂ + .5 C3DIALO2 + .5 C32OH13CO	k1_R02s0R02	Rickard and Pascoe (2009)*
G46494	TrGAroCN	C5CO2DBPAN + OH → HCOCOCHO + CH ₃ CHO + CO ₂ + NO ₂	3.28E-11	Rickard and Pascoe (2009)
G46495	TrGAroCN	C5CO2DBPAN → C5CO2DBCO3 + NO ₂	k_PAN_M	Rickard and Pascoe (2009)
G46496	TrGAroCN	NBZQOOH + OH → NBZQO2	6.68E-11	Rickard and Pascoe (2009)
G46497	TrGAroC	CATEC1OOH + OH → CATEC1O2	k_roohro	Rickard and Pascoe (2009)
G46498	TrGAroC	C6125CO + OH → C5CO14O2 + CO	6.45E-11	Rickard and Pascoe (2009)
G46499a	TrGAroCN	NBZQO2 + HO ₂ → NBZQOOH	KR02H02(6)*(1-rcoch2o2_oh)	Rickard and Pascoe (2009)
G46499b	TrGAroCN	NBZQO2 + HO ₂ → C6CO4DB + NO ₂ + OH	KR02H02(6)*rcoch2o2_oh	Rickard and Pascoe (2009)*
G46500	TrGAroCN	NBZQO2 + NO → C6CO4DB + NO ₂ + NO ₂	KR02N0	Rickard and Pascoe (2009)*
G46501	TrGAroCN	NBZQO2 + NO ₃ → C6CO4DB + NO ₂ + NO ₂	KR02N03	Rickard and Pascoe (2009)*
G46502	TrGAroCN	NBZQO2 → C6CO4DB + NO ₂	k1_R02s0R02	Rickard and Pascoe (2009)*
G46503	TrGAroCN	DNPHENO2 + OH → DNPHENO2	k_roohro	Rickard and Pascoe (2009)
G46504	TrGAroC	CATEC1O2 + HO ₂ → CATEC1OOH	KR02H02(6)	Rickard and Pascoe (2009)
G46505a	TrGAroCN	CATEC1O2 + NO → CATEC1O + NO ₂	KR02N0	Rickard and Pascoe (2009)
G46505b	TrGAroCN	CATEC1O2 + NO ₂ → CATEC1O + NO ₃	k_C6H5O2_NO2	Jagiella and Zabel (2007)*
G46506	TrGAroCN	CATEC1O2 + NO ₃ → CATEC1O + NO ₂	KR02N03	Rickard and Pascoe (2009)
G46507	TrGAroC	CATEC1O2 → CATEC1O	k1_R02s0R02	Rickard and Pascoe (2009)
G46508	TrGAroC	BZEMUCCO3H + OH → BZEMUCCO3	4.37E-11	Rickard and Pascoe (2009)
G46509	TrGAroC	C6H5OOH + OH → C6H5O2	3.60E-12	Rickard and Pascoe (2009)
G46510	TrGAroC	BZEMUCCOOH + OH → BZEMUCCO + OH	1.31E-10	Rickard and Pascoe (2009)
G46511a	TrGAroC	BZEMUCCO3 + HO ₂ → BZEMUCCO2H + O ₃	KAPH02*rc03_o3	Rickard and Pascoe (2009)
G46511b	TrGAroC	BZEMUCCO3 + HO ₂ → BZEMUCCO3H	KAPH02*rc03_oh	Rickard and Pascoe (2009)

49

Table 1: Gas phase reactions (... continued)

#	labels	reaction	rate coefficient	reference
G46511c	TrGAroC	BZEMUCCO3 + HO ₂ → C5DIALO2 + CO ₂ + OH	KAPH02*rc03_oh	Rickard and Pascoe (2009)
G46512	TrGAroCN	BZEMUCCO3 + NO → C5DIALO2 + CO ₂ + NO ₂	KAPNO	Rickard and Pascoe (2009)
G46513	TrGAroCN	BZEMUCCO3 + NO ₂ → BZEMUCPAN	k_CH3CO3_NO2	Rickard and Pascoe (2009)
G46514	TrGAroCN	BZEMUCCO3 + NO ₃ → C5DIALO2 + CO ₂ + NO ₂	KR02N03*1.74	Rickard and Pascoe (2009)
G46515	TrGAroC	BZEMUCCO3 → C5DIALO2 + CO ₂	k1_R02RC03	Rickard and Pascoe (2009)*
G46516	TrGAroC	C6H5O2 + HO ₂ → C6H5OOH	KR02H02(6)	Rickard and Pascoe (2009)
G46517a	TrGAroCN	C6H5O2 + NO → C6H5O + NO ₂	KR02N0	Rickard and Pascoe (2009)
G46517b	TrGAroCN	C6H5O2 + NO ₂ → C6H5O + NO ₃	K_C6H5O2_NO2	Jagiella and Zabel (2007)*
G46518	TrGAroCN	C6H5O2 + NO ₃ → C6H5O + NO ₂	KR02N03	Rickard and Pascoe (2009)
G46519	TrGAroC	C6H5O2 → C6H5O	k1_R02sR02	Rickard and Pascoe (2009)
G46521	TrGAroCN	BZEMUCNO3 + OH → BZEMUCCO + NO ₂	4.38E-11	Rickard and Pascoe (2009)
G46522a	TrGAroC	BZBIPERO2 + HO ₂ → BZBIPEROOH	KR02H02(6)*(1.-rbipero2_oh)	Rickard and Pascoe (2009)
G46522b	TrGAroC	BZBIPERO2 + HO ₂ → OH + GLYOX + HO ₂ + .5 BZFUONE + .5 BZFUONE	KR02H02(6)*rbipero2_oh	Rickard and Pascoe (2009), Bird-sall et al. (2010)*
G46523a	TrGAroCN	BZBIPERO2 + NO → BZBIPERNO3	KR02N0*alpha_AN(9,2,0,0,1,temp,cair)	Rickard and Pascoe (2009)
G46523b	TrGAroCN	BZBIPERO2 + NO → NO ₂ + GLYOX + HO ₂ + .5 BZFUONE + .5 BZFUONE	KR02N0*(1.-alpha_AN(9,2,0,0,1,temp,cair))	Rickard and Pascoe (2009)*
G46524	TrGAroCN	BZBIPERO2 + NO ₃ → NO ₂ + GLYOX + HO ₂ + .5 BZFUONE + .5 BZFUONE	KR02N03	Rickard and Pascoe (2009)*
G46525	TrGAroC	BZBIPERO2 → GLYOX + HO ₂ + BZFUONE	k1_R02sOR02	Rickard and Pascoe (2009)*
G47200	TrGTerCN	CO235C6CHO + NO ₃ → CO235C6CO3 + HNO ₃	KN03AL*5.5	Rickard and Pascoe (2009)
G47201	TrGTerC	CO235C6CHO + OH → CO235C6CO3	6.70E-11	Rickard and Pascoe (2009)
G47202a	TrGTerC	CO235C6CO3 + HO ₂ → CO235C6CO3H	KAPH02*(rc03_oh+rc03_o3)	Rickard and Pascoe (2009)
G47202b	TrGTerC	CO235C6CO3 + HO ₂ → CO235C6O2 + CO ₂ + OH	KAPH02*rc03_oh	Rickard and Pascoe (2009)
G47203	TrGTerCN	CO235C6CO3 + NO → CO235C6O2 + CO ₂ + NO ₂	KAPNO	Rickard and Pascoe (2009)
G47204	TrGTerCN	CO235C6CO3 + NO ₂ → C7PAN3	k_CH3CO3_NO2	Rickard and Pascoe (2009)
G47205	TrGTerC	CO235C6CO3 → CO235C6O2 + CO ₂	k1_R02RC03	Rickard and Pascoe (2009)
G47206	TrGTerC	C235C6CO3H + OH → CO235C6CO3	4.75E-12	Rickard and Pascoe (2009)
G47207	TrGTerCN	C7PAN3 + OH → CO235C5CHO + CO + NO ₂	8.83E-13	Rickard and Pascoe (2009)
G47208	TrGTerCN	C7PAN3 → CO235C6CO3 + NO ₂	k_PAN_M	Rickard and Pascoe (2009)
G47209a	TrGTerC	C716O2 + HO ₂ → C716OOH	KR02H02(7)*rcoch2o2_oh	Rickard and Pascoe (2009), Sander et al. (2018)
G47209b	TrGTerC	C716O2 + HO ₂ → CO13C4CHO + CH ₃ C(O) + OH	KR02H02(7)*rcoch2o2_oh	Rickard and Pascoe (2009), Sander et al. (2018)

50

Table 1: Gas phase reactions (... continued)

#	labels	reaction	rate coefficient	reference
G47210	TrGTerCN	C716O2 + NO → CO13C4CHO + CH ₃ C(O) + NO ₂	KR02N0	Rickard and Pascoe (2009)*
G47211	TrGTerC	C716O2 → CO13C4CHO + CH ₃ C(O)	k1_R02sOR02	Rickard and Pascoe (2009)
G47212	TrGTerC	C716OOH + OH → CO235C6CHO + OH	1.20E-10	Rickard and Pascoe (2009)
G47213	TrGTerC	C721O2 + HO ₂ → C721OOH	KR02H02(7)	Rickard and Pascoe (2009)
G47214	TrGTerCN	C721O2 + NO → C722O2 + NO ₂	KR02N0	Rickard and Pascoe (2009)*
G47215	TrGTerC	C721O2 → C722O2	k1_R02pR02	Rickard and Pascoe (2009)
G47216	TrGTerC	C721OOH + OH → C721O2	1.27E-11	Rickard and Pascoe (2009)
G47217	TrGTerC	C722O2 + HO ₂ → C722OOH	KR02H02(7)	Rickard and Pascoe (2009)
G47218	TrGTerCN	C722O2 + NO → CH ₃ COCH ₃ + C44O2 + NO ₂	KR02N0	Rickard and Pascoe (2009)*
G47219	TrGTerC	C722O2 → CH ₃ COCH ₃ + C44O2	k1_R02tR02	Rickard and Pascoe (2009)
G47220	TrGTerC	C722OOH + OH → C722O2	3.31E-11	Rickard and Pascoe (2009)
G47221	TrGTerC	RO06R3O2 → RO06R5O2	5.68E10*EXP(-8745./TEMP)	Vereecken and Peeters (2012)
G47222	TrGTerCN	RO06R3O2 + NO → RO06R3O + NO ₂	KR02N0	Vereecken and Peeters (2012)*
G47223	TrGTerC	RO06R3O2 + HO ₂ → 7 LCARBON	KR02H02(7)	Vereecken and Peeters (2012)*
G47224	TrGTerC	RO06R3O2 → RO06R3O	k1_R02sR02	Vereecken and Peeters (2012)
G47225	TrGTerC	RO06R3O → 7 LCARBON + HO ₂	5.7E10*EXP(-2949./TEMP)	Vereecken and Peeters (2012)*
G47226	TrGTerC	RO06R5O2 → 7 LCARBON + OH	9.17E10*EXP(-8706./TEMP)	Vereecken and Peeters (2012)*
G47400	TrGAroC	TOLUENE + OH → .07 C6H5CH2O2 + .18 CRESOL + .18 HO ₂ + .65 TLBIPERO2 + .10 TLEPOXMUC + .10 HO ₂	1.8E-12*EXP(340/TEMP)	Rickard and Pascoe (2009)*
G47401	TrGAroC	C6H5CH2O2 + HO ₂ → C6H5CH2OOH	1.5E-13*EXP(1310/TEMP)	Rickard and Pascoe (2009)
G47402a	TrGAroCN	C6H5CH2O2 + NO → C6H5CH2NO3	KR02N0*alpha_AN(7,1,0,0,0,temp,cair)	Rickard and Pascoe (2009)*
G47402b	TrGAroCN	C6H5CH2O2 + NO → BENZAL + HO ₂ + NO ₂	KR02N0*(1.-alpha_AN(7,1,0,0,0,temp,cair))	Rickard and Pascoe (2009)*
G47403	TrGAroCN	C6H5CH2O2 + NO ₃ → BENZAL + HO ₂ + NO ₂	KR02N03	Rickard and Pascoe (2009)*
G47404	TrGAroC	C6H5CH2O2 → BENZAL + HO ₂	2.*(k_CH3O2*2.4E-14*EXP(1620./TEMP))*0.5*R02	Rickard and Pascoe (2009)*
G47405	TrGAroCN	CRESOL + NO ₃ → .103 CRESO2 + .103 HNO ₃ + .506 NCRESO2 + .391 TOLIO + .391 HNO ₃	1.4E-11	Rickard and Pascoe (2009)*
G47406	TrGAroC	CRESOL + OH → .2 CRESO2 + .727 MCATECHOL + .727 HO ₂ + .073 TOLIO	4.65E-11	Rickard and Pascoe (2009)*
G47407a	TrGAroC	TLBIPERO2 + HO ₂ → TLBIPEROOH	KR02H02(7)*(1.-rbipero2_oh)	Rickard and Pascoe (2009)

51

Table 1: Gas phase reactions (... continued)

#	labels	reaction	rate coefficient	reference
G47407b	TrGAroC	TLBIPERO2 + HO ₂ → OH + .6 GLYOX + .4 MGLYOX + HO ₂ + .2 C4MDIAL + .2 C5DICARB + .2 TLFUONE + .2 BZFUONE + .2 MALDIAL	KR02H02(7)*rbipero2_oh	Rickard and Pascoe (2009), Bird-sall et al. (2010)*
G47408a	TrGAroCN	TLBIPERO2 + NO → NO ₂ + .6 GLYOX + .4 MGLYOX + HO ₂ + .2 C4MDIAL + .2 C5DICARB + .2 TLFUONE + .2 BZFUONE + .2 MALDIAL	KR02N0*(1.-alpha_AN(11,2,0,0,1, temp, cair))	Rickard and Pascoe (2009)*
G47408b	TrGAroCN	TLBIPERO2 + NO → TLBIPERNO3	KR02N0*alpha_AN(11,2,0,0,1, temp, cair)	Rickard and Pascoe (2009)*
G47409	TrGAroCN	TLBIPERO2 + NO ₃ → NO ₂ + .6 GLYOX + .4 MGLYOX + HO ₂ + .2 C4MDIAL + .2 C5DICARB + .2 TLFUONE + .2 BZFUONE + .2 MALDIAL	KR02N03	Rickard and Pascoe (2009)*
G47410	TrGAroC	TLBIPERO2 → .6 GLYOX + .4 MGLYOX + HO ₂ + .2 C4MDIAL + .2 C5DICARB + .2 TLFUONE + .2 BZFUONE + .2 MALDIAL	k1_R02s0R02	Rickard and Pascoe (2009)*
G47411	TrGAroCN	TLEPOXMUC + NO ₃ → TLEMUCCO3 + HNO ₃	KN03AL*2.75	Rickard and Pascoe (2009)
G47412	TrGAroC	TLEPOXMUC + O ₃ → EPXC4DIAL + .125 CH ₃ CHO + .695 CH ₃ C(O) + .57 CO + .57 OH + .125 HO ₂ + .1125 CH ₃ COCO ₂ H + .0675 MGLYOX + .0675 H ₂ O ₂ + .25 CO ₂	5.00E-18	Rickard and Pascoe (2009)*
G47413	TrGAroC	TLEPOXMUC + OH → .31 TLEMUCCO3 + .69 TLEMUCO2	7.99E-11	Rickard and Pascoe (2009)*
G47414	TrGAroC	C6H5CH2OOH + OH → BENZAL + OH	2.05E-11	Rickard and Pascoe (2009)
G47415	TrGAroCN	C6H5CH2NO3 + OH → BENZAL + NO ₂	6.03E-12	Rickard and Pascoe (2009)
G47416	TrGAroCN	BENZAL + NO ₃ → C6H5CO3 + HNO ₃	2.40E-15	Rickard and Pascoe (2009)
G47417	TrGAroC	BENZAL + OH → C6H5CO3	5.9E-12*EXP(225/TEMP)	Rickard and Pascoe (2009)
G47418a	TrGAroC	CRESO2 + HO ₂ → CRESOOH	KR02H02(7)*(1-rchohch2o2_oh)	Rickard and Pascoe (2009)
G47418b	TrGAroC	CRESO2 + HO ₂ → .68 C5CO14OH + .68 GLYOX + HO ₂ + .32 PTLQONE + OH	KR02H02(7)*rchohch2o2_oh	Rickard and Pascoe (2009)*
G47419	TrGAroCN	CRESO2 + NO → .68 C5CO14OH + .68 GLYOX + HO ₂ + .32 PTLQONE + NO ₂	KR02N0	Rickard and Pascoe (2009)*
G47420	TrGAroCN	CRESO2 + NO ₃ → .68 C5CO14OH + .68 GLYOX + HO ₂ + .32 PTLQONE + NO ₂	KR02N03	Rickard and Pascoe (2009)*
G47421	TrGAroC	CRESO2 → .68 C5CO14OH + .68 GLYOX + HO ₂ + .32 PTLQONE	k1_R02IS0PD02	Rickard and Pascoe (2009)*
G47422a	TrGAroCN	NCRESO2 + HO ₂ → NCRESOOH	KR02H02(7)*(1-rchohch2o2_oh)	Rickard and Pascoe (2009)

52

Table 1: Gas phase reactions (... continued)

#	labels	reaction	rate coefficient	reference
G47422b	TrGAroCN	NCRESO2 + HO ₂ → C5CO14OH + GLYOX + NO ₂ + OH	KR02H02(7)*rchohch2o2_oh	Rickard and Pascoe (2009)*
G47423	TrGAroCN	NCRESO2 + NO → C5CO14OH + GLYOX + NO ₂ + NO ₂	KR02N0	Rickard and Pascoe (2009)*
G47424	TrGAroCN	NCRESO2 + NO ₃ → C5CO14OH + GLYOX + NO ₂ + NO ₂	KR02N03	Rickard and Pascoe (2009)*
G47425	TrGAroCN	NCRESO2 → C5CO14OH + GLYOX + NO ₂	k1_R02IS0PD02	Rickard and Pascoe (2009)*
G47426	TrGAroCN	TOL1O + NO ₂ → TOL1OHNO2	k_G6H5O_N02	Rickard and Pascoe (2009), Platz et al. (1998)*
G47427	TrGAroC	TOL1O + O ₃ → OXYL1O2	k_C6H5O_03	Rickard and Pascoe (2009), Tao and Li (1999)
G47428	TrGAroCN	MCATECHOL + NO ₃ → MCATEC1O + HNO ₃	1.7E-10*1.0	Rickard and Pascoe (2009)
G47429	TrGAroC	MCATECHOL + O ₃ → MC3ODBC02H + HCOCO ₂ H + HO ₂ + OH	2.8E-17	Rickard and Pascoe (2009)*
G47430	TrGAroC	MCATECHOL + OH → MCATEC1O	2.0E-10*1.0	Rickard and Pascoe (2009)
G47431	TrGAroC	TLBIPEROOH + OH → TLOBIPEROH + OH	9.64E-11	Rickard and Pascoe (2009)
G47432	TrGAroCN	TLBIPERNO3 + OH → TLOBIPEROH + NO ₂	7.16E-11	Rickard and Pascoe (2009)
G47433	TrGAroC	TLOBIPEROH + OH → C5CO14O2 + GLYOX	7.99E-11	Rickard and Pascoe (2009)
G47434a	TrGAroC	TLEMUCCO3 + HO ₂ → C615CO2O2 + CO ₂ + OH	KAPH02*rco3_oh	Rickard and Pascoe (2009)
G47434b	TrGAroC	TLEMUCCO3 + HO ₂ → TLEMUCCO2H + O ₃	KAPH02*rco3_o3	Rickard and Pascoe (2009)
G47434c	TrGAroC	TLEMUCCO3 + HO ₂ → TLEMUCCO3H	KAPH02*rco3_oh	Rickard and Pascoe (2009)
G47435	TrGAroCN	TLEMUCCO3 + NO → C615CO2O2 + CO ₂ + NO ₂	KAPN0	Rickard and Pascoe (2009)
G47436	TrGAroCN	TLEMUCCO3 + NO ₂ → TLEMUCPAN	k_CH3CO3_N02	Rickard and Pascoe (2009)*
G47437	TrGAroCN	TLEMUCCO3 + NO ₃ → C615CO2O2 + CO ₂ + NO ₂	KR02N03*1.74	Rickard and Pascoe (2009)
G47438	TrGAroC	TLEMUCCO3 → C615CO2O2 + CO ₂	k1_R02RC03	Rickard and Pascoe (2009)*
G47439a	TrGAroC	TLEMUCO2 + HO ₂ → TLEMUCOOH	KR02H02(7)*(1-rchohch2o2_oh-rcoch2o2_oh)	Rickard and Pascoe (2009)
G47439b	TrGAroC	TLEMUCO2 + HO ₂ → .5 C3DIALO2 + .5 CO2H3CHO + .5 EPXC4DIAL + .5 MGLYOX + .5 HO ₂ + OH	KR02H02(7)*(rchohch2o2_oh+rcoch2o2_oh)	Rickard and Pascoe (2009)*
G47440a	TrGAroCN	TLEMUCO2 + NO → TLEMUCNO3	KR02N0*alpha_AN(11,2,1,0,0, temp, cair)	Rickard and Pascoe (2009)
G47440b	TrGAroCN	TLEMUCO2 + NO → .5 C3DIALO2 + .5 CO2H3CHO + .5 EPXC4DIAL + .5 MGLYOX + .5 HO ₂ + NO ₂	KR02N0*(1.-alpha_AN(11,2,1,0,0, temp, cair))	Rickard and Pascoe (2009)*
G47441	TrGAroCN	TLEMUCO2 + NO ₃ → .5 C3DIALO2 + .5 CO2H3CHO + .5 EPXC4DIAL + .5 MGLYOX + .5 HO ₂ + NO ₂	KR02N03	Rickard and Pascoe (2009)*

53

Table 1: Gas phase reactions (... continued)

#	labels	reaction	rate coefficient	reference
G47442	TrGAroC	TLEMUCO2 → .5 C3DIALO2 + .5 CO2H3CHO + .5 EPXC4DIAL + .5 MGLYOX + .5 HO2	k1_R02s0R02	Rickard and Pascoe (2009)*
G47443a	TrGAroC	C6H5CO3 + HO2 → C6H5CO3H	1.1E-11*EXP(364./temp)*0.65	Roth et al. (2010)
G47443b	TrGAroC	C6H5CO3 + HO2 → C6H5O2 + CO2 + OH	1.1E-11*EXP(364./temp)*0.20	Roth et al. (2010)
G47443c	TrGAroC	C6H5CO3 + HO2 → PHCOOH + O3	1.1E-11*EXP(364./temp)*0.15	Roth et al. (2010)
G47444	TrGAroCN	C6H5CO3 + NO → C6H5O2 + CO2 + NO2	KAPNO	Rickard and Pascoe (2009)
G47445	TrGAroCN	C6H5CO3 + NO2 → PBZN	k_CH3CO3_NO2	Rickard and Pascoe (2009)*
G47446	TrGAroCN	C6H5CO3 + NO3 → C6H5O2 + CO2 + NO2	KR02N03*1.74	Rickard and Pascoe (2009)
G47447	TrGAroC	C6H5CO3 → C6H5O2 + CO2	k1_R02RC03	Rickard and Pascoe (2009)*
G47448	TrGAroC	CRESOOH + OH → CRESO2	1.15E-10	Rickard and Pascoe (2009)
G47449	TrGAroCN	NCRESOOH + OH → NCRESO2	1.07E-10	Rickard and Pascoe (2009)
G47450	TrGAroCN	TOL1OHNO2 + NO3 → NCRES1O + HNO3	3.13E-13*1.0	Rickard and Pascoe (2009)
G47451	TrGAroCN	TOL1OHNO2 + OH → NCRES1O	2.8E-12	Rickard and Pascoe (2009)
G47452	TrGAroC	OXYL1O2 + HO2 → OXYL1OOH	KR02H02(7)	Rickard and Pascoe (2009)
G47453	TrGAroCN	OXYL1O2 + NO → TOL1O + NO2	KR02N0	Rickard and Pascoe (2009)
G47454	TrGAroCN	OXYL1O2 + NO2 → TOL1O + NO3	K_C6H5O2_NO2	Jagiella and Zabel (2007)*
G47455	TrGAroCN	OXYL1O2 + NO3 → TOL1O + NO2	KR02N03	Rickard and Pascoe (2009)
G47456	TrGAroC	OXYL1O2 → TOL1O	k1_R02sR02	Rickard and Pascoe (2009)
G47457	TrGAroCN	MCATEC1O + NO2 → MNCATECH	k_C6H5O_NO2	Rickard and Pascoe (2009), Platz et al. (1998)
G47458	TrGAroC	MCATEC1O + O3 → MCATEC1O2	k_C6H5O_O3	Rickard and Pascoe (2009), Tao and Li (1999)
G47459	TrGAroC	TLEMUCCO2H + OH → C615CO2O2 + CO2	5.98E-11	Rickard and Pascoe (2009)
G47460	TrGAroC	TLEMUCCO3H + OH → TLEMUCCO3	6.29E-11	Rickard and Pascoe (2009)
G47461	TrGAroCN	TLEMUCPAN + OH → C5DICARB + CO + CO2 + NO2	5.96E-11	Rickard and Pascoe (2009)
G47462	TrGAroCN	TLEMUCPAN → TLEMUCCO3 + NO2	k_PAN_M	Rickard and Pascoe (2009)
G47463	TrGAroC	TLEMUCOOH + OH → TLEMUCCO + OH	7.04E-11	Rickard and Pascoe (2009)
G47464	TrGAroCN	TLEMUCNO3 + OH → TLEMUCCO + NO2	3.06E-11	Rickard and Pascoe (2009)
G47465	TrGAroC	TLEMUCCO + OH → CH3C(O) + EPXC4DIAL + CO	4.06E-11	Rickard and Pascoe (2009)
G47466	TrGAroC	C6H5CO3H + OH → C6H5CO3	4.66E-12	Rickard and Pascoe (2009)
G47467	TrGAroC	PHCOOH + OH → C6H5O2 + CO2	1.10E-12	Rickard and Pascoe (2009)
G47468	TrGAroCN	PBZN + OH → C6H5OOH + CO + NO2	1.06E-12	Rickard and Pascoe (2009)
G47469	TrGAroCN	PBZN → C6H5CO3 + NO2	k_PAN_M*0.67	Rickard and Pascoe (2009)
G47470	TrGAroCN	PTLQONE + NO3 → NPTLQO2	1.00E-12	Rickard and Pascoe (2009)
G47471	TrGAroC	PTLQONE + OH → PTLQO2	2.3E-11	Rickard and Pascoe (2009)

54

Table 1: Gas phase reactions (... continued)

#	labels	reaction	rate coefficient	reference
G47472	TrGAroCN	NCRES1O + NO2 → DNCRES	k_C6H5O_NO2	Rickard and Pascoe (2009), Platz et al. (1998)
G47473	TrGAroCN	NCRES1O + O3 → NCRES1O2	k_C6H5O_O3	Rickard and Pascoe (2009), Tao and Li (1999)
G47474	TrGAroC	OXYL1OOH + OH → OXYL1O2	4.65E-11	Rickard and Pascoe (2009)
G47475	TrGAroCN	MNCATECH + NO3 → MNNCATECO2	5.03E-12	Rickard and Pascoe (2009)
G47476	TrGAroCN	MNCATECH + OH → MNCATECO2	6.83E-12	Rickard and Pascoe (2009)
G47477	TrGAroC	MCATEC1O2 + HO2 → MCATEC1OOH	KR02H02(7)	Rickard and Pascoe (2009)
G47478	TrGAroCN	MCATEC1O2 + NO → MCATEC1O + NO2	KR02N0	Rickard and Pascoe (2009)
G47479	TrGAroCN	MCATEC1O2 + NO2 → MCATEC1O + NO3	K_C6H5O2_NO2	Jagiella and Zabel (2007)*
G47480	TrGAroCN	MCATEC1O2 + NO3 → MCATEC1O + NO2	KR02N03	Rickard and Pascoe (2009)
G47481	TrGAroC	MCATEC1O2 → MCATEC1O	k1_R02s0R02	Rickard and Pascoe (2009)
G47482a	TrGAroCN	NPTLQO2 + HO2 → NPTLQOOH	KR02H02(7)*(1-rcoch2o2_oh)	Rickard and Pascoe (2009)
G47482b	TrGAroCN	NPTLQO2 + HO2 → C7CO4DB + NO2 + OH	KR02H02(7)*rcoch2o2_oh	Rickard and Pascoe (2009)*
G47483	TrGAroCN	NPTLQO2 + NO → C7CO4DB + NO2 + NO2	KR02N0	Rickard and Pascoe (2009)*
G47484	TrGAroCN	NPTLQO2 + NO3 → C7CO4DB + NO2 + NO2	KR02N03	Rickard and Pascoe (2009)*
G47485	TrGAroCN	NPTLQO2 → C7CO4DB + NO2	k1_R02s0R02	Rickard and Pascoe (2009)*
G47486a	TrGAroC	PTLQO2 + HO2 → PTLQOOH	KR02H02(7)*(1-rchohch2o2_oh-rcoch2o2_oh)	Rickard and Pascoe (2009)
G47486b	TrGAroC	PTLQO2 + HO2 → C6CO2OHCO3 + OH	KR02H02(7)*(rchohch2o2_oh+rcoch2o2_oh)	Rickard and Pascoe (2009)*
G47487	TrGAroCN	PTLQO2 + NO → C6CO2OHCO3 + NO2	KR02N0	Rickard and Pascoe (2009)*
G47488	TrGAroCN	PTLQO2 + NO3 → C6CO2OHCO3 + NO2	KR02N03	Rickard and Pascoe (2009)*
G47489	TrGAroC	PTLQO2 → C6CO2OHCO3	k1_R02s0R02	Rickard and Pascoe (2009)*
G47490	TrGAroCN	DNCRES + NO3 → NDNCRESO2	7.83E-15	Rickard and Pascoe (2009)
G47491	TrGAroCN	DNCRES + OH → DNCRESO2	5.10E-14	Rickard and Pascoe (2009)
G47492	TrGAroCN	NCRES1O2 + HO2 → NCRES1OOH	KR02H02(7)	Rickard and Pascoe (2009)
G47493	TrGAroCN	NCRES1O2 + NO → NCRES1O + NO2	KR02N0	Rickard and Pascoe (2009)
G47494	TrGAroCN	NCRES1O2 + NO2 → NCRES1O + NO3	K_C6H5O2_NO2	Jagiella and Zabel (2007)*
G47495	TrGAroCN	NCRES1O2 + NO3 → NCRES1O + NO2	KR02N03	Rickard and Pascoe (2009)
G47496	TrGAroCN	NCRES1O2 → NCRES1O	k1_R02sR02	Rickard and Pascoe (2009)
G47497a	TrGAroCN	MNNCATECO2 + HO2 → MNNCATCOOH	KR02H02(7)*(1-rchohch2o2_oh)	Rickard and Pascoe (2009)
G47497b	TrGAroCN	MNNCATECO2 + HO2 → NC4MDCO2HN + HCOCO2H + NO2 + OH	KR02H02(7)*rchohch2o2_oh	Rickard and Pascoe (2009)*

55

Table 1: Gas phase reactions (... continued)

#	labels	reaction	rate coefficient	reference
G47498	TrGAroCN	MNNCATECO2 + NO → NC4MDCO2HN + HCOCO2H + NO2 + NO2	KR02N0	Rickard and Pascoe (2009)*
G47499	TrGAroCN	MNNCATECO2 + NO3 → NC4MDCO2HN + HCOCO2H + NO2 + NO2	KR02N03	Rickard and Pascoe (2009)*
G47500	TrGAroCN	MNNCATECO2 → NC4MDCO2HN + HCOCO2H + NO2	k1_R02IS0PD02	Rickard and Pascoe (2009)
G47501a	TrGAroCN	MNCATECO2 + HO2 → MNCATECOOH	KR02H02(7)*(1-rchohch2o2_oh)	Rickard and Pascoe (2009)
G47501b	TrGAroCN	MNCATECO2 + HO2 → NC4MDCO2HN + HCOCO2H + HO2 + OH	KR02H02(7)*rchohch2o2_oh	Rickard and Pascoe (2009)*
G47502	TrGAroCN	MNCATECO2 + NO → NC4MDCO2HN + HCOCO2H + HO2 + NO2	KR02N0	Rickard and Pascoe (2009)*
G47503	TrGAroCN	MNCATECO2 + NO3 → NC4MDCO2HN + HCOCO2H + HO2 + NO2	KR02N03	Rickard and Pascoe (2009)*
G47504	TrGAroCN	MNCATECO2 → NC4MDCO2HN + HCOCO2H + HO2	k1_R02IS0PD02	Rickard and Pascoe (2009)*
G47505	TrGAroC	MCATEC1OOH + OH → MCATEC1O2	2.05E-10	Rickard and Pascoe (2009)
G47506	TrGAroCN	NPTLQOOH + OH → NPTLQO2	8.56E-11	Rickard and Pascoe (2009)
G47507	TrGAroC	PTLQOOH + OH → PTLQCO + OH	1.42E-10	Rickard and Pascoe (2009)
G47508	TrGAroC	PTLQCO + OH → C6CO2OHCO3	7.95E-11	Rickard and Pascoe (2009)
G47509a	TrGAroCN	NDNCRESO2 + HO2 → NDNCRESOOH	KR02H02(7)*(1-rchohch2o2_oh)	Rickard and Pascoe (2009)
G47509b	TrGAroCN	NDNCRESO2 + HO2 → NC4MDCO2HN + HNO3 + 2 CO + NO2 + OH	KR02H02(7)*rchohch2o2_oh	Rickard and Pascoe (2009)*
G47510	TrGAroCN	NDNCRESO2 + NO → NC4MDCO2HN + HNO3 + 2 CO + NO2 + NO2	KR02N0	Rickard and Pascoe (2009)*
G47511	TrGAroCN	NDNCRESO2 + NO3 → NC4MDCO2HN + HNO3 + 2 CO + NO2 + NO2	KR02N03	Rickard and Pascoe (2009)*
G47512	TrGAroCN	NDNCRESO2 → NC4MDCO2HN + HNO3 + 2 CO + NO2	k1_R02IS0PD02	Rickard and Pascoe (2009)*
G47513a	TrGAroCN	DNCRESO2 + HO2 → DNCRESOOH	KR02H02(7)*(1-rchohch2o2_oh)	Rickard and Pascoe (2009)
G47513b	TrGAroCN	DNCRESO2 + HO2 → NC4MDCO2HN + HCOCO2H + NO2 + OH	KR02H02(7)*rchohch2o2_oh	Rickard and Pascoe (2009)*
G47514	TrGAroCN	DNCRESO2 + NO → NC4MDCO2HN + HCOCO2H + NO2 + NO2	KR02N0	Rickard and Pascoe (2009)*
G47515	TrGAroCN	DNCRESO2 + NO3 → NC4MDCO2HN + HCOCO2H + NO2 + NO2	KR02N03	Rickard and Pascoe (2009)*
G47516	TrGAroCN	DNCRESO2 → NC4MDCO2HN + HCOCO2H + NO2	k1_R02IS0PD02	Rickard and Pascoe (2009)*
G47517	TrGAroCN	NCRES1OOH + OH → NCRES1O2	1.53E-12	Rickard and Pascoe (2009)
G47518	TrGAroCN	MNNCATCOOH + OH → MNNCATECO2	k_roohro	Rickard and Pascoe (2009)

56

Table 1: Gas phase reactions (... continued)

#	labels	reaction	rate coefficient	reference
G47519	TrGAroCN	MNCATECOOH + OH → MNCATECO2	k_roohro	Rickard and Pascoe (2009)
G47520	TrGAroC	C7CO4DB + OH → CO + CO + CH3C(O) + HCOCOCHO	9.58E-11	Rickard and Pascoe (2009)
G47521a	TrGAroC	C6CO2OHCO3 + HO2 → C5134CO2OH + HO2 + CO + CO2 + OH	KAPH02*rco3_oh	Rickard and Pascoe (2009)
G47521b	TrGAroC	C6CO2OHCO3 + HO2 → C6COOHCO3H	KAPH02*(rco3_oh+rco3_o3)	Rickard and Pascoe (2009)
G47522	TrGAroCN	C6CO2OHCO3 + NO → C5134CO2OH + HO2 + CO + CO2 + NO2	KAPN0	Rickard and Pascoe (2009)
G47523	TrGAroCN	C6CO2OHCO3 + NO2 → C6CO2OHPAN	k_CH3C03_N02	Rickard and Pascoe (2009)
G47524	TrGAroCN	C6CO2OHCO3 + NO3 → C5134CO2OH + HO2 + CO + CO2 + NO2	KR02N03*1.74	Rickard and Pascoe (2009)
G47525	TrGAroC	C6CO2OHCO3 → C5134CO2OH + HO2 + CO + CO2	k1_R02RC03	Rickard and Pascoe (2009)
G47526	TrGAroCN	NDNCRESOOH + OH → NDNCRESO2	k_roohro	Rickard and Pascoe (2009)
G47527	TrGAroCN	DNCRESOOH + OH → DNCRESO2	k_roohro	Rickard and Pascoe (2009)
G47528	TrGAroC	C6COOHCO3H + OH → C6CO2OHCO3	9.29E-11	Rickard and Pascoe (2009)
G47529	TrGAroCN	C6CO2OHPAN + OH → C5134CO2OH + CO + CO + NO2	8.96E-11	Rickard and Pascoe (2009)
G47530	TrGAroCN	C6CO2OHPAN → C6CO2OHCO3 + NO2	k_PAN_M	Rickard and Pascoe (2009)
G48200	TrGTerC	C85O2 → C86O2	k1_R02tR02	Rickard and Pascoe (2009)
G48201	TrGTerC	C85O2 + HO2 → C85OOH	KR02H02(8)	Rickard and Pascoe (2009)
G48202	TrGTerCN	C85O2 + NO → C86O2 + NO2	KR02N0	Rickard and Pascoe (2009)*
G48203	TrGTerC	C85OOH + OH → C85O2	1.29E-11	Rickard and Pascoe (2009)
G48204	TrGTerC	C86O2 → C511O2 + CH3COCH3	k1_R02tR02	Rickard and Pascoe (2009)
G48205	TrGTerCN	C86O2 + NO → C511O2 + CH3COCH3 + NO2	KR02N0	Rickard and Pascoe (2009)*
G48206	TrGTerC	C86O2 + HO2 → C86OOH	KR02H02(8)	Rickard and Pascoe (2009)
G48207	TrGTerC	C86OOH + OH → C86O2	3.45E-11	Rickard and Pascoe (2009)
G48208	TrGTerC	C811O2 → C812O2	k1_R02pR02	Rickard and Pascoe (2009)
G48209	TrGTerC	C811O2 + HO2 → 8 L CARBON	KR02H02(8)	Rickard and Pascoe (2009)
G48210	TrGTerCN	C811O2 + NO → C812O2 + NO2	KR02N0	Rickard and Pascoe (2009)*
G48211	TrGTerC	C812O2 → C813O2	k1_R02t0R02	Rickard and Pascoe (2009)
G48212	TrGTerCN	C812O2 + NO → C813O2 + NO2	KR02N0	Rickard and Pascoe (2009)*
G48213	TrGTerC	C812O2 + HO2 → C812OOH	KR02H02(8)	Rickard and Pascoe (2009)
G48214	TrGTerC	C812OOH + OH → C812O2	1.09E-11	Rickard and Pascoe (2009)
G48215	TrGTerC	C813O2 → CH3COCH3 + C512O2	k1_R02tR02	Rickard and Pascoe (2009)
G48216	TrGTerCN	C813O2 + NO → CH3COCH3 + C512O2 + NO2	KR02N0	Rickard and Pascoe (2009)*

57

Table 1: Gas phase reactions (... continued)

#	labels	reaction	rate coefficient	reference
G48217	TrGTerC	C813O2 + HO2 → C813OOH	KR02H02(8)	Rickard and Pascoe (2009)
G48218	TrGTerC	C813OOH + OH → C813O2	1.86E-11	Rickard and Pascoe (2009)
G48219	TrGTerCN	C721CHO + NO3 → C721CO3 + HNO3	KN03AL*8.5	Rickard and Pascoe (2009)
G48220	TrGTerC	C721CHO + OH → C721CO3	2.63E-11	Rickard and Pascoe (2009)
G48221a	TrGTerC	C721CO3 + HO2 → C721CO3H	KAPH02*rc03_ooH	Rickard and Pascoe (2009)
G48221b	TrGTerC	C721CO3 + HO2 → C721O2 + CO2 + OH	KAPH02*rc03_oh	Rickard and Pascoe (2009)
G48221c	TrGTerC	C721CO3 + HO2 → NORPINIC + O3	KAPH02*rc03_g3	Rickard and Pascoe (2009)
G48222	TrGTerCN	C721CO3 + NO → C721O2 + CO2 + NO2	KAPNO	Rickard and Pascoe (2009)*
G48223	TrGTerCN	C721CO3 + NO2 → C721PAN	k_CH3C03_N02	Rickard and Pascoe (2009)
G48224	TrGTerCN	C721CO3 + NO3 → C721O2 + CO2 + NO2	KR02N03*1.74	Rickard and Pascoe (2009)
G48225	TrGTerC	C721CO3 → C721O2 + CO2	k1_R02RC03*0.9	Sander et al. (2018)
G48226	TrGTerC	C721CO3 → NORPINIC	k1_R02RC03*0.1	Sander et al. (2018)
G48227	TrGTerC	C721CO3H + OH → C721CO3	9.65E-12	Rickard and Pascoe (2009)
G48228	TrGTerC	NORPINIC + OH → C721O2 + CO2	6.57E-12	Rickard and Pascoe (2009)
G48229	TrGTerCN	C721PAN + OH → C721OOH + CO + NO2	2.96E-12	Rickard and Pascoe (2009)
G48230	TrGTerCN	C721PAN → C721CO3 + NO2	k_PAN_M	Rickard and Pascoe (2009)
G48231	TrGTerC	C8BC + OH → C8BCO2	3.04E-12	Rickard and Pascoe (2009)
G48232	TrGTerC	C8BCO2 + HO2 → C8BCOOH	KR02H02(8)	Rickard and Pascoe (2009)
G48233a	TrGTerCN	C8BCO2 + NO → C89O2 + NO2	KR02N0*(1.-alpha_AN(8,2,0,0,0, temp, cair))	Rickard and Pascoe (2009)
G48233b	TrGTerCN	C8BCO2 + NO → C8BCNO3	KR02N0*alpha_AN(8,2,0,0,0, temp, cair)	Rickard and Pascoe (2009)
G48234	TrGTerC	C8BCO2 → C89O2	k1_R02sR02	Rickard and Pascoe (2009)
G48235	TrGTerC	C8BCOOH + OH → C8BCCO + OH	1.62E-11	Rickard and Pascoe (2009)
G48236	TrGTerCN	C8BCNO3 + OH → C8BCCO + NO2	1.84E-12	Rickard and Pascoe (2009)
G48237	TrGTerC	C8BCCO + OH → C89O2	3.94E-12	Rickard and Pascoe (2009)
G48238	TrGTerC	C89O2 + HO2 → C89OOH	KR02H02(8)	Rickard and Pascoe (2009)
G48239a	TrGTerCN	C89O2 + NO → C810O2 + NO2	KR02N0*(1.-alpha_AN(7,2,0,0,0, temp, cair))	Rickard and Pascoe (2009)
G48239b	TrGTerCN	C89O2 + NO → C89NO3	KR02N0*alpha_AN(7,2,0,0,0, temp, cair)	Rickard and Pascoe (2009)
G48240	TrGTerCN	C89O2 + NO3 → C810O2 + NO2	KR02N03	Rickard and Pascoe (2009)
G48241	TrGTerC	C89O2 → C810O2	k1_R02tR02	Rickard and Pascoe (2009)
G48242	TrGTerC	C89OOH + OH → C89O2	3.61E-11	Rickard and Pascoe (2009)
G48243	TrGTerCN	C89NO3 + OH → CH3COCH3 + CO13C4CHO + NO2	2.56E-11	Rickard and Pascoe (2009)

58

Table 1: Gas phase reactions (... continued)

#	labels	reaction	rate coefficient	reference
G48244	TrGTerC	C810O2 + HO2 → C810OOH	KR02H02(8)	Rickard and Pascoe (2009)
G48245a	TrGTerCN	C810O2 + NO → CH3COCH3 + C514O2 + NO2	KR02N0*(1.-alpha_AN(10,3,0,0,0, temp, cair))	Rickard and Pascoe (2009)
G48245b	TrGTerCN	C810O2 + NO → C810NO3	KR02N0*alpha_AN(10,3,0,0,0, temp, cair)	Rickard and Pascoe (2009)
G48246	TrGTerCN	C810O2 + NO3 → CH3COCH3 + C514O2 + NO2	KR02N03	Rickard and Pascoe (2009)
G48247	TrGTerC	C810O2 → CH3COCH3 + C514O2	k1_R02tR02	Rickard and Pascoe (2009)
G48248	TrGTerC	C810OOH + OH → C810O2	8.35E-11	Rickard and Pascoe (2009)
G48249	TrGTerCN	C810NO3 + OH → CH3COCH3 + CO13C4CHO + NO2	4.96E-11	Rickard and Pascoe (2009)
G48400a	TrGAroC	LXYL + OH → TLEPOXMUC + HO2 + LCARBON	0.401E-11	Rickard and Pascoe (2009)*
G48400b	TrGAroC	LXYL + OH → C6H5CH2O2 + LCARBON	0.101E-11	Rickard and Pascoe (2009)*
G48400c	TrGAroC	LXYL + OH → CRESOL + LCARBON	0.261E-11	Rickard and Pascoe (2009)*
G48400d	TrGAroC	LXYL + OH → TLBIPERO2 + HO2 + LCARBON	0.932E-11	Rickard and Pascoe (2009)*
G48401	TrGAroC	LXYL + NO3 → C6H5CH2O2 + HNO3 + LCARBON	3.9E-16	Rickard and Pascoe (2009)*
G48402	TrGAroC	EBENZ + OH → .10 TLEPOXMUC + .07 C6H5CH2O2 + .18 CRESOL + .65 TLBIPERO2 + .28 HO2 + LCARBON	7.00E-12	Rickard and Pascoe (2009)*
G48403	TrGAroCN	EBENZ + NO3 → C6H5CH2O2 + HNO3 + LCARBON	1.20E-16	Rickard and Pascoe (2009)*
G48404	TrGAroCN	STYRENE + NO3 → NSTYRENO2	1.50E-12	Rickard and Pascoe (2009)
G48405	TrGAroC	STYRENE + O3 → .545 HCHO + .1 BENZENE + .28 C6H5O2 + .56 CO + .36 OH + .28 HO2 + .075 PHCOOH + .545 BENZAL + .09 H2O2 + .075 HCOOH + .2 CO2	1.70E-17	Rickard and Pascoe (2009)*
G48406	TrGAroC	STYRENE + OH → STYRENO2	5.80E-11	Rickard and Pascoe (2009)
G48407	TrGAroCN	NSTYRENO2 + HO2 → NSTYRENOOH	KR02H02(8)	Rickard and Pascoe (2009)
G48408	TrGAroCN	NSTYRENO2 + NO → NO2 + NO2 + HCHO + BENZAL	KR02N0	Rickard and Pascoe (2009)*
G48409	TrGAroCN	NSTYRENO2 + NO3 → NO2 + NO2 + HCHO + BENZAL	KR02N03	Rickard and Pascoe (2009)*
G48410	TrGAroCN	NSTYRENO2 → NO2 + HCHO + BENZAL	k1_R02sR02	Rickard and Pascoe (2009)*
G48411	TrGAroCN	NSTYRENOOH + OH → NSTYRENO2	6.16E-11	Rickard and Pascoe (2009)
G48412a	TrGAroC	STYRENO2 + HO2 → STYRENOOH	KR02H02(8)*(1-rchohch2o2_oh)	Rickard and Pascoe (2009)
G48412b	TrGAroC	STYRENO2 + HO2 → HO2 + OH + HCHO + BENZAL	KR02H02(8)*rchohch2o2_oh	Rickard and Pascoe (2009)*
G48413	TrGAroCN	STYRENO2 + NO → NO2 + HO2 + HCHO + BENZAL	KR02N0	Rickard and Pascoe (2009)*
G48414	TrGAroCN	STYRENO2 + NO3 → NO2 + HO2 + HCHO + BENZAL	KR02N03	Rickard and Pascoe (2009)*
G48415	TrGAroC	STYRENO2 → HO2 + HCHO + BENZAL	k1_R02sR02	Rickard and Pascoe (2009)*
G48416	TrGAroC	STYRENOOH + OH → STYRENO2	6.16E-11	Rickard and Pascoe (2009)
G49200	TrGTerC	C96O2 → C97O2	k1_R02pR02	Rickard and Pascoe (2009)

59

Table 1: Gas phase reactions (... continued)

#	labels	reaction	rate coefficient	reference
G49201	TrGTerC	C96O2 + HO2 → C96OOH	KR02H02(9)	Rickard and Pascoe (2009)
G49202a	TrGTerCN	C96O2 + NO → C97O2 + NO2	KR02N0*(1.-alpha_AN(10,1,0,0,0, temp, cair))	Rickard and Pascoe (2009)
G49202b	TrGTerCN	C96O2 + NO → C96NO3	KR02N0*alpha_AN(10,1,0,0,0, temp, cair)	Rickard and Pascoe (2009)
G49203	TrGTerCN	C96NO3 + OH → NORPINAL + NO2	2.88E-12	Rickard and Pascoe (2009)
G49204a	TrGTerC	C96OOH + OH → C96O2	k_roohro	Rickard and Pascoe (2009)
G49205b	TrGTerC	C96OOH + OH → NORPINAL + OH	1.30E-11	Rickard and Pascoe (2009)
G49206	TrGTerC	C97O2 → C98O2	k1_R02tR02	Rickard and Pascoe (2009)
G49207	TrGTerCN	C97O2 + NO → C98O2 + NO2	KR02N0	Rickard and Pascoe (2009)*
G49208a	TrGTerC	C97O2 + HO2 → C97OOH	KR02H02(9)*rcoch2o2_ooH	Rickard and Pascoe (2009), Sander et al. (2018)
G49208b	TrGTerC	C97O2 + HO2 → C98O2 + OH	KR02H02(9)*rcoch2o2_oh	Rickard and Pascoe (2009), Sander et al. (2018)
G49209	TrGTerC	C97OOH + OH → C97O2	1.05E-11	Rickard and Pascoe (2009)
G49210	TrGTerC	C98O2 → C614O2 + CH3COCH3	k1_R02tR02	Rickard and Pascoe (2009)
G49211a	TrGTerCN	C98O2 + NO → C614O2 + CH3COCH3 + NO2	KR02N0*(1.-alpha_AN(12,3,0,0,0, temp, cair))	Rickard and Pascoe (2009)
G49211b	TrGTerCN	C98O2 + NO → 9 LCARBON + LNITROGEN	KR02N0*alpha_AN(12,3,0,0,0, temp, cair)	Rickard and Pascoe (2009)
G49212	TrGTerC	C98O2 + HO2 → C98OOH	KR02H02(9)	Rickard and Pascoe (2009)
G49213	TrGTerC	C98OOH + OH → C98O2	2.05E-11	Rickard and Pascoe (2009)
G49214	TrGTerC	NORPINAL + OH → C85CO3	2.64E-11	Rickard and Pascoe (2009)
G49215	TrGTerCN	NORPINAL + NO3 → C85CO3 + HNO3	KN03AL*8.5	Rickard and Pascoe (2009)
G49216	TrGTerC	C85CO3 → C85O2 + CO2	k1_R02RC03	Rickard and Pascoe (2009)
G49217	TrGTerCN	C85CO3 + NO → C85O2 + CO2 + NO2	KAPNO	Rickard and Pascoe (2009)
G49218	TrGTerCN	C85CO3 + NO2 → C9PAN2	k_CH3C03_N02	Rickard and Pascoe (2009)
G49219a	TrGTerC	C85CO3 + HO2 → C85CO3H	KAPH02*(rco3_ooH+rco3_o3)	Rickard and Pascoe (2009)
G49219b	TrGTerC	C85CO3 + HO2 → C85O2 + CO2 + OH	KAPH02*rco3_oh	Rickard and Pascoe (2009)
G49220	TrGTerCN	C9PAN2 → C85CO3 + NO2	k_PAN_M	Rickard and Pascoe (2009)
G49221	TrGTerCN	C9PAN2 + OH → C85OOH + CO + NO2	6.60E-12	Rickard and Pascoe (2009)
G49222	TrGTerC	C85CO3H + OH → C85CO3	1.02E-11	Rickard and Pascoe (2009)
G49223a	TrGTerC	C89CO3 → .8 C811CO3 + .2 C89O2 + .2 CO2	k1_R02RC03*0.9	Sander et al. (2018)
G49223b	TrGTerC	C89CO3 → C89CO2H	k1_R02RC03*0.1	Sander et al. (2018)
G49224a	TrGTerC	C89CO3 + HO2 → C89CO3H	KAPH02*rco3_ooH	Rickard and Pascoe (2009)

60

Table 1: Gas phase reactions (... continued)

#	labels	reaction	rate coefficient	reference
G49224b	TrGTerC	C89CO3 + HO2 → C89CO2H + O3	KAPH02*rco3_o3	Rickard and Pascoe (2009)
G49224c	TrGTerC	C89CO3 + HO2 → .80 C811CO3 + .20 C89O2 + .2 CO2 + OH	KAPH02*rco3_oh	Rickard and Pascoe (2009)
G49225	TrGTerCN	C89CO3 + NO2 → C89PAN	k_CH3C03_N02	Rickard and Pascoe (2009)
G49226	TrGTerCN	C89CO3 + NO → .8 C811CO3 + .2 C89O2 + .2 CO2 + NO2	KAPNO	Rickard and Pascoe (2009)
G49227	TrGTerC	C89CO2H + OH → .8 C811CO3 + .2 C89O2 + .2 CO2	2.69E-11	Rickard and Pascoe (2009)
G49228	TrGTerC	C89CO3H + OH → C89CO3	3.00E-11	Rickard and Pascoe (2009)
G49229	TrGTerCN	C89PAN → C89CO3 + NO2	k_PAN_M	Rickard and Pascoe (2009)
G49230	TrGTerCN	C89PAN + OH → CH3COCH3 + CO13C4CHO + CO + NO2	2.52E-11	Rickard and Pascoe (2009)
G49231a	TrGTerC	C811CO3 → C811O2 + CO2	k1_R02RC03*0.9	Sander et al. (2018)
G49231b	TrGTerC	C811CO3 → PINIC	k1_R02RC03*0.1	Sander et al. (2018)
G49232a	TrGTerC	C811CO3 + HO2 → C811CO3H	KAPH02*rco3_ooH	Rickard and Pascoe (2009)
G49232b	TrGTerC	C811CO3 + HO2 → PINIC + O3	KAPH02*rco3_o3	Rickard and Pascoe (2009)
G49232c	TrGTerC	C811CO3 + HO2 → C811O2 + CO2 + OH	KAPH02*rco3_oh	Rickard and Pascoe (2009)
G49233	TrGTerCN	C811CO3 + NO → C811O2 + CO2 + NO2	KAPNO	Rickard and Pascoe (2009)
G49234	TrGTerCN	C811CO3 + NO2 → C811PAN	k_CH3C03_N02	Rickard and Pascoe (2009)
G49235	TrGTerC	PINIC + OH → C811O2 + CO2	7.29E-12	Rickard and Pascoe (2009)
G49236	TrGTerC	NOPINONE + OH → NOPINDO2	1.55E-11	Capouet et al. (2008), Rickard and Pascoe (2009)
G49237a	TrGTerC	NOPINDO2 + HO2 → NOPINDOOH	KR02H02(9)*rcoch2o2_ooH	Rickard and Pascoe (2009), Sander et al. (2018)
G49237b	TrGTerC	NOPINDO2 + HO2 → C89CO3 + OH	KR02H02(9)*rcoch2o2_oh	Rickard and Pascoe (2009), Sander et al. (2018)
G49238	TrGTerCN	NOPINDO2 + NO → C89CO3 + NO2	KR02N0	Rickard and Pascoe (2009)*
G49239	TrGTerC	NOPINDO2 → C89CO3	k1_R02pR02	Rickard and Pascoe (2009)
G49240	TrGTerC	NOPINDOOH → NOPINDCO	2.63E-11	Rickard and Pascoe (2009)
G49241	TrGTerC	NOPINDCO + OH → C89CO3	3.07E-12	Rickard and Pascoe (2009)
G49242	TrGTerC	NOPINOO → NOPINONE + H2O2	6.00E-18*c(ind_H20)	Rickard and Pascoe (2009)
G49243	TrGTerC	NOPINOO + CO → NOPINONE + CO2	1.2E-15	Rickard and Pascoe (2009)
G49244	TrGTerCN	NOPINOO + NO → NOPINONE + NO2	1.E-14	Rickard and Pascoe (2009)
G49245	TrGTerCN	NOPINOO + NO2 → NOPINONE + NO3	1.E-15	Rickard and Pascoe (2009)
G49246	TrGTerC	NORPINENOL + OH → HCOOH + OH + C86O2	k_CH2CHOH_OH_HCOOH	Sander et al. (2018), So et al. (2014)*

61

Table 1: Gas phase reactions (... continued)

#	labels	reaction	rate coefficient	reference
G49247	TrGTerC	NORPINENOL + HCOOH → NORPINAL + HCOOH	k_CH2CHOH_HCOOH	Sander et al. (2018), da Silva (2010)*
G49248	TrGTerC	NORPINAL + HCOOH → NORPINENOL + HCOOH	k_ALD_HCOOH	Sander et al. (2018), da Silva (2010)*
G49249	TrGTerC	C811CO3H + OH → C811CO3	1.04E-11	Rickard and Pascoe (2009)
G49250	TrGTerCN	C811PAN → C811CO3 + NO ₂	k_PAN_M	Rickard and Pascoe (2009)
G49251	TrGTerCN	C811PAN + OH → C721CHO + CO + NO ₂	6.77E-12	Rickard and Pascoe (2009)
G49400a	TrGAroC	LTMB + OH → TLEPOXMUC + HO ₂ + 2 LCARBON	0.827E-11	Rickard and Pascoe (2009)*
G49400b	TrGAroC	LTMB + OH → C6H5CH2O2 + 2 LCARBON	0.189E-11	Rickard and Pascoe (2009)*
G49400c	TrGAroC	LTMB + OH → CRESOL + 2 LCARBON	0.141E-11	Rickard and Pascoe (2009)*
G49400d	TrGAroC	LTMB + OH → TLBIPERO2 + HO ₂ + 2 LCARBON	2.917E-11	Rickard and Pascoe (2009)*
G49401	TrGAroCN	LTMB + NO ₃ → C6H5CH2O2 + HNO ₃ + 2 LCARBON	1.52E-15	Rickard and Pascoe (2009)*
G40200	TrGTerC	APINENE + OH → .75 LAPINABO2 + .15 MENTHEN6ONE + .15 HO ₂ + .10 ROO6R1O2	1.2E-11*EXP(440./TEMP)	Atkinson et al. (2006)*
G40201a	TrGTerCN	LAPINABO2 + NO → PINAL + HO ₂ + NO ₂	KR02N0*(1.-(.65*alpha_AN(11,3,0,0,0,temp,cair))+.35*alpha_AN(11,2,0,0,0,temp,cair)))	Rickard and Pascoe (2009), Sander et al. (2018)
G40201b	TrGTerCN	LAPINABO2 + NO → LAPINABNO3	KR02N0*(.65*alpha_AN(11,3,0,0,0,temp,cair))+.35*alpha_AN(11,2,0,0,0,temp,cair))	Rickard and Pascoe (2009), Sander et al. (2018)
G40202a	TrGTerC	LAPINABO2 + HO ₂ → LAPINABOOH	KR02H02(10)*(1.-rchohch2o2_oh)	Rickard and Pascoe (2009), Sander et al. (2018)
G40202b	TrGTerC	LAPINABO2 + HO ₂ → PINAL + HO ₂ + OH	KR02H02(10)*rchohch2o2_oh	Rickard and Pascoe (2009), Sander et al. (2018)
G40203	TrGTerC	LAPINABO2 → PINAL + HO ₂	R02*(0.65*k1_R02t0R02+.35*k1_R02s0R02)	Rickard and Pascoe (2009)*
G40204	TrGTerC	LAPINABOOH + OH → .35 LAPINABO2 + .65 C96CO3	2.77E-11	Rickard and Pascoe (2009)*
G40205	TrGTerCN	LAPINABNO3 + OH → .35 PINAL + .65 C96CO3 + NO ₂	4.29E-12	Rickard and Pascoe (2009)*
G40206	TrGTerC	MENTHEN6ONE + OH → OHMENTHEN6ONEO2	6.46E-11	Vereecken et al. (2007)*
G40207	TrGTerCN	OHMENTHEN6ONEO2 + NO → 2OHMENTHEN6ONE + HO ₂ + NO ₂	KR02N0	Vereecken et al. (2007)*
G40208	TrGTerC	OHMENTHEN6ONEO2 + HO ₂ → 2OHMENTHEN6ONE	KR02H02(10)	Vereecken et al. (2007)
G40209	TrGTerC	OHMENTHEN6ONEO2 → 2OHMENTHEN6ONE + HO ₂	k1_R02t0R02	Vereecken et al. (2007)
G40210	TrGTerC	2OHMENTHEN6ONE + OH → 10 LCARBON	1E-11	Vereecken et al. (2007)
G40211	TrGTerC	PINAL + OH → .772 C96CO3 + .228 PINALO2	5.2E-12*EXP(600./TEMP)	Wallington et al. (2018)*

62

Table 1: Gas phase reactions (... continued)

#	labels	reaction	rate coefficient	reference
G40212	TrGTerCN	PINAL + NO ₃ → C96CO3 + HNO ₃	2.0E-14	Wallington et al. (2018)*
G40213a	TrGTerC	C96CO3 → C96O2 + CO ₂	k1_R02RC03*0.9	Rickard and Pascoe (2009)
G40213b	TrGTerC	C96CO3 → PINONIC	k1_R02RC03*0.1	Rickard and Pascoe (2009)
G40214a	TrGTerC	C96CO3 + HO ₂ → PERPINONIC	KAPH02*rco3_ooH	Rickard and Pascoe (2009)
G40214b	TrGTerC	C96CO3 + HO ₂ → PINONIC + O ₃	KAPH02*rco3_o3	Rickard and Pascoe (2009)
G40214c	TrGTerC	C96CO3 + HO ₂ → C96O2 + OH + CO ₂	KAPH02*rco3_oh	Rickard and Pascoe (2009)
G40215	TrGTerCN	C96CO3 + NO ₂ → C10PAN2	k_CH3C03_N02	Rickard and Pascoe (2009)
G40216	TrGTerCN	C96CO3 + NO → C96O2 + NO ₂ + CO ₂	KAPNO	Rickard and Pascoe (2009)
G40217	TrGTerCN	C96CO3 + NO ₃ → C96O2 + NO ₂ + CO ₂	KR02N03*1.74	Rickard and Pascoe (2009)
G40218	TrGTerCN	C10PAN2 → C96CO3 + NO ₂	k_PAN_M	Rickard and Pascoe (2009)
G40219	TrGTerCN	C10PAN2 + OH → NORPINAL + CO + NO ₂	3.66E-12	Rickard and Pascoe (2009)
G40220	TrGTerC	PINONIC + OH → C96O2 + CO ₂	6.65E-12	Rickard and Pascoe (2009)
G40221	TrGTerC	PERPINONIC + OH → C96CO3	9.73E-12	Rickard and Pascoe (2009)
G40222	TrGTerC	PINALO2 + HO ₂ → PINALOOH	KR02H02(10)	Rickard and Pascoe (2009)
G40223a	TrGTerCN	PINALO2 + NO → C106O2 + NO ₂	KR02N0*(1.-alpha_AN(12,3,0,1,0,temp,cair))	Rickard and Pascoe (2009), Sander et al. (2018)
G40223b	TrGTerCN	PINALO2 + NO → PINALNO3	KR02N0*alpha_AN(12,3,0,1,0,temp,cair)	Rickard and Pascoe (2009), Sander et al. (2018)
G40224	TrGTerC	PINALO2 → C106O2	k1_R02tR02	Rickard and Pascoe (2009)
G40225	TrGTerC	PINALOOH + OH → PINALO2	2.75E-11	Rickard and Pascoe (2009)
G40226	TrGTerCN	PINALNO3 + OH → CO235C6CHO + CH ₃ COCH ₃ + NO ₂	2.25E-11	Rickard and Pascoe (2009)
G40227	TrGTerC	C106O2 + HO ₂ → C106OOH	KR02H02(10)	Rickard and Pascoe (2009)
G40228a	TrGTerCN	C106O2 + NO → C716O2 + CH ₃ COCH ₃ + NO ₂	KR02N0*0.875*(1.-alpha_AN(13,3,0,0,0,temp,cair))	Rickard and Pascoe (2009), Sander et al. (2018)
G40228b	TrGTerCN	C106O2 + NO → C106NO3	KR02N0*0.875*alpha_AN(13,3,0,0,0,temp,cair)	Rickard and Pascoe (2009), Sander et al. (2018)
G40229	TrGTerC	C106O2 → C716O2 + CH ₃ COCH ₃	k1_R02tR02	Rickard and Pascoe (2009)
G40230	TrGTerC	C106OOH + OH → C106O2	8.01E-11	Rickard and Pascoe (2009)
G40231	TrGTerCN	C106NO3 + OH → CO235C6CHO + CH ₃ COCH ₃ + NO ₂	7.03E-11	Rickard and Pascoe (2009)
G40232	TrGTerC	APINENE + O ₃ → .09 APINBOO + .08 PINONIC + .77 OH + .33 NORPINAL + .33 CO + .33 HO ₂ + .06 APINAOO + .44 C109O2	8.05E-16*EXP(-640./TEMP)	Wallington et al. (2018)*
G40233	TrGTerC	APINAOO → PINAL + H ₂ O ₂	1.00E-17*c(ind_H2O)	Rickard and Pascoe (2009)
G40234	TrGTerC	APINAOO + CO → PINAL + CO ₂	1.20E-15	Rickard and Pascoe (2009)

63

Table 1: Gas phase reactions (... continued)

#	labels	reaction	rate coefficient	reference
G40235	TrGTerCN	APINAOO + NO → PINAL + NO ₂	1.00E-14	Rickard and Pascoe (2009)
G40236	TrGTerCN	APINAOO + NO ₂ → PINAL + NO ₃	1.00E-15	Rickard and Pascoe (2009)
G40237a	TrGTerC	APINBOO → PINONIC	1.00E-17*c(ind_H2O)*(0.08+0.15)	Rickard and Pascoe (2009)
G40237b	TrGTerC	APINBOO → PINAL + H ₂ O ₂	1.00E-17*c(ind_H2O)*0.77	Rickard and Pascoe (2009)
G40238	TrGTerC	APINBOO + CO → PINAL + CO ₂	1.20E-15	Rickard and Pascoe (2009)
G40239	TrGTerCN	APINBOO + NO → PINAL + NO ₂	1.00E-14	Rickard and Pascoe (2009)
G40240	TrGTerCN	APINBOO + NO ₂ → PINAL + NO ₃	1.00E-15	Rickard and Pascoe (2009)
G40241	TrGTerC	C109O2 → C89CO3 + HCHO	k1_R02pR02	Rickard and Pascoe (2009)
G40242	TrGTerCN	C109O2 + NO → C89CO3 + HCHO + NO ₂	KR02N0	Rickard and Pascoe (2009)*
G40243a	TrGTerC	C109O2 + HO ₂ → C109OOH	KR02H02(10)*rcoch2o2_ooH	Rickard and Pascoe (2009), Sander et al. (2018)
G40243b	TrGTerC	C109O2 + HO ₂ → C89CO3 + HCHO + OH	KR02H02(10)*rcoch2o2_oh	Rickard and Pascoe (2009), Sander et al. (2018)
G40244	TrGTerC	C109OOH + OH → C109CO + OH	5.47E-11	Rickard and Pascoe (2009)
G40245	TrGTerC	C109CO + OH → C89CO3 + CO	5.47E-11	Rickard and Pascoe (2009)
G40246	TrGTerCN	APINENE + NO ₃ → LNAPINABO2	1.2E-12*EXP(490./temp)	Wallington et al. (2018)*
G40247	TrGTerCN	LNAPINABO2 → PINAL + NO ₂	(0.65*k1_R02tR02 + 0.35*k1_R02sR02)	Rickard and Pascoe (2009)
G40248	TrGTerCN	LNAPINABO2 + NO → PINAL + NO ₂ + NO ₂	KR02N0	Rickard and Pascoe (2009)*
G40249	TrGTerCN	LNAPINABO2 + HO ₂ → LNAPINABOOH	KR02H02(10)	Rickard and Pascoe (2009)
G40250	TrGTerCN	LNAPINABO2 + NO ₃ → PINAL + NO ₂ + NO ₂	KR02N03	Rickard and Pascoe (2009)
G40251	TrGTerCN	LNAPINABOOH + OH → LNAPINABO2	(.65*6.87E-12+.35*1.23E-11)	Rickard and Pascoe (2009)
G40252a	TrGTerC	BPINENE + OH → BPINAO2	1.47E-11*EXP(467./TEMP)	Gill and Hites (2002)*
G40252b	TrGTerC	BPINENE + OH → ROO6R1O2	*0.8326*0.3/(0.8326+0.068)	Gill and Hites (2002)*
G40253a	TrGTerC	BPINAO2 + HO ₂ → BPINAOOH	KR02H02(10)*rcoch2o2_ooH	Rickard and Pascoe (2009), Sander et al. (2018)
G40253b	TrGTerC	BPINAO2 + HO ₂ → NOPINONE + HCHO + HO ₂ + OH	KR02H02(10)*rcoch2o2_oh	Rickard and Pascoe (2009), Sander et al. (2018)
G40254a	TrGTerCN	BPINAO2 + NO → NOPINONE + HCHO + HO ₂ + NO ₂	KR02N0*(1.-alpha_AN(11,3,0,0,0, temp, cair))	Rickard and Pascoe (2009), Sander et al. (2018)
G40254b	TrGTerCN	BPINAO2 + NO → BPINANO3	KR02N0*alpha_AN(11,3,0,0,0, temp, cair)	Rickard and Pascoe (2009), Sander et al. (2018)
G40255	TrGTerC	BPINAO2 → NOPINONE + HCHO + HO ₂	k1_R02tR02	Rickard and Pascoe (2009)

64

Table 1: Gas phase reactions (... continued)

#	labels	reaction	rate coefficient	reference
G40256	TrGTerC	BPINAOOH + OH → BPINAO2	1.33E-11	Rickard and Pascoe (2009)
G40257	TrGTerCN	BPINANO3 + OH → NOPINONE + HCHO + NO ₂	4.70E-12	Rickard and Pascoe (2009)
G40258a	TrGTerCN	ROO6R1O2 + NO → ROO6R3O2 + CH ₃ COCH ₃ + NO ₂	KR02N0*(1.-alpha_AN(13,3,0,0,0, temp, cair))	Vereecken and Peeters (2012)
G40258b	TrGTerCN	ROO6R1O2 + NO → ROO6R1NO3	KR02N0*alpha_AN(13,3,0,0,0, temp, cair)	Vereecken and Peeters (2012)
G40259	TrGTerC	ROO6R1O2 + HO ₂ → 10 LCARBON	KR02H02(10)	Vereecken and Peeters (2012)*
G40260	TrGTerC	ROO6R1O2 → ROO6R3O2 + CH ₃ COCH ₃	k1_R02tR02	Vereecken and Peeters (2012)
G40261a	TrGTerCN	RO6R1O2 + NO → RO6R3O2 + NO ₂	KR02N0*(1.-alpha_AN(12,3,0,0,0, temp, cair))	Vereecken and Peeters (2012)
G40261b	TrGTerCN	RO6R1O2 + NO → RO6R1NO3	KR02N0*alpha_AN(12,3,0,0,0, temp, cair)	Vereecken and Peeters (2012)
G40262	TrGTerC	RO6R1O2 + HO ₂ → 10 LCARBON	KR02H02(10)	Vereecken and Peeters (2012)*
G40263	TrGTerC	RO6R1O2 → RO6R3O2	k1_R02sR02	Vereecken and Peeters (2012)
G40264a	TrGTerCN	RO6R3O2 + NO → 9 LCARBON + HCHO + HO ₂ + NO ₂	KR02N0*(1.-alpha_AN(12,3,0,0,0, temp, cair))	Vereecken and Peeters (2012)
G40264b	TrGTerCN	RO6R3O2 + NO → 10 LCARBON + LNITROGEN	KR02N0*alpha_AN(12,3,0,0,0, temp, cair)	Vereecken and Peeters (2012)
G40265	TrGTerC	RO6R3O2 + HO ₂ → 10 LCARBON	KR02H02(10)	Vereecken and Peeters (2012)
G40266	TrGTerC	RO6R3O2 → 9 LCARBON + HCHO + HO ₂	k1_R02sR02	Vereecken and Peeters (2012)*
G40267a	TrGTerC	BPINENE + O ₃ → NOPINONE + .63 CO + .37 CH ₂ OO + .16 OH + .16 HO ₂	1.35E-15*EXP(-1270./TEMP)	Wallington et al. (2018)*
G40267b	TrGTerC	BPINENE + O ₃ → NOPINO2 + CO ₂	*.051/(1-.027)	Nguyen et al. (2009), Wallington et al. (2018)
G40267c	TrGTerC	BPINENE + O ₃ → NOPINDO2 + CO ₂ + OH	1.35E-15*EXP(-1270./TEMP)	Nguyen et al. (2009), Wallington et al. (2018)
G40267d	TrGTerC	BPINENE + O ₃ → CS8C + 2 CO ₂	*.283/(1-.027)	Nguyen et al. (2009), Wallington et al. (2018)
G40268	TrGTerCN	BPINENE + NO ₃ → LNBPINABO2	1.35E-15*EXP(-1270./TEMP)	Nguyen et al. (2009), Wallington et al. (2018)
G40269	TrGTerCN	LNBPINABO2 + HO ₂ → LNBPINABOOH	*(.104+.167)/(1-.027)	Wallington et al. (2018)*
G40270	TrGTerCN	LNBPINABO2 + NO → NOPINONE + HCHO + NO ₂ + NO ₂	KR02H02(10)	Rickard and Pascoe (2009)
G40271	TrGTerCN	LNBPINABO2 + NO ₃ → NOPINONE + HCHO + NO ₂	KR02N0	Rickard and Pascoe (2009)*
G40272a	TrGTerCN	LNBPINABO2 + NO ₃ → NOPINONE + HCHO + NO ₂ + NO ₂	KR02N03	Rickard and Pascoe (2009)
G40272a	TrGTerCN	LNBPINABO2 → NOPINONE + HCHO + NO ₂	k1_R02tR02*0.7	Rickard and Pascoe (2009)

65

Table 1: Gas phase reactions (... continued)

#	labels	reaction	rate coefficient	reference
G40272b	TrGTerCN	LNBPINABO2 → BPINANO3	k1_R02tR02*0.3	Rickard and Pascoe (2009)
G40273	TrGTerCN	LNBPINABOOH + OH → LNBPINABO2	9.58E-12	Rickard and Pascoe (2009)
G40274	TrGTerCN	ROO6R1NO3 + OH → ROO6R3O2 + CH ₃ COCH ₃ + NO ₂	9.16E-13	Vereecken and Peeters (2012), Gill and Hites (2002)*
G40275	TrGTerCN	RO6R1NO3 + OH → 9 LCARBON + HCHO + HO ₂ + NO ₂	9.16E-13	Vereecken and Peeters (2012), Gill and Hites (2002)
G40276	TrGTerC	PINEOL + OH → HCOOH + OH + NORPINAL	k_CH2CHOH_OH_HCOOH	Sander et al. (2018), So et al. (2014)*
G40277	TrGTerC	PINEOL + HCOOH → PINAL + HCOOH	k_CH2CHOH_HCOOH	Sander et al. (2018), da Silva (2010)*
G40278	TrGTerC	PINAL + HCOOH → PINEOL + HCOOH	k_ALD_HCOOH	Sander et al. (2018), da Silva (2010)*
G40279a	TrGC	CARENE + OH → LAPINABO2	8.8E-11*(.50+.25)	Atkinson and Arey (2003)
G40279b	TrGC	CARENE + OH → MENTHENONE + HO ₂	8.8E-11*.25*.60	Atkinson and Arey (2003)
G40279c	TrGC	CARENE + OH → ROO6R1O2	8.8E-11*.25*.40	Atkinson and Arey (2003)
G40280a	TrGC	CARENE + O ₃ → APINBOO	3.7E-17*.50*.18	Atkinson and Arey (2003)
G40280b	TrGC	CARENE + O ₃ → PINONIC	3.7E-17*.50*.16	Atkinson and Arey (2003)
G40280c	TrGC	CARENE + O ₃ → OH + NORPINAL + CO + HO ₂	3.7E-17*.50*.66	Atkinson and Arey (2003)
G40280d	TrGC	CARENE + O ₃ → APINAOO	3.7E-17*.50*.12	Atkinson and Arey (2003)
G40280e	TrGC	CARENE + O ₃ → OH + C109O2	3.7E-17*.50*(.22+.66)	Atkinson and Arey (2003)
G40281	TrGCN	CARENE + NO ₃ → LNAPINABO2	9.1E-12	Atkinson and Arey (2003)
G40282a	TrGTerC	SABINENE + OH → BPINAO2	1.47E-11*EXP(467./TEMP) *(0.8326*0.3+0.068)/(0.8326+0.068)	Gill and Hites (2002)*
G40282b	TrGTerC	SABINENE + OH → ROO6R1O2	1.47E-11*EXP(467./TEMP) *0.8326*0.7/(0.8326+0.068)	Vereecken and Peeters (2012), Gill and Hites (2002)*
G40283a	TrGTerC	SABINENE + O ₃ → NOPINONE + .63 CO + .37 HOCH ₂ OOH + .16 OH + .16 HO ₂	1.35E-15*EXP(-1270./TEMP) *.051/(1-.027)	Wallington et al. (2018)*
G40283b	TrGTerC	SABINENE + O ₃ → NOPINOO + CO ₂	1.35E-15*EXP(-1270./TEMP) *.368/(1-.027)	Nguyen et al. (2009), Wallington et al. (2018)
G40283c	TrGTerC	SABINENE + O ₃ → NOPINDO2 + CO ₂ + OH	1.35E-15*EXP(-1270./TEMP) *.283/(1-.027)	Nguyen et al. (2009), Wallington et al. (2018)
G40283d	TrGTerC	SABINENE + O ₃ → C8BC + 2 CO ₂	1.35E-15*EXP(-1270./TEMP) *(.104+167)/(1-.027)	Nguyen et al. (2009), Wallington et al. (2018)
G40284	TrGTerCN	SABINENE + NO ₃ → LNBPINABO2	2.51E-12	Wallington et al. (2018)*

66

Table 1: Gas phase reactions (... continued)

#	labels	reaction	rate coefficient	reference
G40285a	TrGTerC	CAMPHENE + OH → BPINAO2	1.47E-11*EXP(467./TEMP) *(0.8326*0.3+0.068)/(0.8326+0.068)	Gill and Hites (2002)*
G40285b	TrGTerC	CAMPHENE + OH → ROO6R1O2	1.47E-11*EXP(467./TEMP) *0.8326*0.7/(0.8326+0.068)	Vereecken and Peeters (2012), Gill and Hites (2002)*
G40286a	TrGTerC	CAMPHENE + O ₃ → NOPINONE + .63 CO + .37 HOCH ₂ OOH + .16 OH + .16 HO ₂	1.35E-15*EXP(-1270./TEMP) *.051/(1-.027)	Wallington et al. (2018)*
G40286b	TrGTerC	CAMPHENE + O ₃ → NOPINOO + CO ₂	1.35E-15*EXP(-1270./TEMP) *.368/(1-.027)	Nguyen et al. (2009), Wallington et al. (2018)
G40286c	TrGTerC	CAMPHENE + O ₃ → NOPINDO2 + CO ₂ + OH	1.35E-15*EXP(-1270./TEMP) *.283/(1-.027)	Nguyen et al. (2009), Wallington et al. (2018)
G40286d	TrGTerC	CAMPHENE + O ₃ → C8BC + 2 CO ₂	1.35E-15*EXP(-1270./TEMP) *(.104+167)/(1-.027)	Nguyen et al. (2009), Wallington et al. (2018)
G40287	TrGTerCN	CAMPHENE + NO ₃ → LNBPINABO2	2.51E-12	Wallington et al. (2018)*
G40400	TrGAroC	LHAROM + OH → .14 TLEPOXMUC + .03 C6H5CH2O2 + .04 CRESOL + .79 TLBIPERO2 + .18 HO ₂ + 4 LCARBON	5.67E-11	Rickard and Pascoe (2009)*
G40401	TrGAroCN	LHAROM + NO ₃ → C6H5CH2O2 + HNO ₃ + 4 LCARBON	2.60E-15	Rickard and Pascoe (2009)*

67

General notes

Three-body reactions

Rate coefficients for three-body reactions are defined via the function $k_3rd(T, M, k_0^{300}, n, k_{inf}^{300}, m, f_c)$. In the code, the temperature T is called `temp` and the concentration of "air molecules" M is called `cair`. Using the auxiliary variables $k_0(T)$, $k_{inf}(T)$, and k_{ratio} , k_3rd is defined as:

$$k_0(T) = k_0^{300} \times \left(\frac{300K}{T}\right)^n \quad (1)$$

$$k_{inf}(T) = k_{inf}^{300} \times \left(\frac{300K}{T}\right)^m \quad (2)$$

$$k_{ratio} = \frac{k_0(T)M}{k_{inf}(T)} \quad (3)$$

$$k_3rd = \frac{k_0(T)M}{1 + k_{ratio}} \times f_c^{\left(\frac{1}{1 + (\log_{10}(k_{ratio}))^2}\right)} \quad (4)$$

A similar function, called `k_3rd_iupac` here, is used by Wallington et al. (2018) for three-body reactions. It has the same function parameters as `k_3rd` and it is defined as:

$$k_0(T) = k_0^{300} \times \left(\frac{300K}{T}\right)^n \quad (5)$$

$$k_{inf}(T) = k_{inf}^{300} \times \left(\frac{300K}{T}\right)^m \quad (6)$$

$$k_{ratio} = \frac{k_0(T)M}{k_{inf}(T)} \quad (7)$$

$$N = 0.75 - 1.27 \times \log_{10}(f_c) \quad (8)$$

$$k_3rd_iupac = \frac{k_0(T)M}{1 + k_{ratio}} \times f_c^{\left(\frac{1}{1 + (0.9 \times 10^{(k_{ratio})/N})^2}\right)} \quad (9)$$

Structure-Activity Relationships (SAR)

Some unmeasured rate coefficients are estimated with structure-activity relationships, using the following parameters and substituent factors:

k for H-abstraction by OH in $\text{cm}^{-3}\text{s}^{-1}$	
<code>k_p</code>	$4.49 \times 10^{-18} \times (T/K)^2 \exp(-320 K/T)$
<code>k_s</code>	$4.50 \times 10^{-18} \times (T/K)^2 \exp(253 K/T)$
<code>k_t</code>	$2.12 \times 10^{-18} \times (T/K)^2 \exp(696 K/T)$
<code>k_rohro</code>	$2.1 \times 10^{-18} \times (T/K)^2 \exp(-85 K/T)$
<code>k_co2h</code>	$0.7 \times k_{\text{CH}_3\text{CO}_2\text{H}+\text{OH}}$
<code>k_roohro</code>	$0.6 \times k_{\text{CH}_3\text{OOH}+\text{OH}}$
<code>f_alk</code>	1.23
<code>f_soh</code>	3.44
<code>f_toh</code>	2.68
<code>f_sooh</code>	8.
<code>f_tooh</code>	8.
<code>f_ono2</code>	0.04
<code>f_ch2ono2</code>	0.20
<code>f_cpan</code>	0.25
<code>f_allyl</code>	3.6
<code>f_cho</code>	0.55
<code>f_co2h</code>	1.67
<code>f_co</code>	0.73
<code>f_o</code>	8.15
<code>f_pch2oh</code>	1.29
<code>f_tch2oh</code>	0.53

k for OH-addition to double bonds in $\text{cm}^{-3}\text{s}^{-1}$	
<code>k_adp</code>	$4.5 \times 10^{-12} \times (T/300 K)^{-0.85}$
<code>k_ads</code>	$1/4 \times (1.1 \times 10^{-11} \times \exp(485 K/T) + 1.0 \times 10^{-11} \times \exp(553 K/T))$
<code>k_adt</code>	$1.922 \times 10^{-11} \times \exp(450 K/T) - k_{ads}$
<code>k_adsecprim</code>	3.0×10^{-11}
<code>k_adtertprim</code>	5.7×10^{-11}
<code>a_pan</code>	0.56
<code>a_cho</code>	0.31
<code>a_coch3</code>	0.76
<code>a_ch2oh</code>	1.7
<code>a_ch2ooh</code>	1.7
<code>a_coh</code>	2.2
<code>a_cooH</code>	2.2
<code>a_co2h</code>	0.25
<code>a_ch2ono2</code>	0.64

RO₂ self and cross reactions

The self and cross reactions of organic peroxy radicals are treated according to the permutation reaction formalism as implemented in the MCM (Rickard and Pascoe, 2009), as described by Jenkin et al. (1997). Every organic peroxy radical reacts in a pseudo-first-order reaction with a rate constant that is expressed as $k^{\text{1st}} = 2 \times \sqrt{k_{\text{self}}} \times k_{\text{CH3O2}} \times [\text{RO}_2]$ where k_{self} = second-order rate coefficient of the self reaction of the organic peroxy radical, k_{CH3O2} = second-order rate coefficient of the self reaction of CH_3O_2 , and $[\text{RO}_2]$ = sum of the concentrations of all organic peroxy radicals.

68

Specific notes

G2110: The rate coefficient is: $k_{\text{H02_H02}} = (3.0\text{E-}13 \times \text{EXP}(460./\text{temp}) + 2.1\text{E-}33 \times \text{EXP}(920./\text{temp}) \times \text{cair}) \times (1 + 1.4\text{E-}21 \times \text{EXP}(2200./\text{temp}) \times \text{C}(\text{ind_H2O}))$.

G2117: Converted to Kc [molec-1 cm3] = $\text{Kp} \times \text{R} \times \text{T} / \text{NA}$, where R is 82.05730 [cm3atmK1mol1].

G2118: Assuming fast equilibrium.

G3109: The rate coefficient is: $k_{\text{N03_N02}} = k_{\text{3rd}}(\text{temp}, \text{cair}, 2.4\text{E-}30, 3.0, 1.6\text{E-}12, -0.1, 0.6)$.

G3110: The rate coefficient is defined as backward reaction divided by equilibrium constant.

G3203: The rate coefficient is: $k_{\text{N02_H02}} = k_{\text{3rd}}(\text{temp}, \text{cair}, 1.9\text{E-}31, 3.4, 4.0\text{E-}12, 0.3, 0.6)$.

G3206: The rate coefficient is: $k_{\text{HN03_OH}} = 1.32\text{E-}14 \times \text{EXP}(527/\text{temp}) + 1 / (1 / (7.39\text{E-}32 \times \text{EXP}(453/\text{temp}) \times \text{cair}) + 1 / (9.73\text{E-}17 \times \text{EXP}(1910/\text{temp})))$

G3207: The rate coefficient is defined as backward reaction divided by equilibrium constant.

G4104b: Methyl nitrate yield according to Banic et al. (2003) but reduced by a factor of 10 according to the upper limit derived from measurements by Munger et al. (1999).

G4109: Same temperature dependence as for $\text{CH}_3\text{CHO} + \text{NO}_3$ assumed.

G4115: The rate coefficient is defined as backward reaction divided by equilibrium constant.

G4116: Same value as for PAN + OH.

G4126: Same as for G4104 but scaled to match the recommended value at 298K.

G4127: Same as for $\text{CH}_3\text{O}_2 + \text{NO}_3$ in G4105.

G4130a: SAR for H-abstraction by OH.

G4130b: SAR for H-abstraction by OH.

G4132: SAR for H-abstraction by OH.

G4133: Lower limit of the rate constant. Products uncertain but CH_3OH can be excluded because of a likely high energy barrier (L. Vereecken, pers. comm.). CH_2OO production cannot be excluded.

G4134: Estimate based on the decomposition lifetime of 3 s (Olzmann et al., 1997) and a 20 kcal/mol energy barrier (Vereecken and Francisco, 2012).

G4135: Rate constant for $\text{CH}_2\text{OO} + \text{NO}_2$ (G4138) multiplied by the factor from Ouyang et al. (2013).

G4136: Average of two measurements.

G4137: Upper limit.

G4138: Average of 7 E-12 and 1.5 E-12.

G4141: HOCH_2OCHO forms and then decomposes to formic anhydride (Cruzdev et al., 1993) which hydrolyses in the humid atmosphere (Conn et al., 1942).

G4142: High-pressure limit.

G4143: Generic estimate for reaction with alcohols.

G4144: Generic estimate for reaction with RO_2 .

G4148: Same value as for $\text{NO}_2 + \text{CH}_3\text{O}_2$.

G4149: Barnes et al. (1985) estimated a decomposition rate equal to that of $\text{CH}_3\text{O}_2\text{NO}_2$.

G4150: Value for $\text{CH}_3\text{O}_2\text{NO}_2 + \text{OH}$, H-abstraction enhanced by the HO-group by `f_soh`.

G4154: Products assumed to be $\text{CH}_3\text{O}_2 + \text{O}_2$ (could also be $\text{HCHO} + \text{O}_2 + \text{OH}$).

G4160b: Half of the H-yield is attributed to fast secondary chemistry.

G4160c: The NH + CO channel is also significant but neglected here.

G4161: No studies below 450 K and only the major channel is considered.

G4164: Upper limit. Dominant pathway under atmospheric conditions.

G42001: The product distribution is from Rickard and Pascoe (2009), after substitution of the energized Criegee intermediate, CH_2OO , by its decomposition products and reaction of the stabilized CI with the water dimer.

G42010: Only major channel considered as the end products are essentially the same.

G42013: The rate coefficient is: $k_{\text{CH3CO3_N02}} = k_{\text{3rd}}(\text{temp}, \text{cair}, 9.7\text{E-}29, 5.6, 9.3\text{E-}12, 1.5, 0.6)$.

G42018: The rate coefficient is the same as for the CH_3 channel in G4107 ($\text{CH}_3\text{OOH} + \text{OH}$).

G42021: The rate coefficient is $k_{\text{PAN_M}} = k_{\text{CH3CO3_N02}}/9.0\text{E-}29 \times \text{EXP}(-14000./\text{temp})$, i.e. the rate coefficient is defined as backward reaction divided by equilibrium constant.

G42022a: Quantum yields and products are from Glowacki et al. (2012).

G42022b: Quantum yields and products are from Glowacki et al. (2012).

G42024a: Rate constant is the high-pressure limit as recommended by Atkinson et al. (2006).

G42024b: Rate constant is the high-pressure limit as recommended by Atkinson et al. (2006).

G42047: Orlando et al. (1998) estimated that about 25% of the $\text{HOCH}_2\text{CH}_2\text{O}$ in this reaction is produced with sufficient excess energy that it decomposes promptly. The decomposition products are 2 HCHO + HO₂.

G42051a: Same as for the CH_3O_2 channel in G4107: $\text{CH}_3\text{OOH} + \text{OH}$.

69

G42058b: The aldehydic H is assumed to be like the analogous H of HOCH₂CHO.

G42074a: Factor of 3 to match the estimate of $k = 1.E-11$ molec/cm³/s by Paulot et al. (2009a).

G42074b: Factor of 3 to match the estimate of $k = 1.E-11$ molec/cm³/s by Paulot et al. (2009a).

G42075: NO₃CH₂CO₂H and NO₃CH₂CO₃H neglected.

G42078: NO₃CH₂CO₂H neglected.

G42082: Same rate constant as for PAN + OH.

G42083a: Rate constant is the high-pressure limit as recommended by Atkinson et al. (2006).

G42083b: Rate constant is the high-pressure limit as recommended by Atkinson et al. (2006).

G42085a: Uncertainties on the kinetics at pressures < 0.1 bar.

G42085b: Channel proposed by Hynes and Wine 1991, OH + HCHO + HOCN, could not be confirmed by Tyndall et al. (2001b). There is no alternative mechanism at the moment. Products assumed to be OH + CH₃CO₃ + NO

G42086b: Assuming HCN is from channel 2h, HCO + H + HCN. HCO is replaced by H + CO.

G42086c: Assuming exothermic channels 2b and 2d are equally important.

G42087: HCOCN is produced but replaced here by its likely oxidation products (HCN + CO₂) as studied by Tyndall et al. (2001b). The rate constant for a typical RO₂ + NO reaction is used.

G42088: NCCH₂OOH is produced but replaced here by its likely oxidation products (HCN + CO₂) as studied by Tyndall et al. (2001b). The rate constant for a typical RO₂ + HO₂ reaction is used.

G42089a: The minor channel with $k=5.2E-12$ is combined with the major one producing HCOOH.

G42090: Theoretical keto-enol tautomerization catalyzed by formic acid (Grenfell et al., 2006).

G42091: Theoretical keto-enol tautomerization catalyzed by formic acid (Grenfell et al., 2006).

G43001a: Branching ratios according to Rickard et al. (1999).

G43001b: Branching ratios according to Rickard et al. (1999).

G43004: The value for the generic RO₂ + HO₂ reaction from Atkinson (1997) is used here.

G43008: The value for the generic RO₂ + HO₂ reaction from Atkinson (1997) is used here.

G43011: Strong positive deviation of k below 240 K compared to the expression recommended by JPL (Burkholder et al., 2015).

G43015a: The same value as for G4107 (CH₃OOH + OH) is used, multiplied by the branching ratio of the CH₃O₂ channel.

G43028: Alkyl nitrate formation neglected. (also not considered in MCM).

G43037: Alkyl nitrate formation neglected. (also not considered in MCM).

G43040a: Rate coefficient estimated with SAR (Taraborrelli, 2010).

G43040b: Rate coefficient estimated with SAR (Taraborrelli, 2010).

G43044: Alkyl nitrate formation neglected.

G43045c: Rate coefficient assumed to equal to the one of hydroxyacetone (ACETOL) for this channel.

G43048: Using the high-pressure limit.

G43049: The pressure fall-off between 1000 and 100 mbar is only 3% (Kirchner et al., 1999).

G43050: Value for CH₃O₂NO₂ + OH, H-abstraction enhanced by the CH₃CO-group by f.co.

G43051c: Products approximated with C₂H₅CHO + HO₂.

G43052: Only major H-abstraction channel considered.

G43059: Products approximated with the major end-product CH₃CHO.

G43060b: Products approximated with the major end-product CH₃CHO.

G43061: Products approximated with the likely end-product CH₃CHO.

G43065: As for HCOCO₃.

G43070a: Branching ratios estimated with SAR for H-abstraction rate constants by OH.

G43070b: Branching ratios estimated with SAR for H-abstraction rate constants by OH.

G43071a: Only this channel considered as the intermediate radical is likely more stable than CHCH(OH)₂.

G43072: Theoretical keto-enol tautomerization catalyzed by formic acid (Grenfell et al., 2006).

G43073: Theoretical keto-enol tautomerization catalyzed by formic acid (Grenfell et al., 2006).

G43074: HCOCOCOCHO would be produced but undergoes fast photolysis (faster than MGLYOX) and is substituted with its products.

G43223: Products simplified

G43419: KDEC C3DIALO → GLYOX + CO + HO₂

G43420: KDEC C3DIALO → GLYOX + CO + HO₂

G43421: Permutation reaction (minor channels removed).

G44000: The LC₄H₉O₂ composition ($nC_4H_9O_2:sC_4H_9O_2$ ratio) is assumed to be equal to the ratio of the production rates at 298K: $k_p/(k_p+k_s) = 0.1273$ and $k_s/(k_p+k_s) = 0.8727$.

70

G44001b: $sC_4H_9O_2$ products are substituted with 0.636 MEK + HO₂ and 0.364 CH₃CHO + C₂H₅O₂ at 1 bar and 298 K.

G44003c: The alkyl nitrate yield is the weighted average yield for the two isomers forming from $nC_4H_9O_2$ and $sC_4H_9O_2$.

G44010b: H-abstraction from primary C and substitution of the resulting peroxy radical with its products from the reaction with NO.

G44011: H-abstraction from primary C and substitution of the resulting peroxy radical with its products from the reaction with NO.

G44015b: Products assumed to be only from H-abstraction from a secondary C bearing the -OOH group.

G44016: Products assumed to be only from H-abstraction from a secondary C bearing the -ONO₂ group.

G44018: LHVMKABO2 is 0.12 HMVKA02 + 0.88 HMVKBO2.

G44019: LMEKO2 represents 0.62 MEKBO2 + 0.38 MEKAO2.

G44021a: The products of MEKAO are substituted with HCHO + CO₂ + HOCH₂CH₂O₂.

G44023a: Products from H-abstraction from the tertiary carbon bearing the ONO₂ group.

G44023b: Products from H-abstraction from the secondary carbon bearing the ONO₂ group.

G44025: Same value as for PAN.

G44026: Products as in G4415. Only the main channels for each isomer are considered. Weighted average for the isomers.

G44035: Rate constant replaced with the one of beta hydroxy RO₂.

G44046b: Using value for secondary nitrate (88% of total).

G44061a: Using value for secondary nitrate (88% of total).

G44061b: Using value for secondary nitrate (88% of total).

G44062a: Simplified products.

G44062b: Simplified products.

G44066: Alkyl nitrate formation neglected.

G44070: Alkyl nitrate formation neglected.

G44076: Alkyl nitrate formation neglected.

G44078: Other channel neglected.

G44081: Alkyl nitrate formation neglected.

G44082: Other channel neglected.

G44085: k for CH₃CHCO from Hatakeyama et al. (1985) adjusted.

G44086: Simplified product distribution.

G44089: The nitrated RO₂ is replaced by its products upon reaction with NO.

G44096: Both LBUT1ENO2 isomers mostly C₂H₅CHO.

G44097a: Branching ratios according to Rickard et al. (1999). CH₃CHO₂CHO is replaced with its major products CH₃CHO + CO + HO₂.

G44097b: Branching ratios according to Rickard et al. (1999).

G44098: The nitrated RO₂ is replaced by its products upon reaction with NO.

G44103b: MEKCOH replaced by its major oxidation products.

G44104: Carbonyl nitrate replaced by its major oxidation products.

G44106: CH3CHOOA products as from C₃H₆ + O₃ reaction.

G44107: The nitrated RO₂ is replaced by its products upon reaction with NO.

G44110: The nitrated RO₂ is replaced by its products upon reaction with NO.

G44124b: Skipping intermediate steps mostly leading to acetone.

G44126: Skipping intermediate steps mostly leading to acetone.

G44127: Only this channel considered as the intermediate radical is likely more stable than CHCH(OH)₂.

G44128: Theoretical keto-enol tautomerization catalyzed by formic acid (Grenfell et al., 2006).

G44129: Theoretical keto-enol tautomerization catalyzed by formic acid (Grenfell et al., 2006).

G44130: Only this channel considered as the intermediate radical is likely more stable than CHCH(OH)₂.

G44131: Theoretical keto-enol tautomerization catalyzed by formic acid (Grenfell et al., 2006).

G44132: Theoretical keto-enol tautomerization catalyzed by formic acid (Grenfell et al., 2006).

G44133: Only this channel considered as the intermediate radical is likely more stable than CHCH(OH)₂.

G44134: Theoretical keto-enol tautomerization catalyzed by formic acid (Grenfell et al., 2006).

G44135: Theoretical keto-enol tautomerization catalyzed by formic acid (Grenfell et al., 2006).

G44136: Only this channel considered as the intermediate radical is likely more stable than CHCH(OH)₂.

G44137: Theoretical keto-enol tautomerization catalyzed by formic acid (Grenfell et al., 2006).

G44138: Theoretical keto-enol tautomerization catalyzed by formic acid (Grenfell et al., 2006).

G44139: Simplified oxidation.

71

G44140: Simplified oxidation.
G44141: Simplified oxidation.
G44142: Simplified oxidation.
G44202: Alkyl nitrate formation neglected.
G44203a: Rate coefficient estimated with SAR (Taraborrelli, 2010).
G44205: Alkyl nitrate formation neglected.
G44210: Alkyl nitrate formation neglected.
G44221: Same k as for MGLYOX + OH (Tyndall et al., 1995).
G44402: KDEC NC4DCO2 → MALANHY + NO2
G44406c: KDEC MALDIALCO2 → 0.6 MALANHY + HO2 + 0.4 GLYOX + 0.4 CO + 0.4 CO2
G44407: KDEC MALDIALCO2 → 0.6 MALANHY + HO2 + 0.4 GLYOX + 0.4 CO + 0.4 CO2
G44409: KDEC MALDIALCO2 → 0.6 MALANHY + HO2 + 0.4 GLYOX + 0.4 CO + 0.4 CO2
G44410: KDEC MALDIALCO2 → 0.6 MALANHY + HO2 + 0.4 GLYOX + 0.4 CO + 0.4 CO2
G44412: KDEC BZFUONOOA → 0.5 BZFUONOO + 0.5 CO + 0.5 CO2 + 0.5 HCOCH2O2 + 0.5 OH and BZFUONOO → 0.625 CO14O3CO2H + 0.375 CO14O3CHO + 0.375 H2O2
G44421: Only major channel.
G44424: KDEC: GLYOOA → 0.125 HCHO + 0.18 GLYOO + 0.82 HO2 + 0.57 OH + 1.265 CO + 0.25 CO2 and H2O substitution GLYOO → 0.625 HCOCO2H + 0.375 GLYOX + 0.375 H2O2
G44425: Merged equations.
G44430: KDEC MALANHYO → HCOCOHCO3
G44431: KDEC MALANHYO → HCOCOHCO3
G44432: Only major channel. KDEC MALANHYO → HCOCOHCO3
G44436: KDEC NBZFUO → 0.5 CO14O3CHO + 0.5 NO2 + 0.5 NBZFUONE + 0.5 HO2
G44437: KDEC NBZFUO → 0.5 CO14O3CHO + 0.5 NO2 + 0.5 NBZFUONE + 0.5 HO2
G44438: KDEC NBZFUO → 0.5 CO14O3CHO + 0.5 NO2 + 0.5 NBZFUONE + 0.5 HO2 and RO2 Only major channel.
G44439: KDEC MALDIALCO2 → 0.6 MALANHY + HO2 + 0.4 GLYOX + 0.4 CO + 0.4 CO2
G44443: KDEC MECOACETO → CH3CO3 + HCHO
G44444: KDEC MECOACETO → CH3CO3 + HCHO
G44445: KDEC MECOACETO → CH3CO3 + HCHO
G44450: KDEC BZFUO → CO14O3CHO + HO2
G44451: KDEC BZFUO → CO14O3CHO + HO2
G44452: KDEC BZFUO → CO14O3CHO + HO2. Only major channel.
G44457: KDEC MALDIALO → GLYOX + GLYOX + HO2
G44458: KDEC MALDIALO → GLYOX + GLYOX + HO2
G44459: KDEC MALDIALO → GLYOX + GLYOX + HO2. Only major channel.
G44461: KBPAN → k.PAN_M
G45019d: Delta-1 and delta-2 LIEPOX are not considered and replaced by beta-LIEPOX formed by ISOP-BOOH and ISOPDOOH.
G45021: SAR estimate within uncertainty range of the experimentally determined rate constant by Solberg et al. (1997), 1.1E-11.
G45037: SAR estimate within uncertainty range of the experimentally determined rate constant by Solberg et al. (1997), 4.2E-11.
G45040: Alkyl nitrate formation neglected.
G45043: Old MCM rate constant 4.16E-11.
G45047: Alkyl nitrate formation neglected.
G45055: Alkyl nitrate formation neglected.
G45071: Alkyl nitrate formation neglected.
G45074: Formic acid production consistent with results of Bates et al. (2014). Here, the high yields of formic acid and hydroxycarbonyls at low NO from oxidation of cis-beta-LIEPOX (the most abundant isomer) are approximated with the production of DB10 which undergo both the Dibble double H-transfer to DB2O2 and HOCH2 elimination yielding HVMK and HMAC (ketovinyl alcohol potentially arising from decomposition of the alkoxy radical resulting from the ring opening after H-abstraction). The rate constant is from Paulot et al. (2009b) and adjusted based on Bates et al. (2014) that determined the single rate constants for the cis- and trans- beta isomer.
G45080: Alkyl nitrate formation neglected.
G45092a: C4MDIAL = CM4DIAL in MCM only from aromatics.
G45092b: Only one acyl peroxy radical considered.
G45093: Two aldehydic sites reacting with NO3 but only one isomer product considered.
G45095: Alkyl nitrate formation neglected.
G45098: Alkyl nitrate formation neglected.
G45100: Alkyl nitrate formation neglected.
G45104a: DB10OH is a hydroperoxide bearing a vinyl alcohol moiety that upon reaction with OH yields HCOOH (Davis et al., 1998).

72

G45107: OH production here is to take into account the hydroperoxidic function formed by the shift of the enolic hydrogen and not present in DB2O2. This approximation leads to spurious HO2 production.
G45108a: Consistent with the results of Bates et al. (2014).
G45108b: Consistent with the results of Bates et al. (2014). Assuming that the enol alkoxy radical partly decomposes yielding a substitute vinyl alcohol.
G45111: Alkyl nitrate formation neglected.
G45114b: Here, formic acid is mechanistically produced by the OH-addition to the vinyl alcohol which, upon RO2-to-RO conversion (skipped here), yields the HOCHOH fragment which in turn reacts with O2 forming HCOOH + HO2. Along CH3COCHOHCHO should be produced but not in the mechanism. Only CH3COCHO2CHO. The rate constant is consistent with predictions by Ganzeveld et al. (2006) for ENOL. OH-addition to the OH-bearing carbon is considered the dominant channel as it is already for the ENOL (Ganzeveld et al., 2006).
G45115: Theoretical keto-enol tautomerization catalyzed by formic acid (Grenfell et al., 2006). The product should be C1ODC3OOHC4OD but it is neglected in the mechanism.
G45116: As for DB1OOH + OH.
G45117: Additional sinks for DB2OOH are neglected.
G45121b: Nitrate assumed to be major isomer that is mostly similar to products of ISOPDO2-chemistry.
G45128: Rate constant by Liljegen and Stevens (2013). A lumped RO2 that upon conversion to RO yields 100% 2-methyl-butenedial (C4MDIAL) although Aschmann et al. (2014) quantified a 38% yield of the Z/E mixture.
G45129: As for 3METHYLFURAN + OH but with additional NO2 production for mass conservation.
G45131: Alkyl nitrate formation neglected.
G45132: Hydroperoxide formation neglected.
G45134b: ZCO2HC23DBCOD formation is neglected. However, it is produced in MCM and in aromatic-related reactions under the name of MC3ODBCO2H.
G45139: LZCPANC23DBCOD is assumed to react like LC5PAN1719.
G45201: Alkyl nitrate formation neglected.
G45207: Alkyl nitrate formation neglected.
G45214: Alkyl nitrate formation neglected.
G45217: Alkyl nitrate formation neglected.
G45225: Alkyl nitrate formation neglected.
G45236: LMBOABO2 = 0.67 MBOAO2 + 0.33 MBOBO2
G45247: Alkyl nitrate formation neglected.
G45400: KDEC NC4MDCO2 → MMALANHY + NO2
G45404: KDEC NTLFUO → ACCOMECHO + NO2
G45405: KDEC NTLFUO → ACCOMECHO + NO2
G45406: KDEC NTLFUO → ACCOMECHO
G45409: KBPAN → k.PAN_M (renaming)
G45413: KFPAN → k.CH3CO3_NO2 (renaming)
G45422: KDEC MMALANHYO → CO2H3CO3
G45423: KDEC MMALANHYO → CO2H3CO3
G45424: KDEC MMALANHYO → CO2H3CO3 and Only major channel.
G45429: KBPAN → k.PAN_M (renamed)
G45430a: KDEC C5CO14CO2 → 0.83 MALANHY + 0.83 CH3 + 0.17 MGLYOX + 0.17 HO2 + 0.17 CO + 0.17 CO2
G45431: KDEC C5CO14CO2 → 0.83 MALANHY + 0.83 CH3 + 0.17 MGLYOX + 0.17 HO2 + 0.17 CO + 0.17 CO2
G45432: KFPAN → k.CH3CO3_NO2 (renaming)
G45433: KDEC C5CO14CO2 → 0.83 MALANHY + 0.83 CH3 + 0.17 MGLYOX + 0.17 HO2 + 0.17 CO + 0.17 CO2
G45434: KDEC C5CO14CO2 → 0.83 MALANHY + 0.83 CH3 + 0.17 MGLYOX + 0.17 HO2 + 0.17 CO + 0.17 CO2 and only major channel.
G45436: KDEC C5CO14CO2 → 0.83 MALANHY + 0.83 CH3 + 0.17 MGLYOX + 0.17 HO2 + 0.17 CO + 0.17 CO2
G45444: KDEC MC3CODOBCO2 → 0.35 GLYOX + 0.35 CH3 + 0.35 CO + 0.35 CO2 + 0.65 MMALANHY + 0.65 HO2
G45452: KDEC TLFUONOAA → 0.5 CO + 0.5 OH + 0.5 MECOACETO2 + 0.5 TLFUONOO and H2O subs TLFUONOO → 0.625 C24O3CCO2H + 0.375 ACCOMECHO + 0.375 H2O2
G45456: KFPAN → k.CH3CO3_NO2 (renaming)
G45476b: KDEC NTLFUO → ACCOMECHO + NO2 and reactions with KRO2HO2.
G45477: KDEC NTLFUO → ACCOMECHO + NO2
G45478: KDEC NTLFUO → ACCOMECHO + NO2
G45479: KDEC NTLFUO → ACCOMECHO + NO2
G45486b: KDEC C5DIALO → MALDIAL + CO + HO2 and reactions with KRO2HO2.
G45487: KDEC C5DIALO → MALDIAL
G45488: KDEC C5DIALO → MALDIAL
G45489: KDEC C5DIALO → MALDIAL
G45491b: Reactions with KRO2HO2.

73

G46492: MGLYOX + GLYOX + HO2 from KDEC substitution

G46493: MGLYOX + GLYOX + HO2 from KDEC substitution

G46494: Permutation reaction (minor channels removed).

G46201: Alkyl nitrate formation neglected.

G46404b: Reactions with KRO2HO2 and KDEC C615CO2O → C5DICARB + CO + HO2.

G46405: KDEC C615CO2O → C5DICARB + CO + HO2

G46406: KDEC C615CO2O → C5DICARB + CO + HO2

G46407: Only major channel.

G46413b: Reactions with KRO2HO2 and KDEC DNPHENO → NC4DCO2H + HNO3 + CO + CO + NO2.

G46414: KDEC DNDPHENO → NC4DCO2H + HNO3 + CO + CO + NO2

G46415: KDEC DNDPHENO → NC4DCO2H + HNO3 + CO + CO + NO2

G46416: KDEC DNDPHENO → NC4DCO2H + HNO3 + CO + CO + NO2

G46418: KDEC CATECOOA → MALDALCO2H + HCOCO2H + HO2 + OH

G46426: KFPAN → k.CH3CO3.NO2

G46430: KDEC GLYOOA → .125 HCHO + .18 GLYOO + .82 HO2 + .57 OH + 1.265 CO

G46432b: Reactions with KRO2HO2 and KDEC NCATECO → NC4DCO2H + HCOCO2H + HO2

G46433: KDEC NCATECO → NC4DCO2H + HCOCO2H + HO2

G46434: KDEC NCATECO → NC4DCO2H + HCOCO2H + HO2

G46435: KDEC NCATECO → NC4DCO2H + HCOCO2H + HO2

G46437b: Reactions with KRO2HO2 and KDEC NPHENO → MALDALCO2H + GLYOX + NO2

G46438: KDEC NPHENO → MALDALCO2H + GLYOX + NO2

G46439: KDEC NPHENO → MALDALCO2H + GLYOX + NO2

G46440: KDEC NPHENO → MALDALCO2H + GLYOX + NO2

G46441: Merged equations.

G46447b: reactions with KRO2HO2 and KDEC NNCATECO → NC4DCO2H + HCOCO2H + NO2

G46448: KDEC NNCATECO → NC4DCO2H + HCOCO2H + NO2

G46449: KDEC NNCATECO → NC4DCO2H + HCOCO2H + NO2

G46450: KDEC NNCATECO → NC4DCO2H + HCOCO2H + NO2

G46457: Merged equations.

G46458: Merged equations.

G46461b: Reactions with KRO2HO2 and KDEC PHENO → 0.71 MALDALCO2H + 0.71 GLYOX + 0.29 PBZQONE + HO2

G46462: KDEC PHENO → 0.71 MALDALCO2H + 0.71 GLYOX + 0.29 PBZQONE + HO2

G46463: KDEC PHENO → 0.71 MALDALCO2H + 0.71 GLYOX + 0.29 PBZQONE + HO2

G46464: KDEC PHENO → 0.71 MALDALCO2H + 0.71 GLYOX + 0.29 PBZQONE + HO2 and Only major channel.

G46468: KFPAN → k.CH3CO3.NO2

G46472b: new channel

G46476: HOC6H4NO2 is a nitro-phenol

G46480b: Reactions with KRO2HO2 and KDEC PBZQO → C5CO2OHCO3

G46481: KDEC PBZQO → C5CO2OHCO3

G46482: KDEC PBZQO → C5CO2OHCO3

G46483: KDEC PBZQO → C5CO2OHCO3 and Only major channel.

G46485b: Reactions with KRO2HO2 and KDEC DNPHENO → NC4DCO2H + HCOCO2H + NO2

G46486: KDEC DNPHENO → NC4DCO2H + HCOCO2H + NO2

G46487: KDEC DNPHENO → NC4DCO2H + HCOCO2H + NO2

G46488: KDEC DNPHENO → NC4DCO2H + HCOCO2H + NO2

G46490b: Reactions with KRO2HO2 and KDEC BZEMUCO → 0.5 EPXC4DIAL + 0.5 GLYOX + 0.5 HO2 + 0.5 C3DIALO2 + 0.5 C32OH13CO.

G46491b: KDEC BZEMUCO → 0.5 EPXC4DIAL + 0.5 GLYOX + 0.5 HO2 + 0.5 C3DIALO2 + 0.5 C32OH13CO.

G46492: KDEC BZEMUCO → 0.5 EPXC4DIAL + 0.5 GLYOX + 0.5 HO2 + 0.5 C3DIALO2 + 0.5 C32OH13CO

G46493: KDEC BZEMUCO → 0.5 EPXC4DIAL + 0.5 GLYOX + 0.5 HO2 + 0.5 C3DIALO2 + 0.5 C32OH13CO and Only major channel.

G46499b: Reactions with KRO2HO2 and KDEC NBZQO → C6CO4DB + NO2.

G46500: KDEC NBZQO → C6CO4DB + NO2

G46501: KDEC NBZQO → C6CO4DB + NO2

G46502: KDEC NBZQO → C6CO4DB + NO2

74

G46505b: New channel.

G46515: Only major channel.

G46517b: New channel.

G46522b: In analogy to TLBIPERO2 from toluene (Birdsall et al., 2010).

G46523b: KDEC BZBIPERO → GLYOX + HO2 + 0.5 BZFUONE + 0.5 BZFUONE

G46524: KDEC BZBIPERO → GLYOX + HO2 + 0.5 BZFUONE + 0.5 BZFUONE

G46525: KDEC BZBIPERO → GLYOX + HO2 + 0.5 BZFUONE + 0.5 BZFUONE and Only major channel.

G47210: Alkyl nitrate formation neglected.

G47214: Alkyl nitrate formation neglected.

G47218: Alkyl nitrate formation neglected.

G47222: Alkyl nitrate formation neglected.

G47223: ROO6R3OOH produced but no sink for it.

G47225: ROO6R4P produced but no sink for it.

G47226: ROO6R5P produced but no sink for it

G47400: Merged.

G47402a: KROPRIM*O2 fast reaction C6H5CH2O = BENZAL + HO2.

G47402b: KROPRIM*O2 fast reaction C6H5CH2O = BENZAL + HO2.

G47403: KROPRIM*O2 fast reaction C6H5CH2O = BENZAL + HO2.

G47404: KROPRIM*O2 fast reaction C6H5CH2O = BENZAL + HO2. C6H5CH2OH replaced by its oxidation product BENZAL.

G47405: Merged.

G47406: Merged.

G47407b: According to Birdsall et al. (2010), the branching ratio rbipero2_oh is set to 0.4 in order to take into account the OH-recycling and summed yield of butendial and methylbutendial.

G47408a: KDEC TLBIPERO → 0.6 GLYOX + 0.4 MGLYOX + HO2 + 0.2 C4MDIAL + 0.2 C5DICARB + 0.2 TLFUONE + 0.2 BZFUONE + 0.2 MALDIAL

G47408b: KDEC TLBIPERO → 0.6 GLYOX + 0.4 MGLYOX + HO2 + 0.2 ZCODC23DB COD + 0.2 C5DICARB + 0.2 TLFUONE + 0.2 BZFUONE + 0.2 MALDIAL

G47409: KDEC TLBIPERO → 0.6 GLYOX + 0.4 MGLYOX + HO2 + 0.2 ZCODC23DB COD + 0.2 C5DICARB + 0.2 TLFUONE + 0.2 BZFUONE + 0.2 MALDIAL

G47410: Only major channel and KDEC TLBIPERO → 0.6 GLYOX + 0.4 MGLYOX + HO2 + 0.2 ZCODC23DB COD + 0.2 C5DICARB + 0.2 TLFUONE + 0.2 BZFUONE + 0.2 MALDIAL

G47412: KDEC MGLOOB → 0.125 CH3CHO + 0.695 CH3CO + 0.57 CO + 0.57 OH + 0.125 HO2 + 0.18 MGLOO + 0.25 CO2

G47413: Merged.

G47418b: Reactions with KRO2HO2 and KDEC CRESO → 0.68 C5CO14OH + 0.68 GLYOX + HO2 + 0.32 PTLQONE.

G47419: KDEC CRESO → 0.68 C5CO14OH + 0.68 GLYOX + HO2 + 0.32 PTLQONE

G47420: KDEC CRESO → 0.68 C5CO14OH + 0.68 GLYOX + HO2 + 0.32 PTLQONE

G47421: KDEC CRESO → 0.68 C5CO14OH + 0.68 GLYOX + HO2 + 0.32 PTLQONE and Only major channel.

G47422b: Reactions with KRO2HO2 and KDEC NCRESO → C5CO14OH + GLYOX + NO2

G47423: KDEC NCRESO → C5CO14OH + GLYOX + NO2

G47424: KDEC NCRESO → C5CO14OH + GLYOX + NO2

G47425: KDEC NCRESO → C5CO14OH + GLYOX + NO2 and Only major channel.

G47426: TOL1OHNO2 is a nitro-phenol

G47429: KDEC MCATECOOA → MC3ODBCO2H + HCOCO2H + HO2 + OH

G47436: KFPAN → k.CH3CO3.NO2

G47438: Only major channel.

G47439b: Reactions with KRO2HO2 and KDEC TLEMUCO → 0.5 C3DIALO2 + 0.5 CO2H3CHO + 0.5 EPXC4DIAL + 0.5 MGLYOX + 0.5 HO2

G47440b: KDEC TLEMUCO → 0.5 C3DIALO2 + 0.5 CO2H3CHO + 0.5 EPXC4DIAL + 0.5 MGLYOX + 0.5 HO2

G47441: KDEC TLEMUCO → 0.5 C3DIALO2 + 0.5 CO2H3CHO + 0.5 EPXC4DIAL + 0.5 MGLYOX + 0.5 HO2

G47442: KDEC TLEMUCO → 0.5 C3DIALO2 + 0.5 CO2H3CHO + 0.5 EPXC4DIAL + 0.5 MGLYOX + 0.5 HO2 and Only major channel.

G47445: KFPAN → k.CH3CO3.NO2

G47447: Only major channel.

G47454: New channel.

G47479: New channel.

G47482b: Reactions with KRO2HO2 and KDEC NPTLQO → C7CO4DB + NO2

G47483: KDEC NPTLQO → C7CO4DB + NO2

G47484: KDEC NPTLQO → C7CO4DB + NO2

G47485: KDEC NPTLQO → C7CO4DB + NO2

G47486b: Reactions with KRO2HO2 and KDEC PTLQO → C6CO2OHCO3

75

G47487: KDEC PTLQO \rightarrow C6CO2OHC03
G47488: KDEC PTLQO \rightarrow C6CO2OHC03
G47489: Only major channel. KDEC PTLQO \rightarrow C6CO2OHC03.
G47494: New channel.
G47497b: Reactions with KRO2HO2 and KDEC MNCATECO \rightarrow NC4MDCO2H + HCOCO2H + NO2
G47498: KDEC MNCATECO \rightarrow NC4MDCO2H + HCOCO2H + NO2
G47499: KDEC MNCATECO \rightarrow NC4MDCO2H + HCOCO2H + NO2
G47501b: Reactions with KRO2HO2 and KDEC MNCATECO \rightarrow NC4MDCO2H + HCOCO2H + HO2
G47502: KDEC MNCATECO \rightarrow NC4MDCO2H + HCOCO2H + HO2
G47503: KDEC MNCATECO \rightarrow NC4MDCO2H + HCOCO2H + HO2
G47504: KDEC MNCATECO \rightarrow NC4MDCO2H + HCOCO2H + HO2
G47509b: Reactions with KRO2HO2 and KDEC DNCRESO \rightarrow NC4MDCO2H + HNO3 + CO + CO + NO2
G47510: KDEC DNCRESO \rightarrow NC4MDCO2H + HNO3 + CO + CO + NO2
G47511: KDEC DNCRESO \rightarrow NC4MDCO2H + HNO3 + CO + CO + NO2
G47512: KDEC DNCRESO \rightarrow NC4MDCO2H + HNO3 + CO + CO + NO2
G47513b: Reactions with KRO2HO2 and KDEC DNCRESO \rightarrow NC4MDCO2H + HCOCO2H + NO2
G47514: KDEC DNCRESO \rightarrow NC4MDCO2H + HCOCO2H + NO2
G47515: KDEC DNCRESO \rightarrow NC4MDCO2H + HCOCO2H + NO2
G47516: KDEC DNCRESO \rightarrow NC4MDCO2H + HCOCO2H + NO2
G48202: Alkyl nitrate formation neglected.
G48205: Alkyl nitrate formation neglected.
G48210: Alkyl nitrate formation neglected.
G48212: Alkyl nitrate formation neglected.
G48216: Alkyl nitrate formation neglected.
G48222: Alkyl nitrate formation neglected.
G48400a: Same products as for toluene. Assuming a 1:1:1 proportion in xylenes emissions the analogous toluene product is produced with a rate constant equal to $(1.36E-11*0.24 + 2.31E-11*0.29 + 1.43E-11*0.155)/3$, where k and coefficients are for the single isomers ortho, meta and para from MCM.
G48400b: Same products as for toluene. Assuming a 1:1:1 proportion in xylenes emissions the analogous toluene product is produced with a rate constant equal to $(1.36E-11*0.05 + 2.31E-11*0.04 + 1.43E-11*0.10)/3$, where k and coefficients are for the single isomers ortho, meta and para from MCM.
G48400c: Same products as for toluene. Assuming a 1:1:1 proportion in xylenes emissions the analogous toluene product is produced with a rate constant equal to $(1.36E-11*0.16 + 2.31E-11*0.17 + 1.43E-11*0.12)/3$, where k and coefficients are for the single isomers ortho, meta and para from MCM.
G48400d: Same products as for toluene. Assuming a 1:1:1 proportion in xylenes emissions the analogous toluene product is produced with a rate constant equal to $(1.36E-11*0.55 + 2.31E-11*0.50 + 1.43E-11*0.625)/3$, where k and coefficients are for the single isomers ortho, meta and para from MCM.
G48401: Same products as for toluene. The rate constant is the average of m, p, o $k=(4.10E-16+2.60E-16+5.00E-16)/3 = 3.9E-16$.
G48402: merged under same rate constant
G48403: Same products as for toluene
G48405: KDEC CH2OOB \rightarrow 0.24 CH2OO + 0.40 CO + 0.36 HO2 + 0.36 CO + 0.36 OH and H2O + PHCHO \rightarrow 0.625 PHCOOH + 0.375 BENZAL + 0.375 H2O2 + 0.2 CO2
G48408: KDEC NSTYRENEO \rightarrow NO2 + HCHO + BENZAL
G48409: KDEC NSTYRENEO \rightarrow NO2 + HCHO + BENZAL
G48410: KDEC NSTYRENEO \rightarrow NO2 + HCHO + BENZAL
G48412b: KDEC STYRENO \rightarrow HO2 + HCHO + BENZAL and reactions with KRO2HO2.
G48413: KDEC STYRENO \rightarrow HO2 + HCHO + BENZAL
G48414: KDEC STYRENO \rightarrow HO2 + HCHO + BENZAL
G48415: KDEC STYRENO \rightarrow HO2 + HCHO + BENZAL
G49207: Alkyl nitrate formation neglected.
G49238: Alkyl nitrate formation neglected.
G49246: Only this channel considered as the intermediate radical is likely more stable than CHCH(OH)₂. Instead of the (lacking) carbonyl a product of further degradation is assumed.
G49247: Theoretical keto-enol tautomerization catalyzed by formic acid (Grenfell et al., 2006).
G49248: Theoretical keto-enol tautomerization catalyzed by formic acid (Grenfell et al., 2006).
G49400a: Same products as for toluene. Assuming a 1:1:1 proportion in xylenes emissions the analogous toluene product is produced with a rate constant equal to $(3.27E-11*0.21 + 3.25E-11*0.30 + 5.67E-11*0.14)/3$, where k and coefficients are for the single isomers 1,2,3-, 1,3,4- and 1,3,5- from MCM.
G49400b: Same products as for toluene. Assuming a 1:1:1 proportion in xylenes emissions the analogous toluene product is produced with a rate constant equal to $(3.27E-11*0.06 + 3.25E-11*0.06 + 5.67E-11*0.03)/3$, where k and coefficients are for the single isomers 1,2,3-, 1,3,4- and 1,3,5- from MCM.
G49400c: Same products as for toluene. Assuming a 1:1:1 proportion in xylenes emissions the analogous toluene product is produced with a rate constant equal to $(3.27E-11*0.03 + 3.25E-11*0.03 + 5.67E-11*0.04)/3$, where k and coefficients are for the single isomers 1,2,3-, 1,3,4- and 1,3,5- from MCM.
G49400d: Same products as for toluene. Assuming a 1:1:1 proportion in xylenes emissions the analogous toluene product is produced with a rate constant equal to $(3.27E-11*0.70 + 3.25E-11*0.61 + 5.67E-11*0.79)/3$, where k and coefficients are for the single isomers 1,2,3-, 1,3,4- and 1,3,5- from MCM.
G49401: Same products as for toluene. The rate constant is the average of m, p, o $k=(1.90+1.80+0.88)E-15/3=1.52E-15$.
G40200: Products from Vereecken et al. (2007). LAP-INAPO2 = 0.65 APINAPO2 + 0.35 APINBO2
G40203: Weighted average for isomers A and B, $k = 0.33*9.20E-14+0.67*8.80E-13$.
G40204: Weighted average for isomers A and B, $k = 0.35*1.83E-11+0.65*3.28E-11$.
G40205: Weighted average for isomers A and B, $k = 0.35*5.50E-12+0.65*3.64E-12$.
G40206: SAR-estimated rate constant, $(k_{ads}+k_{adt})*aco3 = 6.46E-11$ where $k_{ads} = 3.0E-11$, $k_{adt} = 5.5E-11$, $aco3 = 0.76$
G40207: Alkyl nitrate formation neglected.
G40211: Products from Rickard and Pascoe (2009).
G40212: Products from Rickard and Pascoe (2009).
G40232: Products from Capouet et al. (2008).
G40242: Alkyl nitrate formation neglected.
G40246: Products from Rickard and Pascoe (2009).
G40248: Alkyl nitrate formation neglected.
G40252a: Products from Vereecken and Peeters (2012).
G40252b: Products from Vereecken and Peeters (2012).
G40259: RO6R1OOH is produced but no sink for it.
G40262: RO6R1OOH is produced but no sink for it.
G40266: Rate constant modified according to MCM protocol.
G40267a: Products from Nguyen et al. (2009).
G40268: Products from Rickard and Pascoe (2009).
G40270: Alkyl nitrate neglected.
G40274: As for RO6R1NO3 in G4085.
G40276: Only this channel considered as the intermediate radical is likely more stable than CHCH(OH)₂.
G40277: Theoretical keto-enol tautomerization catalyzed by formic acid (Grenfell et al., 2006).
G40278: Theoretical keto-enol tautomerization catalyzed by formic acid (Grenfell et al., 2006).
G40282a: Products from Vereecken and Peeters (2012).
G40282b: Products from Vereecken and Peeters (2012).
G40283a: Products from Nguyen et al. (2009).
G40284: Products from Rickard and Pascoe (2009).
G40285a: Products from Vereecken and Peeters (2012).
G40285b: Products from Vereecken and Peeters (2012).
G40286a: Products from Nguyen et al. (2009).
G40287: Products from Rickard and Pascoe (2009).
G40400: DIET35TOL(from MCM) as representative of higher aromatics
G40401: Same products as for toluene.

Table 2: Photolysis reactions

#	labels	reaction	rate coefficient	reference
J1000a	UpStTrGJ	$O_2 + h\nu \rightarrow O(^3P) + O(^3P)$	jx(ip_D2)	Sander et al. (2014)
J1001a	UpStTrGJ	$O_3 + h\nu \rightarrow O(^1D) + O_2$	jx(ip_01D)	Sander et al. (2014)
J1001b	UpStTrGJ	$O_3 + h\nu \rightarrow O(^3P) + O_2$	jx(ip_03P)	Sander et al. (2014)
J2101	UpStTrGJ	$H_2O_2 + h\nu \rightarrow 2 OH$	jx(ip_H2O2)	Sander et al. (2014)
J3101	UpStTrGJN	$NO_2 + h\nu \rightarrow NO + O(^3P)$	jx(ip_NO2)	Sander et al. (2014)
J3103a	UpStTrGJN	$NO_3 + h\nu \rightarrow NO_2 + O(^3P)$	jx(ip_NO20)	Sander et al. (2014)
J3103b	UpStTrGJN	$NO_3 + h\nu \rightarrow NO + O_2$	jx(ip_NO02)	Sander et al. (2014)
J3104	StTrGJN	$N_2O_5 + h\nu \rightarrow NO_2 + NO_3$	jx(ip_N2O5)	Sander et al. (2014)
J3200	TrGJN	$HONO + h\nu \rightarrow NO + OH$	jx(ip_HONO)	Sander et al. (2014)
J3201	StTrGJN	$HNO_3 + h\nu \rightarrow NO_2 + OH$	jx(ip_HNO3)	Sander et al. (2014)
J3202	StTrGJN	$HNO_3 + h\nu \rightarrow .667 NO_2 + .667 HO_2 + .333 NO_3 + .333 OH$	jx(ip_HNO4)	Sander et al. (2014)
J41000	StTrGJ	$CH_3OOH + h\nu \rightarrow CH_3O + OH$	jx(ip_CH300H)	Sander et al. (2014)
J41001a	StTrGJ	$HCHO + h\nu \rightarrow H_2 + CO$	jx(ip_C0H2)	Sander et al. (2014)
J41001b	StTrGJ	$HCHO + h\nu \rightarrow H + CO + HO_2$	jx(ip_C0H0)	Sander et al. (2014)
J41004	StTrGJN	$CH_3ONO + h\nu \rightarrow CH_3O + NO$	jx(ip_CH3ON0)	Sander et al. (2014)
J41005	StTrGJN	$CH_3ONO_2 + h\nu \rightarrow CH_3O + NO_2$	jx(ip_CH3NO3)	Sander et al. (2014)
J41006	StTrGJN	$CH_3O_2NO_2 + h\nu \rightarrow .667 NO_2 + .667 CH_3O_2 + .333 NO_3 + .333 CH_3O$	jx(ip_CH3O2NO2)	Sander et al. (2014)*
J41007	StTrGJ	$HOCH_2OOH + h\nu \rightarrow HCOOH + OH + HO_2$	jx(ip_CH300H)	Sander et al. (2014)
J41008	StTrGJ	$CH_3O_2 + h\nu \rightarrow HCHO + OH$	jx(ip_CH3O2)	Sander et al. (2014)
J41009	StTrGJ	$HCOOH + h\nu \rightarrow CO + HO_2 + OH$	jx(ip_HCO0H)	Sander et al. (2014)
J41010	StTrGJN	$HOCH_2O_2NO_2 + h\nu \rightarrow .667 NO_2 + .667 HOCH_2O_2 + .333 NO_3 + .333 HCOOH + .333 HO_2$	jx(ip_CH3O2NO2)	Sander et al. (2014)
J42000	TrGJN	$C_2H_5OOH + h\nu \rightarrow CH_3CHO + HO_2 + OH$	jx(ip_CH300H)	von Kuhlmann (2001)
J42001a	TrGJN	$CH_3CHO + h\nu \rightarrow CH_3 + HO_2 + CO$	jx(ip_CH3CHO)	Sander et al. (2014)
J42001b	TrGJN	$CH_3CHO + h\nu \rightarrow CH_2CHOH$	jx(ip_CH3CHO2VINYL)	Clubb et al. (2012)
J42002	TrGJN	$CH_3C(O)OOH + h\nu \rightarrow CH_3 + OH + CO_2$	jx(ip_CH3CO3H)	Sander et al. (2014)
J42004	TrGJCN	$PAN + h\nu \rightarrow .7 CH_3C(O) + .7 NO_2 + .3 CH_3 + .3 CO_2 + .3 NO_3$	jx(ip_PAN)	Sander et al. (2014)*
J42005a	TrGJN	$HOCH_2CHO + h\nu \rightarrow HCHO + 2 HO_2 + CO$	jx(ip_HOCH2CHO)*0.83	Sander et al. (2014)*
J42005b	TrGJN	$HOCH_2CHO + h\nu \rightarrow OH + HCOCH_2O_2$	jx(ip_HOCH2CHO)*0.07	Sander et al. (2014)*
J42005c	TrGJN	$HOCH_2CHO + h\nu \rightarrow CH_3OH + CO$	jx(ip_HOCH2CHO)*0.10	Sander et al. (2014)*
J42006	TrGJN	$HOCH_2CO_3H + h\nu \rightarrow HCHO + HO_2 + OH + CO_2$	jx(ip_CH300H)	Rickard and Pascoe (2009)

78

Table 2: Photolysis reactions (... continued)

#	labels	reaction	rate coefficient	reference
J42007	TrGJCN	$PHAN + h\nu \rightarrow .7 HOCH_2CO + .7 NO_2 + .3 HCHO + .3 HO_2 + .3 CO_2 + .3 NO_3$	jx(ip_PAN)	see note*
J42008	TrGJN	$GLYOX + h\nu \rightarrow 2 CO + 2 HO_2$	jx(ip_GLYOX)	Sander et al. (2014)
J42009	TrGJN	$HCOCO_2H + h\nu \rightarrow 2 HO_2 + CO + CO_2$	jx(ip_MGLYOX)	Rickard and Pascoe (2009)
J42010	TrGJN	$HCOC(O)H + h\nu \rightarrow HO_2 + CO + OH + CO_2$	jx(ip_CH300H)+jx(ip_HOCH2CHO)	Rickard and Pascoe (2009)
J42011	TrGJN	$HYETHO2H + h\nu \rightarrow HOCH_2CH_2O + OH$	jx(ip_CH300H)	Rickard and Pascoe (2009)
J42012	TrGJCN	$ETHOHN03 + h\nu \rightarrow HO_2 + 2 HCHO + NO_2$	j_IC3H7N03	Rickard and Pascoe (2009)
J42013	TrGJN	$HOCH_2CO_3H + h\nu \rightarrow OH + HCHO + CO_2 + OH$	2*jx(ip_CH300H)	Sander et al. (2018)
J42014	TrGC	$HOCH_2CO_2H + h\nu \rightarrow OH + HCHO + HO_2 + CO_2$	jx(ip_CH300H)	Sander et al. (2018)
J42015	TrGC	$CH_2CO + h\nu \rightarrow .4 CO_2 + .8 H + .34 CO + .34 OH + .34 HO_2 + .16 HCHO + .16 O(^3P) + .1 HCOOH + CO$	j_ketene* 0.36	Sander et al. (2018)
J42016	TrGC	$CH_3CHOHOH + h\nu \rightarrow CH_3 + HCOOH + OH$	jx(ip_CH300H)	Sander et al. (2018)
J42017	TrGJCN	$NO_3CH_2CHO + h\nu \rightarrow HO_2 + CO + HCHO + NO_2$	(jx(ip_C2H5N03)+jx(ip_CH3CHO)) *(jx(ip_NOA)+1E-10)/(0.59*j_IC3H7N03+jx(ip_CH3COCH3)+1E-10)	Sander et al. (2018)*
J42018	TrGJN	$HOCH_2CHO + h\nu \rightarrow OH + HCHO + CO + HO_2$	jx(ip_CH300H)+jx(ip_HOCH2CHO)	Sander et al. (2018)
J42019	TrGJCN	$C_2H_5ONO_2 + h\nu \rightarrow CH_3CHO + HO_2 + NO_2$	jx(ip_C2H5N03)	Sander et al. (2018)
J42020	TrGJCN	$NO_3CH_2CHO + h\nu \rightarrow .7 NO_3CH_2CO_3 + .7 NO_2 + .3 HCHO + .3 NO_2 + .3 CO_2 + .3 NO_3$	jx(ip_PAN)	Sander et al. (2018)*
J42021	StTrGJCN	$C_2H_5O_2NO_2 + h\nu \rightarrow .667 NO_2 + .667 C_2H_5O_2 + .333 NO_3 + .333 CH_3CHO + .333 HO_2$	jx(ip_CH3O2NO2)	Sander et al. (2018)*
J43000	TrGJN	$iC_3H_7OOH + h\nu \rightarrow CH_3COCH_3 + HO_2 + OH$	jx(ip_CH300H)	von Kuhlmann (2001)
J43001	TrGJN	$CH_3COCH_3 + h\nu \rightarrow CH_3C(O) + CH_3$	jx(ip_CH3COCH3)	Sander et al. (2014)
J43002	TrGJN	$CH_3COCH_2OH + h\nu \rightarrow .5 CH_3C(O) + .5 HCHO + .5 HO_2 + .5 HOCH_2CO + .5 CH_3$	j_ACETOL	Sander et al. (2014)*
J43003	TrGJN	$MGLYOX + h\nu \rightarrow CH_3C(O) + CO + HO_2$	jx(ip_MGLYOX)	Sander et al. (2014)
J43004	TrGJN	$CH_3COCH_2O_2H + h\nu \rightarrow CH_3C(O) + HCHO + OH$	jx(ip_CH300H)+j_ACETOL	Rickard and Pascoe (2009)
J43005	TrGJN	$HOCH_2COCH_2OOH + h\nu \rightarrow HOCH_2CO + HCHO + OH$	jx(ip_CH300H)+j_ACETOL	Sander et al. (2018)
J43006	TrGJCN	$iC_3H_7ONO_2 + h\nu \rightarrow CH_3COCH_3 + NO_2 + HO_2$	j_IC3H7N03	von Kuhlmann et al. (2003)*
J43007	TrGJCN	$NOA + h\nu \rightarrow CH_3C(O) + HCHO + NO_2$	jx(ip_NOA)	Barnes et al. (1993)
J43009	TrGJN	$HYPPO2H + h\nu \rightarrow CH_3CHO + HCHO + HO_2 + OH$	jx(ip_CH300H)	Rickard and Pascoe (2009)
J43010	TrGJCN	$PR2O2HNO_3 + h\nu \rightarrow NOA + HO_2 + OH$	jx(ip_CH300H)	Rickard and Pascoe (2009)
J43011	TrGJN	$HOCH_2COCHO + h\nu \rightarrow HOCH_2CO + CO + HO_2$	jx(ip_MGLYOX)	Rickard and Pascoe (2009)
J43012	TrGJN	$HCOCOCH_2OOH + h\nu \rightarrow HCOCO + HCHO + OH$	jx(ip_CH300H)+j_ACETOL	Sander et al. (2018)

79

Table 2: Photolysis reactions (... continued)

#	labels	reaction	rate coefficient	reference
J43013	TrGJC	HCOCOC ₂ H ₂ OOH + hν → HOOCCH ₂ CO ₂ + CO + HO ₂	jx(ip_MGLYOX)	Sander et al. (2018)
J43014	TrGJTerC	HCOCH ₂ CHO + hν → HCOCH ₂ O ₂ + HO ₂ + CO	jx(ip_HOCH ₂ CHO)*2.	Rickard and Pascoe (2009)
J43015	TrGJTerC	HCOCH ₂ CO ₂ H + hν → HCOCH ₂ O ₂ + CO ₂ + HO ₂	jx(ip_HOCH ₂ CHO)	Rickard and Pascoe (2009)
J43016	TrGJTerC	HOC ₂ H ₄ CO ₃ H + hν → HOCH ₂ CH ₂ O ₂ + CO ₂ + OH	jx(ip_CH300H)	Rickard and Pascoe (2009)
J43017	TrGJC	HCOCOCHO + hν → HCOCO + HO ₂ + CO	2.*jx(ip_MGLYOX)	Sander et al. (2018)
J43018	TrGJC	CH ₃ COCO ₂ H + hν → .32 CH ₃ CHO + .16 CH ₂ CHOH + .54 CO ₂ + .38 CH ₃ C(O) + .38 HO ₂ + .38 CO ₂ + .07 CH ₃ COOH + .07 CO + .05 CH ₃ C(O) + .05 CO + .05 OH	jx(IP_CH3COC ₂ H)	Sander et al. (2018)*
J43019	TrGC	CH ₃ COCO ₃ H + hν → CH ₃ C(O) + OH + CO ₂	jx(IP_MGLYOX)+jx(ip_CH300H)	Sander et al. (2018)
J43020	TrGC	CH ₃ CHCO + hν → C ₂ H ₄ + CO	j_ketene*0.36*2.	Sander et al. (2018)
J43021	TrGCN	PROPOLNO ₃ + hν → HOCH ₂ CHO + HCHO + HO ₂ + NO ₂	j_IC3H7N03	Sander et al. (2018)
J43022	TrGCN	CH ₃ COCH ₂ OONO ₂ + hν → CH ₃ C(O) + HCHO + NO ₃	jx(ip_CH302N02)+jx(ip_CH3C0CH3)	Sander et al. (2018)
J43023	TrGJC	C ₃ H ₇ OOH + hν → C ₂ H ₅ CHO + HO ₂ + OH	jx(ip_CH300H)	von Kuhlmann (2001)
J43024	TrGJCN	C ₃ H ₇ ONO ₂ + hν → C ₂ H ₅ CHO + NO ₂ + HO ₂	0.59*j_IC3H7N03	see note*
J43025a	TrGJC	C ₂ H ₅ CHO + hν → C ₂ H ₅ O ₂ + HO ₂ + CO	jx(ip_C2H5CHO2HCO)	see note*
J43025b	TrGJC	C ₂ H ₅ CHO + hν → CH ₂ CHCH ₂ OH	jx(ip_C2H5CHO2ENOL)	Andrews et al. (2012), Sander et al. (2018)*
J43026	TrGJCN	PPN + hν → .7 C ₂ H ₅ CO ₃ + .7 NO ₂ + .3 C ₂ H ₅ O ₂ + .3 CO ₂ + .3 NO ₃	jx(ip_PAN)	Sander et al. (2014)
J43027	TrGJC	C ₂ H ₅ CO ₃ H + hν → C ₂ H ₅ O ₂ + CO ₂ + OH	jx(ip_CH300H)	von Kuhlmann (2001)
J43028a	TrGJC	HCOCOC ₂ H ₂ OOH + hν → HOOCCH ₂ CO ₂ + CO + HO ₂	jx(ip_MGLYOX)	Sander et al. (2018)
J43028b	TrGJC	HCOCOC ₂ H ₂ OOH + hν → HCOCO + HCHO + OH	jx(ip_HOCH ₂ CHO)+jx(ip_CH300H)	Sander et al. (2018)
J43200	TrGJTerC	HCOCH ₂ CO ₃ H + hν → HCOCH ₂ O ₂ + CO ₂ + OH	jx(ip_HOCH ₂ CHO)+jx(ip_CH300H)	Rickard and Pascoe (2009)
J43400	TrGJAroC	C3DIALOOH + hν → GLYOX + CO + HO ₂ + OH	jx(ip_HOCH ₂ CHO)*2+jx(ip_CH300H)	Rickard and Pascoe (2009)*
J43401	TrGJAroC	C32OH13CO + hν → GLYOX + HO ₂ + HO ₂ + CO	jx(ip_HOCH ₂ CHO)*2	Rickard and Pascoe (2009)
J43402	TrGJAroC	HCOCOHCO ₃ H + hν → GLYOX + HO ₂ + CO ₂ + OH	jx(ip_CH300H)	Rickard and Pascoe (2009)
J44000a	TrGJC	LC ₁ H ₉ OOH + hν → OH + C ₃ H ₇ CHO + HO ₂	jx(ip_CH300H)*(k_p/(k_p+k_s))	Rickard and Pascoe (2009), Sander et al. (2018)
J44000b	TrGJC	LC ₁ H ₉ OOH + hν → OH + .636 MEK + .636 HO ₂ + .364 CH ₃ CHO + .364 C ₂ H ₅ O ₂	jx(ip_CH300H)*(k_s/(k_p+k_s))	Rickard and Pascoe (2009), Sander et al. (2018)
J44001	TrGJC	MVK + hν → .5 C ₃ H ₆ + .5 CH ₃ C(O) + .5 HCHO + CO + .5 HO ₂	jx(ip_MVK)	Sander et al. (2014)

80

Table 2: Photolysis reactions (... continued)

#	labels	reaction	rate coefficient	reference
J44002	TrGJC	MEK + hν → CH ₃ C(O) + C ₂ H ₅ O ₂	0.42*jx(ip_CHOH)	von Kuhlmann et al. (2003)
J44003	TrGJC	LMEKOOH + hν → .62 CH ₃ C(O) + .62 CH ₃ CHO + .38 HCHO + .38 CO ₂ + .38 HOCH ₂ CH ₂ O ₂ + OH	jx(ip_CH300H)+0.42*jx(ip_CHOH)	Sander et al. (2018)
J44004	TrGJC	BIACET + hν → 2 CH ₃ C(O)	2.15*jx(ip_MGLYOX)	see note*
J44005a	TrGJCN	LC4H9NO ₃ + hν → NO ₂ + C ₃ H ₇ CHO + HO ₂	j_IC3H7N03*(k_p/(k_p+k_s))	see note*
J44005b	TrGJCN	LC4H9NO ₃ + hν → NO ₂ + MEK + HO ₂	j_IC3H7N03*(k_s/(k_p+k_s))	see note*
J44006	TrGJCN	MPAN + hν → .7 MACO ₃ + .7 NO ₂ + .3 MACO ₂ + .3 NO ₃	jx(ip_PAN)	see note*
J44007a	TrGJC	CO ₂ H ₃ CO ₃ H + hν → MGLYOX + HO ₂ + OH + CO ₂	jx(ip_CH300H)	Rickard and Pascoe (2009)
J44007b	TrGJC	CO ₂ H ₃ CO ₃ H + hν → CH ₃ C(O) + HO ₂ + HCOCO ₃ H	j_ACETDL	Rickard and Pascoe (2009)
J44008	TrGJC	MACR + hν → .5 MACO ₃ + .5 CH ₃ C(O) + .5 HCHO + .5 CO + HO ₂	jx(ip_MACR)	Sander et al. (2014)
J44009	TrGJC	MACROOH + hν → MACRO + OH	jx(ip_CH300H)+2.77*jx(ip_HOCH ₂ CHO)	Sander et al. (2018)*
J44010	TrGJC	MACROH + hν → CH ₃ COCH ₂ OH + CO + HO ₂ + HO ₂	2.77*jx(ip_HOCH ₂ CHO)	see note*
J44011	TrGJC	MACO ₃ H + hν → MACO ₂ + OH	jx(ip_CH300H)	Sander et al. (2018)
J44012	TrGJC	LHMVKABOOH + hν → .12 MGLYOX + .12 HO ₂ + .88 CH ₃ C(O) + .88 HOCH ₂ CHO + .12 HCHO + OH	jx(ip_CH300H)+j_ACETDL	Sander et al. (2018)
J44013	TrGJC	CO ₂ H ₃ CHO + hν → MGLYOX + CO + HO ₂ + HO ₂	jx(ip_HOCH ₂ CHO)+j_ACETDL	Sander et al. (2018)
J44014	TrGJC	HO ₁ 2CO ₃ C ₄ + hν → CH ₃ C(O) + HOCH ₂ CHO + HO ₂	j_ACETDL	Rickard and Pascoe (2009)
J44015	TrGJC	BIACETOH + hν → CH ₃ C(O) + HOCH ₂ CO	2.15*jx(ip_MGLYOX)	see note*
J44016	TrGC	HCOCCH ₃ CO + hν → .5 OH + .5 CH ₃ CHO + CO + .5 CH ₃ CHCO + .5 CO	j_KETENE	Sander et al. (2018)
J44017a	TrGC	CH ₃ COCHCO + hν → .0192 CH ₃ COCO ₂ H + .1848 H ₂ O ₂ + .2208 MGLYOX + .36 OH + .36 CO + .56 CH ₃ C(O) + .2 CH ₃ CHO + .2 CO ₂ + .2 HCHO + .2 HO ₂ + CO	j_KETENE*0.5	Sander et al. (2018), Rickard and Pascoe (2009)*
J44017b	TrGC	CH ₃ COCHCO + hν → CH ₃ CHCO + CO	j_KETENE*0.5	Sander et al. (2018)
J44018a	TrGJC	CH ₃ COCOCHO + hν → CH ₃ C(O) + 2 CO + HO ₂	jx(ip_MGLYOX)	Sander et al. (2018)
J44018b	TrGJC	CH ₃ COCOCHO + hν → HCOCO + CH ₃ C(O)	2.15*jx(ip_MGLYOX)	Sander et al. (2018)
J44019	TrGJC	CH ₃ COCOCO ₂ H + hν → CH ₃ C(O) + CO + CO ₂ + HO ₂	3.15*jx(ip_MGLYOX)	Sander et al. (2018)
J44020a	TrGJTerC	CH ₃ COCOCO ₂ HOOH + hν → CH ₃ C(O) + OH + HCHO + CO	jx(ip_CH300H)+j_ACETDL	Rickard and Pascoe (2009)
J44020b	TrGJTerC	CH ₃ COCOCO ₂ HOOH + hν → CH ₃ C(O) + HCOCO	2.15*jx(ip_MGLYOX)	Rickard and Pascoe (2009)
J44021	TrGJTerC	C4OOH + hν → HCOCH ₂ CHO + CO ₂ + HO ₂ + OH	jx(ip_CH300H)	Rickard and Pascoe (2009)
J44022	TrGJTerC	C413COOOH + hν → HCOCH ₂ CO ₃ + HCHO + OH	jx(ip_CH300H)+jx(ip_HOCH ₂ CHO)+j_ACETDL	Rickard and Pascoe (2009)

81

Table 2: Photolysis reactions (... continued)

#	labels	reaction	rate coefficient	reference
J44023a	TrGJTerC	C4CODIAL + $h\nu$ → HCOCOC ₂ H ₂ O ₂ + HO ₂ + CO	jx(ip_HOCH2CHO)	Rickard and Pascoe (2009)
J44023b	TrGJTerC	C4CODIAL + $h\nu$ → HCOCH ₂ CO ₃ + HO ₂ + CO	jx(ip_MGLYOX)	Rickard and Pascoe (2009)
J44024	TrGJTerC	C3I2COCOC ₃ H + $h\nu$ → HCOCOC ₂ H ₂ O ₂ + CO ₂ + OH	jx(ip_CH300H)+jx(ip_MGLYOX)	Rickard and Pascoe (2009)
J44025	TrGJCN	LMEKNO ₃ + $h\nu$ → .62 CH ₃ C(O) + .62 CH ₃ CHO + .38 HCHO + .38 CO ₂ + .38 HOCH ₂ CH ₂ O ₂ + NO ₂	jx(ip_MEKNO3)	Barnes et al. (1993), Sander et al. (2018)*
J44026	TrGJCN	MVKNO ₃ + $h\nu$ → CH ₃ C(O) + HOCH ₂ CHO + NO ₂	jx(ip_MEKNO3)	Barnes et al. (1993), Sander et al. (2018)*
J44027	TrGJCN	MACRNO ₃ + $h\nu$ → CH ₃ COCH ₂ OH + CO + HO ₂ + NO ₂	(2.84*j_IC3H7NO3+jx(ip_CH3CHO)) * (jx(ip_MEKNO3)+1E-10) / (j_IC3H7NO3+0.42*jx(ip_CHOH)+1E-10)	Müller et al. (2014), Sander et al. (2018)*
J44028	TrGJCN	TC4H9NO ₃ + $h\nu$ → CH ₃ COCH ₃ + CH ₃ + NO ₂	2.84*j_IC3H7NO3	Sander et al. (2018)
J44029	TrGJC	TC ₄ H ₉ OOH + $h\nu$ → CH ₃ COCH ₃ + CH ₃ + OH	jx(ip_CH300H)	Sander et al. (2018)
J44030	TrGJCN	IBUTOLBNO ₃ + $h\nu$ → CH ₃ COCH ₃ + HCHO + HO ₂ + NO ₂	2.84*j_IC3H7NO3	Sander et al. (2018)
J44031	TrGJC	IBUTOLBOOH + $h\nu$ → CH ₃ COCH ₃ + HCHO + HO ₂ + OH	jx(ip_CH300H)	Sander et al. (2018)
J44032	TrGJC	LBUT1ENOOH + $h\nu$ → C ₂ H ₅ CHO + HCHO + HO ₂ + OH	jx(ip_CH300H)	Sander et al. (2018)
J44033	TrGJCN	LBUT1ENNO ₃ + $h\nu$ → C ₂ H ₅ CHO + HCHO + HO ₂ + NO ₂	j_IC3H7NO3	Sander et al. (2018)
J44034	TrGJC	BUT2OLOOH + $h\nu$ → 2 CH ₃ CHO + HO ₂ + OH	jx(ip_CH300H)	Sander et al. (2018)
J44035	TrGJCN	BUT2OLNO ₃ + $h\nu$ → 2 CH ₃ CHO + HO ₂ + NO ₂	j_IC3H7NO3	Sander et al. (2018)
J44036	TrGJC	BUT2OLO + $h\nu$ → CH ₃ C(O) + HOCH ₂ CO	j_ACETOL	Sander et al. (2018)
J44037a	TrGJC	C ₃ H ₇ CHO + $h\nu$ → C ₃ H ₇ O ₂ + CO + HO ₂	jx(ip_C3H7CHO2HCO)	Sander et al. (2018)
J44037b	TrGJC	C ₃ H ₇ CHO + $h\nu$ → C ₃ H ₄ + CH ₂ CHOH	jx(ip_C3H7CHO2VINYL)	Sander et al. (2018)*
J44038	TrGJC	IPRCHO + $h\nu$ → iC ₃ H ₇ O ₂ + CO + HO ₂	jx(ip_IPRCHO2HCO)	Sander et al. (2018)
J44039	TrGJCN	IC4H9NO ₃ + $h\nu$ → IPRCHO + NO ₂	j_IC3H7NO3	Sander et al. (2018)
J44040	TrGJC	IC ₄ H ₉ OOH + $h\nu$ → IPRCHO + HO ₂ + OH	jx(ip_CH300H)	Sander et al. (2018)
J44041	TrGJC	PERIBUACID + $h\nu$ → iC ₃ H ₇ O ₂ + CO ₂ + OH	jx(ip_CH300H)	Sander et al. (2018)
J44042	TrGJCN	PIPN + $h\nu$ → .7 IPRCO ₃ + .7 NO ₂ + .3 iC ₃ H ₇ O ₂ + .3 CO ₂ + .3 NO ₃	jx(ip_PAN)	Sander et al. (2018), Sander et al. (2014)
J44043	TrGJC	HVMK + $h\nu$ → MGLYOX + CO + 2 OH	jx(ip_PeDIONE24)	Sander et al. (2018), Nakanishi et al. (1977), Messadia et al. (2015), Yoon et al. (1999)*
J44044	TrGJC	HMAC + $h\nu$ → HCOCCH ₃ CO + 2 OH	jx(ip_PeDIONE24)	Sander et al. (2018), Nakanishi et al. (1977), Messadia et al. (2015), Yoon et al. (1999)*

82

Table 2: Photolysis reactions (... continued)

#	labels	reaction	rate coefficient	reference
J44045a	TrGJC	CO2C3CHO + $h\nu$ → CH ₃ COCH ₂ O ₂ + HO ₂ + CO	jx(ip_C2H5CHO2HCO)	Rickard and Pascoe (2009)
J44045b	TrGJC	CO2C3CHO + $h\nu$ → HVMK	jx(ip_C2H5CHO2ENOL)	Andrews et al. (2012), Sander et al. (2018)
J44046a	TrGJC	IBUTDIAL + $h\nu$ → CH ₃ CHO + CO + HO ₂ + CO ₂ + H ₂ O	jx(ip_C2H5CHO2HCO)*2.	see note*
J44046b	TrGJC	IBUTDIAL + $h\nu$ → HMAC	jx(ip_C2H5CHO2ENOL)*2.	Andrews et al. (2012), Sander et al. (2018)
J44200	TrGJTerC	IBUTALOH + $h\nu$ → CH ₃ COCH ₃ + HO ₂ + HO ₂ + CO	j_ACETOL	Rickard and Pascoe (2009)
J44201	TrGJTerC	IPRHOCO ₃ H + $h\nu$ → CH ₃ COCH ₃ + HO ₂ + CO ₂ + OH	jx(ip_CH300H)	Rickard and Pascoe (2009)
J44400a	TrGJAroC	MALDIALOOH + $h\nu$ → C ₃ HOH ₃ CO + CO + OH + HO ₂	jx(ip_HOCH2CHO)*2	Rickard and Pascoe (2009)
J44400b	TrGJAroC	MALDIALOOH + $h\nu$ → GLYOX + GLYOX + HO ₂ + OH	jx(ip_CH300H)	Rickard and Pascoe (2009)*
J44401	TrGJAroC	BZFUOOH + $h\nu$ → CO1403CHO + HO ₂ + OH	jx(ip_CH300H)	Rickard and Pascoe (2009)*
J44402	TrGJAroC	HOCOC4DIAL + $h\nu$ → HCOCOHCO ₃ + HO ₂ + CO	jx(ip_MGLYOX)+jx(ip_HOCH2CHO)	Rickard and Pascoe (2009)
J44403	TrGJAroCN	NBZFUOOH + $h\nu$ → .5 CO1403CHO + .5 NO ₂ + .5 NBZFUONE + .5 HO ₂ + OH	jx(ip_CH300H)	Rickard and Pascoe (2009)*
J44404a	TrGJAroC	MALDALCO ₃ H + $h\nu$ → HCOCOC ₃ H + HO ₂ + CO + HO ₂ + CO	jx(ip_MACR)	Rickard and Pascoe (2009)
J44404b	TrGJAroC	MALDALCO ₃ H + $h\nu$ → .6 MALANHY + HO ₂ + .4 GLYOX + .4 CO + .4 CO ₂ + OH	jx(ip_CH300H)	Rickard and Pascoe (2009)*
J44405	TrGJAroC	EPXDLCO ₂ H + $h\nu$ → C3DIALO ₂ + CO ₂ + HO ₂	2.77*jx(ip_HOCH2CHO)	Rickard and Pascoe (2009)
J44406	TrGJAroC	MALDIAL + $h\nu$ → .4 BZFUONE + .6 MALDIALCO ₃ + .6 HO ₂	jx(ip_NO2)*0.14	Rickard and Pascoe (2009)
J44407	TrGJAroC	MALANHYOOH + $h\nu$ → HCOCOHCO ₃ + CO ₂ + OH	jx(ip_CH300H)	Rickard and Pascoe (2009)*
J44408	TrGJAroC	EPXDLCO ₃ H + $h\nu$ → C3DIALO ₂ + OH + CO ₂	jx(ip_CH300H)+2.77*jx(ip_HOCH2CHO)	Rickard and Pascoe (2009)
J44409	TrGJAroC	CO2C4DIAL + $h\nu$ → CO + CO + HO ₂ + HO ₂ + CO + CO	jx(ip_MGLYOX)*2	Rickard and Pascoe (2009)
J44410	TrGJAroC	MALDALCO ₂ H + $h\nu$ → HCOCOC ₂ H + HO ₂ + CO + HO ₂ + CO	jx(ip_MACR)	Rickard and Pascoe (2009)
J44411	TrGJAroC	EPXC4DIAL + $h\nu$ → C3DIALO ₂ + CO + HO ₂	2.77*jx(ip_HOCH2CHO)*2	Rickard and Pascoe (2009)
J44412	TrGJAroC	CO1403CHO + $h\nu$ → HO ₂ + CO + HCOCH ₂ O ₂ + CO ₂	jx(ip_MGLYOX)	Rickard and Pascoe (2009)
J44414	TrGJAroC	MECOACEOOH + $h\nu$ → CH ₃ C(O) + HCHO + CO ₂ + OH	jx(ip_CH300H)	Rickard and Pascoe (2009)*
J45002	TrGJC	LISOPACOOH + $h\nu$ → LISOPACO + OH	jx(ip_CH300H)	Rickard and Pascoe (2009)
J45003	TrGJCN	LISOPACNO ₃ + $h\nu$ → LISOPACO + NO ₂	0.59*j_IC3H7NO3	see note*
J45004	TrGJC	ISOPBOOH + $h\nu$ → MVK + HCHO + HO ₂ + OH	jx(ip_CH300H)	Rickard and Pascoe (2009)
J45005	TrGJCN	ISOPBNO ₃ + $h\nu$ → MVK + HCHO + HO ₂ + NO ₂	2.84*j_IC3H7NO3	see note*

83

Table 2: Photolysis reactions (... continued)

#	labels	reaction	rate coefficient	reference
J45006	TrGJC	ISOPDOOH + hν → MACR + HCHO + HO ₂ + OH	jx(ip_CH300H)	Rickard and Pascoe (2009)
J45007	TrGJCN	ISOPDNO ₃ + hν → MACR + HCHO + HO ₂ + NO ₂	j_IC3H7N03	see note*
J45008	TrGJCN	NISOPOOH + hν → NC4CHO + HO ₂ + OH	jx(ip_CH300H)	Rickard and Pascoe (2009)
J45009	TrGJCN	NC4CHO + hν → LHC4ACCO ₃ + NO ₂	(.59*j_IC3H7N03+jx(ip_MACR)) *(jx(ip_MEKN03)+1E-10)/(j_IC3H7N03+0.42*jx(ip_CHOH)+1E-10)	Müller et al. (2014), Sander et al. (2018)*
J45010	TrGJCN	LNISOOH + hν → NOA + OH + .5 HOCHCHO + .5 CO + .5 HO ₂ + .5 CO ₂	jx(ip_CH300H)	Taraborrelli et al. (2009), Sander et al. (2018)
J45011	TrGJC	LHC4ACCHO + hν → .5 LHC4ACCO ₃ + .5 HO ₂ + .5 CO + .5 OH + .25 MACRO ₂ + .25 LHMVKABO ₂	jx(ip_MACR)	Sander et al. (2018)
J45012	TrGJC	LC578OOH + hν → .25 CH ₃ COCH ₂ OH + .75 MGLYOX + .25 HOCHCHO + .75 HOCH ₂ CHO + .75 HO ₂ + OH	jx(ip_CH300H)+ 2.77*jx(ip_HOCH2CHO)	Sander et al. (2018)
J45013	TrGJC	LHC4ACCO ₃ H + hν → OH + .5 MACRO ₂ + .5 LHMVKABO ₂ + OH + CO ₂	j_HPALD	Sander et al. (2018)
J45014	TrGJCN	LC5PAN1719 + hν → .7 LHC4ACCO ₃ + .7 NO ₂ + .15 MACRO ₂ + .15 LHMVKABO ₂ + .3 CO ₂ + .3 NO ₃	jx(ip_PAN)	Sander et al. (2018)
J45015	TrGJC	HCOC ₅ + hν → .65 CH ₃ + .65 CO + .65 HCHO + .35 OH + .35 CH ₃ COCH ₂ O ₂ + HOCH ₂ CO	0.5*jx(ip_MVK)	Sander et al. (2018)*
J45016	TrGJC	C590OH + hν → CH ₃ COCH ₂ OH + HOCH ₂ CO + OH	j_ACETOL+jx(ip_CH300H)	Sander et al. (2018)
J45017	TrGJTerC	C511OOH + hν → CH ₃ C(O) + HCOCH ₂ CHO + OH	jx(ip_CH300H)+jx(ip_HOCH2CHO)	Rickard and Pascoe (2009)
J45018a	TrGJTerC	CO23C4CHO + hν → CH ₃ COCOC ₂ O ₂ + HO ₂ + CO	jx(ip_HOCH2CHO)	Rickard and Pascoe (2009)
J45018b	TrGJTerC	CO23C4CHO + hν → CH ₃ C(O) + HCOCH ₂ CO ₃	2.15*jx(ip_MGLYOX)	Rickard and Pascoe (2009)
J45019	TrGJTerC	CO23C4CO ₃ H + hν → CH ₃ COCOC ₂ O ₂ + CO ₂ + OH	jx(ip_CH300H)+jx(ip_HOCH2CHO)	Rickard and Pascoe (2009)
J45020	TrGJTerC	C512OOH + hν → C513O ₂ + OH	jx(ip_CH300H)+jx(ip_HOCH2CHO)	Rickard and Pascoe (2009)
J45021	TrGJTerC	CO13C4CHO + hν → CHOC ₃ COO ₂ + CO + HO ₂	jx(ip_HOCH2CHO)*2	Rickard and Pascoe (2009)
J45022	TrGJTerC	C513OOH + hν → GLYOX + HOC ₂ H ₄ CO ₃ + OH	jx(ip_CH300H)+jx(ip_HOCH2CHO)	Rickard and Pascoe (2009)
J45023	TrGJTerC	C513CO + hν → HOC ₂ H ₄ CO ₃ + HO ₂ + CO + CO	jx(ip_MGLYOX)+2.15*jx(ip_MGLYOX)	Rickard and Pascoe (2009)
J45024	TrGJTerC	C514OOH + hν → CO13C4CHO + HO ₂ + OH	jx(ip_CH300H)+jx(ip_HOCH2CHO)*2	Rickard and Pascoe (2009)
J45025	TrGJTerCN	C514NO ₃ + hν → CO13C4CHO + HO ₂ + NO ₂	j_IC3H7N03+jx(ip_HOCH2CHO)*2	Rickard and Pascoe (2009)
J45026a	TrGJC	LZCOCDC23DBC ₂ OOH + hν → OH + CO + HVMK + OH	j_HPALD*0.6*0.5	Sander et al. (2018), Jenkin et al. (2015), Peeters et al. (2014)
J45026b	TrGJC	LZCOCDC23DBC ₂ OOH + hν → OH + CO + CH ₃ C(O) + HOCH ₂ CHO	j_HPALD*0.6*0.5	Sander et al. (2018), Jenkin et al. (2015), Peeters et al. (2014)

84

Table 2: Photolysis reactions (... continued)

#	labels	reaction	rate coefficient	reference
J45026c	TrGJC	LZCOCDC23DBC ₂ OOH + hν → OH + CO + HVMK + OH	j_HPALD*0.4*0.5	Sander et al. (2018), Jenkin et al. (2015), Peeters et al. (2014)
J45026d	TrGJC	LZCOCDC23DBC ₂ OOH + hν → OH + CO + CO + CH ₃ COCH ₂ OH + HO ₂	j_HPALD*0.4*0.5	Sander et al. (2018), Jenkin et al. (2015), Peeters et al. (2014)
J45027	TrGJC	LZCO ₃ HC23DBC ₂ OD + hν → .62 EZCH3CO ₂ CHCHO + .38 EZCHOCCH3CHO ₂ + OH + CO ₂	j_HPALD	Sander et al. (2018)
J45028a	TrGJC	C10OHC20OHC4OD + hν → CH ₃ COCH ₂ O ₂ H + OH + 2 CO + HO ₂	2.77*jx(IP_HOCH2CHO)	Sander et al. (2018)
J45028b	TrGJC	C10OHC20OHC4OD + hν → .5 CH ₃ COCH ₂ O ₂ H + .5 HOCHCHO + .5 CO ₂ H ₃ CHO + .5 HCHO + 1.5 OH	2.*jx(IP_CH300H)	Sander et al. (2018)
J45029	TrGC	DB1OOH + hν → DB1O ₂ + OH	jx(IP_CH300H)	Sander et al. (2018)
J45030	TrGC	DB2OOH + hν → .48 CH ₃ COCH ₂ OH + .52 HOCH ₂ CHO + .52 MGLYOX + .48 GLYOX + HO ₂ + OH	jx(ip_CH300H)	Sander et al. (2018)
J45031a	TrGJC	C10DC20OHC4OD + hν → MGLYOX + HOCHCHO + OH	jx(ip_CH300H)	Sander et al. (2018)
J45031b	TrGJC	C10DC20OHC4OD + hν → CO ₂ H ₃ CHO + CO + HO ₂ + OH	2.*2.77*jx(IP_HOCH2CHO)	Sander et al. (2018)
J45032	TrGJC	C4MDIAL + hν → .5 CH ₃ COCHCO + .5 HCOCCH ₃ CO + CO + HO ₂ + OH	jx(ip_N02)*0.1*0.5	Sander et al. (2018)*
J45033	TrGCN	DB1NO ₃ + hν → DB1O ₂ + NO ₂	j_IC3H7N03	Sander et al. (2018)
J45034	TrGJTerC	CHOC ₃ COOOH + hν → CHOC ₃ COO ₂ + CO ₂ + OH	jx(ip_CH300H)+jx(ip_HOCH2CHO) +j_ACETOL	Rickard and Pascoe (2009)
J45200a	TrGJTerC	LMBOABOOH + hν → HOCH ₂ CHO + CH ₃ COCH ₃ + HO ₂ + OH	jx(ip_CH300H)*.67	Rickard and Pascoe (2009), Sander et al. (2018)
J45200b	TrGJTerC	LMBOABOOH + hν → IBUTALOH + HCHO + HO ₂ + OH	jx(ip_CH300H)*.33	Rickard and Pascoe (2009), Sander et al. (2018)
J45201	TrGJTerC	MBOACO + hν → HCHO + HO ₂ + IPRHOCO ₃	j_ACETOL	Rickard and Pascoe (2009)
J45202	TrGJTerC	MBOCOCO + hν → CO + HO ₂ + IPRHOCO ₃	jx(ip_MGLYOX)	Rickard and Pascoe (2009)
J45203a	TrGJTerCN	LNMBOABOOH + hν → NO ₃ CH ₂ CHO + CH ₃ COCH ₃ + HO ₂ + OH	jx(ip_CH300H)*.65	Rickard and Pascoe (2009), Sander et al. (2018)

85

Table 2: Photolysis reactions (... continued)

#	labels	reaction	rate coefficient	reference
J45203b	TrGJTerCN	LNMBOABOOH + hν → IBUTALOH + HCHO + NO ₂ + OH	jx(ip_CH300H)*.35	Rickard and Pascoe (2009), Sander et al. (2018)
J45204	TrGJTerCN	NC4OHC3OH + hν → IBUTALOH + CO ₂ + NO ₂ + OH	jx(ip_CH300H)	Rickard and Pascoe (2009)
J45400	TrGJAroC	C54CO + hν → HO ₂ + CO + CO + CO + CH ₃ C(O)	jx(ip_MGLYOX)+2.15*jx(ip_MGLYOX)*2	Rickard and Pascoe (2009)
J45401	TrGJAroC	C5134CO2OH + hν → CH ₃ COCOCOHO + HO ₂ + CO + HO ₂	jx(ip_HOCH2CHO)+2.15*jx(ip_MGLYOX)	Rickard and Pascoe (2009)
J45402	TrGJAroC	C5DIALOOH + hν → MALDIAL + CO + HO ₂ + OH	jx(ip_CH300H)+jx(ip_MACR)	Rickard and Pascoe (2009)*
J45406	TrGJAroC	C5CO14OH + hν → CH ₃ C(O) + HCOCO ₂ H + HO ₂ + CO	jx(ip_MVK)	Rickard and Pascoe (2009)
J45407	TrGJAroC	C5DICARB + hν → .6 C5CO14O2 + .6 HO ₂ + .4 TLFUONE	jx(ip_NO2)*0.2	Rickard and Pascoe (2009)*
J45408	TrGJAroC	MC3ODBCO2H + hν → CH ₃ COCO ₂ H + HO ₂ + CO + HO ₂ + CO	jx(ip_MACR)	Rickard and Pascoe (2009)
J45409	TrGJAroC	ACCOMMECHO + hν → MECOACETO2 + HO ₂ + CO	jx(ip_HOCH2CHO)	Rickard and Pascoe (2009)
J45410	TrGJAroC	MMALNHYOOH + hν → CO2H3CO3 + CO ₂ + OH	jx(ip_CH300H)	Rickard and Pascoe (2009)*
J45411	TrGJAroC	C5DICAROOH + hν → MGLYOX + GLYOX + HO ₂ + OH	jx(ip_CH300H)+jx(ip_HOCH2CHO)+j_ACETOL	Rickard and Pascoe (2009)*
J45412	TrGJAroCN	NTLFUOOH + hν → ACCOMECHO + NO ₂ + OH	jx(ip_CH300H)	Rickard and Pascoe (2009)*
J45414	TrGJAroC	C5CO14OOH + hν → .83 MALANHY + .83 CH ₃ + .17 MGLYOX + .17 HO ₂ + .17 CO + .17 CO ₂ + OH	jx(ip_CH300H)	Rickard and Pascoe (2009)*
J45415	TrGJAroC	TLFUOOH + hν → ACCOMECHO + HO ₂ + OH	jx(ip_CH300H)	Rickard and Pascoe (2009)*
J45417	TrGJAroC	ACCOMECO3H + hν → MECOACETO2 + CO ₂ + OH	jx(ip_CH300H)	Rickard and Pascoe (2009)
J45418	TrGJAroC	C5DIALCO + hν → MALDIALCO3 + CO + HO ₂	jx(ip_MGLYOX)+jx(ip_MACR)	Rickard and Pascoe (2009)
J46200	TrGJTerCN	C614NO3 + hν → CO23C4CHO + HCHO + HO ₂ + NO ₂	2.15*jx(ip_MGLYOX)	Rickard and Pascoe (2009)
J46201	TrGJTerC	C614OOH + hν → CO23C4CHO + HCHO + HO ₂ + OH	jx(ip_CH300H)+2.15*jx(ip_MGLYOX)	Rickard and Pascoe (2009)
J46202	TrGJTerC	CO235C5CHO + hν → CO23C4CO3 + CO + HO ₂	jx(ip_MGLYOX)	Rickard and Pascoe (2009)
J46203	TrGJTerC	CO235C6OOH + hν → CO23C4CO3 + HCHO + OH	jx(ip_CH300H)+2.15*jx(ip_MGLYOX)	Rickard and Pascoe (2009)
J46400	TrGJAroC	PHENOOH + hν → .71 MALDALCO2H + .71 GLYOX + .29 PBZQONE + HO ₂ + OH	jx(ip_CH300H)	Rickard and Pascoe (2009)*
J46401	TrGJAroC	C6CO4DB + hν → C4CO2DBC03 + HO ₂ + CO	jx(ip_MGLYOX)*2	Rickard and Pascoe (2009)

86

Table 2: Photolysis reactions (... continued)

#	labels	reaction	rate coefficient	reference
J46402	TrGJAroC	C5CO2DCO3H + hν → CH ₃ C(O) + HCOCOCHO + CO ₂ + OH	jx(ip_CH300H)+jx(ip_MGLYOX)	Rickard and Pascoe (2009)
J46403	TrGJAroCN	NDNPHENOOH + hν → NC4DCO2H + HNO ₃ + CO + CO + NO ₂ + OH	jx(ip_CH300H)	Rickard and Pascoe (2009)*
J46404	TrGJAroCN	BZBIPERNO3 + hν → GLYOX + HO ₂ + .5 BZFUONE + .5 BZFUONE + NO ₂	j_IC3H7ND3	Rickard and Pascoe (2009)*
J46405	TrGJAroCN	HOC6H4NO2 + hν → HONO + CPDKETENE	jx(ip_HOC6H4NO2)	Chen et al. (2011)*
J46406	TrGJAroC	CPDKETENE + hν → CO ₂ + CO + 2 HO ₂ + MALDIAL	j_KETENE	see note*
J46407	TrGJAroC	C5COOHCO3H + hν → HOCOC4DIAL + HO ₂ + CO + CO ₂ + OH	jx(ip_CH300H)	Rickard and Pascoe (2009)
J46408	TrGJAroC	BZEPOXMUC + hν → .5 C5DIALO2 + 1.5 HO ₂ + 1.5 CO + .5 MALDIAL	4.E3*jx(ip_MVK)*0.1	Rickard and Pascoe (2009)
J46409	TrGJAroCN	NPHEN1OOH + hν → NPHEN1O + OH	jx(ip_CH300H)	Rickard and Pascoe (2009)
J46410	TrGJAroC	BZEMUCCO + hν → HCOCOHCO3 + C3DIALO2	jx(ip_HOCH2CHO)*2+j_ACETOL	Rickard and Pascoe (2009)
J46411	TrGJAroC	BZEMUCCO2H + hν → C5DIALO2 + CO ₂ + HO ₂	jx(ip_MACR)	Rickard and Pascoe (2009)
J46412	TrGJAroCN	NNCATECOOH + hν → NC4DCO2H + HCOCO ₂ H + NO ₂ + OH	jx(ip_CH300H)	Rickard and Pascoe (2009)*
J46413	TrGJAroC	C615CO2OOH + hν → C5DICARB + CO + HO ₂ + OH	jx(ip_MVK)+jx(ip_CH300H)	Rickard and Pascoe (2009)
J46414	TrGJAroCN	NPHENOOH + hν → MALDALCO2H + GLYOX + OH + NO ₂	j_IC3H7ND3 + jx(ip_CH300H)	Rickard and Pascoe (2009)
J46415	TrGJAroCN	NCATECOOH + hν → NC4DCO2H + HCOCO ₂ H + HO ₂ + OH	jx(ip_CH300H)	Rickard and Pascoe (2009)*
J46416	TrGJAroC	PBZQOOH + hν → C5CO2OHC03 + OH	jx(ip_CH300H)	Rickard and Pascoe (2009)*
J46417	TrGJAroC	BZOBIPEROH + hν → MALDIALCO3 + GLYOX + HO ₂	j_ACETOL	Rickard and Pascoe (2009)
J46418	TrGJAroC	BZBIPEROOH + hν → GLYOX + HO ₂ + .5 BZFUONE + .5 BZFUONE + OH	jx(ip_CH300H)	Rickard and Pascoe (2009)*
J46419	TrGJAroCN	NBZQOOH + hν → C6CO4DB + NO ₂ + OH	jx(ip_CH300H)	Rickard and Pascoe (2009)*
J46420	TrGJAroC	CATEC1OOH + hν → CATEC1O + OH	jx(ip_CH300H)	Rickard and Pascoe (2009)
J46421	TrGJAroC	C6125CO + hν → C5CO14O2 + CO + HO ₂	jx(ip_MGLYOX)+jx(ip_MVK)	Rickard and Pascoe (2009)
J46422	TrGJAroCN	DNPHEOOH + hν → NC4DCO2H + HCOCO ₂ H + NO ₂ + OH	jx(ip_CH300H)	Rickard and Pascoe (2009)*
J46423	TrGJAroC	BZEMUCCO3H + hν → C5DIALO2 + CO ₂ + OH	jx(ip_CH300H)+jx(ip_MACR)	Rickard and Pascoe (2009)
J46424	TrGJAroC	C6H5OOH + hν → C6H5O + OH	jx(ip_CH300H)	Rickard and Pascoe (2009)
J46425	TrGJAroC	BZEMUCOOH + hν → .5 EPXC4DIAL + .5 GLYOX + .5 HO ₂ + .5 C3DIALO2 + .5 C32OH13CO + OH	jx(ip_CH300H)+jx(ip_HOCH2CHO)*2	Rickard and Pascoe (2009)*

87

Table 2: Photolysis reactions (... continued)

#	labels	reaction	rate coefficient	reference
J46427	TrGJAroCN	BZEMUCNO3 + hν → EPXC4DIAL + NO2 + GLYOX + HO2	2.77*jx(ip_HOCH2CHO)	Rickard and Pascoe (2009)
J46428	TrGJAroCN	DNPHEN + hν → HONO + NCPDKETENE	jx(ip_HOC6H4NO2)	Sander et al. (2018)
J46429	TrGJAroCN	NCPDKETENE + hν → CO2 + CO + 2 HO2 + NC4DCO2H	j_KETENE	see note*
J47200	TrGJTerC	CO235C6CHO + hν → CHOC3COCO3 + CH3C(O)	2.15*jx(ip_MGLYOX)	Rickard and Pascoe (2009)
J47201	TrGJTerC	C235C6CO3H + hν → CO235C6O2 + CO2 + OH	jx(ip_CH300H)+2.15*jx(ip_MGLYOX)	Rickard and Pascoe (2009)
J47202	TrGJTerC	C716OOH + hν → CO13C4CHO + CH3C(O) + OH	jx(ip_CH300H)+jx(ip_HOCH2CHO)	Rickard and Pascoe (2009)
J47203	TrGJTerC	C721OOH + hν → C72O2 + OH	jx(ip_CH300H)	Rickard and Pascoe (2009)
J47204	TrGJTerC	C722OOH + hν → CH3COCH3 + C44O2 + OH	jx(ip_CH300H)	Rickard and Pascoe (2009)
J47400	TrGJAroC	TLEPOXMUC + hν → .5 C615CO2O2 + HO2 + CO + .5 EPXC4DIAL + .5 CH3C(O)	4.E3*jx(ip_MVK)*0.1	Rickard and Pascoe (2009)
J47401	TrGJAroC	C6H5CH2OOH + hν → BENZAL + HO2 + OH	jx(ip_CH300H)	Rickard and Pascoe (2009)*
J47402	TrGJAroCN	C6H5CH2NO3 + hν → BENZAL + HO2 + NO2	0.59*j_IC3H7NO3	Rickard and Pascoe (2009)*
J47403	TrGJAroC	BENZAL + hν → HO2 + CO + C6H5O2	jx(ip_BENZAL)	Wallington et al. (2018)
J47404	TrGJAroC	TLBIPEROOH + hν → .6 GLYOX + .4 MGLYOX + HO2 + .2 C4MDIAL + .2 C5DICARB + .2 TLFUONE + .2 BZFUONE + .2 MALDIAL + OH	jx(ip_CH300H)	Rickard and Pascoe (2009)*
J47405	TrGJAroCN	TLBIPERNO3 + hν → .6 GLYOX + .4 MGLYOX + HO2 + .2 C4MDIAL + .2 C5DICARB + .2 TLFUONE + .2 BZFUONE + .2 MALDIAL + NO2	j_IC3H7NO3	Rickard and Pascoe (2009)*
J47406	TrGJAroC	TLOBIPEROH + hν → C5CO14O2 + GLYOX + HO2	j_ACETOL	Rickard and Pascoe (2009)
J47407	TrGJAroC	CRESOOH + hν → .68 C5CO14OH + .68 GLYOX + HO2 + .32 PTLQONE + OH	jx(ip_CH300H)	Rickard and Pascoe (2009)*
J47408a	TrGJAroCN	NCRESOOH + hν → .68 C5CO14OH + .68 GLYOX + HO2 + .32 PTLQONE + OH + NO2	j_IC3H7NO3	Rickard and Pascoe (2009)*
J47408b	TrGJAroCN	NCRESOOH + hν → C5CO14OH + GLYOX + NO2 + OH	jx(ip_CH300H)	Rickard and Pascoe (2009)*
J47409	TrGJAroCN	TOL1OHNO2 + hν → HONO + MCPDKETENE	jx(ip_HOPh3Me2NO2)	see note*
J47410	TrGJAroC	TLEMUCCO2H + hν → C615CO2O2 + CO2 + HO2	jx(ip_MACR)	Rickard and Pascoe (2009)
J47411	TrGJAroCN	TLEMUCCO3H + hν → C615CO2O2 + CO2 + OH	jx(ip_CH300H)+jx(ip_MACR)	Rickard and Pascoe (2009)
J47412	TrGJAroC	TLEMUCOOH + hν → .5 C3DIALO2 + .5 CO2H3CHO + .5 EPXC4DIAL + .5 MGLYOX + .5 HO2 + OH	jx(ip_CH300H)+2.77*jx(ip_HOCH2CHO)+j_ACETOL	Rickard and Pascoe (2009)*
J47413	TrGJAroCN	TLEMUCNO3 + hν → EPXC4DIAL + NO2 + CH3C(O) + CO + HO2	2.77*jx(ip_HOCH2CHO)+j_ACETOL	Rickard and Pascoe (2009)

88

Table 2: Photolysis reactions (... continued)

#	labels	reaction	rate coefficient	reference
J47414	TrGJAroC	TLEMUCCO + hν → CH3C(O) + EPXC4DIAL + CO + HO2	2.77*jx(ip_HOCH2CHO)+2.15*jx(ip_MGLYOX)	Rickard and Pascoe (2009)
J47415	TrGJAroC	C6H5CO3H + hν → C6H5O2 + CO2 + OH	jx(ip_CH300H)	Rickard and Pascoe (2009)
J47416	TrGJAroC	OXYL1OOH + hν → TOL1O + OH	jx(ip_CH300H)	Rickard and Pascoe (2009)
J47417	TrGJAroCN	MNCATECH + hν → HONO + MCPDKETENE	jx(ip_HOPh3Me2NO2)	see note*
J47418	TrGJAroC	MCPDKETENE + hν → CO2 + CO + 2 HO2 + C4MDIAL	j_KETENE	see note*
J47419	TrGJAroCN	DNCRES + hν → HONO + MNCPDKETENE	jx(ip_HOPh3Me2NO2)	see note*
J47420	TrGJAroCN	MNCPDKETENE + hν → CO2 + CO + 2 HO2 + NC4MDCO2HN	j_KETENE	see note*
J47421	TrGJAroC	MCATEC1OOH + hν → MCATEC1O + OH	jx(ip_CH300H)	Rickard and Pascoe (2009)
J47422	TrGJAroCN	NPTLQOOH + hν → C7CO4DB + NO2 + OH	jx(ip_CH300H)	Rickard and Pascoe (2009)*
J47423	TrGJAroC	PTLQOOH + hν → C6CO2OHC O3 + OH	jx(ip_CH300H)	Rickard and Pascoe (2009)*
J47424	TrGJAroCN	NCRES1OOH + hν → NCRES1O + OH	jx(ip_CH300H)	Rickard and Pascoe (2009)
J47425	TrGJAroCN	MNNCATCOOH + hν → NC4MDCO2HN + HCOCO2H + NO2 + OH	jx(ip_CH300H)	Rickard and Pascoe (2009)*
J47426	TrGJAroCN	MNCATECOOH + hν → NC4MDCO2HN + HCOCO2H + HO2 + OH	jx(ip_CH300H)	Rickard and Pascoe (2009)*
J47427	TrGJAroC	C7CO4DB + hν → C5CO2DBC O3 + HO2 + CO	jx(ip_MGLYOX)*2	Rickard and Pascoe (2009)
J47428	TrGJAroCN	NDNCRESOOH + hν → NC4MDCO2HN + HNO3 + CO + CO + NO2 + OH	jx(ip_CH300H)	Rickard and Pascoe (2009)*
J47429	TrGJAroCN	DNCRESOOH + hν → NC4MDCO2HN + HCOCO2H + NO2 + OH	jx(ip_CH300H)	Rickard and Pascoe (2009)*
J47430	TrGJAroC	C6COOHCO3H + hν → C513CO2OH + HO2 + CO + CO2 + OH	jx(ip_CH300H)	Rickard and Pascoe (2009)
J48200	TrGJTerC	C86OOH + hν → C511O2 + CH3COCH3 + OH	jx(ip_CH300H)+ jx(ip_HOCH2CHO)	Rickard and Pascoe (2009)
J48201	TrGJTerC	C812OOH + hν → C813O2 + OH	jx(ip_CH300H)	Rickard and Pascoe (2009)
J48202	TrGJTerC	C813OOH + hν → CH3COCH3 + C512O2 + OH	jx(ip_CH300H)+jx(ip_MGLYOX)	Rickard and Pascoe (2009)
J48203	TrGJTerC	C721CHO + hν → C721O2 + CO + HO2	jx(ip_HOCH2CHO)	Rickard and Pascoe (2009)
J48204	TrGJTerC	C721CO3H + hν → C721O2 + CO2 + OH	jx(ip_CH300H)	Rickard and Pascoe (2009)
J48205	TrGJTerC	C8BCOOH + hν → C89O2 + OH	jx(ip_CH300H)	Rickard and Pascoe (2009)
J48206	TrGJTerC	C89OOH + hν → C810O2 + OH	jx(ip_CH300H)+jx(ip_HOCH2CHO)	Rickard and Pascoe (2009)
J48207	TrGJTerCN	C89NO3 + hν → C810O2 + NO2	jx(ip_CH300H)+jx(ip_HOCH2CHO)	Rickard and Pascoe (2009)
J48208	TrGJTerC	C810OOH + hν → CH3COCH3 + C514O2 + OH	jx(ip_CH300H)+jx(ip_HOCH2CHO)	Rickard and Pascoe (2009)

89

Table 2: Photolysis reactions (... continued)

#	labels	reaction	rate coefficient	reference
J48209	TrGJTerCN	C810NO3 + hν → CH ₃ COCH ₃ + C ₅ H ₄ O ₂ + NO ₂	2.84*j_IC3H7N03+jx(ip_HOCH2CHO)	Rickard and Pascoe (2009)
J48210	TrGJTerCN	C8BNCNO3 + hν → C ₈ H ₂ O ₂ + NO ₂	j_IC3H7N03	Rickard and Pascoe (2009)
J48211	TrGJTerC	C85OOH + hν → C ₈ H ₂ O ₂ + OH	jx(ip_CH300H)+j_ACETOL	Rickard and Pascoe (2009)
J48400	TrGJAroC	STYRENOOH + hν → HO ₂ + HCHO + BENZAL + OH	jx(ip_CH300H)	Rickard and Pascoe (2009)*
J49200	TrGJTerC	C96OOH + hν → C ₉ H ₂ O ₂ + OH	jx(ip_CH300H)+j_ACETOL	Rickard and Pascoe (2009)
J49201	TrGJTerC	C97OOH + hν → C ₉ H ₂ O ₂ + OH	jx(ip_CH300H)+j_ACETOL	Rickard and Pascoe (2009)
J49202	TrGJTerC	C98OOH + hν → C ₆ H ₄ O ₂ + CH ₃ COCH ₃ + OH	(jx(ip_CH300H)+2.15*jx(ip_MGLYOX))	Rickard and Pascoe (2009)
J49203a	TrGJTerC	NORPINAL + hν → C ₈ H ₂ O ₂ + CO + HO ₂	jx(ip_PINAL2HCO)	Rickard and Pascoe (2009), Sander et al. (2018)
J49203b	TrGJTerC	NORPINAL + hν → NORPINENOL	jx(ip_PINAL2ENOL)	Sander et al. (2018), Andrews et al. (2012)
J49204	TrGJTerC	C85CO3H + hν → C ₈ H ₂ O ₂ + CO ₂ + OH	jx(ip_CH300H)+j_ACETOL	Rickard and Pascoe (2009)
J49205	TrGJTerC	C89CO2H + hν → .8 C ₈ H ₁₁ CO ₃ + .2 C ₈ H ₉ O ₂ + .2 CO ₂ + HO ₂	jx(ip_HOCH2CHO)	Rickard and Pascoe (2009)
J49206	TrGJTerC	C89CO3H + hν → .8 C ₈ H ₁₁ CO ₃ + .2 C ₈ H ₉ O ₂ + .2 CO ₂ + OH	jx(ip_CH300H)+jx(ip_HOCH2CHO)	Rickard and Pascoe (2009)
J49207	TrGJTerC	C811CO3H + hν → C ₈ H ₁₁ O ₂ + CO ₂ + OH	jx(ip_CH300H)	Rickard and Pascoe (2009)
J49208	TrGJTerC	NOPINDOOH + hν → C ₈ H ₉ CO ₃ + OH	jx(ip_CH300H)	Rickard and Pascoe (2009)
J40200	TrGJTerC	LAPINABOOH + hν → PINAL + HO ₂ + OH	jx(ip_CH300H)	Rickard and Pascoe (2009)
J40201	TrGJTerC	MENTHENONE + hν → RO6R1O2 + OH	jx(ip_CH300H)	Vereecken et al. (2007)
J40202	TrGJTerC	2OHMENTHENONE + hν → 10 LCARBON + OH	jx(ip_CH300H)	Vereecken et al. (2007)
J40203a	TrGJTerC	PINAL + hν → C ₉ H ₂ O ₂ + CO + HO ₂	jx(ip_PINAL2HCO)	Rickard and Pascoe (2009)
J40203b	TrGJTerC	PINAL + hν → PINEOL	jx(ip_PINAL2ENOL)	Sander et al. (2018), Andrews et al. (2012)*
J40204	TrGJTerC	PERPINONIC + hν → C ₉ H ₂ O ₂ + CO ₂ + OH	jx(ip_CH300H)+j_ACETOL	Rickard and Pascoe (2009)
J40205	TrGJTerC	PINALOOH + hν → C ₁₀ H ₂ O ₂ + OH	jx(ip_CH300H)+jx(ip_HOCH2CHO)	Rickard and Pascoe (2009)
J40206	TrGJTerCN	PINALNO3 + hν → C ₁₀ H ₂ O ₂ + NO ₂	j_IC3H7N03+jx(ip_HOCH2CHO)	Rickard and Pascoe (2009)
J40207	TrGJTerC	C106OOH + hν → C ₇ H ₁₆ O ₂ + CH ₃ COCH ₃ + OH	jx(ip_CH300H)+jx(ip_HOCH2CHO)	Rickard and Pascoe (2009)
J40208	TrGJTerCN	C106NO3 + hν → C ₇ H ₁₆ O ₂ + CH ₃ COCH ₃ + NO ₂	j_IC3H7N03+ jx(ip_HOCH2CHO)	Rickard and Pascoe (2009)
J40209	TrGJTerC	C109OOH + hν → C ₈ H ₉ CO ₃ + HCHO + OH	jx(ip_CH300H)+jx(ip_HOCH2CHO)	Rickard and Pascoe (2009)
J40210	TrGJTerC	C109CO + hν → C ₈ H ₉ CO ₃ + CO + HO ₂	jx(ip_MGLYOX)+jx(ip_HOCH2CHO)	Rickard and Pascoe (2009)
J40211	TrGJTerCN	LNAPINABOOH + hν → PINAL + NO ₂ + OH	jx(ip_CH300H)	Rickard and Pascoe (2009)
J40212	TrGJTerC	BPINAOOH + hν → NOPINONE + HCHO + HO ₂ + OH	jx(ip_CH300H)	Rickard and Pascoe (2009)
J40213	TrGJTerCN	LNPINABOOH + hν → NOPINONE + HCHO + NO ₂ + OH	jx(ip_CH300H)	Rickard and Pascoe (2009)

90

Table 2: Photolysis reactions (... continued)

#	labels	reaction	rate coefficient	reference
J40214	TrGJTerCN	RO06R1NO3 + hν → RO06R3O2 + CH ₃ COCH ₃ + NO ₂	2.84*j_IC3H7N03+jx(ip_CH300H)	Sander et al. (2018)
J40215	TrGJTerCN	RO6R1NO3 + hν → 9 LCARBON + HCHO + HO ₂ + NO ₂	2.84*j_IC3H7N03	Sander et al. (2018)

PH (aqueous)

General notes

j-values are calculated with an external module (e.g., JVAL) and then supplied to the MECCA chemistry.

Values that originate from the Master Chemical Mechanism (MCM) by Rickard and Pascoe (2009) are translated according in the following way:

j(11) → jx(ip_COH2)
j(12) → jx(ip_CHOH)
j(15) → jx(ip_HOCH2CHO)
j(18) → jx(ip_MACR)
j(22) → jx(ip_ACETOL)
j(23)+j(24) → jx(ip_MVK)
j(31)+j(32)+j(33) → jx(ip_GLYOX)
j(34) → jx(ip_MGLYOX)
j(41) → jx(ip_CH300H)
j(53) → j(isopropyl nitrate)
j(54) → j(isopropyl nitrate)
j(55) → j(isopropyl nitrate)
j(56)+j(57) → jx(ip_NOA)

Specific notes

J41006: product distribution as for HNO₄

J42004: Quantum yields from Burkholder et al. (2015).

J42005a: Quantum yields from Burkholder et al. (2015).

J42005b: Quantum yields from Burkholder et al. (2015).

J42005c: Quantum yields from Burkholder et al. (2015).

J42007: It is assumed that J(PHAN) is the same as J(PAN).

J42017: Enhancement of *j* according to Müller et al. (2014).

J42020: It is assumed that j(NO₃CH₂CHO) is the same as j(PAN).

J42021: In analogy to what is assumed for CH₃O₂NO₂ photolysis as in (Sander et al., 2014).

J43002: Following von Kuhlmann et al. (2003), we use j(CH₃COCH₂OH) = 0.11*jx(ip_CHOH). As an additional factor, the quantum yield of 0.65 is taken from Orlando et al. (1999a).

J43006: Following von Kuhlmann et al. (2003), we use J(C₃H₇ONO₂) = 3.7*jx(ip_PAN).

J43018: One third of the acetaldehyde channel is considered to be CH₂CHOH according to Hjorth (2002) EUPHORE Report.

J43024: Assuming J(C₃H₇ONO₂) = 0.59 × J(C₃H₇ONO₂), consistent with the photolysis rate coefficients used in the MCM (Rickard and Pascoe, 2009).

J43025a: Photolysis frequencies very similar to the ones of CH₃CHO.

J43025b: Photolysis frequencies very similar to the ones of CH₃CHO.

J43400: KDEC C3DIALO → GLYOX + CO + HO₂

J44004: It is assumed that J(BIACET) is 2.15 times larger than J(MGLYOX), consistent with the photolysis rate coefficients used in the MCM (Rickard and Pascoe, 2009).

J44005a: It is assumed that J(LC4H9NO₃) is the same as J(C₃H₇ONO₂).

J44005b: It is assumed that J(LC4H9NO₃) is the same as J(C₃H₇ONO₂).

J44006: It is assumed that J(MPAN) is the same as J(PAN).

J44009: It is assumed that J(MACROOH) is 2.77 times larger than J(HOCH₂CHO), consistent with the photolysis rate coefficients used in the MCM (Rickard and Pascoe, 2009).

J44010: It is assumed that J(MACROH) is 2.77 times larger than J(HOCH₂CHO), consistent with the photolysis rate coefficients used in the MCM (Rickard and Pascoe, 2009).

J44015: It is assumed that J(BIACETOH) is 2.15 times larger than J(MGLYOX), consistent with the photolysis rate coefficients used in the MCM (Rickard and Pascoe, 2009).

J44017a: CO-channel yielding CH₃COCH which upon reaction with O₂ produces an excited Criegee Intermediate assumed to be similar to MGLOA in MCM.

91

MGLOOA is produced also in other reactions and is substituted by its decomposition products. Furthermore, the stabilized Criegee Intermediate is assumed to solely react with water.

J44025: J values only for the secondary nitrate.

J44026: Like for LMEKNO3 photolysis

J44027: 2.84*J_IC3H7NO3 like for other tertiary alkyl nitrates (see J4505). Enhancement of J according to Müller et al. (2014).

J44037b: Channel which produces just vinyl alcohol and not a larger enol via keto-enol photo- tautomerization.

J44043: The resulting vinyl peroxy radical is assumed to mostly form with HO₂ a labile hydroperoxide (see ketene formation). The products are further simplified.

J44044: 1,5-H-shift for the resulting vinyl peroxy radical assumed to be dominant.

J44046a: Simplified oxidation.

J44400b: KDEC MALDIALO → GLYOX + GLYOX + HO₂

J44401: KDEC BZFUO → CO14O3CHO + HO₂

J44403: KDEC NBZFUO → 0.5 CO14O3CHO + 0.5 NO₂ + 0.5 NBZFUONE + 0.5 HO₂

J44404b: KDEC MALDIALCO₂ → 0.6 MALANHY + HO₂ + 0.4 GLYOX + 0.4 CO

J44407: KDEC MALANHYO → HCOCOHO₃

J44414: KDEC MECOACETO → CH₃CO₃ + HCHO

J45003: It is assumed that J(LISOPACNO₃) = 0.59 × J(iC₃H₇ONO₂), consistent with the photolysis rate coefficients used in the MCM (Rickard and Pascoe, 2009).

J45005: It is assumed that J(ISOPBNO₃) = 2.84 × J(iC₃H₇ONO₂), consistent with the photolysis rate coefficients used in the MCM (Rickard and Pascoe, 2009).

J45007: It is assumed that J(ISOPDNO₃) is the same as J(iC₃H₇ONO₂).

J45009: 0.59*J_IC3H7NO3 like for other primary alkyl nitrates (see J4503). Enhancement of J according to Müller et al. (2014).

J45015: Consistent with the MCM (Rickard and Pascoe, 2009), we assume that J(HCOC5) is half as large as J(MVK). With exception of HOCH₂CO the products of MACO₂ decomposition without CO₂.

J45032: approximation with 4-oxo-pentenal photolysis combining results of Thner et al(2004) and Xiang et al(2007)

J45402: KDEC C5DIALO → MALDIAL + CO + HO₂

J45407: KDEC TLFUONE → 0.6 C5CO14O₂ + 0.6 HO₂ + 0.4 TLFUONE

J45410: KDEC MMALANHYO → CO₂H₃CO₃

J45411: KDEC C5DICARBO → MGLYOX + GLYOX + HO₂

J45412: KDEC NTLFUO → ACCOMECHO + NO₂

J45414: KDEC C5CO14CO₂ → 0.83 MALANHY + 0.83 CH₃ + .17 MGLYOX + .17 HO₂ + .17 CO + .17 CO₂

J45415: KDEC TLFUO → ACCOMECHO + HO₂

J46400: KDEC PHENO → 0.71 MALDALCO₂H + 0.71 GLYOX + 0.29 PBZQONE + HO₂

J46403: KDEC NDNPHENO → NC4DCO₂H + HNO₃ + CO + CO + NO₂

J46404: KDEC BZBIPERO → GLYOX + HO₂ + 0.5 BZFUONE + 0.5 BZFUONE

J46405: new channel created for nitrophenol decomposition

J46406: new channel created for nitrophenol decomposition

J46412: KDEC NNCATECO → NC4DCO₂H + HCOCO₂H + NO₂

J46415: KDEC NCATECO → NC4DCO₂H + HCOCO₂H + HO₂

J46416: KDEC PBZQO → C5CO₂OHC₃O

J46418: KDEC BZBIPERO → GLYOX + HO₂ + 0.5 BZFUONE + 0.5 BZFUONE

J46419: KDEC NBZQO → C6CO₄DB + NO₂

J46422: KDEC DNPHENO → NC4DCO₂H + HCOCO₂H + NO₂

J46425: KDEC BZEMUCO → 0.5 EPXC₄DIAL + .5 GLYOX + .5 HO₂ + .5 C₃DIALO₂ + .5 C₃OH₁₃CO

J46429: new channel

J47401: KROPRIM*O₂ fast reaction C₆H₅CH₂O = BENZAL + HO₂

J47402: KROPRIM*O₂ fast reaction C₆H₅CH₂O = BENZAL + HO₂

J47404: KDEC TLBIPERO → 0.6 GLYOX + 0.4 MGLYOX + HO₂ + 0.2 C₄MDIAL + 0.2 C₅DICARB + 0.2 TLFUONE + 0.2 BZFUONE + 0.2 MALDIAL

J47405: KDEC TLBIPERO → 0.6 GLYOX + 0.4 MGLYOX + HO₂ + 0.2 C₄MDIAL + 0.2 C₅DICARB + 0.2 TLFUONE + 0.2 BZFUONE + 0.2 MALDIAL

J47407: KDEC CRESO → 0.68 C₅CO₁₄OH + 0.68 GLYOX + HO₂ + 0.32 PTLQONE

J47408a: KDEC CRESO → 0.68 C₅CO₁₄OH + 0.68 GLYOX + HO₂ + 0.32 PTLQONE

J47408b: KDEC NCRESO → C₅CO₁₄OH + GLYOX + NO₂

J47409: Using J for 3-methyl-2-nitrophenol.

J47412: KDEC TLEMUCO → 0.5 C₃DIALO₂ + 0.5 CO₂H₃CHO + 0.5 EPXC₄DIAL + 0.5 MGLYOX + 0.5 HO₂

J47417: Using J for 3-methyl-2-nitrophenol.

J47418: new channel

J47419: Using J for 3-methyl-2-nitrophenol.

J47420: new channel

J47422: KDEC NPTLQO → C₇CO₄DB + NO₂

J47423: KDEC PTLQO → C₆CO₂OHC₃O

J47425: KDEC MNNCATECO → NC4MDCO₂H + HCOCO₂H + NO₂

J47426: KDEC MNCATECO → NC4MDCO₂H + HCOCO₂H + HO₂

J47428: KDEC NDNCRESO → NC4MDCO₂H + HNO₃ + CO + CO + NO₂

J47429: KDEC DNCRESO → NC4MDCO₂H + HCOCO₂H + NO₂

J48400: KDEC STYRENO → HO₂ + HCHO + BENZAL

J40203b: Substituted vinyl alcohol in analogy to CH₃CHO photolysis.

Table 3: Reversible (Henry’s law) equilibria and irreversible (“heterogenous”) uptake

#	labels	reaction	rate coefficient	reference
---	--------	----------	------------------	-----------

General notes

The forward (`k_exf`) and backward (`k_exb`) rate coefficients are calculated in subroutine `mecca_aero_calc_k_ex` in the file `messy_mecca_aero.f90` using accommodation coefficients and Henry’s law constants from `chemprop` (see `chemprop.pdf`).

For uptake of X (X = N₂O₅, ClNO₃, or BrNO₃) and

subsequent reaction with H₂O, Cl⁻, and Br⁻ in H3201, H6300, H6301, H6302, H7300, H7301, H7302, H7601, and H7602, we define:

$$k_{\text{ext}}(X) = \frac{k_{\text{mt}}(X) \times \text{LWC}}{[\text{H}_2\text{O}] + 5 \times 10^2[\text{Cl}^-] + 3 \times 10^5[\text{Br}^-]}$$

Here, k_{mt} = mass transfer coefficient, and LWC = liquid water content of the aerosol. The total uptake rate of X is only determined by k_{mt} . The factors only affect

the branching between hydrolysis and the halide reactions. The factor 5×10^2 was chosen such that the chloride reaction dominates over hydrolysis at about $[\text{Cl}^-] > 0.1 \text{ M}$ (see Fig. 3 in Behnke et al. (1997)), i.e. when the ratio $[\text{H}_2\text{O}]/[\text{Cl}^-]$ is less than 5×10^2 . The ratio $5 \times 10^2/3 \times 10^5$ was chosen such that the reactions with chloride and bromide are roughly equal for sea water composition (Behnke et al., 1994). These ratios were measured for uptake of N₂O₅. Here, they are also used for ClNO₃ and BrNO₃.

Table 4: Heterogeneous reactions

#	labels	reaction	rate coefficient	reference
---	--------	----------	------------------	-----------

General notes

Heterogeneous reaction rates are calculated with an external module (e.g., MECCA_KHET) and then supplied to the MECCA chemistry (see www.messy-interface.org for details)

Table 5: Acid-base and other equilibria

#	labels	reaction	$K_0 [M^{m-n}]$	$-\Delta H/R[K]$	reference
---	--------	----------	-----------------	------------------	-----------

Specific notes

Table 6: Aqueous phase reactions

#	labels	reaction	$k_0 [M^{l-n}s^{-1}]$	$-E_a/R[K]$	reference
---	--------	----------	-----------------------	-------------	-----------

Specific notes

References

- Albaladejo, J., Jiménez, E., Notario, A., Cabañas, B., and Martínez, E.: CH₃O yield in the CH₃ + O₃ reaction using the LP/LIF technique at room temperature, *J. Phys. Chem. A*, 106, 2512–2519, doi:10.1021/jp012249o, 2002.
- Andrews, D. U., Heazlewood, B. R., Maccarone, A. T., Conroy, T., Payne, R. J., Jordan, M. J. T., and Kable, S. H.: Photo-tautomerization of acetaldehyde to vinyl alcohol: a potential route to tropospheric acids, *Science*, 337, 1203–1206, doi:10.1126/science.1220712, 2012.
- Aschmann, S. M., Nishino, N., Arey, J., and Atkinson, R.: Products of the OH radical-initiated reactions of furan, 2- and 3-methylfuran, and 2,3- and 2,5-dimethylfuran in the presence of NO, *J. Phys. Chem. A*, 118, 457–466, doi:10.1021/jp410345k, 2014.
- Atkinson, R.: Gas-phase tropospheric chemistry of volatile organic compounds: 1. Alkanes and alkenes, *J. Phys. Chem. Ref. Data*, 26, 215–290, doi:10.1063/1.556012, 1997.
- Atkinson, R.: Kinetics of the gas-phase reactions of OH radicals with alkanes and cycloalkanes, *Atmos. Chem. Phys.*, 3, 2233–2307, doi:10.5194/ACP-3-2233-2003, 2003.
- Atkinson, R. and Arey, J.: Atmospheric degradation of volatile organic compounds, *Chem. Rev.*, 103, 4605–4638, doi:10.1021/cr020642o, 2003.
- Atkinson, R., Baulch, D. L., Cox, R. A., Crowley, J. N., Hampson, R. F., Hynes, R. G., Jenkin, M. E., Rossi, M. J., Troe, J., and IUPAC Subcommittee: Evaluated kinetic and photochemical data for atmospheric chemistry: Volume II – gas phase reactions of organic species, *Atmos. Chem. Phys.*, 6, 3625–4055, doi:10.5194/ACP-6-3625-2006, 2006.
- Baeza-Romero, M. T., Glowacki, D. R., Blitz, M. A., Heard, D., Pilling, M. J., Rickard, A. R., and Seakins, P. W.: A combined experimental and theoretical study of the reaction between methylglyoxal and OH/OD radical: OH regeneration, *Phys. Chem. Chem. Phys.*, 9, 4114–4128, doi:10.1039/b702916k, 2007.
- Banic, C. M., Beauchamp, S. T., Tordon, R. J., Schroeder, W. H., Steffen, A., Anlauf, K. A., and Wong, H. K. T.: Vertical distribution of gaseous elemental mercury in Canada, *J. Geophys. Res.*, 108D, 4264, doi:10.1029/2002JD002116, 2003.
- Barnes, I., Becker, K. H., Fink, E. H., Reimer, A., Zabel, F., and Niki, H.: FTIR spectroscopic study of the gas-phase reaction of HO₂ with H₂CO, *Chem. Phys. Lett.*, 115, 1–8, doi:10.1016/0009-2614(85)80091-9, 1985.
- Barnes, I., Becker, K. H., and Zhu, T.: Near UV absorption-spectra and photolysis products of difunctional organic nitrates – possible importance as NO_x reservoirs, *J. Atmos. Chem.*, 17, 353–373, doi:10.1007/BF00696854, 1993.
- Bates, K. H., Crouse, J. D., St. Clair, J. M., Bennett, N. B., Nguyen, T. B., Seinfeld, J. H., Stoltz, B. M., and Wennberg, P. O.: Gas phase production and loss of isoprene epoxydiols, *J. Phys. Chem. A*, 118, 1237–1246, doi:10.1021/jp4107958, 2014.
- Baulch, D. L., Bowman, C. T., Cobos, C. J., Cox, R. A., Just, T., Kerr, J. A., Pilling, M. J., Stocker, D., Troe, J., Tsang, W., Walker, R. W., and Warnatz, J.: Evaluated kinetic data for combustion modeling: Supplement II, *J. Phys. Chem. Ref. Data*, 34, 757–1397, doi:10.1063/1.1748524, 2005.
- Becker, K. H., Kurtenbach, R., Schmidt, F., and Wiesen, P.: Kinetics of the NCO radical reacting with atoms and selected molecules, *Combust. Flame*, 120, 570–577, doi:10.1016/S0010-2180(99)00108-X, 2000.
- Behnke, W., Scheer, V., and Zetzsch, C.: Production of BrNO₂, Br₂ and ClNO₂ from the reaction between sea spray aerosol and N₂O₅, *J. Aerosol Sci.*, 25, S277–S278, doi:10.1016/0021-8502(94)90369-7, 1994.
- Behnke, W., George, C., Scheer, V., and Zetzsch, C.: Production and decay of ClNO₂ from the reaction of gaseous N₂O₅ with NaCl solution: Bulk and aerosol experiments, *J. Geophys. Res.*, 102D, 3795–3804, doi:10.1029/96JD03057, 1997.
- Beyersdorf, A. J., Blake, D. R., Swanson, A., Meinardi, S., Rowland, F. S., and Davis, D.: Abundances and variability of tropospheric volatile organic compounds at the South Pole and other Antarctic locations, *Atmos. Environ.*, 44, 4565–4574, doi:10.1016/j.atmosenv.2010.08.025, 2010.
- Birdsall, A. W., Andreoni, J. F., and Elrod, M. J.: Investigation of the role of bicyclic peroxy radicals in the oxidation mechanism of toluene, *J. Phys. Chem. A*, 114, 10655–10663, doi:10.1021/jp105467e, 2010.
- Bossolasco, A., Faragó, E. P., Schoemaeker, C., and Fittschen, C.: Rate constant of the reaction between CH₃O₂ and OH radicals, *Chem. Phys. Lett.*, 503, 7–13, doi:10.1016/j.cplett.2013.12.052, 2014.
- Buras, Z. J., Elsamra, R. M. I., and Green, W. H.: Direct determination of the simplest Criegee intermediate (CH₂OO) self reaction rate, *J. Phys. Chem. Lett.*, 5, 2224–2228, doi:10.1021/jz5008406, 2014.
- Burkholder, J. B., Sander, S. P., Abbatt, J., Barker, J. R., Huie, R. E., Kolb, C. E., Kurylo, M. J., Orkin, V. L., Wilmouth, D. M., and Wine, P. H.: Chemical Kinetics and Photochemical Data for Use in Atmospheric Studies, Evaluation No. 18, JPL Publication 15-10, Jet Propulsion Laboratory, Pasadena, <http://jpldataeval.jpl.nasa.gov>, 2015.
- Butkovskaya, N., Kukui, A., and Le Bras, G.: Pressure and temperature dependence of ethyl nitrate formation in the C₂H₅O₂ + NO reaction, *J. Phys. Chem. A*, 114, 956–964, doi:10.1021/jp910003a, 2010.
- Butkovskaya, N., Kukui, A., and Le Bras, G.: Pressure and temperature dependence of methyl nitrate formation in the CH₃O₂ + NO reaction, *J. Phys. Chem. A*, 116, 5972–5980, doi:10.1021/jp210711d, 2012.
- Canosa-Mas, C. E., King, M. D., Lopez, R., Percival, C. J., Wayne, R. P., Shallcross, D. E., Pyle, J. A., and Daele, V.: Is the reaction between CH₃(O)O₂ and NO₂ important in the night-time troposphere?, *J. Chem. Soc. Faraday Trans.*, 92, 2211–2222, doi:10.1039/FT9969202211, 1996.
- Capouet, M., Müller, J.-F., Ceulemans, K., Compernelle, S., Vereecken, L., and Peeters, J.: Modeling aerosol formation in alpha-pinene photo-oxidation experiments, *J. Geophys. Res.*, 113D, doi:10.1029/2007JD008995, 2008.
- Chai, J., Hu, H., Dibble, T. S., Tyndall, G. S., and Orlando, J. J.: Rate constants and kinetic isotope effects for methoxy radical reacting with NO₂ and O₂, *J. Phys. Chem. A*, 118, 3552–3563, doi:10.1021/jp501205d, 2014.
- Chao, W., Hsieh, J.-T., Chang, C.-H., and Lin, J. J.-M.: Direct kinetic measurement of the reaction of the simplest Criegee intermediate with water vapor, *Science*, 347, 751–754, doi:10.1126/science.1261549, 2015.
- Chen, J., Wenger, J. C., and Venables, D. S.: Near-ultraviolet absorption cross sections of nitrophenols and their potential influence on tropospheric oxidation capacity, *J. Phys. Chem. A*, 115, 12235–12242, doi:10.1021/jp206929r, 2011.
- Clubb, A. E., Jordan, M. J. T., Kable, S. H., and Osborn, D. L.: Phototautomerization of acetaldehyde to vinyl alcohol: a primary process in UV-irradiated acetaldehyde from 295 to 335 nm, *J. Phys. Chem. Lett.*, 3, 3522–3526, doi:10.1021/jz301701x, 2012.
- Conn, J. B., Kistiakowsky, G. B., Roberts, R. M., and Smith, E. A.: Heats of organic reactions. XIII. Heats of hydrolysis of some acid anhydrides, *Journal of the American Chemical Society*, 64, 1747–1752, doi:10.1021/ja01260a001, 1942.
- da Silva, G.: Carboxylic acid catalyzed keto-enol tautomerizations in the gas phase, *Angew. Chem.*, 122, 7685–7687, doi:10.1002/ange.201003530, 2010.
- Davis, D., Chen, G., Kasibhatla, P., Jefferson, A., Tanner, D., Eisele, F., Lenschow, D., Neff, W., and Berresheim, H.: DMS oxidation in the Antarctic marine boundary layer: Comparison of model simulations and field observations of DMS, DMSO, DMSO₂, H₂SO₄(g), MSA(g), and MSA(p), *J. Geophys. Res.*, 103D, 1657–1678, doi:10.1029/97JD03452, 1998.
- Dulitz, K., Amedro, D., Dillon, T. J., Pozzer, A., and Crowley, J. N.: Temperature (208–318 K) and pressure (18–696 Torr) dependent rate coefficients for the reaction between OH and HNO₃, *Atmos. Chem. Phys.*, 18, 2381–2394, doi:10.5194/acp-18-2381-2018, 2018.
- Feierabend, K. J., Zhu, L., Talukdar, R. K., and Burkholder, J. B.: Rate coefficients for the OH + HC(O)C(O)H (glyoxal) reaction between 210 and 390 K, *J. Phys. Chem. A*, 112, 73–82, doi:10.1021/JP0768571, 2008.
- Flocke, F., Atlas, E., Madronich, S., Schaufli, S. M., Aikin, K., Margitan, J. J., and Bui, T. P.: Observations of methyl nitrate in the lower stratosphere during STRAT: implications for its gas phase production mechanisms, *Geophys. Res. Lett.*, 25, 1891–1894, doi:10.1029/98GL01417, 1998.
- Francisco-Marquez, M., Alvarez-Idaboy, J. R., Galano, A., and Vivier-Bunge, A.: Theoretical study of the initial reaction between OH and isoprene in tropospheric conditions, *Phys. Chem. Chem. Phys.*, 5, 1392–1399, doi:10.1039/B211185C, 2003.
- Ganzeveld, L., Klemm, O., Rappenglück, B., and Valverde-Canossa, J.: Evaluation of meteorological parameters over a coniferous forest in a single-column chemistry-climate model, *Atmos. Environ.*, 40, S21–S27, doi:10.1016/J.ATMOSENV.2006.01.061, 2006.
- Gill, K. J. and Hites, R. A.: Rate constants for the gas-phase reactions of the hydroxyl radical with isoprene, α - and β -pinene, and limonene as a function of temperature, *J. Phys. Chem. A*, 106, 2538–2544, doi:10.1021/jp013532q, 2002.
- Glowacki, D. R., Lockhart, J., Blitz, M. A., Klippenstein, S. J., Pilling, M. J., Robertson, S. H., and Seakins, P. W.: Interception of excited vibrational quantum states by O₂ in atmospheric association reactions, *Science*, 337, 1066–1069, doi:10.1126/science.1224106, 2012.
- Grenfell, J. L., Lehmann, R., Mieth, P., Langematz, U., and Steil, B.: Chemical reaction pathways affect-

- ing stratospheric and mesospheric ozone, *J. Geophys. Res.*, 111D, doi:10.1029/2004JD005713, 2006.
- Groß, C. B. M., Dillon, T. J., Schuster, G., Lelieveld, J., and Crowley, J. N.: Direct kinetic study of OH and O₃ formation in the reaction of CH₃C(O)O₂ with HO₂, *J. Phys. Chem. A*, 1, 974–985, doi:10.1021/jp412380z, 2014.
- Gruzdev, A. N., Elokho, A. S., Makarov, O. V., and Mokhov, I. L.: Some recent results of Russian measurements of surface ozone in Antarctica. A meteorological interpretation, *Tellus*, 45B, 99–105, doi:10.3402/TELLUSB.V45I2.15584, 1993.
- Hatakeyama, S., Honda, S., and Akimoto, H.: Rate constants and mechanism for reactions of ketenes with OH radicals in air at 299±2 K, *Bull. Chem. Soc. Jpn.*, 58, 2157–2162, doi:10.1246/BCSJ.58.2157, 1985.
- Hermans, I., Müller, J.-F., Nguyen, T. L., Jacobs, P. A., and Peeters, J.: Kinetics of α -hydroxy-alkylperoxy radicals in oxidation processes. HO₂-initiated oxidation of ketones/aldehydes near the tropopause, *J. Phys. Chem. A*, 109, 4303–4311, doi:10.1021/jp444080v, 2005.
- Jagiella, S. and Zabel, F.: Reaction of phenylperoxy radicals with NO₂ at 298 K, *Phys. Chem. Chem. Phys.*, 9, 5036–5051, doi:10.1039/B705193J, 2007.
- Jenkin, M., Saunders, S. M., and Pilling, M. J.: The tropospheric degradation of volatile organic compounds: A protocol for mechanism development, *Atmos. Environ.*, 31, 81–104, doi:10.1016/S1352-2310(96)00105-7, 1997.
- Jenkin, M. E., Young, J. C., and Rickard, A. R.: The MCM v3.3.1 degradation scheme for isoprene, *Atmos. Chem. Phys.*, 15, 11433–11459, doi:10.5194/acp-15-11433-2015, 2015.
- atmospheric pressure and 298 K, *Int. J. Chem. Kinetics*, 23, 1095–1109, doi:10.1002/kin.550231204, 1991.
- Ogryzlo, E. A., Paltenghi, R., and Bayes, K. D.: The rate of reaction of methyl radicals with ozone, *Int. J. Chem. Kinetics*, 13, 667–675, doi:10.1002/kin.550130707, 1981.
- Olmann, M., Kraka, E., Cremer, D., Gutbrod, R., and Andersson, S.: Energetics, kinetics, and product distributions of the reactions of ozone with ethene and 2,3-dimethyl-2-butene, *J. Phys. Chem. A*, 101, 9421–9429, doi:10.1021/JP971663E, 1997.
- Orlando, J. J. and Tyndall, G. S.: The atmospheric chemistry of the HC(O)CO radical, *Int. J. Chem. Kinetics*, 33, 149–156, doi:10.1002/1097-4601(200103)33:3(149::AID-KIN1008)3.0.CO;2-1, 2001.
- Orlando, J. J. and Tyndall, G. S.: Laboratory studies of organic peroxy radical chemistry: an overview with emphasis on recent issues of atmospheric significance, *Chem. Soc. Rev.*, 41, 6294–6317, doi:10.1039/C2CS35166H, 2012.
- Orlando, J. J., Tyndall, G. S., Bilde, M., Ferronato, C., Wallington, T. J., Vereecken, L., and Peeters, J.: Laboratory and theoretical study of the oxy radicals in the OH- and Cl-initiated oxidation of ethene, *J. Phys. Chem. A*, 102, 8116–8123, doi:10.1021/JP981937D, 1998.
- Orlando, J. J., Tyndall, G. S., Fracheboud, J. M., Estupinan, E. G., Haberkorn, S., and Zimmer, A.: The rate and mechanism of the gas-phase oxidation of hydroxyacetone, *Atmos. Environ.*, 33, 1621–1629, doi:10.1016/S1352-2310(98)00386-0, 1999a.
- Orlando, J. J., Tyndall, G. S., and Paulson, S. E.: Mechanism of the OH-initiated oxidation of methacrolein, *Geophys. Res. Lett.*, 26, 2191–2194, doi:10.1029/1999GL900453, 1999b.
- Orlando, J. J., Tyndall, G. S., Bertman, S. B., Chen, W., and Burkholder, J. B.: Rate coefficient for the reaction of OH with CH₂=C(CH₃)C(O)OONO₂ (MPAN), *Atmos. Environ.*, 36, 1895–1900, doi:10.1016/S1352-2310(02)00090-0, 2002.
- Ouyang, B., McLeod, M. W., Jones, R. L., and Bloss, W. J.: NO₃ radical production from the reaction between the Criegee intermediate CH₂OO and NO₂, *Phys. Chem. Chem. Phys.*, 15, 17070–17075, doi:10.1039/c3cp53024h, 2013.
- Paulot, F., Crouse, J. D., Kjaergaard, H. G., Kroll, J. H., Seinfeld, J. H., and Wennberg, P. O.: Isoprene photooxidation: new insights into the production of acids and organic nitrates, *Atmos. Chem. Phys.*, 9, 1479–1501, doi:10.5194/ACP-9-1479-2009, 2009a.
- Paulot, F., Crouse, J. D., Kjaergaard, H. G., Kürten, A., St. Clair, J. M., Seinfeld, J. H., and Wennberg, P. O.: Unexpected epoxide formation in the gas-phase photooxidation of isoprene, *Science*, 325, doi:10.1126/science.1172910, 2009b.
- Paulot, F., Wunch, D., Crouse, J. D., Toon, G. C., Millet, D. B., DeCarlo, P. F., Vigouroux, C., Deutscher, N. M., González Abad, G., Notholt, J., Warneke, T., Hannigan, J. W., Warneke, C., de Gouw, J. A., Dunlea, E. J., De Maziere, M., Griffith, D. W. T., Bernath, P., Jimenez, J. L., and Wennberg, P. O.: Importance of secondary sources in the atmospheric budgets of formic and acetic acids, *Atmos. Chem. Phys.*, 11, 1989–2013, doi:10.5194/acp-11-1989-2011, 2011.
- Peeters, J. and Nguyen, T. L.: Unusually fast 1,6-H shifts of enolic hydrogens in peroxy radicals: formation of the first-generation C₂ and C₃ carbonyls in the oxidation of isoprene, *J. Phys. Chem. A*, 116, 6134–6141, doi:10.1021/jp211447q, 2012.
- Peeters, J., Müller, J.-F., Stavrou, T., and Nguyen, V. S.: Hydroxyl radical recycling in isoprene oxidation driven by hydrogen bonding and hydrogen tunneling: the upgraded LMI mechanism, *J. Phys. Chem. A*, 118, 8625–8643, doi:10.1021/jp5033146, 2014.
- Platz, J., Nielsen, O. J., Wallington, T. J., Ball, J. C., Hurley, M. D., Straccia, A. M., Schneider, W. F., and Sehested, J.: Atmospheric chemistry of the phenoxy radical, C₆H₅O(·): UV spectrum and kinetics of its reaction with NO, NO₂, and O₂, *J. Phys. Chem. A*, 102, 7964–7974, doi:10.1021/jp982221i, 1998.
- Rickard, A. and Pascoe, S.: The Master Chemical Mechanism (MCM), <http://mcm.leeds.ac.uk>, 2009.
- Rickard, A. R., Johnson, D., McGill, C. D., and Marston, G.: OH yields in the gas-phase reactions of ozone with alkenes, *J. Phys. Chem. A*, 103, 7656–7664, doi:10.1021/JP9916992, 1999.
- Roth, E., Chakir, A., and Ferhati, A.: Study of a benzoylperoxy radical in the gas phase: ultraviolet spectrum and C₆H₅C(O)O₂ + HO₂ reaction between 295 and 357 K, *J. Phys. Chem. A*, 114, 10367–10379, doi:10.1021/jp1021467, 2010.
- Sander, R., Jöckel, P., Kirner, O., Kumert, A. T., Landgraf, J., and Pozzer, A.: The photolysis module JVAL-14, compatible with the MESSy standard, and the JVal PreProcessor (JVPP), *Geosci. Model Dev.*, 7, 2653–2662, doi:10.5194/GMD-7-2653-2014, 2014.
- Sander, R., Baumgaertner, A., Cabrera-Perez, D., Frank, F., Groöb, J.-U., Gromov, S., Harder, H., Huijnen, V., Jöckel, P., Karydis, V. A., Niemeyer, K., McCabe, D. C., Gierczak, T., Talukdar, R. K., and Ravishankara, A. R.: Kinetics of the reaction OH + CO under atmospheric conditions, *Geophys. Res. Lett.*, 28, 3135–3138, doi:10.1029/2000GL012719, 2001.
- Mellouki, A. and Mu, Y.: On the atmospheric degradation of pyruvic acid in the gas phase, *J. Photochem. Photobiol. A: Chem.*, 157, doi:10.1016/S1010-6030(03)00070-4, 2003.
- Messaadia, L., Dib, G. E., Ferhati, A., and Chakir, A.: UV-visible spectra and gas-phase rate coefficients for the reaction of 2,3-pentanedione and 2,4-pentanedione with OH radicals, *Chem. Phys. Lett.*, 626, 73–79, doi:10.1016/j.cplett.2015.02.032, 2015.
- Müller, J.-F., Peeters, J., and Stavrou, T.: Fast photolysis of carbonyl nitrates from isoprene, *Atmos. Chem. Phys.*, 14, 2497–2508, doi:10.5194/acp-14-2497-2014, 2014.
- Munger, J. W., Jacob, D. J., Fan, S.-M., Colman, A. S., and Dibb, J. E.: Concentrations and snow-atmosphere fluxes of reactive nitrogen at Summit, Greenland, *J. Geophys. Res.*, 104D, 13721–13734, doi:10.1029/1999JD900192, 1999.
- Nakanishi, H., Morita, H., and Nagakura, S.: Electronic structures and spectra of the keto and enol forms of acetylacetone, *Bull. Chem. Soc. Jpn.*, 50, 2255–2261, doi:10.1246/bcsj.50.2255, 1977.
- Nguyen, T. L., Peeters, J., and Vereecken, L.: Theoretical study of the gas-phase ozonolysis of β -pinene (C₁₀H₁₆), *Phys. Chem. Chem. Phys.*, 11, 5643–5656, doi:10.1039/b822984h, 2009.
- Nielsen, O. J., Sidebottom, H. W., Donlon, M., and Treacy, J.: Rate constants for the gas-phase reactions of OH radicals and Cl atoms with *n*-alkyl nitrates at

- Pozzer, A., Riede, H., Schultz, M., Taraborrelli, D., and Tauer, S.: The atmospheric chemistry box model CAABA/MECCA-4.0gmd, *Geosci. Model Dev. Discuss.*, doi:10.5194/gmd-2018-201, 2018.
- Scribano, Y., Goldman, N., Saykally, R. J., and Lefortier, C.: Water dimers in the atmosphere III: Equilibrium constant from a flexible potential, *J. Phys. Chem. A*, 110, 5411–5419, doi:10.1021/jp056759k, 2006.
- Schested, J., Christensen, L. K., Nielsen, O. J., Bilde, M., Wallington, T. J., Schneider, W. F., Orlando, J. J., and Tyndall, G. S.: Atmospheric chemistry of acetone: Kinetic study of the $\text{CH}_3\text{C}(\text{O})\text{CH}_2\text{O}_2 + \text{NO}/\text{NO}_2$ reactions and decomposition of $\text{CH}_3\text{C}(\text{O})\text{CH}_2\text{O}_2\text{NO}_2$, *Int. J. Chem. Kinetics*, 30, 475–489, doi:10.1002/(SICI)1097-4601(1998)30:7<475::AID-KIN4>3.0.CO;2-P, 1998.
- Sivakumaran, V., Hölscher, D., Dillon, T. J., and Crowley, J. N.: Reaction between OH and HCHO: temperature dependent rate coefficients (202–399 K) and product pathways (298 K), *Phys. Chem. Chem. Phys.*, 5, 4821–4827, doi:10.1039/B306859E, 2003.
- So, S., Wille, U., and da Silva, G.: Atmospheric chemistry of enols: a theoretical study of the vinyl alcohol + OH + O₂ reaction mechanism, *Environ. Sci. Technol.*, 48, 6694–6701, doi:10.1021/es500319q, 2014.
- Solberg, S., Stordal, F., and Hov, Ø.: Tropospheric ozone at high latitudes in clean and polluted air masses, a climatological study, *J. Atmos. Chem.*, 28, 111–123, doi:10.1023/A:1005766612853, 1997.
- Stone, D., Blitz, M., Daubney, L., Howes, N. U. M., and Seakins, P.: Kinetics of CH₂OO reactions with SO₂, NO₂, NO, H₂O and CH₃CHO as a function of pressure, *Phys. Chem. Chem. Phys.*, 16, 1139–1149, doi:10.1039/c3cp54391a, 2014.
- Strekowski, R. S., Nicovich, J. M., and Wine, P. H.: Kinetic and mechanistic study of the Reactions of O(¹D₂) with HCN and CH₃CN, *Chem. Phys. Chem.*, 11, 3942–3955, doi:10.1002/cphc.201000550, 2010.
- Tao, Z. and Li, Z.: A kinetics study on reactions of C₆H₅O with C₆H₅O and O₃ at 298 K, *Int. J. Chem. Kinetics*, 31, 65–72, doi:10.1002/(SICI)1097-4601(1999)31:1(65::AID-KINS)3.0.CO;2-J, 1999.
- Taraborrelli, D.: Isoprene oxidation and its impacts on the atmospheric composition, Ph.D. thesis, Johannes Gutenberg-Universität, Mainz, Germany, <http://d-nb.info/1003538770/34>, 2010.
- Taraborrelli, D., Lawrence, M. G., Butler, T. M., Sander, R., and Lelieveld, J.: Mainz Isoprene Mechanism 2 (MIM2): an isoprene oxidation mechanism for regional and global atmospheric modelling, *Atmos. Chem. Phys.*, 9, 2751–2777, doi:10.5194/ACP-9-2751-2009, 2009.
- Tyndall, G. S., Staffelbach, T. A., Orlando, J. J., and Calvert, J. G.: Rate coefficients for the reactions of OH radicals with methylglyoxal and acetaldehyde, *Int. J. Chem. Kinetics*, 27, 1009–1020, doi:10.1002/KIN.550271006, 1995.
- Tyndall, G. S., Cox, R. A., Granier, C., Lesclaux, R., Moortgat, G. K., Pilling, M. J., Ravishankara, A. R., and Wallington, T. J.: The atmospheric chemistry of small organic peroxy radicals, *J. Geophys. Res.*, 106D, 12 157–12 182, doi:10.1029/2000JD900746, 2001a.
- Tyndall, G. S., Orlando, J. J., Wallington, T. J., and Hurley, M. D.: Products of the chlorine-atom and hydroxyl-radical-initiated oxidation of CH₃CN, *J. Phys. Chem. A*, 105, 5380–5384, doi:10.1021/jp004318p, 2001b.
- Vereecken, L. and Francisco, J. S.: Theoretical studies of atmospheric reaction mechanisms in the troposphere, *Chem. Soc. Rev.*, 41, 6259–6293, doi:10.1039/c2cs35070j, 2012.
- Vereecken, L. and Peeters, J.: A theoretical study of the OH-initiated gas-phase oxidation mechanism of β -pinene (C₁₀H₁₆): first generation products, *Phys. Chem. Chem. Phys.*, 14, 3802–3815, doi:10.1039/c2cp23711e, 2012.
- Vereecken, L., Müller, J.-F., and Peeters, J.: Low-volatility poly-oxygenates in the OH-initiated atmospheric oxidation of α -pinene: impact of non-traditional peroxy radical chemistry, *Phys. Chem. Chem. Phys.*, 9, 5241–5248, doi:10.1039/b708023a, 2007.
- Vereecken, L., Harder, H., and Novelli, A.: The reaction of Criegee intermediates with NO, RO₂, and SO₂, and their fate in the atmosphere, *Phys. Chem. Chem. Phys.*, 14, 14 682–14 695, doi:10.1039/c2cp42300f, 2012.
- Vereecken, L., Harder, H., and Novelli, A.: The reactions of Criegee intermediates with alkenes, ozone, and carbonyl oxides, *Phys. Chem. Chem. Phys.*, 16, 4039–4049, doi:10.1039/c3cp54514h, 2014.
- von Kuhlmann, R.: Tropospheric photochemistry of ozone, its precursors and the hydroxyl radical: A 3D-modeling study considering non-methane hydrocarbons, Ph.D. thesis, Johannes Gutenberg-Universität, Mainz, Germany, 2001.
- von Kuhlmann, R., Lawrence, M. G., Crutzen, P. J., and Rasch, P. J.: A model for studies of tropospheric implications, *Angew. Chem.*, 126, 4635–4638, doi:10.1002/ange.201400964, 2014.
- Yoon, M.-C., Choi, Y. S., and Kim, S. K.: The OH production from the $\pi - \pi^*$ transition of acetylacetone, *Chem. Phys. Lett.*, 300, 207–212, doi:10.1016/S0009-2614(98)01373-6, 1999.
- Zellner, R., Hartmann, D., Karthäuser, J., Rhäsa, D., and Weibring, G.: A laser photolysis/LIF study of the reactions of O(³P) atoms with CH₃ and CH₃O₂ radicals, *J. Chem. Soc. Faraday Trans. 2*, 84, 549–568, doi:10.1039/f29888400549, 1988.
- ozone and nonmethane hydrocarbons: Model description and ozone results, *J. Geophys. Res.*, 108D, 4294, doi:10.1029/2002JD002893, 2003.
- Wallington, T. J., Ammann, M., Cox, R. A., Crowley, J. N., Herrmann, H., Jenkin, M. E., McNeill, V., Mellouki, A., Rossi, M. J., and Troe, J.: IUPAC Task group on atmospheric chemical kinetic data evaluation: Evaluated kinetic data, <http://iupac.pole-ether.fr>, 2018.
- Welz, O., Savee, J. D., Osborn, D. L., Vasu, S. S., Percival, C. J., Shallcross, D. E., and Taatjes, C. A.: Direct kinetic measurements of Criegee intermediate (CH₂OO) formed by reaction of CH₂I with O₂, *Science*, 335, 204–207, doi:10.1126/science.1213229, 2012.
- Welz, O., Eskola, A. J., Sheps, L., Rotavera, B., Savee, J. D., Scheer, A. M., Osborn, D. L., Lowe, D., Booth, A. M., Xiao, P., Khan, M. A. H., Percival, C. J., Shallcross, D. E., and Taatjes, C. A.: Rate coefficients of C1 and C2 Criegee intermediate reactions with formic and acetic acid near the collision limit: Direct kinetics measurements and atmospheric implications, *Angew. Chem.*, 126, 4635–4638, doi:10.1002/ange.201400964, 2014.

E. Support figures for the CO_{calc} discussion.

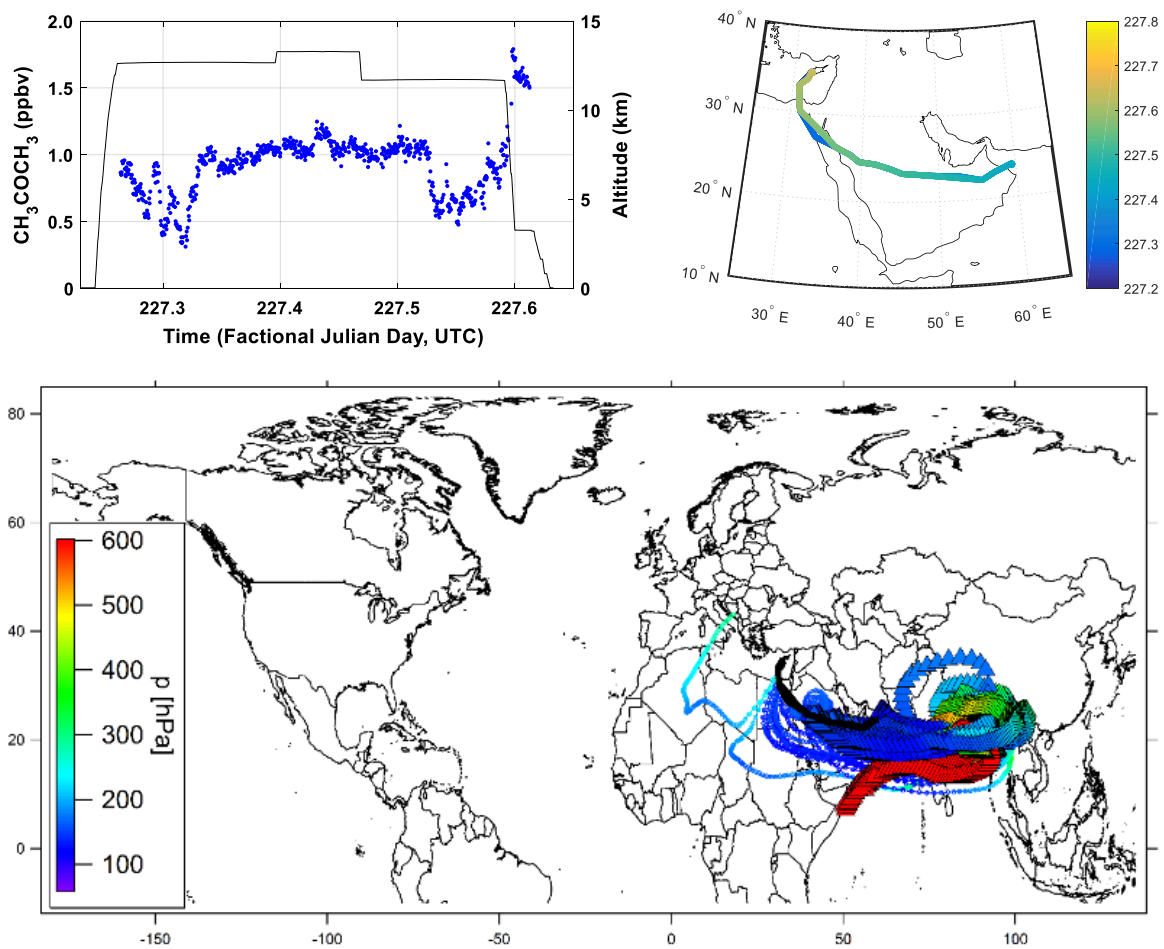


Figure E.1.: Flight 20 (15.08.2015), acetone measurements and altitude (top left panel), flight track colored by time as fractional Julian day, UTC (top right panel), and 12 day backward trajectory analysis taken from the supplementary material of Tomsche et al. (2019) (bottom panel).

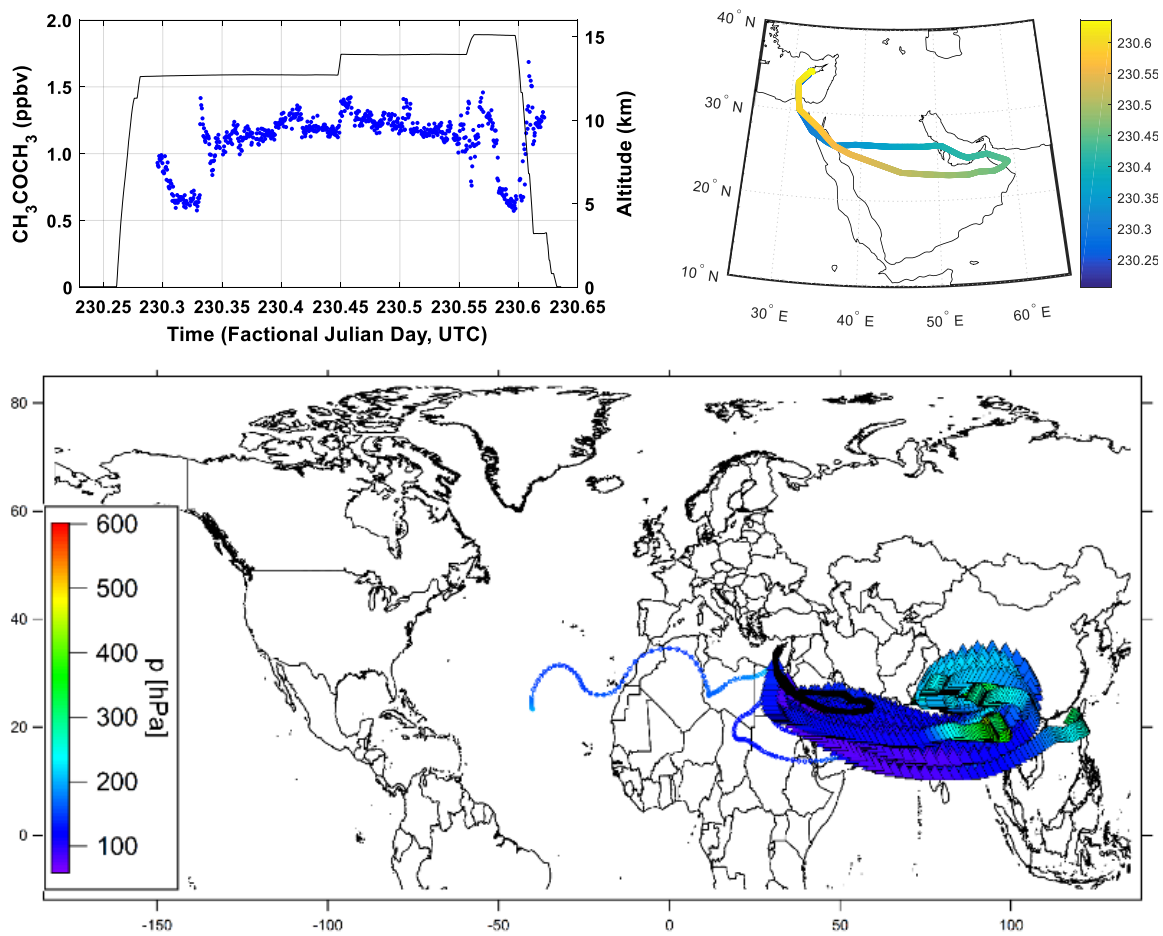


Figure E.2.: Flight 21 (18.08.2015), acetone measurements and altitude (top left panel), flight track colored by time as fractional Julian day, UTC (top right panel), and 12 day backward trajectory analysis taken from the supplementary material of Tomsche et al. (2019) (bottom panel).

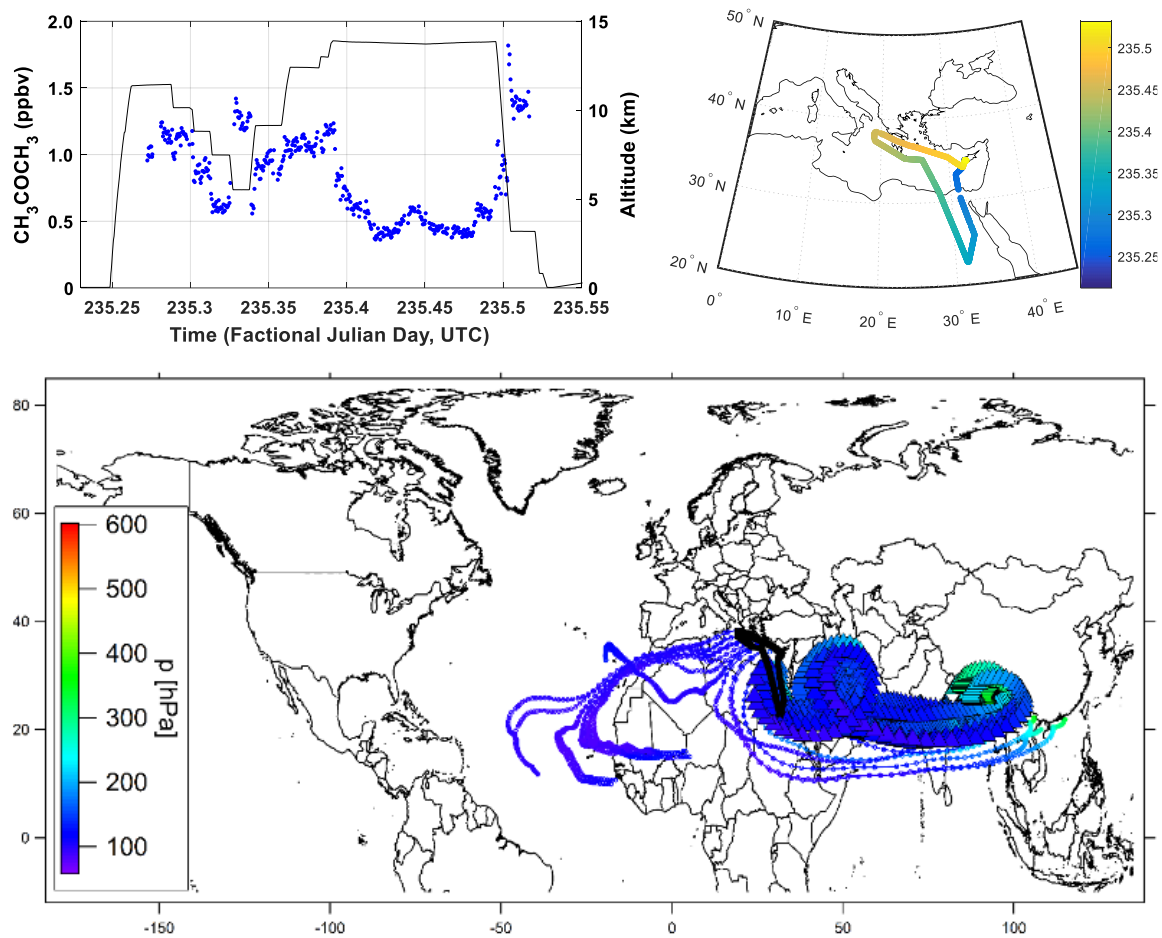


Figure E.3.: Flight 22 (23.08.2015), acetone measurements and altitude (top left panel), flight track colored by time as fractional Julian day, UTC (top right panel), and 12 day backward trajectory analysis taken from the supplementary material of Tomsche et al. (2019) (bottom panel).

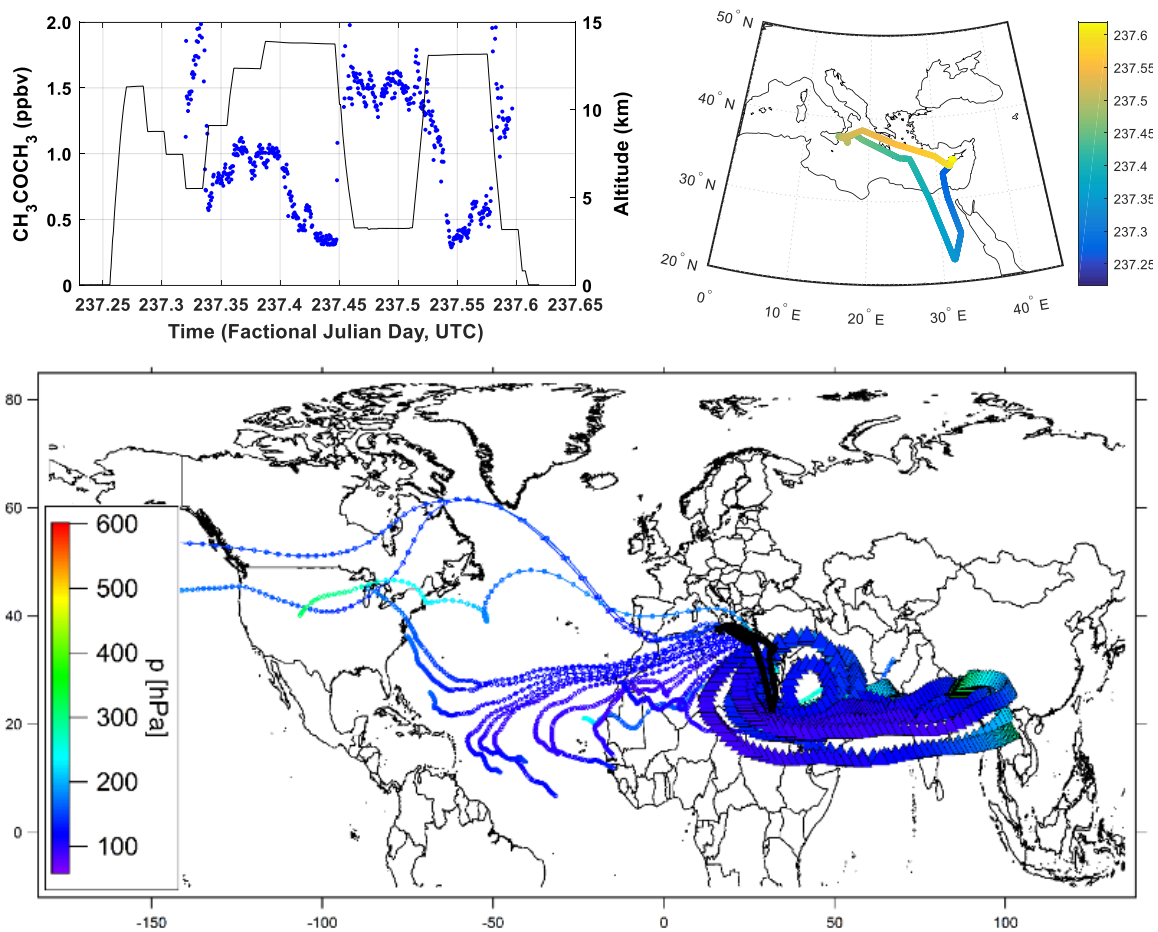


Figure E.4.: Flight 23 (25.08.2015), acetone measurements and altitude (top left panel), flight track colored by time as fractional Julian day, UTC (top right panel), and 12 day backward trajectory analysis taken from the supplementary material of Tomsche et al. (2019) (bottom panel).

F. Abbreviations

AMA	<i>Asian Monsoon Anticyclone</i>
APACHE	<i>All Pressure Altitude-based Calibrator for HO_x Experimentation</i>
CAABA-MECCA	<i>Chemistry As A Box Model Application – Module Efficiently Calculating the Chemistry of the Atmosphere</i>
CFC	<i>Chlorofluorocarbons</i>
CI	<i>Chemical Ionization</i>
CIMS	<i>Chemical Ionization Mass Spectrometry</i>
CPC	<i>Condensation Particle Counter</i>
DEM	<i>Dual Enzyme Monitor</i>
DOAS	<i>Differential Optical Absorption Spectroscopy</i>
EPR	<i>Electron Paramagnetic Resonance</i>
ESR	<i>Electron Spin Resonance</i>
GABRIEL	<i>Guyanas Atmosphere-Biosphere Exchange and Radicals Intensive Experiment with the Learjet, Oct. 2005, Suriname</i>
GC-MS	<i>Gas Chromatography – Mass Spectrometry</i>
GTHOS	<i>Ground-based Tropospheric Hydrogen Oxides Sensor</i>
HALO	<i>High Altitude and LOng Range Research Aircraft</i>
HOPE	<i>HOhenpeissenberg Photochemistry Experiment</i>
HORUS	<i>HydrOxyl Radical Measurement Unit based on fluorescence Spectroscopy</i>
HOVOC	<i>Highly Oxidized Volatile Organic Compounds</i>
HUMPPA	<i>Hyttiälä United Measurements of Photochemistry and Particles in Air</i>
IPI	<i>Inlet Pre-Injector</i>
ITMS	<i>Ion Trap Mass Spectrometry</i>
LIF	<i>Laser Induced Fluorescence</i>
LIF-FAGE	<i>Laser Induced Fluorescence – Fluorescence Assay by Gas Expansion</i>
LT	<i>Lower Troposphere</i>
MCM	<i>Master Chemical Mechanism</i>
MCP	<i>Micro Channel Plate</i>
MFC	<i>Mass Flow Controller</i>
MIM	<i>Mainz Isoprene Mechanism</i>
MOM	<i>Mainz Organic Mechanism</i>
NH	<i>Northern Hemisphere</i>
NMHC	<i>Non-Methane HydroCarbon</i>
NMVOC	<i>Non-Methane Volatile Organic Compound</i>
NOPR	<i>Net Ozone Production Rate</i>
OMO	<i>Oxidation Mechanism Observation</i>
OOMPH	<i>Ocean Organics Modifying Particles in both Hemispheres</i>
PARADE	<i>PARTICLES and RADICALS: Diel observations of the impact of urban and biogenic Emissions</i>
PTR-MS	<i>Proton Transfer Reaction Mass Spectroscopy</i>
RACM	<i>Regional Atmospheric Chemistry Mechanism</i>

SoS99	<i>Southern Oxidants Study 1999</i>
SR-A	<i>Spectral Actinic Radiation.</i>
TDLAS	<i>Tunable Diode Laser Absorption Spectroscopy</i>
TexAQS	<i>Texas Air Quality Study</i>
Trace-P	<i>Transport and Chemical Evolution over the Pacific</i>
UT	<i>Upper Troposphere</i>
UTC	<i>Universal Time Coordinates</i>
UTLS	<i>Upper Troposphere Lower Stratosphere</i>
VOC	<i>Volatile Organic Compound</i>

Bibliography

- Artaxo, P., Rizzo, L. V., Brito, J. F., Barbosa, H. M. J., Arana, A., Sena, E. T., Cirino, G. G., Bastos, W., Martin, S. T. and Andreae, M. O.: "Atmospheric aerosols in Amazonia and land use change: from natural biogenic to biomass burning conditions." *Faraday Discussions* **165**: 203-235 DOI: 10.1039/c3fd00052d, (2013)
- Atkinson, R., Baulch, D. L., Cox, R. A., Crowley, J. N., Hampson, R. F., Hynes, R. G., Jenkin, M. E., Rossi, M. J. and Troe, J.: "Evaluated kinetic and photochemical data for atmospheric chemistry: Volume I - gas phase reactions of O-x, HOx, NOx and SOx species." *Atmospheric Chemistry and Physics* **4**: 1461-1738 DOI: 10.5194/acp-4-1461-2004, (2004)
- Atkinson, R., Baulch, D. L., Cox, R. A., Crowley, J. N., Hampson, R. F., Hynes, R. G., Jenkin, M. E., Rossi, M. J. and Troe, J.: "Evaluated kinetic and photochemical data for atmospheric chemistry: Volume II - gas phase reactions of organic species." *Atmospheric Chemistry and Physics* **6**: 3625-4055 DOI: DOI 10.5194/acp-6-3625-2006, (2006)
- Aumont, B., Chervier, F. and Laval, S.: "Contribution of HONO sources to the NOx/HOx/O-3 chemistry in the polluted boundary layer." *Atmospheric Environment* **37**,4: 487-498, (2003)
- Bailey, A. E., Heard, D. E., Henderson, D. A. and Paul, P. H.: "Collisional quenching of OH(A(2)Sigma(+), $\nu=0$) by H2O between 211 and 294 K and the development of a unified model for quenching." *Chemical Physics Letters* **302**,1-2: 132-138 DOI: Doi 10.1016/S0009-2614(99)00076-7, (1999)
- Bailey, A. E., Heard, D. E., Paul, P. H. and Pilling, M. J.: "Collisional quenching of OH (A(2)Sigma(+), $\nu=0$) by N-2, O-2 and CO2 between 204 and 294 K. Implications for atmospheric measurements of OH by laser-induced fluorescence." *Journal of the Chemical Society-Faraday Transactions* **93**,16: 2915-2920 DOI: DOI 10.1039/a701582h, (1997)
- Baker, A. K., Schuck, T. J., Brenninkmeijer, C. A. M., Rauthe-Schoch, A., Slemr, F., van Velthoven, P. F. J. and Lelieveld, J.: "Estimating the contribution of monsoon-related biogenic production to methane emissions from South Asia using CARIBIC observations." *Geophysical Research Letters* **39**, (2012)
- Bobrowski, N., Honninger, G., Lohberger, F. and Platt, U.: "IDOAS: A new monitoring technique to study the 2D distribution of volcanic gas emissions." *Journal of Volcanology and Geothermal Research* **150**,4: 329-338, (2006)
- Bourtsoukidis, E., Helleis, F., Tomsche, L., Fischer, H., Hofmann, R., Lelieveld, J. and Williams, J.: "An aircraft gas chromatograph-mass spectrometer System for Organic Fast Identification Analysis (SOFIA): design, performance and a case study of Asian monsoon pollution outflow." *Atmospheric Measurement Techniques* **10**,12: 5089-5105 DOI: 10.5194/amt-10-5089-2017, (2017)
- Bozem, H., Butler, T. M., Lawrence, M. G., Harder, H., Martinez, M., Kubistin, D., Lelieveld, J. and Fischer, H.: "Chemical processes related to net ozone tendencies in the free troposphere." *Atmospheric Chemistry and Physics* **17**,17: 10565-10582, (2017)
- Brasseur, G. P., Orlando, J. J. and Tyndall, G. S.: "Atmospheric Chemistry and Global Change." Oxford University Press, (1999)
- Brown, S. S., Dube, W. P., Peischl, J., Ryerson, T. B., Atlas, E., Warneke, C., de Gouw, J. A., Hekkert, S. T., Brock, C. A., Flocke, F., Trainer, M., Parrish, D. D., Feshenfeld, F. C. and Ravishankara, A. R.: "Budgets for nocturnal VOC oxidation by nitrate radicals aloft during the 2006 Texas Air Quality Study." *Journal of Geophysical Research-Atmospheres* **116**, DOI: Artn D24305/10.1029/2011jd016544, (2011)
- Brune, W. H., Faloon, I. C., Tan, D., Weinheimer, A. J., Campos, T., Ridley, B. A., Vay, S. A., Collins, J. E., Sachse, G. W., Jaeglé, L. and Jacob, D. J.: "Airborne in-situ OH and HO2 observations in the cloud-free troposphere and lower stratosphere during SUCCESS." *Geophysical Research Letters* **25**,10: 1701-1704 DOI: 10.1029/97GL03098, (1998)

- Burkholder, J. B., Sander, S. P., Abbatt, J., Barker, J. R., Huie, R. E., Kolb, C. E., Kurylo, M. J., Orkin, V. L., Wilmoth, D. M. and Wine, P. H.: "Chemical Kinetics and Photochemical Data for Use in Atmospheric Studies, Evaluation No. 18." JPL Publication 15-10, (2015)
- Butkovskaya, N., Kukui, A. and Le Bras, G.: "Pressure and Temperature Dependence of Methyl Nitrate Formation in the CH₃O₂+NO Reaction." *Journal of Physical Chemistry A* **116**,24: 5972-5980, (2012)
- Cantrell, C. A., Edwards, G. D., Stephens, S., Mauldin, R. L., Zondlo, M. A., Kosciuch, E., Eisele, F. L., Shetter, R. E., Lefer, B. L., Hall, S., Flocke, F., Weinheimer, A., Fried, A., Apel, E., Kondo, Y., Blake, D. R., Blake, N. J., Simpson, I. J., Bandy, A. R., Thornton, D. C., Heikes, B. G., Singh, H. B., Brune, W. H., Harder, H., Martinez, M., Jacob, D. J., Avery, M. A., Barrick, J. D., Sachse, G. W., Olson, J. R., Crawford, J. H. and Clarke, A. D.: "Peroxy radical behavior during the Transport and Chemical Evolution over the Pacific (TRACE-P) campaign as measured aboard the NASA P-3B aircraft." *Journal of Geophysical Research-Atmospheres* **108**,D20, (2003)
- Cariolle, D., Evans, M. J., Chipperfield, M. P., Butkovskaya, N., Kukui, A. and Le Bras, G.: "Impact of the new HNO₃-forming channel of the HO₂+NO reaction on tropospheric HNO₃, NO_x, HO_x and ozone." *Atmospheric Chemistry and Physics* **8**,14: 4061-4068 DOI: DOI 10.5194/acp-8-4061-2008, (2008)
- Chai, J. J., Hu, H. Y., Dibble, T. S., Tyndall, G. S. and Orlando, J. J.: "Rate Constants and Kinetic Isotope Effects for Methoxy Radical Reacting with NO₂ and O-2." *Journal of Physical Chemistry A* **118**,20: 3552-3563, (2014)
- Chakrabarty, R. K., Gyawali, M., Yatavelli, R. L. N., Pandey, A., Watts, A. C., Knue, J., Chen, L. W. A., Pattison, R. R., Tsiabart, A., Samburova, V. and Moosmuller, H.: "Brown carbon aerosols from burning of boreal peatlands: microphysical properties, emission factors, and implications for direct radiative forcing." *Atmospheric Chemistry and Physics* **16**,5: 3033-3040 DOI: 10.5194/acp-16-3033-2016, (2016)
- Chan, C. Y., Hard, T. M., Mehrabzadeh, A. A., George, L. A. and Obrien, R. J.: "3rd-Generation Fage Instrument for Tropospheric Hydroxyl Radical Measurement." *Journal of Geophysical Research-Atmospheres* **95**,D11: 18569-18576 DOI: DOI 10.1029/JD095iD11p18569, (1990)
- COMSOL. (2019). Multiphysics Documentation, version 5.4, [software] "available at, <https://www.comsol.com>", 2019
- Crawford, J., Davis, D., Olson, J., Chen, G., Liu, S., Fuelberg, H., Hannan, J., Kondo, Y., Anderson, B., Gregory, G., Sachse, G., Talbot, R., Viggiano, A., Heikes, B., Snow, J., Singh, H. and Blake, D.: "Evolution and chemical consequences of lightning-produced NO_x observed in the North Atlantic upper troposphere." *Journal of Geophysical Research-Atmospheres* **105**,D15: 19795-19809 DOI: Doi 10.1029/2000jd900183, (2000)
- Creasey, D. J., Evans, G. E., Heard, D. E. and Lee, J. D.: "Measurements of OH and HO₂ concentrations in the Southern Ocean marine boundary layer." *Journal of Geophysical Research-Atmospheres* **108**,D15, DOI: Artn 4475/10.1029/2002jd003206, (2003)
- Creasey, D. J., Heard, D. E. and Lee, J. D.: "Absorption cross-section measurements of water vapour and oxygen at 185 nm. Implications for the calibration of field instruments to measure OH, HO₂ and RO₂ radicals." *Geophysical Research Letters* **27**,11: 1651-1654 DOI: Doi 10.1029/1999gl011014, (2000)
- Dieke, G. H. and Crosswhite, H. M.: "The Ultraviolet Bands of OH - Fundamental Data." *Journal of Quantitative Spectroscopy & Radiative Transfer* **2**,2: 97-& DOI: Doi 10.1016/0022-4073(62)90061-4, (1962)
- Dilecce, G., Ambrico, P. F. and De Benedictis, S.: "An ambient air RF low-pressure pulsed discharge as an OH source for LIF calibration." *Plasma Sources Science & Technology* **13**,2: 237-244 DOI: Pii S0963-0252(04)76086-7/10.1088/0963-0252/13/2/007, (2004)

- Dorn, H. P., Neuroth, R. and Hofzumahaus, A.: "Investigation of OH Absorption Cross-Sections of Rotational Transitions in the $\alpha(2)\Sigma^+$, $V'=0$ [$-X(2)\Pi$, $V''=0$] Band under Atmospheric Conditions - Implications for Tropospheric Long-Path Absorption-Measurements." *Journal of Geophysical Research-Atmospheres* **100**,D4: 7397-7409 DOI: 10.1029/94JD03323, (1995)
- Dusanter, S., Vimal, D. and Stevens, P. S.: "Technical note: Measuring tropospheric OH and HO₂ by laser-induced fluorescence at low pressure. A comparison of calibration techniques." *Atmospheric Chemistry and Physics* **8**,2: 321-340 DOI: DOI 10.5194/acp-8-321-2008, (2008)
- Edwards, G. D., Cantrell, C. A., Stephens, S., Hill, B., Goyea, O., Shetter, R. E., Mauldin, R. L., Kosciuch, E., Tanner, D. J. and Eisele, F. L.: "Chemical ionization mass spectrometer instrument for the measurement of tropospheric HO₂ and RO₂." *Analytical Chemistry* **75**,20: 5317-5327 DOI: 10.1021/ac034402b, (2003)
- Ehhalt, D. H.: "Photooxidation of trace gases in the troposphere." *Physical Chemistry Chemical Physics* **1**,24: 5401-5408, (1999)
- Eisele, F. L., Mauldin, R. L., Tanner, D. J., Fox, J. R., Mouch, T. and Scully, T.: "An inlet/sampling duct for airborne OH and sulfuric acid measurements." *Journal of Geophysical Research-Atmospheres* **102**,D23: 27993-28001, (1997)
- Eisele, F. L. and Tanner, D. J.: "Ion-Assisted Tropospheric OH Measurements." *Journal of Geophysical Research-Atmospheres* **96**,D5: 9295-9308, (1991)
- Engel, V., Staemmler, V., Vanderwal, R. L., Crim, F. F., Sension, R. J., Hudson, B., Andresen, P., Hennig, S., Weide, K. and Schinke, R.: "Photodissociation of Water in the 1st Absorption-Band - a Prototype for Dissociation on a Repulsive Potential-Energy Surface." *Journal of Physical Chemistry* **96**,8: 3201-3213 DOI: DOI 10.1021/j100187a007, (1992)
- Faloona, I., Tan, D., Brune, W. H., Jaegle, L., Jacob, D. J., Kondo, Y., Koike, M., Chatfield, R., Poeschel, R., Ferry, G., Sachse, G., Vay, S., Anderson, B., Hannon, J. and Fuelberg, H.: "Observations of HO_x and its relationship with NO_x in the upper troposphere during SONEX." *Journal of Geophysical Research-Atmospheres* **105**,D3: 3771-3783, (2000)
- Faloona, I. C., Tan, D., Leshner, R. L., Hazen, N. L., Frame, C. L., Simpas, J. B., Harder, H., Martinez, M., Di Carlo, P., Ren, X. R. and Brune, W. H.: "A laser-induced fluorescence instrument for detecting tropospheric OH and HO₂: Characteristics and calibration." *Journal of Atmospheric Chemistry* **47**,2: 139-167 DOI: DOI 10.1023/B:JOCH.0000021036.53185.0e, (2004)
- Felton, C. C., Sheppard, J. C. and Campbell, M. J.: "Measurements of the Diurnal OH Cycle by a C-14 Tracer Method." *Nature* **335**,6185: 53-55 DOI: DOI 10.1038/335053a0, (1988)
- Filipiak, M. J., Harwood, R. S., Jiang, J. H., Li, Q. B., Livesey, N. J., Manney, G. L., Read, W. G., Schwartz, M. J., Waters, J. W. and Wu, D. L.: "Carbon monoxide measured by the EOS Microwave Limb Sounder on Aura: First results." *Geophysical Research Letters* **32**,14, DOI: Artn L14825 10.1029/2005gl022765, (2005)
- Fischer, E. V., Jacob, D. J., Yantosca, R. M., Sulprizio, M. P., Millet, D. B., Mao, J., Paulot, F., Singh, H. B., Roiger, A., Ries, L., Talbot, R. W., Dzepina, K. and Deolal, S. P.: "Atmospheric peroxyacetyl nitrate (PAN): a global budget and source attribution." *Atmospheric Chemistry and Physics* **14**,5: 2679-2698 DOI: 10.5194/acp-14-2679-2014, (2014)
- Freeman, A. J.: "Configuration Interaction Study of the Electronic Structure of the OH Radical by the Atomic and Molecular Orbital Methods." *Journal of Chemical Physics* **28**,2: 230-243 DOI: Doi 10.1063/1.1744098, (1958)
- Fu, R., Hu, Y. L., Wright, J. S., Jiang, J. H., Dickinson, R. E., Chen, M. X., Filipiak, M., Read, W. G., Waters, J. W. and Wu, D. L.: "Short circuit of water vapor and polluted air to the global stratosphere by convective transport over the Tibetan Plateau." *Proceedings of the National Academy of Sciences of the United States of America* **103**,15: 5664-5669 DOI: 10.1073/pnas.0601584103, (2006)

- Fuchs, H., Bohn, B., Hofzumahaus, A., Holland, F., Lu, K. D., Nehr, S., Rohrer, F. and Wahner, A.: "Detection of HO₂ by laser-induced fluorescence: calibration and interferences from RO₂ radicals." *Atmospheric Measurement Techniques* **4**,6: 1209-1225 DOI: 10.5194/amt-4-1209-2011, (2011)
- Fuchs, H., Dorn, H. P., Bachner, M., Bohn, B., Brauers, T., Gomm, S., Hofzumahaus, A., Holland, F., Nehr, S., Rohrer, F., Tillmann, R. and Wahner, A.: "Comparison of OH concentration measurements by DOAS and LIF during SAPHIR chamber experiments at high OH reactivity and low NO concentration." *Atmospheric Measurement Techniques* **5**,7: 1611-1626, (2012)
- Garny, H. and Randel, W. J.: "Dynamic variability of the Asian monsoon anticyclone observed in potential vorticity and correlations with tracer distributions." *Journal of Geophysical Research-Atmospheres* **118**,24: 13421-13433 DOI: 10.1002/2013jd020908, (2013)
- Ghude, S. D., Kulkarni, S. H., Jena, C., Pfister, G. G., Beig, G., Fadnavis, S. and van der A, R. J.: "Application of satellite observations for identifying regions of dominant sources of nitrogen oxides over the Indian Subcontinent." *Journal of Geophysical Research-Atmospheres* **118**,2: 1075-1089 DOI: 10.1029/2012jd017811, (2013)
- Hard, T. M., George, L. A. and O'brien, R. J.: "Fage Determination of Tropospheric OH and HO₂." *Journal of the Atmospheric Sciences* **52**,19: 3354-3372 DOI: 10.1175/1520-0469(1995)052<3354:Fdotha>2.0.Co;2, (1995)
- Hard, T. M., George, L. A. and O'Brien, R. J.: "An absolute calibration for gas-phase hydroxyl measurements." *Environmental Science & Technology* **36**,8: 1783-1790 DOI: 10.1021/es015646l, (2002)
- Hard, T. M., O'Brien, R. J., Chan, C. Y. and Mehrabzadeh, A. A.: "Tropospheric free radical determination by FAGE." *Environ. Sci. Technol.; (United States): Medium: X; Size: Pages: 768-777*, (1984)
- Hard, T. M., Obrien, R. J., Cook, T. B. and Tsongas, G. A.: "Interference Suppression in HO Fluorescence Detection." *Applied Optics* **18**,19: 3216-3217 DOI: Doi 10.1364/Ao.18.003216, (1979)
- Heard, D. E. and Pilling, M. J.: "Measurement of OH and HO₂ in the troposphere." *Chemical Reviews* **103**,12: 5163-5198 DOI: 10.1021/cr020522s, (2003)
- Hegglin, M. I., Brunner, D., Peter, T., Hoor, P., Fischer, H., Staehelin, J., Krebsbach, M., Schiller, C., Parchatka, U. and Weers, U.: "Measurements of NO, NO_y, N₂O, and O-3 during SPURT: implications for transport and chemistry in the lowermost stratosphere." *Atmospheric Chemistry and Physics* **6**: 1331-1350, (2006)
- Hens, K.: "OH and HO₂ radical measurements in a boreal forest environment using laser induced fluorescence spectroscopy." *Dissertation*, (2013)
- Hens, K., Novelli, A., Martinez, M., Auld, J., Axinte, R., Bohn, B., Fischer, H., Keronen, P., Kubistin, D., Nolscher, A. C., Oswald, R., Paasonen, P., Petaja, T., Regelin, E., Sander, R., Sinha, V., Sipila, M., Taraborrelli, D., Ernest, C. T., Williams, J., Lelieveld, J. and Harder, H.: "Observation and modelling of HO_x radicals in a boreal forest." *Atmospheric Chemistry and Physics* **14**,16: 8723-8747, (2014)
- Herbin, H., Hurtmans, D., Clarisse, L., Turquety, S., Clerbaux, C., Rinsland, C. P., Boone, C., Bernath, P. F. and Coheur, P. F.: "Distributions and seasonal variations of tropospheric ethene (C₂H₄) from Atmospheric Chemistry Experiment (ACE-FTS) solar occultation spectra." *Geophysical Research Letters* **36**, (2009)
- Hofzumahaus, A., Brauers, T., Aschmutat, U., Brandenburger, U., Dorn, H. P., Hausmann, M., Hessling, M., Holland, F., PlassDulmer, C., Sedlacek, M., Weber, M. and Ehhalt, D. H.: "The measurement of tropospheric OH radicals by laser-induced fluorescence spectroscopy during the POPCORN field campaign and Intercomparison of tropospheric OH radical measurements by multiple folded long-path laser absorption and laser induced

- fluorescence - Reply." *Geophysical Research Letters* **24**,23: 3039-3040 DOI: Doi 10.1029/97gl02947, (1997)
- Holland, F., Hessling, M. and Hofzumahaus, A.: "In-Situ Measurement of Tropospheric OH Radicals by Laser-Induced Fluorescence - a Description of the Kfa Instrument." *Journal of the Atmospheric Sciences* **52**,19: 3393-3401 DOI: 10.1175/1520-0469(1995)052<3393:ismoto>2.0.Co;2, (1995)
- Holland, F., Hofzumahaus, A., Schafer, R., Kraus, A. and Patz, H. W.: "Measurements of OH and HO₂ radical concentrations and photolysis frequencies during BERLIOZ." *Journal of Geophysical Research-Atmospheres* **108**,D4, DOI: Artn 8246/10.1029/2001jd001393, (2003)
- International Energy Agency. (2020, 08/2020). "Energy Consumption." Retrieved 03/2020"available at, <https://www.iea.org/data-and-statistics/?country=WORLD&fuel=Energy%20consumption&indicator=Carbon%20intensity%20of%20industry%20energy%20consumption>", 2020
- Irei, S., Takami, A., Sadanaga, Y., Nozoe, S., Yonemura, S., Bandow, H. and Yokouchi, Y.: "Photochemical age of air pollutants, ozone, and secondary organic aerosol in transboundary air observed on Fukue Island, Nagasaki, Japan." *Atmospheric Chemistry and Physics* **16**,7: 4555-4568, (2016)
- Ivanov, A. V., Trakhtenberg, S., Bertram, A. K., Gershenson, Y. M. and Molina, M. J.: "OH, HO₂, and ozone gaseous diffusion coefficients." *J Phys Chem A* **111**,9: 1632-1637 DOI: 10.1021/jp066558w, (2007)
- Jaegle, L., Jacob, D. J., Brune, W. H. and Wennberg, P. O.: "Chemistry of HO_x radicals in the upper troposphere." *Atmospheric Environment* **35**,3: 469-489 DOI: Doi 10.1016/S1352-2310(00)00376-9, (2001)
- Jenkin, M. E., Young, J. C. and Rickard, A. R.: "The MCM v3.3.1 degradation scheme for isoprene." *Atmospheric Chemistry and Physics* **15**,20: 11433-11459, (2015)
- Khalil, M. A. K.: "Atmospheric methane: an introduction, in: Atmospheric Methane." Springer, Berlin, Heidelberg, Germany: 1-8, (2000)
- Kleffmann, J., Gavriloaiei, T., Hofzumahaus, A., Holland, F., Koppmann, R., Rupp, L., Schlosser, E., Siese, M. and Wahner, A.: "Daytime formation of nitrous acid: A major source of OH radicals in a forest." *Geophysical Research Letters* **32**,5, (2005)
- Kleinman, L. I., Daum, P. H., Lee, Y. N., Nunnermacker, L. J., Springston, S. R., Weinstein-Lloyd, J., Hyde, P., Doskey, P., Rudolph, J., Fast, J. and Berkowitz, C.: "Photochemical age determinations in the Phoenix metropolitan area." *Journal of Geophysical Research-Atmospheres* **108**,D3, (2003)
- Krotkov, N. A., McLinden, C. A., Li, C., Lamsal, L. N., Celarier, E. A., Marchenko, S. V., Swartz, W. H., Bucsele, E. J., Joiner, J., Duncan, B. N., Boersma, K. F., Veefkind, J. P., Levelt, P. F., Fioletov, V. E., Dickerson, R. R., He, H., Lu, Z. F. and Streets, D. G.: "Aura OMI observations of regional SO₂ and NO₂ pollution changes from 2005 to 2015." *Atmospheric Chemistry and Physics* **16**,7: 4605-4629 DOI: 10.5194/acp-16-4605-2016, (2016)
- Kubistin, D. OH- und HO₂ radikale über dem tropischen Regenwald. Ph.D. thesis, Johannes Gutenberg-Universität Mainz, 2009
- Kubistin, D., Harder, H., Martinez, M., Rudolf, M., Sander, R., Bozem, H., Eerdeken, G., Fischer, H., Gurk, C., Klupfel, T., Königstedt, R., Parchatka, U., Schiller, C. L., Stickler, A., Taraborrelli, D., Williams, J. and Lelieveld, J.: "Hydroxyl radicals in the tropical troposphere over the Suriname rainforest: comparison of measurements with the box model MECCA." *Atmospheric Chemistry and Physics* **10**,19: 9705-9728 DOI: 10.5194/acp-10-9705-2010, (2010)
- Kukui, A., Ancellet, G. and Le Bras, G.: "Chemical ionisation mass spectrometer for measurements of OH and Peroxy radical concentrations in moderately polluted atmospheres." *Journal of Atmospheric Chemistry* **61**,2: 133-154 DOI: 10.1007/s10874-009-9130-9, (2008)

- Langhoff, S. R., Sink, M. L., Pritchard, R. H. and Kern, C. W.: "Theoretical-Study of the Spin-Orbit-Coupling in the X2-Pi State of OH." *Journal of Molecular Spectroscopy* **96**,1: 200-218, (1982)
- Lanz, V. A., Henne, S., Staehelin, J., Hueglin, C., Vollmer, M. K., Steinbacher, M., Buchmann, B. and Reimann, S.: "Statistical analysis of anthropogenic non-methane VOC variability at a European background location (Jungfrauoch, Switzerland)." *Atmospheric Chemistry and Physics* **9**,10: 3445-3459, (2009)
- Lawrence, M. G. and Lelieveld, J.: "Atmospheric pollutant outflow from southern Asia: a review." *Atmospheric Chemistry and Physics* **10**,22: 11017-11096 DOI: 10.5194/acp-10-11017-2010, (2010)
- Lelieveld, J., Bourtsoukidis, E., Bruhl, C., Fischer, H., Fuchs, H., Harder, H., Hofzumahaus, A., Holland, F., Marno, D., Neumaier, M., Pozzer, A., Schlager, H., Williams, J., Zahn, A. and Ziereis, H.: "The South Asian monsoon-pollution pump and purifier." *Science* **361**,6399: 270-+ DOI: 10.1126/science.aar2501, (2018)
- Lelieveld, J., Dentener, F. J., Peters, W. and Krol, M. C.: "On the role of hydroxyl radicals in the self-cleansing capacity of the troposphere." *Atmospheric Chemistry and Physics* **4**: 2337-2344, (2004)
- Lelieveld, J., Gromov, S., Pozzer, A. and Taraborrelli, D.: "Global tropospheric hydroxyl distribution, budget and reactivity." *Atmospheric Chemistry and Physics* **16**,19: 12477-12493 DOI: 10.5194/acp-16-12477-2016, (2016)
- Lelieveld, J., Peters, W., Dentener, F. J. and Krol, M. C.: "Stability of tropospheric hydroxyl chemistry." *Journal of Geophysical Research-Atmospheres* **107**,D23, DOI: Artn 4715/10.1029/2002jd002272, (2002)
- Lelieveld, J., Pozzer, A., Poschl, U., Fnais, M., Haines, A. and Munzel, T.: "Loss of life expectancy from air pollution compared to other risk factors: a worldwide perspective (vol 116, pg 1334, 2020)." *Cardiovascular Research* **116**,7: 1334-1334, (2020)
- Levy, H.: "Normal Atmosphere - Large Radical and Formaldehyde Concentrations Predicted." *Science* **173**,3992: 141-& DOI: DOI 10.1126/science.173.3992.141, (1971)
- Logan, J. A., Prather, M. J., Wofsy, S. C. and McElroy, M. B.: "Tropospheric chemistry: A global perspective." *Journal of Geophysical Research: Oceans* **86**,C8: 7210-7254 DOI: 10.1029/JC086iC08p07210, (1981)
- Mallik, C., Tomsche, L., Bourtsoukidis, E., Crowley, J. N., Derstroff, B., Fischer, H., Hafermann, S., Huser, I., Javed, U., Kessel, S., Lelieveld, J., Martinez, M., Meusel, H., Novelli, A., Phillips, G. J., Pozzer, A., Reiffs, A., Sander, R., Taraborrelli, D., Sauvage, C., Schuladen, J., Su, H., Williams, J. and Harder, H.: "Oxidation processes in the eastern Mediterranean atmosphere: evidence from the modelling of HOx measurements over Cyprus." *Atmospheric Chemistry and Physics* **18**,14: 10825-10847 DOI: 10.5194/acp-18-10825-2018, (2018)
- Mao, J., Ren, X., Zhang, L., Van Duin, D. M., Cohen, R. C., Park, J. H., Goldstein, A. H., Paulot, F., Beaver, M. R., Crounse, J. D., Wennberg, P. O., DiGangi, J. P., Henry, S. B., Keutsch, F. N., Park, C., Schade, G. W., Wolfe, G. M., Thornton, J. A. and Brune, W. H.: "Insights into hydroxyl measurements and atmospheric oxidation in a California forest." *Atmospheric Chemistry and Physics* **12**,17: 8009-8020 DOI: 10.5194/acp-12-8009-2012, (2012)
- Marno, D., Ernest, C., Hens, K., Javed, U., Klimach, T., Martinez, M., Rudolf, M., Lelieveld, J. and Harder, H.: "Calibration of an airborne HOx instrument using the All Pressure Altitude-based Calibrator for HOx Experimentation (APACHE)." *Atmos. Meas. Tech.* **13**,5: 2711-2731 DOI: 10.5194/amt-13-2711-2020, (2020)
- Martinez, M., Harder, H., Kovacs, T. A., Simpas, J. B., Bassis, J., Leshner, R., Brune, W. H., Frost, G. J., Williams, E. J., Stroud, C. A., Jobson, B. T., Roberts, J. M., Hall, S. R., Shetter, R. E., Wert, B., Fried, A., Alicke, B., Stutz, J., Young, V. L., White, A. B. and Zamora, R. J.: "OH and HO₂ concentrations, sources, and loss rates during the Southern Oxidants Study in Nashville,

- Tennessee, summer 1999." *Journal of Geophysical Research-Atmospheres* **108**,D19, DOI: 10.1029/2003jd003551, (2003)
- Martinez, M., Harder, H., Kubistin, D., Rudolf, M., Bozem, H., Eerdeken, G., Fischer, H., Klupfel, T., Gurk, C., Konigstedt, R., Parchatka, U., Schiller, C. L., Stickler, A., Williams, J. and Lelieveld, J.: "Hydroxyl radicals in the tropical troposphere over the Suriname rainforest: airborne measurements." *Atmospheric Chemistry and Physics* **10**,8: 3759-3773, (2010)
- Mather, J. H., Stevens, P. S. and Brune, W. H.: "OH and HO₂ measurements using laser-induced fluorescence." *Journal of Geophysical Research-Atmospheres* **102**,D5: 6427-6436 DOI: Doi 10.1029/96jd01702, (1997)
- Mihelcic, D., Ehhalt, D. H., Kulassa, G. F., Klomfass, J., Trainer, M., Schmidt, U. and Rohrs, H.: "Measurements of Free-Radicals in Atmosphere by Matrix-Isolation and Electron-Paramagnetic Resonance." *Pure and Applied Geophysics* **116**,2-3: 530-536 DOI: Doi 10.1007/Bf01636905, (1978)
- Miller, J. B., Lehman, S. J., Montzka, S. A., Sweeney, C., Miller, B. R., Karion, A., Wolak, C., Dlugokencky, E. J., Southon, J., Turnbull, J. C. and Tans, P. P.: "Linking emissions of fossil fuel CO₂ and other anthropogenic trace gases using atmospheric (CO₂)-C-14." *Journal of Geophysical Research-Atmospheres* **117**, DOI: Artn D08302 10.1029/2011jd017048, (2012)
- Motley, H. L., Smart, R. H. and Leftwich, C. I.: "Effect of Polluted Los Angeles Air (Smog) on Lung Volume Measurements." *Jama-Journal of the American Medical Association* **171**,11: 1469-1477, (1959)
- Muller, J. B. A., Elste, T., Plass-Dulmer, C., Stange, G., Holla, R., Claude, A., Englert, J., Gilge, S. and Kubistin, D.: "A novel semi-direct method to measure OH reactivity by chemical ionization mass spectrometry (CIMS)." *Atmospheric Measurement Techniques* **11**,7: 4413-4433, (2018)
- Novelli, A., Hens, K., Ernest, C. T., Kubistin, D., Regelin, E., Elste, T., Plass-Dulmer, C., Martinez, M., Lelieveld, J. and Harder, H.: "Characterisation of an inlet pre-injector laser-induced fluorescence instrument for the measurement of atmospheric hydroxyl radicals." *Atmospheric Measurement Techniques* **7**,10: 3413-3430 DOI: 10.5194/amt-7-3413-2014, (2014)
- Oppenheimer, C., Tsanev, V. I., Braban, C. F., Cox, R. A., Adams, J. W., Aiuppa, A., Bobrowski, N., Delmelle, P., Barclay, J. and McGonigle, A. J. S.: "BrO formation in volcanic plumes." *Geochimica Et Cosmochimica Acta* **70**,12: 2935-2941, (2006)
- Ortgies, G., Gericke, K. H. and Comes, F. J.: "Is UV Laser-Induced Fluorescence a Method to Monitor Tropospheric OH." *Geophysical Research Letters* **7**,11: 905-908 DOI: DOI 10.1029/GL007i011p00905, (1980)
- Pandis, S. N. and Seinfeld, J. H.: "Atmospheric chemistry and physics: From air pollution to climate change." Wiley, Hoboken, New Jersey, USA,,: 41-42, (2006)
- Park, M., Randel, W. J., Emmons, L. K., Bernath, P. F., Walker, K. A. and Boone, C. D.: "Chemical isolation in the Asian monsoon anticyclone observed in Atmospheric Chemistry Experiment (ACE-FTS) data." *Atmospheric Chemistry and Physics* **8**,3: 757-764 DOI: DOI 10.5194/acp-8-757-2008, (2008)
- Park, M., Randel, W. J., Kinnison, D. E., Garcia, R. R. and Choi, W.: "Seasonal variation of methane, water vapor, and nitrogen oxides near the tropopause: Satellite observations and model simulations." *Journal of Geophysical Research-Atmospheres* **109**,D3, DOI: Artn D03302 10.1029/2003jd003706, (2004)
- Paulson, S. E., Gallimore, P. J., Kuang, X. B. M., Chen, J. R., Kalberer, M. and Gonzalez, D. H.: "A light-driven burst of hydroxyl radicals dominates oxidation chemistry in newly activated cloud droplets." *Science Advances* **5**,5, DOI: ARTN eaav7689 10.1126/sciadv.aav7689, (2019)

- Petaja, T., Mauldin, R. L., Kosciuch, E., McGrath, J., Nieminen, T., Paasonen, P., Boy, M., Adamov, A., Kotiaho, T. and Kulmala, M.: "Sulfuric acid and OH concentrations in a boreal forest site." *Atmospheric Chemistry and Physics* **9**,19: 7435-7448, (2009)
- Ploeger, F., Gottschling, C., Griessbach, S., Grooss, J. U., Guenther, G., Konopka, P., Muller, R., Riese, M., Strohm, F., Tao, M., Ungermann, J., Vogel, B. and von Hobe, M.: "A potential vorticity-based determination of the transport barrier in the Asian summer monsoon anticyclone." *Atmospheric Chemistry and Physics* **15**,22: 13145-13159 DOI: 10.5194/acp-15-13145-2015, (2015)
- Ploeger, F., Konopka, P., Walker, K. and Riese, M.: "Quantifying pollution transport from the Asian monsoon anticyclone into the lower stratosphere." *Atmospheric Chemistry and Physics* **17**,11: 7055-7066 DOI: 10.5194/acp-17-7055-2017, (2017)
- Prinn, R.: "Is the cleansing capability of the atmosphere (OH concentration) changing?" *Abstracts of Papers of the American Chemical Society* **226**: U24-U24, (2003)
- Randel, W. J., Park, M., Emmons, L., Kinnison, D., Bernath, P., Walker, K. A., Boone, C. and Pumphrey, H.: "Asian Monsoon Transport of Pollution to the Stratosphere." *Science* **328**,5978: 611-613, (2010)
- Regelin, E., Harder, H., Martinez, M., Kubistin, D., Ernest, C. T., Bozem, H., Klippel, T., Hosaynali-Beygi, Z., Fischer, H., Sander, R., Jockel, P., Konigstedt, R. and Lelieveld, J.: "HOx measurements in the summertime upper troposphere over Europe: a comparison of observations to a box model and a 3-D model." *Atmospheric Chemistry and Physics* **13**,21: 10703-10720 DOI: 10.5194/acp-13-10703-2013, (2013)
- Reiner, T., Hanke, M. and Arnold, F.: "Atmospheric peroxy radical measurements by ion molecule reaction mass spectrometry: A novel analytical method using amplifying chemical conversion to sulfuric acid." *Journal of Geophysical Research-Atmospheres* **102**,D1: 1311-1326 DOI: Doi 10.1029/96jd02963, (1997)
- Ren, X. R., Harder, H., Martinez, M., Leshner, R. L., Olliger, A., Simpas, J. B., Brune, W. H., Schwab, J. J., Demerjian, K. L., He, Y., Zhou, X. L. and Gao, H. G.: "OH and HO₂ chemistry in the urban atmosphere of New York City." *Atmospheric Environment* **37**,26: 3639-3651 DOI: 10.1016/S1352-2310(03)00459-X, (2003)
- Ren, X. R., Olson, J. R., Crawford, J. H., Brune, W. H., Mao, J. Q., Long, R. B., Chen, Z., Chen, G., Avery, M. A., Sachse, G. W., Barrick, J. D., Diskin, G. S., Huey, L. G., Fried, A., Cohen, R. C., Heikes, B., Wennberg, P. O., Singh, H. B., Blake, D. R. and Shetter, R. E.: "HOx chemistry during INTEX-A 2004: Observation, model calculation, and comparison with previous studies." *Journal of Geophysical Research-Atmospheres* **113**,D5, DOI: Artn D05310 10.1029/2007jd009166, (2008)
- Roach, P. E.: "The Generation of Nearly Isotropic Turbulence by Means of Grids." *International Journal of Heat and Fluid Flow* **8**,2: 82-92 DOI: Doi 10.1016/0142-727x(87)90001-4, (1987)
- Rohrer, F., Lu, K. D., Hofzumahaus, A., Bohn, B., Brauers, T., Chang, C. C., Fuchs, H., Haseler, R., Holland, F., Hu, M., Kita, K., Kondo, Y., Li, X., Lou, S. R., Oebel, A., Shao, M., Zeng, L. M., Zhu, T., Zhang, Y. H. and Wahner, A.: "Maximum efficiency in the hydroxyl-radical-based self-cleansing of the troposphere." *Nature Geoscience* **7**,8: 559-563, (2014)
- Rudolph, J. and Johnen, F. J.: "Measurements of Light Atmospheric Hydrocarbons over the Atlantic in Regions of Low Biological-Activity." *Journal of Geophysical Research-Atmospheres* **95**,D12: 20583-20591, (1990)
- Saito, T., Kawamura, K., Tsunogai, U., Chen, T. Y., Matsueda, H., Nakatsuka, T., Gamo, T., Uematsu, M. and Huebert, B. J.: "Photochemical histories of nonmethane hydrocarbons inferred from their stable carbon isotope ratio measurements over east Asia." *Journal of Geophysical Research-Atmospheres* **114**, (2009)
- Sander, R., Baumgaertner, A., Cabrera-Perez, D., Frank, F., Gromov, S., Grooss, J. U., Harder, H., Huijnen, V., Jockel, P., Karydis, V. A., Niemeyer, K. E., Pozzer, A., Hella, R. B., Schultz, M.

- G., Taraborrelli, D. and Tauer, S.: "The community atmospheric chemistry box model CAABA/MECCA-4.0." *Geoscientific Model Development* **12**,4: 1365-1385, (2019)
- Sander, S. P., Finlayson-Pitts, B. J., Friedl, R. R., Golden, D. M., Huie, R. E., Kolb, C. E., Kurylo, M. J., Molina, M. J., Moortgat, G. K., Orkin, V. L. and Ravishankara, A. R.: "Chemical Kinetics and Photochemical Data for Use in Atmospheric Studies." JPL Publication 02-25, (2003)
- Sander, S. P., Friedl, R. R., Golden, D. M., Kurylo, M. J., Moortgat, G. K., Wine, P. H., Ravishankara, A. R., Kolb, C. E., Molina, M. J. and Finlayson-Pitts, B. J.: "Chemical kinetics and photochemical data for use in atmospheric studies, Evaluation Number 15." JPL Publication **06-2**, (2006)
- Santee, M. L., Manney, G. L., Livesey, N. J., Schwartz, M. J., Neu, J. L. and Read, W. G.: "A comprehensive overview of the climatological composition of the Asian summermonsoon anticyclone based on 10 years of Aura Microwave Limb Sounder measurements." *Journal of Geophysical Research-Atmospheres* **122**,10: 5491-5514 DOI: 10.1002/2016jd026408, (2017)
- Scheeren, H. A., Lelieveld, J., Roelofs, G. J., Williams, J., Fischer, H., de Reus, M., de Gouw, J. A., Warneke, C., Holzinger, R., Schlager, H., Klupfel, T., Bolder, M., van der Veen, C. and Lawrence, M.: "The impact of monsoon outflow from India and Southeast Asia in the upper troposphere over the eastern Mediterranean." *Atmospheric Chemistry and Physics* **3**: 1589-1608 DOI: DOI 10.5194/acp-3-1589-2003, (2003)
- Schlosser, E., Brauers, T., Dorn, H. P., Fuchs, H., Haseler, R., Hofzumahaus, A., Holland, F., Wahner, A., Kanaya, Y., Kajii, Y., Miyamoto, K., Nishida, S., Watanabe, K., Yoshino, A., Kubistin, D., Martinez, M., Rudolf, M., Harder, H., Berresheim, H., Elste, T., Plass-Dulmer, C., Stange, G. and Schurath, U.: "Technical Note: Formal blind intercomparison of OH measurements: results from the international campaign HOxComp." *Atmospheric Chemistry and Physics* **9**,20: 7923-7948 DOI: DOI 10.5194/acp-9-7923-2009, (2009)
- Schumann, U. and Huntrieser, H.: "The global lightning-induced nitrogen oxides source." *Atmospheric Chemistry and Physics* **7**,14: 3823-3907 DOI: DOI 10.5194/acp-7-3823-2007, (2007)
- Seinfeld, J. H. and Pandis, S. N.: "Atmospheric Chemistry and Physics, From Air Pollution to Climate Change." New York. John Wiley and Sons, Incorporated, (1998)
- Selvam, B. P., Lapierre, J. F., Guillemette, F., Voigt, C., Lamprecht, R. E., Biasi, C., Christensen, T. R., Martikainen, P. J. and Berggren, M.: "Degradation potentials of dissolved organic carbon (DOC) from thawed permafrost peat." *Scientific Reports* **7**, DOI: ARTN 45811 10.1038/srep45811, (2017)
- Sherwood, S. C. and Dessler, A. E.: "A model for transport across the tropical tropopause." *Journal of the Atmospheric Sciences* **58**,7: 765-779 DOI: Doi 10.1175/1520-0469(2001)058<0765:Amftat>2.0.Co;2, (2001)
- Skerlak, B., Sprenger, M. and Wernli, H.: "A global climatology of stratosphere-troposphere exchange using the ERA-Interim data set from 1979 to 2011." *Atmospheric Chemistry and Physics* **14**,2: 913-937 DOI: 10.5194/acp-14-913-2014, (2014)
- Smith, S. C., Lee, J. D., Bloss, W. J., Johnson, G. P., Ingham, T. and Heard, D. E.: "Concentrations of OH and HO₂ radicals during NAMBLEX: measurements and steady state analysis." *Atmospheric Chemistry and Physics* **6**: 1435-1453 DOI: DOI 10.5194/acp-6-1435-2006, (2006)
- Stevens, P. S., Mather, J. H. and Brune, W. H.: "Measurement of Tropospheric Oh and Ho₂ by Laser-Induced Fluorescence at Low-Pressure." *Journal of Geophysical Research-Atmospheres* **99**,D2: 3543-3557 DOI: 10.1029/93jd03342, (1994)
- Stockwell, W. R., Kirchner, F., Kuhn, M. and Seefeld, S.: "A new mechanism for regional atmospheric chemistry modeling." *Journal of Geophysical Research-Atmospheres* **102**,D22: 25847-25879, (1997)

- Streets, D. G., Yarber, K. F., Woo, J. H. and Carmichael, G. R.: "Biomass burning in Asia: Annual and seasonal estimates and atmospheric emissions." *Global Biogeochemical Cycles* **17**,4, DOI: Artn 1099 10.1029/2003gb002040, (2003)
- Tadic, I., Parchatka, U., Konigstedt, R. and Fischer, H.: "In-flight stability of quantum cascade laser-based infrared absorption spectroscopy measurements of atmospheric carbon monoxide." *Applied Physics B-Lasers and Optics* **123**,5, DOI: ARTN 146 10.1007/s00340-017-6721-z, (2017)
- Tan, D., Faloon, I., Simpas, J. B., Brune, W., Olson, J., Crawford, J., Avery, M., Sachse, G., Vay, S., Sandholm, S., Guan, H. W., Vaughn, T., Mastromarino, J., Heikes, B., Snow, J., Podolske, J. and Singh, H.: "OH and HO₂ in the tropical Pacific: Results from PEM-Tropics B." *Journal of Geophysical Research-Atmospheres* **106**,D23: 32667-32681 DOI: 10.1029/2001jd900002, (2001)
- Tang, M. J., Cox, R. A. and Kalberer, M.: "Compilation and evaluation of gas phase diffusion coefficients of reactive trace gases in the atmosphere: volume 1. Inorganic compounds." *Atmospheric Chemistry and Physics* **14**,17: 9233-9247 DOI: 10.5194/acp-14-9233-2014, (2014)
- Tanner, D. J. and Eisele, F. L.: "Present OH Measurement Limits and Associated Uncertainties." *Journal of Geophysical Research-Atmospheres* **100**,D2: 2883-2892 DOI: 10.1029/94jd02609, (1995)
- Taraborrelli, D., Lawrence, M. G., Butler, T. M., Sander, R. and Lelieveld, J.: "Mainz Isoprene Mechanism 2 (MIM2): an isoprene oxidation mechanism for regional and global atmospheric modelling." *Atmospheric Chemistry and Physics* **9**,8: 2751-2777, (2009)
- Taraborrelli, D., Lawrence, M. G., Crowley, J. N., Dillon, T. J., Gromov, S., Gross, C. B. M., Vereecken, L. and Lelieveld, J.: "Hydroxyl radical buffered by isoprene oxidation over tropical forests." *Nature Geoscience* **5**,3: 190-193, (2012)
- Tomsche, L., Pozzer, A., Ojha, N., Parchatka, U., Lelieveld, J. and Fischer, H.: "Upper tropospheric CH₄ and CO affected by the South Asian summer monsoon during the Oxidation Mechanism Observations mission." *Atmospheric Chemistry and Physics* **19**,3: 1915-1939, (2019)
- Umezawa, T., Matsueda, H., Sawa, Y., Niwa, Y., Machida, T. and Zhou, L. X.: "Seasonal evaluation of tropospheric CO₂ over the Asia-Pacific region observed by the CONTRAIL commercial airliner measurements." *Atmospheric Chemistry and Physics* **18**,20: 14851-14866 DOI: 10.5194/acp-18-14851-2018, (2018)
- van Aardenne, J. A., Dentener, F. J., Olivier, J. G. J., Goldewijk, C. G. M. K. and Lelieveld, J.: "A 1 degrees x 1 degrees resolution data set of historical anthropogenic trace gas emissions for the period 1890-1990." *Global Biogeochemical Cycles* **15**,4: 909-928 DOI: Doi 10.1029/2000gb001265, (2001)
- Verreycken, T. and Bruggeman, P. J.: "OH density measurements in nanosecond pulsed discharges in atmospheric pressure N₂-H₂O mixtures." *Plasma Sources Science & Technology* **23**,1, DOI: Artn 015009/10.1088/0963-0252/23/1/015009, (2014)
- Voigt, C., Marushchak, M. E., Lamprecht, R. E., Jackowicz-Korczynski, M., Lindgren, A., Mastepanov, M., Granlund, L., Christensen, T. R., Tahvanainen, T., Martikainen, P. J. and Biasi, C.: "Increased nitrous oxide emissions from Arctic peatlands after permafrost thaw." *Proceedings of the National Academy of Sciences of the United States of America* **114**,24: 6238-6243 DOI: 10.1073/pnas.1702902114, (2017)
- Volz-Thomas, A., Geiss, H., Hofzumahaus, A. and Becker, K. H.: "Introduction to special section: Photochemistry experiment in BERLIOZ." *Journal of Geophysical Research-Atmospheres* **108**,D4, (2003)
- Vranckx, S., Peeters, J. and Carl, S. A.: "Absolute rate constant and O((3)P) yield for the O((1)D)+N((2)O) reaction in the temperature range 227K to 719K." *Atmospheric Chemistry and Physics* **8**,20: 6261-6272 DOI: DOI 10.5194/acp-8-6261-2008, (2008)

- Wang, C. C. and Davis, L. I.: "Measurement of Hydroxyl Concentrations in Air Using a Tunable UV Laser-Beam." *Physical Review Letters* **32,7**: 349-352 DOI: DOI 10.1103/PhysRevLett.32.349, (1974)
- Watanabe, T., Yoshida, M., Fujiwara, S., Abe, K., Onoe, A., Hirota, M. and Igarashi, S.: "Spin Trapping of Hydroxyl Radical in the Troposphere for Determination by Electron-Spin Resonance and Gas-Chromatography Mass-Spectrometry." *Analytical Chemistry* **54,14**: 2470-2474 DOI: 10.1021/ac00251a015, (1982)
- Wennberg, P. O., Cohen, R. C., Hazen, N. L., Lapson, L. B., Allen, N. T., Hanisco, T. F., Oliver, J. F., Lanham, N. W., Demusz, J. N. and Anderson, J. G.: "Aircraft-Borne, Laser-Induced Fluorescence Instrument for the in-Situ Detection of Hydroxyl and Hydroperoxyl Radicals." *Review of Scientific Instruments* **65,6**: 1858-1876 DOI: Doi 10.1063/1.1144835, (1994)
- White, J. U.: "Long optical paths of large aperture." *Journal of the Optical Society of America* **32,5**: 285-288 DOI: Doi 10.1364/Josa.32.000285, (1942)
- Winiberg, F. A. F., Smith, S. C., Bejan, I., Brumby, C. A., Ingham, T., Malkin, T. L., Orr, S. C., Heard, D. E. and Seakins, P. W.: "Pressure-dependent calibration of the OH and HO₂ channels of a FAGE HO_x instrument using the Highly Instrumented Reactor for Atmospheric Chemistry (HIRAC)." *Atmospheric Measurement Techniques* **8,2**: 523-540 DOI: 10.5194/amt-8-523-2015, (2015)
- Zhang, D. H., Collins, M. A. and Lee, S. Y.: "First-principles theory for the H+H₂O, D₂O reactions." *Science* **290,5493**: 961-963 DOI: DOI 10.1126/science.290.5493.961, (2000)

Danksagung

When attempting or completing a PhD, I believe that the biggest lessons learned, beyond those of academic or technical in nature, are those of oneself. Throughout the PhD emotional roller coaster of stress, setbacks, eureka moments, and progression, you learn a lot about your capacity to temper expectation, utilize frustration, and gain strength from elation in order to reach your personal goals and achieve your version of success.

I give my deepest gratitude to my friends, family, and particularly my wife who have always believed in me and never subsided in their love and support.

Curriculum Vitae

Name Daniel Richard Marno

Education

Since May 2015 PhD student at the Max-Planck Institute for Chemistry in the Air chemistry department, in cooperation with Johannes Gutenberg-University, Mainz, Germany. Thesis Topic: "The Oxidation Capacity of the Summertime Asian Monsoon Anticyclone - Airborne measurements of OH and HO₂ radicals in the Upper Troposphere using Laser Induced Fluorescence Spectroscopy"

Sep. 2013 to Sep. 2014 MRes – Masters (by research) in Environmental Science at Lancaster University, Lancaster, UK. Thesis Topic: "Seasonal Changes in Troposphere Ozone from the Pre-industrial to the end of the 21st century from the Atmospheric Chemistry and Climate Model Intercomparison Project (ACCMIP)".

Oct. 2010 – Jun. 2013 BSc of Natural Sciences at Lancaster University, Lancaster, UK

Sep. 2008 – Jul. 2010 A-levels in Biology, Chemistry, Physics, and Geography

Field Campaigns

Aug – Sep 2018 Chemistry of the Atmosphere – *Field Experiment in Africa (CAFE-Africa 2018)*

Sep – Nov 2015 Amazonian Tall Tower Observatory (ATTO-2015)

Jul – Sept 2015 Oxidation Mechanism Observations (OMO-Asia 2015)

Publications

Hottmann, B., Hafermann, S., Tomsche, L., **Marno, D.**, Martinez, M., Harder, H., Pozzer, A., Neumaier, M., Zahn, A., Bohn, B., Ziereis, H., Lelieveld, J. and Fischer, H.: "Impact of the South Asian monsoon outflow on atmospheric hydroperoxides in the upper troposphere." *Atmos. Chem. Phys. Discuss.* 2020: 1-31 DOI: 10.5194/acp-2020-93, (2020)

Lelieveld, J., Bourtsoukidis, E., Bruhl, C., Fischer, H., Fuchs, H., Harder, H., Hofzumahaus, A., Holland, F., **Marno, D.**, Neumaier, M., Pozzer, A., Schlager, H., Williams, J., Zahn, A. and Ziereis, H.: "The South Asian monsoon-pollution pump and purifier." *Science* 361,6399: 270-+ DOI: 10.1126/science.aar2501, (2018)

Marno, D., Ernest, C., Hens, K., Javed, U., Klimach, T., Martinez, M., Rudolf, M., Lelieveld, J. and Harder, H.: "Calibration of an airborne HO_x instrument using the All Pressure Altitude-based Calibrator for HO_x Experimentation (APACHE)." *Atmos. Meas. Tech.* 13,5: 2711-2731 DOI: 10.5194/amt-13-2711-2020, (2020)

1st Author Conference Contributions

Marno, D., Künstler, C., Hens, K., Ernest, C., Martinez, M., Fuchs H., Bourtsoukidis, E., Williams, J., Holland, F., Hofzumahaus, A., Tomsche, L., Hottmann, B., Fischer, H., Bohn, B., Lelieveld, J., Harder, H.: “OH and HO₂ concentration observations in the upper troposphere inside and outside of Asian monsoon influenced air”, Poster at IGAC, 4.086, (2018).

Marno, D., Künstler, C., Hens, K., Ernest, C., Broch, S., Fuchs, H., Martinez, M., Bourtsoukidis, E., Williams, J., Holland, F., Hofzumahaus, A., Tomsche, L., Fischer, H., Klausner, T., Schlager, H., Eirenschmalz, L., Stratmann, G., Stock, P., Ziereis, H., Roiger, A., Bohn, B., Zahn, A., Wahner, A., Lelieveld, J., Harder, H.: “Observed OH and HO₂ concentrations in the upper troposphere inside and outside of Asian monsoon influenced air”, Talk at AGU Fall Meeting, A41I-02, (2016)